ALUNITE AND HIGH SULFIDATION GOLD–SILVER–COPPER MINERALIZATION IN THE EL INDIO–PASCUA BELT, CHILE–ARGENTINA

by

CARI L. DEYELL

B.Sc.H., Queen's University, 1995

A thesis submitted in partial fulfillment of the
requirements for the degree of

DOCTOR OF PHILOSOPHY

in

The Faculty of Graduate Studies

(Department of Earth and Ocean Sciences)

We accept this thesis as conforming to the required standard

THE UNIVERSITY OF BRITISH COLUMBIA

December, 2001

In presenting this thesis in partial fulfilment of the requirements for an advanced degree at the University of British Columbia, I agree that the Library shall make it freely available for reference and study. I further agree that permission for extensive copying of this thesis for scholarly purposes may be granted by the head of my department or by his or her representatives. It is understood that copying or publication of this thesis for financial gain shall not be allowed without my written permission.

Department of Earth + Ocean Sciences

The University of British Columbia
Vancouver, Canada

Date Dec. 17/01

DE-6 (2/88)

ABSTRACT

High sulfidation precious-metal deposits, one of the principal styles of epithermal mineralization, are characterized by minerals diagnostic of a high sulfidation state (pyrite, enargite) and acidic hydrothermal conditions, particularly alunite ($KAl_3(SO_4)_2(OH)_6$) and alunite-group minerals. One of the world's foremost high sulfidation districts, the El Indio-Pascua Belt, straddles the Chile-Argentina border in the Cordillera Principal of the Andes. The region contains the world-class El Indio mine, the extensive Pascua-Lama and Veladero exploration projects, and several smaller prospects and mineralized alteration zones. This belt has been the subject of numerous studies at both a regional- and deposit-scale, and provides an excellent site to constrain genetic and exploration models for high sulfidation deposits.

The genesis and timing of high sulfidation deposits in the El Indio-Pascua Belt has been constrained by detailed field studies, supplemented by geochemical, stable isotopic, and ^{40}Ar-^{39}Ar analyses of alunite, a critical mineral throughout the paragenesis of most systems in this region. Widespread barren, pre-mineral alteration containing abundant alunite may have provided permeability controls and metals for subsequent mineralization. Economic mineralization in the district formed between *ca.* 6 to 9.5 Ma, and is associated commonly with syn-mineral alunite. This alunite has textural, chemical and isotopic characteristics consistent with a magmatic-hydrothermal origin and requires the presence of relatively oxidizing, acidic, and sulfur-rich mineralizing fluids. Data suggest that these fluids were derived from the condensation of a magmatic vapor plume, further supported by the presence of syn-ore magmatic steam alunite at the Tambo deposit. This conclusion is consistent with emerging evidence from other systems indicating the importance of vapor transport for metals in high sulfidation systems.

Alteration and mineralization in the El Indio-Pascua Belt were dominated by magmatic fluids, even in the near-surface environment. The negligible contribution of meteoric fluids is attributed to prolonged magmatic activity, an arid climate, and depressed water tables resulting from tectonic uplift and repeated incision. These features provide new constraints for the genetic model for high sulfidation deposits, although the specific setting of the El Indio-Pascua Belt may have provided a unique combination of processes explaining the formation and preservation of these prolific mineralizing systems.

TABLE OF CONTENTS

LIST OF TABLES

LIST OF FIGURES

ACKNOWLEDGEMENTS

I came to U.B.C. nearly six years ago with the intention of doing a M.Sc. in acid rock drainage, and somehow got diverted into this economic geology project along the way. This was largely the fault of John Thompson, and I found myself working on a small high sulfidation property in north-central B.C. within a few months of my arrival in Vancouver. After a year or so, the option arose to expand the project into a Ph.D. thesis. At that time, all I knew was that it would involve travelling to South America, which seemed like a pretty good deal. I diligently signed up for an introductory Spanish course, but quickly discovered upon my arrival in La Serena that my abilities to count to 10 just weren't going to help that much. Chileans are generally incomprehensible, even to fellow Latinos, and I was thoroughly confused. My plans to study the supergene remobilization of precious-metals were erased within hours of my arrival in Chile, after my first meeting with Dave Heberlein. Luckily Alan Clark, one of my previous professors from Queen's University, was present at the time, and all of a sudden I found myself about to embark on a comprehensive study of 'alunita' in the El Indio-Pascua Belt. Needless to say, my first field season was considerably overwhelming. I eventually managed to pick up enough spanish to figure out at what time the miners would be blasting in the pit I was working in that day - although I didn't always get that one quite right. Obviously I survived (minus one truck), and immediately signed myself up for another season.

After all this time, there are so many people that I would like to thank for their contributions to this thesis. First and foremost, I would like to thank the Thompson family for putting up with me for all these years. I am indebted to John for the scientific support and constant reminders to not panic at every turn. I am sure Teck will be glad to have his full attention once again. Just one more to go, John! I am also sure that Anne will be very glad to see an end to my impositions on countless evenings and weekends. I thank her for her enthusiasm for the research topic. Her knowledge of the subject, including field and PIMA expertise, was invaluable.

I also wish to thank Lee Groat for accepting me to U.B.C. in the first place, and allowing this project to evolve in the direction that it did. I appreciate all the resources that Lee put at my disposal throughout this process.

This project was funded by Barrick Gold Corporation, with additional support from NSERC scholarships and grants. I would like to thank Jay Hodgson at Barrick for setting up the financial support for this project, and Dave Heberlein for the initial research ideas and providing all of the administrative and logistical support required, both in the field and in La Serena.

This thesis would not have been possible without the collaboration of Barrick geologists and consultants, who provided the geological framework that my project depends on. Kevin Heather was a great help my first season, and I thank him for his interest in the project. Others

on this list include: Raúl Guerra and all the geologists at Km. 34.; Nivaldo Rojas at El Indio; Dean Williams; Luis Perez and the other Del Carmen geologists; Bob Leonardson, Jean-François Metail, and the Pascua boys - Javier Vega, Pedro Vera, Fernando Rojas; José Noriega and the Lama exploration staff; Jack Hamilton, Graham Nixon, and Raymond Jannas. Logistical support and practical assistance was provided by numerous people, particularly Jessica Cuellar, Gabriel Sanchéz, and John Kieley. A special thanks to Toño Traslavina and the Pascua crew for the salsa instruction.

My fellow researchers were of immense help, and made life in Chile very enjoyable. Thomas Bissig provided thoughtful discussion and exchange of samples, maps, data, and ideas. I also thank him for making sure my samples made it through the Queen's Geochron Lab. Annick (a.k.a. Miss Pascua) Chouinard was a pleasure to work with, and her knowledge of Pascua was an invaluable resource. I am sure 'Club Resort Pascua' will never be the same - and I have the photos to prove it!

A large component of this thesis is based on a stable isotope study that was completed at the U.S.G.S. Denver facility. I am indebted to Bob Rye for his support and his knowledge of acid sulfate systematics. It is a pleasure working with him, and his scientific contributions are very much appreciated. Cyndi Kester provided infinite assistance in the lab and this project would not have been possible without her. I thank her for her quick response to my many queries over the past few years. Gary Landis is also thanked for his persistence with the fluid inclusion gas analyses and his contributions to this project.

Many other individuals at U.B.C. have made important contributions to this thesis. Shane Ebert is gratefully acknowledged for his prompt reviews of many versions of these chapters and numerous discussions on all things epithermal. I thank Greg Dipple for his patience in helping me get through the frightening world of thermodynamics and Margules parameters. Dick Tosdal was a great source of contacts at the U.S.G.S. and is thanked for his comments on several of these chapters. Steve Rowins is acknowledged for his assistance with the fluid inclusion stage. My committee members, K Fletcher and John Jambor, are thanked for their input. Many of their suggestions have been incorporated into this version of the thesis. I would also like to thank my friends and fellow graduate students at U.B.C. over the years. Shannon Shaw and Anita Lam provided wise advice upon my arrival in Vancouver. I thank Craig Nichol, Mike Buchanan, Vanessa Gale, Mike St. Pierre, Meghan Lewis, and Emily Chastain for the countless caffeine and sugar breaks; Tina Roth for the gallons of tea, commiseration, and helpful advice; and Scott Heffernan for providing welcome distraction and understanding over the last year.

And finally, I want to thank my family for their support through this long process. Their constant questions of ' Are you done yet?', and the inevitable follow-up, 'Well, what the .... are you doing out there anyway?', were a continual source of motivation. And, most importantly, I actually managed to beat my brother to the 'doctor' title, with a few months to spare!

Chapter 1

INTRODUCTION

HIGH SULFIDATION DEPOSITS

Epithermal deposits were originally recognized by Lindgren (1933) as a distinct class of precious-metal deposit that formed at relatively low temperatures and shallow depths. High sulfidation deposits are one of the two principal types of epithermal systems, and are characterized by the presence of high sulfidation state minerals (e.g., enargite and luzonite) and acid sulfate alteration assemblages (quartz, alunite, kaolinite, pyrophyllite: Hedenquist, 1987; Arribas, 1995). Deposits of this type were previously termed enargite-gold (Ashley, 1982), high sulfur (Bonham, 1984; 1986), quartz-alunite gold (Berger, 1986), acid-sulfate (Heald et al., 1987), and alunite-kaolinite (Hayba et al., 1985), in reference to either the alteration mineralogy or conditions of formation.

Intensive exploration and the discovery of several world-class epithermal deposits in the last 10 to 20 years have greatly advanced our understanding of the high sulfidation environment. Research has focused on the mineralizing environment and ore-forming processes at specific deposits (e.g., Stoffregen, 1987; Vennemann et al., 1993; Sillitoe and Lorsen, 1994; Arribas et al., 1995; Hedenquist et al., 1998; Jannas et al., 1999). Studies in many areas are hindered by the pervasive nature of alteration, the depth of oxidation, and the lack of good quality fluid inclusions. Regardless, the major elements of the genetic model are broadly accepted as follows:

- Deposits form in subduction-related arc settings and are typically associated with volcanic centers. Mineralization is coeval with local volcanic rocks and related intrusions.
- In many deposits, pervasive pre-ore alteration is widespread. Alteration results from the condensation of magmatic vapors that are generated by phase separation of exsolved magmatic fluids. Disproportionation or dissociation of SO_2 and HCl, respectively, create extremely low pH, reactive fluids. Vuggy residual quartz is the product of extreme base leaching and marks the principal fluid upflow channel. Alteration typically grades outwards to an acid sulfate alteration zone containing quartz, alunite ± clays, and surrounding advanced argillic, argillic and propylitic assemblages (Table 1.1). This sequence reflects the progressive neutralization and cooling of acidic fluids outwards from the main fluid conduit.

Table 1.1 Alteration assemblages relevant to the high sulfidation environment, as used in this study (modified from Thompson and Thompson, 1996 and Hedenquist et al., 2000).

Assemblage	Diagnostic Mineralogy	Accessory phases	Occurrence
Residual (vuggy) Quartz	quartz	rutile, pyrite, S°, hematite, cristobalite	Typically core of high sulfidation system and principal ore-host.
Silicic	quartz	chalcedony, rutile, barite, pyrite, opaline silica	Partial to massive silicification, quartz veins, and silicified breccias.
Acid sulfate[1]	alunite[2], quartz	kaolinite/dickite-pyrophyllite, pyrite, S°, diaspore, zunyite, APS[3]	Either hypogene, steam-heated, or supergene in origin.
Advanced argillic	kaolinite/dickite-pyrophyllite, quartz	Illite/smectite, pyrite, diaspore, alunite	Typically surrounds silicic cores and hypogene acid sulfate alteration zones.
Argillic	illite/smectite	kaolinite, montmorillonite, quartz, pyrite	Halo to hypogene acid sulfate or advanced argillic assemblages.
Propylitic	chlorite, illite/smectite	calcite, epidote, pyrite	Typically widespread, peripheral alteration.
Sericitic	sericite[4]	quartz, pyrite	Typically a deeper (higher temperature) equivalent to advanced argillic alteration.

[1] includes both acid-chloride sulfate and acid sulfate assemblages as summarized in Hedenquist et al. (2000).
[2] includes alunite-group minerals.
[3] APS = alumino-phosphate-sulfate minerals of beudantite or crandallite groups.
[4] field term used for fine-grained white mica and includes illite, muscovite, and intermediate K-dioctahedral micas

- Mineralization postdates regional alteration and is focused in veins, breccia zones, and permeable or reactive lithologies. The composition of ore-fluids is poorly constrained. These fluids are typically inferred to be less acidic and less oxidized than the early alteration fluids, and possibly of mixed magmatic-meteoric origin. This two-stage model is invoked to explain localized mineralization and conversely, the lack of mineralization in many regional alteration zones (lithocaps).
- Formation of these deposits at shallow levels, close to the paleosurface, influence their geometry, the vertical zonation of alteration with respect to temperature and pressure (depth), and the potential interaction of deep ascending and shallow descending fluids. The nature of landforms, elevation, relief, and access to meteoric water will affect both deposit formation and preservation.

THE EL INDIO-PASCUA BELT

The El Indio-Pascua Belt is situated in the Central Andean Cordillera Principal and straddles the Chile-Argentina border between latitudes 29°20' and 30°30' S (Fig. 1.1). This region has been the subject of intensive exploration for approximately twenty years, resulting in the development of several mines (e.g., El Indio, Tambo), delineation of extensive resources (e.g., Pascua-Lama, Veladero), and discovery of numerous mineralized alteration zones. It is one of the foremost districts of high sulfidation mineralization in the world. Total production from the district to date has been over 310 t gold, 31,000 t silver, and 1 Mt of copper, mostly from the El Indio mine. Mining activities at El Indio are diminishing however, and the adjacent Tambo mine was recently closed (in 2000). Exploration is currently focused in the Pascua-Lama and Veladero districts, at the northern limit of the belt.

The El Indio-Pascua Belt is located in the "flat slab" segment of the Andes, between two other well-known mineralized areas: the Maricunga porphyry Au and high sulfidation Au-Ag belt to the north (26-28° S), and the Los Pelambres – El Teniente porphyry Cu-Mo belt to the south (32-34° S). The Maricunga Belt occurs at the northern margin or transition zone of the "flat slab" region, but the mineralized systems in the belt formed before or during the very early stages of slab flattening, 24-20 and 14-13 Ma respectively (Vila and Sillitoe, 1991; Muntean and Einaudi, 2001). In contrast, porphyry Cu-Mo deposits in the Los Pelambres – El Teniente district formed in the late Miocene (10-5 Ma: Skewes and Stern, 1994; Kay et al., 1999), and are coeval with high sulfidation systems in the El Indio-Pascua Belt. Several metallogenetic models

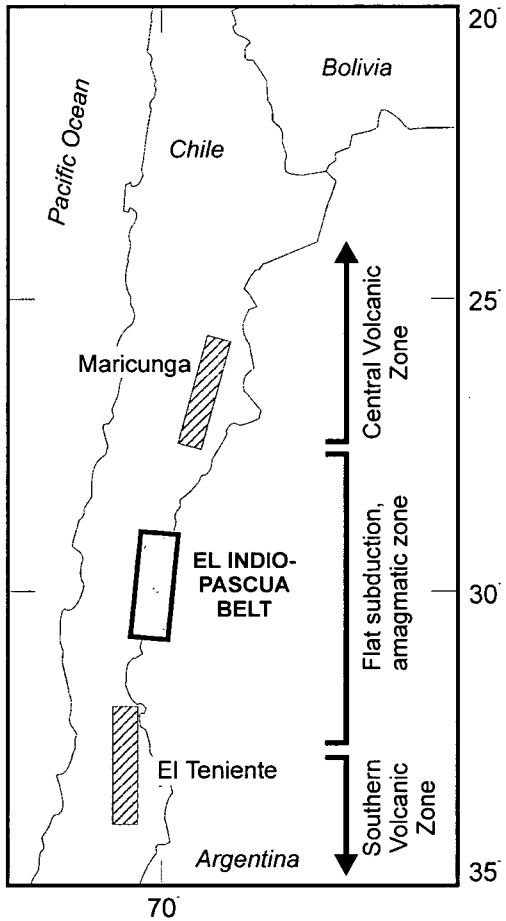

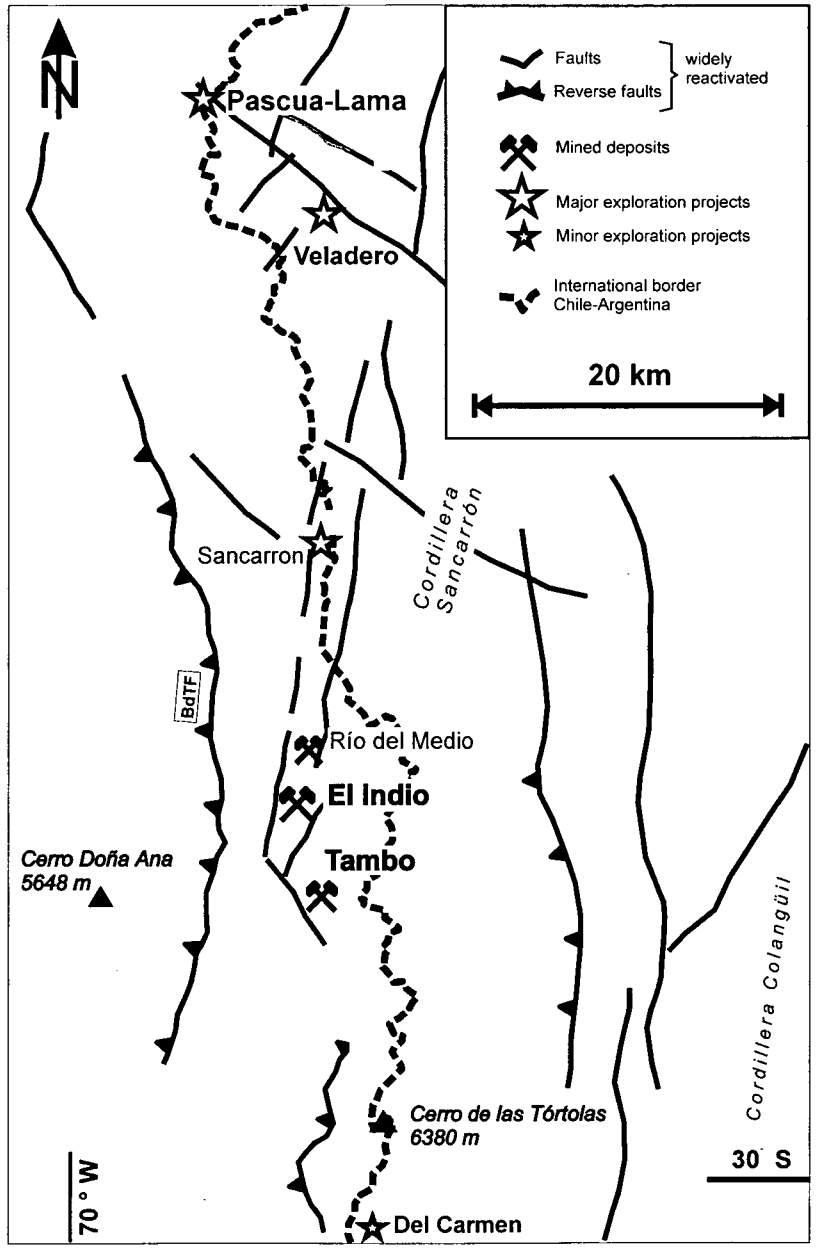

Figure 1.1. The El Indio-Pascua Belt. Location map on left shows the principal Tertiary metallogenetic belts of northern Chile (and Argentina), and the location of the amagmatic flat-slab segment of the Central Andes (after Sillitoe, 1991). Major deposits and prospects in the El Indio-Pascua Belt are given in map to right.

have been proposed for the flat-slab region and its borders (Skewes and Stern, 1994; Sasso and Clark, 1998; Kay et al., 1999; Kay and Mpodozis, 2001), including the most recent contribution from Bissig (2001).

Hydrothermal alteration of late Eocene to late Miocene age is recognized throughout the El Indio-Pascua Belt, but economic Au (Cu, Ag) mineralization is restricted to a narrow interval between 6 to 9.5 Ma (Bissig, 2001). Most deposits and prospects are of the high sulfidation-type. Low sulfidation-style mineralization is recognized only in the Rio del Medio vein, located near El Indio, although El Indio itself has characteristics of both high and low sulfidation environments (Jannas et al., 1999; Bissig, 2001). Ore deposition throughout the region is inferred to have occurred beneath a relatively flat landscape, at a time when magmatism was minimal (Bissig, 2001). There is no evidence for major volcanic edifices related to mineralizing centres. The current topography of the belt is attributed to post-Miocene valley incision and glaciation (Viet, 1996; Bissig, 2001).

The El Indio-Pascua Belt provides an excellent site for studying epithermal processes and high sulfidation deposits for several reasons.

- The systems in this region are typically well preserved, due to their young age and favorable tectonic and climatic conditions. Near-surface features of these deposits are preserved as steam-heated alteration zones and regional planar landforms (Bissig, 2001).
- Access is possible via the extensive mining and exploration activities of Barrick Gold Corporation, the predominant landholder in the region. This company has been operating in the belt for over 20 years and all drill core, underground workings, and exploration data were made available for the purposes of this study.
- A relatively complete geological framework has been determined for this region, based on numerous studies at both a deposit- (e.g., Siddeley and Araneda, 1986; Jannas et al., 1999; Chouinard and Williams-Jones, 1999) and regional-scale (e.g., Thiele, 1964; Maksaev et al., 1984; Martin et al., 1995; Kay and Mpodozis, 2001; Bissig, 2001).
- Alunite is spatially and genetically associated with precious metal mineralization in many deposits and prospects, and hence provides direct information on mineralizing processes (see below).

THE ROLE OF ALUNITE

Alunite ($KAl_3(SO_4)_2(OH)_6$) and alunite-group minerals (Table 1.2) are the key constituents in acid sulfate alteration. Alteration of this type is a characteristic feature of high sulfidation epithermal gold deposits (Cooke and Simmons, 2000; and references therein) and forms under conditions of low pH and highly oxidized fluid chemistry (Holland, 1965; Henley and McNabb, 1978; Stoffregen, 1987). These conditions can be generated by several mechanisms in the epithermal environment, related to either hypogene magmatic condensates, steam-heated processes, or supergene oxidation.

The abundance and variability of alunite in high sulfidation systems has been recognized by several authors (e.g., Bethke, 1984; Rye et al., 1992; Sillitoe, 1993; Thompson, 1992; Arribas, 1995; Hedenquist et al., 2000). Recent studies indicate that alunite can be used to determine the nature of alteration fluids and the physio-chemical environment of mineral deposition. The presence of syn-mineral alunite in the El Indio-Pascua Belt also provides direct information on ore-forming processes. Research to date has focused on specific characteristics of alunite-group minerals, including:

- Field relations: The distribution, textures, mineral associations, and paragenesis of acid sulfate alteration are commonly used as an exploration tool to differentiate between ore-proximal, hypogene alteration and near-surface assemblages (e.g., Thompson, 1992; Sillitoe, 1993; Hedenquist et al., 2000).

Table 1.2 Minerals of the alunite supergroup (current usage: Jambor, 1999).

	Al > Fe		Fe > Al	
Alunite-jarosite group	alunite	$KAl_3(SO_4)_2(OH)_6$	jarosite	$KFe_3(SO_4)_2(OH)_6$
	natroalunite	$NaAl_3(SO_4)_2(OH)_6$	natrojarosite	$NaFe_3(SO_4)_2(OH)_6$
	minamiite	$(Na,K,Ca)_2Al_6(SO_4)_4(OH)_{12}$	hydronium jarosite	$(H_3O)Fe_3(SO_4)_2(OH)_6$
	huangite	$CaAl_6(SO_4)_4(OH)_{12}$	argentojarosite	$AgFe_3(SO_4)_2(OH)_6$
	walthierite	$BaAl_6(SO_4)_4(OH)_{12}$	beaverite	$Pb(Fe,Cu)_3Fe_3(SO_4)_2(OH,H_2O)_6$
	ammonioalunite	$NH_4Al_3(SO_4)_2(OH)_6$	ammoniojarosite	$(NH_4)Fe_3(SO_4)_2(OH)_6$
	schlossmacherite	$(H_3O,Ca)Al_3(SO_4)_2(OH)_6$	plumbojarosite	$PbFe_6(SO_4)_4(OH)_{12}$
Beudantite group	svanbergite	$SrAl_3[(P,S)O_4)]_2(OH,H_2O)_6$	beaudantite	$PbFe_3[(As,S)O_4)]_2(OH,H_2O)_6$
	woodhouseite	$CaAl_3[(P,S)O_4)]_2(OH,H_2O)_6$		
	hinsdalite	$PbAl_3[(P,S)O_4)]_2(OH,H_2O)_6$		
Crandallite group	crandallite	$CaAl_3[(PO_3(O_{1/2}(OH)_{1/2}]_2(OH)_6$		
	goyazite	$SrAl_3[(PO_3(O_{1/2}(OH)_{1/2}]_2(OH)_6$		
	gorceixite	$BaAl_3(PO_4)(PO_3{\bullet}OH)(OH)_6$		
	plumbogummite	$PbAl_3(PO_4)_2(OH,H_2O)_6$		
	florencite-(Ce)	$CeAl_3(PO_4)_2(OH)_6$		
	florencite-(La)	$LaAl_3(PO_4)_2(OH)_6$		

- Geochemistry: Several experimental (Hemley et al., 1969; Stoffregen and Cygan, 1990) and empirical studies (e.g., Aoki, 1991; Aoki et al., 1993; Thompson, 1992; Hedenquist et al., 1994; Arribas et al., 1995) have correlated variations in alunite-group chemistry to specific environments or temperatures of deposition. The temperature dependence of K:Na substitution is of particular interest in mineral exploration, since this feature can be readily identified in the field by the use of portable short-wave infrared (SWIR) spectrometers (e.g., PIMA, FieldSpec Pro).

- Stable-isotope systematics: Alunite-group minerals contain four stable-isotope sites; $D_{(OH)}$, $^{34}S_{(SO4)}$, $^{18}O_{OH}$, and $^{18}O_{SO4}$, more than any other common mineral. Isotopic variations are related to the source and type of fluids, rates of processes, and the physical-chemical environment of deposition (Rye et al., 1992). Isotopic studies are particularly useful in conjunction with analyses of coexisting minerals such as clays (kaolinite, dickite, pyrophyllite), sericite, and sulfides.

- Geochronology: Alunite is useful for age determinations by K-Ar and $^{40}Ar/^{39}Ar$ methods due to the large concentration of potassium in end-member alunite (and jarosite). Alunite age data have been applied to supergene and weathering events (see Vasconcelos, 1999 for details) and paleoclimate studies (e.g., Bird et al., 1990; Sillitoe et al., 1991; Arehart and O'Neil, 1993; Vasconcelos et al., 1994). Hypogene alunite can also be used to date hydrothermal events and associated precious- or base-metal mineralization (e.g., Alpers and Brimhall, 1988; Sillitoe et al., 1991; Perello, 1994; Arribas et al., 1995; Bissig, 2001; this study), provided alteration is coeval with mineralization.

Using a combination of these characteristics and previous stable-isotope studies, Rye et al. (1992) defined four specific environments of acid sulfate alteration (Fig. 1.2). These are:

- The magmatic-hydrothermal environment, where the disproportionation of magmatic SO_2 in condensed magmatic vapor forms H_2S and H_2SO_4 below *ca.* 350°C. The resulting acidic fluids react with wall rock to form extensive zones of acid sulfate alteration (this assemblage is equivalent to hypogene chloride-sulfate alteration as summarized in Hedenquist et al., 2000).

- The magmatic steam environment, where alunite is believed to form from the expansion of rapidly ascending SO_2-rich magmatic vapor following sudden depressurization of the hydrothermal system (Rye, 1993).

- The steam-heated environment, where alunite forms from the condensation of vapour derived from an underlying hydrothermal system and the oxidation of H_2S gas above the water table.
- The supergene environment, where the supergene oxidation of sulfides can produce an assemblage of kaolinite ± quartz, alunite, jarosite, with iron oxide and oxyhydroxide minerals.

The terminology and relations defined by Rye et al. (1992) are used throughout this dissertation to specify different origins of alunite and acid sulfate alteration assemblages.

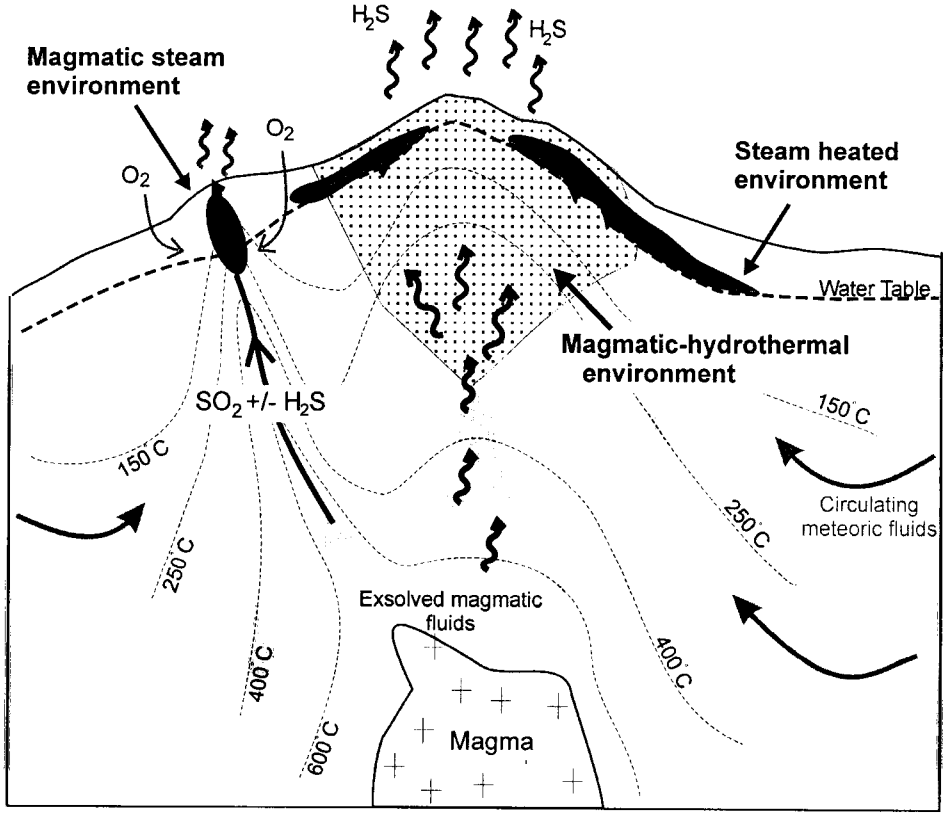

Figure 1.2. Schematic diagram of a high sulfidation epithermal system showing environments magmatic-hydrothermal, magmatic steam, and steam-heated alteration. Supergene processes not shown. Modified from Rye et al. (1992).

SCIENTIFIC CONTRIBUTIONS OF THIS STUDY

The principal goal of this thesis is to better constrain genetic and exploration models for high sulfidation systems in the premier district for this deposit-type, the El Indio-Pascua Belt, and to improve the general understanding of this deposit-type worldwide. Prior to this study, only limited data were available on alteration and ore-forming events in the El Indio-Pascua Belt. Investigations were carried out in association with exploration activities and concurrent research in this region to clarify the relation between alteration and high sulfidation mineralization. In particular, research presented in this dissertation is focused on:

- The origin and importance of early alteration. Economic mineralization in the El Indio-Pascua Belt was preceded by the development of numerous and widespread barren alteration zones. Pre-mineral, barren alteration is typical of most high sulfidation systems and may be an important factor in the development of some economic deposits. The distribution and characteristics of pre-mineral alteration, and the timing with respect to ore formation in the Tambo and Pascua-Lama districts, are addressed.
- Nature of alunite-natroalunite stability relationships. Very little information is available regarding occurrences of natroalunite and the nature of the alunite-natroalunite solid solution. This relationship is of particular interest in mineral exploration, given the potential to distinguish ore-proximal, hypogene alteration from lower temperature assemblages. The present study examines the distribution of alunite-natroalunite throughout the El Indio Pascua Belt, using stable-isotope and geochronological data to constrain the origin of alteration. Experimental data from Stoffregen and Cygan (1990) is used to predict the effect of fluid compositions on the alunite-natroalunite solid solution.
- Mineralizing processes. While there is general consensus that source of fluids and metals in high sulfidation deposits is magmatic (e.g., Hedenquist and Lowenstern, 1994; Arribas, 1995; Cooke and Simmons, 2000), there is still considerable uncertainty regarding the physical nature of the ore fluids. In particular, the relative contributions of vapor versus hypersaline liquid to the transport and deposition of gold, silver, and copper are the cause of much debate. Data from this study are used to generate a model for high sulfidation mineralization in the El Indio-Pascua Belt, with implications for epithermal environments in general.
- The transition from magmatic-hydrothermal to supergene processes. Late-stage processes in the El Indio-Pascua Belt include the deposition of magmatic steam alunite and late-stage acid

sulfate alteration. Magmatic steam processes are currently poorly understood, but new data from this study are used to clarify the nature of these events and their relation to magmatic-hydrothermal alteration. An environment transitional between magmatic-hydrothermal and supergene processes is defined based on stable-isotope and ^{40}Ar-^{39}Ar data for late-stage acid sulfate alteration.

- The near-surface environment. Despite the importance of near-surface alteration to the recognition of high sulfidation environments, very few data are available regarding the characteristics of these assemblages. ^{40}Ar-^{39}Ar alunite ages are used to constrain the timing of steam-heated alteration relative to underlying mineralization in the El Indio-Pascua Belt. Stable-isotope data, in conjunction with paleoclimate and physiographic data, record the relative contributions of meteoric and magmatic fluids in near-surface processes.

PRESENTATION

This dissertation is organized in manuscript format in accordance with the requirements of the University of British Columbia. Each chapter represents either a complete manuscript or a major contribution to future publications. A brief description of each chapter, listing co-authors and their respective contributions, is given below.

Chapter 2: The nature of hydrothermal alteration at the Pascua–Lama high sulfidation deposit, Chile-Argentina. *Deyell, C.L., Leonardson, R., Chouinard, A., Rye, R.O., and Bissig, T.*

This chapter presents detailed work by the author on the characteristics and distribution of hydrothermal alteration in the Pascua-Lama district, with new ^{40}Ar-^{39}Ar ages to constrain the timing of alteration events. The data presented herein is based on field studies, combined with detailed short-wave infrared (SWIR), petrographic, and geochemical analyses by the author. All stable-isotope data were collected by the author at Bob Rye's U.S.G.S. facility. The regional geological framework is based on the recent study by Bissig (2001), with additional information from R. Leonardson and the exploration staff at Barrick Chile Ltda. and Barrick Exploraciónes Argentina. The styles and distribution of mineralization in the Brecha Central area (the central part of the Pascua system) are the subject of A. Chouinard's Ph.D. thesis (currently in progress at McGill University). Work by the author is focused on the broader system. This paper represents the major contribution to a manuscript in preparation for submission to Economic Geology.

Detailed results from A. Chouinard's study will be submitted as a companion paper.

Chapter 3: Alunite in an evolving magmatic-hydrothermal system: The Tambo high sulfidation deposit, El Indio district, Chile. *Deyell, C.L., Rye, R.O., Landis, G.P., and Bissig, T.*

This paper presents a model for the evolution of the Tambo high sulfidation system, based on new field, paragenetic, geochronologic, and geochemical constraints determined by the author. The paper emphasizes differences of scale and controls between Tambo and Pascua-Lama, but documents a similar hydrothermal evolution. The manuscript has been submitted to Chemical Geology for publication in a special volume on 'Sulfate Minerals in Hydrothermal Environments'. The paper has also been informally reviewed by two U.S.G.S. scientists and J. Hedenquist. Their comments are greatly appreciated and have been incorporated into this version of the paper. The regional geological framework for the deposit is based on recent work by Bissig (2001) and previous studies in this area (Jannas et al., 1999; Siddeley and Araneda, 1990). All stable-isotope analyses were performed by the author at R. Rye's U.S.G.S. laboratory. G. Landis and R. Rye are responsible for fluid inclusion gas analyses and the interpretation of this data summarized herein.

Chapter 4. The role of alunite in exploration. Evidence from high sulfidation deposits in the El Indio-Pascua Belt, Chile–Argentina. *Deyell, C.L. and Thompson, A.J.B.*

The chapter provides an evaluation of the use of alunite and acid sulfate alteration for mineral exploration in the El Indio-Pascua Belt. Field relations, paragenetic constraints, and physical, geochemical, and stable-isotopic characteristics for different alteration assemblages are summarized, based on research by the author in the El Indio-Pascua Belt. Particular emphasis is placed on the characteristics of magmatic-hydrothermal alteration and its relation to precious-metal mineralization. The paper is intended for submission to the Journal of Geochemical Exploration. Several ideas on the use of alunite in exploration have evolved from previous work by A. Thompson (and E.U. Petersen) in hydrothermal systems in Utah and northern Chile (unpub. data).

Chapter 5. Alunite–natroalunite stability relationships. *Deyell, C.L. and Dipple, G.M.*

The focus of this paper is the nature of the alunite–natroalunite solid-solution and the occurrence of these minerals in the El Indio-Pascua Belt. Experimental data of Stoffregen and

Cygan (1990) are used to predict the effect of variable temperature and fluid K:Na contents on the composition of alunite–natroalunite solid-solution.

Chapter 6. Formation of high sulfidation precious metal deposits: New evidence from the El Indio-Pascua Belt, Chile-Argentina. *Deyell, C.L.*

This paper provides new constraints on the genetic model for high sulfidation systems based on data from the El Indio-Pascua Belt. This chapter is the major contribution to a collaborative paper (in preparation) with J. Thompson, T. Bissig, and A. Chouinard and is intended to summarize results of recent research in this belt. J. Thompson contributed his ideas to the regional framework of high sulfidation mineralization and relations to other systems in the Andean Cordillera.

REFERENCES

Alpers, C.N., and Brimhall, G.H., 1988. Middle Miocene climatic change in the Atacama Desert, northern Chile: Evidence from supergene mineralization at La Escondida. Geological Society of America Bulletin, 100, 1640-1656.

Aoki, M., 1991. Mineralogical features and genesis of alunite solid solution in high temperature magmatic-hydrothermal systems. Journal of the Geological Survey of Japan, 277, 31-32.

Aoki, M., Comsti, E.C., Lazo, F.B., and Matsuhisa, Y., 1993. Advanced argillic alteration and geochemistry of alunite in an evolving hydrothermal system at Baguio, northern Luzon, Phillipines. Resource Geology, 43, 155-164.

Arehart, G.B. and O'Neil, J.R., 1993. D/H ratios of supergene alunite as an indicator of paleoclimate in continental settings: Climate change in continental isotope records. Geophysics Monographs, 78, 277-284.

Arribas, A., Jr., 1995. Characteristics of high sulfidation epithermal deposits, and their relation to magmatic fluids. *In* Thompson, J.F.H., ed., Magmas, Fluids and Ore Deposits. Mineralogical Association of Canada Short Course Notes, 23, 419-454.

Arribas, A., Jr., Cunningham, C.G., Rytuba, J.J., Rye, R.O., Kelly, W.C., McKee, E.H., Podwysocky, M.H., and Tosdal, R.M., 1995. Geology, geochronology, fluid inclusions, and

stable isotope geochemistry of the Rodalquilar Au alunite deposit, Spain. Economic Geology, 90, 795-822.

Ashley, R.P., 1982. Occurrence model for enargite-gold deposits. U.S. Geological Survey Open File Report 82-795, 144-147.

Bethke, P.M., 1984. Controls on base- and precious-metal mineralization in deeper epithermal environments. U.S. Geological Survey Open File Report 84-890, 40 p.

Berger, B.R, 1986. Descriptive model of epithermal quartz-alunite Au. *In* Cox, D.P., and Singer, D.A., eds., Mineral Deposit Models. U.S. Geological Survey Bulletin 1693, p.158.

Bird, M.I., Chivas, A.R., and McDougall, I., 1990. An isotopic study of surficial alunite in Australia: 2. Potassium-argon geochronomogy. Chemical Geology, 80, 133-145.

Bissig, T., 2001. Metallogenesis of the Miocene El Indio-Pascua gold-silver-copper belt, Chile/ Argentina: Geodynamic, geomorphological and petrochemical controls on epithermal mineralization. Unpublished Ph.D. thesis, Queen's University.

Bonham, H.F., Jr, 1984. Three major types of epithermal precious metal deposits. Geological Society of America Abstracts with Program, 16, 449.

Bonham, H.F., Jr., 1986. Models for volcanic-hosted epithermal precious metal deposits: A review. *In* Proceedings of the International Volcanological Congress, Symposium 5, Hamilton, New Zealand 1986. Aukland, New Zealand, 13-17.

Chouinard, A. and Williams-Jones, A.E. 1999. Mineralogy and petrography of ore and alteration assemblages at the Pascua Au-Ag-Cu deposit, Chile. Internal for Barrick Gold and Barrick Chile Ltda.

Cooke, D.R. and Simmons, S.F., 2000. Characterisitcs and genesis of epithermal gold deposits. *In* Hagemann. S.G., and Brown, P.E., eds., Reviews in Economic Geology, v. 13, 221-244.

Hayba, D.O., Bethke, P.M., Heald, P, and Foley, N.K., 1985. Geologic, mineralogic, and geochemical characteristics of volcanic-hosted epithermal precious-metal deposits. Reviews in Economic Geology v. 2, 129-167.

Heald, P., Foley, N.K., and Hayba, D.O., 1987. Comparative anatomy of volcanic-hosted epithermal deposits: acid-sulfate and adularia-sericite types. Economic Geology, 82, 1-26.

Hedenquist, J.W., 1987. Mineralization asscoiated with volcanic-related hydrothermal systems in the Circum-Pacific basin. *In* Horn, M.K., ed., Transactions of the Fourth Circum-Pacific Energy and Mineral Resources Conference, August, 1986. Singapore, American Association of Petroleum Geologists, Tulsa, OK, 513-524.

Hedenquist, J.W, Arribas, A., Jr., and Gonzalez-Urien, E., 2000. Eploration for epithemal gold

deposits. *In* Hagemann, S.G. and Brown, P.E., eds., Gold 2000. Reviews in Economic Geology, vol. 13., 245-277.

Hedenquist, J.W., Arribas, Jr., A., and Reynolds, T.J., 1998. Evolution of an intrusion-centered hydrothermal system: Far Southeast-Lepanto porphyry and epithermal Cu-Au deposits, Phillipines. Economic Geology, 93, 373-404.

Hedenquist, J.W. and Lowenstern, J.B., 1994. The role of magmas in the formation of hydrothermal ore deposits. Nature, 370 (6490), 519-527.

Hemley, J.J., Hostetler, P.B., Gude, A.J., and Mountjoy, W.T., 1969. Some stability relations of alunite. Economic Geology, 64, 599-612.

Henley, R.W., and McNabb, 1978. Magmatic vapor plumes and ground-water interaction in porphyry copper emplacement. Economic Geology, 73, 1-20.

Holland, H.D., 1965. Some applications of thermodynamic dta to problems of ore deposits, II. Mineral assemblages and the composition of ore-forming fluids. Economic Geology, 60, 1101-1166.

Jannas, R.R., Bowers, T.S., Petersen, U., Beane, R.E., 1999. High-sulfidation deposit types in the El Indio District, Chile. *In* B.J. Skinner, ed., Geology and ore deposits of the Central Andes. SEG Special Publication #7, 27-59.

Kay, S.M., Mpodozis, C., and Coira, B., 1999. Neogene magmatism, tectonism, and mineral deposits of the Central Andes (22° to 33° S latitude). *In* Skinner, B.J., ed., Geology and Ore Deposits of the Central Andes, SEG Special Publication #7, 27-59.

Kay, S.M., and Mpdozis, C., 2001. Central Andean ore deposits linked to evolving shallow subduction systems and thickening crust. GSA Today, 11(3), 4-9.

Lindgren, W., 1933. Mineral deposits, 4th Edition. McGraw-Hill Book Company, New York, 930 p.

Maksaev, V., Moscoso, R., Mpodozis, C., and Nasi, C., 1984. Las unidades volcánicas y plutonicas del cenozoico superior en la Alta Cordillera del Norte Chico (29°-31° S): Geología, alteración hidrothermal y mineralisacion. Revista Geológica de Chile, 21, 11-51.

Martin, M, Clavero, J., and Mpodozis, C., 1995. Estudio geologico regional del Franja El Indio, Cordillera de Coquimbo. Servicio National de Geologia y Minera, Santiago, Chile. Registered report IR-95-06, 232p.

Martin, M.W., Clavero, J.R., Mpodozis, C., 1999. Late Paleozoic to Early Jurassic tectonic development of the high Andean Principal Cordillera, El Indio Region, Chile (29-30° S). Journal of South American Earth Sciences, 12, 33-49.

Muntean, J.L., and Einaudi, M.T., 2001. Porphyry-epithermal transition: Maricunga Belt, Northern Chile. Economic Geology, 96 (4), 1445-1472.

Perello, J.A., 1994. Geology, porphyry Cu-Au, and epithermal Cu-Au-Ag mineralization of the Tombulilato district, North Sulawesi, Indonesia. Journal of Geochemical Exploration, 50, 221-256.

Rye, R.O., 1993. The evolution of magmatic fluids in the epithermal environment: The stable isotope perspective. Economic Geology, 88, 733-753.

Rye, R.O., Bethke, P.M., and Wasserman, M.D., 1992. The stable isotope geochemistry of acid sulfate alteration. Economic Geology, 87 (2), 225-262.

Sasso, A.M., and Clark, A.H., 1998. The Farallón Negro Group, Northwest Argentina: Magmatic hydrothermal and tectonic evolution and implications for Cu-Au metallogeny in the Andean back-arc. Society of Economic Geologists Newsletter, 34, 8-18.

Siddeley, G, and Areneda, R., 1985. Gold-silver occurences of the El Indio belt, Chile. Geology of the Andes and its relation to mineral and energy resources. Symposium, Chile, 18 p.

Sillitoe, R.H., 1993. Epithermal models: Genetic types, geometric controls, and shallow features. *In* R.V. Kirkham, W.D. Sinclair, R.I. Thorpe and J.M. Duke, eds., Mineral Deposit Modelling. Geological Association of Canada Special Paper 40, 403-417.

Sillitoe, R.H., 1999. Styles of high sulfidation gold, silver and copper mineralization in the porphyry and epithermal environments. PacRim '99. Bali, Indonesia, 10-13 October, Proceedings, 29-44.

Sillitoe, R.H., and Lorson, R,C, 1994. Epithermal gold-silver-mercury deposits at Paradise Peak, Nevada: Ore controls, porphyry gold association, detachment faulting, and supergene oxidation. Economic Geology, 89, 1228-1248.

Sillitoe, R.H., McKee, E.H., and Vila T., 1991. Reconnaissance K-Ar geochronology of the Maricunga gold-silver belt, northern Chile. Economic Geology, 86, 1261-1270.

Skewes, M.A., and Stern, C.R., 1994. Tectonic trigger for the formation of late Miocene Cu-rich breccia pipes in the Andes of central Chile. Geology, 22 (6), 551-554.

Stroffregen, R., 1987. Genesis of acid-sulfate alteration and Au-Cu-Ag mineralization at Summitville, Colorado. Economic Geology, 82, 1575-1591.

Stoffregen, R.E., and Cygan, G., 1990. An experimental study of Na-K exchange between alunite and aqueous sulfate solutions. American Mineralogist. 75, 209-220.

Thompson, A.J.B, 1992. Alunite compositions and textures: Relationships to precious metal

mineralization. *In* New Developments in Lithogeochemistry, Mineral Deposit Research Unit Short Course #8, 20-21 February.

Thompson, A.J.B., and Thompson, J.F.H., 1996. Atlas of alteration: A field and petrographic guide to hydrothermal alteration minerals. Geological Association of Canada – Mineral Deposits Division. 119 p.

Vasconcelos, P.M., 1999. $^{40}Ar/^{39}Ar$ geochronology of supergene processes in ore deposits. *In* Lambert, D.D., Ruiz, J., eds., Application of radiogenic Isotopes to Ore Deposits Research and Exploration. Reviews in Economic Geology vol 12, 73-113.

Vasconcelos, P.M., Brimhall, G.H., Becker, T.M., and Renne, P.R., 1994. $^{40}Ar/^{39}Ar$ analysis of supergene jarosite and alunite: Implications to the paleoweathering history of the western USA and West Africa. Geochimica et Cosmochimica Acta, 58, 401-420.

Venneman, T.W., Muntean, J.L., Kesler, S.E., O'Neil, J.R., Valley, J.W., and Russell, N., 1993. Stable isotope evidence for magmatic fluids in the Pueblo Viejo epithermal acid sulfate Au-Ag deposit, Dominican Republic. Economic Geology, 88, 55-71.

Viet, H., 1996. Southern westerlies during the Holocene deduced from geomorphological and pedological studies in the Norte Chico, northern Chile (27-33 degrees S). Paleogeography, Paleoclimatology, Paleoecology, 123, 107-119.

Vila, T., and Sillitoe, R.H., 1991. Gold-rich porphyry systems in the Maricunga Belt, northern Chile. Economic Geology, 86 (6), 1238-1260.

Chapter 2

THE NATURE OF HYDROTHERMAL ALTERATION AT THE PASCUA-LAMA HIGH SULFIDATION DEPOSIT; CHILE-ARGENTINA

INTRODUCTION

The Pascua-Lama Au-Cu-Ag deposit is located at the north end of the El Indio-Pascua Belt, in the Cordillera Principal of Chile (Region III) and Argentina (San Juan province; Fig. 2.1). The deposit occurs at approximately 4500 to 5100 metres above sea level (a.s.l.) in an area hosting widespread zones of hydrothermal alteration that are visible as distinct colour anomalies and topographic features. The recognition of these zones led to the discovery of high sulfidation gold mineralization in the Cerro Nevado area (Chile) in 1977 by Compañía Minera San José S.A. The project was explored by a series of operators, including Lac Minerals Ltd., until the acquisition of this company by Barrick Gold Corporation in 1994. Continued exploration has uncovered several zones of both sulfide-rich and oxidized (sulfide-poor) mineralization to the east of the original Cerro Nevada discovery. Estimated proven- and probable-resources at Pascua-Lama total 269 Mt at 1.95 g/t Au and 66 g/t Ag (1.1 g/t Au cut-off: data from Mining Journal, London, April, 2001).

Pascua-Lama is classified as a high sulfidation deposit on the basis of the abundance of acid-sulfate alteration and minerals of high sulfidation state, such as enargite. Several stages of alteration and alunite deposition are recognized from the near paleosurface to several hundred metres depth. The Au-Cu-Ag ore occurs in many forms. The largest deposit is Brecha Central (Fig. 2.2) which hosts high-grade gold ore in alunite-pyrite-enargite breccia matrix fill and banded veins, and in extensive alteration zones of silica-pyrite ± Fe-sulfate. The Frontera area, east of Brecha Central, straddles the Chile-Argentina border and hosts similar styles of mineralization. Smaller, high grade oxidized veins and breccias occur in the Esperanza and Penelope deposits, located to the SW and SE of Brecha Central, respectively (Fig. 2.2). Several other mineralized zones have been discovered recently in the Lama district, including El Morro Oueste and Filo Frederico Norte. New $^{40}Ar/^{39}Ar$ data suggest that Au-Ag mineralization (and

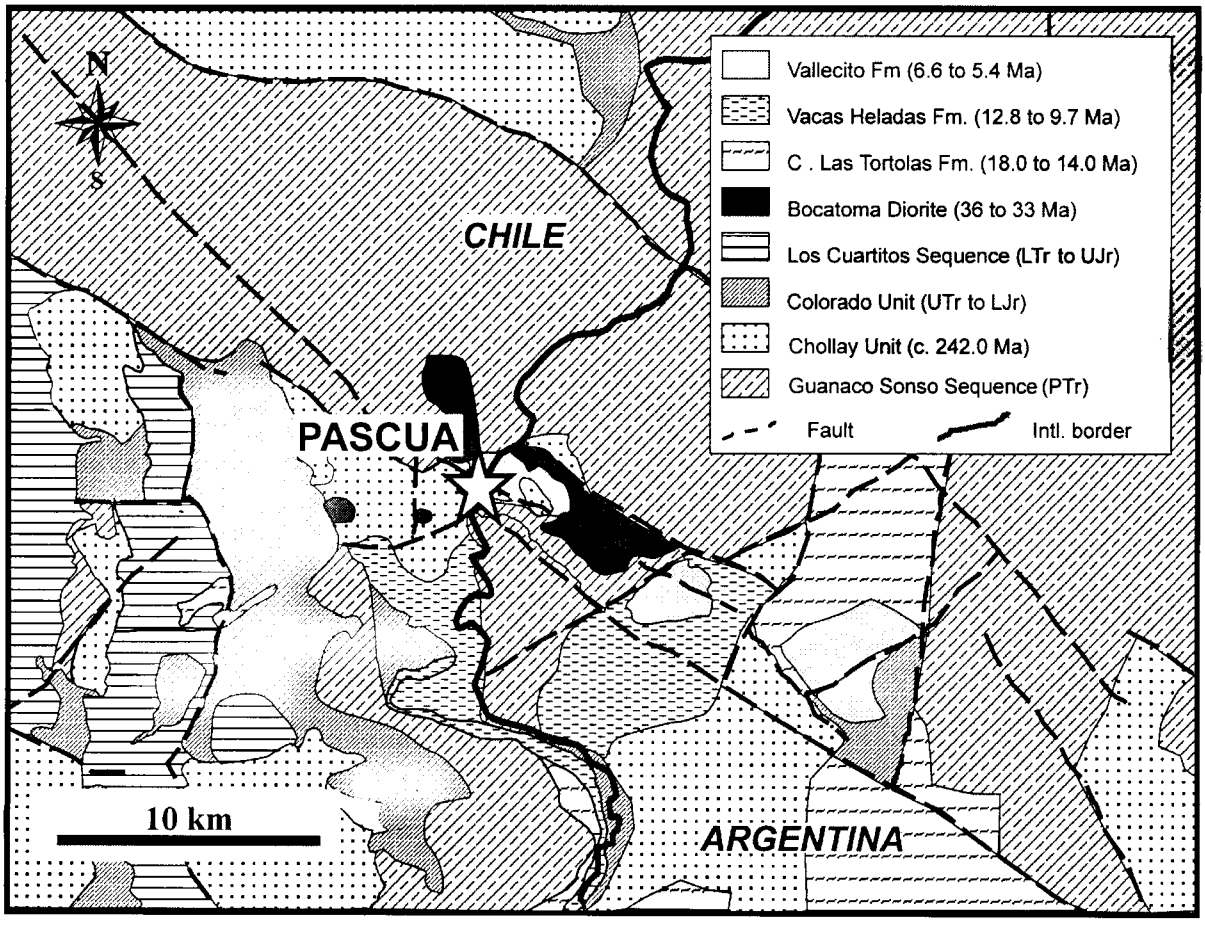

Figure 2.1. Regional geology of the Pascua-Lama area. Adapted from Martin et al. (1995) using unpublished data from D. Heberlein. See text for descriptions of lithological units.

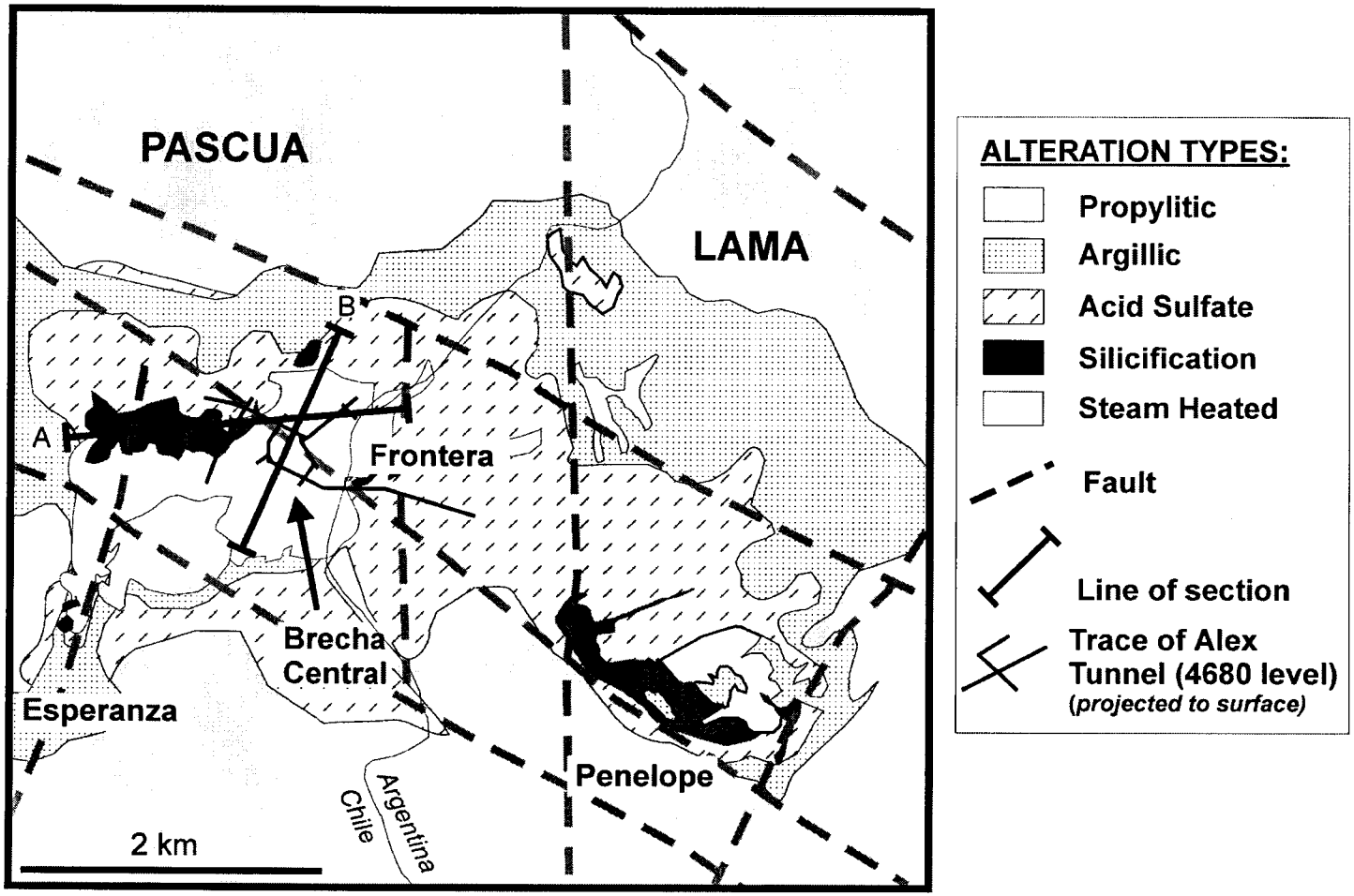

Figure 2.2. Pascua-Lama property map showing the distribution of alteration zones at surface. Pascua refers to the side of the property located in Chile, Lama to that in Argentina. Also shown are locations of the two detailed alteration sections, CA-EW (line A) and CA-00 (line B) refered to in the text. Adapted from Caceres et al. (1997) using unpublished data from D. Heberlein.

related alteration) at Lama may have narrowly pre-dated the main Au-Cu-Ag event at Pascua (Bissig, 2001) and will not be considered here.

In this paper, we examine the nature and distribution of alteration in the Pascua district to constrain the origin and evolution of the deposit. Focus is placed on the relation between alunite and ore-stage events, and its implications for magmatic-hydrothermal processes in the near-surface environment.

GEOLOGICAL FRAMEWORK

The El Indio-Pascua Belt (Fig. 2.1) straddles the Chile-Argentina border in the Cordillera Principal of the Andes, between latitudes 29°20' and 30°30' S. In addition to Pascua-Lama, the district hosts widespread zones of hydrothermal alteration and several world-class epithermal deposits and prospects, including El Indio, which has produced over 10 Moz of gold, and Veladero, with resources of 15 Moz Au and 230 Moz Ag. These hydrothermal systems were emplaced within a NNE-SSW striking tectonic depression bound by the steeply W-dipping high-angle reverse Baños del Toro fault to the west and opposing structures in the Valle del Cura region in the east. Upper Paleozoic -to- lower Jurassic basement in this block consists predominantly of calc-alkaline felsic intrusive suites and volcanic rocks (Martin et al., 1999) and is overlain by up to 1500 m of Tertiary subaerial volcanic strata. The latter are extensively preserved in the southern part of the belt, but are less widespread in the vicinity of Pascua-Lama and Veladero (Martin et al., 1995; Maksaev et al., 1984).

The Tertiary volcanic sequence (summarized in Bissig, 2001 and Martin et al., 1995) consists of a thick succession (up to 1200 m) of dacitic and rhyodacitic tuffs and subordinate basaltic and andesitic flows of the 23-27 Ma Tilito Formation. The overlying 17.5-21 Ma Escabroso Formation is composed predominantly of andesitic lavas and hypabyssal intrusive bodies as well as volcaniclastic sediments. Following a minor deformation event, continued igneous activity is represented by the 14-17 Ma andesitic Cerro de las Tórtolas Formation and the contemporaneous Infiernillo intrusive unit. Magmatism decreased markedly thereafter and is recorded only as isolated occurrences of dacitic tuffs of the Vacas Heladas Formation (11 to 12.7 Ma). A single 7.8 Ma dacite dike, the only igneous rock roughly coeval with the mineralization in the district, is reported from Pascua (Bissig, 2001). Rhyolitic tuffs of the Vallecito Formation (5.5-6.2 Ma) are restricted to the Valle del Cura (Ramos et al., 1989) and some occurrences in the wider El Indio-Tambo area. Volcanism finally ceased in the Upper

Pliocene after the eruption of the 2 Ma Cerro de Vidrio rhyolite dome in the NE of the belt (Bissig, 2001).

In the immediate Pascua area, the geology is dominated by intrusive rocks of the Pastos Blancos group (Upper Paleozoic to Lower Jurassic) that outcrop to the north of Brecha Central and the Frontera zone. The intrusions are largely fine- to coarse-grained porphyritic granites and small stocks of dacite porphyry and granodiorite. Crystal and pumice tuffs of mostly dacitic composition and of probable Paleozoic age occur on the western edge of the Esperanza zone. Dacitic tuffs of Vacas Heladas age (11 to 12.7 Ma) are also recognized in the eastern part of the property (Sector Morro). Both the extrusive and intrusive units are intruded by small stocks of Bocatoma-age (36-30 Ma) hornblende-biotite diorite and various small dikes of andesitic to rhyolitic composition.

The Pascua-Lama deposit occurs roughly at the intersection of two structural corridors; the E-SE oriented Pascua corridor and the N-NE oriented Pedro corridor (Hamilton, 1998). Numerous pre- or syn-mineral breccias are sited on, and are elongate parallel to, ESE fractures of the Pascua system. The largest of these is Brecha Central, which is a polymictic, matrix-supported breccia. Breccia fragments are typically altered to a quartz-alunite assemblage and the matrix is composed exclusively of alunite and pyrite-enargite. Other matrix- and clast-supported breccias occur east of Brecha Central in the Penelope area in Argentina, and also further SW in the Esperanza area. The character and geometry of the breccias suggest that they are phreatomagmatic in origin, although a few post-mineral breccias of magmatic origin are also present. Structural indicators suggest that breccias were emplaced during a period of extension that is related to local intrusive activity and the development of small-scale horst–graben structures and block faults in the Pascua area (Hamilton, 1998). Down-dropped blocks in between the Quebrada de Pedro and Quebrada de Pascua systems contain late volcaniclastic and lacustrine sequences of probable Vacas Heladas age that are not preserved elsewhere (Nixon, 1998). There is also a suggestion that normal movement along the Pedro fault system has down-dropped the area west of this zone.

MINERALIZATION

There are two principal styles of Au (and Cu ± Ag) mineralization in the Brecha Central and Frontera areas. Alunite-pyrite-enargite (APE) mineralization is concentrated in the matrix of the phreatic breccias and as banded alunite-sulfide veins and minor disseminations in a

surrounding stockwork zone (Fig 2.3). Pyrite-szomolnokite (PZ) mineralization is characterized by pyrite and szomolnokite ($FeSO_4 \cdot H_2O$) in strongly silicified, partly leached alteration zones.

The APE mineralizing event is the largest in terms of volume. It consists of alunite, enargite, and pyrite in various amounts. Barite is common and occurs as individual grains and massive aggregates. Native sulfur occurs with alunite and enargite-pyrite in the matrix of Brecha Central but is rarely observed in the banded veins. Accessory minerals include diaspore, anglesite, pyrophyllite, stibnite, cassiterite, goldfieldite, covellite, galena, and trace chalcopyrite. Gold occurs primarily as native gold and calaverite ($AuTe_2$) as inclusions in enargite, rarely in pyrite or alunite, and occasionally in fractures cross-cutting sulfide grains. Minor 'electrum' also occurs as inclusions in both pyrite and enargite. APE-type mineralization occurs primarily in the deeper parts of the deposit, typically between about 4450-4700 m (all elevations are reported as metres above sea level), and below PZ mineralization. Average Au grades are about 1.2-2 g/t Au (values vary slightly between Brecha Central and stockwork samples). APE ore also contains some of the highest Au and Cu grades – up to 20 g/t and 2% respectively.

The PZ style of mineralization is distributed above and lateral to the APE assemblage. Mean Au grades in the PZ zone (2.1 g/t) are slightly higher than APE grades, and Cu contents average 0.2%. Copper is attributed to minor enargite that is commonly partly replaced by arsenolite or szomolnokite. Other accessory minerals include anglesite, barite, and rare covellite, gypsum, voltaite, and paracoquimbite. Gold and silver are thought to occur as sub-microscopic inclusions in pyrite and enargite.

A third style of gold mineralization (which is equivalent to silica-gold mineralizing facies of Chouinard and Williams-Jones, 1999) is concentrated in the Esperanza area. Occurrences are also present locally in the Brecha Central and Frontera zones, usually above PZ-type mineralization. Gold occurs almost exclusively in native form associated with selective to massive silicic alteration. Jarosite, alunite, barite, and scorodite are common but sulfides are rare to absent (Caceres et al., 1997). Trace electrum and Ag-Cu sulfosalts occur locally. Gold grades average about 1.2 g/t (in Brecha Central) and Cu mineralization is insignificant. The timing of mineralization in the Esperanza zone is unclear but is thought to be roughly contemporaneous with the main Au events in the district. The occurrence of visible gold as fine coatings on oxidized fracture surfaces at Esperanza also suggests supergene remobilization of the primary mineralizing assemblage.

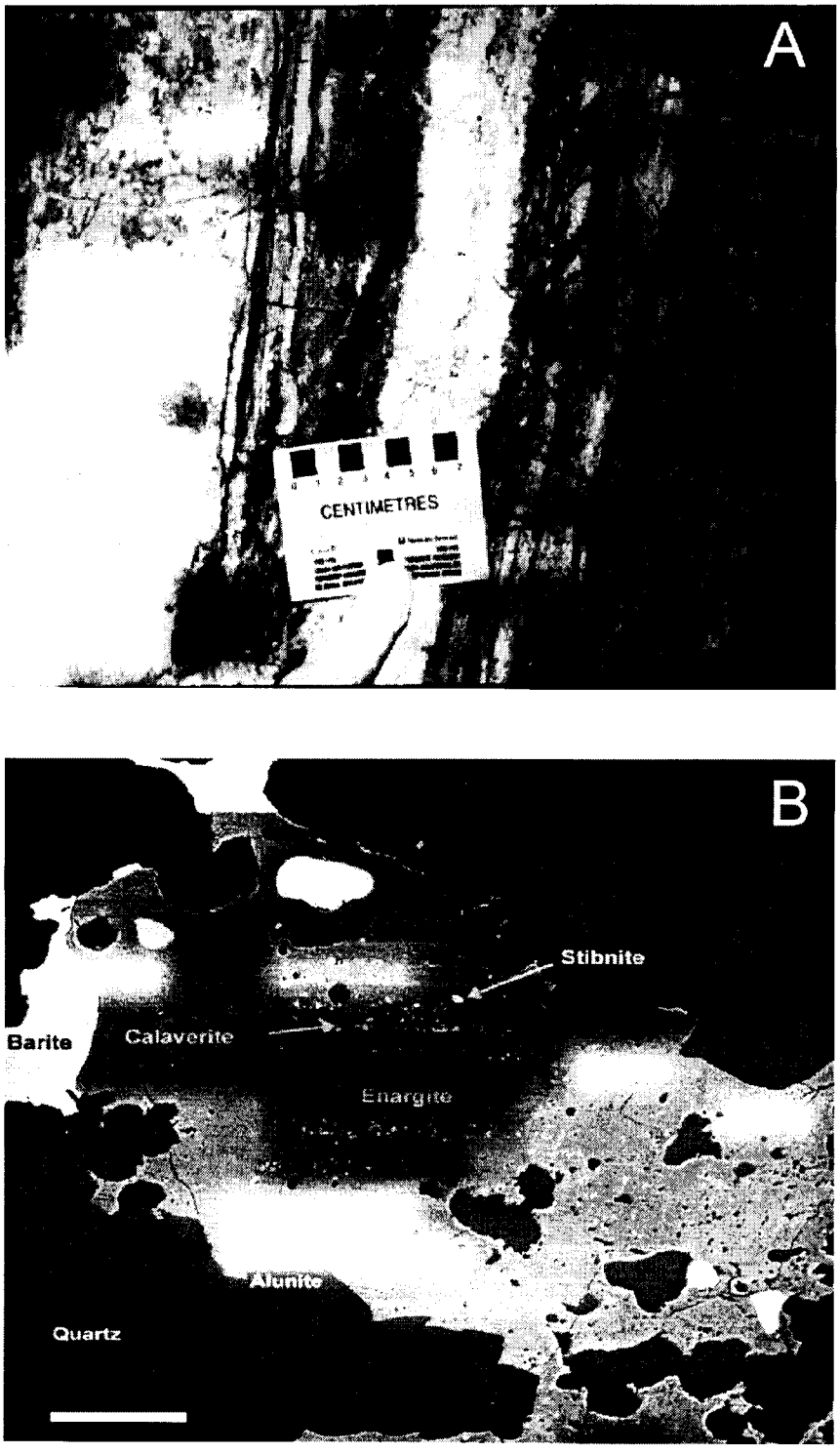

Figure 2.3. Examples of APE mineralization.
(A) Banded alunite-pyrite-enargite veins in silicified and AS I altered-wall rock. Alunite = white bands, sulfides = dark bands. Maria Tunnel.
(B) SEM backscatter image of the AS II assemblage. Enargite has inclusions of calaverite ($AuTe_2$) and one inclusion of stibnite (Sb_2S_3), and is intergrown with alunite, barite, and quartz. Alex Tunnel. Scale bar = 100 μm. *Photo courtesy of A. Chouinard.*

Silver is concentrated in the upper parts of the Brecha Central and Frontera zones, as black Ag-rich veinlets and disseminations in silicified alteration zones. This assemblage consists of fine-grained native silver, electrum, native selenium, iodargyrite (AgI), chlorargyrite (AgCl), and barite. Accessory phases include jarosite, galena, aguilarite (Ag_4SeS), native gold, and tiemannite (HgSe). Silver-enriched zones are typically found above and/or slightly offset from the zones of highest Au and Cu concentrations and overprints both APE and PZ-type mineralization.

ALTERATION: CHARACTERISTICS AND DISTRIBUTION

Alteration is widespread in the Pascua district, occurring in an area of approximately 15 km^2. Alteration types identified on the property include intense acid sulfate and silicic assemblages with peripheral argillic and propylitic alteration. Deep quartz-muscovite alteration has been described in early company reports (R. Guerra, pers. comm.) but was not observed over the course of this study. Alteration is typically pervasive and texturally destructive, making it difficult to identify original rock types and controls on the distribution of alteration. The relations between assemblages are complex and subtle changes in mineralogy, particularly when clay and sericitic minerals are present, are not easily identified in the field.

Methods of identification

An extensive study was initiated in 1998 to refine pre-existing alteration maps and to provide detailed information regarding the distribution of specific alteration minerals. Alunite is of particular interest because it is directly associated with the APE and silica-gold styles of mineralization. Samples were selected from surface and underground exposures, drill core, and reverse-circulation drillholes (RDH). The character and mineralogy of the assemblages were determined by systematic short-wave infrared spectroscopy (SWIR) techniques, with supplemental petrography and X-ray diffraction. Samples for SWIR analysis were taken every 10-20 m from the Alex Tunnel and from selected drill core along cross-sections CA-EW, and CA-00. Several drill holes located approximately within the 4680 m level were also sampled to supplement the Alex Tunnel data. All analyses were made using a Portable Infrared Mineral Analyzer (PIMA) - a field portable spectrometer that measures reflectance spectra in the SWIR band. Spectra were analyzed using PIMAView 3.0 software. Mineral identification is made by comparison of wavelength positions, intensity and shape of absorption troughs, and the overall

shape of the spectrum in comparison to standards in the SPECMIN database (e.g., Thompson et al., 1999). PIMA samples were carefully selected to minimize intergrown sulfides and surficial sulfate or alunogen material that can obscure the SWIR spectra (Thompson et al., 1999). Abundant jarosite was also avoided during sampling because its strong spectral response can conceal the presence of other, less abundant, minerals.

Alteration Types

1. Acid Sulfate Alteration

a) Early Acid Sulfate (AS I)

The earliest recognized alunite-bearing alteration in the Pascua area is characterized by fine-grained intergrowths of alunite ± quartz, clays (kaolinite-dickite-pyrophyllite) and pyrite. This stage of alteration formed prior to brecciation and is superimposed by the main mineralizing event (Chouinard and Williams-Jones, 1999). The assemblage is widespread and extends from surface to the maximum depth investigated by drilling (*ca.* 4100 m).

AS I alteration occurs as aggregates that replaced feldspar phenocrysts, as disseminations in the wallrock matrix, and rarely as irregular alunite veinlets and stringers (Fig. 2.4a). Only primary quartz phenocrysts and rare rutile remain from the original wallrock. Alunite is the main constituent of the assemblage and comprises 10 to 40 volume percent of the altered rocks. Alunite is white, cream, yellow, or pink and forms lath-like, elongate tabular or anhedral crystals 25 to 200 μm in length. Fine to medium-grained bladed alunite crystals also infill vugs within a silicified matrix that appear to have formed from the complete dissolution of feldspars or tuff fragments. Rare inclusions of alumino-phospho-sulfate (APS) minerals are present.

AS I accessory minerals include pyrite, diaspore, and zunyite. Pyrite occurs as a minor to trace constituent interstitial to, or as inclusions in, alunite. Locally, small vugs in alunite appear to have resulted from the leaching of pyrite grains. Zunyite occurs exclusively at depths greater than 4500 m and only where pyrophyllite is present. Diaspore is slightly more abundant than zunyite and occurs as clusters of subequant grains, locally as inclusions in alunite. Diaspore also occurs in the deeper parts of the deposit, below about 4550 m.

AS I alteration is overprinted by at least one silicification event ("silicification selectiva"; Chouinard and Williams-Jones, 1999). This event is characterized by fine-grained,

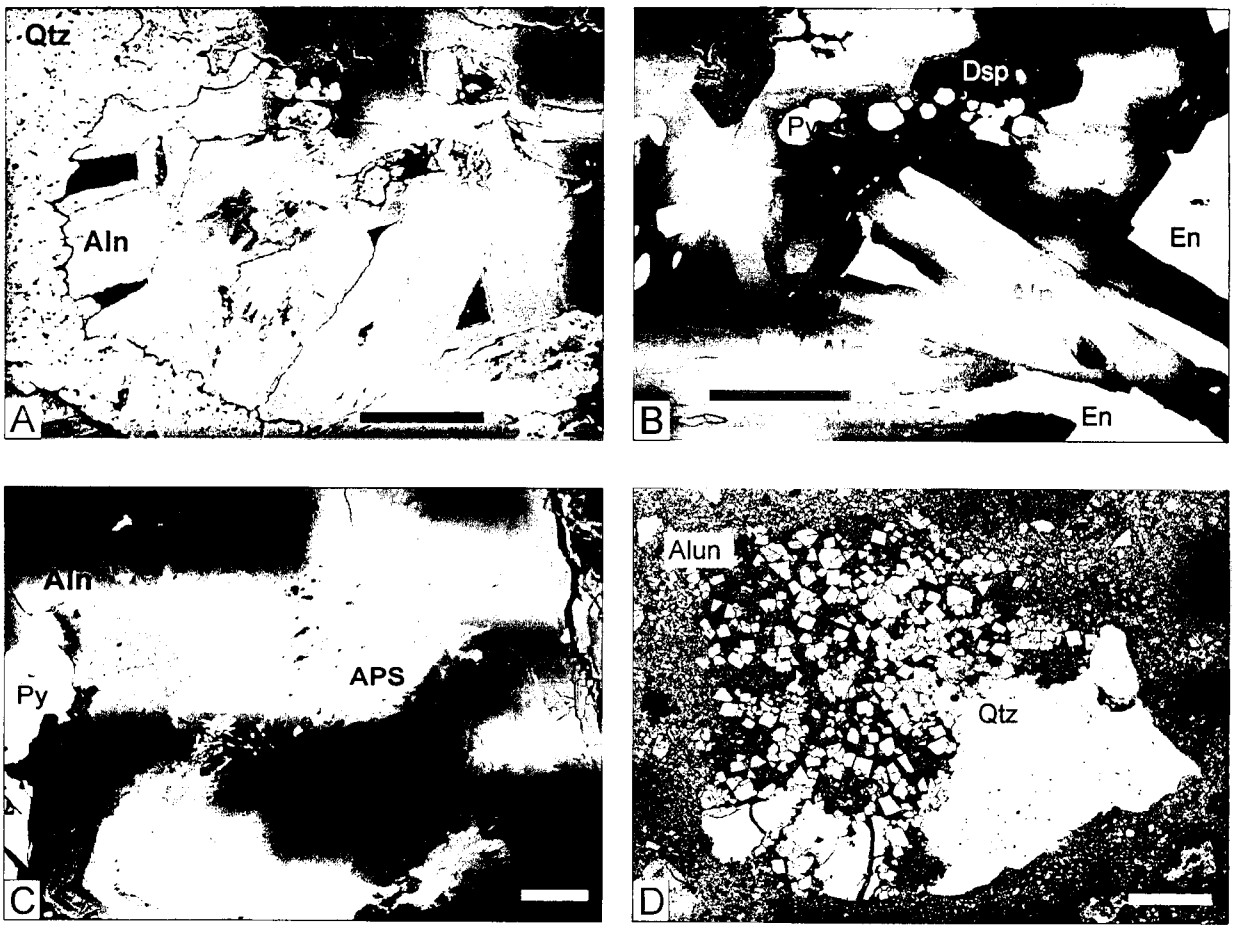

Figure 2.4.

(A) SEM backscatter image showing irregular APS grains (bright zones) in cores of AS I alunite. DDH-116, 289m. Scale bar = 25 μm.

(B) SEM backscatter image of AS II alteration with K-rich (light) and Na-rich (dark) alunite associated with diaspore, pyrite, and enargite. Lama DDH-05, 337m. Scale bar = 50 μm.

(C) SEM backscatter image of REE-bearing APS inclusions in AS II alunite. DDH-111, 189.85m. Scale bar = 20 μm

(D) SEM backscatter image of steam heated alteration from near-surface above the Frontera Zone. DDH-119, 47m. Scale bar = 200 μm.

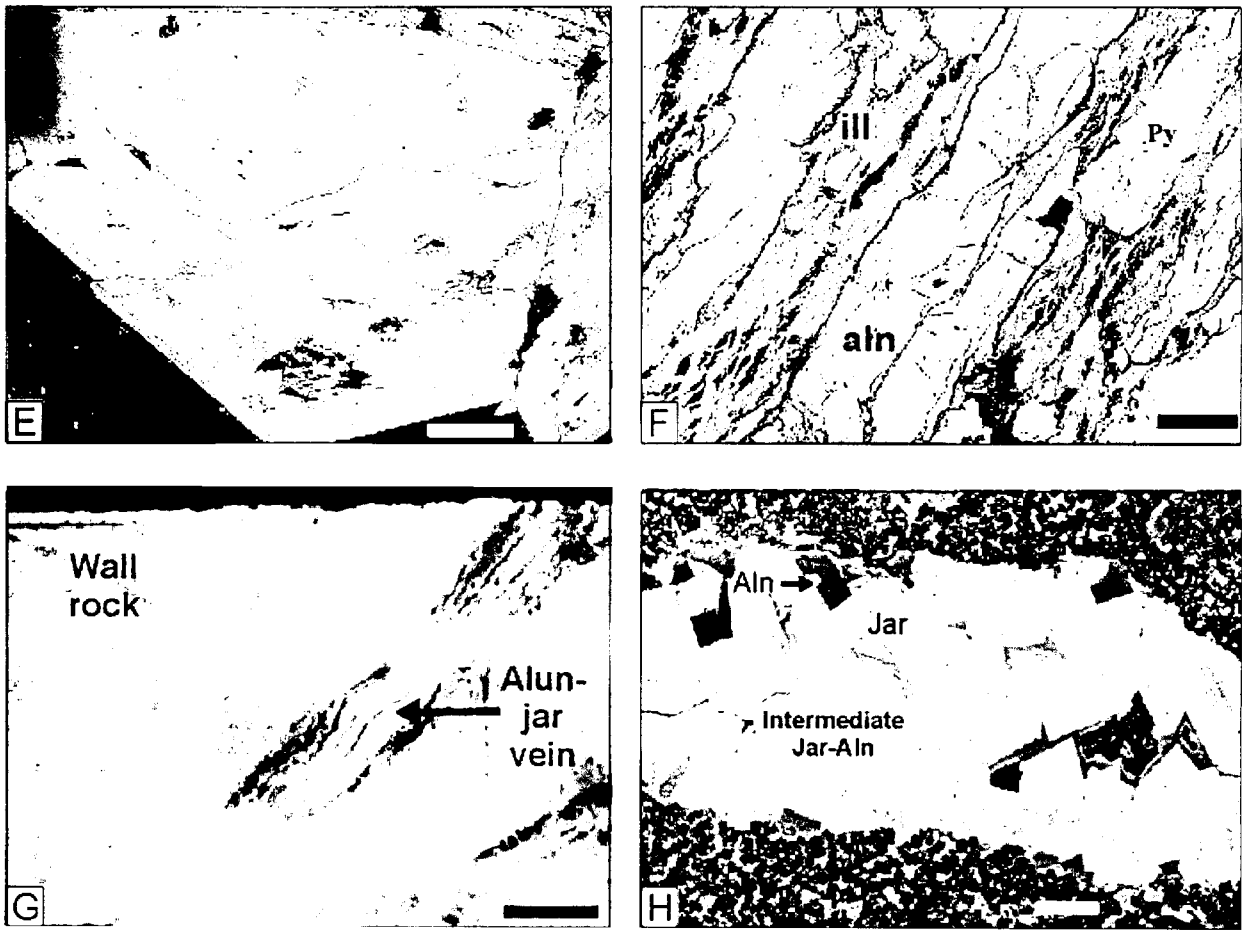

Figure 2.4. (Continued)

(E) SEM backscatter image showing oscillatory PO_4 ± Sr zoning (light bands) in coarse-grained AS III alunite (sample PS-26c). Scale bar = 100 μm.

(F) SEM backscatter image of fine-grained illite (ill) cross-cutting and replacing AS I alunite (alun). DDH-111, 120m. Scale bar = 50 μm.

(G) Alunite ± jarosite late stage veinlets cross-cutting AS I altered wall rock. DDH-057, 154m. Scale bar = 1 cm.

(H) SEM backscatter image showing supergene alunite, jarosite and intermediate alunite-jarosite solid solution Sample PM-33, Alex Tunnel. Scale bar = 20 μm.

granular quartz that locally dominates over the acid sulfate assemblage. Locally, alunite is also replaced by pyrophyllite, dickite, or fine-grained illite (see discussion below). Trace to significant amounts of jarosite also overprint the AS I assemblage. All jarosite is late and occurs exclusively in open spaces in the rock matrix, overprinting alunite, and as small cross-cutting veinlets.

b) *Acid Sulfate II (AS II)*

A second stage of alunite is coeval with APE-type mineralization. As noted above, this event is characterized by alunite-pyrite-enargite deposition as disseminations and open-space fill in the Brecha Central area, and as banded alunite-sulfide veins in the surrounding stockwork zone. Locally, alunite and sulfides are intimately intergrown, particularly in underground exposures in the Maria Tunnel, with smooth grain boundaries. Narrow silicified alteration halos surround the banded veins and indicate that AS II fluids interacted with the surrounding wallrock. This interaction was of limited extent (Chouinard and Williams-Jones, 1999) and it has not been possible to determine the effect of the AS II event on previously AS I-altered rock by observation and petrography alone. For this reason, the following descriptions are limited to matrix and vein alunite clearly associated with APE sulfides.

AS II alunite occurs as coarse-grained clusters and rosettes in open vugs of the breccia matrix and as densely intergrown euhedral crystals in the banded veins. Grains are typically tabular to bladed, ranging from 30 μm to >2 cm in length. Colours range from white to grey to pink. Barite inclusions are common and occur along growth planes in coarse alunite crystals. Trace inclusions of pyrite, enargite, galena, anglesite, APS (Fig. 2.4c), and rare diaspore are also present (Fig. 2.4b). Native sulfur occurs intergrown with alunite and sulfides in the matrix of Brecha Central. Farther east in the Frontera zone, massive alunite-enargite-pyrite veins occur with accessory pyrophyllite and diaspore (Fig. 2.4b). In this zone, two phases of alunite are identifiable, with K-dominant tabular alunite grains overgrown and cemented by a more Na-rich alunite. Both varieties are intergrown with the AS II sulfides and are considered to be part of the same event. In the Esperanza area, the absence of sulfides makes it difficult to distinguish between acid sulfate alteration events. However, larger vugs and open space in breccia matrices are filled with coarse, white to cream, bladed alunite crystals up to 1 cm long that texturally and chemically resemble the AS II alunite identified in the Brecha Central and Frontera zones.

Vertical zonation in the AS II assemblage is difficult to determine because of limited

drill-core data above the 4680 level. A near-surface vein assemblage of alunite-gypsum ± native sulphur cross-cuts AS I alteration above Brecha Central. This assemblage is thought to represent the shallow (i.e., low temperature) equivalent of the banded alunite-sulfide veins, but paragenetic relationships are unclear.

c) Surficial Alteration Blanket

A third acid sulfate assemblage occurs at or near the present-day surface and consists of silica minerals (cristobalite) ± kaolinite, alunite, and native sulfur. Alteration forms a blanket-like zone at elevations greater than approximately 4900 m and locally penetrates to greater depths along structures. Alteration is typically pervasive and commonly occurs as powdery, friable masses. Although original textures are rarely preserved, locally the rocks have been affected only by strong leaching, leaving a residual vuggy quartz rock with discernable porphyritic textures. Minor opaline silica intermixed with fine-grained quartz also occurs in irregular patches near the base of the alteration zone. The mineralogy, texture, and distribution of this assemblage are consistent with the steam-heated environment (e.g., Schoen et al., 1974).

Alunite is a minor constituent in the surficial blanket assemblage. Alteration is locally zoned with an upper layer of residual or vuggy quartz (cristobalite) that grades downwards into a kaolinite and/or alunite-bearing zone. Where present, alunite occurs in irregular patches and disseminations in veinlets and open spaces. It is extremely fine-grained (< 5 μm) and forms pseudo-cubic, tabular, and anhedral crystals that appear as grey, irregular masses in thin section (Fig. 2.4d). Fine-grained jarosite occurs locally as overgrowths on alunite and linings of open vugs.

d) Near-surface, Open-space Fill Alunite (AS III)

A third stage of alunite deposition occurs in isolated surface exposures of coarse vug- and matrix-fill alunite above the Alex Tunnel. The alunite is medium- to coarse-grained, clear to golden yellow, and occurs as a lining in vugs in the matrix of the surficial breccia (Fig. 2.4e). Rare inclusions of barite and jarosite are present. Similar occurrences are noted as coarse vein and vug-fill alunite that cross-cuts AS I alteration in several near-surface drillholes, but the relationship of this event to AS II and steam-heated alteration is unclear.

e) Late-stage alunite (± jarosite) veins

A late-stage of alunite occurs as veins, veinlets and local disseminations throughout the Pascua district. Jarosite is commonly associated with alunite but is always late. Accessory quartz is present locally. Alteration may occur in a fine-grained, granular to powdery assemblage, forming cryptocrystalline, hard lenses and veins, or as medium- to coarse-grained, euhedral veins (Fig. 2.4g). Local euhedral tabular crystals line veins and cavities. Veins are white to yellow to orange-brown, depending on the amount of jarosite present. Alunite is commonly fine- to medium-grained with tabular to anhedral crystals locally intermixed with silica. A pseudo-cubic crystal habit is observed in some finer-grained (<5 μm) samples. Cross-cutting relations indicate that this stage of alteration post-dates both the AS I and AS II events.

f) Supergene jarosite (± alunite)

As noted, jarosite is present as a late mineral in association with acid sulfate, silicic, and argillic alteration assemblages. It occurs interstitial to alunite, quartz, and illite as fine-grained disseminations, granular crystals in vugs and open spaces, and locally as veinlets that dissect alunite grains or cross-cut AS I and argillic alteration. The distribution of jarosite is strongly fault and fracture controlled and extends to the maximum depths investigated by drilling (about 4100 m). Accessory hematite is present locally. Alunite rarely occurs intergrown with supergene jarosite, in thin veinlets and fine-grained aggregates in the rock matrix. The two cannot be distinguished in thin section but SEM-EDS analysis shows pseudo-cubic alunite grains (<5 μm) overgrown by successive bands of jarosite and compositional zones intermediate to alunite-jarosite end-members (Fig. 2.4h).

2. Silicic Alteration and Silicification

At least four different silicification events can be distinguished on the basis of mineral associations and paragenetic relations. The terminology provided in parentheses is from Chouinard and Williams-Jones (1999). Minor vuggy silica (Vuggy Silica I) and locally massive, grey silicification (Silicification I) pre-date the emplacement of Brecha Central, on the basis of the presence of grey, densely silicified and locally strongly leached, vuggy silica fragments in the breccia. Most silicification occurred post-Brecha Central, however, and is contemporaneous with silica-gold-, pyrite-, and pyrite-szomolnokite –type mineralization. This stage of alteration includes the patchy development of vuggy silica (Vuggy Silica II) in which

primary feldspars and mafic minerals are partly to completely leached. Primary quartz phenocrysts are typically preserved, and the groundmass is completely replaced by fine-grained granular quartz. Rutile occurs as tiny clusters along grain margins of the original quartz grains, but there is also evidence for the local redistribution and remobilization of Ti during this event (Chouinard and Williams-Jones, 1999). Silicic II alteration also formed post-Brecha Central and comprises massively silicified rocks, selectively silicified, partly leached rocks, and localized silica stockwork and veins. The white to grey-coloured silica alteration consists of massive, fine-grained quartz commonly with later syn-ore minerals (e.g. pyrite, enargite, szomolnokite) that infill leached vugs and cavities.

3. Argillic Alteration

Argillic alteration is characterized by kaolinite, quartz ± illite, montmorillonite, interlayered illite-smectite, and rare gypsum and dickite. Feldspars are partly to completely replaced by fine-grained, platy masses of clay minerals that can only be differentiated by XRD or SWIR analysis. Accessory pyrite and late jarosite occur interstitially to kaolinite-illite. Alteration is typically pervasive, although original granitic textures are locally visible.

Argillic alteration is typically gradational to acid sulfate and propylitic assemblages at the lateral margins of the Brecha Central and Frontera zones. Illite (± kaolinite and quartz) also locally cross-cuts and overprints AS I alteration in close proximity to Brecha Central (e.g., "illite overprint" in Chouinard and Williams-Jones, 1999). Some fragments in Brecha Central also contain illite. This alteration is rarely recognizable in hand specimen, but petrographic and SEM-EDS analyses show that illite corroded and replaced AS I alunite grains (Fig. 2.4f). Observations suggest that the alteration occurred following the AS I event but before brecciation and mineralization. The distribution of this assemblage is not well-constrained and it is unclear how, or if, it relates to the widespread argillic alteration assemblage.

4. Propylitic Alteration

A weak alteration assemblage of chlorite ± kaolinite, gypsum, pyrite, and illite with rare epidote and smectite occurs peripheral to the zones of intense alteration and the major breccia and vein systems in the Pascua-Lama area. Typically, feldspars, biotite, or hornblende are partly to completely replaced by fine-grained masses of sericite (kaolinite-illite-smectite), chlorite, and minor Ti-oxide. Minor patches and disseminations of epidote are common. Rare

fine-grained pyrite occurs as clusters and disseminations in the rock matrix. Seams of kaolinite-illite, gypsum, and patchy limonite-hematite locally cross-cut the propylitic assemblage.

Distribution of Alteration

The distribution of alteration assemblages is illustrated at surface (Fig. 2.2) and in two cross-sections; CA-EW (Fig. 2.5) and CA-00 (Fig. 2.6). Section CA-EW is oriented nearly E-W and extends from Esperanza to the Frontera zone. Section CA-00 is oriented roughly orthogonal to CA-EW and transects both high-grade Au and Cu mineralization in Brecha Central and relatively weakly altered rocks to the north and south. Alteration maps were completed by systematic SWIR analyses from selected drill core and RC chips (individual data points shown; Figs. 2.6 to 2.8) and by extrapolating drill core logs from other holes on section (not shown). Only certain alteration assemblages are mapable at the scale of these diagrams. Due to the difficulties in separating the AS I and AS II assemblages, the two are combined as 'Acid Sulfate Alteration' for the purposes of this compilation. Most of the alteration is presumed to have formed during the earlier event, due to the consistency in style and mineralogy of the assemblage. Likewise, individual silicification events are also not differentiated and are grouped as one unit.

Results from this study illustrate differences in the styles of alteration between the Esperanza and Brecha Central/Frontera zones. At Esperanza, silicic alteration is prevalent at and near surface and is underlain by extensive acid sulfate alteration (Fig. 2.7). Kaolinite is the most common clay mineral associated with the acid sulfate assemblage. Dickite and pyrophyllite occur locally. A small siliceous knob composed mostly of opaline silica outcrops at the top of the Esperanza zone. This may represent silica precipitation at the water table coincident with the base of an eroded steam-heated zone (e.g., Schoen et al., 1974). Isolated occurrences of argillic alteration, intermixed with patchy chlorite-bearing propylitic alteration (not shown) occur at the base of the silicic zone. This assemblage is largely hosted in a small stock of diorite and, on the basis of sparse drill core data, does not appear to extend into the surrounding granitic rocks. Jarosite is prevalent beneath the silicic alteration zone. Abundant veins and disseminations of jarosite ± alunite also cross-cut the silicic alteration zone but are too irregular to be shown at the scale of this diagram.

East of the Esperanza area, silicic alteration is present primarily as irregular pods or lens-like bodies at intermediate elevations (approximately 4700-4900 m) and is surrounded by

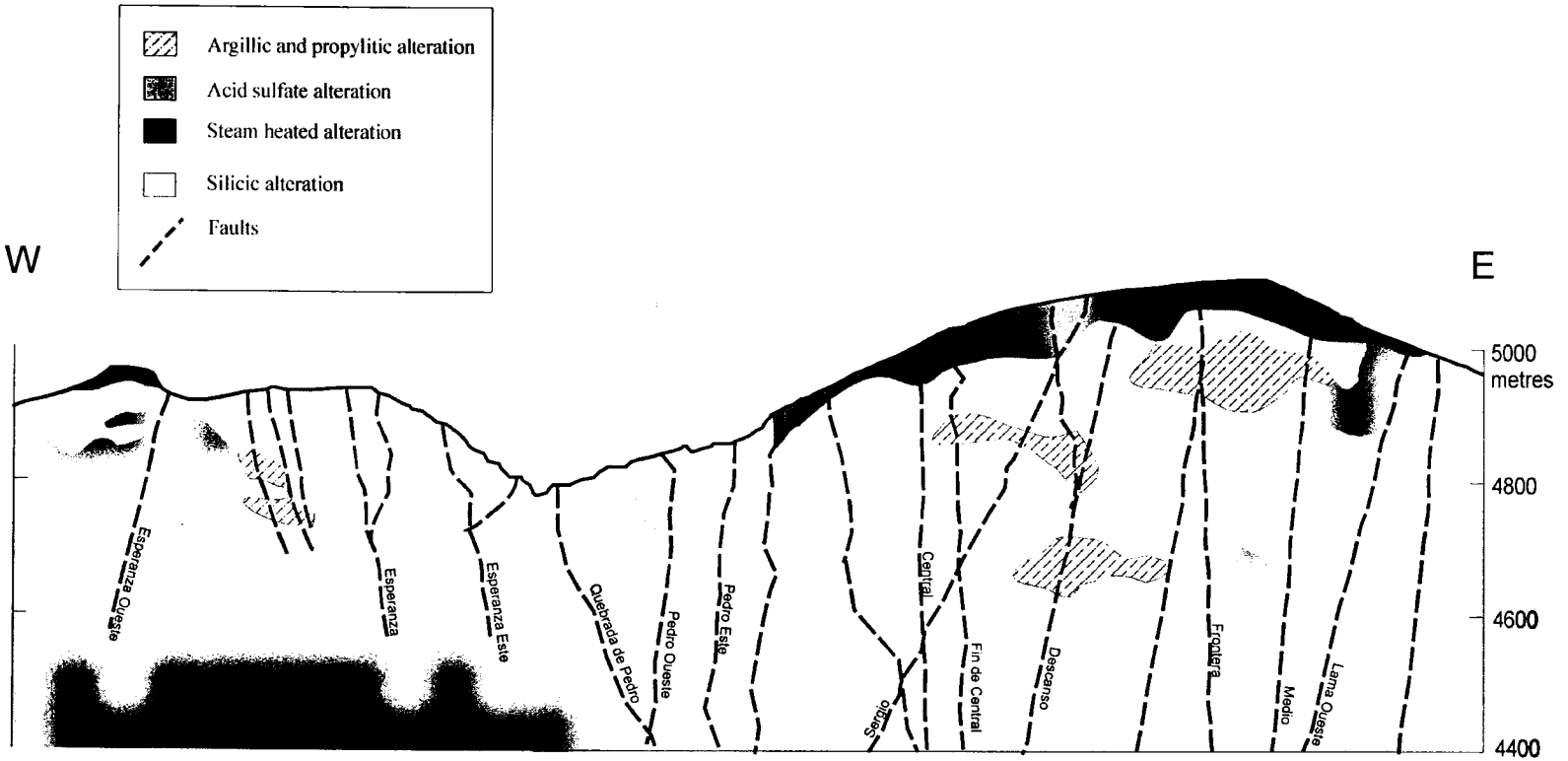

Figure 2.5. Section CA-EW showing distribution of alteration in Esperanza, Brecha Central, and Frontera zones. Mapping is based on systematic PIMA analyses (see Figures 2.7 and 2.8), drill core logging, and surface outcrops.

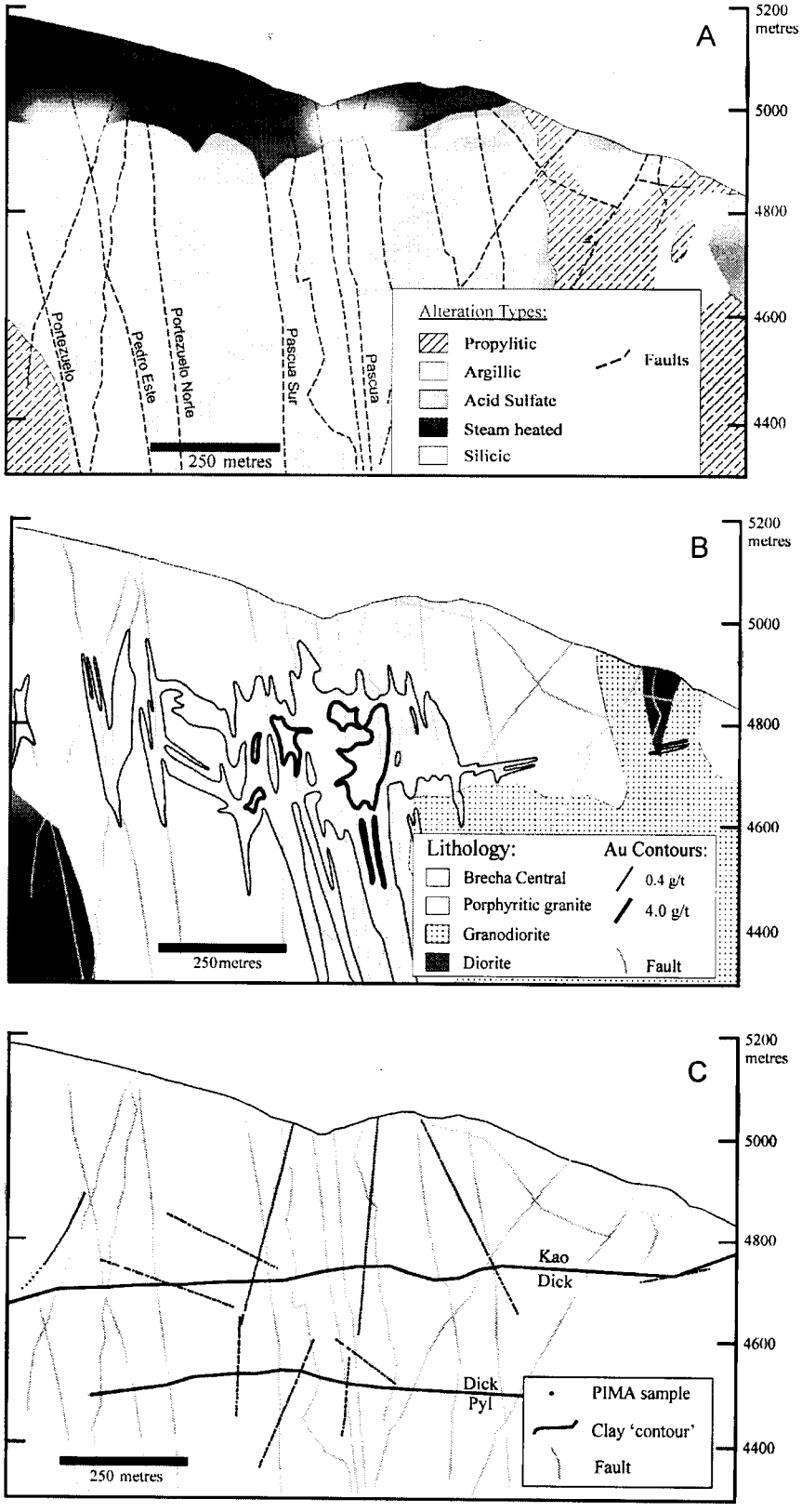

Figure 2.6. Section CA-00. (a) Distribution of alteration zones. Also shown are locations of major faults. (b) Major lithological units and distribution of Au mineralization. (c) Locations of PIMA sample points and distribution of dominant clay mineralogy.

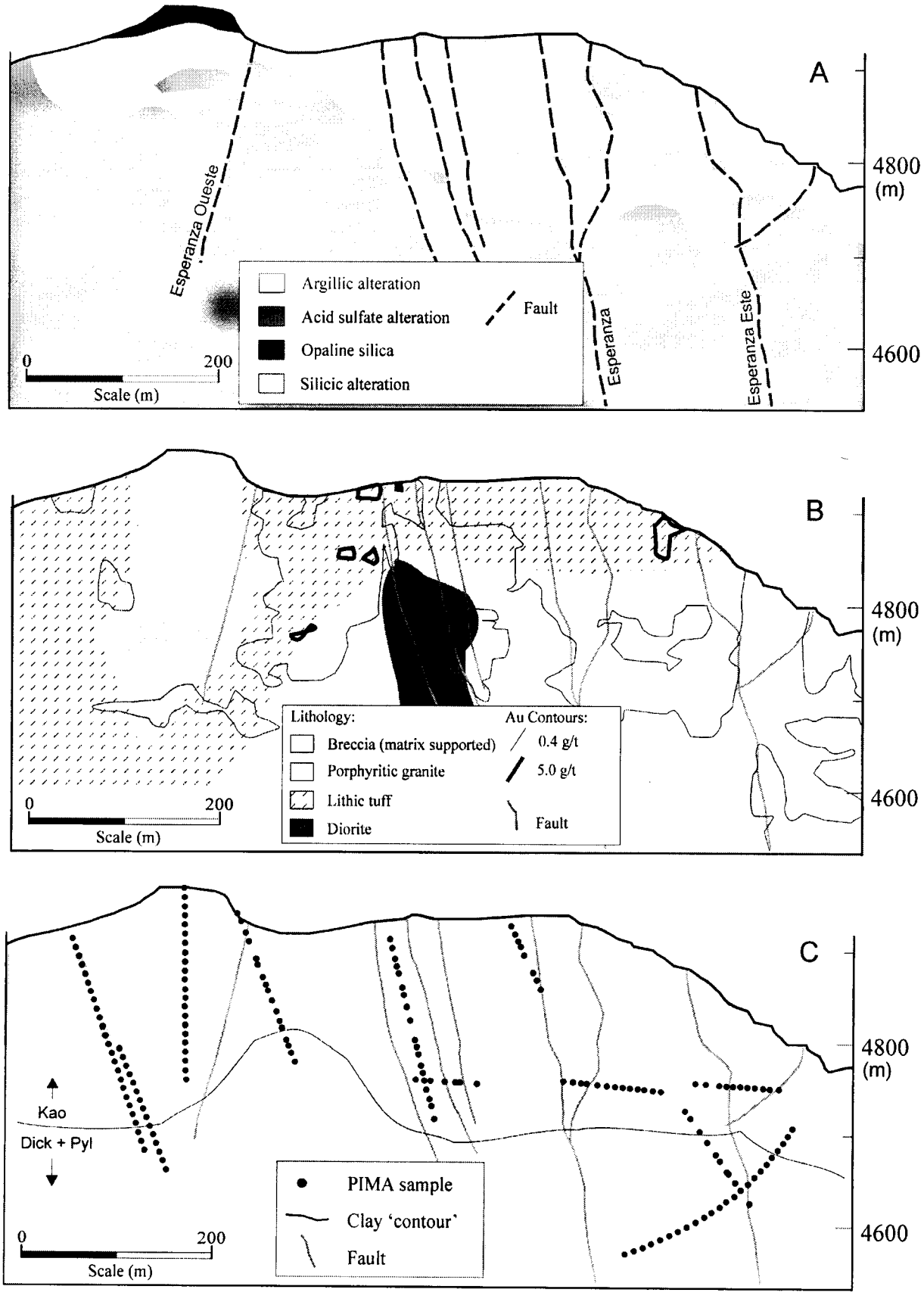

Figure 2.7. Detailed section of Esperanza area from section CA-EW. (a) Distribution of alteration zones. Also shown are locations of major faults. (b) Major lithological units and distribution of Au mineralization. (c) Locations of PIMA sample points and distribution of dominant clay mineralogy.

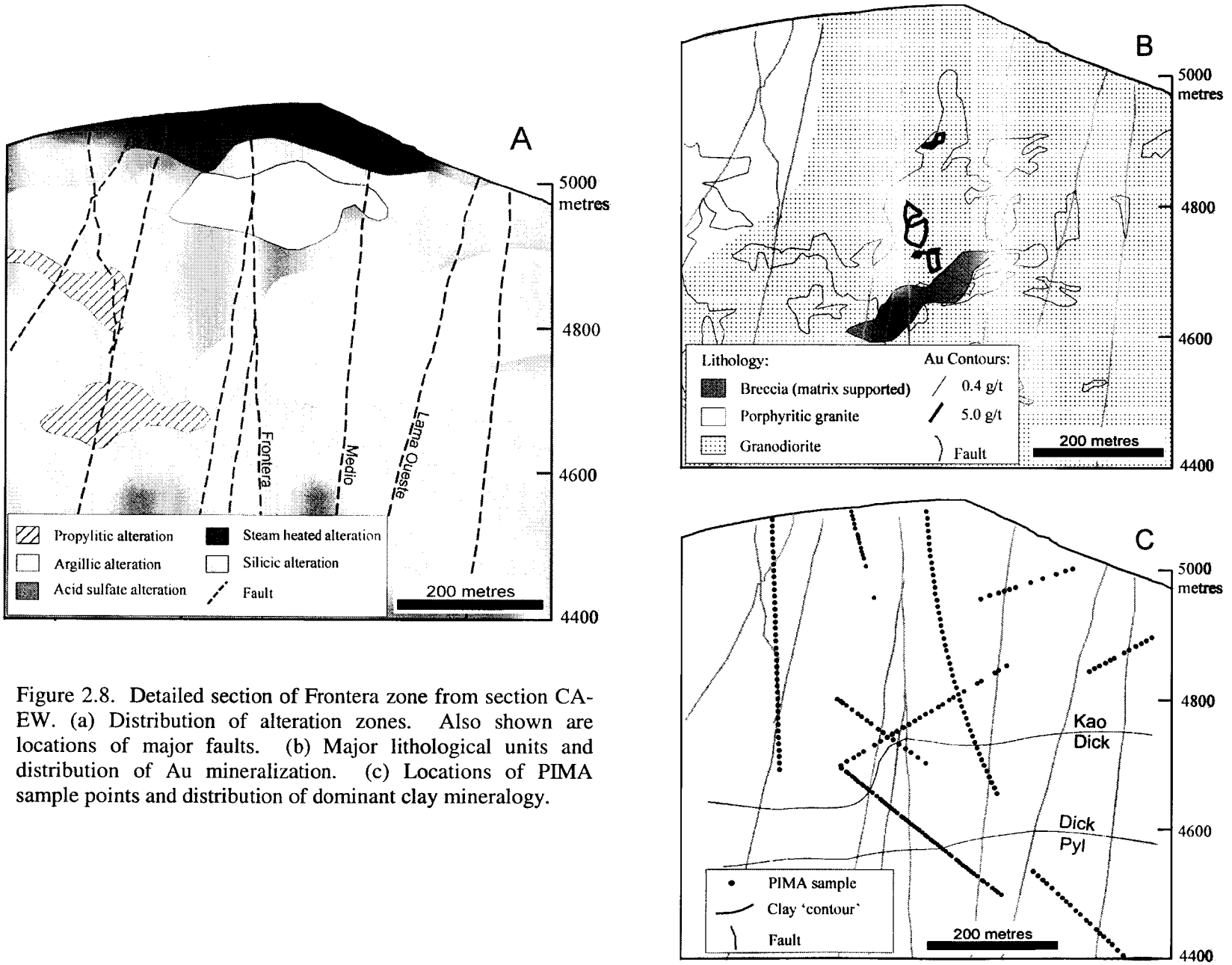

Figure 2.8. Detailed section of Frontera zone from section CA-EW. (a) Distribution of alteration zones. Also shown are locations of major faults. (b) Major lithological units and distribution of Au mineralization. (c) Locations of PIMA sample points and distribution of dominant clay mineralogy.

acid sulfate assemblages (Fig. 2.5, 2.6). Surficial blanket-type alteration occurs in an irregular, tabular zone that extends from surface to about 4900 m. Locally, this zone is underlain by kaolinite-rich argillic alteration and silicic assemblages (Fig. 2.8) that do not appear to be associated with the overlying steam-heated zone. Between the Central and Frontera faults, alteration is less intense, with irregular occurrences of kaolinite ± illite-bearing argillic alteration and the absence of significant silicic alteration. This area coincides with very low Au grades, and is hosted primarily in granodiorite with cross-cutting diorite dikes (not shown).

Alteration in and at the margins of Brecha Central (Fig. 2.6) is dominated by silicic and acid sulfate assemblages. To the north of the breccia, alteration grades outward to more widespread propylitic and illite/smectite-bearing argillic assemblages. Jarosite is generally restricted to granitic rocks at the margins of Brecha Central and is concentrated at intermediate to low elevations, peripheral to areas with the highest Au and Cu grades.

A strong vertical zonation in clay mineralogy associated with acid sulfate alteration is evident in both the Brecha Central and Frontera zones (Figs. 2.6, 2.8). Pyrophyllite occurs almost exclusively below about 4550 m. Dickite is dominant above this zone to about 4700 m. Kaolinite is most common at elevations above 4700 to 4750 m.

ALUNITE GEOCHEMISTRY

To evaluate the variability of alunite in each alteration assemblage, the chemical compositions of different stages of alunite were determined by analysis of individual alunite grains and sample composites. End-member alunite is represented by the formula $KAl_3(SO_4)_2(OH)_6$ but naturally occurring minerals of the alunite supergroup can show a wide range of chemical substitutions (e.g., Jambor, 1999). The most common substitution of Na for K defines the alunite-natroalunite solid solution. Other substitutions for K^+ may include Ca, Ba, Sr, REE (Ce, La), Pb, Ag, H_3O, and NH_4. Substitution of Fe^{3+} for Al^{3+} defines the alunite-jarosite solid solution and substitution of $(PO_4)^{2-}$ for $(SO_4)^{2-}$ forms APS minerals of the crandallite or beudantite groups (Table 2.1; Jambor, 1999; Stoffregen et al., 2000).

Analytical methods

Samples from each stage of alteration were classified on the basis of distribution, mineral associations, and paragenetic relations. These observations were supplemented by detailed petrographic study, and only samples clearly belonging to each alteration type were

used for further geochemical and isotope analyses. Alunite grain mounts and polished sections were analyzed by SEM-EDS and electron probe microanalysis (EPMA). EPMA data were collected on a fully-automated CAMECA SX-50 microprobe, operating in the wavelength-dispersion mode with the following operating conditions: excitation voltage, 15 kV; beam current, 10 nA; beam diameter, 15 μm; and total count time under 65 seconds. Analytical parameters were chosen to minimize beam damage caused by the volatilization of alkali elements (e.g., Petersen and Thompson, 1992). However, the large beam size results in poor representation of finer-grained samples (supergene and steam-heated alteration in particular) and thin oscillatory zones and/or growth bands. Details of analytical methods are given in Appendix A.

Based on petrographic and EPMA results, representative samples were selected for ICP-MS trace-metal and REE analysis (details Appendix A). Supergene alunite could not be adequately separated from intermixed jarosite ± quartz, but all other alunite types were analyzed. The purity of separates was verified by powder X-ray diffraction but trace amounts (≤10 %) of quartz or clays may be present.

Table 2.1. Selected minerals of the alunite-jarosite family.

Alunite-jarosite group	alunite	$KAl_3(SO_4)_2(OH)_6$
	natroalunite	$NaAl_3(SO_4)_2(OH)_6$
	minamiite	$(Na,K,Ca)_2Al_6(SO_4)_4(OH)_{12}$
	huangite	$CaAl_6(SO_4)_4(OH)_{12}$
	walthierite	$BaAl_6(SO_4)_4(OH)_{12}$
	jarosite	$KFe_3(SO_4)_2(OH)_6$
Beudantite group	svanbergite	$SrAl_3(PO_4)(SO_4)(OH)_6$
	woodhouseite	$CaAl_3(PO_4)(SO_4)(OH)_6$
Crandallite group	crandallite	$CaAl_3[(PO_3(O_{1/2}(OH)_{1/2}]_2(OH)_6$
	florencite-(Ce)	$CeAl_3(PO_4)_2(OH)_6$
	florencite-(La)	$LaAl_3(PO_4)_2(OH)_6$

Analytical results

EPMA and trace-element geochemical data for all stages of alunite are summarized in Table 2.2. Alunite K and Na data for all EPMA analyses collected during this study are plotted in Figure 2.9. REE data (Fig. 2.10) are normalized to a sample of unaltered basement granite from the Pascua area (sample 99thb139a, Colorado Unit; Table 2.3). Also shown in Figure 2.10 is the normalized REE composition of a dacite dike that is coeval with mineralization in the district (sample 99thb130b, Table 2.3).

Table 2.2a. Summary of EPMA data for all Pascua alunite samples, as atoms per formula unit (a.p.f.u.). The mean, standard deviation at 95% confidence level (2σ), and maximum and minimum values for each element are given. Data below detection limits (0.02 a.p.f.u. for Na; 0.01 a.p.f.u. for all other elements) are not shown. *n* = total number of analyses. Also given are the number of samples represented in each stage.

	AS I *n=351 (18 samples)*				**AS II** *n=316 (10 samples)*				**AS III** *n=31 (2 samples)*				**SH** *n=20 (2 samples)*				**LV** *n=36 (4 samples)*			
Element	Mean	2σ	Max	Min	Mean	2σ	Max	Min	Mean	2σ	Max	Min	Mean	2σ	Max	Min	Mean	2σ	Max	Min
K	0.89	0.27	1.03	0.29	0.86	0.32	1.05	0.06	0.96	0.07	1.00	0.85	0.90	0.17	0.99	0.69	1.00	0.04	1.03	0.96
Na	0.15	0.25	0.63	-	0.15	0.23	0.58	-	0.06	0.08	0.16	-	0.13	0.17	0.33	0.04	0.04	0.03	0.06	-
Ca	-	-	0.07	-	-	-	0.68	-	-	-	-	-	-	-	-	-	-	-	-	-
Ba	-	-	0.06	-	-	-	0.10	-	-	-	0.02	-	-	-	-	-	-	-	-	-
Sr	-	-	0.01	-	-	-	0.11	-	-	-	-	-	-	-	0.02	-	-	-	-	-
P	-	-	0.10	-	0.03	0.21	0.92	-	-	-	0.04	-	0.02	0.02	0.03	-	-	-	0.02	-
S	1.99	0.02	2.00	1.90	1.97	0.21	2.00	1.08	1.99	0.02	2.00	1.96	1.98	0.02	2.00	1.97	1.99	0.01	2.00	1.98
Fe	-	-	0.12	-	-	-	0.13	-	-	-	0.01	-	-	-	0.04	-	0.02	0.04	0.06	-
Al	3.08	0.11	3.23	3.03	3.05	0.13	3.22	2.92	3.03	0.08	3.19	2.97	3.15	0.12	3.26	3.02	3.11	0.09	3.19	3.03

Table 2.2b. Selected ICP-MS trace element and REE concentrations for bulk (~1 gram) alunite samples. Trace contaminants may be present. Data below detection limits (0.1 ppm for REE; 2 ppm for Zn) not shown. Estimates of precision, based on duplicate analyses, given in Appendix B.

	AS I *		AS II		AS III	Steam Heated		Late Stage Veins
Sample #:	*P09*	*P11*	*P06*	*P05*	*P32*	*P-SH*	*P15*	*P17*
P (ppm)	110	135	470	580	840	740	790	2260
Sr	41.4	187.3	878	137	615	1095	685	2400
Ba	220	230	6170	6120	1720	1140	1240	2180
Pb	340	554	696	2530	1765	688	128	3170
Sb	12.2	22.7	1	5	31	4	2	1.5
Ag	3.5	2.7	1.2	0.4	2.8	1.0	0.4	1.4
Cu	31	12	22	122	21	54	28	27
Bi	13.1	10.3	0.2	0.4	4.5	0.9	0.6	0.2
Zn	16	2	-	18	-	2	-	48
La	15	14.8	17.5	20	39	37.5	39	32
Ce	29.5	26.8	19.5	20	33	54.5	51.5	65
Pr	3.2	2.7	1.5	1.7	1.4	5.5	4.5	8.7
Nd	8.5	5.8	3.5	4	2	16.5	14	37
Sm	1	0.4	0.3	0.4	0.1	2	2.3	11.3
Eu	0.1	-	0.1	-	-	0.4	0.4	2.8
Gd	0.5	0.2	0.2	0.3	0.1	1.4	1.7	11.1
Tb	-	-	-	-	-	0.1	0.2	1.3
Dy	0.3	0.4	-	0.1	-	0.8	1	3.6
Ho	-	0.1	-	-	-	0.1	0.2	0.3
Er	0.1	0.7	-	-	-	0.6	0.6	0.3
Tm	-	0.1	-	-	-	0.1	-	-
Yb	0.2	1.6	-	-	-	0.9	0.8	0.3
Lu	-	0.4	-	-	-	0.1	0.1	-

* may contain up to 10% quartz.

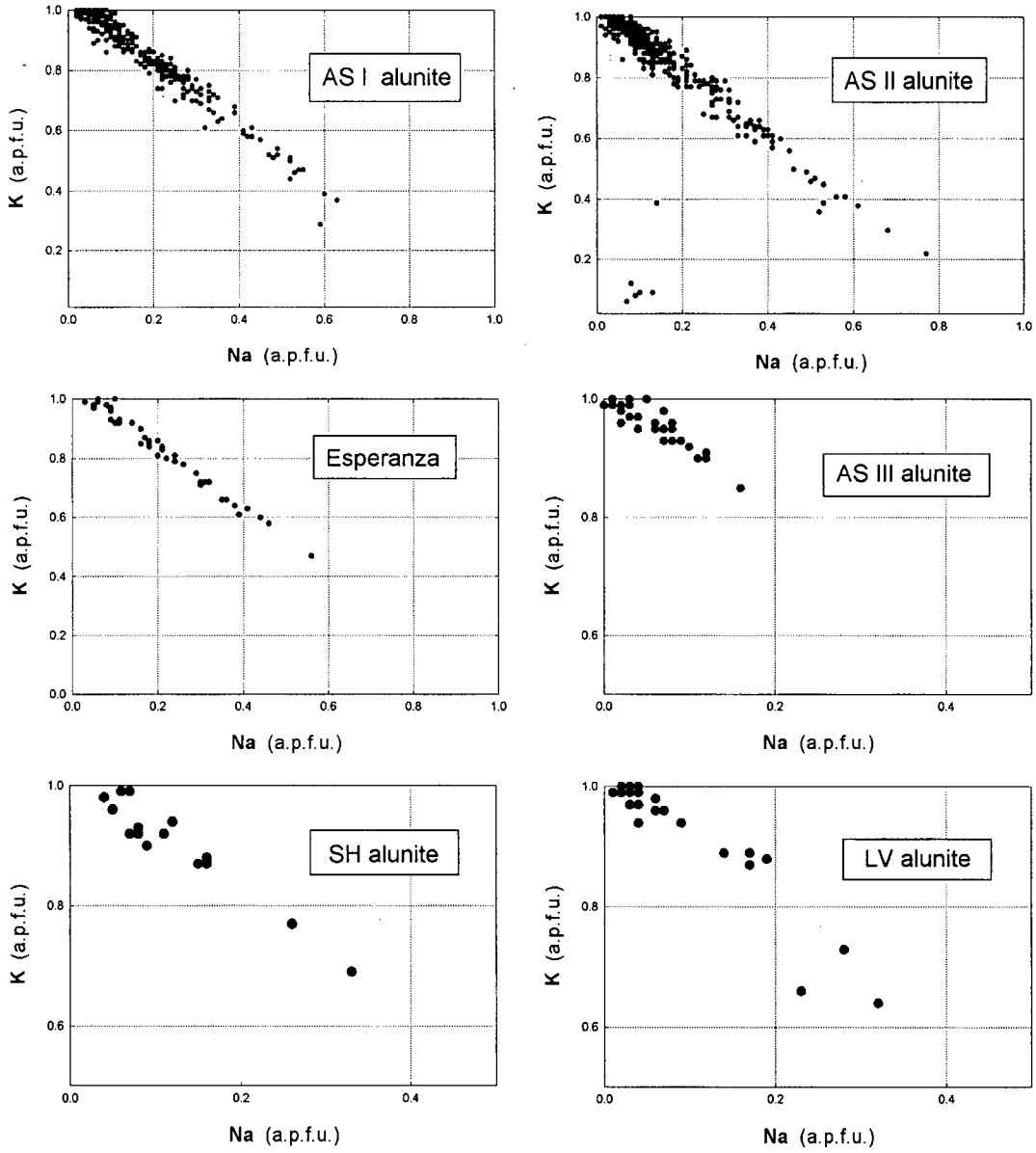

Figure 2.9. K versus Na contents for each stage of Pascua alunite based on EPMA results. Each point represents one analysis from a total of *m* samples for each stage: AS (m=18); AS II (m=10); Esperanza (m=3); AS III (m=2); steam heated (SH; m=2); and late vein (m=4). Data points below detection limits for K (0.01 a.p.f.u.) and Na (0.2 a.p.f.u.) not shown.

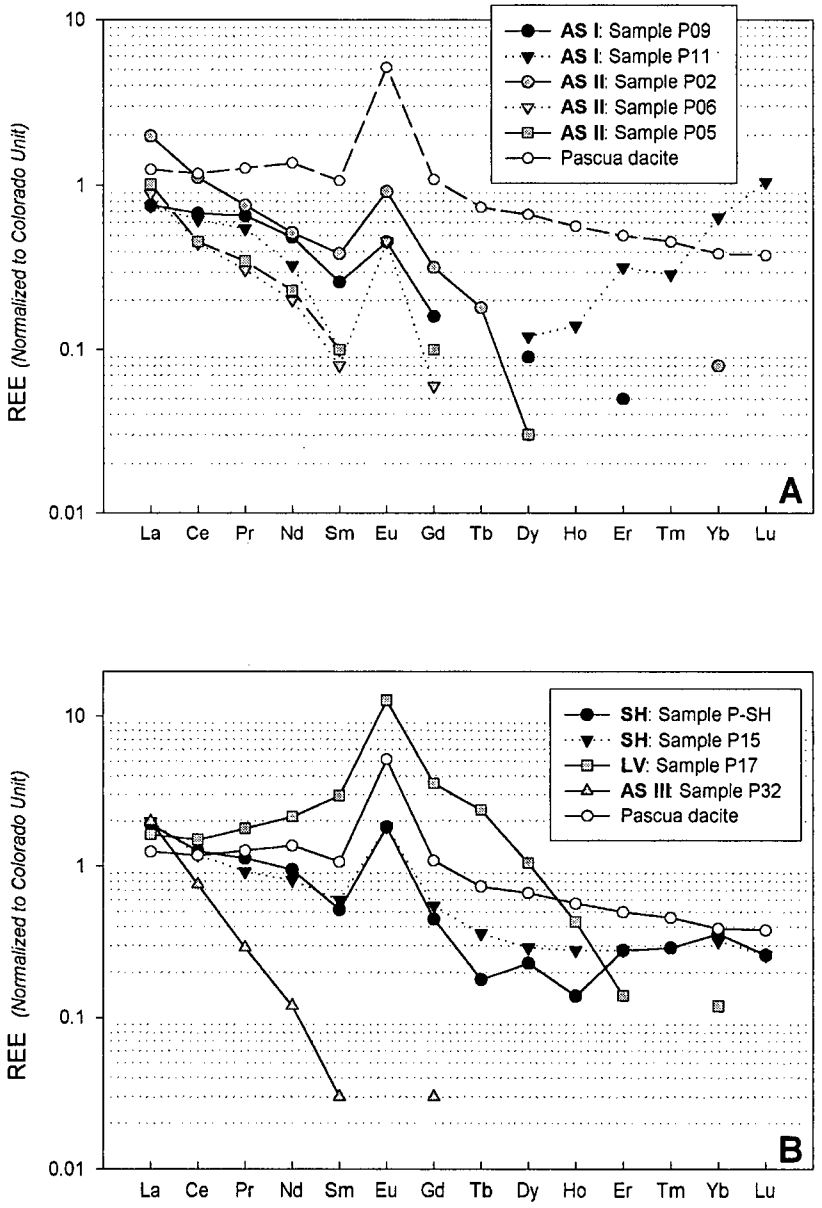

Figure 2.10. REE data for Pascua alunite normalized to a sample of host granite (Colorado Unit). Also shown is normalized REE data for one sample of dacite (Pascua dacite) that is contemporaneous with alteration and mineralization in the area. (A) AS I, AS II samples (sample number given in parentheses). (B) AS III, steam heated (SH), and late vein (LV) alunite. Data points below detection not plotted.

Table 2.3. Geochemical data for unaltered host rock (Colorado Unit) used for normalization of alunite REE. Data for Pascua dacite given for comparison. *Unpub. data, T. Bissig.*

	Pascua Dacite	**Colorado Unit**
Sample #	*99thb130b*	*99thb139a*
Na_2O (wt %)	2.94	3.32
K_2O	1.84	4.39
CaO	5.68	0.36
MgO	2.07	0.11
MnO	0.27	0.05
Fe_2O_3 (Fe total)	4.45	0.82
Al_2O_3	16.99	12.28
P_2O_5	0.19	0.01
SiO_2	63.06	76.35
TiO_2	0.66	0.08
Total	**98.23%**	**97.79%**
REE ICP-MS (ppm)		
La	24.7	19.7
Ce	51.2	43.3
Pr	6.2	4.9
Nd	23.7	17.3
Sm	4.1	3.8
Eu	1.1	0.2
Gd	3.4	3.1
Tb	0.4	0.6
Dy	2.3	3.4
Ho	0.4	0.7
Er	1.1	2.2
Tm	0.2	0.3
Yb	1.0	2.5
Lu	0.1	0.4

Acid Sulfate I: AS I alunite is dominantly potassic. Substitution of Na ranges from below detection to 0.6 atoms per formula unit (a.p.f.u.), based on EPMA analyses (Fig. 2.9). Irregular compositional zoning is common with trace P, Sr, and Ba substitution. Rare oscillatory zoning is present in deeper samples, in which compositions alternate in bands of nearly pure alunite, alunite with minor Na, and thin Ba or Ca-bearing alumino-phospho-sulfate (APS) zones. APS grains also occur locally as inclusions and as cores of AS I alunite. Where present, APS minerals contain minor Sr, REE, and trace Ba. Many of these APS inclusions and zones are too narrow (<5-10 μm) to obtain accurate EPMA analyses. Trace-element contents are better represented by the ICP-MS data that indicate elevated Sb and Bi concentrations,

particularly in comparison to AS II alunite. REE contents are variable. One sample (P09) is relatively depleted in REE and exhibits strong fractionation of heavy-REE (HREE) compared to host-rock compositions. The second sample (P11) is depleted in mid-REE (MREE), but high HREE contents may be attributed to the presence of REE-bearing APS zones that are visible by SEM backscatter imaging.

Acid Sulfate II: The chemistry of AS II alunite is more variable than AS I alteration. The range of Na substitution is similar for the two stages, but APS zoning with Ca, Ba, Sr ± REE is more common in the AS II event. Walthierite is present as rare irregular zones or bands, particularly in alunite sampled from the Maria Tunnel. Substitution of Ca locally approaches end-member huangite in irregular zones from a vein at the margins of Brecha Central. Again, geochemical variability is not adequately represented by EPMA data due to the small size of APS inclusions and chemical zonation. ICP-MS data show significantly elevated Sr, Ba, and Pb concentrations in AS II alunite, in comparison to the AS I samples. All samples show strong fractionation in HREE compared to the host lithology.

Acid Sulfate III: SEM-EDS analysis indicates crystals are nearly stoichiometric (≥ 0.8 a.p.f.u. K) with minor Na or P substitution in oscillatory growth zones. Sb and Pb contents are higher than average and data reflect extreme fractionation in HREE relative to host-rock compositions.

Blanket zone: Alunite in this assemblage is typically homogenous and K-dominant, with up to 0.3 a.p.f.u Na substitution. Trace amounts of P and Sr ± Fe occur in irregular zones. Sr and Sb are elevated relative to most other alunite types, but Ba and Pb contents are low. Alunite exhibits limited REE fractionation with respect to the granite host rock.

Late-stage alunite veins: Alunite of this stage is nearly stoichiometric, with Na substitution rarely exceeding 0.2 a.p.f.u. ICP-MS data indicate significantly elevated P, Sr, and Pb, relative to all other alunite types. This sample also exhibits a very different REE fractionation pattern, with strong enrichment of MREE and depletion in HREE. The strong Eu anomaly is similar to increased Eu contents in the coeval dacite.

Interpretation of results

With few exceptions, AS I and AS II alunite are similar in their major-element compositions. Average Na contents are comparable for both stages but the distribution of Na- versus K-rich alunite differs between the two events. AS II alunite on average shows increasing

Na contents with increasing depth, which is not observed in AS I samples (Fig. 2.11). As well, Na contents are higher in AS II samples from the eastern (Lama) side of the property, in comparison to AS II alunite in the Brecha Central and Frontera zones (significant difference at 95% confidence level, based on t-test results; Appendix A). Alunite veins at Lama were sampled to greater depths than those in Pascua however, and hence the increase in average Na/K may reflect the depth (and therefore temperature) of formation rather than a spatial distribution. High concentrations of Na have been correlated with elevated temperatures of alunite formation in other deposits (Stroffregen and Alpers, 1987; Stoffregen and Cygan, 1990; Aoki, 1991; Hedenquist et al., 1994; Aoki et al., 1993; A.J.B. Thompson, unpub. data). Results from this study also indicate that AS I and AS II alunite are generally enriched in Ba, Ca $\pm$ PO_4, Sr, REE in comparison to AS III and near-surface, blanket zone alunite occurrences. Similar observations are noted in other high sulfidation environments (e.g., Aoki, 1991; Stoffregen et al., 2000; Thompson and Petersen, unpub. data). Late-stage alunite, however, exhibits variable compositions that are consistent with the range of data reported for supergene alunite in other studies (e.g., Stoffregen and Alpers, 1987; Dill, 2001).

REE fractionation patterns are extremely variable. AS I alteration in particular has very different REE signatures for the two samples analyzed. Results for sample P09 are similar to those reported in recent studies of advanced argillic alteration in other high sulfidation environments (e.g. Fulignati et al., 1999; Arribas et al., 1995). The observed loss of HREE may be the result of preferential uptake of LREE into the alunite structure (Schwab et al., 1990). However, grains with elevated zones of Sr $\pm$ PO_4 in the second sample (P11) are correlated with much higher HREE contents. This enrichment may be attributed to mineralogical controls on REE substitution and the stabilization of the alunite crystal structure by larger bivalent ions such as Sr and Ba (Schwab et al., 1990). REE contents may also be controlled by the replacement of apatite grains in the host rock (Stoffregen and Alpers, 1987) or local variations in temperature, redox conditions, or fluid/rock ratios (e.g., Michard, 1989; Lottermoser, 1992). REE contents of AS III alunite, and to a lesser extent AS II, exhibit extreme fractionation of HREE compared to host-rock compositions. We propose that the data reflect differential partitioning of REE into the source fluids (Flynn and Burnham, 1978; Reed, 1995) and minimal wallrock interaction. Results for AS III alunite are similar to those obtained for magmatic steam alunite in the Tambo deposit (Chap. 3).

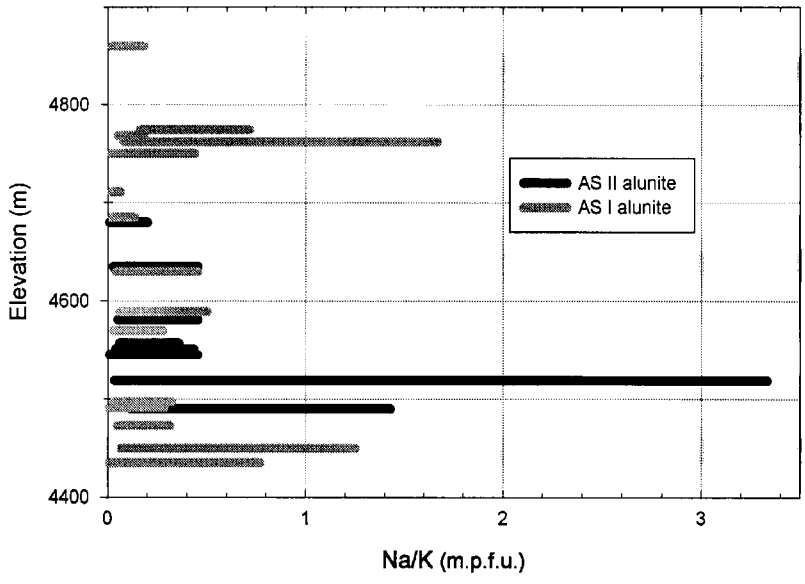

Figure 2.11. Range of Na/K ratios for AS I and AS II alunite with elevation. Based on EPMA results for a total of *n* data points (AS I *n*=351; AS II *n*=316).

STABLE-ISOTOPE STUDY

Complete stable-isotope systematics ($\delta^{34}S$, δD, $\delta^{18}O_{SO4}$, and $\delta^{18}O_{OH}$) were determined for alunite and associated alteration minerals in order to characterize the source of these components. Only samples clearly belonging to each paragenetic stage were analyzed. Alunite from each stage of alteration and two samples of jarosite were analyzed for $\delta^{34}S$, and a sub-set of samples was selected for δD and $\delta^{18}O$ analysis. Sulfur data were also obtained for AS II-stage pyrite, enargite, and barite. Clay minerals are not included in this study because material could not be adequately separated for analysis.

All data were collected at the U.S. Geological Survey Isotope Laboratory in Denver. The $\delta^{34}S$ analyses were determined by an on-line method using an elemental analyzer coupled to a Micromass Optima mass spectrometer following Giesemann et al. (1994). Analyses of δD were performed by a step heated technique modified from Godfrey (1962). Oxygen-isotope data were collected for alunite (both sulfate and hydroxyl groups) and barite. Analyses were done using the conventional BrF_5 method described in Wasserman et al. (1992). Several samples were also analyzed by pyrolysis with a Finnigan TC/EA coupled to a Finnigan Delta Plus XL mass spectrometer using continuous-flow methods modified from Kornexl et al. (1999). Details of sample preparation and analytical methods are reported in Appendix B. Brief sample descriptions and all isotope data are listed in Table 2.4.

Sulfur-Isotope Relations

All sulfur-isotope results are summarized in Fig. 2.12. The $\delta^{34}S$ value of bulk sulfur in the magma ($\delta^{34}S_{\Sigma S}$) cannot be directly determined, since no large bodies of syn-ore volcanic rocks have been identified in the Pascua district. Estimation of $\delta^{34}S_{\Sigma S}$ (2 to 4‰; Fig. 2.5) is therefore based on data for magmatic steam alunite (AS III; see discussion below). The main results from this study are:

- The range of $\delta^{34}S$ values for AS I and AS II alunite are similar, from 13 to 25‰. Data for AS II barite (22.1‰) and Esperanza alunite (18.3‰) also fall within this range.
- AS II enargite and pyrite data are narrowly clustered around -3 to -6‰. AS I pyrite could not be separated in sufficient quantity for analysis, but Beane (1988) reported a $\delta^{34}S$ value of -3.5‰ for disseminated pyrite intergrown with alunite in quartz monzonite from the Brecha Central area. This value is plotted for comparison on Figure 2.12.

Table 2.4a. Sample descriptions and stable isotope results for Pascua alunite. All data is given in per mil, elevation in metres above sea level. Stages are: Acid Sulfate I (AS I); Acid Sulfate II (AS II); Acid Sulfate III (AS III); Steam heated (SH); Late stage veins (LV); Esperanza (Esp); and Supergene (SP). Abbreviated mineral names; alunite (alun), quartz (qtz), kaolinite (kao), dickite (dick), pyrophyllite (pyl), jarosite (jar), enargite (enarg), sil (silica), bar (barite), native sulfur (S).

Sample	Lab #	Stage	Elev. (m)	Description	δD	$\delta^{34}S$	$\delta^{18}O_{SO4}$	$\delta^{18}O_{OH}$ [1]
DDH-137A, 23.1m	P09a	AS I	4665	Qtz-alun alteration of monzonite	-37	24.7	19.9	9.2
DDH-184, 441.3m	P10a	AS I	4616	Qtz-alun alteration of diorite	-52	22.0	13.8	12.4
DDH-195A, 242.0m	P11a	AS I	4612	Qtz-alun alteration of monzonite	-33	24.5	16.9	12.2
DDH-154, 185.9m	P12a	AS I	4570	Qtz-alun-dick alteration; Frontera	-52	15.7		
LM-20, 94.8m	P13a	AS I	4990	Qtz-alun-py alteration of monzonite	-29	21.0	20.7	14.7
DDH-116, 289.5m	P21a	AS I	4435	Qtz-alun alteration; Lama		15.3		
DDH-152, 107.0m	P22a	AS I	4630	Qtz-alun-dick alteration; Frontera		12.6		
PSD-98-108, 374m	P23a	AS I	4435	Qtz-alun-pyl-zuny alteration	-43	18.5	15.6	9.4
DDH-017, 122.5	P24a	AS I	4369	Qtz-alun-pyl alteration; near Esperanza		17.1		
DDH-017, 108.0m	P28a	AS I	4369	Qtz-alun-pyl alteration; near Esperanza		16.7		
DDH-168, 260m	P33a	AS I	4647	Qtz-alun-pyl alteration	-27	20.4		
DDH-116, 157.0m	P01a	AS II	4551	Alun-py-enarg banded vein	-46	17.6	15.8	10.9
DDH-137A, 113.9m	P02a	AS II	4580	Brecha Central Sur matrix; alun-enarg-py	-34	19.8	16.5	13.0
DDH-137A, 152.1m	P03a	AS II	4544	Alun-py-enarg banded vein	-51	14.7	17.4	15.6
DDH-154, 224.3m	P04a	AS II	4545	Matrix alun-enarg-py; Frontera	-44	22.2	15.7	10.7
PS-99-03	P05a	AS II	4680	Brecha Central matrix; alun-enarg-py-S	-41	14.1	18.0	13.6
PS-98-16d	P06a	AS II	4674	Alun-enarg vein; Tunel Maria	-40	24.7	19.6	10.4
LM-03, 301.0m	P07a	AS II	4519	Alun-py-enarg vein; Lama		17.9		
DDH-172, 435.1m	P25a	AS II	4393	Alun-jar vein	-47	18.9	15.6	14.4*
Annick 440	P27a	AS II	4680	Brecha Central matrix; alun-enarg-py	-36	12.6	18.2	15.5*
PS-26c	P32a	AS III	4995	Near-surface, coarse matrix alun	-41	2.8	20.4	13.5
DDH-129, 111.6m	P14a	LV	4582	Alun-jar vein	-40	7.0	20.7	13.5
DR-368NE, PM-33	P16a	LV	4680	Alun-jar +/- silica vein; Tunel Alex	-72	4.3	9.7	9.0
DDH-154, 310.5m	P17a	LV	4489	Alun +/- jar vein	-79	6.2	12.7	5.5
LM-20, 160.1m	P15a	SH	4960	Alun-jar matrix; Lama, near surface	-48	1.6	19.1	13.1*
DDH-119, 47.7m	P18a	SH	4994	Alun-sil +/- kao, S; near surface	-42	-0.1	16.9	13.2
DDH-122, 4.3m	P19a	SH	5089	Alun-sil +/- kao, S; near surface	-68	6.1		
DDH-119. 34.0m	P20a	SH	5006	Alun-sil +/- kao, S; near surface	-58	2.4	18.7	13.3
DDH-057, 76.5m	P26a	Esp	4873	Alun in bx matrix; Esperanza	-35	18.3	17.4	12.4

[1] calculated using BrF_5 total oxygen data, except continuous flow samples marked with "*". See discussion in text.

Table 2.4b. Sample descriptions and stable isotope results for jarosite, barite, and sulfides. Abbreviations as in Table 2.4a.

Sample	Lab #	Stage	Elev. (m)	Description	δD	$\delta^{34}S$	$\delta^{18}O_{SO4}$	$\delta^{18}O_{OH}$
Jarosite:								
DDH-135, 162.7m	Pj30	SP	4528	Jar +/- alun vein cutting QA alteration	-129	-2.5		
DDH-198, 168m	Pj31	SP	4718	Matrix of opaline qtz bx	-178	3.3	4.5	2.3
Barite:								
Annick 440	Pb29	AS II	4680	Barite breccia matrix in Dr-440-SE		22.1	14.4	
Pyrite:								
DDH-137A, 113.9m	P02p	AS II	4580	Brecha Central Sur matrix; alun-enarg-py		-3.8		
DDH-137A, 152.1m	P03p	AS II	4544	Alun-py-enarg banded vein		-5.3		
LM-03, 301.0m	P07p	AS II	4519	Alun-py-enarg vein; Lama		-3.4		
Enargite:								
DDH-137A, 113.9m	P02e	AS II	4580	Brecha Central Sur matrix; alun-enarg-py		-6.0		
DDH-154, 224.3m	P04e	AS II	4545	Matrix alun-enarg-py; Frontera		-3.6		
PS-98-16d	P06e	AS II	4674	Alun-enarg vein; Tunel Maria		-4.5		
LM-03a, 433m	P08e	AS II	4398	Massive vein enarg		-5.6		

- AS III alunite was sampled from coarse grained, euhedral crystals obtained near-surface in the matrix of Brecha Central. The alunite has a low $\delta^{34}S$ value of 2.8‰.
- $\delta^{34}S$ values for alunite in the near-surface, blanket zone (0 to 6‰) are slightly enriched relative to sulfides in the deposit.
- Samples of late-stage alunite were selected from drill core and underground exposures in the Alex Tunel. The $\delta^{34}S$ values range from 4 to 7‰ and are also enriched relative to AS II sulfides.
- Jarosite (sample Pj31) was separated from a series of fine-grained veinlets that cross-cut a strongly silicified alteration zone approximately 300 m below the present-day surface. This sample has the lightest $\delta^{34}S$ value (-2.5‰) of all sulfates in the deposit. Sample Pj31, from veinlets that cross-cut AS I altered wallrock, has $\delta^{34}S$ data (3.3‰) similar to those of late-stage alunite.

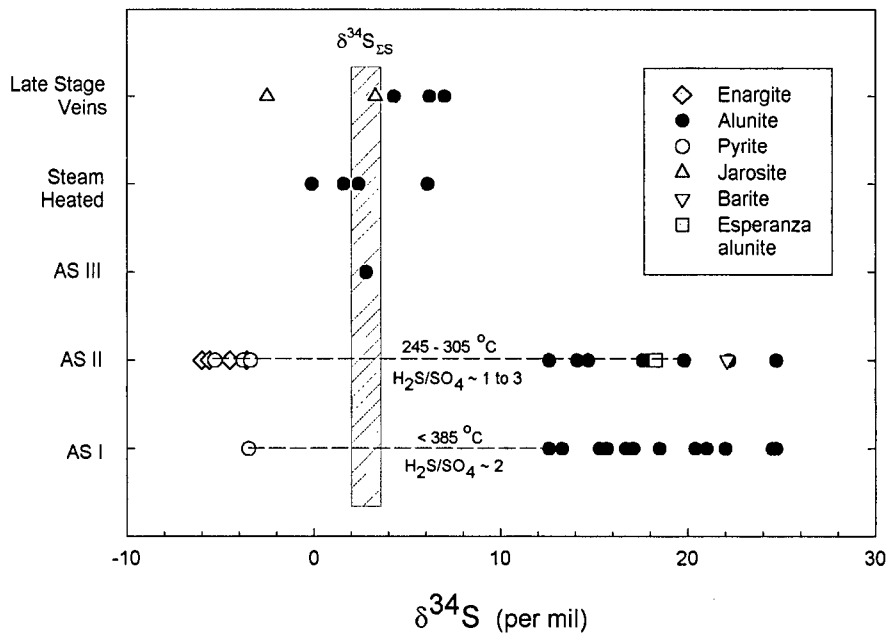

Figure 2.12. Range in $\delta^{34}S$ data (in ‰) for all stages of Pascua alunite. Also shown is data for associated sulfides, jarosite, and barite. Estimated $\delta^{34}S_{\Sigma S}$ ~ 2 to 4 per mil. Range of $\Delta^{34}S_{alun\text{-}py}$ temperatures for AS I and AS II stages are given, as well as estimated H_2S/SO_2 ratios. See text for discussion.

The high $\delta^{34}S$ values for AS I, AS II, and Esperanza alunite are significantly different from all other stages of alunite and jarosite in the deposit. The 14 to 30‰ difference between alunite and sulfides is consistent with sulfate derived from the disproportionation of SO_2 (Rye et al., 1992; Rye, 1993) and is interpreted to reflect a magmatic-hydrothermal origin. The large variation in alunite $\delta^{34}S$ values is attributed to deposition over a range of temperatures. These temperatures can be estimated by the isotopic fractionation equation of Ohmoto and Lasaga (1982) for coexisting alunite and pyrite. Data for the one AS I sample reported in Beane (1988) give an equilibrium $\Delta^{34}S_{alun\text{-}py}$ temperature of 380° C. This represents a maximum depositional temperature for the AS I event. Using an average $\delta^{34}S$ pyrite value of -4‰, depositional temperatures for other AS I alunite samples are estimated at 190° to 350°C. Likewise, equilibrium temperatures calculated for three AS II alunite-pyrite pairs (samples P02, P03, and P07) range from 245° to 305° C.

Calculated sulfide–sulfate (H_2S/SO_4) ratios for AS I and AS II fluids are approximately 1 to 3. These values are in the range of magmatic-hydrothermal processes (Rye et al., 1992; Rye, 1993) and suggest mildly reducing fluid conditions during alunite deposition in both pre- and syn-mineral events.

Low $\delta^{34}S$ values for all AS III, blanket zone, and late-stage alunite are interpreted to reflect different origins. Sulfur-isotope data for AS III alunite, in conjunction with oxygen-isotope results, are consistent with a magmatic steam origin. Alunite of this type is considered to have $\delta^{34}S$ values close to that of the bulk sulfur in the magma, based on relationships determined by Cunningham et al. (1984) and Rye et al. (1992) for alunite at Marysvale, Utah. The $\delta^{34}S$ values for blanket-type alunite, combined with high $\delta^{18}O_{SO4}$ values, are consistent with a steam-heated origin, although data indicate limited sulfur isotope exchange between aqueous SO_4 and H_2S. The $\delta^{34}S$ data for jarosite sample Pj31 are consistent with sulfate derived from the oxidation of pre-cursor sulfides. The slightly heavier sulfur values for late-stage alunite are interpreted to represent either sulfate derived from the oxidation of sulfides or H_2S degassed during the collapse of the hydrothermal system. In either case, limited sulfur-isotope exchange between sulfate and sulfide species is inferred, on the basis of the range of $\delta^{34}S$ values. Oxygen-isotope systematics provide further clues as to their origin (see below).

Oxygen-Isotope Relations

Oxygen-isotope systematics for each stage of alteration, including both sulfur-oxygen and oxygen-hydrogen relationships, are given in Figures 2.13 and 2.14. Also shown are the range of calculated fluid compositions in equilibrium with alunite of each stage. The composition of paleo- meteoric waters is estimated at $\delta D = -100 \pm 10‰$ (B. Taylor, pers. comm.). However, data from this study and from Jannas et al. (1999) indicate that this value may have been slightly lighter (*ca.* -125‰). Variations of this magnitude are expected over the duration of the hydrothermal system, and a range of meteoric δD values is shown on all isotope plots accompanying the following discussions.

AS I and AS II alunite: Depositional temperatures calculated from $\Delta^{18}O_{SO4\text{-}OH}$ values for AS I and AS II alunite are unreasonable, ranging from –50° to >800° C. Oxygen isotopic temperatures for individual samples are also consistently higher than those determined by $\Delta^{34}S_{alun\text{-}py}$ fractionations. These results are attributed to disequilibrium effects due to retrograde OH exchange (Rye et al., 1992).

Fluid compositions for the two alteration events are nearly identical (Fig. 2.13) and are shown as one field with δD_{H2O} between -25 and -47‰. These data overlap with values for felsic magmatic fluids (Taylor, 1992) and the volcanic vapor field (Giggenbach, 1992), and indicate a dominant magmatic component in the source fluids for both paragenetic stages. Lower δD_{H2O} values are generally accompanied by a downward shift in $\delta^{18}O_{H2O}$ and are interpreted to represent limited mixing between magmatic fluids and meteoric waters. This trend is not attributed to δD depletion by open-system degassing (Taylor, 1988) since there is no systematic depletion over time, from the early AS I to the later AS II assemblage.

AS III: The equilibrium fluid composition for AS III alunite (Fig. 2.14b) overlaps with the range of AS I and AS II fluids and indicates a dominant magmatic fluid signature. However, the depositional temperature calculated from $\Delta^{18}O_{SO4\text{-}OH}$ is lower than expected (110 °C), and may indicate equilibration with a low δD_{H2O} fluid. Overall the isotope data, combined with textural and geochemical observations, are consistent with a magmatic steam origin for AS III alunite (Rye et al., 1992).

Blanket zone: Calculated $\Delta^{18}O_{SO4\text{-}OH}$ temperatures of deposition for alunite of this stage are 130°, 150° and 270 °C. The lower temperature data are reasonable for environments in which aqueous sulfate forms at shallow levels from the oxidation of H_2S by atmospheric oxygen, and indicate that oxygen-isotope equilibrium was obtained between the aqueous sulfate

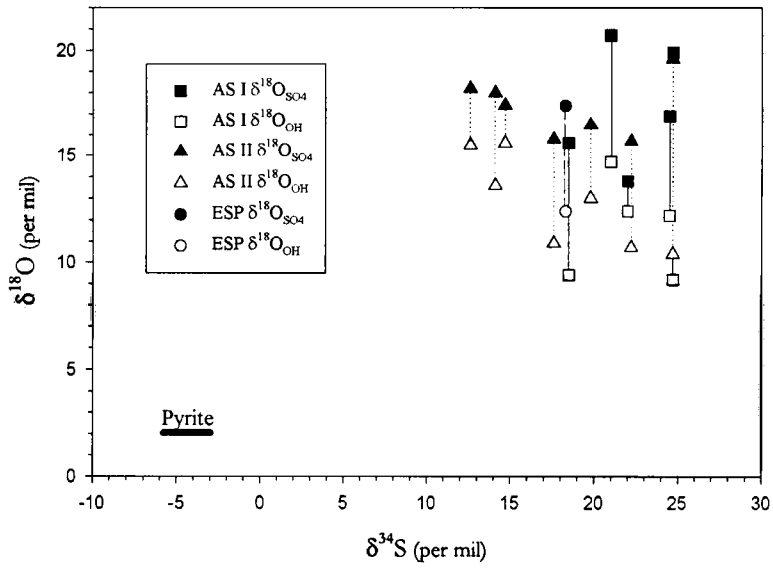

Figure 2.13a. $\delta^{34}S$ and $\delta^{18}O$ data for alunite from stages AS I, AS II, and Esperanza (ESP). $\delta^{18}O_{SO4}$, and $\delta^{18}O_{OH}$ values for each sample are joined by lines. Range of $\delta^{34}S$ data for AS II pyrite is given for reference.

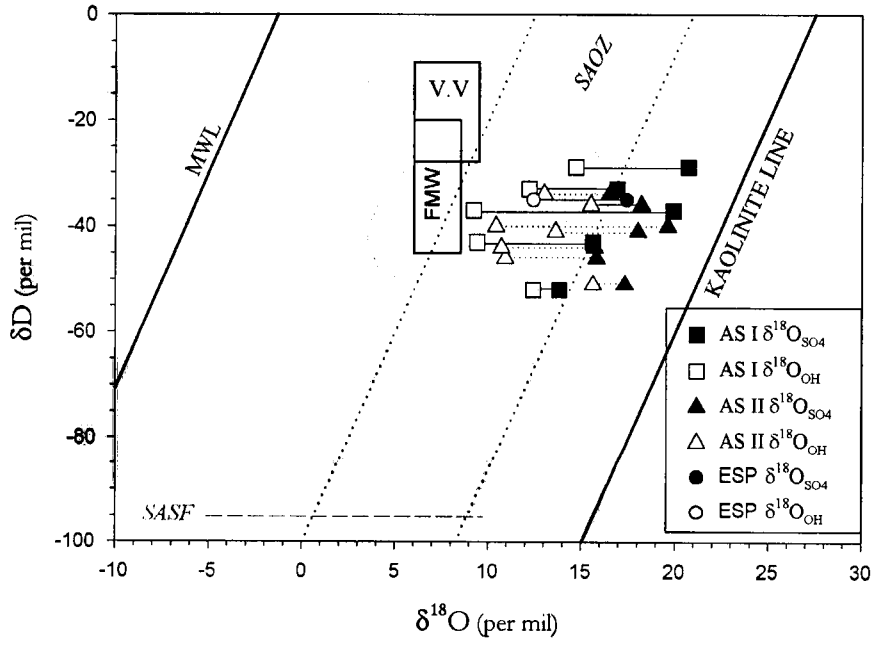

Figure 2.13b. δD, $\delta^{18}O_{SO4}$, and $\delta^{18}O_{OH}$ values for alunite from stages AS I, AS II, and Esperanza (ESP). Range of calculated δD_{H2O} and $\delta^{18}O_{H2O}$ for fluids in equilibrium with AS I and AS II are shown as one shaded fields. Fluid compositions calculated from equations of Stoffregen et al.. (1994) and Rye and Stoffregen (1995). Temperatures used for calculations (AS I; 200-380°C: AS II; 240-350°C) are derived from textural, $\Delta^{34}S_{alun-py}$, and $\Delta^{18}O_{SO4-OH}$ isotope data. Lines and fields are MWL = meteoric water line of Craig (1961); FMW = composition of fluids dissolved in felsic magmas (Taylor, 1988); kaolinite line of Savin and Epstein (1970); V.V (volcanic vapor) = range of water compositions discharged from high temperature fumaroles (Giggenbach, 1992); SASF (light grey) = supergene alunite SO_4 field; and SAOZ = supergene alunite OH zone as described in Rye et al. (1992).

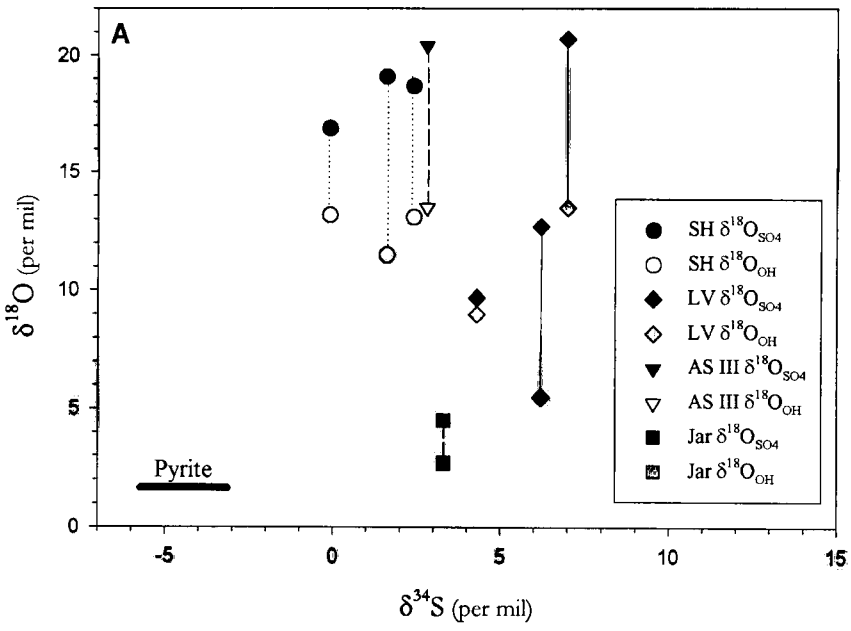

Figure 2.14a. $\delta^{34}S$ and $\delta^{18}O$ data for steam heated (SH), late vein (LV) and AS III alunite, and one sample of jarosite (jar). $\delta^{18}O_{SO4}$, and $\delta^{18}O_{OH}$ values for each sample are joined by lines. Range of $\delta^{34}S$ data for AS II pyrite is given for reference.

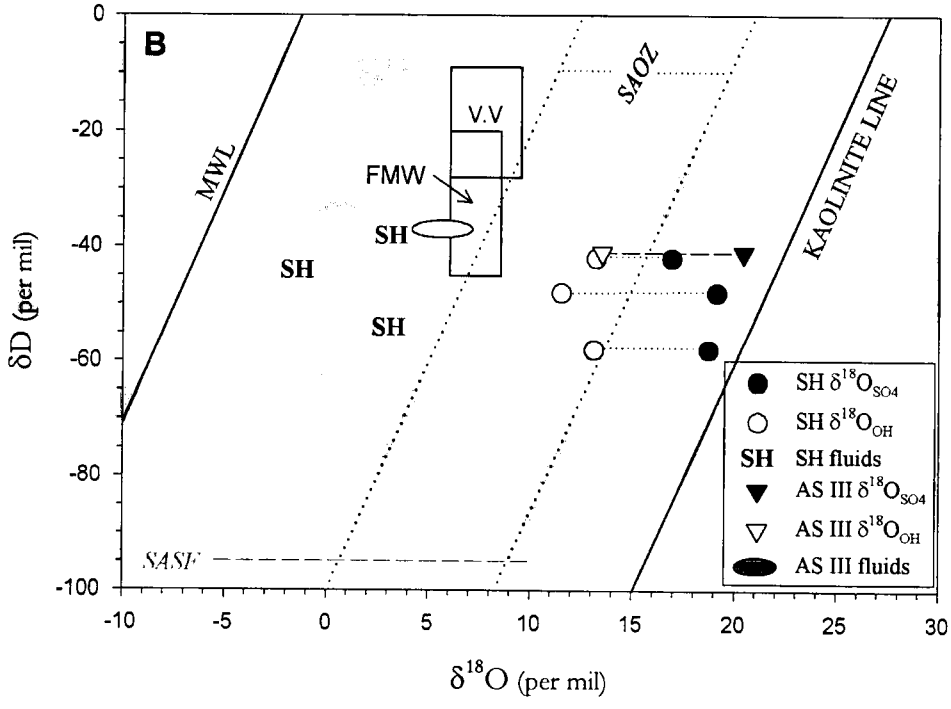

Figure 2.14b. δD, $\delta^{18}O_{SO4}$, and $\delta^{18}O_{OH}$ values steam heated (SH) and AS III alunite. Range of calculated δD_{H2O} and $\delta^{18}O_{H2O}$ for fluids in equilibrium with alunite are given - calculated from equations of Stoffregen et al. (1994) and Rye and Stoffregen (1995). Temperatures used for calculations are derived from textural and $\Delta^{18}O_{SO4\text{-}OH}$ isotope data. Lines and fields as described in Fig. 2.13b.

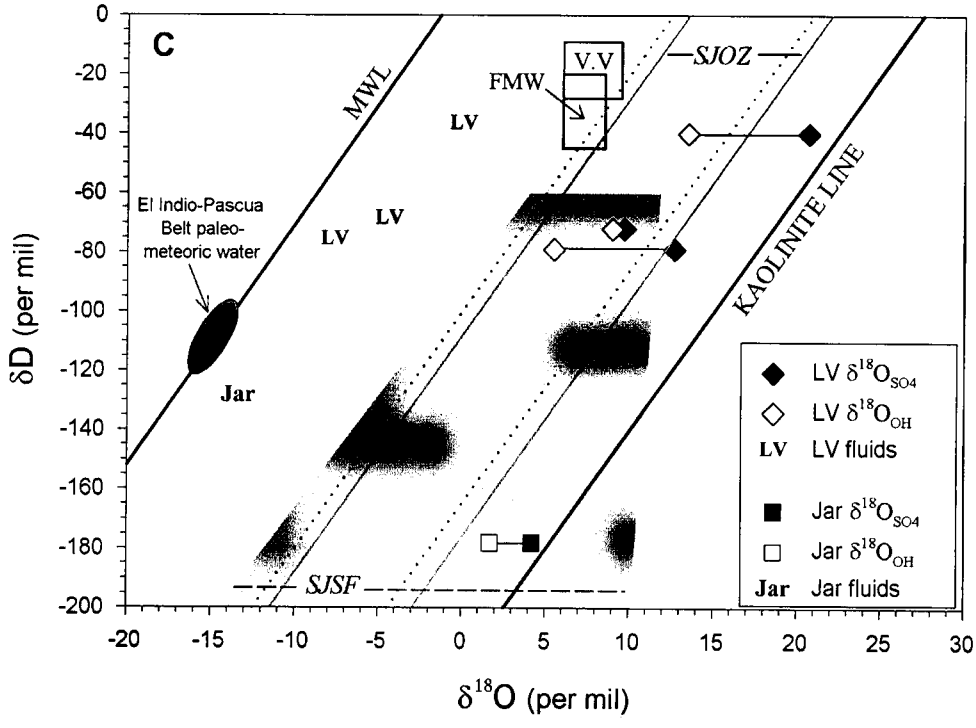

Figure 2.14c. δD, $\delta^{18}O_{SO4}$, and $\delta^{18}O_{OH}$ values late vein alunite (LV) and jarosite (jar). Range of calculated δD_{H2O} and $\delta^{18}O_{H2O}$ for fluids in equilibrium with each sample are given - calculated from equations of Stoffregen et al.. (1994) and Rye and Stoffregen (1995). Temperatures used for calculations are derived from textural and $\Delta^{18}O_{SO4\text{-}OH}$ isotope data. Lines and fields as per Fig. 2.13b. Also shown is SJOZ = supergene jarosite OH zone and SJSF = supergene jarosite sulfate field as described in Rye and Alpers (1997); and the estimated composition of paleo-meteoric water.

and water in the fluid. The third sample gives an unreasonably high $\Delta^{18}O_{SO4\text{-}OH}$ temperature, given its shallow depth of formation, which suggests that $\Delta^{18}O_{SO4\text{-}OH}$ may have been affected by post depositional exchange.

Calculated fluid compositions in equilibrium with alunite (Fig. 2.14b) have δD_{H2O} values of -40 to -55‰ and $\delta^{18}O_{H2O}$ data between -2 and +3‰. The values are significantly heavier than those of paleometeoric water and are not typical of steam-heated environments (e. g., Rye et al., 1992). Some of this enrichment may be attributed to evaporation effects (Henley and Stewart, 1983), but the degree of enrichment (> 45‰) is much greater than that in any system reported to date (J. Hedenquist, pers. comm.). Based on these results, we propose that steam-heated alteration involved a significant magmatic fluid component.

Late-stage alunite: Fig. 2.14c highlights reference fields for supergene alunite and jarosite as given in Rye et al. (1992) and Rye and Alpers (1997), respectively, for comparison to late-stage alunite and jarosite from this study. Alunite $\delta^{18}O_{OH}$ data plot within the Supergene Alunite OH Zone (SAOZ), but two of the three $\delta^{18}O_{SO4}$ values fall outside of the Supergene Alunite Sulfate Field (SASF). The latter samples have large, positive $\Delta^{18}O_{SO4\text{-}OH}$ values that are not consistent with a supergene origin (Rye et al., 1992). Depositional $\Delta^{18}O_{SO4\text{-}OH}$ temperatures average 85°C, higher than expected for the supergene environment. Temperature calculations for these two alunite samples suggest sufficient residence time of aqueous sulfate following oxidation that allowed for oxygen isotopic equilibrium with water in the fluid. The third sample exhibits obvious disequilibrium between oxygen-isotope species.

Calculated δD_{H2O} values for late-stage alunite (Fig. 2.14c) range between -35 and -75‰ with $\delta^{18}O_{H2O}$ less than 0‰. The lowest $\delta^{18}O_{H2O}$ values are correlated with progressively lighter $\delta^{18}O_{H2O}$ contents, suggesting a substantial magmatic contribution to the source fluids mixed with varying amounts of meteoric water.

Overall, data for late-stage alunite are not consistent with a supergene origin. Results can be interpreted to reflect either the oxidation of precursor sulfides or of H_2S degassed from the hydrothermal system. Based on the abundance of sulfide in the Pascua deposit and visible signs of oxidation, we suggest the former is more likely. Oxidation could result from atmospheric processes above the water table. Alternatively, recent evidence for alteration in the Tambo deposit (Chap. 3) indicates that oxidation by SO_2-rich magmatic vapors could be significant in the late-stages of a shallow hydrothermal system. Similar processes may be applicable at Pascua, given the evidence for near-surface magmatic steam alunite.

Jarosite: Oxygen-isotope data are available only for one sample of jarosite (Pj31). The $\delta^{18}O_{OH}$ data is slightly heavier than the Supergene Jarosite OH Zone (SJOZ) defined by Rye and Alpers (1997), but $\delta^{18}O_{SO4}$ data fall within the Supergene Jarosite Sulfate Field (SASF; Rye and Alpers, 1997). These values may indicate limited OH exchange with low pH waters (Rye and Alpers, 1997) or formation from partly exchanged meteoric waters. The composition of fluid calculated in equilibrium with jarosite is close to the predicted composition of paleometeoric waters and is consistent with formation in the supergene environment.

GEOCHRONOLOGY

Alunite from four paragenetic stages and one sample of jarosite were selected for $^{40}Ar/^{39}Ar$ dating. AS III alunite (sample P32) was collected and dated previously (Bissig, 2001) and is included here for comparison. The objective of this study was to determine the duration of magmatic-hydrothermal activity in the Pascua area and to confirm the timing of different alteration events.

All analyses were carried out at the Queen's University (Kingston, Canada) ^{40}Ar-^{39}Ar laboratory, equipped with a Mass Analyzer Products MAP 216 mass spectrometer. About 10 mg of each sample was irradiated for 7.5 h at the McMaster nuclear reactor in Hamilton, Canada using biotite standard Mac-83 as a radiation-flux monitor (24.36 ± 0.17 Ma; Sandeman et al., 1999). Samples were step-heated using a defocused LEXEL 3500 Ar laser-beam. Ages were calculated using the decay constants suggested by Steiger and Jäger (1977), and all errors are given at 2σ. Analytical details are provided in Appendix C.

Results and Interpretation:

Of the four alunite samples dated, only one (sample P05) yielded a reasonable plateau age (Table 2.5). This sample consists of coarse-grained AS II alunite from the matrix of Brecha Central. The alunite is intergrown with pyrite, enargite and native sulfur and is therefore considered to be coeval with the APE-ore event. Its age (8.78 ± 0.63 Ma) is consistent with the range of ages reported in Bissig (2001) for APE mineralization (8.7 ± 0.2 to 8.1 ± 0.1 Ma). The relatively large error for this sample is attributed to poor absorption of the laser-beam and insufficient release of argon.

Table 2.5. $^{40}Ar/^{39}Ar$ results for alunite and jarosite (calculated from data given in Appendix D). All ages reported in this study are within error, due to analytical difficulties (see text). Data for sample P32 is reported in Bissig (2001) and listed here for comparison.

Sample	Stage		Lab no.	Integrated date (Ma +/- 2SD)	Plateau Age (Ma +/- 2SD)	% ^{39}Ar in the plateau	Correlation date (Ma +/- 2SD)	% ^{39}Ar in the correlation	MSWD	Initial $^{40}Ar/^{39}Ar$ (+/- 2SD)
P05	AS II	Alunite	TU-128	9.18 (1.41)	8.78 (0.63)	95.0	8.74 (2.66)	100.0	0.07	296.85 (144.89)
P32	AS III	Alunite			8.38 (0.17)					
P18	SH	Alunite	TB-108	8.24 (3.95)	9.14 (1.98)	77.7	9.85 (17.31)	100.0	0.03	293.76 (755.00)
P17	LV	Alunite	TB-105	9.38 (2.94)	7.97 (1.59)	64.2	7.24 (1.98)	100.0	0.99	298.75 (118.29)
Pj31	SP	Jarosite	TU-129	8.18 (0.64)	7.98 (0.43)	95.4	8.13 (0.69)	100.0	0.980	292.81 (37.88)

AS III alunite, sampled at surface from coarse vug-fill crystals at the margin of Brecha Central, yielded an age of 8.38 ± 0.17 Ma (Bissig, 2001). Based on these results, this alunite is coeval with AS II alteration and ore deposition.

A sample of late jarosite (sample Pj31) also yielded a reasonable age (7.98 ± 0.43 Ma) on the second dating attempt. This sample is characterized by a supergene isotopic signature and is the youngest alteration event recorded in the Pascua-Lama district.

Samples of late vein and steam-heated alunite did not release sufficient argon and their reported ages represent only rough estimates (7.97 ± 1.59 and 9.14 ± 1.98 Ma, respectively). Repeated attempts to date AS I alunite were unsuccessful.

DISCUSSION: CONTROLS ON ALTERATION

The distribution of alteration and mineralization in high sulfidation systems is strongly controlled by the focus of fluid flow and the related permeability of the host rocks (Sillitoe, 1999). Permeability can be generated by structural, hydrothermal, or lithological processes, and the relative importance of each will vary with the local environment (Sillitoe, 1993). Lithological and hydrothermal brecciation are typically important controls in shallow epithermal systems (< 500 m depth; Sillitoe, 1999). Preferential alteration and precious-metal deposition in poorly lithified, porous, clastic, and volcaniclastic sedimentary rocks are common in several deposits (e.g., Pierina, Volkert et al., 1998; Pueblo Viejo, Kesler et al., 1981). Hydrothermal-induced permeability is attributed to rock fragmentation, brecciation, and rock leaching (Sillitoe, 1999), and several deposits host alteration and mineralization in hydrothermal breccias (e.g. Paradise Peak, Nevada, John et al., 1991; Tambo, Chile, Jannas et al., 1999). Structural controls dominate at the intermediate levels of high sulfidation systems (Sillitoe, 1999). These controls include either regional-scale features or structures related to the emplacement of shallow intrusions (Sillitoe, 1999; Hedenquist et al., 2000).

Topographical effects are also important in the shallow epithermal environment. These effects are particularly evident in deposits where steam-heated alteration (generated above paleo-water tables) is preserved. Progressive or intermittent lowering of the water table during hydrothermal activity can cause overprinting of deeper high sulfidation mineralization and magmatic-hydrothermal alteration assemblages by the steam-heated environment.

The nature of alteration at Pascua has many similarities with other high sulfidation

systems. On a broad scale, intense silicic and acid sulfate alteration zones grade outward to argillic and propylitic assemblages. Detailed mapping and SWIR analyses have shown that the distribution of alteration on a smaller scale is often much more complex however, and is influenced by several factors including elevation and lithological, structural, and topographical controls. The effects of each of these factors are described below.

Lithology: Lithological controls are subordinate at Pascua. The deposit is largely hosted in intrusive rocks of the Pastos Blancos group that are relatively homogenous with respect to composition and texture. Permeability controls are apparent only in the Esperanza area where tuffaceous units with a high degree of primary porosity are altered to massive, silica-rich assemblages (section CA-EW). Compositional variations in host lithology appear to influence alteration only on a local scale. For example, less intense argillic and propylitic alteration in the Esperanza area is associated with a small stock of presumed Bocatoma-age diorite that intrudes the Pastos Blancos sequence. Similarly, intrusions of granodioritic and dioritic composition occur peripheral to Brecha Central (section CA-00) and are altered to argillic and propylitic assemblages, whereas the adjacent granitic rocks are intensely altered. In this case, lithological effects were likely combined with the progressive reduction and cooling of acid sulfate fluids away from the main breccia conduit.

Structure and brecciation: The distribution of alteration is strongly influenced by structural controls, especially in the Brecha Central and Frontera areas. The AS II assemblage in particular is preferentially hosted in intra-mineral breccias and surrounding stockwork zones. Breccias formed along pre-existing ESE- and N- to NNE-trending structures of the Quebrada de Pascua and Quebrada de Pedro fault systems (Hamilton, 1998). North-trending faults and sub-horizontal fracture zones also control the AS II assemblage and stockwork mineralization in the Maria Tunnel and Pedro Este area. Likewise, steam-heated and late-stage acid sulfate alteration used existing structures to propagate downwards from surface and from the margins of the deposit.

Elevation: Elevation has had a strong effect on the mineralogy and distribution of several alteration assemblages, due to both topographical and temperature–depth relationships. Topography has had the largest influence on the distribution of steam-heated and supergene assemblages, since the acid sulfate fluids responsible for alteration in each case were generated above the paleo-water table. The blanket-type distribution of steam-heated alteration at Pascua is typical of this environment (e.g. Schoen et al., 1974) and its preservation indicates that limited erosion has taken place in this region over the past 8 m.yr. The predominance of

jarosite and scorodite also appear to have been controlled by present-day topography (Chouinard and Williams-Jones, 1999). Jarosite is most abundant at the margins of Brecha Central, on the flanks of Quebrada de Pedro, roughly enveloping the sulfide-rich ore.

A consistent vertical zonation in the mineralogy of the AS I assemblage indicates a gradual cooling of magmatic-hydrothermal fluids with increasing elevation. The co-existence of alunite, pyrophyllite, zunyite, and diaspore at depths greater than about 4500 m is consistent with temperatures of 200-380°C (Hemley et al., 1980; Reyes, 1990). The kaolinite-dominant assemblage at higher elevations suggests that temperatures had cooled to less than about 150-200°C. Similarly, silicic alteration typically occurs above AS II alteration in the Brecha Central and Frontera zones, at elevations between 4600 to 4900 m. This suggests a decrease in silica solubility with gradual cooling or neutralization of the upwelling fluids. Equivalent lateral zonation is present in both the AS I and silicic assemblages at the margins of the hydrothermal system as alteration grades outwards to argillic and propylitic assemblages.

SUMMARY: ALTERATION PARAGENESIS IN AN EVOLVING HYDROTHERMAL SYSTEM

Data from this study, combined with $^{40}Ar/^{39}Ar$ ages presented in Bissig (2001), indicate that episodic magmatic-hydrothermal activity occurred in the Pascua-Lama region over a period of at least 1 to 2 m.yr. The deposit is complex, with multiple stages of alteration and several forms of Au, Cu, and Ag mineralization. In this study, we have focussed on the nature of alteration in the Esperanza, Brecha Central, and Frontera areas but several newly discovered zones in the Lama district have not been considered. The combined areal extent of this district is over 15 km^2 and recent resource estimates indicate that this region, including Veladero, is one of the largest high sulfidation systems discovered to date.

Throughout this study, we have examined the relation between alunite-bearing alteration assemblages and ore-stage events, using petrographic, SWIR, geochemical, and isotopic methods. Based on these results, we can group alteration in the Pascua district into 3 intervals, according to the relation between alteration and precious-metal deposition. These are: (1) pre-mineral magmatic-hydrothermal alteration that occurred prior to *ca.* 8.8 Ma; (2) syn-mineral magmatic-hydrothermal alteration and related Au and Cu mineralization between about 8.8-8.1 Ma; and (3) limited post-mineral, late-stage oxidation and supergene alteration that record the collapse of the hydrothermal system. The features of each of these stages are described in the following section and are illustrated schematically in Figure 2.15.

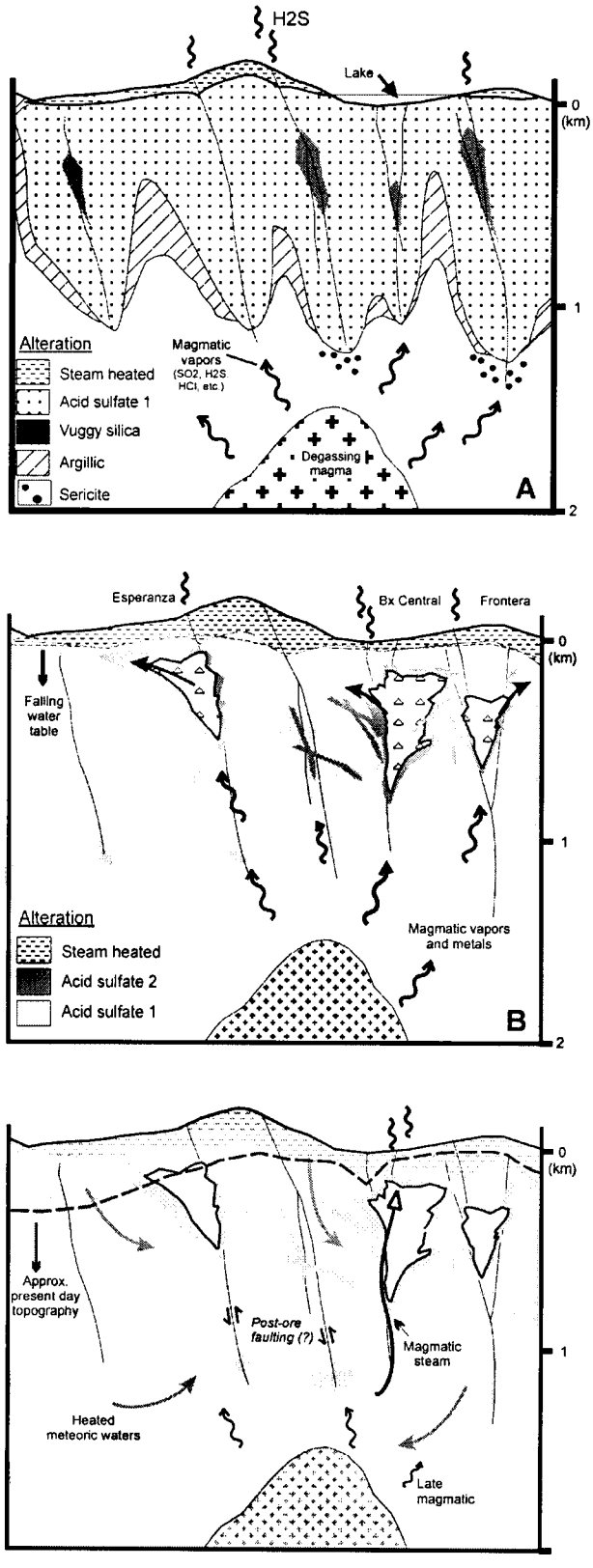

Figure 2.15. Schematic cross sections showing the evolution of the Pascua deposit from pre-mineral (A), syn-mineral (B), and post-mineral (C) stages. A. Widespread, early hydrothermal alteration in the greater Pascua region (prior to ~ 8.8 Ma). B. The initiation of brecciation and Au-Ag-Cu mineralization in the Esperanza, Brecha Central, and Frontera areas (age ~ 8.8-8.1 Ma). C. Late stage processes with local incursion of meteoric fluids and late pulses of magmatic steam. Post-ore faulting is inferred.

Pre-mineral alteration:

The consistency of style and distribution of most wallrock alteration in the Pascua district suggests the alteration was generated by a single, large event. These features, combined with stable-isotope data of alunite and associated alteration minerals, indicate a magmatic-hydrothermal origin for this stage of alteration. The widespread acid sulfate (AS I) assemblage is consistent with the condensation of high-temperature magmatic vapors and subsequent disproportionation of magmatic SO_2 at temperatures <400° C (Holland, 1965). Isotope data indicate that vapors were absorbed into fluids with magmatic H- and O-isotope signatures and there is no evidence for significant mixing with meteoric waters. These fluids would have become increasingly acid and oxidizing following the dissociation of H_2SO_4 and HCl with decreasing temperature. Variations in the clay mineralogy of the AS I assemblage record a progressive cooling of these hydrothermal fluids with increasing elevation. Similarly, the zonation of acid sulfate and silicic assemblages to surrounding argillic and propylitic alteration is typical of high sulfidation systems and indicates progressive neutralization of hypogene hydrothermal fluids by wallrock reaction outward from the main fluid conduits (e.g. Stoffregen, 1987; Arribas, 1995). Vuggy silica alteration, which is generated from leaching by hydrothermal fluids of pH <2 and temperatures less than about 250° C (Stoffregen, 1987), is relatively scarce in the Pascua area. This scarcity suggests that either the early magmatic-hydrothermal fluids were not sufficiently acidic to leach Al from the host rock, or that fluids rose along multiple conduits and were not focused in any one area. Given the large areal extent of alteration and the abundance of pre-existing structural conduits, we consider the latter explanation the more likely.

Syn-mineral alteration:

Deposition of AS II alunite and associated Cu and Au mineralization occurred in the Brecha Central and Frontera zones at approximately 8.8-8.1 Ma. Wallrock alteration appears to be limited to structurally controlled acid sulfate (AS II) and silicic assemblages. Abundant alunite precipitated with the sulfide-rich APE mineralizing facies along open fractures and in the matrix of hydrothermal breccias. Isotopic data for this stage are nearly identical to the early acid sulfate alteration event and again indicate a dominantly magmatic fluid source and depositional temperatures between 200-350° C. Data are consistent with the condensation of high temperature magmatic vapors into fluids of dominantly magmatic origin (e.g., Rye et al., 1992). These fluids ascended to elevations of *ca.* 4500-4700 m, where they precipitated an

assemblage of alunite with enargite, pyrite, and native sulfur. The fO_2 and pH conditions of mineral deposition can be modeled on the basis of this assemblage, at temperatures calculated from alunite-pyrite isotope pairs (Fig. 2.16). These calculations indicate that ore precipitated from relatively oxidized, acidic, and sulfur-rich fluids. These findings are not consistent with a near-neutral, reduced ore-fluid that is inferred for many high sulfidation deposits (e.g., Hedenquist et al., 1998: details see Chap. 6).

The occurrence of coarse-grained magmatic steam alunite above Brecha Central suggests that episodic pulses of high-pressure, high temperature magmatic vapors were released to the near-surface environment (e.g., Rye, 1993: details see Chap. 3). The timing of steam-heated alteration above the Brecha Central and Frontera areas is unconstrained. The $^{40}Ar/^{39}Ar$ ages are inconclusive, and alteration may be related to either pre- or syn-mineral magmatic-hydrothermal activity, or likely both. Steam-heated alteration forms only under sub-aerial conditions and the relatively large thickness of this alteration zone suggests a progressive descent of the water table. However, isotopic data for alunite indicate that there was little, if any, meteoric water involved in the alteration process.

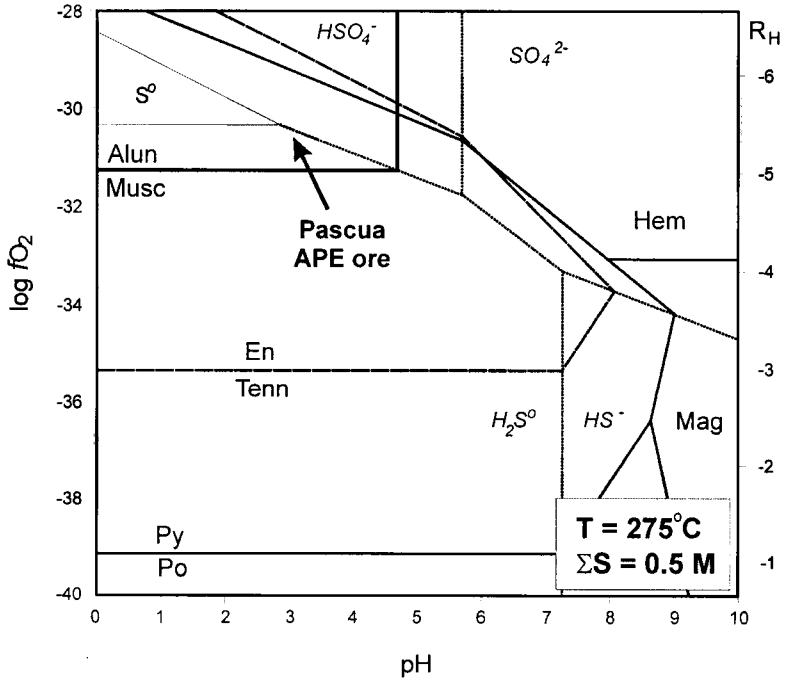

Figure 2.16. The Pascua APE mineralizing event in terms of pH and the fugacity of O_2 at 275°C and 0.5 molal total dissolved sulfur. Stability relations among minerals are calculated using reactions given in Appendix D. Pressure equals vapour saturation at temperature. The grey area represents the chemical characteristics of APE mineralizing fluids and is contained within the stability fields of alunite, pyrite, enargite, and native sulfur. Mineral abbreviations: alunite (alun), enargite (en), hematite (hem), magnetite (mag), muscovite (musc), pyrrhotite (po), pyrite (py), native sulfur (S^o), tennantite (tenn).

Post-mineral alteration:

Late-stage acid sulfate alteration events record the gradual collapse of the magmatic-hydrothermal system. Isotopic data indicate a progressive mixing of magmatic and meteoric fluids as temperatures cooled to ≤100° C. Alunite ± quartz and jarosite precipitated as thin veins and disseminations from sulfate-rich fluids that we propose were generated from the oxidation of precursor sulfides. Due to the overlap in $^{40}Ar/^{39}Ar$ age data, these processes may have been active at surface or at the margins of the system even as magmatic-dominated fluids were still ascending at depth in the core of the deposit. The wide range of trace-element (eg., Pb, Ba, Zn) contents in late-stage alunite was likely derived from the remobilization of the precursor AS II sulfide assemblage. These late-stage, acidic, moderate-temperature fluids may have been responsible for the enrichment of Ag observed at higher elevations in the Brecha Central area (discussed in Chouinard and Williams-Jones, 1999).

Supergene jarosite has been identified based on paragenetic observations and stable-isotope data. The occurrence of supergene jarosite suggests that most magmatic activity in this region had stopped by 7.5 Ma at the latest. This is the youngest alteration event recognized in the district. Evidence for the supergene remobilization of Au is observed in the Esperanza area, where visible Au occurs as coatings on high-level, oxidized fracture surfaces. Similar processes are apparent at the Penelope deposit on the Lama side of the property and are important factors in determining the economic feasibility of the region as a whole.

REFERENCES

Aoki, M., 1991. Mineralogical features and genesis of alunite solid solution in high temperature magmatic-hydrothermal systems. Journal of the Geological Survey of Japan, 277, 31-32.

Aoki, M., Comsti, E.C., Lazo, F.B., and Matsuhisa, Y., 1993. Advanced argillic alteration and geochemistry of alunite in an evolving hydrothermal system at Baguio, northern Luzon, Phillipines. Resource Geology, 43, 155-164.

Arribas, A., Jr., 1995. Characteristics of high sulfidation epithermal deposits, and their relation to magmatic fluids. Mineralogical Association of Canada Short Course Notes, v. 23, 419-454.

Arribas, A., Jr., Cunningham, C.G., Rytuba, J.J., Rye, R.O., Kelly, W.C., McKee, E.H.,

Podwysocky, M.H., and Tosdal, R.M., 1995. Geology, geochronology, fluid inclusions, and stable isotope geochemistry of the Rodalquilar Au alunite deposit, Spain. Economic Geology, 90, 795-822.

Beane, R.E., 1988. Hydrothermal alteration and mineralization at the Nevada prospect, Chile. Unpublished company report, Barrick Corp.

Bissig, T., 2001. Metallogenesis of the Miocene El Indio-Pascua gold-silver-copper belt, Chile/ Argentina: Geodynamic, geomorphological and petrochemical controls on epithermal mineralization. Unpublished Ph.D. thesis, Queen's University.

Caceres, C., Cordova, M., Rojas, F., and Vega, J., 1997. Projecto Mina Pascua – Informe de exploraciones: Temporada 1996-1997. Internal company report.

Chouinard, A. and Williams-Jones, A.E. 1999. Mineralogy and petrography of ore and alteration assemblages at the Pascua Au-Ag-Cu deposit, Chile. Internal for Barrick Gold and Barrick Chile Ltda.

Cooke, D.R. and Simmons, S.F., 2000. Characterisitcs and genesis of epithermal gold deposits. *In* Hagemann, S.G. and Brown, P.E., eds., Gold 2000. Reviews in Economic Geology, 13, 221-244.

Craig, H., 1961. Isotopic variations in meteoric waters. Science, 133, 1702-1703.

Cunningham, C.G., Rye, R.O., Steven, T.A., and Mehnert, H.H., 1984. Origins and exploration signficance of replacement and vein-type alunite deposits in the Marysvale volcanic field, west central Utah. Economic Geology, 79: 50-71.

Dill, H.G., 2001. The geology of aluminum phosphates and sulfates of the alunite group minerals; a review. Earth-Science Reviews, 53, 35-93.

Flynn, F.R., and Burnham, C.W., 1978. An experimental determination of rare earth partition coefficients between a chloride-containing vapor phase and silicate melts. Geochimica et Cosmochimica Acta, 42, 685-701.

Fulignati, P., Gioncada, A., and Sbrana, A., 1999. Rare-earth element behaviour in the alteration facies of the active magmatic-hydrothermal systems of Vulcano (Aeolian Islands, Italy). Journal of Volcanology and Geothermal Research, 88, 325-342.

Gieseman, A., Jager, H.J., Norman, A.L., Krouse, H.R., and Brand, W.A., 1994. On-line sulfur-isotope determination using and elemental analyzer coupled to a mass spectrometer. Analytical Chemistry, 65(18).

Giggenbach, W.F., 1992. Magma degassing and mineral deposition in hydrothermal systems along convergent plate boundaries. Economic Geology, 87, 1927-1944.

Godfrey, J.D., 1962. The deuterium content of natural waters and other substances. Geochimica et Cosmochimica Acta, 27: 43-52.

Hamilton, J.V. 1998. Aspects of the structural setting, alteration, and Au-Ag-Cu mineralization at the Pascua deposit, east-central Chile. Unpublished company report, Barrick Corp.

Hedenquist, J.W., Arribas, A.R., and Gonzalez-Urien, E., 2000. Exploration for epithermal gold deposits. *In* Hagemann, S.G. and Brown, P.E., eds., Gold 2000. Reviews in Economic Geology, 13, 245-278.

Hedenquist, J.W., Matsuhisa, Y., Izawa, E., White, N.C., Giggenbach, W.F., and Aoki, M., 1994. Geology, geochemistry, and origin of high sulfidation Cu-Au mineralization in the Nansatsu District, Japan. Economic Geology, 89, 1-30.

Hemley, J.J., Montoya, J.W., Marinenko, J.W., and Luce, R.W., 1980. Equilibria in the system Al_2O_3-SiO_2-H_2O and some general implications for alteration/mineralization processes. Economic Geology, 75, 210-228.

Henley, R.W., and Stewart, M.K., 1983. Chemical and isotopic changes in the hydrololoy of the Tauhara geothermal field due to exploitation at Wairakei. Journal of Volcanology and Geothermal Research, 15, 285-314.

Holland, H.D., 1965. Some applications of thermochemical data to problems of ore deposits, II. Mineral assemblages and the composition of ore-forming fluids. Economic Geology, 60, 1101-1166.

Jannas, R.R., Bowers, T.S., Petersen, U., Beane, R.E., 1999. High-sulfidation deposit types in the El Indio District, Chile. *In* Skinner, B.J. ed., Geology and ore deposits of the Central Andes, SEG special pub. #7, 27-59.

Jambor, 1999. Nomenclature of the alunite supergroup. Canadian Mineralogist, 37. 1323-1341.

John, D.A., Nash, J.T., Clark, C.W., and Wulftange, W.H., 1991. Geology, hydrothermal alteration, and mineralization at the Paradise Peak gold-silver-mercury deposit, Nye County, Nevada. *In* Raines, G.L., Lisle, R.E., Schafer, R.W., and Wilkinson, W.H., eds., Geology and Ore deposits of the Great Basin, Symposium Proceedings. Geological Society of Nevada, Reno, 1020-1050.

Kesler, S.E., Russel, N., Seaward, M., Rivera, J., McCurdy, K., Cumming, G.L., and Sutter, J. F., 1981. Geology and geochemistry of sulfide mineralization underlying the Pueblo Viejo gold-silver-oxide deposit, Dominican Republic. Economic Geology, 76, 1096-1117.

Kornexl, B. E., Gehre, M., Höfling, R., and Werner, R.A., 1999. On-line $\delta^{18}O$ measurement of

organic and inorganic substances. Rapid Communications in Mass Spectrometry, 13, 1685-1693.

Lottermoser, B.J., 1992. Rare earth elements and hydrothermal ore formation processes. Ore Geology Reviews, 7, 25-41.

Maksaev, V., Moscoso, R., Mpodozis, C., and Nasi, C., 1984. Las unidades volcánicas y plutonicas del cenozoico superior en la Alta Cordillera del Norte Chico (29°-31° S): Geología, alteración hidrothermal y mineralisacion: Revista geológica de Chile, 21, 11-51.

Martin, M, Clavero, J., and Mpodozis, C., 1995. Estudio geologico regional del Franja El Indio, Cordillera de Coquimbo. Servicio National de Geologia y Minera, Santiago, Chile. Registered report IR-95-06, 232p.

Martin, M.W., Clavero, J.R., Mpodozis, C., 1999. Late Paleozoic to Early Jurassic tectonic development of the high Andean Principal Cordillera, El Indio Region, Chile (29-30° S). Journal of South American Earth Sciences, 12, 33-49.

Michard, A., 1989. Rare earth element systematics in hydrothermal fluids. Geochimica et Cosmochimica Acta, 53, 745-750.

Nixon, G.T., 1998. The volcanic geology of Pascua: Implications for mineral exploration. Unpublished company report, Barrick Corp.

Ohmoto, H., and Lasaga, A.C., 1982. Kinetics of reactions between aqueous sulfates and sulfides in hydrothermal systems. Geochemica et Cosmochimica Acta, 46, 1727-1746.

Petersen, E.U., and Thompson, A.J.B., 1992. Analysis of alunite and other thermally sensitive minerals. Microprobe Analyst (Internal report for the Dept. of Geology and Geophysics, University of Utah), April, 2-6.

Ramos, V. A., Mahlburg Kay, S, Page, R. N. and Munizaga, F., 1989. La ignimbrita Vacas Heladas y el cese del volcanismo en el Valle del Cura, Provincia de San Juan. Revista Asociación Geológica Argentina, 44, 336-352.

Reed, M.J., 1995, Distribution of rare earth elements between aqueous fluids and granitic melt. Ph.D. thesis, Univ of Maryland at College Park.

Reyes, A.G., 1990. Petrology of Phillipine geothermal systems and the application of alteration mineralogy to their assessment. Journal of Volcanology and Geothermal Research, 43, 279-309.

Rye, R.O., 1993. The evolution of magmatic fluids in the epithermal environment: The stable isotope perspective. Economic Geology, 88, 733-753.

Rye, R.O., and Alpers, C.N., 1997. The stable isotope geochemistry of jarosite. USGS Open

File Report 97-88, 28 p.

Rye, R.O., Bethke, P.M., and Wasserman, M.D., 1992. The stable isotope geochemistry of acid sulfate alteration. Economic Geology, 87, 225-262.

Rye, R.O, and Stoffregen, R.E., 1995. Jarosite-water oxygen and hydrogen isotope fractionations: preliminary experimental data. Economic Geology, 90, 2336-2342.

Sandeman, H.A., Archibald, D.A.; Grant, J.W.; Villneuve, M.E. and Ford, F.D. 1999. Characterisation of the chemical composition and ^{40}Ar-^{39}Ar systematics of intralaboratory standard MAC-83 biotite. *In* Radiogenic Age and Isotopic Studies: Report 12; Geological Survey of Canada, Current Research 1999-F, p.13-26.

Savin, S.M., and Epstein, S., 1970. The oxygen and hydrogen isotope geochemistry of clay minerals. Geochimica et Cosmochimica Acta, 34, 24-42.

Schwab, R.G., Herold, H, Gotz, C. and de Oliveira, N.P., 1990. Compounds of the crandallite type: Synthesis and properties of pure rare earth element phosphates. Neues Jahrbuch fuer Mineralogie, 6, 241-254.

Schoen, R., White, D.E., and Hemley. J.J., 1974. Argillization by descending acid at Steamboat Springs, Nevada. Clays and Clay Minerals, 22, 1-22.

Sillitoe, R.H., 1993. Epithermal models: Genetic types, geometric controls, and shallow features. *In* Kirkham, R.V., Sinclair, W.D., Thorpe, R.I., and Duke, J.M., eds. Mineral Deposit Modelling; Geological Association of Canada, Special Paper 40, p.403-417.

Sillitoe, R.H., 1999. Styles of high sulfidation gold, silver and copper mineralization in the porphyry and epithermal environments. PacRim '99. Bali, Indonesia, 10-13 October, Proceedings, p. 29-44.

Stoffregen, R., 1987. Genesis of acid sulfate alteration and Au-Cu-Ag mineralization at Summitville, Colorado. Economic Geology, 82, 1575-1591.

Stoffregen, R.E. and Alpers, C.N., 1987. Woodhouseite and svanbergite in hydrothermal ore deposits: Products of apatite destruction during advanced argillic alteration. Canadian Mineralogist, 25, 201-211.

Stoffregen, R.E., Alpers, C.N, and Jambor, J.L., 2000. Alunite-jarosite crystallography, thermodynamics, and geochronology. *In* Alpers, C.N., Jambor, J.L., and Nordstrom, D.K., eds., Sulfate Minerals; Crystallography, geochemistry, and environmental significance. Reviews in Mineralogy and Geochemistry, 40, p. 454-480.

Stoffregen, R.E., and Cygan, G., 1990. An experimental study of Na-K exchange between alunite and aqueous sulfate solutions. American Mineralogist. 75, 209-220.

Stoffregen, R.E., Rye, R.O., and Wasserman, M.D., 1994. Experimental studies of alunite: I. ^{18}O-^{16}O and D-H fractionation factors between alunite and water at 250-450°C. Geochimica et Cosmochimica Acta, 58, 903-916.

Steiger, R. H. and Jäger, E., 1977. Subcommission on geochronology: convention on the use of decay constants in geo- and cosmochronology. Earth and Planetary Science Letters, 36, 359-362.

Taylor, B.E., 1988. Degassing of rhyolitic magmas: Hydrogen isotope evidence and implications for magmatic-hydrothermal ore deposits. Canadian Institute of Mining and Mineralogy Special Volume, 39, 33-49.

Thompson, A.J.B., Hauff, P.L., and Robitaille, A.J. 1999. Alteration mapping in exploration: Application of short-wave infrared (SWIR) spectroscopy. SEG newsletter, October 1999.

Thompson, A.J.B., and Petersen, E.U., 1995. Characteristics of alunite in relation to ore-forming environment. Unpublished data.

Volkert, D.F., McEwan, C.J.A., Garay, E., 1998. Pierina Au-Ag deposit, Cordillera Negra, North-Central Peru. *In* Pathways '98: Extended Abstracts Volume.

Chapter 3

ALUNITE IN AN EVOLVING MAGMATIC-HYDROTHERMAL SYSTEM; THE TAMBO HIGH SULFIDATION DEPOSIT, EL INDIO DISTRICT, CHILE

INTRODUCTION

The Tambo high sulfidation gold deposit is located in the El Indio-Pascua Belt, within the Main Cordillera of Chile (Fig. 3.1). This belt hosts widespread zones of hydrothermal alteration and several world-class epithermal deposits and prospects, including El Indio (>10 Moz Au produced), Pascua-Lama (proven and probable resources of 17 Moz Au and 560 Moz Ag) and Veladero (15 Moz Au, 230 Moz Ag). The Tambo deposit is relatively small in comparison, with a total production of just over 0.8 Moz Au from several tectonic-hydrothermal breccias and high-grade veins.

Previous studies of the El Indio district (Siddeley and Areneda, 1985; Bennet, 1995; Jannas, 1995; Jannas et al., 1999) have constrained the geological setting of the Tambo deposit. This region has many features in common with other high sulfidation systems, although the deposit is unique in several aspects.

1. Limited erosion has preserved many features of the hydrothermal system, including the near-paleosurface. As such, multiple stages of alunite ($KAl_3(SO_4)_2(OH)_6$) and acid sulfate alteration can be recognized over several hundred metres of vertical extent. These stages include each of the four major types of acid sulfate alteration described by Rye et al. (1992): magmatic-hydrothermal, magmatic steam, steam-heated, and supergene.
2. Mineralization is sulfide- and Cu- poor in comparison to most other deposits of this type (e. g., Cooke and Simmons, 2000; Sillitoe, 1999). Ore is hosted primarily in barite and alunite ± quartz.
3. A second stage of Au mineralization is hosted in, and associated with, alunite of magmatic steam origin (this study; Jannas et al., 1999).

In this paper, we examine shallow-level magmatic-hydrothermal processes within a well-constrained geological framework. The goal of this investigation was to clarify the evolution of the Tambo deposit and, in particular, to determine the role of magmatic fluids, the mechanisms

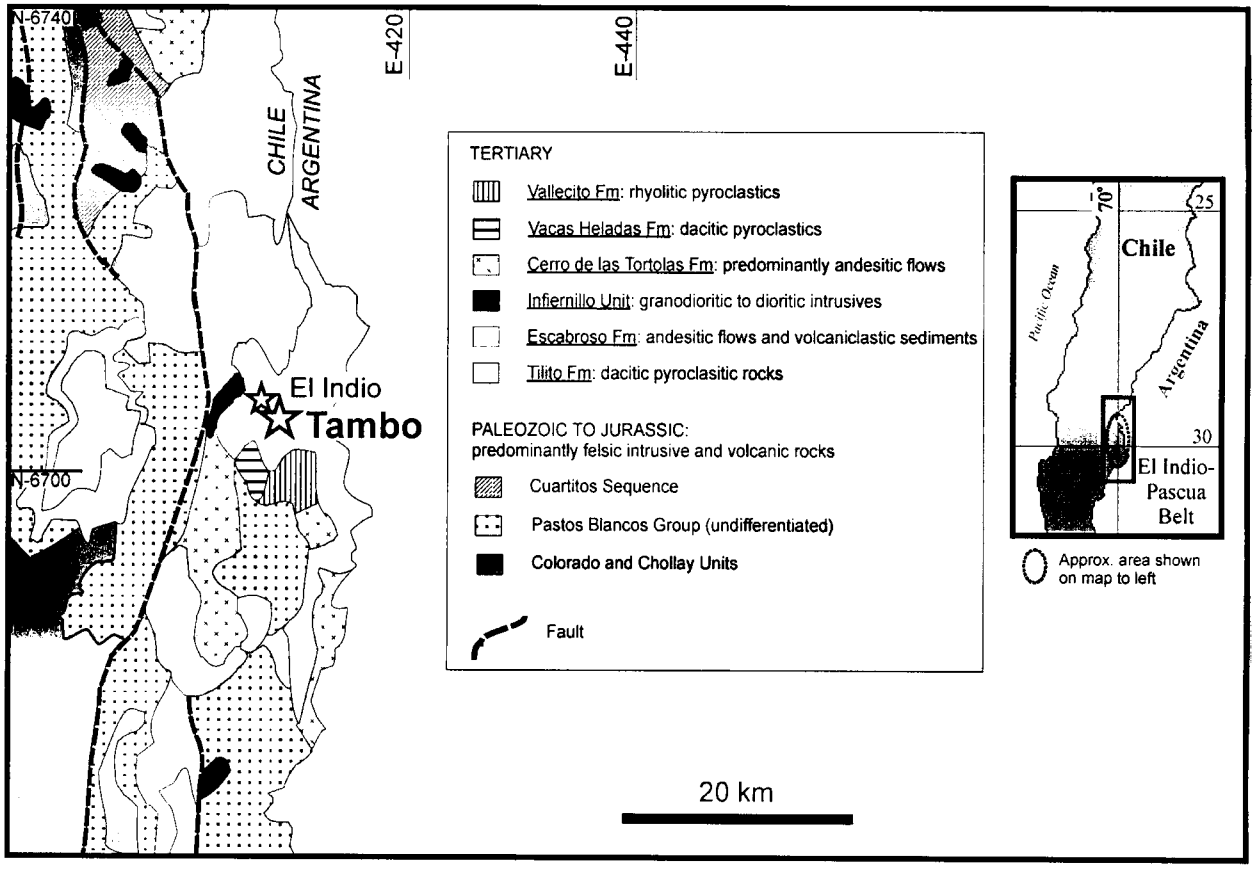

Figure 3.1. Geology of the El Indio district adapted from Jannas et al. (1999). Locations of the Tambo and El Indio properties are shown. See inset map for area location.

of ore-metal transport, and the nature of magmatic steam processes. Emphasis is placed on the temporal and spatial relationship between alunite and Au mineralization, because the isotopic, geochronologic, and geochemical characteristics of alunite can be used to resolve the nature of source fluids (e.g., Bethke, 1984; Rye et al., 1992). Eight different stages of alunite have been recognized at the Tambo deposit. The relative timing of each event was determined from the paragenetic sequence defined by Jannas (1995), with additional constraints from field relations and new $^{40}Ar/^{39}Ar$ ages for alunite.

GEOLOGICAL FRAMEWORK

Regional geology

The El Indio-Pascua Belt is located in the center of a presently amagmatic segment of the Andean Cordillera. The lack of recent volcanism is attributed to subhorizontal subduction of the Nazca plate beneath the South American continent between 27° 30' and 33° S (Barazangi and Isacks, 1976). The district is approximately 100 km long and 30-40 km wide and straddles the Chile–Argentina border (Fig. 3.1). Hydrothermal systems formed within a NNE-SSW-striking tectonic depression bounded by the steeply west-dipping high-angle reverse Baños del Toro Fault to the west and opposing structures in the Valle del Cura region to the east. Within this block, an Upper Paleozoic to lower Jurassic basement, predominantly composed of calc-alkaline felsic intrusive suites and volcanic rocks (Martin et al., 1999), is overlain by up to 1500 m of Tertiary subaerial volcanic strata. The latter are extensively preserved in the southern part of the belt, where the Tambo and El Indio mines are located (Fig. 3.1), but are less widespread in the northern extremity of the district near Pascua-Lama and Veladero (Martin et al., 1995; Maksaev et al., 1984). The Tertiary volcanic sequence is briefly summarized here after Bissig (2001) and Martin et al. (1995). A thick succession (up to 1200 m) of dacitic and rhyodacitic tuffs with volcaniclastic sediments and subordinate basaltic and andesitic flows comprises the 23-27 Ma Tilito Formation. It is separated from the overlying 17.5-21 Ma Escabroso Formation by an angular unconformity marked by a persistent regolith horizon. The latter consists predominantly of andesitic lavas and hypabyssal intrusive bodies as well as volcaniclastic sedimentary rocks. After a brief deformation event, igneous activity continued and is represented by the 14-17 Ma andesitic Cerro de las Tórtolas Formation and the contemporaneous Infiernillo Intrusive Unit. Magmatism decreased markedly thereafter. Dacitic tuffs of the Vacas Heladas Formation erupted from isolated centers between 11 and 12.7

Ma. A single 7.8 Ma dacite dike, the only igneous rock coeval with mineralization in the district, is reported from Pascua (Bissig, 2001). The 5.5-6.2 Ma Vallecito Formation rhyolitic tuffs are restricted to an ignimbrite sheet in the Valle del Cura (Ramos et al., 1989) and some occurrences in the El Indio-Tambo area. Volcanism ceased in the Upper Pliocene after eruption of the 2 Ma Cerro de Vidrio rhyolite dome in the northeast corner of the belt (Bissig, 2001).

Local geology

The geology of the El Indio-Tambo district is dominated by an upper Oligocene to Upper Miocene sequence of intensely fractured volcanic and volcaniclastic rocks. The epithermal mineralization is hosted by rhyolitic ash-flow tuffs of the Tilito Formation ("Amiga tuff"; Jannas et al., 1999) and, at El Indio, is overlain by Escabroso Formation andesitic lavas. Intrusive units and hydrothermal alteration of Escabroso and Infiernillo age are also present in the area. However, $^{40}Ar/^{39}Ar$ ages for both El Indio and Tambo mineralization are significantly younger than these intrusions. The El Indio vein system formed between 7.8 and 6.2 Ma (Bissig, 2001), whereas the Tambo ore was deposited between 7 and 9 Ma (this study; Bissig, 2001). Tuffs of the Vacas Heladas Formation were deposited to the southwest of El Indio in the Azufreras region, and rhyolites of the Vallecito Formation occur ca. 4 km south of Tambo.

The structural grain of the El Indio-Tambo district is dominated by NNE- and NW-trending normal and high-angle reverse faults and conjugate shear faults (Martin et al. 1995; Caddey, 1993). Mineralization is thought to have occurred during an early compressional event that was followed by regional relaxation and the development of shear fractures and normal oblique-slip faults (Caddey, 1993).

Mineralization

Gold (and Ag) mineralization at Tambo is hosted in three major hydrothermal breccias and several small high-grade veins. Two of the major breccia deposits, Kimberly and Wendy, are on the north-west and south flanks of Cerro Elefante, respectively (Fig. 3.2 and 3.3). These deposits have lateral and vertical dimensions of up to 300 m and 400 m, respectively, and consist of matrix-supported, monolithic breccias that contain altered fragments of Amiga tuff (Jannas et al., 1999). The main ore zone occurs between 4200 m and 4000 m a.s.l., with grades up to 4-10 g/t Au and 10 g/t Ag (Jannas et al., 1999). The Canto Sur deposit is located at a higher elevation on Cerro Canto, which separates the El Indio and Tambo mines. All three breccias are located at, or close to, the intersection of north-northwest and east-northeast fault

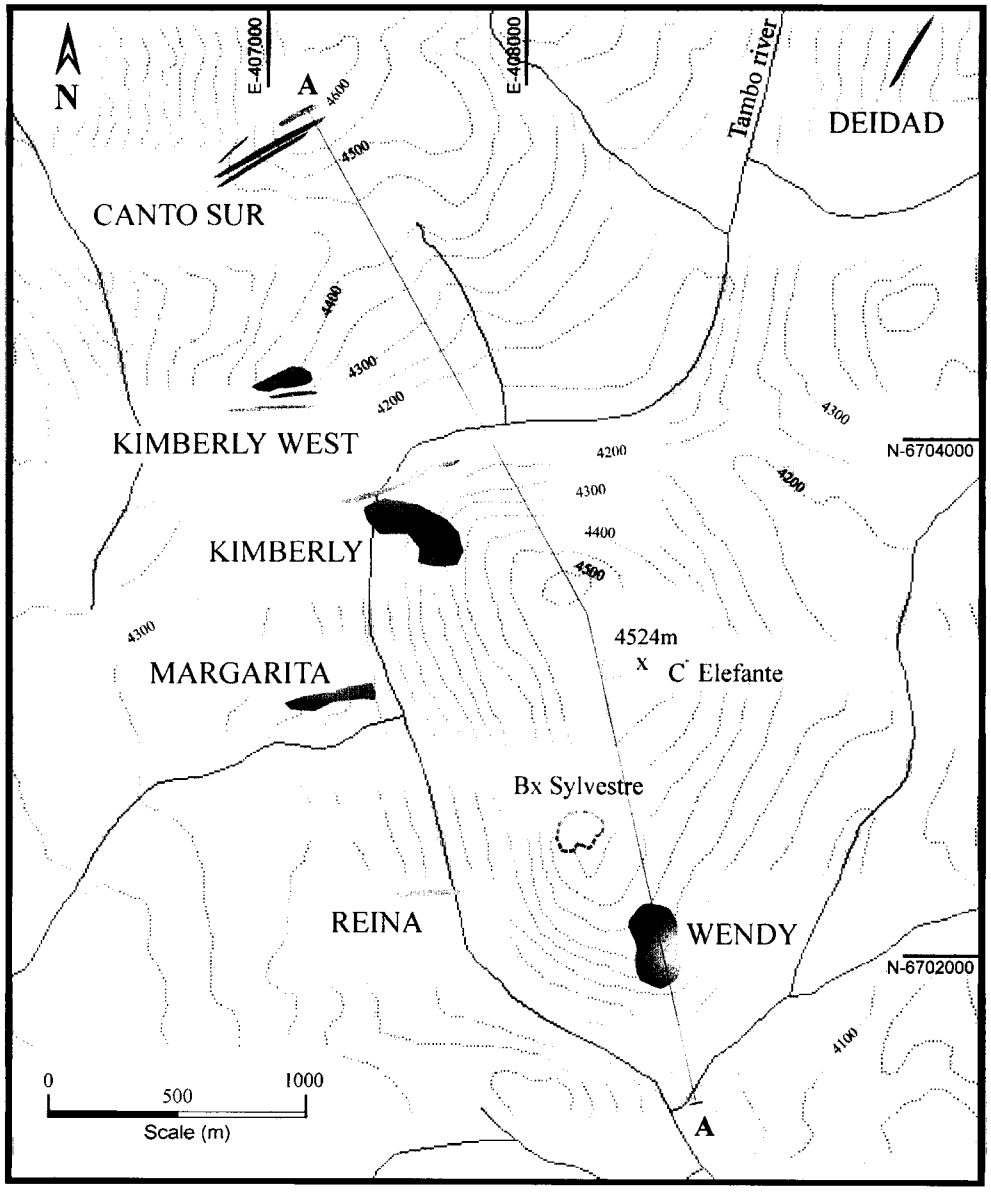

Figure 3.2. Map of the Tambo property modified from Jannas et al. (1999). Shaded areas indicate zones of mineralization.

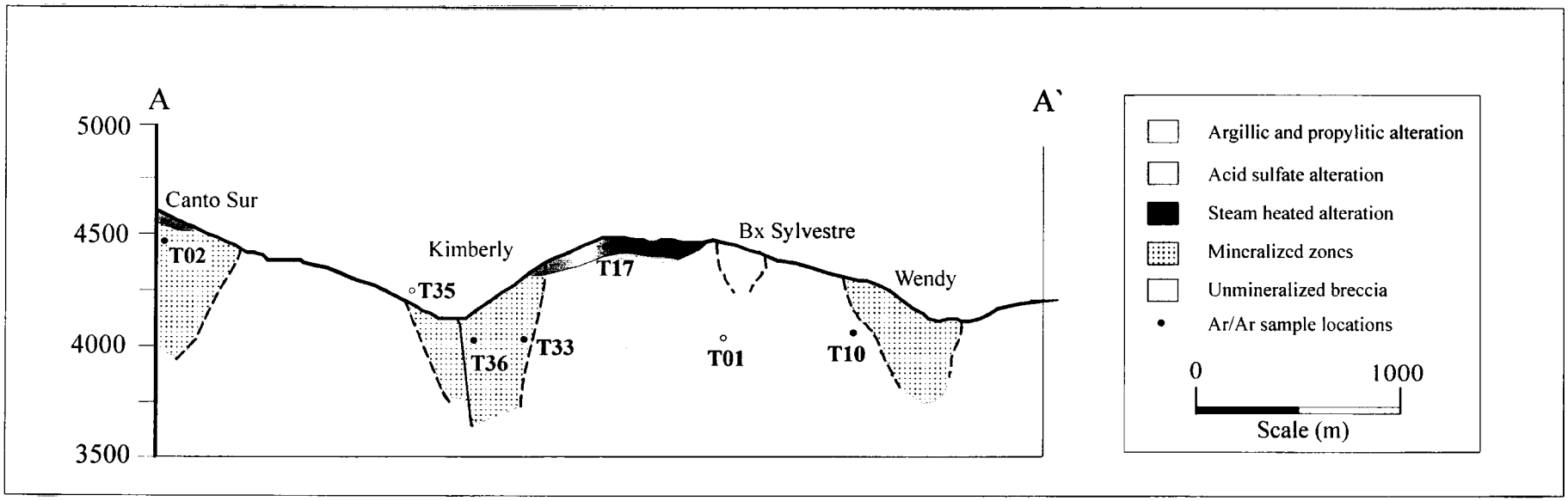

Figure 3.3. Schematic section showing a projection of the three major mineralized breccias (Canto Sur, Kimberly, and Wendy) and zones of alteration at Tambo. Line of section is marked on Figure 2.2. Also shown are locations of $^{40}Ar/^{39}Ar$ samples; open symbols indicate samples projected onto the section.

systems in areas of intense shears and extensional joints (Jannas et al., 1999). Barite is common in both the Canto Sur and Kimberly breccias, and the original matrix has been completely replaced by barite-alunite ± quartz cement. No barite is present at Wendy, however, and the breccia matrix consists entirely of alunite ± quartz. Vein mineralization at Tambo is primarily hosted by the Reina, Deidad, and Indigena structures (Fig. 3.2). These veins are typically narrow (1-4 m wide), of limited vertical extent (< 200 m), and consist of primarily barite and alunite ± quartz. Ore grades average 15 g/t Au and 30 g/t Ag, but locally exceed 1000 g/t Au (Jannas et al., 1999).

Two stages of mineralization were recognized by Jannas et al. (1999). Early Au mineralization (Stage 2; Table 3.1) is closely associated with barite in both the veins and the breccia deposits. Electrum, minor sulfides (including enargite, galena, and pyrite), native tellurium, other Te minerals, and native gold are concentrated along growth planes in the barite. Trace sulfides and gold occur interstitial to alunite overgrowths on barite grains. Gold also occurs locally on the rims of the breccia fragments. The second stage of mineralization (Stage 3; Table 3.1) is characterized by native gold that occurs in fractures and vugs, and interstitial to grains of alunite, hematite, jarosite, and barite. Inclusions of native gold also occur in alunite. Sulfides are rare, although minor enargite occurs at depth in the Wendy breccia, intergrown with coarse alunite grains. Early tellurides are typically replaced by minerals such as poughite, rodalquilarite, and tellurite (Jannas et al., 1999).

METHODS OF ANALYSIS

Alteration assemblages were identified by field and petrographic observations, using the paragenetic relations described by Jannas et al. (1999). Field work was carried out between February, 1998 and April, 1999. Access at the time was limited to surficial outcrops, open pits (Kimberly, Wendy, and Canto Sur), and drill core. The mineralogy and character of each paragenetic stage were determined by examination of thin and polished sections using standard optical methods and X-ray diffraction (XRD). In addition, short-wave infrared (SWIR) analyses were made *in situ* using a Portable Infrared Mineral Analyzer (PIMA), a field-portable spectrometer that measures reflectance spectra in the SWIR band. Spectra were analyzed using PIMAView 3.0 software, and mineral identification was made by comparison to standards in the SPECMIN database (Thompson et al., 1999). Representative samples from each

Table 3.1: Paragenetic sequence and characteristics of the 8 different stages of alunite formation at Tambo. Abbreviated mineral names; alunite (alun), quartz (qtz), kaolinite (kao), dickite (dick), pyrophyllite (pyl), walthierite (wal), jarosite (jar), enargite (en), galena (gn), pyrite (py), hematite (hem), huangite (huag). Reported Ar/Ar ages in bold are from this study; other ages are reported in Bissig et al (in prep).

	Brecha Sylvestre	**Stage 1**	**Stage 2**	**Stage 3**	**Banded Veins**	**Steam Heated**	**Huangite-bearing Veins**	**Late Stage Oxidation**
$^{40}Ar/^{39}Ar$ age	10.42 ± 0.28	**11.00 ± 0.27**	**8.71 ± 0.21**	8.24 ± 0.15	-	**8.86 ± 0.38**	**8.63 ± 0.41**	**7.25 ± 0.14**
Alunite Occurrence	Matrix fill; with qtz and late jar	Qtz-alun ± kao, dick, pyl alteration of Amiga tuff	Vein and bx matrix alun associated with bar, wal, trace qtz, and late jar	Fine-grained to coarse, breccia and vein filling alun	Coarse, banded alun veins with hem	Surficial qtz - kao - S^o ± alun alteration	Fine-grained, thin pink alun-huag veinlets with trace kao	Fine-grained alun with minor qtz; late jar
Mineralization	-	-	Electrum, minor sulfides (en, gn, py), native Te, Te-Au minerals, native Au	Native Au, trace en	-	-	-	-

paragenetic stage were selected for further analysis.

Six samples were dated by $^{40}Ar/^{39}Ar$ laser step-heating methods. All analyses were carried out at the Queen's University ^{40}Ar-^{39}Ar laboratory equipped with a Mass Analyzer Products MAP 216 mass spectrometer. About 10 mg of each sample were irradiated for 7.5 h at McMaster nuclear reactor in Hamilton, Canada, using biotite standard Mac-83 as a radiation flux monitor (24.36 ± 0.17 Ma; Sandeman et al., 1999). J-values for individual samples were determined by second-order polynomial interpolation and, for the samples discussed in this article, were about 2.4×10^{-3} and varied by less than 0.02×10^{-3}. Samples were step-heated using a defocused LEXEL 3500 Ar laser-beam. Ages were calculated using the decay constants suggested by Steiger and Jäger (1977), and all errors are given at 2σ.

Geochemical characteristics of alunite were determined by analysis of individual grains and sample composites. Grain mounts and polished sections were analyzed by scanning-electron microscopy with energy-dispersion spectroscopy (SEM-EDS) and electron-probe microanalysis (EPMA). EPMA data were collected on a fully-automated CAMECA SX-50 microprobe, operating in the wavelength-dispersion mode with the following operating conditions: 15 keV excitation voltage, 10 nA beam current, 15 μm beam diameter, and total count time under 65 seconds. Analytical parameters were chosen to minimize beam damage caused by the volatilization of alkali elements (Petersen and Thompson, 1992). Data reduction was done with the 'PAP' method of Pouchou and Pichoir (1985). Alunite separates (approximately 1 g samples) were carefully hand-picked and treated using a 1:1 HF/H_2O solution to remove silicate contaminants (Wasserman et al., 1992). The purity of separates was verified by XRD, but trace to minor amounts (i.e., ≤ 10 volume %) of quartz, clays, or other impurities may be present. Samples were analyzed by inductively-coupled plasma mass spectrometry (ICP-MS) for trace metal and rare-earth-element (REE) contents by ALS Chemex Laboratories, Canada. For trace metal analysis, samples were dissolved in a mixture of perchloric, nitric and hydrofluoric acids to ensure total dissolution. For REE determination, samples were fused with lithium metaborate prior to analysis. Alunite REE data are normalized to average REE content of volcanic tuffs from the Tilito Formation (T. Bissig, unpub. data; average values given in Table 3.2) that host ore in the El Indio district.

Table 3.2: Average major and rare earth element geochemical data for unaltered rocks of the Tilito Fm (n=3). Data from Bissig (2001).

	Tilito Fm
Na_2O (wt %)	2.85
K_2O	3.85
CaO	4.48
MgO	1.25
MnO	0.07
Fe_2O_3 (Fe total)	4.33
Al_2O_3	16.03
P_2O_5	0.15
SiO_2	63.39
TiO_2	0.57
Total	**97.35%**
REE ICP-MS (ppm)	
La	31.6
Ce	62.6
Pr	7.2
Nd	25.2
Sm	4.8
Eu	1.0
Gd	3.9
Tb	0.6
Dy	3.5
Ho	0.7
Er	2.1
Tm	0.3
Yb	2.1
Lu	0.3

Complete stable isotopic analyses ($\delta^{34}S$, δD, $\delta^{18}O_{SO4}$, and $\delta^{18}O_{OH}$) were determined for alunite from each paragenetic stage. Sulfur-isotope data were also obtained for selected barite and enargite samples. All data were collected at the U.S. Geological Survey Isotope Laboratory in Denver, USA. Samples were separated and prepared according to the procedure of Wasserman et al. (1992). Sulfur isotopic analyses were determined by an on-line method using an elemental analyzer coupled to a Micromass Optima mass spectrometer (Giesemann et al., 1994). Analytical precision is better than ± 0.2‰. D/H analyses were performed by a step-heated technique modified from Godfrey (1962), with analytical precision better than ± 3‰. Alunite oxygen-isotope data were collected for both sulfate and hydroxyl oxygen. For $\delta^{18}O_{SO4}$

analysis, alunite was dissolved in a hot NaOH solution, and sulfate was precipitated as $BaSO_4$ (Wasserman et al., 1992). The $BaSO_4$ precipitate was then analyzed by fluorination with BrF_5 at 580°C in accordance with the standard analytical procedure of Clayton and Mayeda (1963), and as used by Pickthorn and O'Neil (1985). Analytical precision is estimated at ± 0.15‰. $\delta^{18}O_{OH}$ was determined by material balance using the total-O isotopic composition of alunite (measured by fluorination with BrF_5, described above) and $\delta^{18}O_{SO4}$ results. Several oxygen-isotope analyses were also determined by pyrolysis with a Finnigan TC/EA coupled to a Finnigan Delta Plus XL mass spectrometer using continuous-flow methods modified from Kornexl et al. (1999; details in Appendix B). Analytical precision is better than ± 0.3‰.

Fluid-inclusion gas analyses were carried out at the U.S. Geological Survey fluid-inclusion and noble-gas laboratories in Denver, USA. All samples were initially crushed in a sealed stainless steel tube to mechanically release gas from inclusions. After analysis of this gas, the crushed alunite was heated at 200°C for 1 h in the same tube to generate thermally released gas. The temperature chosen was sufficient to decrepitate fluid inclusions (especially vapor-rich) that still remained after crushing, yet avoided thermal decomposition of alunite. The released gases from both extractions were split for gas-composition analysis on a calibrated quadrupole mass spectrometer (Pfeiffer Vacuum Prisma) and the remaining gas was analyzed for He and Ne isotopes on a high-resolution MAP 215-50 noble-gas instrument. Gas species were analyzed at approximately 10^{-8} torr, with each analysis consisting of an average of 40 to 60 matrix calculations that correct for ion sensitivity and gas ionization fragmentation, and which calibrate the intensity response to standards. Results were determined as mole % summed to 100% when normalized to nitrogen. The remaining gas was then processed to extract He and Ne by cryogenically removing other gases on charcoal, gettering the gas (Saes ST707), and concentrating the purified He and Ne in a small-volume charcoal trap. Helium, and then Ne, were separately analyzed by selective thermal desorption from the charcoal and expansion into the mass spectrometer. Helium and Ne calibration was achieved by processing laboratory air corrected for barometric pressure, temperature, and relative humidity using identical procedures (^4He=6.414 e^{-12} mol/volt ± 0.016%, ^3He=9.951 e^{-20} mol/cps ± 0.144%, $^3He/^4He$ detector discrimination = 1.03074 ± 1.68%; Ne isotopes are treated as normalized percentages and ratios only, but corrected for $^{40}Ar^{++}$ and CO_2^{++} isobaric interferences to ^{20}Ne and ^{22}Ne).

ALUNITE PARAGENESIS IN THE TAMBO SYSTEM

Eight stages of alunite are recognized in the Tambo district. The paragenetic sequence (Table 3.1) is based on field and petrographic observations, using relations and terminology (e. g., Stages 1, 2, and 3) presented in Jannas et al. (1999). The characteristics of each stage are described below.

a) *Brecha Sylvestre*: Brecha Sylvestre is a relatively small, barren breccia body at the southwestern end of Cerro Elephante (Fig. 3.2). The breccia occurs between 4430 and 4480 m (all elevations are reported as elevation above sea level), approximately 200 m above the zones of highest gold production in the Wendy and Kimberly orebodies. The breccia is mainly clast-supported, locally silicified, and shows evidence of strong acid-leaching which resulted in removal of most of the matrix material (Bennet, 1995). The matrix consists of open vugs lined with alunite and minor quartz (Fig. 3.4a). Alunite typically occurs as pale white to yellow, elongate bladed to acicular crystals from 20 to 200 μm in length. Jarosite is also common and overgrows silicified breccia fragments and matrix crystals.

b) *Stage 1 - Pre-ore acid sulfate alteration*: Widespread acid sulfate alteration of Amiga Tuff wallrock is recognized throughout the Tambo area (Stage 1). This assemblage is surrounded by argillic- and propylitic- altered rocks away from the main orebodies (this study; Jannas, 1995). The occurrence of altered clasts with silicified rims in the hydrothermal breccias indicates that alteration occurred prior to brecciation and subsequent mineralization. Alteration occurs as fine intergrowths of alunite-quartz that selectively replaced feldspar crystals and locally forms massive clusters in the matrix of the Amiga tuff (Fig. 3.4b). Pumice clasts within dacite tuff fragments in the breccia pipes are also replaced (Jannas, 1995). Original rock textures are generally preserved. Associated minerals include clays (kaolinite-dickite), pyrophyllite, rare pyrite, and diaspore. Alunite commonly occurs as clusters of tabular to bladed crystals between 50 μm to 2 mm in length. Crystals locally have cores of alumino-phospho-sulfate (APS) minerals, including woodhouseite, svanbergite, and florencite (Table 3.3). Alunite grains are also locally pitted with corroded margins, and are rarely overprinted by fine-grained (10-20 μm) alunite ± quartz.

c) *Stage 2 - Early Gold Mineralization*: Stage 2 alunite post-dates the emplacement of the three major breccias and is closely associated early Au deposition. Alunite typically occurs as euhedral, golden-yellow bladed crystals up to 1 cm long that have overgrown barite and breccia fragments. Finer-grained tabular crystals less than 50 μm in length also occur. Alunite

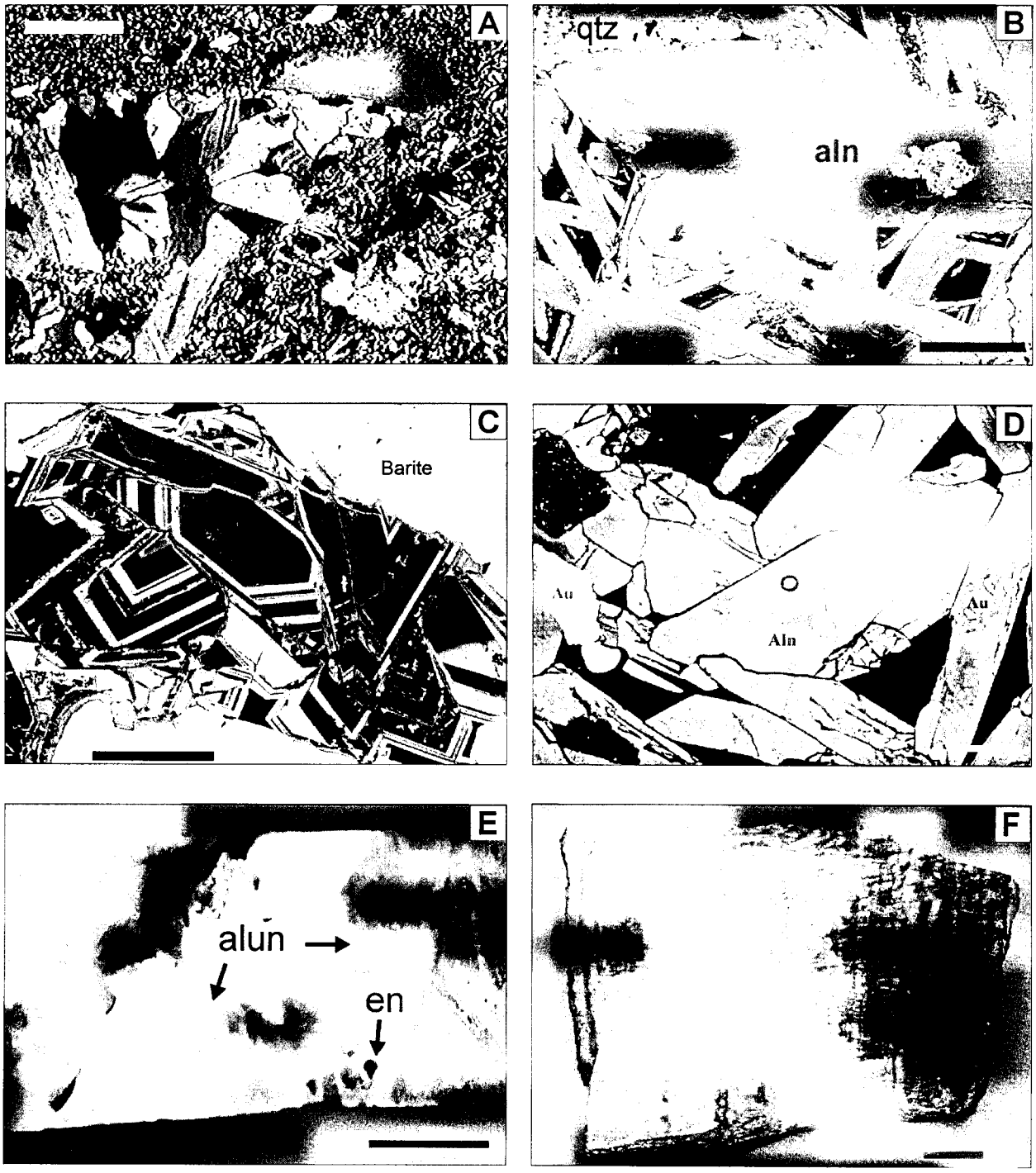

Figure 3.4.

A) Medium-grained, tabular alunite crystals in the matrix of Brecha Sylvestre (PTS, crossed polars). Scale bar = 50 μm.

B) SEM backscatter image of Stage 1 quartz (qtz)-alunite (alun) alteration. Bright zones within alunite grains are inclusions of woodhouseite-svanbergite. Scale bar = 25 μm.

C) Walthierite (light grey)-alunite (dark grey) zoning in Stage 2 alunite from the Canto Sur deposit (SEM back-scatter image). Alunite is hosted in barite (white). Scale bar = 50 μm (SEM backscatter image).

D) Native Au (white) associated with alunite (grey) from Wendy (DDH-92a , 206.7m; SEM backscatter image). Bright circle in centre of image due to electron beam damage. Scale bar = 25 μm.

E) Fine-grained (white) Stage 3 alunite (alun) overgrowing coarser-grained Stage 3 alunite (grey) in the matrix of the Wendy breccia. Minor enargite (en) is associated with coarse-grained alunite. Scale bar = 1 cm.

F) Banded alunite-hematite vein from the Kimberly deposit. Scale bar = 1 cm.

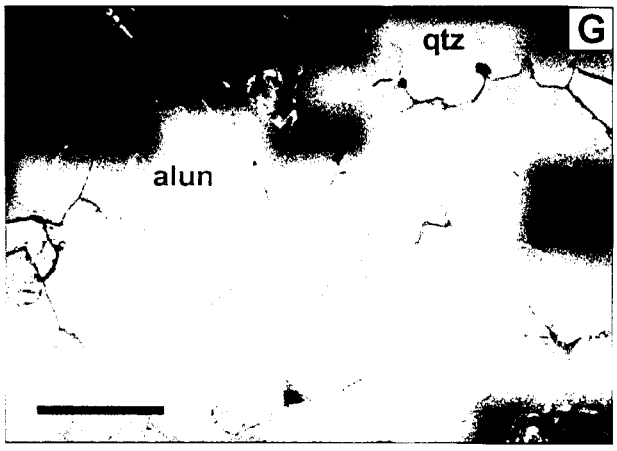

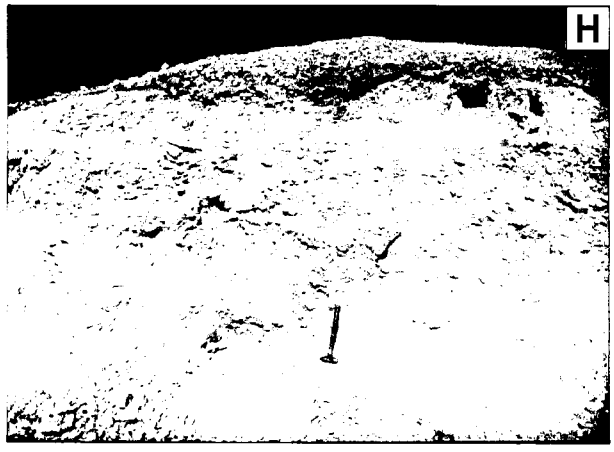

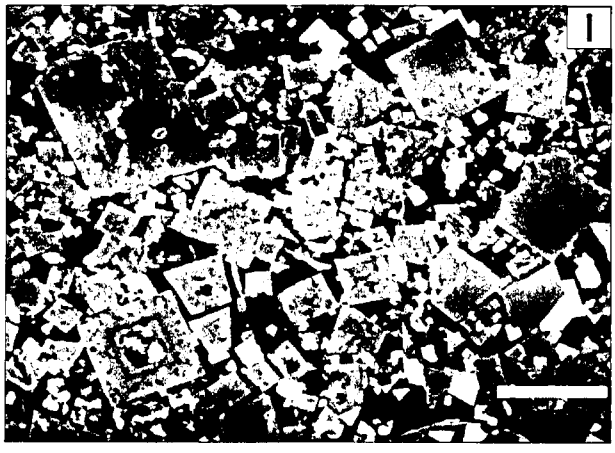

Figure 3.4. (Continued)
G) Zoned alunite (light grey)- huangite (dark grey)-woodhouseite/svanbergite (white) grains from the Kimberly pit (SEM backscatter image). Scale bar = 10 μm.
H) Steam heated alteration in outcrop near the top of Cerro Elefante. Hammer for scale.
I) Fine-grained, pseudocubic alunite grains (grey) with minor jarosite (white). Scale bar = 10 μm (SEM backscatter image).

of this stage is recognized by complex compositional zoning and the presence of walthierite (Ba alunite end-member; Table 3.3). Walthierite was first recognized in the Reina vein (Beane, 1991; Li et al., 1992), where it forms irregular to oscillatory compositional zones (Fig. 3.4c) and aggregates in coarse-grained alunite crystals. Stage 2 alunite also occurs in the Kimberly and Canto Sur breccias in close association with barite and trace quartz.

d) *Stage 3 - Late Gold Mineralization*: Deposition of Stage 3 alunite overlapped with the later stage of Au deposition and continued after mineralization ceased. Alunite is characterized by its nearly stoichiometric composition and variable crystal size and shape. Fine-grained alunite occurs as lath-like to thin bladed crystals, rarely greater than 30 μm long, that form overgrowths on breccia fragments and Stage 2 barite crystals in the Kimberly and Canto Sur breccia pipes. Alunite commonly exhibits the characteristic 'earthy' texture described by Jannas et al. (1999) and locally contains inclusions of native gold (Fig. 3.4d). Coarser grained varieties (up to 2 cm) of white to pinkish-brown, bladed alunite occur in veins, as cement to breccia fragments, as overgrowths on Stage 2 alunite crystals, and as local

intergrowths with enargite (Fig. 3.4e). Fine-grained alunite crystals also postdate the coarser bladed veins and breccia matrix. Minor amounts of quartz and kaolinite are associated with this stage. Late jarosite and scorodite that overprint Stage 3 alunite are common.

e) *Coarse banded alunite (± hematite) veins*: Coarsely crystalline veins up to 20 cm wide of alunite ± hematite (Fig. 3.4f) are common in the upper and marginal parts of the Kimberly open pit, and occur locally in the Wendy deposit. The veins cross-cut both Stage 1 alteration and hydrothermal breccias, but the timing of the veins relative to Stage 3 alunite is unknown. The veins are characterized by coarse alunite crystals (1 to 5 mm long) that grew in successive bands outward from the wallrock. Minor hematite and rare quartz ± jarosite occur interstitial to the alunite crystals. The presence of hematite gives the veins a distinct reddish colour that allows them to be easily distinguished from the surrounding wallrock. Where hematite is absent, the veins have a cream-white colour.

f) *Huangite-bearing veins*: Another variety of late veins occurs in the Kimberly and Kimberly West open pits. These veinlets are thin, pink to white, cryptocrystalline, and are composed of alunite, huangite (Ca alunite end-member; Table 3.3) ± kaolinite, quartz, and trace pyrite (Fig. 3.4g). Alunite occurs as clusters of tabular to anhedral grains averaging 50 to 100μm in length, locally overprinted by late jarosite and scorodite. The veinlets cut Stage 1 alteration, but timing with respect to Stage 2 or later events is unknown. Huangite had not been recognized previously in the Tambo area, but was first described in the El Indio district in association with kaolinite and pyrite (± alunite, pyrophyllite, sericite, minamiite, woodhouseite) adjacent to the El Indio Campana B vein (Li et al., 1992). Alunite in this vein has been dated at 6.21 ± 0.26 Ma and represents the youngest alteration event in the district (Bissig, 2001).

Table 3.3. Minerals of the alunite supergroup identified in the Tambo area.

Alunite-jarosite group	alunite	$KAl_3(SO_4)_2(OH)_6$
	natroalunite	$NaAl_3(SO_4)_2(OH)_6$
	minamiite	$(Na,K,Ca)_2Al_6(SO_4)_4(OH)_{12}$
	huangite	$CaAl_6(SO_4)_4(OH)_{12}$
	walthierite	$BaAl_6(SO_4)_4(OH)_{12}$
	jarosite	$KFe_3(SO_4)_2(OH)_6$
Beudantite group	svanbergite	$SrAl_3(PO_4)(SO_4)(OH)_6$
	woodhouseite	$CaAl_3(PO_4)(SO_4)(OH)_6$
Crandallite group	crandallite	$CaAl_3[(PO_3(O_{1/2}(OH)_{1/2}]_2(OH)_6$
	florencite-(Ce)	$CeAl_3(PO_4)_2(OH)_6$
	florencite-(La)	$LaAl_3(PO_4)_2(OH)_6$

g) *Near-surface alteration*: A powdery, friable assemblage of silica– kaolinite ± alunite and native sulfur is present at higher elevations (4300 – 4500 m) in the Tambo district (Fig. 3.4h) and occurs as alteration blankets on top of Cerro Elephante, Cerro Canto, and the adjacent Azufreras and Sol Poniente areas. Alteration is commonly pervasive, with the matrix of the host rocks and feldspars in tuff fragments completely replaced. Alteration also extends downward along fractures, particularly beneath the surficial alteration zone on Cerro Elefante, and locally overprints older acid sulfate assemblages. Alunite in the near-surface zone is restricted to irregular pods and lenses and occurs as fine-grained (<15-20 μm), tabular, and less commonly pseudo-cubic crystals intergrown with fine-grained silica. The mineralogy and distribution of this assemblage is typical of steam-heated alteration (e.g., Schoen et al., 1974).

h) *Late alunite veins ± jarosite*: Late, fine-grained to cryptocrystalline alunite ± jarosite veinlets are common in the Tambo area. These veins occur at all depths investigated by drilling (down to 3800 m elevation) and cross-cut all other alteration types. Alunite is typically fine- to medium-grained (10-50 μm), tabular to bladed in habit, and is locally intermixed with quartz. Alunite is commonly overgrown and locally cross-cut by fine-grained jarosite. In rare occurrences, extremely fine-grained (2-10 μm), pseudo-cubic alunite is intergrown with kaolinite ± jarosite (Fig. 3.4i) in veinlets that cross-cut wallrock altered by illite-smectite ± chlorite. Sufficient alunite of this last style could not be separated for further analysis.

GEOCHRONOLOGY

Six alunite samples were dated by the $^{40}Ar/^{39}Ar$ laser step-heating method to supplement existing age data for the Tambo area (Jannas et al., 1999; Bissig, 2001) and to confirm the relative timing of the alteration events. Results (Table 3.4) indicate that Stage 1 wallrock alteration (11.0 ± 0.3 Ma) occurred 2 to 3 m.yr. prior to either Stage 2 or Stage 3 ore deposition. Alteration is contemporaneous with Vacas Heladas volcanism, and extensive hydrothermal alteration of this age can be traced throughout the El Indio-Pascua Belt (Bissig, 2001). A sample of coarse, vug-fill alunite from Brecha Sylvestre, dated at 10.4 ± 0.3 Ma (Bissig, 2001), is also pre-ore and may overlap with Stage 1 alteration.

The timing of Stage 2 mineralization is constrained by $^{40}Ar/^{39}Ar$ data (8.7 ± 0.2 Ma) for a sample of coarse-grained alunite from the Reina vein that contains inclusions of gold. Alunite in this sample is also intergrown with barite that contains precious metals. Stage 3

Table 3.4. ^{40}Ar-^{39}Ar results for six stages of Tambo alunite. Abbreviations: Ca-vein = huangite-bearing vein; SH= steam-heated, LV = late vein; BV = banded vein. Calculated from data given in Appendix C.

Stage	Sample	Lab no.	Integrated date (Ma +/- 2σ)	**Plateau Age (Ma +/- 2σ)**	% ^{39}Ar in the plateau	Correlation date (Ma +/- 2σ)	% ^{39}Ar in the correlation	MSWD	Initial $^{40}Ar/^{39}Ar$ (+/- 2σ)
1	T10a	TB-106	10.87 (0.34)	**11.00 (0.27)**	94.4	11.10 (1.46)	100.0	0.16	291.17 (92.11)
2	T01	TB-110	8.71 (0.21)	-	-	8.72 (0.63)	100.0	0.43	290.79 (166.77)
Ca-vein	T35	TB-103	8.61 (0.45)	**8.63 (0.41)**	87.2	6.97 (6.28)	100.0	3.70	526.85 (1419.61)
SH	T17	TB-101	8.68 (0.59)	**8.86 (0.38)**	91.7	8.97 (3.45)	100.0	0.02	293.77 (183.44)
LV	T02a	TB-104	7.18 (0.15)	**7.25 (0.14)**	88.4	7.27 (0.13)	100.0	0.52	226.54 (247.77)
BV	T33	TB-111	7.38 (2.88)	**7.70 (2.80)**	90.3	8.15 (12.78)	100.0	0.04	293.76 (672.32)

mineralization is slightly younger, based on data for medium-grained alunite (8.2 ± 0.2 Ma) sampled from the matrix of the Kimberly breccia.

The near-surface, blanket style of alteration (8.9 ± 0.4 Ma) was sampled from Cerro Elephante, above the Kimberly deposit. Alteration overlaps in time with Stage 2 and may represent the surficial expression of early gold mineralization.

The timing of huangite-bearing veins (8.6 ± 0.4 Ma) relative to mineralization is uncertain. The relatively large error for this analysis is attributed to the small grain size of alunite and a smaller quantity of Ar gas released during heating. These veins may overlap with either Stage 2 or Stage 3, or may be intermediate between the two. Cross-cutting relations could not be determined in the field. It is clear, however, that alunite in these veins is unrelated to the much younger huangite-bearing Campana B vein at El Indio (6.2 ± 0.3 Ma; Bissig, 2001).

Late stage alunite (± jarosite) was sampled from thin veinlets that cross-cut Stage 1 alteration in the Canto Sur deposit. The plateau age for this sample (7.3 ± 0.1 Ma) is approximately 1 m.yr. younger than the main mineralizing events in the Kimberly and Wendy areas. It should be noted, however, that Bissig (2001) reported an age of 7.1 ± 0.2 Ma for alunite thought to be related to Au deposition in the Canto Sur breccia. The paragenesis of this sample is unclear. The style and mineralogy of both alteration and ore assemblages at Canto Sur are similar to those in other parts of the Tambo deposit. These features suggest a common origin. If mineralization in this area is younger, however, then late-stage alteration is coeval with, and not younger than, Canto Sur ore-stage alunite.

STABLE-ISOTOPE STUDY

Stable-isotope analyses of alunite and associated alteration minerals were determined for each paragenetic stage. Alunite contains four stable-isotope sites ($\delta^{34}S$, δD, $\delta^{18}O_{SO4}$, and $\delta^{18}O_{OH}$) and data can be used to characterize the fluid source and environment of deposition for each stage of alteration (Rye et al., 1992). Sample descriptions and isotope results are presented in Table 3.5. The data show considerable variation in alunite $\delta^{34}S$, with values ranging from 0 to +27‰ (Fig. 3.5). Limited data for Stage 3 enargite range from about –2 to –4‰, consistent with values reported in Jannas et al. (1999).

Estimation of $\delta^{34}S$ for bulk sulfur in the magma (1-3‰; Fig. 3.5) is based on data for magmatic steam alunite (cf. Rye et al., 1992) and agrees with estimates presented by Jannas et

Table 3.5. Sample descriptions and stable isotope results for all Tambo alunite, barite, and enargite samples. Elevation given in metres above sea level. Abbreviated mineral names; alunite (alun), quartz (qtz), kaolinite (kao), dickite (dick), pyrophyllite (pyl), walthierite (wal), jarosite (jar), enargite (enarg), scorodite (scord), hematite (hem), bar (barite), native sulfur (S).

Sample	Lab #	Stage	Deposit	Elev. (m)	Description	δD	$\delta^{34}S$	$\delta^{18}O_{SO4}$	$\delta^{18}O_{OH}$[1]
						(per mil)			
Alunite:									
WND-92A, 190.0m	T09a	1	Wendy	4113	Qtz-alun alteration	-98	6.2	9.4	3.7
WND-92A, 290.8m	T10a	1	Wendy	4135	Qtz-alun alteration	-53	22.1	15.8	10.1
KBD-85, 16.0m	T16a	1	Kimberly	4113	Qtz-alun-pyl alt		7.2		
KBD-85, 306.8m	T29a	1	Kimberly	3887	Qtz-alun alteration	-32	23.1	17.2	14.3
KBD-85, 94.1m	T30a	1	Kimberly	4052	Qtz-alun alteration	-30	1.1	20.3	14.3
WND-92a, 82.7m	T31a	1	Wendy	4090	Qtz-alun-dick alteration		12.4		
RA-01	T01a	2	Reina	4010	Vein alun with bar, walth, Au	-28	27.3	21.0	15.5
RA-4, 41.6m	T24a	2	Reina	4025	Coarse alun with walth	-27	27.4	20.3	16.3
CS-29	T26a	2	Canto Sur	4522	Fine-grained alun, bar with Au	-55	27.3	16.5	10.8
CS-01b	T27a	3	Canto Sur	4474	Alun with bar in breccia matrix	-38	2.1	19.6	15.3
CS-08	T02b	3	Canto Sur	4474	Matrix alun over bar	-78	1.8	10.1	3.6
LN-24	T03a	3	Kimberly West	4130	Matrix alun, overgrowing T03b	-47	5.5	17.7	13.2
LN-24	T03b	3	Kimberly West	4130	Matrix alun, overgrowing qtz	-46	1.3	19.2	12.8
WND-86, 155.0m	T04a	3	Wendy	4017	Matrix alun, with enarg and scord	-63	1.7	15.0	8.1
WND-86, 237m	T06a	3	Wendy	3960	Matrix alun hosting enarg	-85	1.7	11.9	5.7
CS-04	T20a	3	Canto Sur	4475	Matrix alun	-41	-0.2		
WND-92a, 37.5m	T21a	3	Wendy	4080	Matrix alun hosting enarg	-80	1.7	15.9	4.9
WND-92a, 231.8m	T22a	3	Wendy	4122	Matrix alun	-54	2.8	19.7	14.7
KB-43	T23a	3	Kimberly	4075	Matrix alun	-79	0.7		
LN-09	T25a	2	Kimberly West	4240	Matrix alun with bar, qtz	-42	25.7	19.6	16.4
WND-92a, 13.7m	T28a	3	Wendy	4075	Fine-grained matrix alun	-98	2.8	11.1	3.6
KB-08	T36a	3	Kimberly	4050	Matrix alun with scord	-51	3.5	18.0	12.0
KB-47	T07a	MS	Kimberly		Coarse banded vein with minor hem	-40	0.5	20.5	14.0
KB-33B	T08a	MS	Kimberly	4100	Coarse banded vein with hem	-48	1.1	16.4	8.8
WN-07	T32a	MS	Wendy	4180	Banded vein with hem	-69	1.4	15.9	9.7
KB-01	T33a	MS	Kimberly	4050	Coarse banded vein	-60	0.4	18.8	15.6*
KB-44	T34a	MS	Kimberly	4075	Coarse banded vein with hem	-74	0.3	11.3	
KB-09	T14a	Ca	Kimberly	4060	Thin veinlet cross-cutting altered tuff	-118	1.8	11.7	3.2
LN-02	T35a	Ca	Kimberly West	4260	Thin veinlet cross-cutting altered tuff	-56	9.2	20.6	14.2
KB-37B	T13a	SH	Kimberly	4480	Near-surface qtz-kao-alun-S alteration	-53	5.9	18.8	12.3
KB-40	T17a	SH	Kimberly	4460	Near-surface qtz-kao-alun-S alteration	-13	4.9	23.2	18.8
WN-14	T18a	SH	Cerro Elephante	4450	Powdery qtz-alun veinlets	-62	16.6	15.4	11.9*
CS-08	T02a	LV	Canto Sur	4474	Fine-grained alun-jar over Stage 3 alun	-111	-0.2	10.0	2.5
KBD-85, 306.8m V	T11a	LV	Kimberly	3887	Alun-jar veinlet in Stage 1 alteration	-110	5.4	7.0	1.3
KBD-85, 125.7m	T12a	LV	Kimberly	4027	Alun-qtz (jar) veinlet	-57	2.0	15.7	9.8
WND-86, 226.5m	T15a	LV	Wendy	3969	Brown jar-alun vein	-68	4.3	16.1	9.3
Barite:									
RA-01	Tb01	2	Reina	4050	Coarse vein fill, associated with T01a		26.8	13.8	
CS-08	Tb02	2	Canto Sur	4474	Coarse matrix crystals, with alun		24.5	17.3	
CS-30	Tb03	2	Canto Sur	4396	Coarse matrix crystals, mineralized		23.8	17.1	
Enargite:									
WND-86, 155.0m	T04e	3	Wendy	4017	Enarg intergrown with alun		-2.4		
WND-86, 237m	T06e	3	Wendy	3960	Enarg intergrown with alun		-3.7		

[1] calculated using BrF_5 total oxygen data, except samples marked by *

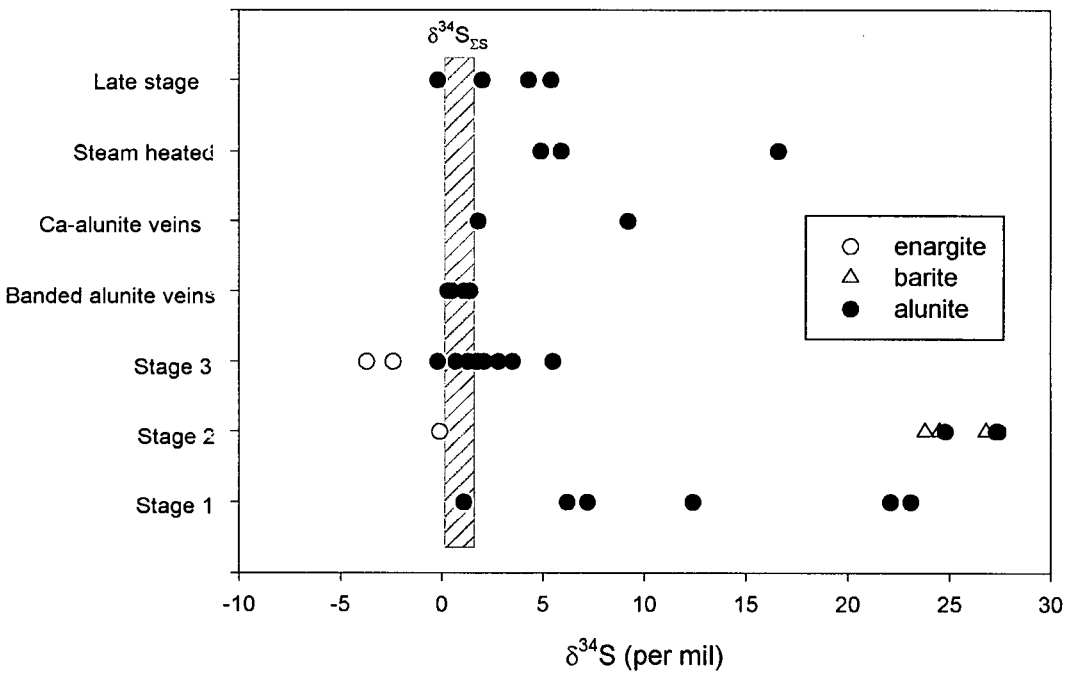

Figure 3.5. Range in $\delta^{34}S$ data (in ‰) for all stages of Tambo alunite. Also shown is data for associated enargite (this study; Jannas et al, 1999) and barite from Stages 2 and 3. Estimated $\delta^{34}S_{\Sigma S} \sim 1$ to 3 per mil. See text for discussion.

al. (1999). The composition of paleometeoric waters is estimated at $\delta D = -100 \pm 10‰$ (B. Taylor, pers. comm.). However, isotope data for jarosite of supergene origin from the Pascua deposit (Chap. 2), located to the north of El Indio-Tambo, suggest that this value has been slightly lighter (*ca.* -125‰). Variations of this magnitude are expected during the 3-4 m.yr. duration of the Tambo hydrothermal system, and a range of meteoric δD values is shown on all isotope plots accompanying the following discussions.

Stable-isotope systematics for each paragenetic stage are presented below. For ease of data interpretation and discussion, some samples are grouped with other, related, stages. In each section, $\delta^{34}S$ data are discussed first, followed by $\delta^{18}O$ and δD relations.

Brecha Sylvestre, Stage 1, and Stage 2: Magmatic-hydrothermal alunite

Figure 3.6 summarizes the $\delta^{34}S$, δD, and $\delta^{18}O$ data for Brecha Sylvestre, Stage 1 and Stage 2 alunite. Stage 1$\delta^{34}S$ data range from 1 to 23‰ (Fig. 3.6a). Stage 2 alunite is heavier, with $\delta^{34}S$ values of 26 to 27‰. Sulfur data for the two Brecha Sylvestre samples (14 and 15‰) are lighter than Stage 2 alunite, but are intermediate to Stage 1 values.

Alunite δD and $\delta^{18}O$ values are shown in Figure 3.6b, along with the range of calculated fluid compositions in equilibrium with samples from each alteration event (calculated from equations in Stoffregen et al., 1994). Both Stage 2 and Brecha Sylvester alunite fluids overlap with the compositions of fluids in felsic magmas (Taylor, 1992). Most Stage 1 alunite fluids also plot within this range, indicating a dominant magmatic fluid component. One lighter δD_{H2O} value (-94‰) suggests local mixing with meteoric fluids. In both Stages 1 and 2, there is a linear trend to lighter isotopic values.

Discussion: The large range in Stage 1 $\delta^{34}S$ data is unusual. The heaviest $\delta^{34}S$ values (22 to 23‰) are consistent with derivation from sulfate that equilibrated with H_2S during disproportionation of SO_2 (Rye et al., 1992; Rye, 1993), but other data are not. We propose two alternative explanations for this variability.

1) Data may represent magmatic-hydrothermal alunite formed from aqueous sulfate sulfur species that did not always reach isotopic equilibrium with H_2S during disproportionation of SO_2. This could result from shorter residence times for aqueous sulfate during early vapor-plume development, condensation, and alunite precipitation in Stage 1.
2) Alternatively, data can be interpreted as magmatic-hydrothermal alunite that is partially to completely replaced by either magmatic steam or steam-heated alunite.

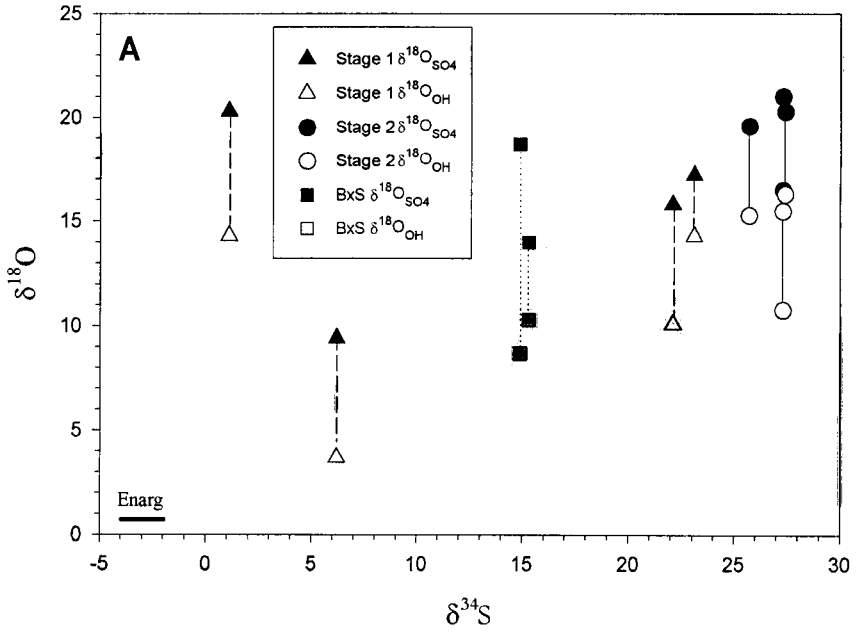

Figure 3.6a. $\delta^{34}S$ and $\delta^{18}O$ data (in ‰) for alunite from Stage 1, Stage 2, and Brecha Sylvestre (BxS). $\delta^{18}O_{SO4}$, and $\delta^{18}O_{OH}$ values for each sample are joined by lines. Range of $\delta^{34}S$ data for associated sulfides is also given.

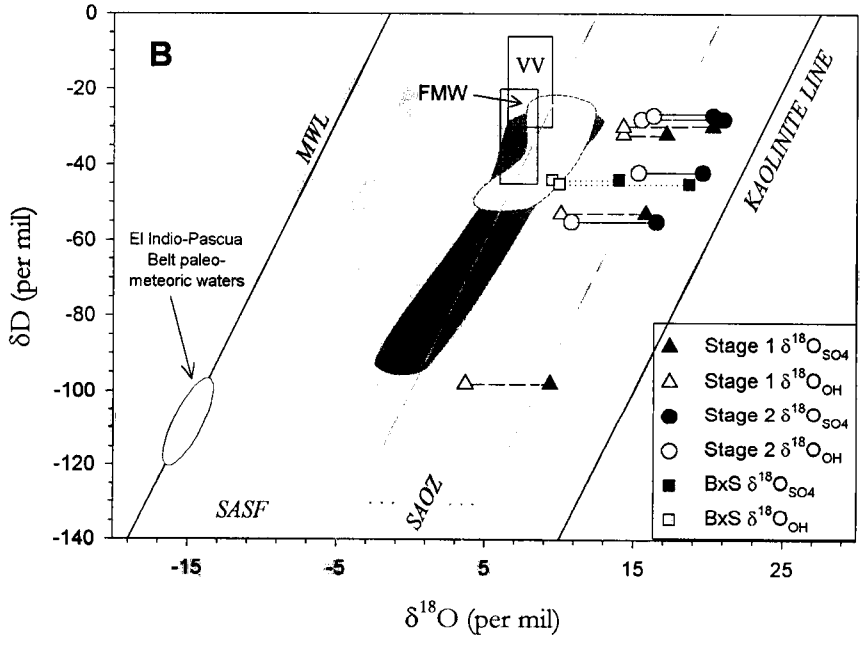

Figure 3.6b. δD, $\delta^{18}O_{SO4}$, and $\delta^{18}O_{OH}$ values for alunite from Stage 1, Stage 2, and Brecha Sylvestre (BxS). Range of calculated δD_{H2O} and $\delta^{18}O_{H2O}$ for fluids in equilibrium with each stage are shown as shaded fields (grey = Stage 1; 200-280°C: white = Stage 2; 180-250°C). Fluid compositions calculated from equations of Stoffregen et al (1994). Temperatures used for calculations are derived from textural, $\Delta^{34}S_{alun-py}$, and $\Delta^{18}O_{SO4-OH}$ isotope data. Lines and fields are MWL = meteoric water line of Craig (1961); FMW = composition of waters dissolved in felsic magmas (Taylor, 1988); kaolinite line of Savin and Epstein (1970); V.V (volcanic vapor) = range of water compositions discharged from high temperature fumaroles (Giggenbach, 1992); SASF (light grey) = supergene alunite SO_4 field; and SAOZ = supergene alunite OH zone as described in Rye et al. (1992). Also shown (white circle) is the estimated composition of paleo-meteoric waters (B. Taylor, pers. comm.).

Based on textural and petrographic observations for Stage 1 alunite, the second model is preferred. Alunite with the lowest $\delta^{34}S$ values has macroscopic characteristics of Stage 1 alteration but the alunite is not associated with clays or APS inclusions typical of the Stage 1 alunite. These grains appear to have precipitated in open vugs created by the leaching of feldspar phenocrysts. Partial replacement of APS-bearing alunite by a more homogeneous, K-rich variety is also observed in one sample. Similar processes are inferred at El Salvador (J. Hedenquist, pers. comm.), where partial replacement of hypogene by supergene alunite resulted in intermediate $\delta^{34}S$ values. Magmatic fluid signatures for most samples of Stage 1alunite are also consistent with a magmatic-hydrothermal origin.

High $\delta^{34}S$ values for Stage 2 alunite (and barite) and fluid compositions in the magmatic range are consistent with a magmatic-hydrothermal origin for this stage of alteration. Homogenization temperatures determined by Jannas (1995) for fluid inclusions in Stage 2 barite range from 140° to 280°C. Calculated $\Delta^{18}O_{SO4\text{-}OH}$ temperature values (e.g., Rye et al., 1992; Stoffregen et al., 1994) for Stage 2 alunite are nearly identical (140° to 240 °C) and suggest that equilibrium between oxygen species was maintained.

Stage 3 and Banded Alunite Veins; Transitional and Magmatic Steam alunite

Figure 3.7 summarizes the $\delta^{34}S$, δD, and $\delta^{18}O$ data for Stage 3 and banded vein alunite. $\delta^{34}S$ values for both events are slightly greater than the values of Stage 3 enargite (about -2 to -4‰). Stage 3 alunite exhibit almost no $\delta^{34}S$ variation (± 0.2‰) between coarse breccia-fill alunite and fine-grained alunite overgrowths (Appendix B). Only minor $\delta^{34}S$ zoning is noted within large (1 to 2 cm) Stage 3 crystals with values ranging between 1.0 to 2.0‰.

Banded vein alunite has consistently lower $\delta^{34}S$ values (about 0 to 1.5‰) than Stage 3 samples. Only minor $\delta^{34}S$ variation is reported between different banded vein samples or between growth bands in a single vein (Appendix B). The narrow range of values for both banded vein and Stage 3 alunite indicates that alunite sulfur isotope equilibrium was not attained between aqueous sulfate and H_2S.

Calculated fluid compositions for alunite are shown in Figure 3.7b. Stage 3 fluids have δD_{H2O} values between about –30 and -95‰, and $\delta^{18}O_{H2O}$ between -1 and 13‰. Banded vein alunite fluids occur in a more restricted range, with δD_{H2O} values between -35 and -65‰. Data for both events overlap with magmatic waters (Taylor, 1992), but Stage 3 and banded vein fluids are typically depleted in deuterium relative to Stage 2 magmatic-hydrothermal fluids. A

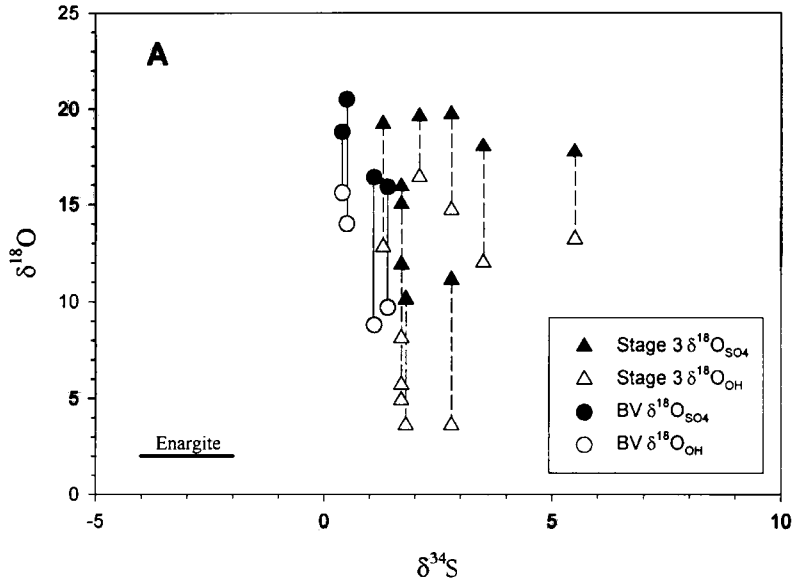

Figure 3.7a. $\delta^{34}S$ and $\delta^{18}O$ data (in ‰) for Stage 3 and banded vein (BV) alunite. $\delta^{18}O_{SO4}$, and $\delta^{18}O_{OH}$ values for each sample are joined by lines. Range of $\delta^{34}S$ data for Tambo sulfides is also given.

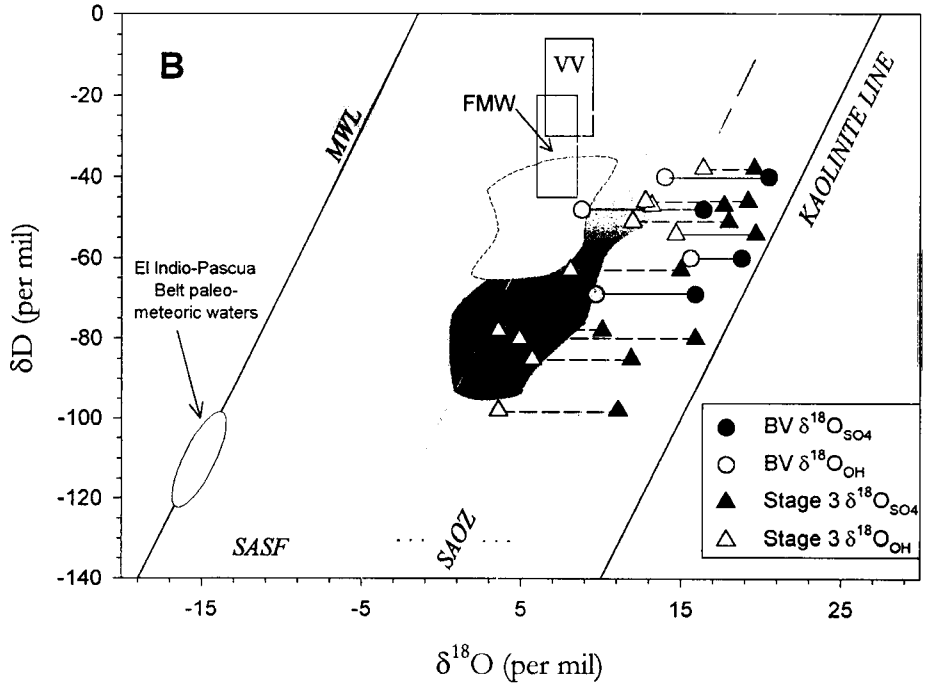

Figure 3.7b. δD, $\delta^{18}O_{SO4}$, and $\delta^{18}O_{OH}$ values for Stage 3 and banded vein (BV) alunite. Range of calculated δD_{H2O} and $\delta^{18}O_{H2O}$ for fluids in equilibrium with each stage are shown as shaded fields (grey = Stage 3; 200-300°C: white = BV; 200-300°C). Fluid compositions calculated from equations of Stoffregen et al (1994). Temperatures used for calculations are derived from textural, $\Delta^{34}S_{alun-py}$, and $\Delta^{18}O_{SO4-OH}$ isotope data. Lines and fields are given in Figure 3.6.

correlation between decreasing δD_{H2O} and $\delta^{18}O_{H2O}$ values for both alunite types suggests that this depletion can be attributed mainly to mixing between magmatic and meteoric fluids. Deuterium depletion of late-stage magmatic fluids (Taylor, 1988) may also contribute to this trend.

Discussion: Data for banded vein alunite indicate a major magmatic component in the source fluids. Results are consistent with a magmatic steam origin. Stage 3 data are more variable and show greater degrees of mixing between magmatic and meteoric fluids. This variation suggests episodic pulses of vapor released from the magma rather than continued, open-system degassing. The larger range of $\delta^{34}S$ values for alunite of this stage suggests limited exchange between aqueous sulfur species. Deposition is thought to have occurred in an environment that is transitional between magmatic-hydrothermal and magmatic steam.

Depositional temperatures calculated from $\Delta^{18}O_{SO4\text{-}OH}$ for banded vein alunite average about 110°C, with the exception of one higher value at 320°C (sample T33a). Independent temperature estimates are not available for this stage of alteration, but temperatures are expected to be at least as high as those encountered in the magmatic-hydrothermal environment (i.e., 180 to 300°C). Retrograde isotopic exchange is not expected given the coarse grain size of the alunite; hence, the origin of the low $\delta^{18}O_{OH}$ values is unclear. Similar behaviour is reported for magmatic steam alunite at Alunite Ridge, Utah (Rye et al., 1992).

The range in $\Delta^{18}O_{SO4\text{-}OH}$ temperatures for Stage 3 alunite is greater than for the banded veins (10° to 330°C), but most values are below 200°C. Again, several temperatures are unreasonably low but others are within the expected range for shallow environments of deposition.

Huangite-bearing vein alunite

$\delta^{34}S$, δD, and $\delta^{18}O$ data for two samples of huangite-bearing vein alunite are plotted in Figure 3.8. Results for the two samples are significantly different. One sample has low $\delta^{34}S$ (1.8‰) and $\delta^{18}O_{SO4}$ (11.7‰) values. The other sample has a $\delta^{34}S$ value of about 9‰, and has $\delta^{18}O$ data in the range of magmatic-hydrothermal alunite. Calculated δD_{H2O} compositions in equilibrium with the two samples are –115 and –52‰, respectively. The first sample (T35) has a fluid composition which overlaps that of Tambo magmatic-hydrothermal and magmatic steam occurrences. Data for the latter (sample T14a) indicate a dominant meteoric fluid component.

Discussion: Depositional temperatures for the two huangite-bearing samples are

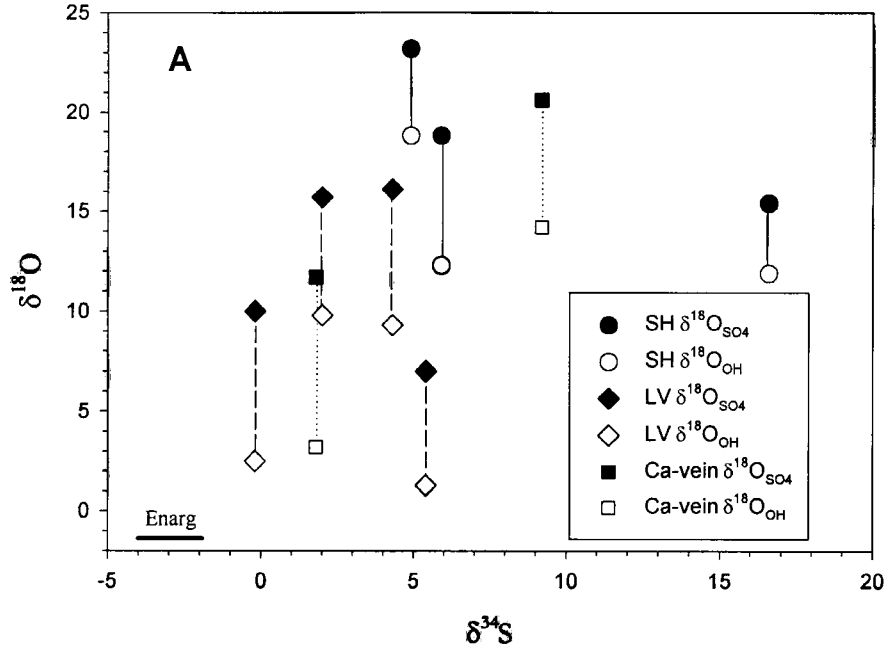

Figure 3.8a. $\delta^{34}S$ and $\delta^{18}O$ data (in ‰) for steam heated (SH), late vein (LV) and huangite-bearing vein (Ca-vein) alunite. $\delta^{18}O_{SO4}$, and $\delta^{18}O_{OH}$ values for each sample are joined by lines. Range of $\delta^{34}S$ data for Tambo sulfides is given for reference.

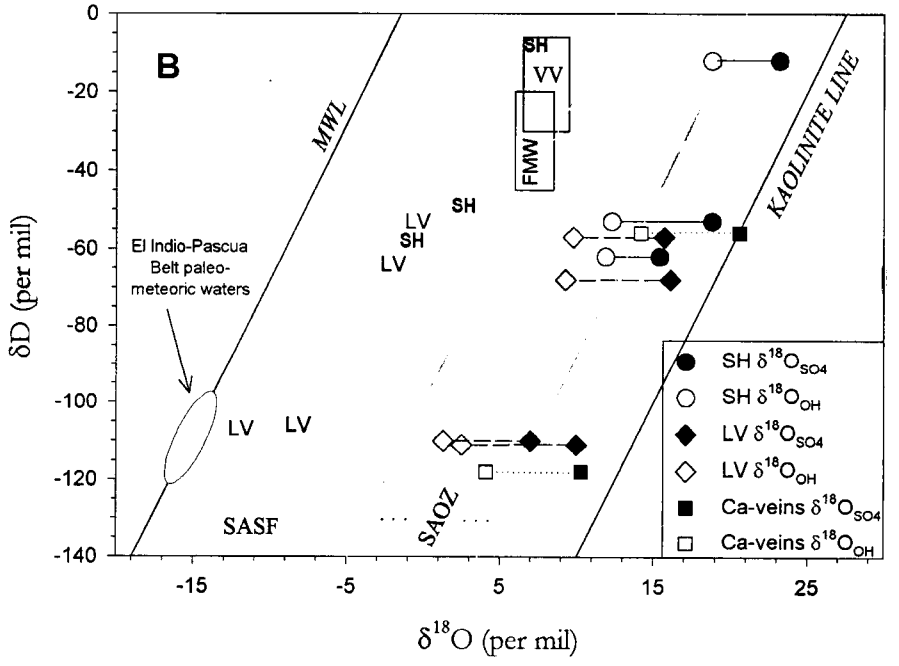

Figure 3.8b. δD, $\delta^{18}O_{SO4}$, and $\delta^{18}O_{OH}$ values for steam heated (SH), late vein (LV) and huangite-bearing vein (Ca-vein) alunite. Range of calculated δD_{H2O} and $\delta^{18}O_{H2O}$ for fluids in equilibrium with each stage are shown as symbols (SH = steam heated fluids; LV = late vein fluids). Fluid compositions calculated from equations of Stoffregen et al (1994). Temperatures used for calculations are derived from textural, $\Delta^{34}S_{alun-py}$, and $\Delta^{18}O_{SO4-OH}$ isotope data. Lines and fields are given in Figure 3.6.

similar and average 105°C. No independent temperature estimates are available for these veins however and it is unclear whether these values are reasonable. Temperatures of formation for the mineralogically similar El Indio Campana vein were estimated to be 225-275°C (Jannas, 1995), but lower temperature occurrences of Ca-rich alunite have been reported elsewhere (e.g., Stoffregen and Alpers, 1987; Arribas et al., 1995). The origin of these veins and their relation to other alteration or mineralizing events is uncertain.

Near-surface alteration

Figure 3.8 summarizes the $\delta^{34}S$, δD, and $\delta^{18}O$ data for alunite sampled from the near-surface alteration blanket on Cerro Elefante. Two samples (T13, T17) have $\delta^{34}S$ values slightly enriched relative to bulk sulfur in the deposit, and have high $\delta^{18}O_{SO4}$ values. The third sample (T18), selected from white, powdery veins that cross-cut Stage 1 alteration just below the blanket zone, has a much larger $\delta^{34}S$ value (16.6‰) and lower $\delta^{18}O_{SO4}$ value (15.4‰) compared to the first two samples.

Calculated fluid compositions in equilibrium with alunite are plotted in Figure 3.8b. δD_{H2O} data for the first two samples vary between about −10 and -55‰, with $\delta^{18}O_{H2O}$ data between 2 and 7‰. These values are significantly enriched relative to those for meteoric water, and indicate a dominant magmatic fluid component. Deuterium enrichment by evaporation (Henley and Stewart, 1983) is inferred for the highest δD value.

Discussion: Sulfur and oxygen isotopic data for this stage of alteration are consistent with a steam-heated origin. Limited S-isotope exchange between aqueous SO_4 and H_2S is inferred for the first two samples. Calculated $\Delta^{18}O_{SO4\text{-}OH}$ temperatures of deposition are 110° and 210 °C. Results are reasonable, although perhaps slightly high in the latter, for environments in which aqueous sulfate forms at shallow levels from the oxidation of H_2S by atmospheric oxygen (Rye et al., 1992; Ebert and Rye, 1997). Oxygen isotopic temperatures also suggest that oxygen-isotope equilibrium was obtained between the aqueous sulfate and water in the fluid. The third sample, given its shallow depth, has an unreasonably high $\Delta^{18}O_{SO4\text{-}OH}$ temperature of 290 °C, although $\delta^{18}O_{OH}$ data are in the range of the previous two samples. Significant sulfur isotope exchange occurred between aqueous SO_4 and H_2S, but $\Delta^{18}O_{SO4\text{-}OH}$ may have been affected by post-depositional exchange.

Late vein alunite

Sulfur data for late vein alunite are slightly greater than values for sulfides in the deposit (Fig. 3.8a). All $\delta^{18}O_{OH}$ results plot within the Supergene Alunite OH Zone (SAOZ) defined by Rye et al. (1992); however, all but one alunite $\delta^{18}O_{SO4}$ data plot outside of the Supergene Alunite Sulfate Field (SASF; Rye et al., 1992). These results, combined with large positive $\Delta^{18}O_{SO4\text{-}OH}$ values, are not consistent with a supergene origin. Similarly, calculated $\Delta^{18}O_{SO4\text{-}OH}$ temperatures average about 100° C and are higher than expected for deposition in the supergene environment.

Calculated fluid compositions in equilibrium with alunite samples are shown in Figure 3.8b. Two samples with the lowest δD_{H2O} and $\delta^{18}O_{H2O}$ values have fluids very close to the predicted composition of meteoric waters. The other two samples have much larger δD_{H2O} and $\delta^{18}O_{H2O}$ values, indicating a substantial magmatic contribution. These fluid compositions overlap those for magmatic-hydrothermal and magmatic steam occurrences.

Discussion: Results indicate that the late alunite veins were not generated under supergene conditions. Alunite formed from mixed magmatic-meteoric fluids at moderate temperatures (*ca.* 100°C). The absence of significant sulfides in the orebody and surrounding host rocks requires that the majority of sulfur must have been derived from condensed magmatic vapors (either H_2S or SO_2). Data are consistent with aqueous sulfate that formed from the oxidation of degassed H_2S as the hydrothermal system cooled. Alternatively, pulses of SO_2-rich magmatic steam rapidly condensed into mixed magmatic-meteoric fluids in the final stages of the system.

GEOCHEMISTRY OF ALUNITE

Major and trace-element compositions were determined to evaluate the variability of alunite and alunite-group minerals in each alteration assemblage. End-member alunite is represented by the formula $KAl_3(SO_4)_2(OH)_6$ but naturally occurring minerals of the alunite supergroup can have a wide range of chemical substitutions (Jambor, 1999). The most common substitution of Na for K defines the alunite-natroalunite solid solution. Other substitutions for K^+ may include Ca, Ba, Sr, REE (Ce, La), Pb, Ag, H_3O, and NH_4. Substitution of Fe^{3+} for Al^{3+} defines the alunite-jarosite solid solution, and substitution of $(PO_4)^{2-}$ for $(SO_4)^{2-}$ forms APS minerals of the crandallite and beudantite groups (Table 3.3: as summarized in Jambor, 1999).

Several experimental (Hemley et al., 1969; Stoffregen and Cygan, 1990) and empirical studies (e.g., Aoki, 1991; Aoki et al, 1993; Thompson, 1992; Hedenquist et al., 1994; Arribas et al., 1995) have correlated variations in alunite-group chemistry to specific environments or temperatures of deposition. Similarly, published data on REE contents of acid sulfate-altered rocks suggest that REEs may be influenced by a number of factors including; (a) crystallographic controls (Schwab et al., 1990); (b) the availability and type of complexing agents (Wood, 1990a; Wood, 1990b; Lottermoser, 1992); and (c) environmental controls such as pH, Eh, temperature (e.g., Michard, 1989). It is also likely that vapor-melt partition coefficients (Flynn and Burnham, 1978; Candela and Piccoli, 1995; Reed, 1995) affect the REE content of magmatic vapors, and subsequent alteration, in the epithermal environment.

Summary of Results

Chemical data for all stages of Tambo alunite are given in Table 3.6. EPMA data (Table 3.6a) are summarized for each paragenetic stage. The large beam size required for analysis resulted in poor representation of finer-grained samples (supergene and steam-heated alteration in particular) and thin oscillatory zones and growth bands. Selected ICP-MS trace metal concentrations are listed in Table 3.6b. REE results presented in this study (Fig. 3.9) are normalized to average REE contents of unaltered host rock (Tilito Formation: Table 3.2). Data for each paragenetic stage are summarized in the following discussion.

Magmatic-hydrothermal alunite, represented by Brecha Sylvestre, Stage 1, and Stage 2 alteration, exhibits a wide range of compositions. Brecha Sylvestre alunite samples are compositionally simple, with local enrichment in Pb and Sb, minor Na, and trace P, Sr, and Ba. Alunite is depleted in REE relative to host-rock values, and moderate HREE fractionation is apparent. In contrast, Stage 1 alunite is chemically heterogeneous, with irregular trace-element (Na, Ca, Ba, P, Sr) substitution. Average Na contents are the highest among the analyzed alunite types (statistically significant at 95% confidence limit, based on t-test results: Appendix A). Calcium and Ba substitutions locally approach huangite and walthierite end-member compositions. REE results show Stage 1 alunite samples are depleted in mid-REE (MREE) relative to the host Tilito Formation, and exhibit minor light-REE (LREE) fractionation.

Stage 2 alunite has a unique geochemical signature characterized by high Ba and the presence of walthierite. Compositions intermediate between walthierite and alunite are common and a nearly complete solid-solution exists between the two end-members (Fig. 3.10). Stage 2 alunite in the Kimberly and Canto Sur deposits are commonly oscillatory zoned (Fig.

Table 3.6a. Summary of EPMA data for all Tambo alunite samples. Results are listed as atoms per formula unit (a.p.f.u.), recalculated based on 2X (Jambor, 1999). The mean, standard deviation at 95% confidence level (2σ), and maximum and minimum values for each element are given. Data below detection limits (0.02 a.p.f.u. for Na; 0.01 a.p.f.u. for all other elements) are not shown. *n* = total number of analyses. Also given are the number of samples represented in each stage.

	Stage 1 *n=85 (5 samples)*				Stage 2 *n=59 (4 samples)*				Stage 3 *n=76 (3 samples)*				Banded Vein *n=33 (2 samples)*			
Element	Mean	2σ	Max	Min	Mean	2σ	Max	Min	Mean	2σ	Max	Min	Mean	2σ	Max	Min
K	0.81	0.46	1.03	-	0.58	0.80	1.04	0.02	0.89	0.31	1.05	0.26	0.87	0.20	1.02	0.61
Na	0.19	0.34	0.81	-	0.09	0.27	0.90	-	0.11	0.26	0.62	-	0.10	0.15	0.33	-
Ca	0.03	0.27	0.83	-	-	-	0.02	-	-	-	0.02	-	-	-	-	-
Ba	-	-	0.03	-	0.18	0.40	0.51	-	-	-	0.06	-	-	-	0.04	-
Sr	-	-	0.09	-	-	-	-	-	-	-	-	-	-	-	0.02	-
P	0.05	0.43	1.35	-	-	-	0.05	-	-	-	0.06	-	0.02	0.04	0.08	-
S	1.95	-	2.00	0.65	1.99	0.02	2.00	1.95	1.99	0.03	2.00	1.94	1.98	0.04	2.00	1.92
Fe	-	-	0.06	-	0.04	0.55	2.13	-	-	-	0.17	-	-	-	-	-
Al	3.08	0.12	3.25	2.95	3.11	0.55	3.26	1.14	3.16	0.13	3.29	3.01	3.14	0.11	3.24	3.04

	Ca Veins *n=58 (2 samples)*				SH *n=31 (2 samples)*				Late Stage *n=11 (2 samples)*			
Element	Mean	2σ	Max	Min	Mean	2σ	Max	Min	Mean	2σ	Max	Min
K	0.46	0.71	1.03	-	0.98	0.10	1.04	0.84	0.92	0.10	1.02	0.85
Na	0.10	0.24	0.58	-	0.04	0.08	0.16	-	0.12	0.10	0.21	0.02
Ca	0.24	0.33	0.49	-	-	-	0.03	-	-	-	0.02	-
Ba	-	-	0.03	-	-	-	-	-	-	-	-	-
Sr	-	-	0.06	-	-	-	-	-	-	-	-	-
P	0.03	0.18	0.39	-	-	-	0.03	-	-	-	0.04	-
S	1.97	0.18	2.00	1.61	1.99	0.02	2.00	1.97	1.99	0.02	2.00	1.96
Fe	-	-	0.05	-	-	-	0.02	-	0.04	0.11	0.21	-
Al	3.12	0.11	3.20	3.06	3.13	0.09	3.23	3.05	3.13	0.18	3.25	2.94

Table 3.6b. ICP-MS trace element and REE concentrations for bulk (~1 gram) alunite samples. Trace contaminants may be present. Data below detection limits (0.1 ppm for REE) not shown. Estimates of precision, based on duplicate analyses, given in Appendix B.

	Stage 1*		Stage 2		Stage 3			
Sample #:	T09	T10	T01	T27	T03b	T04	T22	T28
P (ppm)	970	380	1570	120	1180	1210	1700	1270
Sr	668	208	511	461	411	696	728	1580
Ba	340	630	4080	3850	3600	600	280	1470
Pb	116	856	1515	1745	251	608	428	338
Sb	-	11	317	10	10	29.5	31	15
Ag	2.7	0.9	79.4	4.0	5.8	21.4	0.2	3.0
Cu	1218	10	32	20	17	53	18	69
Bi	22	1.5	6.5	0.8	13.4	102.0	2.3	32.0
Zn	4	2	-	2	6	48	-	46
La	45.3	25.5	10.5	13.3		66.5	90.3	
Ce	86.5	45	9.5	9.2		79.5	81.3	
Pr	9.2	4.3	0.6	0.5		4.1	5.1	
Nd	24.8	11.5	1.5	0.8		6	6.8	
Sm	3.3	1.6	0.2	-		0.2	0.1	
Eu	0.3	0.3	0.2	0.2		0.2	0.1	
Gd	1.8	1.3	0.1	-		0.3	0.1	
Tb	0.2	0.3	-	-		-	-	
Dy	1	1.1	-	-		0.2	-	
Ho	0.2	0.3	-	-		-	-	
Er	1	1.1	-	-		-	-	
Tm	0.1	0.3	-	-		-	-	
Yb	1.4	1.6	-	-		-	-	
Lu	0.2	0.3	-	-		-	-	

* May contain up to 10% quartz.

Table 3.6b. (Continued)

	Banded Vein		Ca-vein	Steam-Heated	Late Stage		Bx Sylvestre
Sample #:	T33	T32	T14	T17	T11	T02A	B03
P	2300	1410	630	940	1490	1580	680
Sr	1535	582	246	353	2760	677	511
Ba	1120	450	830	1030	2140	2430	650
Pb	580	628	59	916	486	2240	1700
Sb	28.5	22	0.5	10	14.5	14.3	78.5
Ag	-	0.6	-	1.4	3.0	7.9	0.8
Cu	18	19	18	44	44	1	25
Bi	0.3	46.2	0.6	1.0	32.3	6.0	29.2
Zn	-	2	8	18	70	-	2
La	156	81.5	48	47.5	29	77	33
Ce	198	116.5	109.5	85	50	47	3
Pr	13.4	7.9	15.5	8.7	5.9	2.1	8
Nd	24	13	65.5	27.5	22	3	0.6
Sm	1.1	0.6	16.8	3.7	5	0.2	0.1
Eu	0.3	0.1	2.5	0.5	0.9	0.4	0.5
Gd	1	0.5	9.3	2.3	3.2	0.1	-
Tb	0.1	-	0.6	0.2	0.4	-	0.1
Dy	0.3	0.1	0.7	0.7	1.1	-	-
Ho	-	-	-	0.1	0.1	-	0.1
Er	0.1	-	-	0.5	0.3	-	-
Tm	-	-	-	-	-	-	0.1
Yb	0.1	-	0.1	0.8	0.3	0.1	-
Lu	-	-	-	0.1	-	-	-

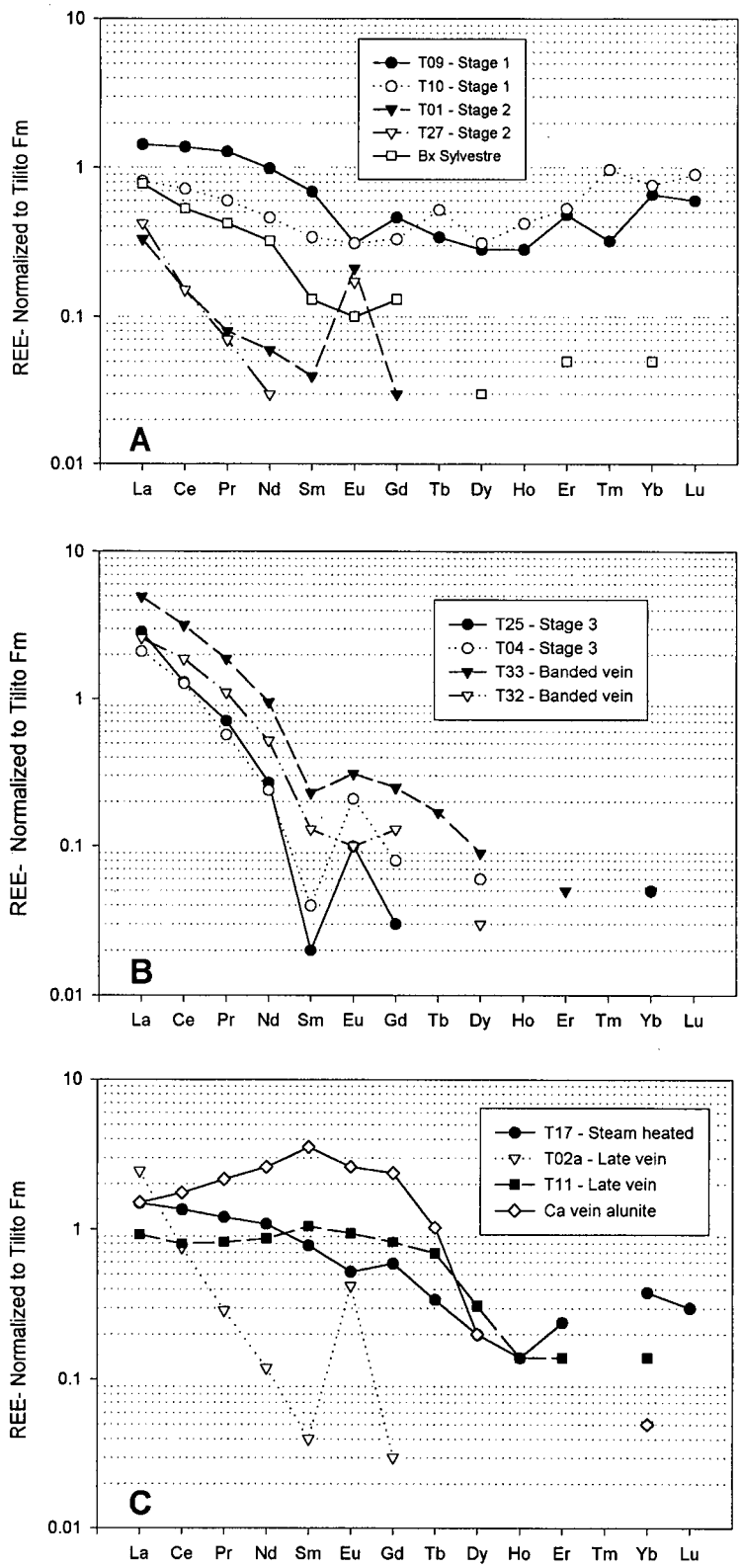

Figure 3.9. REE data for all stages of Tambo alunite normalized to average REE composition of the Tilito Fm. Individual sample numbers are given in the legend accompanying each plot. Data points below detection are not plotted. (A) Bx Sylvestre, Stage 1 and Stage 2 alunite. (B) Stage 3 and Banded vein alunite. (C) Huangite-bearing vein alunite (Ca-vein), steam heated, and late vein samples.

3.4c), typically with a core of Na-bearing alunite overgrown by walthierite and rimmed by nearly stoichiometric alunite. Walthierite has not been identified in the Wendy deposit, and Stage 2 alunite in this area occurs as coarse bladed crystals that are zoned in Ca, Na, P, and minor Ba. Stage 2 alunite is typically Na-poor (less than 0.2 a.p.f.u.), although the mineral locally approaches natroalunite end-member compositions. Barium, Pb, Sb, and Ag contents on average are the highest in Stage 2 compared to the contents in other alunite types. Stage 2 alunite exhibits strong fractionation in LREE, no detectable heavy-REE (HREE), and a strong, positive Eu anomaly.

Stage 3 and banded vein alunite are chemically similar. Both are nearly stoichiometric, with minor Na (< 0.4 a.p.f.u) and trace-metal substitution. Oscillatory zoning with $PO_4 \pm Sr$ substitution is common, and banded vein alunite in particular has the highest P contents compared to other stages of alunite. In contrast, Ca, Ba, and Pb contents are low. EPMA analyses indicate almost no chemical variation across successive growth bands in the alunite veins. Stage 3 and banded vein alunite are both enriched in LREE, with values two to five times higher than those of the host rock, but are significantly depleted in HREE. These trends are more pronounced in the banded vein samples with $(La/Yb)_n$ ratios >100.

As their name suggests, huangite-bearing veins are characterized by the presence of huangite. It typically occurs as thick overgrowths on alunite grains that have woodhouseite-svanbergite cores. EPMA data indicate a full range of substitution between alunite and huangite end-member compositions (Fig. 3.11). Oscillatory zoning between huangite and minamiite compositions occurs locally. ICP-MS results confirm very high Ca contents with elevated Na concentrations and few trace elements. Alunite of this stage is significantly enriched in LREE and MREE relative to all other alunite types. HREE are strongly fractionated.

Chemical data for steam-heated alunite samples are limited, due to the small grain size and relatively rare occurrence of alunite in the steam-heated alteration zone. This alunite is nearly stoichiometric, with minor Na, Sr, and P substitution. Fractionation of HREE is moderate, with minor enrichment in LREE compared to the host Tilito Formation.

Geochemical data for the late veins are limited because of the fine-grained nature of the alunite. Results indicate that the mineral is chemically variable, with high Sr contents and locally elevated PO_4, Ba, Pb, Cu, and Zn. Sodium contents are low, and REE contents are extremely variable. One sample (T11) shows no LREE fractionation relative to host-rock values but has a significant depletion in HREE. Another sample (T02a) shows similar behavior

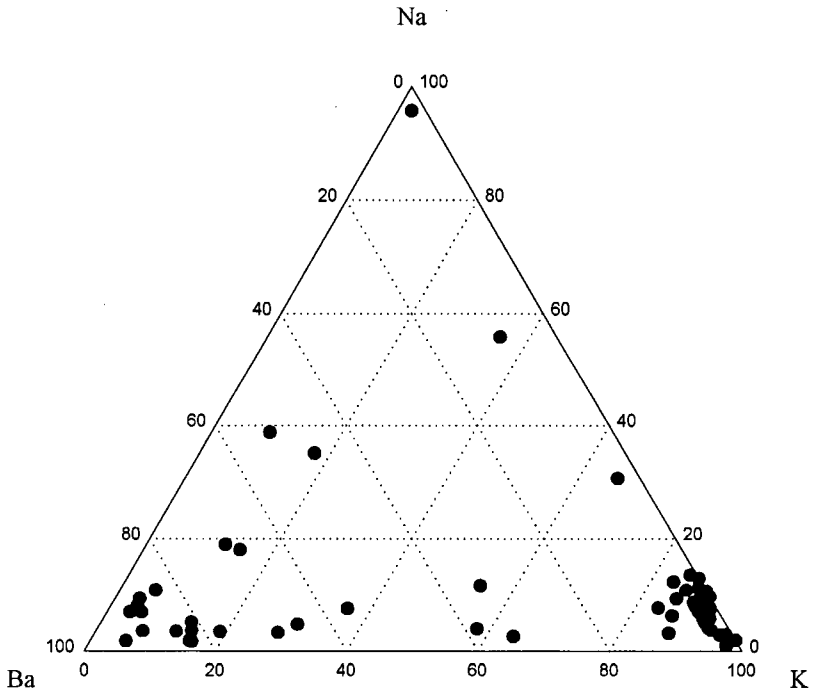

Figure 3.10. Normalized K-Na-Ba compositions of Stage 2 alunite. Based on recalculated EPMA data (58 analyses total from 4 samples).

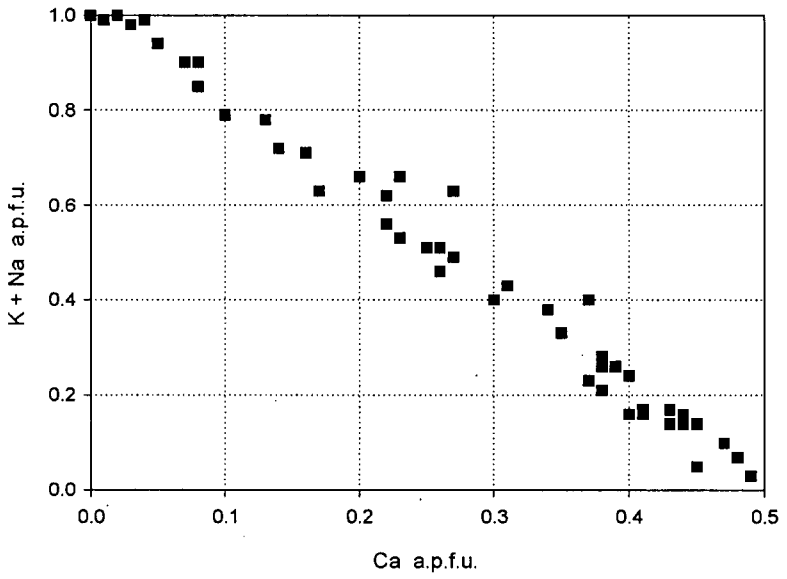

Figure 3.11. Measured K+Na versus Ca content of huangite-bearing vein alunite. Axes are given as atoms per formula unit (a.p.f.u.). Data taken from EPMA analyses (n=47) of multiple grains in two samples, KB-09 and LN-02.

to Stage 2 alunite, with extreme HREE fractionation and a large, positive Eu anomaly. EPMA analyses of extremely fine-grained, pseudo-cubic alunite from irregular veinlets indicate nearly stoichiometric compositions, minor Na substitution (<0.2 a.p.f.u.), and trace Fe. Slightly larger (10-15 μm) pseudo-cubic grains of Ca- and Sr-bearing APS minerals (likely woodhouseite-svanbergite) occur intergrown with alunite and kaolinite in these veins.

Interpretation

Chemical data for Tambo magmatic-hydrothermal alunite are consistent with other studies that report heterogeneous alunite compositions and elevated concentrations of Na, Ba, Ca, Sr, PO_4, and REE in high temperature environments (Stroffregen and Alpers, 1987; Stoffregen and Cygan, 1990; Aoki, 1991; Aoki et al., 1993; Hedenquist et al., 1994; A.J.B. Thompson, unpub. data). These elements typically occur as APS minerals overgrown by alunite or alunite-natroalunite (e.g., Stoffregen and Alpers, 1987; Aoki et al., 1993), as observed in Stage 1 samples from this study. The abundance of walthierite in Stage 2 is unusual, although similar compositions are noted for ore-stage alteration at the Pascua deposit, located at the northern end of the El Indio-Pascua Belt (Chap. 2).

Little geochemical information is available for near-surface alunite occurrences. Limited data for steam-heated alteration show significant variations (Ebert and Rye, 1997; A.J. B. Thompson, unpub. data), with compositions extending to the alunite and natroalunite end-member. The former is consistent with results reported in this study. Supergene alunite is generally K-rich in comparison to that in higher temperature occurrences, although trace-element concentrations are extremely variable, with Ca, Sr, REE and PO_4 substitutions reported (Stoffregen and Alpers, 1987; Arribas et al., 1995). The elevated trace-metal concentrations for samples of late vein alunite examined in this study are attributed to the metal content of source fluids, since stable-isotope results are not consistent with the oxidation of precursor sulfides.

Few chemical analyses have been published for magmatic steam alteration. Alunite in the Tambo banded veins is chemically similar to that from Alunite Ridge, Utah, and both are characterized by fine-scale, sawtooth bands of PO_4 and Sr substitution (Cunningham et al., 1984). Barium substitution is more common at Alunite Ridge however, and is rarely detected in the Tambo banded veins.

Recent studies on the REE contents of hydrothermal fluids (Michard, 1989; Lewis et al., 1997, 1998) and of hydrothermally altered rocks (Hopf, 1993; Arribas et al., 1995; Fulignati et al., 1999), have shown that REE can be mobilized under the conditions of acid sulfate

alteration. Magmatic-hydrothermal alteration has been characterized by strong fractionation of HREE with respect to LREE, when compared to fresh-rock equivalents (Arribas et al., 1995; Fulignati et al., 1999). However, compositional data for REE in Stage 1 alunite at Tambo and the host-rocks are not consistent with these published trends. We propose that the presence of APS inclusions and growth zones with elevated PO_4 and Sr contents contribute to the 'capturing effect' described by Schwab et al. (1990) and allow for the incorporation of HREE into the alunite crystal structure. Similar behavior is noted for Tambo steam-heated alunite which shows relatively minor HREE fractionation compared to host-rock values. Results are analogous to those described by Lewis et al. (1998) for altered rocks at Yellowstone National Park.

Alunite sampled from Stages 2 and 3 and the banded veins all exhibit strong fractionation of HREE compared to the host-rock composition. This trend is most pronounced in the Stage 3 and banded vein samples, whereas Stage 2 samples have comparatively lower REE concentrations. In all three stages, alunite precipitated in open spaces (either in veins or breccia matrices) with little evidence for wallrock interaction. The chemistry of these alunites should therefore reflect their source fluid composition. Experimental studies of REE partitioning between a Cl-bearing supercritical fluid (i.e., 'vapors') and a residual melt have shown a relative enrichment in LREE compared to HREE in the vapor phase (Flynn and Burnham, 1978; Reed, 1995). No information is available for these phases at lower temperatures, but the chemical signature of the Stage 2, Stage 3, and banded vein alunite may reflect the composition of a HREE-depleted fluid derived from the supercritical vapor-phase. In contrast, other forms of alunite derived their REE contents from a combination of magmatic fluids and REEs leached from the host rocks.

CHEMISTRY OF FLUID-INCLUSION GASES

Bulk sample fluid-inclusion techniques are widely used for the analysis of inclusion volatiles, mainly H_2O, CO_2, CH_4, N_2, H_2, and the noble gases (Shepperd and Rankin, 1998). Quadrupole mass spectrometric (QMS) analysis in particular has been applied to the identification of a large number of gases at low concentration in a variety of ore deposits and geothermal systems (e.g., Guha et al., 1990; Landis and Hofstra, 1991; Graney and Kesler, 1995b; Lindaas et al., 1998). A thorough review of this technique and its limitations are given in Graney and Kesler (1995a).

Compositions of fluid-inclusion gas in Tambo alunite were determined by QMS analysis (Landis and Rye, *in prep.*) in order to characterize Stage 2 and 3 ore fluids and banded vein alunite (i.e., magmatic steam) fluids. Repeated attempts to analyze fine-grained Stage 1, steam-heated, and late vein alunite failed to release sufficient quantities of gas. We present herein only a summary of results and the reader is referred to Landis and Rye (*in prep.*) for details.

Alunite samples were selected from coarse-grained assemblages and were examined petrographically prior to analysis. Stage 2 alunite, selected from the Reina vein, contains mostly small (<10 μm), apparently primary, vapor-rich inclusions, but the results of necking are common. Other, slightly larger inclusions (10-15 μm) have irregular shapes and may be secondary or pseudo-secondary in origin. These inclusions are vapor-dominant, but with more variable liquid-to-vapor ratios. Stage 3 alunite was selected from the Canto Sur deposit and contains many small (5-10 μm), vapor-dominant inclusions. Banded vein alunite, sampled from the Kimberly deposit, typically contains small, irregular, vapor-rich inclusions tightly clustered along growth zones.

Results and Interpretation

Data for crush- and thermally-released gas from alunite samples are reported in Table 3.7. The quantity of gas released by crushing is significantly smaller than that by thermal release, and is likely the result of opening very few and mostly larger inclusions along secondary planes in the alunite. The genetic significance of these mechanically released gases is not known, but the gases probably represent mixtures of multiple generations and secondary trapping events. Thermally-released gases are derived from decrepitation of the much more uniform occurrence of small primary inclusions (after removal of anomalous and secondary inclusions by crushing). These gases are generally considered to be representative of magmatic volatiles at the time of deposition (Graney and Kesler, 1995a). However, due to analytical effects, measured H_2S concentrations are considered a minimum value (Graney and Kesler, 1995b). The presence of sulfide daughter minerals would indicate significant post-depositional changes in sulfur gas species, but none were detected at Tambo. Similarly, significant reaction of SO_2 gas with sulfate bound in the structure of alunite is unlikely (Landis and Rye, *in prep.*).

Ratios of major gas species, H_2S-SO_2-HCl (Fig. 3.12a), for the three alunite depositional events illustrate a distinct transition in volatile chemistry. Stage 2 fluids are H_2S-dominant ($H_2S/SO_2 \sim 6$), whereas magmatic steam alunite (banded vein sample) is characterized by a

Table 3.7. Fluid inclusion gas chemistry data for Stage 2, Stage 3, and banded vein alunite. Abbreviations: MH = magmatic hydrothermal, MS = magmatic steam, a = atmosphere, cps = counts per second. Blank fields are not detected. Accuracy is 3-5% based on prepared standard gas mixtures and analysis of synthetic fluid inclusions.

Sample	T01a		T02b		T08a	
Description	**Stage 2**		**Stage 3**		**Banded Vein**	
Method	Crush	Thermo	Crush	Thermo	Crush	Thermo
Weight (g)	8	8	6.6	6.6	7.4	7.4
N_2 %	13.6131	0.1961	19.5394	0.5174	48.6233	20.2117
O_2 ppm	48	44	19	59	127	1045
Ar ppm	4070	200	4431	654	14228	54992
H_2 %	65.09	1.44	65.65	6.68	13.59	45.38
H_2O%	11.3008	97.551	4.0415	91.1306	21.7247	29.9172
H_2S ppm	20	17	12	12	22	1
SO_2 ppm	38	3	24	30	43	48
HCl ppm	47	8	9	41	10	3
HF ppm	313	2672	90	2234	0	673
CH_4 %	0.212	0.014	0.43	0.083	0.143	0.5
CO_2 %	1.637	0.458	2.173	0.764	1.141	3.264
CO %	7.69	0.045	7.712	0.52	20.128	–
He ppm						44
^{4}He volts	0.085718	1.479663	0.029593	0.945581	0.425582	0.107442
^{4}He moles-gm^{-1}	6.872E-14	1.186E-12	2.876E-14	9.189E-13	3.689E-13	9.313E-14
^{3}He cps	2.771531	8.834217	1.057146	9.002538	17.721322	2.350376
^{3}He moles-gm^{-1}	3.447E-20	1.099E-19	1.594E-20	1.357E-19	2.383E-19	3.161E-20
R=^{3}He/^{4}He	5.016E-07	9.263E-08	5.542E-07	1.477E-07	6.460E-07	3.394E-07
R/R_a	0.3625	0.0669	0.4004	0.1067	0.4668	0.2452
^{20}Ne	91.772	90.009	91.35	91.564	85.109	90.098
^{21}Ne	0.29924	0.28346	0.2571	0.25246	4.23851	0.39388
^{22}Ne	7.92907	9.70787	8.39272	8.1838	10.65245	9.50805
^{21}Ne/^{20}Ne	0.0033	0.0031	0.0028	0.0028	0.0498	0.0044
^{21}Ne/^{22}Ne	0.0377	0.0292	0.0306	0.0308	0.3979	0.0414
^{22}Ne/^{20}Ne	0.0864	0.1079	0.0919	0.0894	0.1252	0.1055

disequilibrium gas assemblage with high H_2, abundant reduced carbon species, and high SO_2. This chemical shift is also illustrated in Figure 3.12b, with compositions recast to modeled equilibrium mole fractions at approximated temperatures and pressures for each alunite stage (using the NASA-CEA program and thermochemical data set; Gordon and McBride, 1994; McBride and Gordon, 1996: details see Landis and Rye, *in prep.*).

Helium is commonly used as a tracer in studies of fluid flow in hydrothermal systems, because isotopic compositions of He from atmospheric, upper-mantle, and crustal or radiogenic sources differ substantially. The atmospheric $^3He/^4He$ ratio (R_a) is 1.39 ± 0.01 (e.g., Mamyrin et al., 1969) and is typically used as a reference for comparison to $^3He/^4He$ (R) gas data in the form R/R_a. Mantle-derived He has R/R_a values greater than 8 (Craig and Lupton, 1981; Lupton, 1983) whereas crustal ^4He is enriched from both radiogenic U-Th decay and nuclear spallation reactions, creating low R/R_a values of < 0.01 in upper crustal elevated U-Th rocks (Gerling et al., 1971; Morrison and Pine, 1955). Thermal release $^3He/^4He$ and R/R_a in this study range from 9.3e-8 to 3.4e-7 and 0.06 to 0.25, respectively. There is no indication of elevated ^3He of mantle origin in any of the samples in this study, and data suggest a crustal magmatic component. In particular, banded vein samples have the highest R/R_a values. Stable isotopic analyses indicate minor meteoric fluid was involved during any of these stages; hence, the volatiles and magmatic steam in particular must have been derived directly from magma, with He incorporated in the melt during partial melting in the lower crust.

Similarly, the isotopic and elemental composition of Ne of the earth is significantly different from that of the present atmosphere, and can provide further indications of fluid source and the amount of crustal versus magmatic interaction. Neon isotopes are typically compared against end-member compositions of the atmosphere and of mid-ocean-ridge basalts (MORB), which show enrichment in ^{20}Ne and ^{21}Ne relative to ^{22}Ne (e.g., Poreda et al, 1984; Marty, 1989). In contrast, crustal fluids typically are enriched in ^{21}Ne and ^{22}Ne relative to ^{20}Ne from crustal nucleogenic-radiogenic processes (Kennedy et al., 1990). Neon isotopic data from this study are consistent with He results and suggest a crustal enrichment in ^{21}Ne and ^{22}Ne relative to ^{20}Ne (Table 3.7).

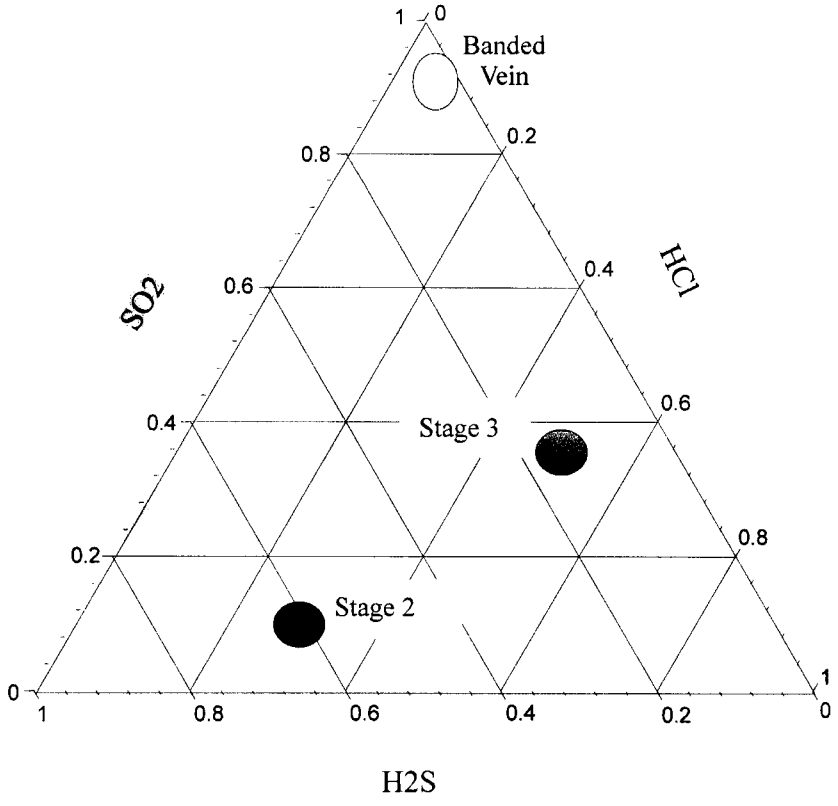

Figure 3.12a. Ternary H_2S-SO_2-HCl data from fluid inclusion analyses of Tambo alunite.

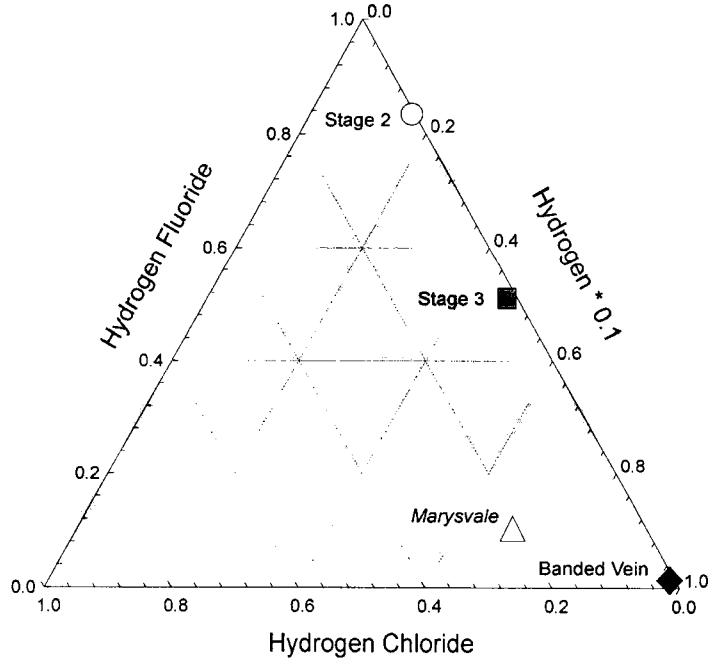

Figure 3.12b. Ternary HCl-HF-H_2 data from fluid inclusion analyses of Tambo alunite. Methods of mole fraction recalculation detailed in Landis and Rye (in prep.)

DISCUSSION

Fluid-inclusion and isotopic studies of several high sulfidation deposits have indicated that magmatic fluids contribute to both alteration and mineralization within these systems (e.g., Hedenquist and Lowenstern, 1994; Arribas, 1995; Cooke and Simmons, 2000). This magmatic component originates from the exsolution of a fluid from the melt during retrograde (or resurgent) boiling (Burhnam, 1979; Burnham and Ohmoto, 1980). When the exsolved fluid reaches its solvus, the inception of aqueous immiscibility leads to the formation of low-density vapor and dense hypersaline liquid. Evidence for phase separation is seen in fluid inclusions from many porphyry copper deposits, which contain both hypersaline liquid-rich inclusions and associated vapor-rich inclusions (Burnham, 1979; Roedder, 1984; Bodnar, 1985). This process is critical for the partitioning of ore metals from the melt to the hydrothermal system (Candela and Piccoli, 1995; Williams et al., 1995), and the strong effect on the physical behavior of the system is due to the large density contrast between the vapor and liquid phases. The aqueous vapor will rise to shallow depths and either discharge at surface as volcanic fumaroles, or become absorbed into the groundwater system. The dense, hypersaline liquid remains at depth and is recorded as saline fluid inclusions in intrusive rocks and porphyry ore deposits (Hedenquist and Lowenstern, 1994 and references therein). Ore-metal partitioning between these two phases will determine where (potential) mineralization will occur (see discussion below).

As fluids ascend from their underlying magma source, they are further influenced by the transition from brittle to plastic behavior in the lithosphere (Fournier, 1999). This transition typically occurs at about 370° to 400°C in continental hydrothermal systems (Fournier, 1999). Abrupt changes in the pressure regime across this transition zone are thought to be responsible for porphyry Cu mineralization in several systems (e.g., Fournier, 1967; Gustafson and Hunt, 1975; Cunningham, 1978), and more recently for porphyry Au mineralization (Muntean and Einuadi, 2000). Similarly, several authors have related epithermal mineralization to the escape of magmatic fluids into hydrostatically pressured hydrothermal systems (e.g. Fournier, 1987; Rye, 1993; Deen et al., 1994; Hedenquist et al., 1998).

In the following discussion, we examine the role of magmatic fluids in the Tambo high sulfidation system and the nature of magmatic steam processes.

Role of Magmatic Fluids in Alteration

It is generally accepted that hypogene acid sulfate alteration results from oxidized and acidic fluids that are generated by the condensation of magmatic volatiles enriched in SO_2, HCl, and HF. The disproportionation of these acid species at temperatures below *ca.* 300-350°C (Hemley et al., 1969) creates acidic fluids with a pH of about 1. These fluids are sufficiently acidic to leach most components from the host rock, leaving a vuggy quartz residue. The progressive neutralization of these fluids by reaction with wallrock forms successive alteration envelopes of acid sulfate, advanced argillic, argillic, and propylitic assemblages outward from the main fluid conduit (e.g., Steven and Ratte, 1960).

Stable-isotope evidence indicates that the degree of meteoric water interaction during hypogene alteration is variable. At the Julcani deposit for example, the condensed liquids responsible for acid sulfate alteration were of magmatic origin (Deen et al., 1994). Rodalquilar also has evidence for a strong magmatic component during hypogene alteration (Arribas et al., 1995). In contrast, many other high sulfidation deposits have evidence for mixed magmatic and meteoric alteration-fluids (e.g., Summitville, Rye et al., 1990; Nansatsu, Hedenquist et al., 1994; Pueblo Viejo, Venneman et al., 1993).

Magmatic contributions to the near-surface environment are less well defined. Steam-heated alteration forms from the oxidation of H_2S gas at or above the water table (Schoen et al., 1974). The fluids responsible for alteration typically have a meteoric isotopic signature (e.g., Rye et al., 1992; Ebert and Rye, 1997), however deuterium enrichment (10 to 20‰) is common in steam-heated fluids from active geothermal systems. This enrichment is attributed to the effects of either subsurface boiling (Truesdell et al., 1977) or evaporation (Henley and Stewart, 1983).

At Tambo, the large difference between isotopically light meteoric water and significantly heavier magmatic fluids emphasizes processes involving these two components. Stable-isotope evidence indicates that there is a dominant magmatic component in all stages of hypogene alteration and alunite deposition. Minor meteoric water is involved in Stage 1 and Stage 3 alteration, but overall, magmatic-hydrothermal and magmatic steam processes from initial Stage 1 alteration through to the banded alunite veins involve a significant magmatic fluid contribution. Similarly, fluids responsible for steam-heated alteration are significantly enriched in deuterium (by up to 100‰) compared to local meteoric water. This enrichment is much greater than that attributed to either boiling or evaporation mechanisms to date (maximum of *ca.* 40‰; J. Hedenquist, pers. comm.). Thus, whereas evaporation may have played a role in

steam-heated processes, we conclude that much of the water involved in alteration was of magmatic origin.

Late stage alteration at Tambo also involved a large magmatic fluid component. On the basis of stable isotopic data, we suggest that alteration resulted from the mixing of magmatic fluids (either magmatic steam or condensed magmatic vapors) with meteoric waters. This magmatic fluid signature is recorded in alunite deuterium values that show a maximum 50‰ enrichment above that of meteoric water.

Overall, there is a strong magmatic fluid component to alteration at the Tambo deposit, even in near-surface and late-stage processes. These fluids likely consisted of condensed magmatic vapors that accumulated from episodic magmatic activity over a period of 4 m.y. These fluids effectively displaced, or overwhelmed, meteoric groundwaters in the immediate vicinity. We propose that this process is attributed to local climatic and physiographic effects, related to an semi-arid climate and regional erosional events that are thought to have significantly depressed water tables throughout the El Indio-Pascua Belt (Bissig, 2001; details see Chap. 6).

Role of Magmatic Fluids in Mineralization

Although the consensus is that high sulfidation ore metals are of magmatic origin (e.g., Hedenquist and Lowenstern, 1994; Arribas, 1995; Cooke and Simmons, 2000), there is considerable debate regarding the nature of these fluids, and particularly the relative contributions of vapor versus hypersaline liquid to the formation of Au, Ag, and Cu mineralization. Based on fluid-inclusion and isotopic studies on several high sulfidation deposits, the nature of mineralizing fluids were summarized by Cooke and Simmons (2000). Three possible ore-fluids were given as:

a) Low-salinity, acid waters with high concentrations of reduced sulfur. Under these conditions, Au (and possibly Cu) would be transported as bisulfide complexes. Fluids could result from either the mixing of magmatic volatiles with meteoric waters (Sillitoe, 1983; Arribas, 1995), particularly under high pressure conditions (Hedenquist, 1995), or at the base of a rising vapor plume (Rye, 1993).
b) Metal-bearing, acidic brines derived from a magma carrying chloride-complexed metals (White, 1991; Hedenquist et al., 1994).
c) Reduced magmatic vapors transporting Au and Cu in the vapor phase as sulfide or chloride species (Arribas, 1995; Mountain, 1999).

Given recent studies of metal fractionation between magmatic brines and vapors and evidence from fluid and melt inclusions, there is growing evidence that supports the proposal that magmatic vapors have the capacity to transport metals such as Cu and Au (Lowenstern et al., 1991; Heinrich et al., 1992; Shinohara, 1994; Audétat et al., 1998; Heinrich et al., 1999; Ulrich et al., 1999). In some cases, Au, Ag, and Cu have been shown to partition preferentially into a high-pressure vapor phase (Heinrich et al., 1999). These results are particularly significant to epithermal mineralization, given the much larger mobility and mass flux of a vapor phase relative to brine.

At Tambo, Stage 2 ore is characterized by vapor-rich, H_2S-dominant, low-salinity fluids (this study; Jannas et al., 1999). There is no evidence for a hypersaline fluid component; nearly all fluid-inclusions measured by Jannas (1995) contain less than 4 wt. % NaCl equivalent, and measured concentrations of Cl in inclusion gases are negligible. We conclude that Au was transported as sulfide-complexed metals in a magmatic vapor phase, either as volatile species (e.g., $AuS_{(g)}$) or as bisulfide complexes, as inferred by Heinrich et al. (1999) for Au transport in their experiments. The S-rich, Fe-poor nature of the Stage 2 assemblage is consistent with vapor separation from a brine (Heinrich et al., 1999). Similarly, the high Te content of the mineralizing assemblage is also consistent with vapor-phase transport (Cooke and McPhail, 2000).

The mechanisms of Stage 3 mineralization are less clear, but again there is no evidence for a hypersaline brine component. Stage 3 fluids are vapor-rich, although more oxidized (SO_2-rich) than those responsible for Stage 2 Au deposition. There are two viable scenarios for mineralization. Gold may have precipitated directly from the magmatic vapor phase without prior condensation, as postulated for magmatic steam alunite (see discussion below). Alternatively, Stage 3 ore fluids may have represented mixed magmatic vapor condensates (analogous to Stage 2 fluids) and SO_2-rich magmatic steam. Gold was either transported in the ascending mixture of vapor + steam as sulfide-complexes or volatiles species, or was present in previously condensed magmatic fluids. In the latter case, Au deposition would result from oxidation caused by periodic pulses of magmatic steam that mix with residual vapor condensates.

Origins of Magmatic Steam

The magmatic steam environment was initially defined by Rye et al. (1992), based on data for coarsely crystalline alunite veins from Marysvale, Utah (Cunningham et al., 1984).

Alunite in these veins is characterized by near-equilibrium oxygen-isotope values but disequilibrium sulfur-isotope values and δD in the magmatic range. Documented occurrences of this type are rare, and the mechanism of magmatic steam deposition is poorly understood. Magmatic steam processes are a significant part of the Tambo deposit however, due to their abundance and association with Stage 3 ore. Stable-isotope and fluid-inclusion data from this study have helped to characterize the magmatic steam environment. Important considerations are summarized below.

- Magmatic steam fluids are SO_2-rich. This was inferred by Cunningham et al. (1984) on the basis of the absence of sulfide in the Marysvale veins. Fluid-inclusion data from this study confirm a transition from H_2S-rich magmatic-hydrothermal fluids to SO_2-rich magmatic steam fluids.

- Alunite is characterized by nearly constant $\delta^{34}S$ values close to the value of bulk sulfur in the magma (Rye et al., 1992). Given that sulfur-isotope equilibrium between aqueous sulfate and sulfide is obtained quickly at high temperature (Ohmoto and Lasaga, 1982), a rapid rate of vapor ascent and mineral deposition is required once fluids are exsolved from the magma (Rye et al., 1992; Rye, 1993).

- Inclusion fluids are vapor-rich and of low salinity. These data indicate that magmatic steam fluids consisted mostly of vapor that had already undergone phase separation. However, under low pressure conditions, some Cl may be incorporated into the vapor-phase as HCl° (Fournier, 1999).

- Magmatic steam alunite forms late in the development of the hydrothermal system. A similar transition from early magmatic-hydrothermal to late magmatic steam processes has also been documented at the Red Mountain deposit, Colorado (Bove et al., 1990; Rye et al., 1992).

On the basis of these constraints and the ideas presented in Fournier (1999), we propose a conceptual model for the origin of magmatic steam alunite at Tambo. This model is illustrated schematically in Fig. 3.13, on the basis of physical parameters given in Fig. 3.14. Magmatic steam processes were initiated by the emplacement of a magma body within 1 to 2 km of surface (Fig. 3.14). Given the shallow depth of emplacement, and perhaps coupled with the thermal collapse of the previous magmatic-hydrothermal system, a high thermal gradient would have existed across the brittle–plastic transition zone. Fluids exsolved from the magma

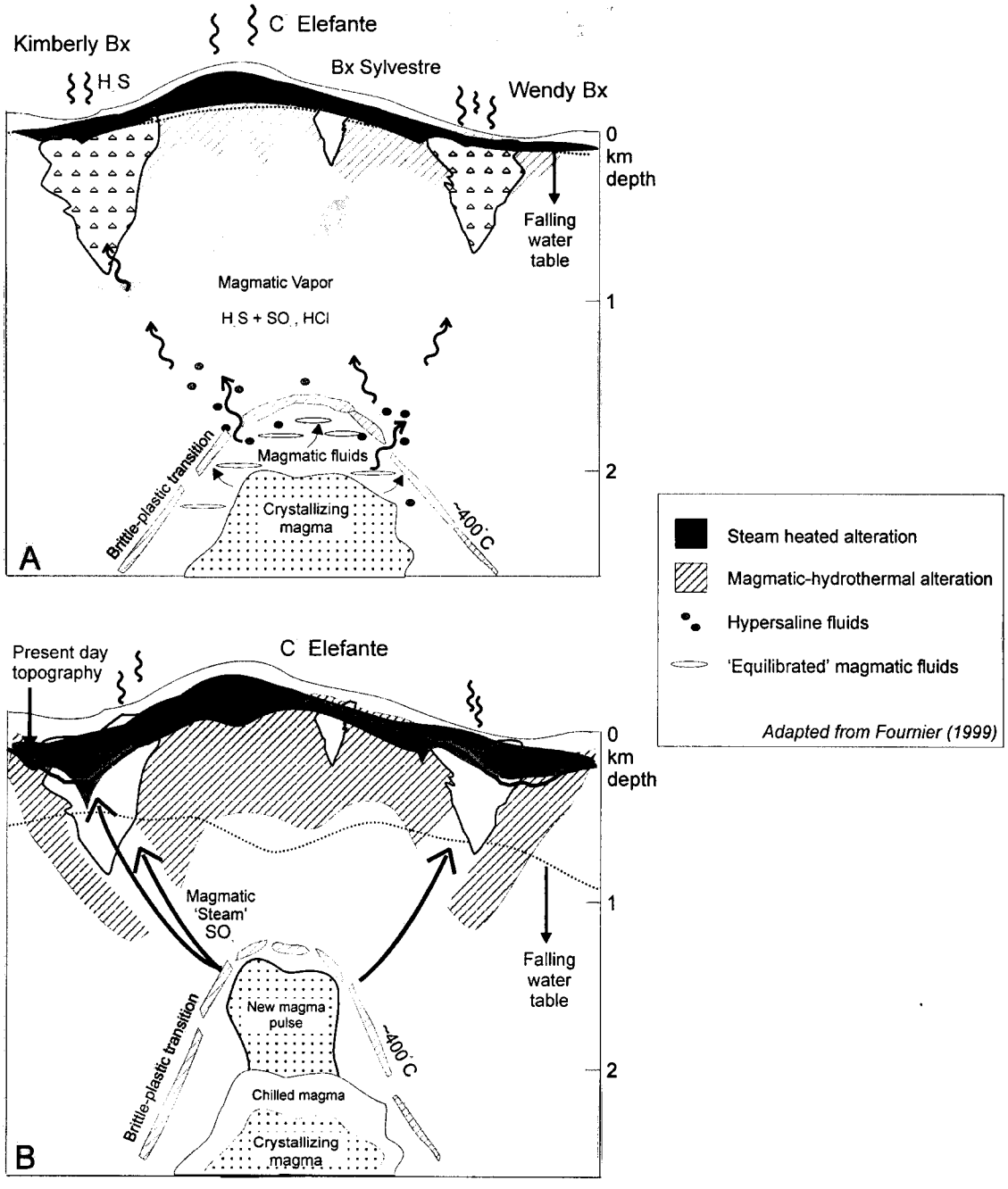

Figure 3.13. Schematic section of Cerro Elefante depicting the proposed model for (A) Stage 2 alteration and Au ore formation and (B) magmatic steam processes. Stable isotope data indicate Stage 2 alunite and barite formed from condensed magmatic vapor with $H_2S/SO_2 \sim 6$ and equilibrated sulfur species with no evidence for meteoric fluid involvement. Magmatic fluids likely evolved from deep crystalline rocks between the brittle-plastic transition and carapace of the magma (Rye, 1993) during episodic rupture of the brittle-plastic transition (Fournier, 1999). Steam heated alteration was active near-surface during the magmatic-hydrothermal event. Magmatic steam alunite formed from SO_2-dominant magmatic vapors that exsolved from a new pulse of magma emplaced to shallow depth. Decompression and rapid cooling would have resulted due to high temperature gradients and progressive lowering of the water table (Bissig et al., submitted, b). A vapor + brine mixture was released into the hydrostatic regime. The vapor quickly ascended along pre-existing structures and alunite (+ trace quartz, hematite) precipitated along fracture surfaces.

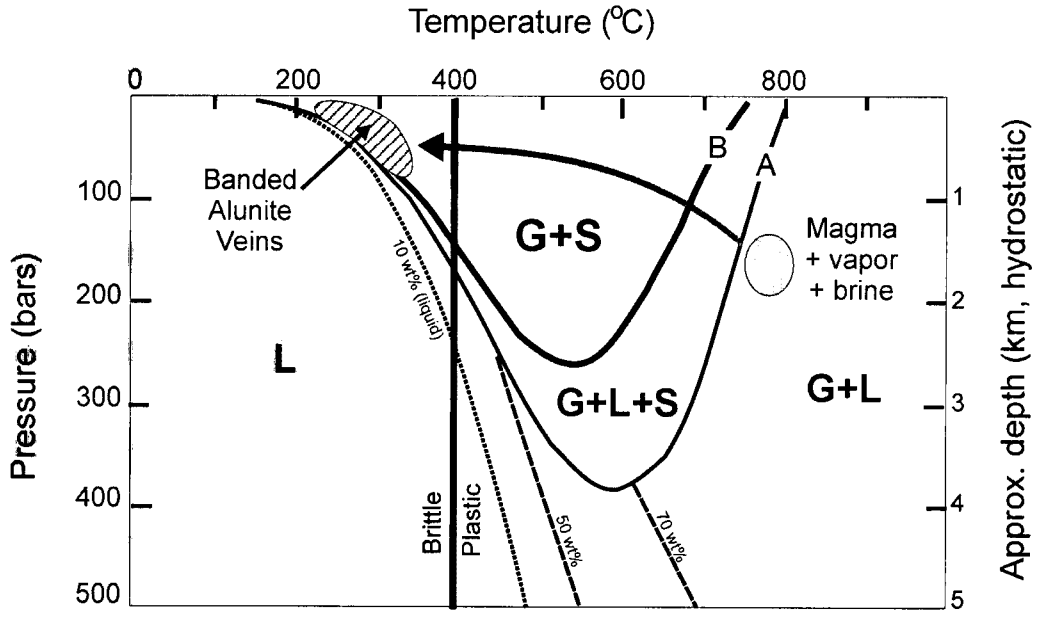

Figure 3.14. Diagram showing phase relations in the system NaCl-H_2O (modified from Fournier (1999)). Depths assuming 1g/cm^3 hydrostatic load are given. G = gas, L = liquid, S = solid salt. Curve A shows the three-phase boundary, G+L+S for the system NaCl-H_2O. Curve B shows the three phase boundary, G+L+S, for the system NaCl-KCl-H_2O, with Na/K in solution fixed by equilibration with albite and K feldspar at the indicated temperatures. Approximate position of the brittle-plastic transition is given. Reference lines: dotted line = condensation point curves for magmatic vapor containing 10 wt % dissolved NaCl: dashed lines = contours of constant wt % NaCl dissolved in brine. This diagram is used to illustrate the origin of magmatic steam alunite veins from fluids exsolved from a magma emplaced at shallow depth (1-2 km).

and released across this boundary would therefore experience a sudden decompression (i.e., 'flashing') and rapid cooling (Fournier, 1999). These fluids were likely a mixture of vapor + brine, but the large volume of 'vapor' generated under these conditions would have ascended very quickly, away from the parent brine. These vapors would have been SO_2-dominant, due to the shallow depth of vapor release (Gerlach and Casadevall, 1986; Carroll and Webster, 1994) and sudden decompression buffered H_2S/SO_2 gases in the magmatic fluids (Gerlach, 1993). According to Fournier (1999), the vapors would also have been capable of carrying minor Si and moderate HCl^o. Under these low-pressure conditions, however, the solubility of quartz in vapor is too low to permit major silica deposition (Fournier and Potter, 1982), in contrast to the occurrence of banded quartz veins in some porphyry gold deposits (e.g., Muntean and Einaudi, 2000). Flashing of the vapor-rich fluids would result in gas + salt (Fig. 3.14) and apparent supersaturation with respect to alunite (with trace quartz and hematite). The mechanisms of alunite precipitation are unclear, but it is likely that SO_2 in the vapors would react with H_2 upon cooling (Gerlach, 1993) to form sulfate. Any HCl^o in the vapor would remain unreactive in the absence of liquid water (Fournier, 1999). Given the semi-arid conditions and depressed water table in the Tambo area at this time (Bissig, 2001), little excess water would have been present at the depths of alunite deposition (within about 500-800 m of the surface), and any HCl^o would have remained in the vapor phase.

SUMMARY

The geological framework determined by Jannas et al. (1999) for the Tambo deposit has allowed a detailed study of shallow-level magmatic-hydrothermal processes. Tambo is characterized by several alteration and mineralizing events, related to episodic magmatic activity over a period of at least 4 m.y. We have focussed on the characteristics of alunite and acid sulfate alteration assemblages. Textural and paragenetic observations, combined with geochronologic, stable-isotope, and geochemical data, have helped to define the evolution of alunite source fluids and depositional processes in the epithermal environment. Results from this study have shown:

1. There is a strong magmatic signature to all stages of alteration and ore-related events in the Tambo area. Meteoric fluid contribution is minimal, even in the near-surface steam-heated environment and during the final stages of the hydrothermal system.

2. Vapor-phase Au transport is inferred for both Stage 2 and Stage 3 mineralization. There is no evidence for a magmatic brine contribution to ore-stage fluids.

3. The fluids responsible for both alteration and mineralization evolve from a high-temperature magmatic vapor plume. The transition from magmatic-hydrothermal alteration to magmatic steam-dominated processes reflects changes in pressure conditions and the hydrodynamic regime into which magmatic volatiles were released.

REFERENCES

Aoki, M., 1991. Mineralogical features and genesis of alunite solid solution in high temperature magmatic-hydrothermal systems. Journal of the Geological Survey of Japan, 277: 31-32.

Aoki, M., Comsti, E.C., Lazo, F.B., and Matsuhisa, Y., 1993. Advanced argillic alteration and geochemistry of alunite in an evolving hydrothermal system at Baguio, northern Luzon, Phillipines. Resource Geology, 43: 155-164.

Arribas, A., Jr., 1995. Characteristics of high sulfidation epithermal deposits, and their relation to magmatic fluids. *In* Thompson, J.F.H. ed., Magmas, Fluids and Ore Deposits. Mineralogical Association of Canada Short Course Notes, 23: 419-454.

Arribas, A., Jr., Cunningham, C.G., Rytuba, J.J., Rye, R.O., Kelly, W.C., McKee, E.H., Podwysocky, M.H., and Tosdal, R.M., 1995. Geology, geochronology, fluid inclusions, and stable isotope geochemistry of the Rodalquilar Au alunite deposit, Spain. Economic Geology, 90: 795-822.

Audétat, A., Günther, D., and Heinrich, C.A., 1998. Formation of magmatic-hydrothermal ore deposit: Insights with LA-ICP-MS analysis of fluid inclusions. Science, 279: 2091-2094.

Barazangi, M. and Isacks, B. L., 1976. Spatial distribution of earthquakes and subduction of the Nazca Plate beneath South America. Geology, 4: 686-692.

Beane, R.E., 1991. Deposit correlations in the El Indio Belt, Chile: Mineral paragenesis, fluid inclusions, and sulfur isotopes. Internal report for Barrick Gold Corporation.

Bennet, R.E., 1995. A combined hydrothermal alteration study and exploration target evaluation of the Tambo mining district, El Indio mineral belt, Region IV, Chile. Internal report for Companià Minera San José Ltda.

Bethke, P.M., 1984. Controls on base- and precious-metal mineralization in deeper epithermal environments. U.S. Geological Survey Open File Report 84-890, 40 p.

Bissig, T., 2001. Metallogenesis of the Miocene El Indio-Pascua gold-silver-copper belt, Chile/ Argentina: Geodynamic, geomorphological and petrochemical controls on epithermal mineralization. Unpublished Ph.D. thesis, Queen's University, Kingston, Canada.

Bodnar, R.J., 1995. Fluid-inclusion evidence for a magmatic source of metals in porphyry copper deposits. Mineralogical Association of Canada Short Course Series, 23: 139-152.

Bove, D.J., Rye, R.O., and Hon, K., 1990. Evolution of the Red Mountain alunite deposits, Lake City, Colorado. US Geological Survey Open File Report, 90-0235.

Burham, C.W., 1979. Magmas and hydrothermal fluids. *In* Barnes, H.L., ed., Geochemistry of Hydtrothermal Ore Deposits. New York, Wiley: 71-36.

Burham, W.C., and Ohomoto, H., 1980. Late-stage processes of felsic magmatism. Mining Geology Special Issue 8: 1-11.

Caddey, S.W., 1993. Structural analysis of the El Indio-Tambo mining district, Chile: exploration guides, ore controls, and target areas. Internal report for Barrick Gold Corporation.

Candela, P.A. and Piccoli, P.M., 1995. Model ore-metal partitioning from melts into vapor and vapor-brine mixtures. *In* Thompson, J.F.H., ed., Magmas, Fluids, and Ore Deposits. Mineralogical Association of Canada Short Course Series, 23: 101-127.

Carroll, M.R., and Webster, J.D., 1994. Solubilities of sulfur, noble gases, nitrogen, chlorine, and fluorine in magmas. Reviews in Mineralogy, 30: 231-279.

Cooke, D.R., and McPhail, D.C., 2000. Epithermal Au-Ag-Te mineralization, Acupan, Baguio District, Phillipines: numerical simulations of mineral deposition. Economic Geology, 96: 109-131.

Cooke, D.R. and Simmons, S.F., 2000. Characterisitcs and genesis of epithermal gold deposits. *In* Hagemann, S.G. and Brown, P.E. ed., Gold 2000. Reviews in Economic Geology, 13: 221-244.

Craig, H., 1961. Isotopic variations in meteoric waters. Science, 133: 1702-1703.

Craig, H., and Lupton, J.E., 1981. ^{3}He and mantle volatiles in the ocean and the ocean crust. *In* Emiliani, C, ed., The Sea: 391-428.

Cunningham, C.G., 1978. Pressure gradients and boiling as mechanisms for localizing ore in porphyry systems. US Geological Survey Journal of Research, 6: 745-754.

Cunningham, C.G., Rye, R.O., Steven, T.A., and Mehnert, H.H., 1984. Origins and exploration

signficance of replacement and vein-type alunite deposits in the Marysvale volcanic field, west central Utah. Economic Geology, 79: 50-71.

Deen, J.A., Rye, R.O., Munoz, J.L., and Drexler, J.W., 1994. The magmatic-hydrothermal system at Julcani, Peru: Evidence from fluid inclusions and hydrogen and oxygen isotopes. Economic Geology, 89: 1924-1938.

Ebert, S.W. and Rye, R.O., 1997. Secondary precious metal enrichment by steam-heated fluids in the Crowfoot-Lewis hotspring gold-silver deposit and relation to paleoclimate. Economic Geology, 92: 578-600.

Fournier, R.O., 1967. The porphyry copper deposit exposed in the Liberty open-pit mine near Ely, Nevada. Part I. Syngenetic formation. Economic Geology, 62: 57-81.

Fournier, R.O., 1987. Conceptual models of brine evolution in magmatic-hydrothermal systems. US Geological Survey Professional Paper, 1350, v.2: 1487-1506.

Fournier, R.O., and Potter, R.W., 1982. An equation correlating the solubility of quartz in water from 25 to 900°C at pressures up to 10,000 bars. Geochimica et Cosmochimica Acta, 46: 1969-1973.

Fournier, 1999. Hydrothermal processes related to movement of fluid from plastic into brittle rock in the magmatic-hydrothermal environment. Economic Geology, 94: 1193-1212.

Flynn, F.R., and Burnham, C.W., 1978. An experimental determination of rare earth partition coefficients between a chloride-containing vapor phase and silicate melts. Geochimica et Cosmochimica Acta, 42: 685-701.

Fulignati, P., Gioncada, A., and Sbrana, A., 1999. Rare-earth element behaviour in the alteration facies of the active magmatic-hydrothermal systems of Vulcano (Aeolian Islands, Italy). Journal of Volcanology and Geothermal Research, 88: 325-342.

Fulignati, P. and Sbrana, A., 1998. Presence of native gold and tellurium in the activee high-sulfidation hydrothermal system of the La Fossa volcano (Vulcano, Italy). Journal of Volcanology and Geothermal Research, 86: 187-198.

Gammons, C.H., and William-Jones, A.E., 1997. Chemical mobility of gold in the porphyry-epithermal environment. Economic Geology, 92: 43-59.

Gerlach, T.M., 1993. Oxygen buffering of Kilauea volcanic gases and the oxygen fugacity of Kilauea basalt. Geochimica et Cosmochimica Acta, 57: 795-814.

Gerlach, T.M., and Casadevall, T.J., 1986. Evaluation of gas data from high-temperature fumaroles at Mount St. Helens, 1980-1982. Journal of Volcanology and Geothermal Research, 28 (1-2): 107-140.

Gerling E., K., Mamyrin, B.A.,a nd Tolstikhin, I.N., 1971. Helium isotope composition in some rocks. Geochemical International, 8: 755-761.

Gieseman, A., Jager, H.J., Norman, A.L., Krouse, H.R., and Brand, W.A., 1994. On-line sulfur-isotope determination using and elemental analyzer coupled to a mass spectrometer. Analytical Chemistry, 65 (18).

Giggenbach, W.F., 1992. Magma degassing and mineral deposition in hydrothermal systems along convergent plate boundaries. Economic Geology, 87: 1927-1944.

Godfrey, J.D., 1962. The deuterium content of natural waters and other substances. Geochimica et Cosmochimica Acta, 27: 43-52.

Gordon, S., and McBride, B.J., 1994. Computer Program for Calculation of Complex Chemical Equilibrium Compositions and Applications. I. Analysis. NASA Reference Publication 1311.

Graney, J.R., and Kesler, S.E, 1995a. Gas composition of inclusion fluid in ore deposits: Is there a relation to magmas?. *In* Thompson, J.F.H., ed., Magmas, Fluids, and Ore Deposits. Mineralogical Association of Canada Short Course vol. 23: 221-246.

Graney, J.R., and Kesler, S.E., 1995b. Factors affecting gas analysis of inclusion fluid by quadrupole mass spectrometry. Geochimica et Cosmochimica Acta, 59: 3977-3986.

Guha, J., Lu, L.Z., and Gagnon, M., 1990. Gas composition of fluid inclusions using solid probe mass spectrometry and its application to study of mineralizing processes. Geochimica et Cosmochimica Acta, 54: 553-558.

Gustafson, L.B., and Hunt, J.P., 1975. The porphyry copper deposit at El Salvador, Chile. Economic Geology, 70: 857-912.

Hedenquist, J.W., 1995. The ascent of magmatic fluid: Discharge versus mineralization. Mineralogical Association of Canada Short Course Series, v. 23: 263-289.

Hedenquist, J.W. and Arribas, A., Jr., 1999. Epithermal gold deposits: I. Hydrothermal processes in intrusion-related systems, and II. Characteristics, examples, and origin of epithermal gold deposits. *In* F. Molnar, J. Lexa, and J.W. Hedenquist, eds., Epithermal Mineralization of the Western Carpathians. Society of Economic Geologists, Guidebook Series, 31: 13-63.

Hedenquist, J.W. and Lowenstern, J.B., 1994. The role of magmas in the formation of hydrothermal ore deposits. Nature, 370: 519-527.

Hedenquist, J.W., Simmons, S.F., Giggenbach, W.F., and Eldridge, C.S., 1993. White Island, New Zealnad, volcanic-hydrothermal system represent the geochemical environment of

high sulfidation Cu and Au ore deposition. Geology, 21: 731-734.

Hedenquist, J.W., Matsuhisa, Y., Izawa, E., White, N.C., Giggenbach, W.F., and Aoki, M., 1994. Geology, Geochemistry, and origin of high sulfidation Cu-Au mineralization in the Nansatsu District, Japan. Economic Geology, 89: 1-30.

Heinrich, C.A., Gunther, D., Audetat, A., Ulrich, T., and Frischknecht, R., 1999. Metal fractionation between magmatic brine and vapor, determined by microanalysis of fluid inclusions. Geology, 27: 755-758.

Heinrich, C.A., Ryan, C.G., Mernagh, T.P., and Eadington, P.J., 1992. Segregation of ore metals between magmatic brine and vapor: A fluid inclusion study using PIXE micranalysis. Economic Geology, 87: 1566-1583.

Hemley, J.J., Hostetler, P.B., Gude, A.J., and Mountjoy, W.T., 1969. Some stability relations of alunite. Economic Geology, 64: 599-612.

Henley, R.W., and Stewart, M.K., 1983. Chemical and isotopic changes in the hydrololoy of the Tauhara geothermal field due to exploitation at Wairakei. Journal of Volcanology and Geothermal Research, 15: 285-314.

Hopf, S., 1993. Behavior of rare earth elements in goethermal systems of New Zealand. Journal of Geochemical Exploration, 47: 333-357.

Jambor, J.L., 1999. Nomenclature of the alunite supergroup. Canadian Mineralogist, 37: 1323-1341.

Jannas, R.R., 1995. Reduced and oxidized high sulfidation deposits of the El Indio deposit, Chile. Ph.D. thesis, Cambridge, Massachusetts, Harvard University, 421 p.

Jannas, R.R., Bowers, T.S., Petersen, U., Beane, R.E., 1999. High-sulfidation deposit types in the El Indio District, Chile. *In* Skinner, B.J., ed., Geology and ore deposits of the Central Andes. SEG special publication #7: 27-59.

Kavaleris, I., 1994. High Au, Ag, Mo, Pb V, and W content of fumarolic deposits at Merapi volcano, Central Java, Indonesia. Journal of Geochemical Exploration, 50: 480-492.

Kennedy, B.M., Hiyagon, H., and Reynolds, J.H., 1990. Crustal neon: a striking uniformity. Earth Science Planetary Letters, 98: 277-286.

Kornexl, Barbara E., Matthias Gehre, Reiner Höfling, and Roland A. Werner, 1999. On-line $\delta^{18}O$ measurement of organic and inorganic substances. Rapid Communications in Mass Spectrometry 13: 1685-1693.

Landis, G.P., and Hofstra, A.H., 1991. Fluid inclusion gas chemistry as a potential mineral exploration tool: Case studies from Crede, CO, Jerrit Canyon, NV, Coeur d'Alene district,

ID and MT, southern Alaska epithermal veins, and mid-continent MVT's. Journal of Geochemical Exploration, 42: 25-60.

Lewis, A.J., Palmer, M.R., Sturchio, N.C., and Kemp, A.J., 1997. The rare earth element geochemistry of acid-sulphate and acid-sulphate-chloride geothermal systems from Yellowstone National Park, Wyoming, USA. Geochimica et Cosmochimica Acta, 61: 695-706.

Lewis, A.J., Komminou, A., Yardley, B.W.D., and Palmer, M.R., 1998. Rare earth element speciation in geothermal fluids from Yellowstone National Park, Wyoming, USA. Geochimica et Cosmochimica Acta, 62: 657-663.

Li, G., Peacor, D.R., Essene, E.J., Brosnahan, D.R., and Beane, R.E., 1992. Walthierite and huangite; two new minerals of the alunite group from the Coquimbo region, Chile. American Mineralogist, 77: 1275-1284.

Lindaas, S.E., Chomiak, B.A., Campbell, A.R., and Norman, D.I., 1998. Enargite-hosted fluid inclusion gases from the Lepanto, Philippines, high-sulfidation Cu-Au deposit. Abstracts with Programs - Geological Society of America. 30 (7): 20.

Lottermoser, B.J., 1992. Rare earth elements and hydrothermal ore formation processes. Ore Geology Reviews, 7: 25-41.

Lowenstern, J.B., Mahood, G.A., Rivers, M.L., and Sutton, S.R., 1991. Evidence for extreme partitioning of copper into a magmatic vapor phase. Science, 257: 1405-1409.

Lupton, J.E., 1983. Terrestrial inert gases: istope tracer studies and clues to primordial components in the mantle. Annual Reviews in Earth Science, 11: 371-414.

Maksaev, V., Moscoso, R., Mpodozis, C., and Nasi, C., 1984. Las unidades volcánicas y plutonicas del cenozoico superior en la Alta Cordillera del Norte Chico (29°-31° S): Geología, alteración hidrothermal y mineralisacion. Revista geológica de Chile, 21: 11-51.

Mamyrin, B.A., Anufriev, G.S., Kamenski, I.L., and Tolstikhin, I.N., 1969. Determination of the isotopic composition of atmospheric helium. Geochemistry International, 7: 498-505.

Martin, M, Clavero, J., and Mpodozis, C., 1995. Estudio geologico regional del Franja El Indio, Cordillera de Coquimbo. Servicio National de Geología y Minería, Santiago, Chile. Registered report IR-95-06, 232p.

Martin, M.W., Clavero, J.R., Mpodozis, C., 1999. Late Paleozoic to Early Jurassic tectonic development of the high Andean Principal Cordillera, El Indio Region, Chile (29-30°S). Journal of South American Earth Sciences, 12: 33-49.

Marty, B. 1989. Neon and xenon isotopes in MORB: implications for the earth-atmosphere

evolution. Earth Science Planetary letters, 94: 45-56.

McBride, B.J., and Gordon, S., 1996. Computer Program for Calculation of Complex Chemical Equilibrium Compositions and Applications. II. Users Manual and Program Description. NASA Reference Publication 1311: 177p.

Michard, A., 1989. Rare earth element systematics in hydrothermal fluids. Geochimica et Cosmochimica Acta, 53: 745-750.

Morrison, P., and Pine, J., 1955. Radiogenic origin of the helium isotopes in rock. New York Academy Science Annals, 62: 71-92.

Mountain, B.W., 1999. Trace metals in geothermal fluids: I. Metal behavior at the deep source. *In* Simmons, S.F., Morgan, O.E., and Dunstall, M, eds., New Zealand Geothermal Workshop: 21^{sr}, Aukland, November, 1999. Proceedings: 61-66.

Muntean, J.L., and Einaudi, M.T., 2000. Porphyry gold deposits of the Refugio District, Maricunga Belt, Northern Chile. Economic Geology, 95: 1445-1472.

Ohmoto, H., and Lasaga, A.C., 1982. Kinetics of reactions between aqueous sulfates and sulfdies in hydrothermal systems. Geochimica et Cosmochimica Acta, 46: 1727-1746.

Petersen, E.U., and Thompson, A.J.B., 1992. Analysis of alunite and other thermally sensitive minerals. Microprobe Analyst (Internal report for the Dept. of Geology and Geophysics, University of Utah), April: 2-6.

Pickthorn, W.J., and O'Neil, J.R., 1985. ^{18}O relations in alunite mineral: potential single mineral thermometer. Geological Society of America Abstracts with Programs, 17(7): 686.

Poreda, R., Radicati di Brozolo, F., 1984. Neon in mid-Atlantic ridge basalts. Earth Science Planetary Letters, 69: 277-289.

Pouchou, J.L. & Pichoir, F., 1985. PAP $\phi(\rho Z)$ procedure for improved quantitative microanalysis. Microbeam Analysis, 1985: 104-106.

Ramos, V. A., Mahlburg Kay, S, Page, R. N. and Munizaga, F., 1989. La ignimbrita Vacas Heladas y el cese del volcanismo en el Valle del Cura, Provincia de San Juan. Revista Asociación Geológica Argentina, 44: 336-352.

Reed, M.H., 1992. Origin of diverse hydrothermal fluids by reaction of magmatic volatiles with wallrock. Japan Geological Survey Report, 279: 135-140.

Reed, M.J., 1995. Distribution of rare earth elements between aqueous fluids and granitic melt. Ph.D. thesis, University of Maryland at College Park.

Roedder, E., 1984. Fluid inclusions. Reviews in Mineralogy, 12, 644 p.

Rye, R.O., 1993. The evolution of magmatic fluids in the epithermal environment: The stable

isotope perspective. Economic Geology, 88: 733-753.

Rye, R.O., Bethke, P.M., and Wasserman, M.D., 1992. The stable isotope geochemistry of acid sulfate alteration. Economic Geology, 87: 225-262.

Sandeman, H.A., Archibald, D.A.; Grant, J.W.; Villneuve, M.E. and Ford, F.D. 1999. Characterisation of the chemical composition and ^{40}Ar-^{39}Ar systematics of intralaboratory standard MAC-83 biotite. Radiogenic Age and Isotopic Studies: Report 12; Geological Survey of Canada, Current Research 1999-F: 13-26.

Savin, S.M., and Epstein, S., 1970. The oxygen and hydrogen isotope geochemistry of clay minerals. Geochimica et Cosmochimica Acta. 34: 24-42.

Schoen, R., White, D., and Hemley, J.J., 1974. Argillization by descending acid at Steamboat Springs, Nevada. Clays and Clay Minerals, 22: 1-22.

Schwab, R.G., Herold, H, Gotz, C. and de Oliveira, N.P., 1990. Compounds of the crandallite type: Synthesis and properties of pure rare earth element phosphates. Neues Jahrbuch fuer Mineralogie, 6: 241-254.

Shepperd, T.J., and Rankin, A.H., 1998. Fluid Inclusin Techniques of Analysis. *In* Richards, J. P., and Larson, P.B., eds., Reviews in Economic Geology, vol. 10: 125-150.

Shinohara, H., 1994. Exsolution of immiscible apor and liquid phases from a crystallizing silicate melt: Implications for chlorine and metal transport. Geochimica et Cosmochimica Acta, 58: 5215-5221.

Siddeley, G, and Areneda, R., 1985. Gold-silver occurences of the El Indio belt, Chile. Geology of the Andes and its relation to mineral and energy resources. Symposium, Chile, 18 p.

Sillitoe, R.H., 1983. Enargite-bearing massive sulfide deposits high in porphyry copper systems. Economic Geology, 78: 348-352.

Sillitoe, R.H., 1993. Epithermal models: Genetic types, geometric controls, and shallow features. *In* R.V. Kirkham, W.D. Sinclair, R.I. Thorpe and J.M. Duke, eds., Mineral Deposit Modelling; Geological Association of Canada, Special paper 40: 403-417.

Sillitoe, R.H., 1999. Styles of high sulfidation gold, silver and copper mineralization in the porphyry and epithermal environments. PacRim '99. Bali, Indonesia, 10-13 October, Proceedings: 29-44.

Steiger, R. H. and Jäger, E., 1977. Subcommission on geochronology: convention on the use of decay constants in geo- and cosmochronology. Earth and Planetary Science Letters, 36: 359-362.

Steven, T.A., and Ratte, J.C., 1960. Geology of ore deposits of the Summitville district, San

Juan Mountains, Colorado. US Geological Survey Professional Paper 343: 70 p.

Stoffregen, R.E. and Alpers, C.N., 1987. Woodhouseite and svanbergite in hydrothermal ore deposits: Products of apatite destruction during advanced argillic alteration. Canadian Mineralogist, 25: 201-211.

Stoffregen, R.E., Rye, R.O., and Wasserman, M.D., 1994. Experimental studies of alunite: I. ^{18}O-^{16}O and D-H fractionation factors between alunite and water at 250-450°C. Geochimica et Cosmochimica Acta, 58: 903-916.

Stoffregen, R.E., and Cygan, G., 1990. An experimental study of Na-K exchange between alunite and aqueous sulfate solutions. American Mineralogist. 75: 209-220.

Taran, Y.A., Bernard, A., Gavilanes, J-C., and Africano, F., 2000. Native gold in mineral precipitates from high-temperature volcanic gases of Colima volcano, Mexico. Applied Geochemistry, 15: 337-346.

Taylor, B.E., 1988. Degassing of rhyolitic magmas: Hydrogen isotope evidence and implications for magmatic-hydrothermal ore deposits. Canadian Institute of Mining and Mineralogy Special Volume, 39: 33-49.

Taylor, H.P., Jr., 1979. Oxygen and hydrogen isotope relationships in hydrothermal mineral deposits. *In* Barnes, H.L. ed., Geochemistry of Hydrothermal Ore Deposits. Wiley Interscience, New York: 236-277.

Thompson, A.J.B, 1992. Alunite compositions and textures: Relationships to precious metal mineralization. Mineral Deposit Research Unit Short Course #8: New Developments in Lithogeochemistry. University of B.C., Canada.

Thompson, A.J.B., Hauff, P.L., and Robitaille, A.J. 1999. Alteration mapping in exploration: Application of short-wave infrared (SWIR) spectroscopy. Society of Economic Geologists Newsletter, Oct 1999: 39.

Truesdell, A.H., Nathenson, M., and Rye, R.O., 1977. The effects of boiling and dilution on the isotopic compositions of Yellowstone thermal waters. Journal of Geophysical Research, 82: 3694-3704.

Ulrich, T., Gunther, D. and Heinrich, C.A., 1999. Gold concentrations of magmatic brines and the metal budget of porphyry copper deposits. Nature, 399: 676-679.

Venneman, T.W., Muntean, J.L., Kesler, S.E., O'Neil, J.R., Valley, J.W., and Russell, N., 1993. Stable isotope evidence for magmatic fluids in the Pueblo Viejo epithermal acid sulfate Au-Ag deposit, Dominican Republic. Economic Geology, 88, 55-71.

Wasserman, M.D., Rye, R.O., Bethke, P.M., and Arribas, Jr., A., 1992. Methods for separation

and total stable isotope analysis of alunite. Open file report 92-9, US Department of the Interior, Geological Survey.

White, N.C., 1991. High sulfidation epithermal gold deposits: Characteristics and a a model for their origin. Geological Survey of Japan Report 277: 9-20.

Williams, T.J., Candela, P.A., and Piccoli, P.M., 1995. The partitioning of copper betweem silicate melts and two-phase aqueous fluids: An experimental investigation at 1 kbar, 800°C and 0.5 kbar, 850°C. Contributions to Mineralogy and Petrology, 121: 388-399.

Wood, S.A., 1990a. The aqueous geochemistry of the rare-earth elements and yttrium 1. Review of available low-temperature data for inorganic complexes and the inorganic REE speciation of natural waters. Chemical Geology, 82: 159-186.

Wood, S.A., 1990b. The aqueous geochemistry of the rare-earth elements and yttrium 2. Theorectical predictions of speciation in hydrothermal solutions to 350°C at saturation water vapor pressure. Chemical Geology, 88: 99-125.

Chapter 4

THE ROLE OF ALUNITE IN EXPLORATION: EVIDENCE FROM HIGH SULFIDATION DEPOSITS IN THE EL INDIO-PASCUA BELT, CHILE

INTRODUCTION

Acid sulfate alteration is a characteristic feature of high sulfidation epithermal gold deposits (Cooke and Simmons, 2000; and references therein). Alteration is defined by alunite ± kaolinite (or dickite, pyrophyllite), quartz, and pyrite (Hemley and Jones, 1964; Meyer and Hemley, 1967) and forms under conditions of low pH and highly oxidized fluid chemistry (Holland, 1965; Henley and McNabb, 1978; Stoffregen, 1987). These conditions can be generated by several mechanisms in both the epithermal environment and in lithocaps overlying porphyry deposits. Four specific environments of acid sulfate alteration were defined by Rye et al. (1992; Fig. 4.1) on the basis of field characteristics, paragenetic associations, geochemical signatures, and stable-isotope systematics; each of which may be present within high sulfidation systems. These include:

- The magmatic-hydrothermal environment, where the disproportionation of magmatic SO_2 in condensed magmatic vapor forms H_2S and H_2SO_4 below *ca.* 350°C. The resulting acidic fluids react with wallrock to form extensive zones of acid (chloride-) sulfate alteration.
- The magmatic steam environment, where alunite is believed to form from the expansion of rapidly ascending SO_2-rich magmatic vapor following sudden depressurization of the hydrothermal system (Rye, 1993).
- The steam-heated environment, where alunite forms from the condensation of vapour derived from an underlying hydrothermal system and the oxidation of H_2S gas above the water table.
- The supergene environment, where the supergene oxidation of sulfides can produce an assemblage of kaolinite ± quartz, alunite, jarosite, with iron oxide and oxyhydroxide minerals.

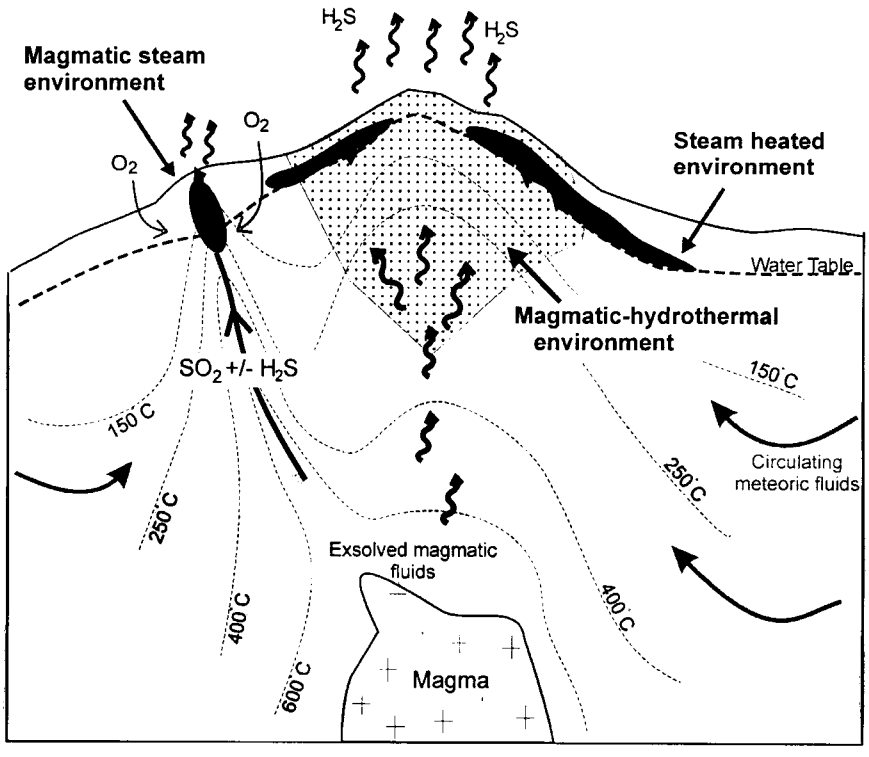

Figure 4.1. Schematic diagram of a high sulfidation epithermal system showing environments magmatic-hydrothermal, magmatic steam, and steam heated alteration. Supergene processes not shown.

Effective exploration for high sulfidation deposits requires an understanding of the origin of acid sulfate alteration, since each assemblage has different genetic and spatial relation to potential mineralization (Bethke, 1984; Thompson, 1992; Sillitoe, 1993). Alunite and associated alteration minerals are now easily and routinely identified in the field by short-wave infrared (SWIR) field spectrometers and hyperspectral techniques (including airborne surveys), but the identification of critical ore-related assemblages is often difficult due to multiple or superimposed alteration events.

To date, a number of techniques have been used to differentiate between the environments of acid sulfate alteration. These include field characteristics (e.g., distribution, mineral assemblages, textures, paragenetic relations), chemical composition, age dating, and stable isotopic signatures of alunite and associated minerals (e.g., Bethke, 1984; Rye et al., 1992; Sillitoe, 1993; Thompson, 1992; Arribas et al., 1995; Jannas et al., 1999; Thompson et al., 1999; Hedenquist et al., 2000). Few studies however include detailed data for more than one type of alteration from a single deposit or district. These observations are critical for

exploration at either a regional- or deposit-scale if complex alteration patterns are apparent.

In this paper, we present results from an extensive study of alteration associated with high sulfidation Au-Cu-Ag mineralization in the El Indio-Pascua Belt. This belt straddles the Chile-Argentina border between latitudes 29°20' and 30° S in the Main Andean Cordillera (Fig. 4.2). The region hosts widespread zones of hydrothermal alteration and several world-class epithermal deposits, including El Indio-Tambo, which has produced over 11 Moz of gold, Pascua-Lama (proven-and-probable resources 17 Moz Au and 560 Moz Ag), and Veladero (15 Moz Au, 230 Moz Ag). Many smaller occurrences such as the Del Carmen and Salitrales prospects are also recognized. The comprehensive nature of this study is possible because:

- The deposits in this region are young (*ca.* 6 to 9 Ma; Bissig, 2001) and typically well preserved, due to favorable tectonic and climatic conditions.
- Several deposits have been previously studied in detail (e.g., El Indio-Tambo, Jannas et al., 1999; Pascua-Lama, Chouinard and Williams-Jones, 1999), and metallogenetic and geochronologic constraints have been determined (Bissig, 2001).
- Access is available via the extensive mining and exploration operations of Barrick Gold Corporation, the principal operator in the region.
- Multiple stages of acid sulfate alteration are recognized in each deposit, including one or several magmatic-hydrothermal, magmatic steam, steam-heated, and/or supergene assemblages.

We present herein a summary of the physical, chemical, stable-isotope, and age characteristics of alunite-group minerals, and their role in differentiating between origins of acid sulfate alteration. Our discussion is focused on high sulfidation systems in the El Indio-Pascua Belt, but applications to exploration in other epithermal districts are addressed.

GEOLOGY OF THE EL INDIO-PASCUA BELT

The El Indio-Pascua Belt (Fig. 4.2) host several high sulfidation deposits and prospects in Paleozoic intrusions and volcanic rocks (e.g., Pascua-Lama, Veladero) and Oligocene to Middle Miocene volcanic and volcaniclastic rocks (e.g., El Indio-Tambo, Sancarron). Mineralization in the belt occurred *ca.* 9 to 6 Ma, between Vacas Heladas and Vallecito age volcanism (Bissig 2001; Jannas et al., 1999). The geology and styles of alteration at the El

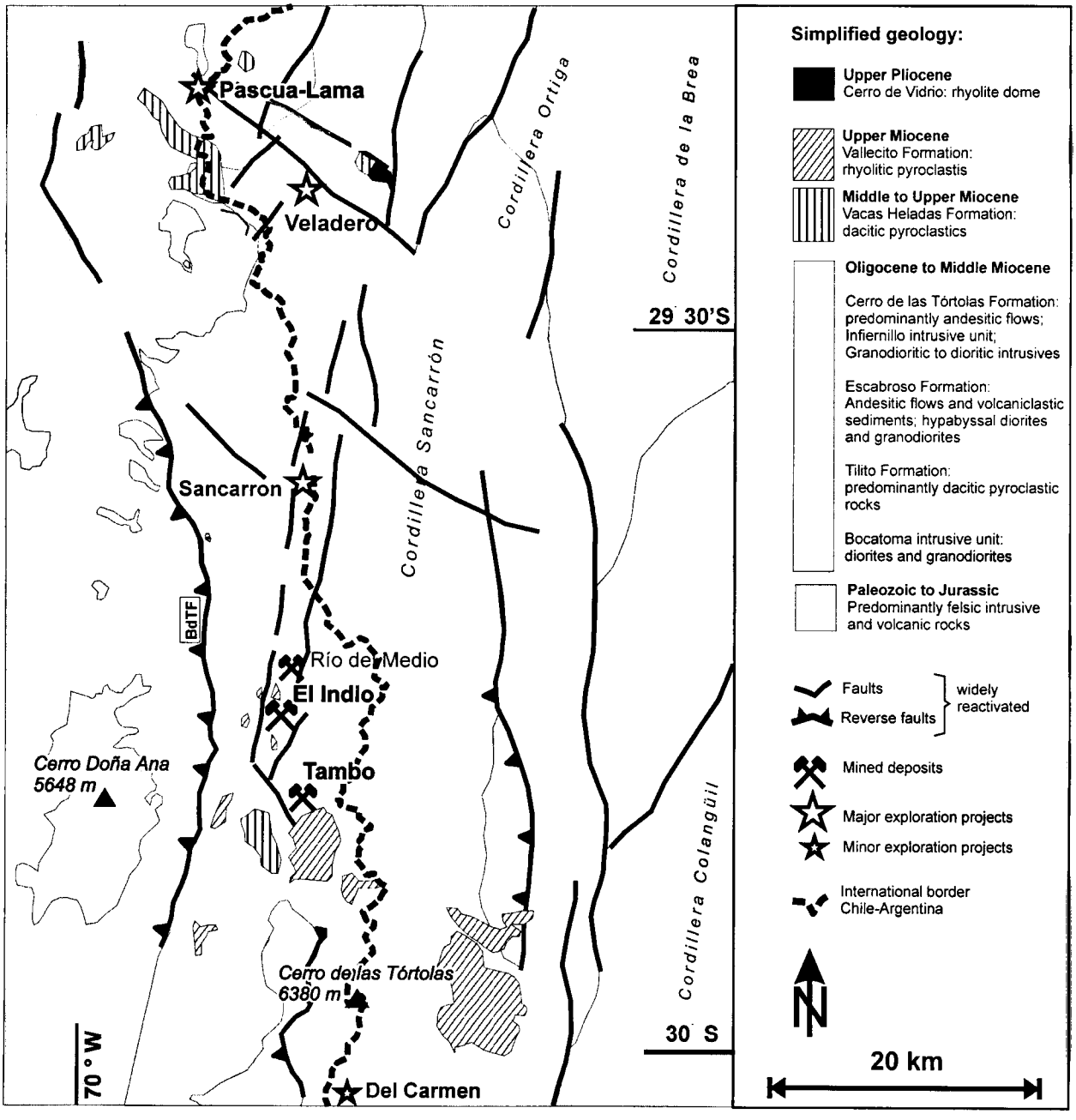

Figure 4.2. Map of the El Indio-Pascua Belt showing locations of epithermal deposits and prospects. Simplified geology is given according to the stratigraphy defined in Bissig (2001). BdTF = Banos del Toro fault. *Adapted from Bissig (2001).*

Indio and Tambo deposits have been described previously (see Chap. 3: Jannas et al., 1999; Jannas et al., 1990; Siddeley and Areneda, 1986). Both deposits are hosted in intensely altered Tertiary rhyodacitic volcanic rocks. El Indio is characterized by sulfide-rich mineralization in complex enargite-pyrite (copper dominant) and later gold-quartz vein systems (Jannas et al., 1999). Silicic, argillic, and sericitic alteration assemblages are dominant. Alunite is rare. It occurs in patchy kaolinite- and sericite-bearing alteration assemblages in the proximity of the Campana, Viento, and Mula Muerta copper veins and as banded alunite-enargite-pyrite veins in the Campana and Brechita-Huantina areas (Jannas et al., 1999). In contrast, mineralization at the Tambo deposit is hosted in sulfide-poor alunite-barite-gold breccias and several high grade alunite-barite veins. The deposit contains at least six stages of acid sulfate alteration, including magmatic-hydrothermal (Stages 1 and 2), magmatic steam (includes Stage 3 and banded alunite veins), steam-heated, and apparent supergene (details see Chap. 3).

The Pascua property is located at the northern end of the El Indio-Pascua Belt, straddling the Chile-Argentina border. Gold, copper, and silver mineralization occurs in several forms (Chouinard and Williams-Jones, 1999). These include abundant alunite-pyrite-enargite breccia matrix fill and banded veins, and extensive silica-pyrite ± Fe-sulfate alteration zones. Several smaller, high grade oxidized veins and breccias occur in the Esperanza and Penelope deposits. Mineralization and alteration is hosted primarily in intrusive rocks of the Carboniferous-Lower Triassic Pastos Blancos group. Several stages of acid sulfate alteration are recognized (Chap. 2). Pre-ore (AS I) and syn-ore (AS II) alteration are both magmatic-hydrothermal in origin. Magmatic steam alunite (AS III) occurs locally near-surface. Steam-heated and supergene assemblages are also recognized.

Del Carmen is a smaller prospect located south of the El Indio mine in the San Juan province of Argentina. Gold (± copper, silver) mineralization occurs as veins, infilling breccia matrices, or disseminations in association with sulfides; principally pyrite and enargite (Noriega and Perez, 1997). Rare native Au is observed. Stratigraphy in the project area consists of a sequence of pyroclastic flows and lapilli tuff flows that correspond to the upper part of the Doña Ana Formation. Andesitic to dacitic tuffs and lavas of the Cerro de Tortalas Formation overlie the Doña Ana rocks and are interbedded with pyroclastic flows and volcanic breccias (Gallardo, 1995). Hydrothermal breccias outcrop as isolated bodies intruding the tuff sequences. Alteration is associated primarily with the Cerro de las Tortalas Formation and assemblages grade laterally from vuggy silica to quartz-alunite to quartz-alunite-kaolinite-illite

to smectite-pyrite (Noriega and Perez, 1997).

The Salitrales prospect is located a few kilometers south-east of El Indio. The area has not been explored extensively, but contains several anomalous Au showings (Paleczeck et al., 1996). The property consists of a small porphyritic dacite stock that intrudes a sequence of Miocene volcanics. Anomalous Au, Ag, As, Sb, Pb, Hg, and Bi concentrations occur in soils related to siliceous (vuggy quartz) and acid sulfate alteration assemblages. Alteration is typically structurally controlled and is concentrated in and around several strongly silicified breccias of probable hydrothermal origin (Paleczeck et al., 1996). Minor pyrite and enargite are found at surface. Alunite is typically overprinted with late jarosite ± scorodite.

METHODS OF ANALYSIS

Methods used for the characterization of alunite and acid sulfate alteration in the El Indio-Pascua Belt are summarized below. A detailed account of sample preparation and analytical techniques is provided in Appendices A, B, and C.

Field Techniques: Detailed alteration mapping and sampling at El Indio-Pascua Belt properties was completed between 1998 and 1999. Access was made possible through the extensive mining and exploration activities of Barrick Gold Corporation. This allowed an examination of both surface and underground exposures, and detailed sampling of drill core, wherever available. Considerable effort was made to study complete vertical and lateral sections across alteration zones.

Petrography: Detailed petrographic studies are required to accurately determine the paragenesis of alteration minerals and/or assemblages. Both transmitted and reflected light techniques were used throughout this study. Scanning electron microscopy was often necessary to identify fine-grained assemblages and intergrowths of alunite and clays that could not be distinguished in thin section.

SWIR Spectroscopy: Alunite and associated minerals are easily detected with field portable SWIR spectrometers (e.g., PIMA, FieldSpec Pro). The spectrometers detect the energy generated by vibrations within molecular bonds, in the 1300 to 2500 nm region of the electromagnetic spectrum (Thompson et al., 1999). SWIR is particularly sensitive to certain molecules and radicals, including OH^-, H_2O, NH_4^+, CO_3^{2-}, and cation-OH^- bonds such as Al-OH, Mg-OH, and Fe-OH. Minerals are distinguished on the basis of distinctive features and wavelength positions, and by the character of the SWIR profile. SWIR spectroscopy is suitable

for many alteration minerals such as phylosilicates, clays, carbonates, and selected sulfates – including alunite (Thompson et al., 1999). In this study, a PIMA instrument was used in the field for regional reconnaissance work and more detailed alteration mapping at Pascua (details see Chap. 2). A database of over 5000 SWIR spectra was collected from samples across the El Indio-Pascua Belt. This study complements initial SWIR analyses compiled by Bennet (1995) for the Tambo region.

Geochemistry: Alunite belongs to a large group of minerals, the alunite supergroup, that consists of over 40 mineral species. Minerals have the general formula $DG_3(TO_4)_2(OH,H_2O)_6$ and can be sub-divided into 3 groups based on the T-site occupancy (Jambor, 1999). The alunite group is characterized by $(SO_4)^{2-}$ dominant minerals; the beudantite group contains both SO_4 and either PO_4 or AsO_4; and TO_4 in the crandallite group represents one or both of PO_4 and AsO_4. End-member compositions are rarely attained in natural alunite occurrences and extensive solid solution is typical for one or more of the D, G, and T sites (Stoffregen et al., 2000). The most common and naturally abundant minerals belong to the alunite-natroalunite and jarosite-natrojarosite solid solution series, but many other minerals are known to occur in high sulfidation epithermal environments (Table 4.1).

In this study, geochemical characteristics of alunite-group minerals (hereafter referred to as alunite, except where specified) were determined by analysis of individual grains and sample composites. Grain mounts and polished sections were analysed by scanning electron microscope with energy-dispersion spectroscopy (SEM-EDS) and electron probe microanalysis (EPMA). EPMA analytical parameters were chosen in order to minimize beam damage caused by the volatilization of alkali elements (Petersen and Thompson, 1992). This requires a large beam size (15-20 μm), that results in poor representation of finer-grained samples (i.e. particularly supergene and steam-heated alunite) and thin compositional growth bands.

Alunite separates were also analyzed by inductively-coupled plasma mass spectrometry (ICP-MS) for trace metal and rare earth element (REE) contents. Approximately 1 gram of material from each sample was separated for analysis and treated using a 1:1 HF/H_2O solution to remove silicate contaminants, if present (Wasserman et al., 1992). The purity of separates was verified by powder X-ray diffraction (XRD) but trace amounts of quartz, clays, or other impurities may be present. Samples were digested with perchloric, nitric and hydrofluoric acids for trace-metal analysis. REE were determined by lithium metaborate fusion and ICP-MS techniques.

Stable-isotope Systematics: Alunite-group minerals contain four stable-isotope sites; D

Table 4.1. Minerals of the alunite super-group reported in high sulfidation environments (currrent usage: Jambor, 1999).

	Al > Fe		Fe > Al	
Alunite-jarosite group	alunite	$KAl_3(SO_4)_2(OH)_6$	jarosite	$KFe_3(SO_4)_2(OH)_6$
	natroalunite	$NaAl_3(SO_4)_2(OH)_6$	natrojarosite	$NaFe_3(SO_4)_2(OH)_6$
	minamiite	$(Na,K,Ca)_2Al_6(SO_4)_4(OH)_{12}$	hydronium jarosite	$(H_3O)Fe_3(SO_4)_2(OH)_6$
	huangite	$CaAl_6(SO_4)_4(OH)_{12}$	argentojarosite	$AgFe_3(SO_4)_2(OH)_6$
	walthierite	$BaAl_6(SO_4)_4(OH)_{12}$	beaverite	$Pb(Fe,Cu)_3Fe_3(SO_4)_2(OH,H_2O)_6$
	ammonioalunite	$NH_4Al_3(SO_4)_2(OH)_6$	ammoniojarosite	$(NH_4)Fe_3(SO_4)_2(OH)_6$
	schlossmacherite	$(H_3O,Ca)Al_3(SO_4)_2(OH)_6$	plumbojarosite	$PbFe_6(SO_4)_4(OH)_{12}$
Beudantite group	svanbergite	$SrAl_3[(P,S)O_4)]_2(OH,H_2O)_6$	beaudantite	$PbFe_3[(As,S)O_4)]_2(OH,H_2O)_6$
	woodhouseite	$CaAl_3[(P,S)O_4)]_2(OH,H_2O)_6$		
	hinsdalite	$PbAl_3[(P,S)O_4)]_2(OH,H_2O)_6$		
Crandallite group	crandallite	$CaAl_3[(PO_3(O_{1/2}(OH)_{1/2}]_2(OH)_6$		
	goyazite	$SrAl_3[(PO_3(O_{1/2}(OH)_{1/2}]_2(OH)_6$		
	gorceixite	$BaAl_3(PO_4)(PO_3{\bullet}OH)(OH)_6$		
	plumbogummite	$PbAl_3(PO_4)_2(OH,H_2O)_6$		
	florencite-(Ce)	$CeAl_3(PO_4)_2(OH)_6$		
	florencite-(La)	$LaAl_3(PO_4)_2(OH)_6$		

$_{(OH)}$, $^{34}S_{(SO4)}$, $^{18}O_{OH}$, and $^{18}O_{SO4}$. Isotopic variations are related to the source and type of fluids, rates of processes, and the physical-chemical environment of deposition (Rye et al., 1992). Isotopic studies are particularly useful in conjunction with analyses on coexisting minerals such as clays (kaolinite, dickite, pyrophyllite), muscovite/sericite, and sulfides. The stable-isotope systematics of the four environments of acid sulfate alteration are described in detail in Rye et al. (1992) and Rye (1993). All data for this study (Appendix B) was collected at the U.S. Geological Survey Isotope Laboratory in Denver.

Geochronology: Alunite is useful for age determinations by K-Ar and $^{40}Ar/^{39}Ar$ methods due to the large concentration of potassium in end-member alunite (and jarosite). Alunite age data have been applied to supergene and weathering events (see Vasconcelos, 1999 for details) and paleoclimate studies (e.g., Vasconcelos et al., 1994; Arehart and O'Neil, 1993; Sillitoe et al., 1991; Bird et al., 1990). Hypogene alunite can also be used to date hydrothermal events and associated precious- or base-metal mineralization (e.g., Bissig, 2001; Arribas et al., 1995; Perello, 1994; Sillitoe et al., 1991; Alpers and Brimhall, 1988; etc.), provided alteration is coeval with mineralization.

Data for this study were collected at the Queen's University ^{40}Ar-^{39}Ar laboratory, equipped with a Mass Analyzer Products MAP 216 mass spectrometer. About 10 mg of each sample was irradiated for 7.5 hours at McMaster nuclear reactor in Hamilton, Canada using biotite standard Mac-83 as a radiation flux monitor (24.36 ± 0.17 Ma; Sandeman et al., 1999). Samples were step-heated using a defocused LEXEL 3500 Ar laser-beam. Ages are calculated using the decay-constants suggested by Steiger and Jäger (1977) and all errors are given at 2σ.

Fluid inclusions: Fluid inclusions data for alunite are rare. These studies are difficult because inclusions are typically small, necking and decrepitation are common (this study; Jannas et al., 1999; Beane, 1988), and it is often difficult to determine the paragenesis of inclusion populations. Associated phases such as quartz, barite, and/or sulfides may be suitable for fluid inclusion analysis, provided they are coeval with alteration. In this study, only relatively coarse-grained alunite (e.g., magmatic-hydrothermal and magmatic steam) contained sufficiently large inclusions to study petrographically. Enargite samples from both Pascua and Tambo were unsuitable for analysis (A. Chouinard, pers comm.).

Analyses of gas species contained in fluid inclusions were determined for several coarse-grained alunite samples from the Tambo area. Thermally released gas from *ca.* 1 gram alunite separates was analyzed by Pfeiffer quadrupole mass spectrometer (Prisma) at the U.S.G. S. facilities in Denver. Analytical details provided in Chapter 3.

ENVIRONMENTS OF ACID SULFATE ALTERATION

Characteristics of the four environments of acid sulfate alteration in the El Indio-Pascua Belt are summarized in Table 4.2. The nature of each of these environments is described in the following section, with particular reference to their relation to potential high sulfidation ore. Detailed physical, chemical, and isotopic data specifically for alunite-group minerals within each assemblage are also given (Table 4.3).

1. Magmatic-Hydrothermal Environment

Magmatic-hydrothermal alteration is most closely related to potential high sulfidation (hypogene) mineralization (e.g., Sillitoe, 1999; Hedenquist et al., 2000). Alteration results from high temperature acidic fluids produced from the condensation of magmatic volatiles containing SO_2, H_2S, HCl^o, and HF. The dissociation of dominant acidic species, HCl and H_2SO_4, below about 300 to 350°C (Hemley et al., 1969; Knight, 1977) creates acidic fluids with a pH of about 1. These fluids are sufficiently acid to leach most components from the host rock, often leaving a vuggy quartz residue. The progressive neutralization of these fluids by reaction with wallrock forms successive alteration envelopes of alunite ± dickite/kaolinite, to kaolinite/dickite ± pyrophyllite, to illite-smectite, and smectite-chlorite outward from the main fluid conduit. Strong structural or lithological controls can influence the shape and distribution of alteration as fluids flow down the hydraulic gradient, along the most permeable channel. The permeability provided by early stage residual quartz commonly controls subsequent fluid flow and precious-metal deposition (e.g., Summitville; Stoffregen, 1987). In some deposits however, the silicic zone is absent and gold ore is hosted in acid sulfate (e.g., la Mejicana, Losada-Calderon and McPhail, 1996) or advanced argillic assemblages (e.g., Pueblo Viejo, Kesler et al., 1981).

Characteristics of magmatic-hydrothermal alteration in the El Indio-Pascua Belt are extremely variable. Alteration occurs as widespread acid sulfate and silicic assemblages that grade outwards to argillic and propylitic alteration on a broad scale in both the El Indio-Tambo and Pascua-Lama districts. This style of alteration ('wallrock' alteration) typically pre-dates precious metal mineralization. Acid sulfate alteration is also directly associated with precious-metal mineralization in the Tambo, Pascua, and Del Carmen areas. Alteration of this type ('gangue' alunite) is strongly structurally controlled and occurs as disseminations and open-space filling in sulfate-rich (e.g., Tambo) and sulfide-rich (e.g., Pascua, Del Carmen) breccias

Table 4.2. Characteristics of the 4 environments of acid sulfate alteration in the El Indio-Pascua Belt.

	Magmatic-Hydrothermal		**Magmatic Steam**	**Steam Heated**	**Supergene**
	Wallrock	Gangue			
Distribution	Widespread, grades outwards from silicic assemblages into argillic and propylitic alteration	Structural controlled: hydrothermal breccias, veins	Banded veins ± breccia matrices, open space fill	Topographically controlled blanket-style zones; locally extends downwards along fractures	Thin veinlets and disseminations, fracture coatings. Typically topographically controlled but occurs at all depths investigated by mining operations.
Mineral assemblage	Alun, qtz ± kao, dick, pyl, dsp, zuny	Alun ± bar, py, en, S^{o}, qtz (cov, Te-min, dsp, pyl)	Alun ± hem (qtz, jar)	Sil (opal, tryd, crist) ± kao, S^{o} (alun)	Jar, Fe-oxides ± alun, scorodite, Fe-sulfates
Relationship to ore (spatial)	Envelopes ore	Hosts ore or ore-bearing minerals	Usually unrelated: locally hosts ore (Stage 3, Tambo deposit)	Above ore	Rarely cross-cuts sulfide ore. Locally hosts remobilized Au or late Ag-ore (Pascua).
Relationship to ore (age)	Pre-ore (up to 3 Ma or < 1 Ma before mineralization)	Syn-ore (typically 7-9 Ma)	Usually post-ore. Syn-ore at Tambo (Stage 3)	Syn-ore (or syn- magmatic-hydrothermal alteration)	Post- sulfide ore. Contemporaneous with remobilized or late Au-Ag ore. (< 8 Ma)

Table 4.3. Physical, geochemical, and isotopic characteristics of alunite in the El Indio-Pascua Belt.

	Magmatic-Hydrothermal		Magmatic Steam	Steam Heated	Supergene
	Wallrock Alunite	Gangue Alunite			
Occurrence and texture	Disseminated crystals and aggregates replacing phenocrysts, tuff fragments, in vugs. Irregular stringers.	Banded veins, coarse fracture fill, breccia matrix cement.	Banded, mono-mineralic veins. Rarely earthy or fine-grained masses.	Powdery, friable masses Infilling vugs and replacing feldspars phenocrysts.. Irregular veinlets.	Irregular veinlets and disseminations. Fine-grained to porcellaneous to powdery masses.
Crystal habit	Bladed, tabular. Rarely acicular.	Tabular, bladed.	Tabular. Rarely bladed or anhedral.	Anhedral to pseudo-cubic. Rarely tabular.	Pseudo-cubic. Locally anhedral.
Grain size	Med- to coarse-grained. Typically 20-250 μm.	Med- to coarse-grained. Typically 50-500 μm.	Med- to coarse-grained (50-500 μm). Less commonly <30 μm)	Fine- to med-grained. Typically 5-50μm.	Fine-grained. < 10 μm.
Geochemical signature	Variable. Common Na, P, Ca, Sr, Ba, Pb substitution.	Variable. Usually elevated Ba (± Ca) in comparison to wallrock alteration.	Nearly stoichiometric alunite. Locally elevated P, Sr.	Nearly pure alunite. Locally elevated Sr, Sb, Fe, P.	Variable. Nearly pure alun to alun-jar solid solution. Local APS grains or substitution with Ca, Sr, Ba, P.
REE fractionation (vs. host rocks)	MREE depletion. 'U' shaped diagram.	Strong HREE fractionation.	Extreme HREE fractionation.	Similar to host rock, Local MREE depletion and 'U' shaped pattern.	Variable. Local MREE enrichment.
Zoning	APS or Na-rich cores. Local oscillatory or irregular zoning.	Common. Oscillatory or irregular Na, Ba and/or APS substitution.	PO_4 ± Sr oscillatory bands.	None.	Usually none. Rarely K-Na oscillatory zoning. Local alun-jar compositional zones.
Stable isotope characteristics	High $\delta^{34}S$ (typically >15 ‰)[1]. $\Delta^{34}S_{alun\text{-}py}$ give reasonable temperature estimates, usually 200-350°C. Dominant magmatic fluid contribution (based on $\delta^{18}O_{H2O}$ and δD_{H2O}).		Near zero $\delta^{34}S$ (average 1-3‰). Dominant magmatic fluid contribution (based on $\delta^{18}O_{H2O}$ and δD_{H2O})[2].	$\delta^{34}S_{alun}$ slightly greater than $\delta^{34}S_{py}$. $\Delta^{18}O_{SO4\text{-}OH}$ temperatures = 90-150°C. High δD_{H2O} values.	$\delta^{34}S_{alun} \approx \delta^{34}S_{py}$[3] Disequilibrium $\Delta^{18}O_{SO4\text{-}OH}$. δD_{H2O} close to paleo-meteoric values.
Fluid inclusions	Variable L/V ratios. Rare daughter minerals. Necking is common. $H_2S > SO_2$.		Small (<5μm). V-rich. $SO_2 >> H_2S$.	-	-

[1] Magmatic-hydrothermal alunite from Brechita-Huantina vein (El Indio deposit) is an exception (see discussion in text).
[2] With exception for Stage 3 alunite, Tambo deposit which indicates limited mixing between magmatic and meteoric fluids.
[3] Data based on supergene jarosite, Pascua deposit. Discussion of late stage alunite provided in the text.

and veins. Paragenetic and textural observations indicate that alunite is coeval with mineralization in these deposits. This close temporal and spatial relationship between alunite and hypogene ore is rare. Similar observations are documented only at la Mejicana deposit, Argentina (Losada-Calderon and McPhail, 1996) and, to a much lesser extent, at Lepanto in the Philippines (Hedenquist et al., 1998). Differences between gangue and wallrock alteration will be highlighted in the following discussion, to emphasize ore-proximal characteristics.

Physical characteristics

Mineral associations: Wallrock alteration occurs as aggregates replacing feldspar phenocrysts, disseminated in the wallrock matrix, infilling vugs left from the leaching of fragments or feldspar phenocrysts, and as irregular alunite veinlets and stringers. Original lithic textures are commonly but not always preserved. Alunite is typically intergrown with quartz, pyrite ± kaolinite ± dickite ± pyrophyllite and common accessory minerals; diaspore, zunyite, APS (Fig. 4.3a). Alteration can be vertically and horizontally zoned with quartz-alunite-kaolinite near surface and at external margins, grading to pyrophyllite-zunyite and/or diaspore at depth. Vertical zonation is particularly apparent at Pascua, where alunite-pyrophyllite (± zunyite, diaspore) assemblages occur at depths below about 4550 metres above sea level (m.a.s.l.; all elevations reported hereafter are a.s.l.). Alunite-dickite is most common between 4550-4750 m, and kaolinite-alunite alteration is dominant above this zone.

Gangue alunite occurs in association with barite, sulfides (pyrite, enargite-luzonite, covellite, tetrahedrite-tennantite, chalcopyrite) ± quartz, native sulfur (Fig. 4.3b). At Tambo, alunite overgrows barite and cements breccia fragments or occurs in coarse-grained veins intergrown with barite and lesser quartz. At Pascua, alunite occurs in the matrix of several hydrothermal breccias, intergrown with precious metal-bearing sulfides. Banded veins in surrounding stockwork zones contain coarse-grained alunite, pyrite, and enargite in successive bands parallel to the vein wall. Accessory diaspore and pyrophyllite occur locally.

Crystal size and habit: Magmatic-hydrothermal alunite is typically medium to coarse-grained (*ca.* 20-250 μm), but grain size can range between 5 μm to 2 cm. Degree of crystallinity and crystal morphology are variable. Bladed and tabular habits are common. Very thin, elongate to acicular grains are found locally in open spaces of vugs and breccia matrices. Pseudo-cubic forms are rare. Alunite colour ranges from white, pink, yellow, cream, to grey, and single crystals are locally visibly zoned (Fig. 4.4). Colour is often related to inclusions of

sulfides, jarosite, or hematite contained in alunite. No consistent relation between alunite composition and colour has been determined.

Figure 4.3.
(A) *on left.* Typical disseminated magmatic-hydrothermal acid sulfate alteration with alunite, pyrophyllite, and pyrite. Small APS grains are found in cores to some alunite grains. (DDH - LM03, 300.1m; Pascua-Lama).
(B) *on right.* Banded alunite (white-cream)-pyrite-enargite (dark) vein from Pascua deposit (Maria tunnel).

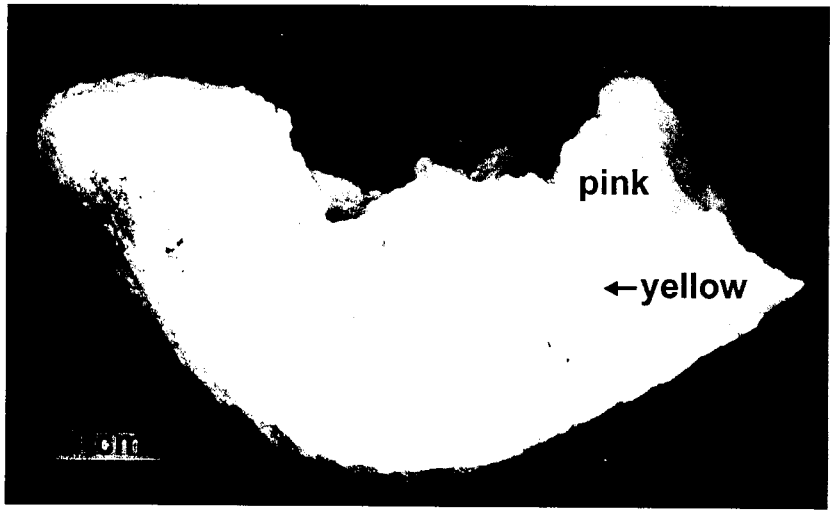

Figure 4.4. Coarse-grained magmatic-hydrothermal alunite from Del Carmen. Individual crystals are visibly zoned.

Geochemical characteristics

Compositional variability is common in magmatic-hydrothermal alunite from the El Indio-Pascua Belt (Table 4.4). Most minerals belong to the alunite-natroalunite solid-solution series but walthierite, minamiite, huangite, beudantite-group (e.g., woodhouseite, svanbergite) and crandallite-group (e.g., florencite) compositions occur locally. Data are consistent with other studies that indicate elevated PO_4 with variable Na, Ca, Sr, Ba, Pb, and/or REE in alunite of magmatic-hydrothermal origin (e.g., Aoki, 1991; Aoki et al, 1993; Thompson, 1992). Results from this study are also consistent with experimental (Stoffregen and Cygan, 1990) and empirical evidence (as summarized in Stoffregen et al., 2000) that indicate greater Na substitution is favored at higher depositional temperatures (Fig. 4.5). Elevated Ba and, to a lesser extent Ca, are also characteristic of magmatic-hydrothermal alunite at several localities (Fig. 4.6).

Zoning: Compositional variations in alunite occur as intracrystalline growth bands or irregular zones, rather than as discrete grains of homogeneous composition. Disseminated alunite are commonly cored with phosphate ± Ca, Sr, REE-rich compositions surrounded by alunite-natroalunite solid-solution (this study; Aoki, 1991). At Salitrales, these cores are typically Na-rich and are rimmed with PO_4 ± Ca ± Sr and finally K-rich alunite. Oscillatory zoning between alunite-natroalunite and beudantite or crandallite compositions is also common, both in wallrock and gangue alunite. This zoning is particularly evident in Stage 2 alunite at Tambo, where alunite (or alunite-natroalunite) cores are overgrown by successive bands of walthierite and K-dominant alunite (Fig. 4.7a). Other well developed zoning is noted between huangite-alunite compositions (see Fig. 3.4g). PO_4 enrichment is often coupled with Sr or Ca substitution (Fig. 4.8), likely by the reaction $SO_4^{2-} + D^{+} \leftrightarrow PO_4^{3-} + D^{2+}$, where D represents the cation site in 12-fold coordination (Stoffregen et al., 2000). Irregular geochemical zoning is also observed at several El Indio-Pascua belt localities, particularly between alunite and natroalunite compositions (Fig 4.7b). Similar features are reported in the Baguio district, Philippines (Aoki et al., 1993) where they are interpreted to represent post-depositional Na depletion.

Compositional zoning is rarely evident in thin section, due to similarities in optical properties of the alunite-group minerals (Stoffregen et al., 2000). Zoning that is visible petrographically rarely corresponds to significant compositional differences and may represent inclusions or impurities concentrated along growth surfaces. Backscatter imaging is most

Table 4.4. Summary of EPMA data for El Indio-Pascua Belt alunite. Data is given as atoms per formula unit and classified according to alteration type. Total number of analyses for each group is indicated by *n*. Data below detection limit (0.2 a.p.f.u. for Na, 0.1 for all other elements) not shown.

	Magmatic-Hydrothermal *n = 976*				Magmatic Steam *n = 138*				Steam-Heated *n = 47*				Late Stage *n= 43*			
Element	Mean	2σ	Max	Min	Mean	2σ	Max	Min	Mean	2σ	Max	Min	Mean	2σ	Max	Min
K	0.83	0.42	1.05	0.01	0.90	0.26	1.05	0.26	0.95	0.15	1.04	0.69	0.94	0.17	1.03	0.64
Na	0.17	0.28	0.90	-	0.10	0.21	0.62	-	0.07	0.15	0.33	-	0.09	0.16	0.32	0.01
Ca	0.01	0.12	0.83	-	-	-	0.02	-	-	-	0.03	-	-	-	0.05	-
Ba	0.02	0.12	0.51	-	0.01	0.02	0.06	-	-	-	0.01	-	-	-	0.02	-
Sr	-	-	0.11	-	-	-	0.02	-	-	-	0.02	-	-	-	0.06	-
P	0.02	0.18	1.35	-	0.01	0.03	0.08	-	0.01	0.02	0.03	-	0.01	0.04	0.13	-
S	1.98	0.18	2.00	0.65	1.99	0.03	2.00	1.92	1.99	0.02	2.00	1.97	1.99	0.04	2.00	1.87
Fe	0.01	0.14	2.13	-	-	-	0.17	-	0.01	0.02	0.04	0.00	0.34	1.30	2.03	-
Al	3.12	0.18	3.23	1.14	3.15	0.12	3.19	3.01	3.14	0.10	3.26	3.02	2.80	1.34	3.25	1.08

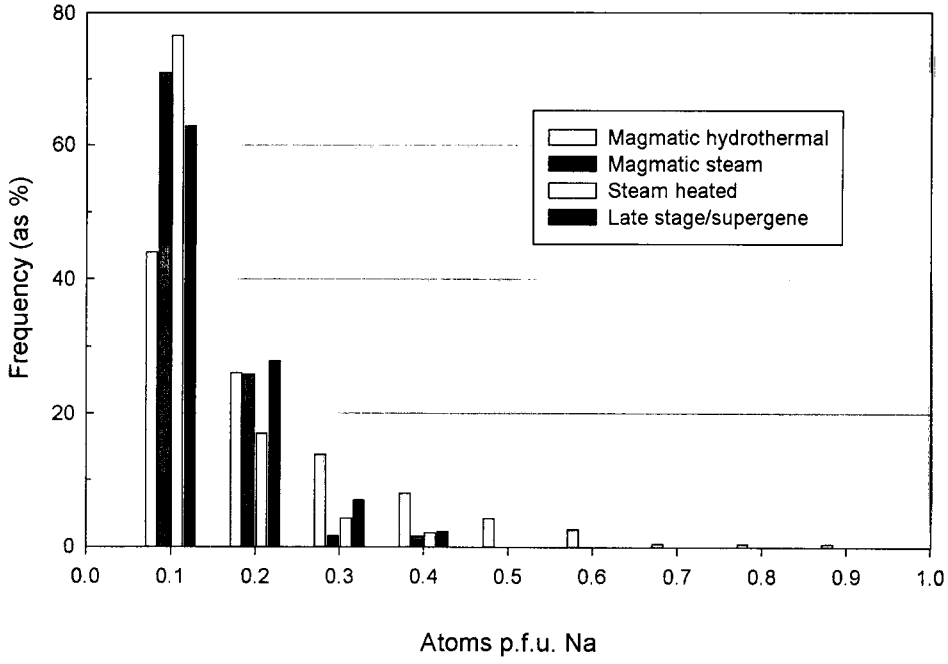

Figure 4.5. Histogram showing the range of Na substitution in alunite from 4 environments of acid sulfate alteration. Based on EPMA data from El Indio-Pascua Belt properties, including Pascua-Lama, El Indio, Tambo, Del Carmen, and Salitrales. Details of analytical procedures given in Appendix A. Total number analyses (*n*): magmatic-hydrothermal $n = 976$; magmatic steam $n = 138$; steam heated $n = 47$; late stage and supergene $n = 43$.

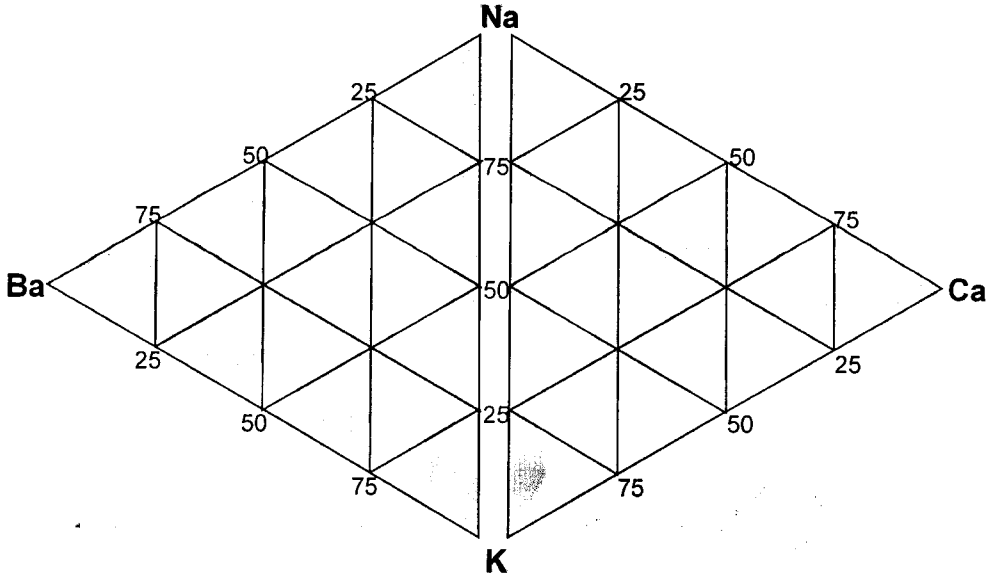

Figure 4.6. Ternary diagrams showing range of compositions (K-Na-Ba and K-Na-Ca) for all El Indio-Pascua Belt magmatic-hydrothermal alunite. Based on EPMA results.

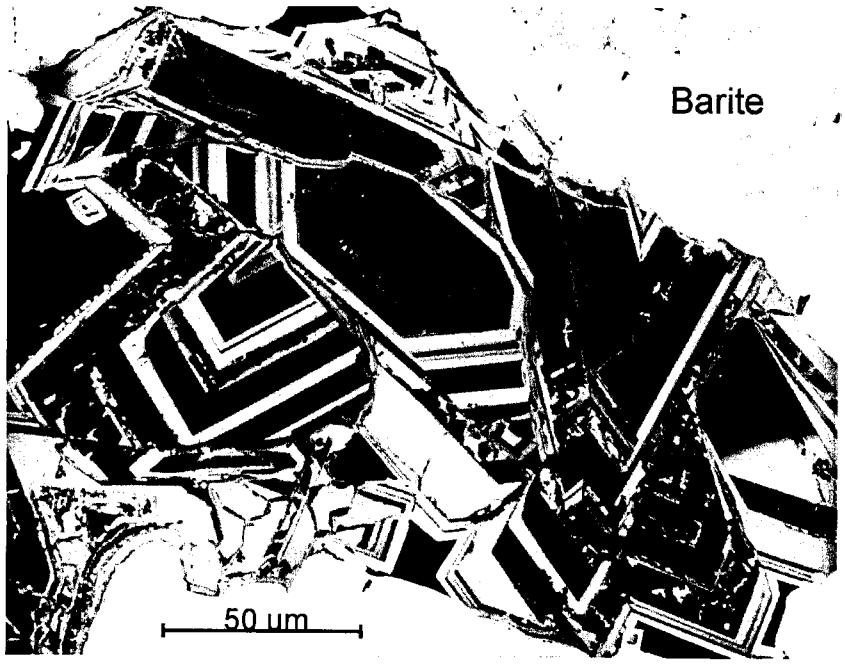

Figure 4.7a. Oscillatory zoning between alunite (dark) and walthierite (light) compositions (Canto Sur area, Tambo).

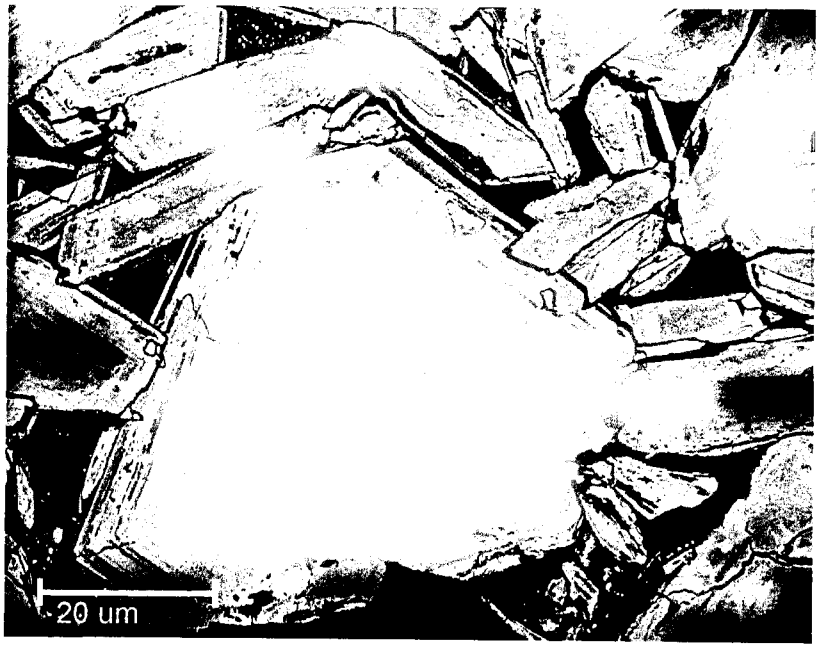

Figure 4.7b. Irregular zoning between K-rich (light) and Na-rich (dark) compositions in alunite (Campana B vein, El Indio).

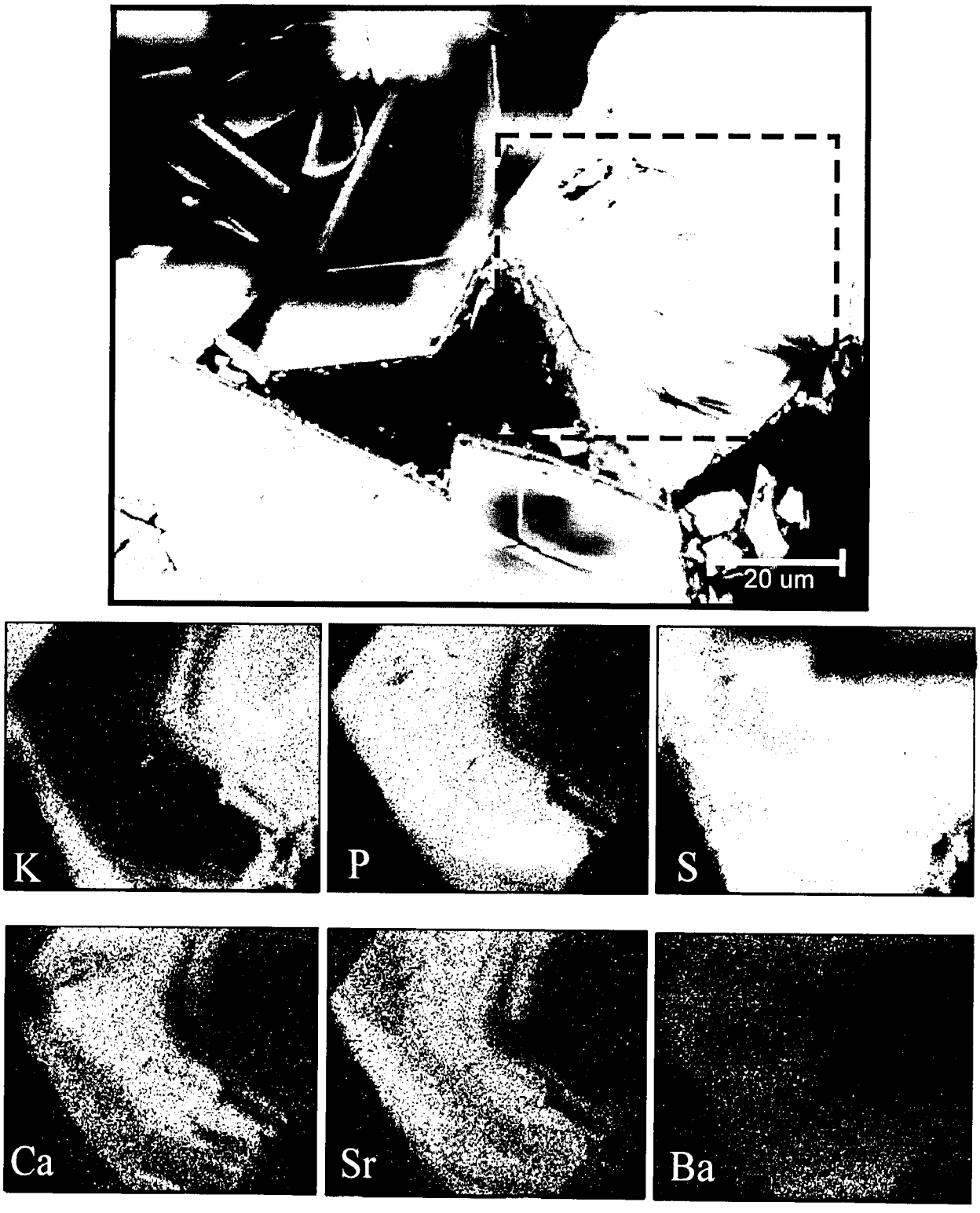

Figure 4.8. SEM photomicrograph (top) showing compositional zoning in magmatic-hydrothermal alunite (Tambo, Stage 2. Wendy deposit. DDH-92a, 290m). Qualitative EDS element maps (bottom) show distribution of K, S, P, Ca, Sr, and Ba. Lightest coloured zones correlate with highest concentration of each element.

effective for identifying (qualitatively) geochemical variations in alunite. In some cases, these variations can also be detected by SWIR analyses (Fig. 4.9) or by X-ray diffraction (XRD), if phases are present in sufficient quantity.

In general, compositional zoning is best developed in alunite that occurs in small vugs or open spaces, either within wallrock or large barite and sulfide crystals. Alunite sampled from larger veins and breccias is typically more homogeneous. These observations suggest that geochemical zonation is not strongly affected by large-scale variations in external factors such as pressure, temperature, or composition of the source fluid, as suggested for strong growth zoning in hydrothermal garnets (e.g., Jamtveit, 1999; Crowe et al., 2001). Instead, variations in alunite-group mineral chemistry may be attributed to feedback mechanisms associated with supersaturation and growth kinetics, in a method analogous to the porous media experiments of Putnis et al. (1992) and Prieto et al. (1997).

REE signature: REE data for magmatic-hydrothermal alunite are summarized in Fig. 4.10. Results indicate that while magmatic-hydrothermal alunite cannot be distinguished from other alteration types on the basis of REE fractionation trends, REE patterns can be used to separate wallrock and gangue alunite. Gangue alunite is characterized by a strong fractionation of heavy REE (HREE) when normalized to host rock composition. In contrast, wallrock alunite typically has a U-shaped REE distribution with variable enrichment of light REE (LREE) and HREE, and depletion in middle REE (MREE). Similar patterns were observed by Terakado and Fujitani (1998) for magmatic-hydrothermal alteration in southwestern Japan. These differences are likely related to fluid-rock ratios and the amount of fluid-rock interaction (e.g., Lottermoser, 1992), and are discussed in detail in Chapters 2 and 3.

Stable-isotope characteristics

Isotopic equilibrium between all sulfur and oxygen species is expected in the magmatic-hydrothermal environment, due to the highly acidic fluids and high temperatures of formation. However, the alunite OH-site is prone to retrograde isotopic exchange during cooling (Rye et al., 1992). Alunite in the El Indio-Pascua Belt are characterized by high $\delta^{34}S$ values (Fig. 4.11a) and overlap with data for barite, where available. One exception is alunite from the Brechita-Huantina vein (El Indio deposit) that has much lighter $\delta^{34}S$ values of 6 to 7‰. Sulfur-isotope data for pyrite from this vein is similarly depleted. In general, alunite samples provide reliable $\Delta^{34}S_{alunite\text{-}pyrite}$ temperature estimates, *ca.* 200-350°C, and indicate equilibrium

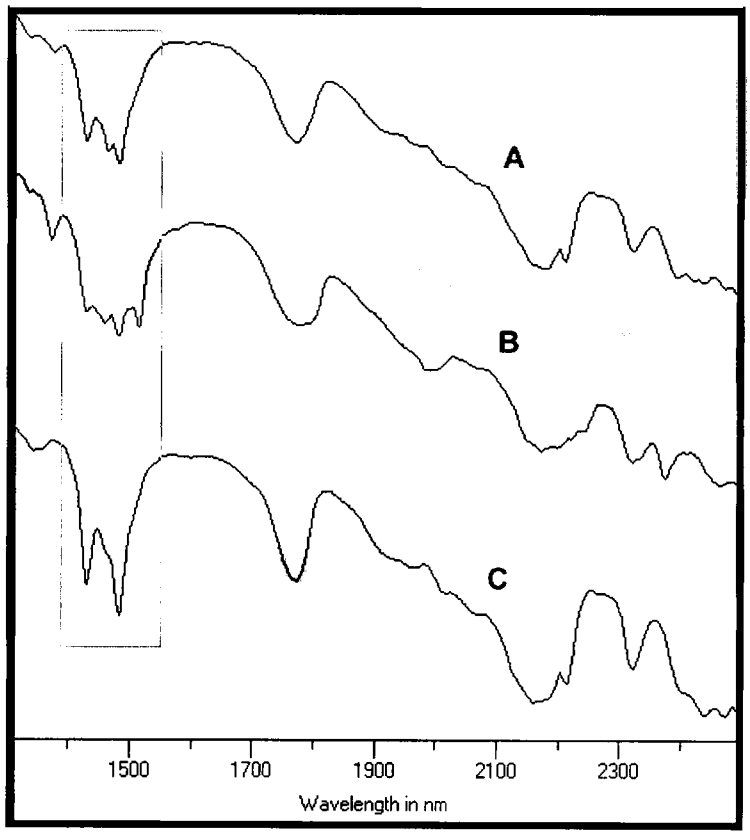

Figure 4.9. PIMA spectra for three samples of magmatic-hydrothermal alteration from the El Indio-Tambo district. Compositional variation is evident from features in the *ca.* 1480 nm range (enclosed in box). A) alunite-waltherite zoning (Canto Sur deposit, Tambo); B) alunite-huangite zoning (Kimberly deposit, Tambo); and C) typical example of pure alunite (Pascua deposit).

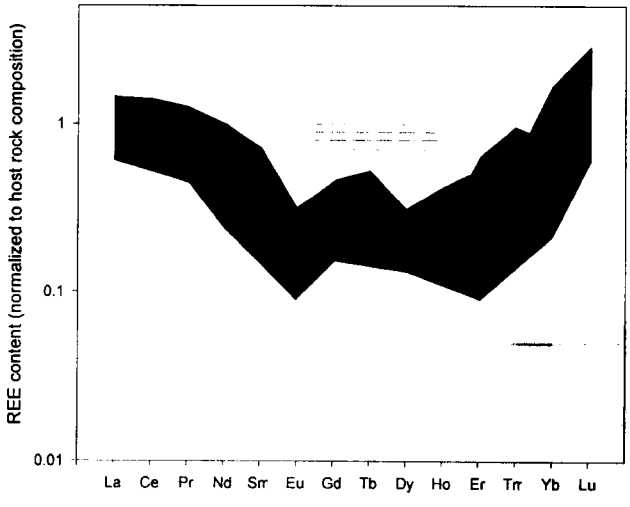

Figure 4.10. Range of REE data for El Indio-Pascua Belt magmatic-hydrothermal alunite, normalized to average host rock compositions for each area. Shown are range of values for disseminated, wallrock alteration (black; n=4) and gangue alteration (grey; n=9).

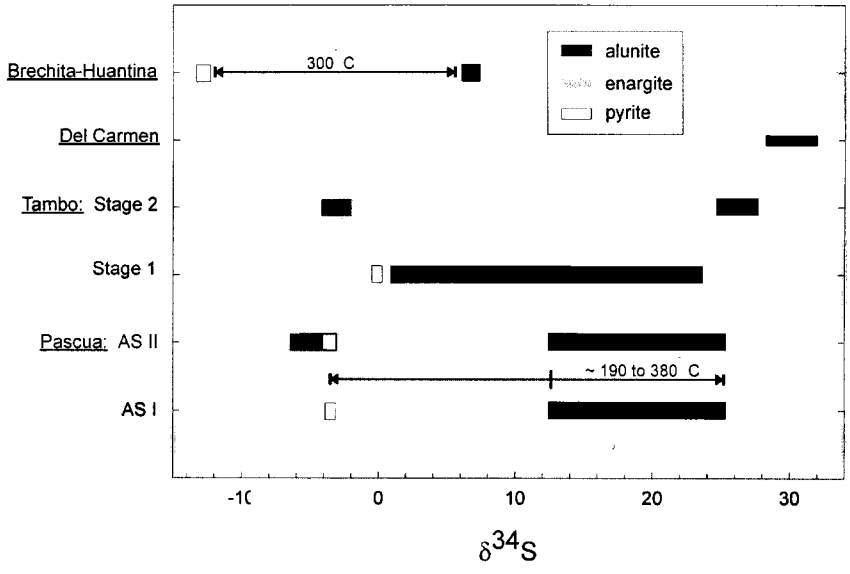

Figure 4.11a. Range of $\delta^{34}S$ data for El Indio-Pascua Belt magmatic-hydrothermal alunite and associated sulfides, where available. Data for each paragenetic stage of at Tambo and Pascua separated (details see Chap. 2 and 3). Also shown are range of depositional temperatures calculated from $\Delta^{34}S_{alun\text{-}py}$ (Ohmoto and Lasaga, 1982), where possible.

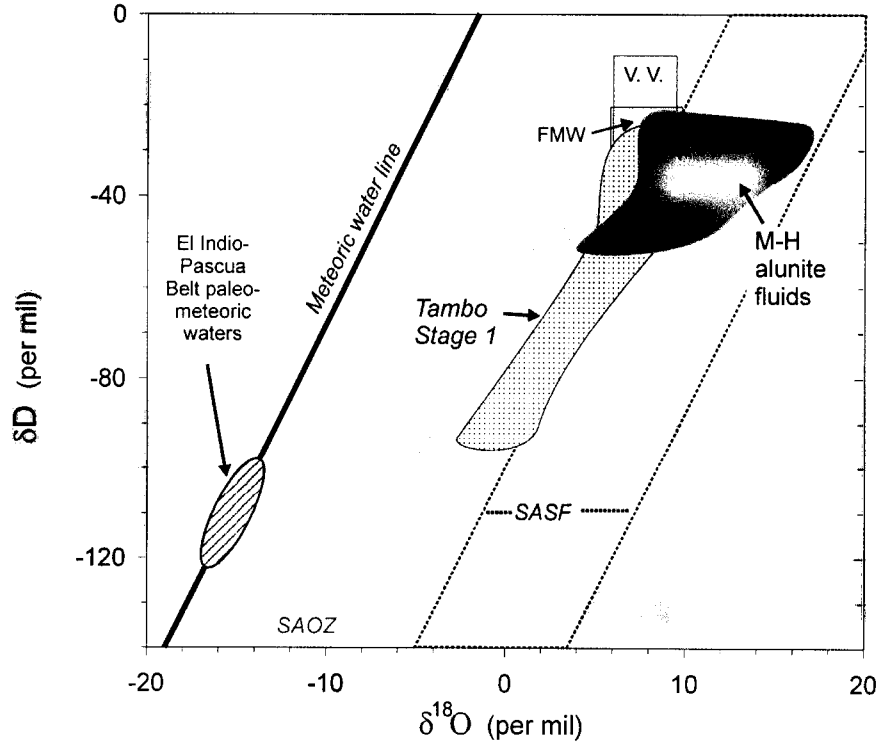

Figure 4.11b. Range of $\delta^{18}O$ and δD for fluids calculated in equilibrium with magmatic-hydrothermal (M-H) alunite (dark grey) from all study areas. Also shown is range of alunite fluids for Tambo Stage 1 alunite (stippled area), which has been overprinted by later steam heated or magmatic steam fluids (see discussion in text). Lines and reference fields: meteoric water line (Craig, 1961); PMW = primary magmatic water field of Taylor (1979); volcanic vapor = range of water compositions discharged from high temperature fumaroles (Giggenbach, 1992); SASF = supergene alunite SO_4 field and SAOZ = supergene alunite OH zone as described in Rye et al. (1992).

fractionation between aqueous H_2S and SO_4.

Fluid compositions in equilibrium with alunite can be calculated based on fractionation data from Stoffregen et al. (1994). $\delta^{18}O_{H2O}$ and δD_{H2O} results indicate that most alunite fluids have a dominant magmatic signature (Fig. 4.12b) and little meteoric water was involved during alteration. However, a large range in alunite $\delta^{18}O_{H2O}$ and δD_{H2O} are calculated for an early stage of alteration at the Tambo deposit (Stage 1). This variation is attributed to the overprinting of previously altered wallrock by later magmatic steam or descending steam-heated fluids (details see Chap. 3).

Fluid inclusions

Fluid inclusions in wallrock alunite are typically too small to study (< 2μm). Coarser-grained vein and open space filling alunite generally contain larger, 2-phase inclusions (5-10μm). Inclusions are typically vapor-rich, although results of necking are common. Daughter crystals are observed only in samples of gangue alunite from Pascua (AS II alteration). These include a translucent phase, probably halite or sylvite, and locally an unknown opaque phase, possibly sulfide or hematite (Fig. 4.12). Most attempts to measure inclusion homogenization or freezing temperatures were unsuccessful due to decrepitation.

Fluid inclusion gas chemistry data for alunite are limited at this time, but results from the Tambo deposit indicate that magmatic-hydrothermal fluids are characterized by high H_2S/SO_2 ratios (Fig. 4.13). Measured Cl contents are low and are consistent with petrographic observations and limited fluid inclusion data from Jannas et al. (1999) that show no evidence for highly saline mineralizing fluids in this deposit.

Age relations

The relation of magmatic-hydrothermal alteration to gold mineralization in the El Indio-Pascua Belt is complex. Evidence from this study and Bissig (2001) indicate that the El Indio-Tambo and Pascua-Lama districts are characterized by multiple alteration and mineralizing events. In each region however, at least one stage of magmatic-hydrothermal alteration occurred prior to the main stage of precious-metal mineralization, which is typical of most high sulfidation systems (e.g., Cooke and Simmons, 2000; Hedenquist et al., 2000). At Tambo, barren wallrock alteration occurs up to 3 m. yr. prior to mineralizing events. At Pascua, the time gap between early wallrock alteration and mineralization is at most 0.5 m. yr.

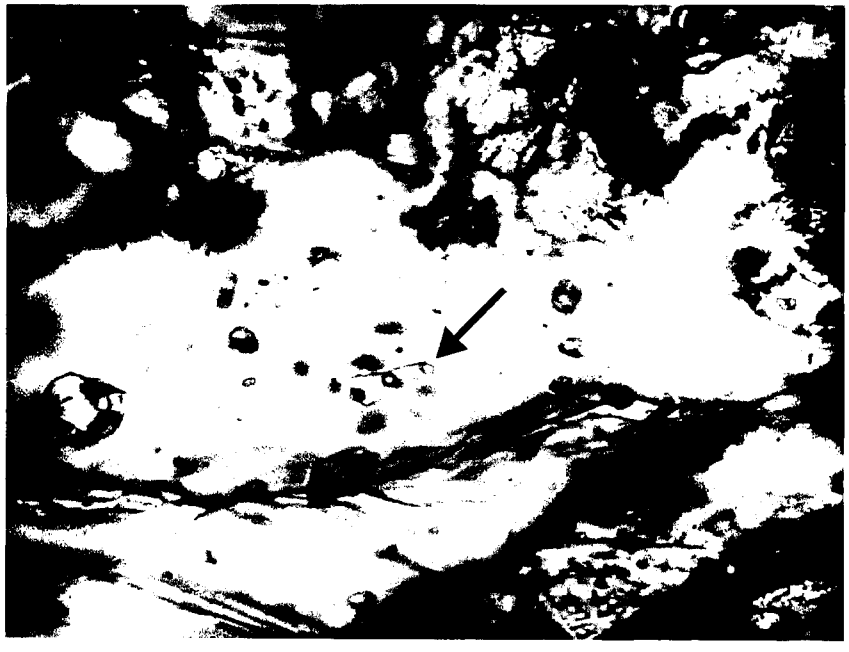

Figure 4.12. Fluid inclusion in magmatic-hydrothermal alunite (Pascua deposit; DDH-137a, 152.1m) with small vapor bubble and two daughter crystals.

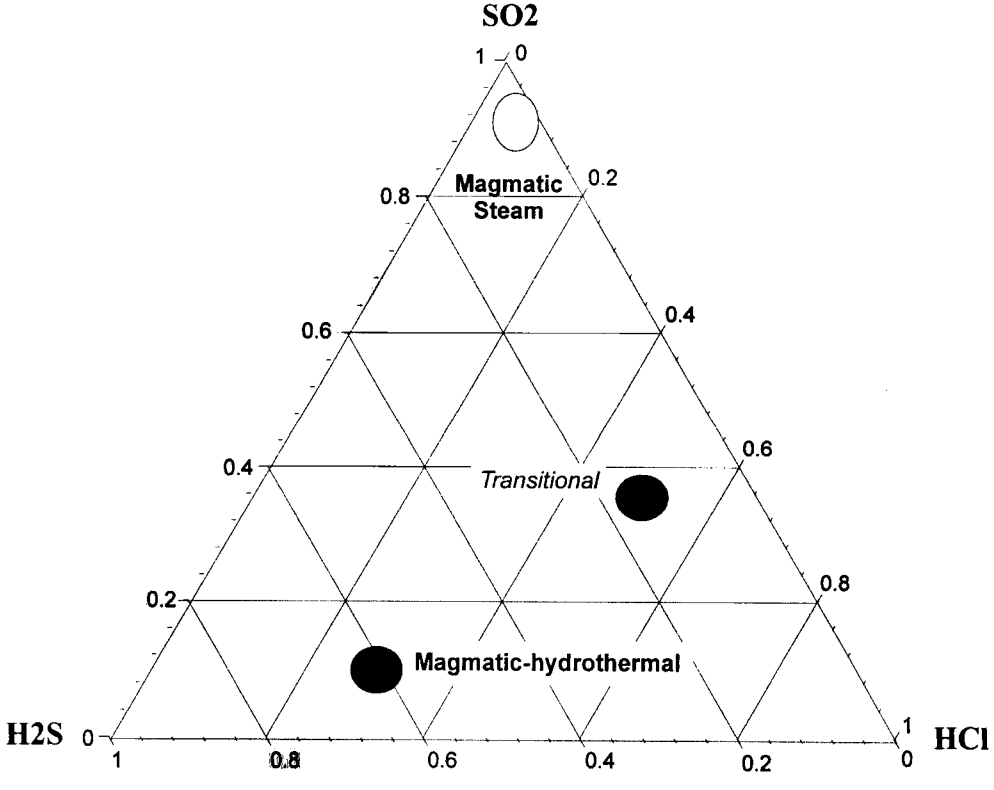

Figure 4.13. Ternary H_2S-SO_2-HCl data from fluid inclusion analyses of Tambo alunite (details see Chap. 3). Range of data for magmatic-hydrothermal and magmatic steam are shown. Also shown is data for Stage 3 alunite from Tambo that is transitional between magmatic-hydrothermal and magmatic steam (circle labeled '*transitional*').

A second stage of alunite deposition is coeval with mineralization at both Tambo and Pascua, as well as locally at El Indio (Brechita-Huantina and Campana veins; Jannas et al., 1999). In each of these cases alunite is intergrown with, or host to, precious-metal bearing sulfides or native gold. A similar relation is inferred for Del Carmen, where alunite is locally intergrown with enargite and pyrite, but age constraints are not available for this region. The presence of abundant syn-mineral alunite is unique to the El Indio-Pascua Belt, and its significance is discussed in a later chapter (Chap. 6).

2. Magmatic Steam Environment

The nature of magmatic steam alunite is poorly understood at this time, and documented occurrences are rare. Alunite of this type occurs in abundance at Alunite Ridge in Marysvale, Utah in coarse-grained mono-mineralic veins up to 20 metres wide (Cunningham et al., 1984), and at the Red Mountain deposit in Colorado as coarse-grained crystals cementing breccia fragments and infilling veins (Bove et al., 1990; Rye et al., 1992). Magmatic steam alunite is of particular interest in the El Indio-Pascua Belt because of its abundance and association with late gold mineralization at the Tambo deposit (Chap. 3). Localized occurrences of magmatic steam alunite are also documented near-surface in at Pascua. Alunite of this type is thought to form from the expansion of rapidly ascending SO_2-rich magmatic vapor (Rye et al., 1992), resulting either from the sudden depressurization of the hydrothermal system (Rye, 1993), or from magma emplaced to shallow depths (Fournier, 1999; Gerlach and Casadevall, 1986). A detailed discussion on this topic is included in Chapter 3, and only a summary of physical and geochemical data from the El Indio-Pascua Belt will be presented here.

Physical characteristics

Magmatic steam alunite is most abundant in the Tambo deposit, where it occurs in several forms.

- Coarse-grained crystals (1 to 5 mm) occur in mono-mineralic, sub-vertical, banded veins (Fig. 4.14). Hematite is common and occurs as inclusions in, or small grains interstitial to, alunite and trace quartz.
- Coarse-grained (1-3 mm) alunite also occurs in stockwork veins and cementing breccia fragments. Alunite is locally overgrown or banded with much finer-grained (<50μm), lath-shaped alunite crystals.

- A third variety of alunite (Stage 3) occurs as fine-grained (<30 μm), lath-like to thin bladed crystals in sugary, earthy masses. Native gold occurs interstitial to, or as inclusions in, alunite of this stage.

At Pascua, magmatic steam alunite occurs near-surface as coarse-grained (1-3 mm) crystals lining open vugs and veins. Minor jarosite is found as overgrowths on magmatic steam alunite at both deposits, but its origins are unclear. Jarosite may form from a magmatic steam phase (Rye and Alpers, 1997), or represent an overprinting supergene event.

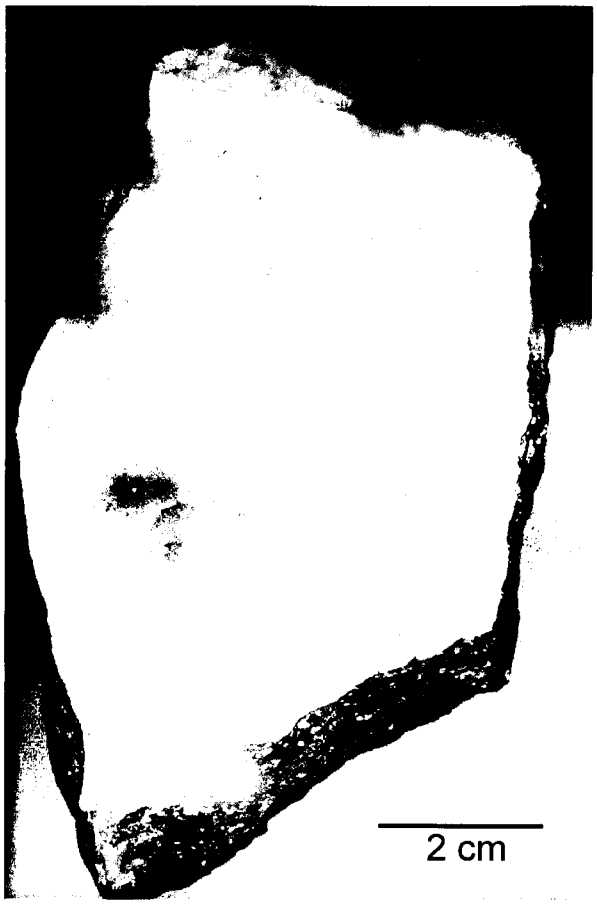

Figure 4.14. Banded magmatic-steam alunite vein (Kimberly deposit, Tambo) in contact with wallrock (at left).

Geochemical characteristics

Magmatic steam alunite is K-dominant with less than 0.2 atoms per formula unit (a.p.f. u.) Na substitution, on average (Fig. 4.5). Elevated Sr and PO_4 concentrations are common and typically occur in oscillatory growth zones detectable by EDS backscatter imaging (Fig. 4.15). Results are similar to those reported for Alunite Ridge, Utah (Cunningham et al., 1986; Stoffregen and Alpers, 1987). However, Cunningham et al. (1986) also report locally elevated Ba concentrations, inversely correlated with Sr and PO_4 zoning, in magmatic steam alunite from Alunite Ridge. Similar trends were not seen in this study and nearly all Ba is below detection (Table 4.4).

REE signature: Magmatic steam alunite from both Tambo and Pascua exhibit extreme HREE fractionation and limited enrichment of La and Ce, compared to host rock values (Fig. 4.16). Results are similar to data for magmatic-hydrothermal gangue alunite reported above. Both forms of alunite are precipitated in open spaces, likely without significant wallrock interaction. REE signatures should therefore reflect the composition of the source fluids/ vapors. Several experimental studies have demonstrated the differential partitioning of LREE into an exsolved magmatic vapor phase (e.g., Flynn and Burnham, 1978; Reed, 1995), although crystallographic controls on REE substitution described by Schwab et al. (1990) may also account for the significant depletion of HREE in magmatic steam alunite.

Stable-isotope characteristics

Magmatic steam alunite in the El Indio-Pascua Belt is characterized by near zero $\delta^{34}S$ values (Fig. 4.17a). At Tambo, only minor $\delta^{34}S$ variation is reported between different samples of banded vein alunite or between growth bands in a single vein (Table 4.5). These nearly constant $\delta^{34}S$ values should be close to the $\delta^{34}S$ of bulk sulfur in the magma (Rye et al., 1992) and likely reflect the quantitative, disequilibrium oxidation of magmatic SO_2 (and possibly H_2S: Cunningham et al., 1997). Alunite δD and $\delta^{18}O_{SO4}$ values are near magmatic values and suggest that little to no meteoric water was present in the source fluid (Fig. 4.17b). Depositional temperatures calculated from $\Delta^{18}O_{SO4\text{-}OH}$ are typically in the range of 70-200°C and are considered too low for precipitation from a magmatic vapor phase. Similar observations are noted by Rye et al. (1992) for Marysvale alunite.

Isotopic results from the Tambo deposit also indicate that there is a transitional phase between magmatic-hydrothermal and magmatic steam environments (Chap. 3). Sulfur data for

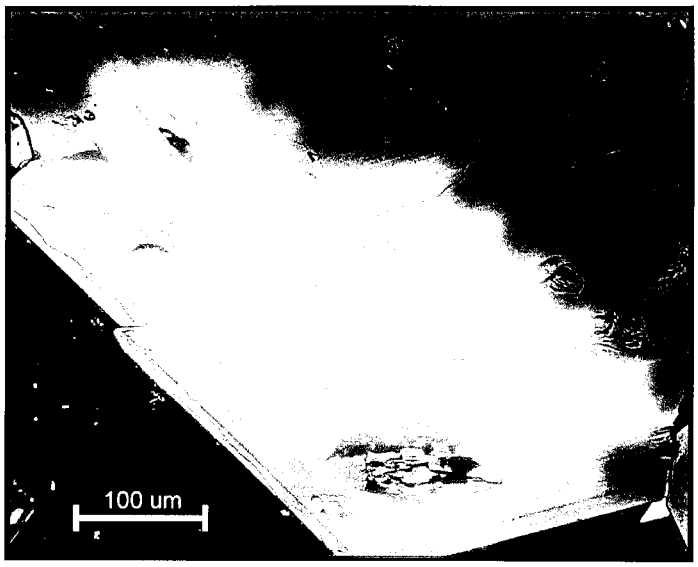

Figure 4.15. Backscatter image showing $PO_4 \pm Sr$ zoning (light grey/white) in magmatic steam alunite (Pascua deposit).

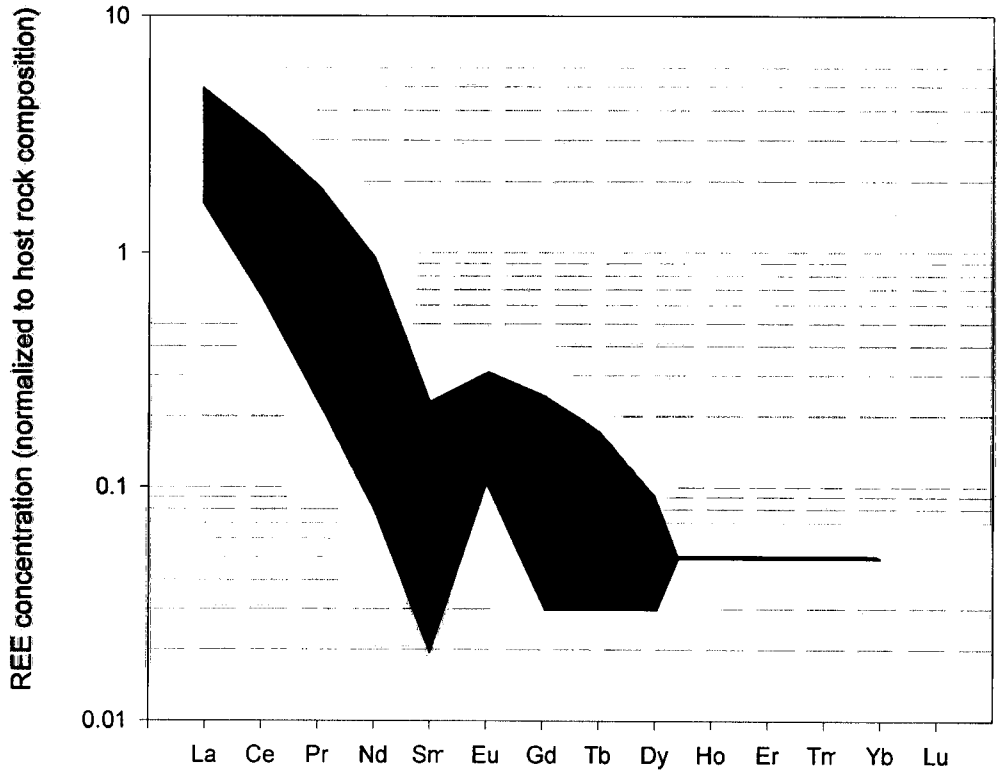

Figure 4.16. Range of REE data for El Indio-Pascua Belt magmatic steam alunite (n=5; including samples of Stage 3 alteration from Tambo). Data are normalized to average host rock compositions for each region.

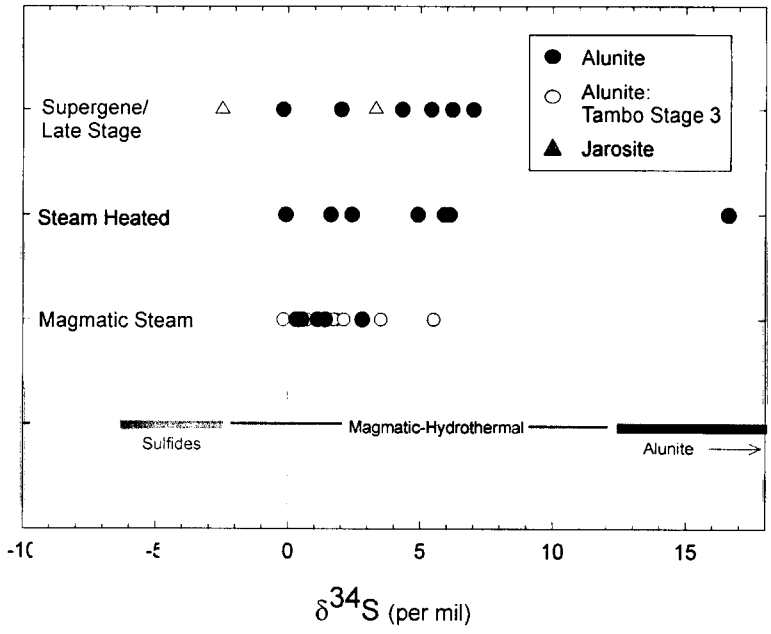

Figure 4.17a. Sulfur isotope data for magmatic steam, steam heated and supergene/late stage alunite and jarosite for the El Indio-Pascua Belt. Range of data for magmatic-hydrothermal alunite and sulfides is given for reference.

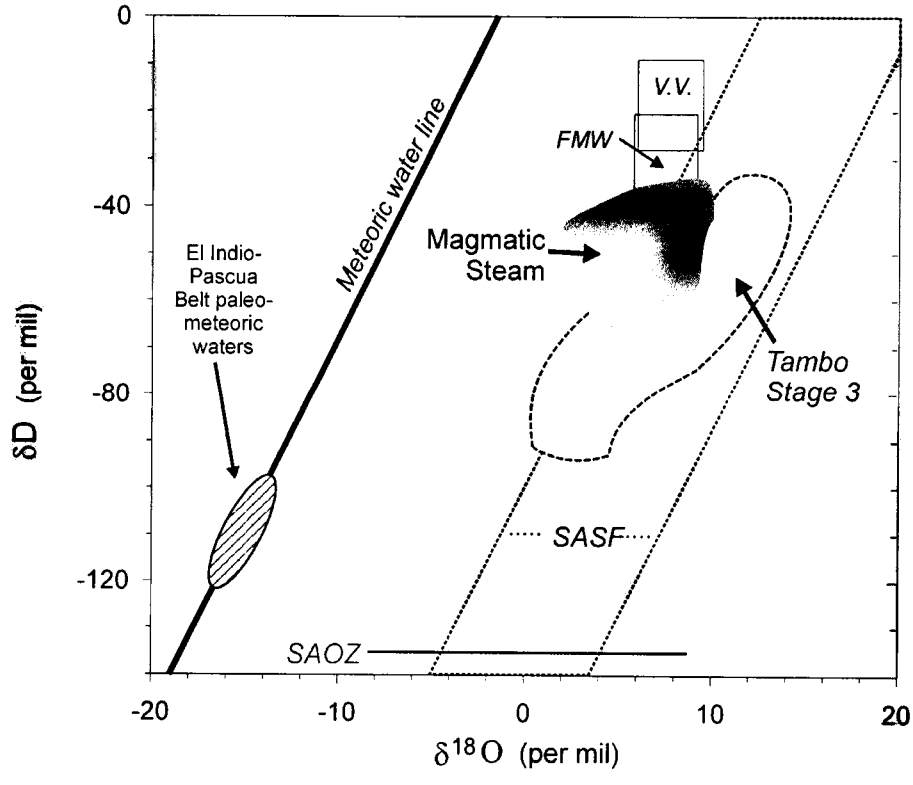

Figure 4.17b. Range of $\delta^{18}O$ and δD for fluids calculated in equilibrium with magmatic steam alunite (dark grey) from all study areas. Also shown is range of alunite fluids for Tambo Stage 3 alunite (white), transitional between magmatic-hydrothermal and magmatic steam environments (see discussion in text). Descriptions of lines and fields as per Fig. 4.11b.

Stage 3 alunite ($\delta^{34}S$ up to 5.5‰) are slightly heavier than values from the banded veins. This suggests incomplete sulfur isotope exchange between SO_4 and H_2S species in some samples, possibly due to slightly longer fluid residence times. Also, in contrast to banded vein samples, calculated fluid compositions in equilibrium with Stage 3 alunite show limited mixing between magmatic and meteoric fluids.

Fluid inclusions

Fluid inclusions in magmatic steam alunite are typically very small (<5 μm) and vapor-rich (this study; Jannas et al., 1999). Gas analyses indicate that they are SO_2-dominant (Fig. 4.11), particularly in comparison to magmatic-hydrothermal alunite. H_2S and HCl concentrations are extremely low, but abundant reduced carbon species are detected. Overall data suggest that volatiles were derived directly from the magma (further details provided in Chap. 3).

Table 4.5. Variation in sulfur isotope data (in per mil) for magmatic steam alunite from a single vein.

Sample #	Analysis	$\delta^{34}S$	Sample #	Analysis	$\delta^{34}S$
KB-02a	1	-0.1	**KB-02b**	1	0.4
	2	0.8		2	-0.2
	3	1.1		3	0.1
	4	1.6		4	-0.2
	5	1.8		5	0.0
	6	1.0		6	-0.7
	7	0.7		7	0.2
	8	0.6		8	0.1
	9	-1.1		9	-0.7
	10	-0.2		10	0.2
	11	0.0			
	12	-0.4			
	13	-0.4			
	14	-0.5			
	15	-0.1			
	16	0.8			
	17	-0.8			
	18	-0.2			
	19	0.4			

Age relations

Paragenetic and geochronologic evidence indicate that magmatic steam alunite formed late in the development of magmatic-hydrothermal systems in the El Indio-Pascua Belt. $^{40}Ar/^{39}Ar$ dating of magmatic steam alunite at Pascua indicates that it is slightly younger than, or contemporaneous with, the main gold mineralizing event (Chap. 2). At Tambo, Stage 3 alunite (8.2 ± 0.2) is younger than the gold-bearing magmatic-hydrothermal Stage 2 event (8.7 ± 0.2). However, the coarse-grained banded magmatic steam alunite veins did not yield accurate $^{40}Ar/^{39}Ar$ ages, despite several dating attempts.

3. Steam-heated Environment

Steam-heated alteration forms from the condensation of vapour derived from an underlying hydrothermal system and the oxidation of H_2S. Sulfuric acid is produced by the reaction: $H_2S + 2O_2 \leftrightarrow H_2SO_4$ (Schoen et al., 1974). This reaction takes place at or above the water table, and therefore at temperatures below 100°C, but fluids may descend along fractures to depths where higher temperatures are encountered, usually in the range of 90-160°C (Rye et al., 1992). Steam-heated alteration typically occurs as tabular, blanket-like zones that are defined by the paleo-water table (Fig. 4.18). These zones will be thicker where paleo-water tables are deep, such as in arid regions or beneath topographic highs (like stratavolcanoes) in mountainous terrain (Sillitoe, 1993). There is no direct genetic relation between steam-heated alteration and precious metal mineralization, but alteration occurs above or lateral to the mineralizing system, if present. In cases of groundwater table collapse (e.g., Simmons and Browne, 1990; Ebert and Rye, 1997), alteration may overprint epithermal mineralization.

Most our of knowledge of steam-heated processes is taken from low sulfidation systems and active geothermal areas. Much less information is available for steam-heated alteration above high sulfidation deposits, likely because the paleosurface is preserved in few systems (e. g., La Coipa, Paradise Peak, Yanacocha, Pierina; Sillitoe, 1999). In the El Indio-Pascua belt, steam-heated alteration occurs at upper elevations as visibly distinct, discontinuous alteration zones. In the El Indio-Tambo region, steam-heated assemblages occur above the Kimberly, Wendy, and Canto Sur deposits and as extensive alteration zones in the nearby, barren, Azufreras and Sol Poniente areas. At Pascua, alteration forms a nearly continuous blanket-type zone above the Brecha Central area at elevations above 4950 m.

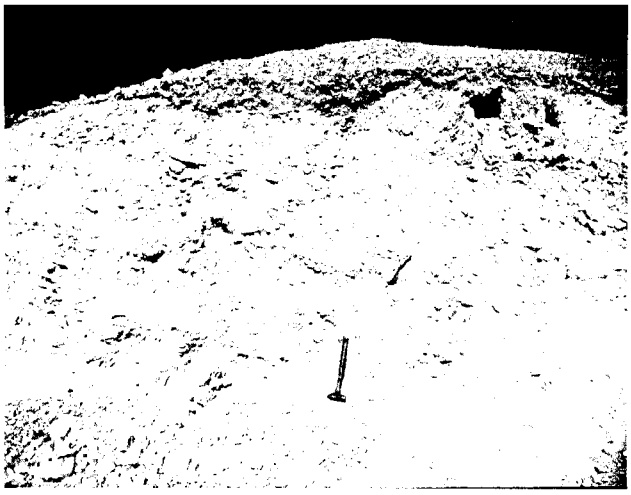

Figure 4.18. Steam heated alteration at Cerro Elephante, Tambo deposit.

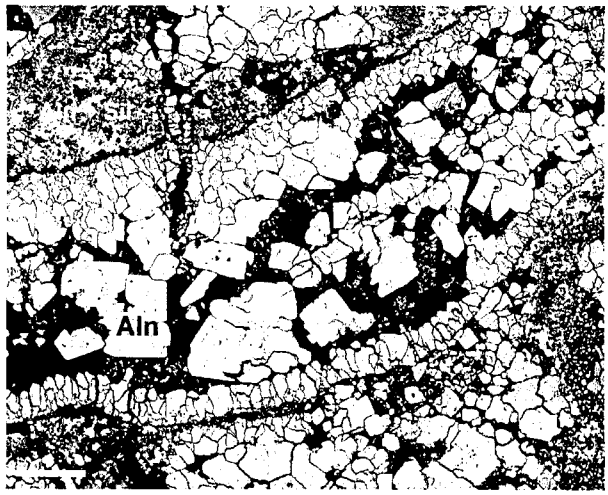

Figure 4.19. SEM micrograph of typical steam heated alteration, Pascua deposit (DDH-119, 47.7m). Scale bar = 10 μm.

Physical characteristics

Steam-heated alteration in the El Indio-Pascua Belt consists of kaolinite, cristobalite (± trydimite), native sulfur ± trace opal. Alunite is relatively rare. Where present, it is restricted to irregular pods and lenses of fine-grained (*ca.* 5-50 μm), tabular, lath-shaped, pseudo-cubic and less commonly acicular crystals that appear as grey, irregular masses in thin section (Fig. 4.19). Alteration is typically distributed in massive to extremely porous, friable zones, although cross-cutting veins and disseminations of this assemblage typically extend to greater depth along fractures. Alteration in several steam-heated systems is vertically zoned (Sillitoe, 1993; Hedenquist et al., 2000) and at Pascua, an upper layer of residual, vuggy quartz grades downwards into a kaolinite and/or alunite-bearing zone.

Geochemical characteristics

Geochemical data for steam-heated alunite in the El Indio-Pascua Belt are limited, due to the relatively scarcity of alunite and fine-grained nature of alteration. Overall, our results indicate that alunite is nearly stoichiometric with minor Na and locally elevated Sr, Sb, Fe, and PO_4 contents (Table 4.4). No zoning is visible. Geochemical data from other steam-heated alteration zones are also limited but generally show both alunite and natroalunite end-member compositions (Thompson and Petersen, 1995; Ebert and Rye, 1997). Other substitutions are rare.

REE signatures: Steam-heated alunite typically show slight HREE fractionation compared to host rock values (Fig. 4.20). Some samples exhibit a U-shaped MREE depletion trend, similar to magmatic-hydrothermal wallrock alteration. REE fractionation patterns of El Indio-Pascua Belt alunite are similar to those of acid-sulfate waters in Yellowstone National Park and suggest REE are complexed by sulphate and fluoride in acidic, low temperature, low salinity fluids (Lewis et al., 1998).

Stable-isotope characteristics

Sulfur-isotope data for steam-heated alunite are variable (Fig. 4.17a). $\delta^{34}S$ values average 4‰ and are slightly to significantly heavier than data for underlying sulfides. Data reflect partial sulfur isotope exchange with H_2S, possibly as a result of longer fluid residence times with aqueous sulfate, or the interaction of steam-heated fluids with higher temperature magmatic steam. These values are not typical of other steam-heated environments, where alunite $\delta^{34}S$ are nearly equal to H_2S derived from the hydrothermal fluid and equivalent to underlying sulfides, if present (Rye et al., 1992).

Depositional temperatures based on $\Delta^{18}O_{SO4\text{-}OH}$ for steam-heated alunite average between 90° and 150 °C and are consistent with data from other studies (e.g., Rye et al., 1992). Results indicate oxygen isotopic equilibrium between alunite and the fluid. Few samples give unreasonably high temperatures however, suggesting post-depositional oxygen-isotope exchange.

Calculated $\delta^{18}O_{H2O}$ and δD_{H2O} values for El Indio-Pascua Belt alunite are shown in Figure 21. These values are much heavier than the paleo-meteoric water composition, estimated at $\delta D = -100 \pm 10$‰ (B. Taylor, pers. comm.). Data are inconsistent with the predictions of Rye et al. (1992) and results from other studies (Ebert and Rye, 1997), which indicate steam-heated fluids are typically derived from meteoric waters. Our results suggest that much of the water present in the steam-heated zone in the El Indio-Pascua Belt formed from the condensation of vapors derived from magmatic fluids. This is attributed to prolonged magmatic-hydrothermal activity in the area and a progressive lowering of the water table induced by regional erosional events (Bissig, 2001).

Age relations

Steam-heated acid sulfate alteration is often considered to be coincident with underlying

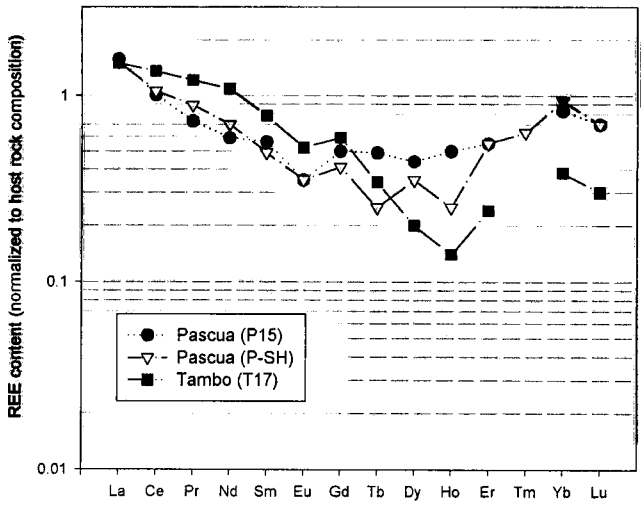

Figure 4.20. REE data for steam heated alteration, Pascua and Tambo deposits. All data normalized to average host rock compositions. Data below detection not plotted.

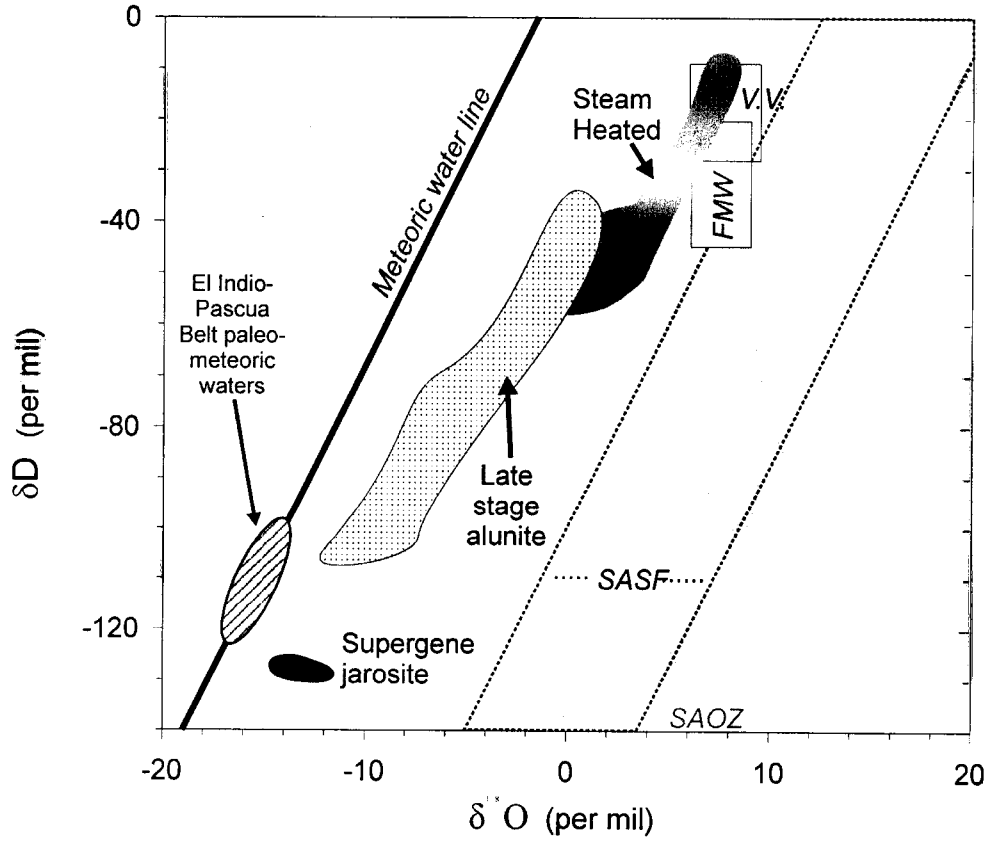

Figure 4.21. Range of $\delta^{18}O$ and δD for fluids calculated in equilibrium with steam-heated (dark grey) and late stage oxidation (stippled) alunite from all study areas. Also shown is range of supergene jarosite fluids (black) from the Pascua deposit. Descriptions of lines and fields as per Fig. 4.11b.

mineralization, if present (Rye et al., 1992). Age relations in the El Indio-Pascua Belt are more complex however. Deposits occur in regions with evidence for multiple stages of alteration and mineralization than span several million years. Steam-heated processes could have been associated with any, or all, of these events. The only reliable age data for steam-heated alteration overlying mineralization in this region is from the Tambo deposit (8.9 ± 0.4 Ma), and shows that alteration is coeval with the earliest stage of ore deposition (Stage 2).

4. Supergene Environment

Supergene acid sulfate alteration results from the weathering of any sulfide-rich zone under atmospheric conditions. In the strictest sense, supergene oxidation therefore only occurs above (or locally immediately below) the water table and has no genetic relation to epithermal precious-metal mineralization. Alteration typically occurs in topographically controlled zones but acid fluids may drain downward locally along faults and open fractures, resulting in cross-cutting veins and disseminations in the weathering profile. The development of supergene alunite is also strongly controlled by climate and local environmental effects (e.g., Sillitoe, 1999). Well-developed supergene profiles are expected only in semi-arid to arid environments where relatively low water/rock ratios can result in acidic, sulfate-rich waters during weathering. Temperatures of formation typically average 20-40°C, depending on the local environment, but oxidation reactions are strongly exothermic and temperatures may reach up to 80°C (Rye et al., 1992).

Supergene processes are apparent throughout the El Indio-Pascua Belt. The effects of oxidation include ubiquitous iron oxide and hematite staining on surficial and near surface exposures of both mineralized and barren host rock. Secondary gypsum is abundant locally, particularly in surface outcrops in the Pascua district and in the Del Carmen area. Hydrous iron sulfates such as szomolnokite, voltaite, and coquimbite are found in-situ in underground exposures of sulfide-rich ore in the Pascua area and also develop rapidly on the surface of drill core once exposed to surficial atmospheric conditions, and particularly to added water.

In contrast, definitive occurrences of supergene acid sulfate alteration are rare. Supergene jarosite is recognized at the Pascua district (Chap. 2) and localized occurrences of alunite-jarosite are also considered supergene in origin, based on paragenetic characteristics (described below). Thin veinlets and disseminations of porcellaneous alunite ± late jarosite are

common, but textural and isotopic evidence has shown that alteration is not of typical supergene origin (Chap. 2, 3). Instead, alteration ('late stage alteration') is thought to have occurred during the final stages of the hydrothermal systems, from mixing of magmatic and meteoric fluids at temperatures *ca.* 80° to 150°C. These assemblages can rarely be distinguished from true supergene alteration on the basis of field or textural characteristics, unless cross-cutting relations are evident. The distinction may be of importance in exploration however, since the higher temperatures of late stage alteration and involvement of magmatic fluids have a greater potential for remobilization or enrichment of hypogene precious-metal mineralization. At Pascua for example, late stage acidic, moderate temperature fluids may have been responsible for Ag enrichment at high elevations in the Brecha Central area (A. Chouinard, pers. comm.). Characteristics of both late stage and supergene alteration are described in the following section, and any differences between the two assemblages are emphasized.

Physical characteristics

As mentioned, late stage and supergene acid sulfate alteration are difficult to distinguish on a textural basis. Late stage alteration throughout the El Indio-Pascua Belt occurs as chalky, porcellaneous masses, fine powdery aggregates, fracture coatings, and thin, cryptocrystalline veinlets that cross-cut mineralization and all other alteration types (Fig 22). Alunite is common, and occurs as fine- to medium-grained (10-50 μm), tabular to bladed crystals, often intermixed with quartz. Locally, alunite is overgrown or cross-cut by fine-grained jarosite, with ubiquitous iron oxides and common scorodite. This later assemblage is considered supergene in origin. Rare alunite is present and typically occurs as fine-grained (0.5-5 μm) pseudo-cubic crystals (Fig. 4.23a), although grains up to 30μm are found locally. Anhedral, lath-like to rhombohedral forms are rare. Pseudocubic to subhedral grains of woodhouseite-svanbergite composition are also observed in thin veinlets cross-cutting argillically altered rock in the Tambo deposit (Kimberly Oueste), intermixed with kaolinite and pseudo-cubic alunite grains (Fig. 4.23b). Based on these relations, the APS grains are considered supergene in origin. Similar observations have been reported in other supergene environments (e.g., Stoffregen and Alpers, 1987, Dill et al., 1997).

Geochemical characteristics

Only qualitative geochemical data is available for supergene alunite in the El Indio-

Figure 4.22. Late stage alunite-jarosite veinlets cross-cutting altered volcanic tuff (Wendy deposit, Tambo). Scale bar in centimetres.

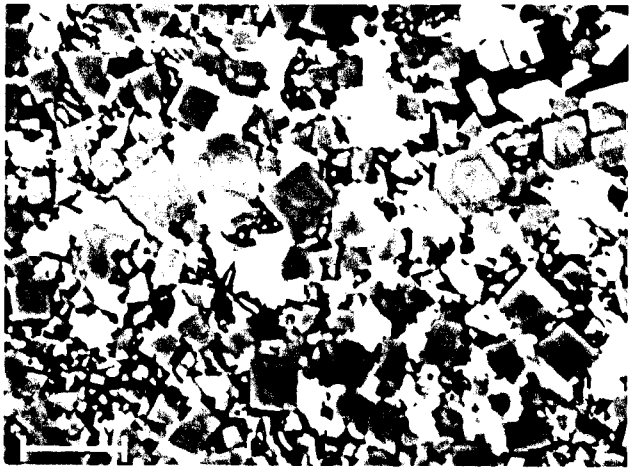

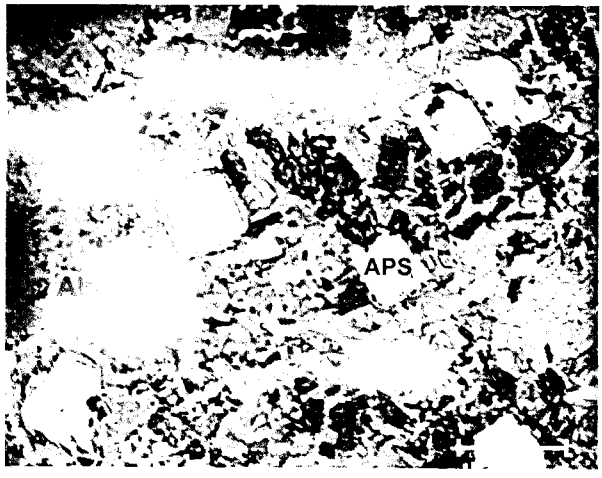

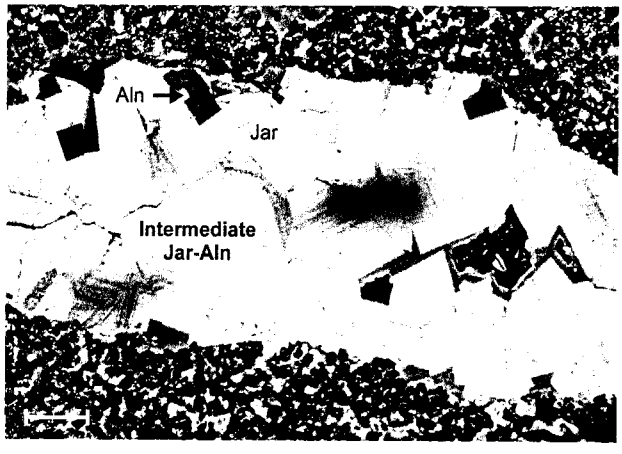

Figure 4.23.
(a) *top left.* SEM micrograph of pseudocubic alunite crystals (grey) showing oscillatory compositional zoning between alunite and more Na-rich compositions. Jarosite (white) occurs interstitial to alunite grains. Scale bar = 5μm.
(b) *top right.* SEM micrograph of supergene APS (light grey) with alunite (grey) and kaolinite (dark grey). Scale bar = 10μm.
(c) *bottom.* SEM micrograph of veinlet with supergene alunite overgrown by jarosite and alunite-jarosite solid solution (Pascua deposit, 4680 level). Scale bar = 20μm.

Pascua Belt, due to the fine-grained nature of alteration and relatively rare occurrence of alunite in the supergene assemblage. Alunite is typically K-dominant (Table 4.4), and rarely exhibits very fine oscillatory zoning between K-dominant and more Na-rich compositions. Solid solution between alunite and jarosite end-member compositions also occurs in thin veinlets at the Pascua deposit (Fig. 4.23c). Geochemical data for late stage alteration (Fig. 4.5) indicate that average alunite compositions are K-rich in comparison to higher temperature occurrences (at 95% confidence level, based on t-test statistics: Appendix A). Trace element concentrations are extremely variable with locally elevated Ca, Sr, PO_4 ± REE and trace metal concentrations (Pb, Cu, Zn ± Ba) that are likely derived from hypogene sulfides. Data are consistent with other studies that report variable supergene alunite compositions, largely depending on the contents of precursor sulfides and the availability of ions in the weathering profile (Arribas et al., 1995; Stoffregen and Alpers, 1987; ibid, 1992, Thompson and Petersen 1995, Dill et al., 1997).

REE signatures: REE data are available only for late vein alunite since sufficient material of supergene alunite could not be separated. Results are given in Figure 24 and show variable patterns of REE fractionation. One sample exhibits strong depletion in HREE. The other two samples have concave-shaped patterns of MREE enrichment and also show significant depletion in HREE. The pattern of MREE enrichment is opposite to the U-shaped pattern observed in magmatic-hydrothermal wallrock alteration and steam-heated samples (Figs. 10 and 16), although to a lesser degree. We suggest that REE fractionation is affected by temperature variations and differences in the availability of complexing agents with increasing meteoric water contribution (Wood, 1990; Lottermoser, 1992), but more data is required to fully understand these processes.

Stable-isotope characteristics

Stable-isotope data are available only for samples of late stage alunite (Fig. 4.25) and one sample of supergene jarosite from Pascua. The alunite is characterized by low $\delta^{34}S$ (typically less than 6‰) and $\delta^{18}O_{OH}$ (less than 10‰) values. Data generally do not fall within the reference fields defined by Rye et al. (1992) for supergene alunite. El Indio-Pascua Belt alunite $\Delta^{18}O_{SO4\text{-}OH}$ values are all positive and therefore also not consistent with a supergene origin (e.g., Rye et al., 1992). Several samples give $\Delta^{18}O_{SO4\text{-}OH}$ temperatures between 80° to 140 °C. These values are considered reasonable for late stage oxidation in the presence of

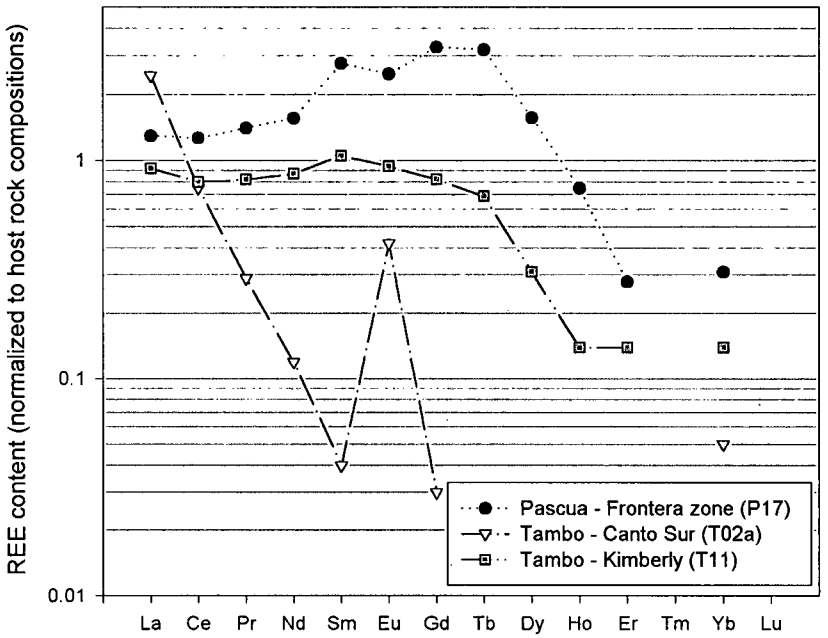

Figure 4.24. REE data for late stage acid sulfate alteration; Pascua and Tambo deposits. All data normalized to host rock compositions. Data below detection limits not shown.

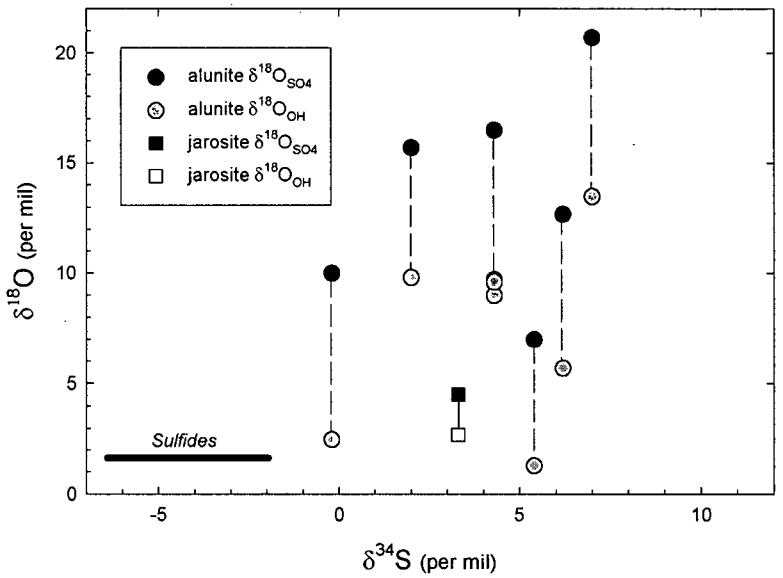

Figure 4.25. Sulfur and oxygen isotope data for El Indio-Pascua Belt late stage alunite and supergene jarosite. $\delta^{18}O_{SO4}$ and $\delta^{18}O_{OH}$ data for each sample joined by lines. Range of $\delta^{34}S$ data for hypogene sulfides given for reference.

magmatic fluids. Other $\Delta^{18}O_{SO4\text{-}OH}$ values are grossly out of equilibrium and suggest non-equilibrium or kinetic controls on alunite $\delta^{18}O_{SO4}$ values. Calculated alunite $\delta^{18}O_{H2O}$ and δD_{H2O} data indicate variable mixing between magmatic and meteoric fluids (see Fig. 4.21).

Jarosite $\delta^{34}S$ data from the Pascua deposit are slightly enriched relative to sulfides in the deposit. Jarosite $\delta^{18}O$ data generally fall within the reference fields defined by Rye and Alpers (1997) for supergene environments. However, $\delta^{18}O_{OH}$ data are slightly heavier than the Supergene Jarosite OH Zone (SJOZ) and may indicate formation from partially exchanged meteoric waters. Jarosite calculated fluid compositions are nearly identical to the estimated composition of paleo-meteoric waters (see Fig. 4.21).

Age relations

Results from the El Indio-Pascua Belt illustrate that the timing of supergene or oxidation processes within magmatic-hydrothermal systems can be complicated. Both supergene and late stage acid sulfate assemblages post-date alteration and mineralization related to the magmatic-hydrothermal system. $^{40}Ar/^{39}Ar$ ages reported for the Pascua deposit (Chap. 2; Bissig, 2001) indicate supergene jarosite (7.98 ± 0.43 Ma) formed within 1 Ma of the main mineralizing event. Similarly, late stage alunite (± jarosite) veins from the Tambo deposit (Canto Sur pit: 7.25 ± 0.14 Ma) formed *ca.* 1 Ma after the main period of mineralization in the Kimberly and Wendy areas, although these veins may be contemporaneous with Au mineralization in this area (Bissig, 2001).

DISCUSSION: IMPLICATIONS FOR EXPLORATION

Recognition of the different types of acid sulfate alteration is critical for effective exploration in high sulfidation systems, particularly in poorly exposed terrains. In the field, the identification of these assemblages will rely mostly on the spatial distribution of alteration, macroscopic textures, and mineral assemblages. Rigorous field work and careful mapping are required. Particular attention must be paid to local features such as climate (both current and paleo- conditions), topography, lithology, and structure that can affect both the distribution and nature of alteration zones. For example, both alteration and mineralization in high sulfidation systems are strongly controlled by permeability, which can be generated by either structural,

hydrothermal, or lithological processes. The relative importance of each will vary with the local environment (Sillitoe, 1993). The distribution of alteration can be further complicated by superimposed alteration events, particularly in areas of groundwater table collapse (Simmons and Browne, 1990; Ebert and Rye, 1997).

Field mapping in epithermal systems can be aided by in-situ SWIR analyses, which are particularly helpful for identifying fine-grained mixtures and subtle changes in mineralogy (e. g., kaolinite-dickite-pyrophyllite) that can be difficult to distinguish in hand specimen. In some cases, SWIR techniques can also be used to determine the chemistry of alunite-group minerals (Thompson et al., 1999) and may aid in the identification of higher temperature alteration assemblages. In areas with multiple stages of alteration, field work should be combined with careful petrographic observations and simple XRD or SEM-EDS analysis, in order to better define paragenetic relations and mineral chemistry. Detailed isotopic or fluid-inclusion studies can provide additional information regarding the nature of the source fluids and physio-chemical environment of deposition. Successful use of such complementary information can distinguish higher temperature, magmatic-hydrothermal alteration zones that have a direct spatial (and possibly temporal) relation to potential precious-metal mineralization.

Exploration in the El Indio-Pascua Belt

The El Indio-Pascua Belt is a unique region which hosts several world-class Au (Cu-Ag) deposits and extensive areas of hydrothermal alteration. High sulfidation systems within this belt have many features in common with other deposits, although several differences can be identified. For example;

- There is only limited evidence for syn-ore magmatic activity (Bissig, 2001).
- Deposits and prospects are not associated with major volcanic edifices.
- The largest (most economic) deposits in this region have evidence for multiple, superimposed alteration and mineralizing events.
- A shallow erosional level has preserved many features of the near paleo-surface.
- Abundant alunite is coeval with, and host to, precious-metal mineralization.

Results from this study have highlighted the complexity of relations between acid sulfate assemblages of different origin. Effective exploration in this region (as in other regions) must therefore focus on identifying ore-related, hypogene alteration assemblages. Several key considerations are outlined below.

1. Magmatic-hydrothermal alteration can be differentiated from lower temperature steam-heated and supergene occurrences by a combination of factors which include:
   - Mineral associations, and particularly a direct spatial and genetic relation of alunite with sulfides or high-temperature alteration minerals (e.g., dickite, pyrophyllite, diaspore, zunyite).
   - Alunite crystal habit: coarse-grained crystals with a bladed to tabular habit.
   - Variable alunite geochemistry, specifically elevated Ba contents and complex or oscillatory geochemical zoning.
2. Differentiating between barren wallrock alteration and potentially ore-bearing (gangue) alunite is much more difficult. In the El Indio-Pascua Belt, mineralization and associated gangue is typically strongly structurally controlled and exploration should therefore focus on determining favorable structural fluid conduits – after magmatic-hydrothermal alteration zones have been delimited.
3. Magmatic steam alunite may also host gold ore, but cannot reasonably be targeted by regional-scale exploration programs. Alunite of this type is extremely variable in texture and physical characteristics, and it may be difficult to distinguish visually from magmatic-hydrothermal and even steam-heated assemblages. Detailed paragenetic, petrographic, and isotopic studies would be required to confirm alunite of magmatic steam origin.
4. Steam-heated alteration overlies precious metal mineralization in all of the areas included in this study, with the exception of Salitrales. Alteration is coeval with gold deposition in the Tambo deposit, and possibly in the Pascua area as well. However, large areas of barren steam-heated alteration also occur to the south of El Indio-Tambo. Without an in-depth examination of these barren alteration zones, we have no means to distinguish potential 'ore-related' steam-heated alteration.
5. The economic feasibility of deposits in the El Indio-Pascua Belt is not dependent on supergene or late-stage oxidation processes. However, enrichment or remobilization of precious-metal assemblages can occur on a local scale.

Applications to Exploration World-wide

While the above features apply specifically to the El Indio-Pascua Belt, general exploration criteria can be applied to high sulfidation systems world-wide. A decision-tree

(Fig. 4.26) highlights the use of alunite and the critical observations that must be made to explore effectively for deposits of this type. Emphasis is placed on distinguishing between types of acid sulfate alteration. Reference is made to Tables 4.2 and 4.3, which summarize characteristics of alunite and associated alteration assemblages in the El Indio-Pascua Belt. Many of these features may apply to high sulfidation systems in general, but specific alunite characteristics, and particularly alunite chemical compositions, will vary in different geological settings.

Alunite may be of particular use in two common exploration scenarios; 1) regions with poor outcrop, or 2) regions with widespread alteration but no obvious mineralization. In both cases, a combination of paragenetic, textural, or geochemical features of alunite could help by first confirming that alteration is magmatic-hydrothermal in origin, and secondly, by providing focus to exploration activities by identifying higher-temperature, and therefore potentially ore-proximal, assemblages. Specifically, coarse-grained alunite, associated with kaolinite or dickite and sulfides, are characteristic of a magmatic-hydrothermal origin. Complex chemical zoning and elevated Na, Ba, P, and Ca contents are also indicative of magmatic-hydrothermal alunite. These determinations could be made from simple petrographic or geochemical (SWIR, XRD) analyses. In some cases, more detailed SEM-EDS and EPMA analyses may also be useful to identify zoning and trace-element variations in alunite minerals.

Figure 4.26 emphasizes the importance of the combination of techniques needed to explore successfully for high sulfidation systems. Careful field mapping, with emphasis on alteration assemblages and structural features, can be supplemented by more detailed petrographic and alunite chemical analyses to generate viable drill targets.

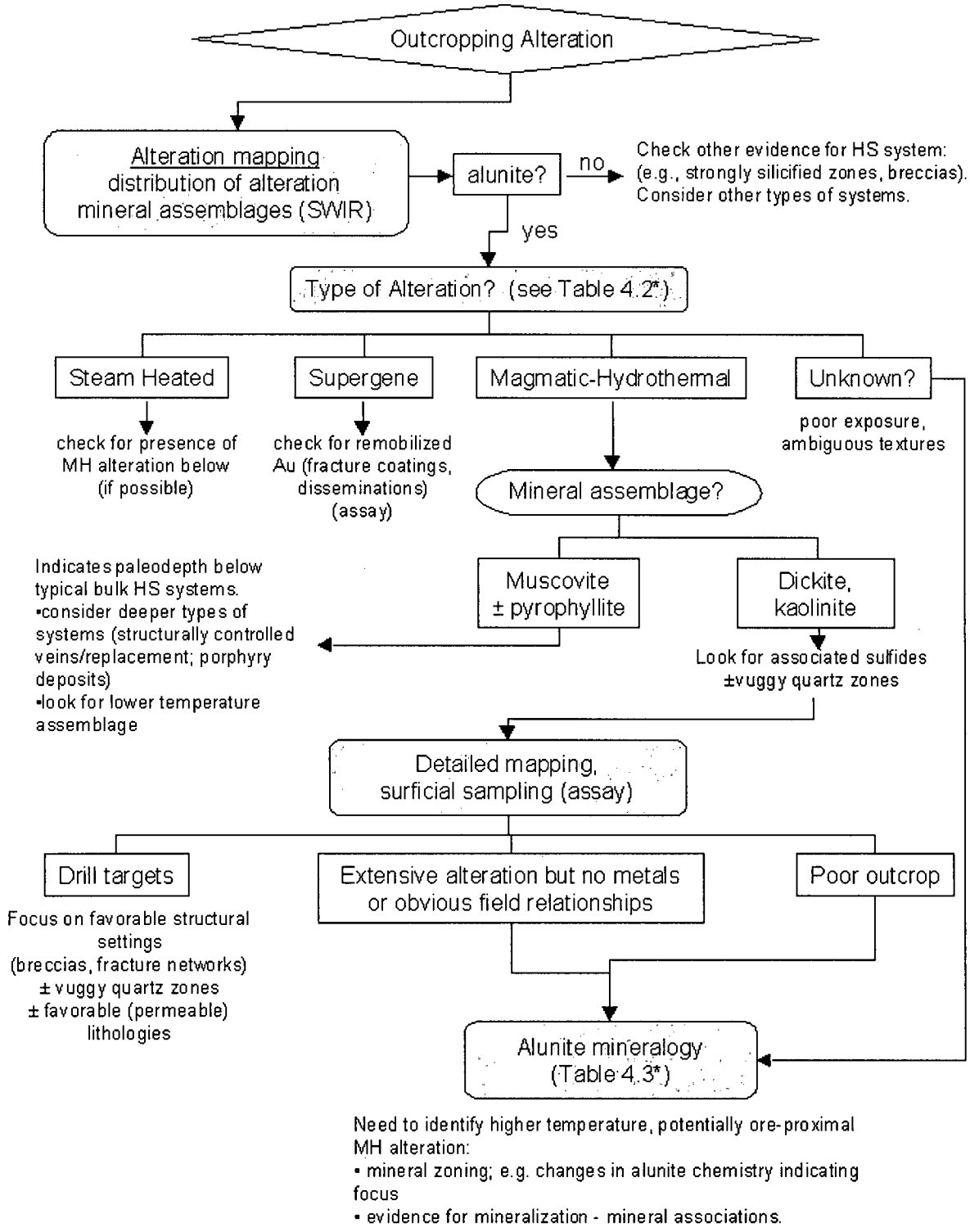

Figure 4.26. Decision-tree illustrating the use of alunite in mineral exploration. *Reference is made to Tables 4.2 and 4.3 that apply specifically to the El Indio-Pascua Belt, but many features may apply to high sulfidation systems in general.

REFERENCES

Alpers, C.N., and Brimful, G.H., 1988. Middle Miocene climatic change in the Atacama Desert, northern Chile: Evidence from supergene mineralization at La Escondida. Geological Society of America Bulletin, 100, 1640-1656.

Aoki, M., 1991. Mineralogical features and genesis of alunite solid solution in high temperature magmatic-hydrothermal systems. Journal of the Geological Survey of Japan, 277, 31-32.

Aoki, M., Comsti, E.C., Lazo, F.B., and Matsuhisa, Y., 1993. Advanced argillic alteration and geochemistry of alunite in an evolving hydrothermal system at Baguio, northern Luzon, Phillipines. Resource Geology, 43, 155-164.

Arehart, G.B. and O'Neil, J.R., 1993. D/H ratios of supergene alunite as an indicator of paleoclimate in continental settings: Climate change in continental isotope records. Geophysics Monographs, 78, 277-284.

Arribas, A., Jr., Cunningham, C.G., Rytuba, J.J., Rye, R.O., Kelly, W.C., McKee, E.H., Podwysocky, M.H., and Tosdal, R.M., 1995. Geology, geochronology, fluid inclusions, and stable-isotope geochemistry of the Rodalquilar Au alunite deposit, Spain. Economic Geology, 90, 795-822.

Beane, R.E., 1988. Hydrothermal alteration and mineralization at the Nevada prospect, Chile. Unpublished company report, Barrick Corp.

Bennet, R.E., 1995. A combined hydrothermal alteration study and exploration target evaluation of the Tambo mining district, El Indio mineral belt, Region IV, Chile. Internal report for Compania Minera San Jose Ltda.

Bethke, P.M., 1984. Controls on base- and precious-metal mineralization in deeper epithermal environments. U.S. Geological Survey Open File Report 84-890, 40 p.

Bird, M.I., Chivas, A.R., and McDougall, I., 1990. An isotopic study of surficial alunite in Australia: 2. Potassium-argon geochronomogy. Chemical Geology, 80, 133-145.

Bissig, T., 2001. Metallogenesis of the Miocene El Indio-Pascua gold-silver-copper belt, Chile/ Argentina: Geodynamic, geomorphological and petrochemical controls on epithermal mineralization. Unpublished Ph.D. thesis, Queen's University, Kingston, Canada.

Bove, D.J., Rye, R.O., and Hon, K., 1990. Evolution of the Red Mountain alunite deposits, Lake City, Colorado. US Geological Survey Open File Report, 90-0235, 29 p.

Cooke, D.R. and Simmons, S.F., 2000. Characterisitcs and genesis of epithermal gold deposits.

In Hagemann, S.G. and Brown, P.E., eds., Gold 2000. Reviews in Economic Geology, vol. 13., 221-244.

Chouinard, A. and Williams-Jones, A.E., 1999. Mineralogy and petrography of ore and alteration assemblages at the Pascua Au-Ag-Cu deposit, Chile. Internal Report for Barrick Gold Corp.

Crowe, D.E., Riciputi, L.R., Bezenek, S., Ignatiev, A., 2001. Oxygen isotope and trace element zoning in hydrothermal garnets: Windows into large-scale fluid-flow behavior. Geology, 29, 479-482.

Cunningham, C.G., Rye, R.O., Bethke, P.M., Logan, M.A.V., 1997. Vein alunite formed by degassing of an epizonal stock. EOS, Transactions 78, F746.

Cunningham, C.G., Rye, R.O., Steven, T.A., and Mehnert, H.H., 1984. Origins and exploration significance of replacement and vein-type alunite deposits in the Marysvale volcanic field, west central Utah. Economic Geology, 79, 50-71.

Dill, H.G., Bosse, H.R., Henning, K.H., Fricke, A., Ahrendt, H., 1997. Mineralogical and chemical variations in hypogene and supergene kaolin deposits in a mobile fold belt; the Central Andes of northwestern Peru. Mineralium Deposita, 32, 149-163.

Ebert, S.W. and Rye, R.O., 1997. Secondary precious metal enrichment by steam-heated fluids in the Crowfoot-Lewis hotspring gold-silver deposit and relation to paleoclimate. Economic Geology, 92, 578-600.

Fournier, 1999. Hydrothermal processes related to movement of fluid from plastic into brittle rock in the magmatic-hydrothermal environment. Economic Geology, 94, 1193-1212.

Flynn, F.R., and Burnham, C.W., 1978. An experimental determination of rare earth partition coefficients between a chloride-containing vapor phase and silicate melts. Geochimica et Cosmochimica Acta, 42, 685-701.

Gallardo, V., 1995. Proyecto Del Carmen; Provincia de San Juan, Argentina. Internal Report for Barrick Gold Corporation.

Gerlach, T.M., and Casadevall, T.M., 1986. Fumarole emissions at Mount St. Helens volcano, June 1980 to October, 1981: Degassing of a magma-hydrothermal system. Journal of Volcanology and Geothermal Research, 28, 141-160.

Hedenquist, J.W, Arribas, A., Jr., and Gonzalez-Urien, E., 2000. Eploration for epithemal gold deposits. *In* Hagemann, S.G. and Brown, P.E., eds., Gold 2000. Reviews in Economic Geology, vol. 13., 245-277.

Hedenquist, J.W., Arribas, Jr., A., and Reynolds, T.J., 1998. Evolution of an intrusion-centered

hydrothermal system: Far Southeast-Lepanto porphyry and epithermal Cu-Au deposits, Phillipines. Economic Geology, 93, 373-404.

Henley, R.W., and McNabb, 1978. Magmatic vapor plumes and ground-water interaction in porphyry copper emplacement. Economic Geology, 73, 1-20.

Hemley, J.J., and Jones, W.R., 1964. Chemical aspects of hydrothermal alteration with emphasis of hydrogen metasomatism. Economic Geology, 59, 538-569.

Hemley, J.J., Hostetler, P.B., Gude, A.J., and Mountjoy, W.T., 1969. Some stability relations of alunite. Economic Geology, 64, 599-612.

Holland, H.D., 1965. Some applications of thermodynamic dta to problems of ore deposits, II. Mineral assemblages and the composition of ore-forming fluids. Economic Geology, 60, 1101-1166.

Jambor, J.L., 1999. Nomenclature of the alunite supergroup. Canadian Mineralogist, 37, 1323-1341.

Jamveit, B., 1999. Crystal growth and intracrystalline zonation pattern in hydrothermal environments. *In* Jamtveit, B. and Meakin, P., eds., Growth, Dissolution and Pattern Formation in Geosystems, 65-84.

Jannas, R.R., Beane, R.E., Ahler, B.A., and Brosnahan, D.R., 1990. Gold and copper mineralization at the El Indio deposit, Chile. Journal of Geochemical Exploration, 36, 233-266.

Jannas, R.R., Bowers, T.S., Petersen, U., Beane, R.E., 1999. High-sulfidation deposit types in the El Indio District, Chile. *In* Skinner, B.J. ed., Geology and ore deposits of the Central Andes, SEG special pub. #7, p.27-59.

Kesler, S.E., Russell, N., Seaward, M., Rivera, J., McCurdy, K, Cumming, G.L., and Sutter, J. F., 1981. Geology and geochemistry of sulfide mineralization underlying the Pueblo Viejo gold-silver oxide depoist, Dominican Republic. Economic Geology, 76, 1096-1117.

Knight, J.E., 1977. A thermochemical study of alunite, enargite, luzonite, and tennantite deposits. Economic Geology, 72, 1321-1336.

Losada-Calderon, A.J., and McPhail, D.C., 1996. Porphyry and high-sulfidation epithermal mineralization iin the Nevados del Famatina Mining District, Argentina. *In* Camus, F., Sillitoe, R.H., and Petersen, R., eds., Andean copper deposits: New discoveries, mineralization, styles, and metallogeny. Society of Economic Geologists Special Publication No. 5, 91-118.

Lottermoser, B.J., 1992. Rare earth elements and hydrothermal ore formation processes. Ore

Geology Reviews, 7, 25-41.

Meyer, C.A. and Hemley, J.J., 1967. Wallrock alteration. *In* Barnes, H.L., ed., Geochemistry of Hydrothermal Ore Deposits. New York, Holt, Rinehart, and Winston, 166-235.

Noriega, J. and Perez, L., 1997. Proyecto Del Carmen - Informe temporada 1997. Internal report for Barrick Gold Corporation.

Perello, J.A., 1994. Geology, porphyry Cu-Au, and epithermal Cu-Au-Ag mineralization of the Tombulilato district, North Sulawesi, Indonesia. Journal of Geochemical Exploration, 50, 221-256.

Petersen, E.U., and Thompson, A.J.B., 1992. Analysis of alunite and other thermally sensitive minerals. Microprobe Analyst (Newsletter for Laboratory for Electron Microprobe Analysis, University of Utah), April 1992. 2-5.

Prieto, M., Feernandez-Gonzalez, A., Putnis, A., and Fernandez-Diaz, L., 1997. Nucleation, growth, and zoning phenomena in cystallizing $(Ba,Sr)CO_3$, $Ba(SO_4,CrO_4)$, $(Ba,Sr)SO_4$, and $(Cd,Ca)CO_3$ solid solutions from aqueous solutions. Geochimica et Cosmochimica Acta, 61, 3383-3397.

Putnis, A., Prieto, M., and Fernandez-Diaz, L., 1995. Fluid supersaturation and crystallization in porous media. Geological Magazine, 132, 1-13.

Reed, M.J., 1995. Distribution of rare earth elements between aqueous fluids and granitic melt. Ph.D. thesis, University of Maryland at College Park.

Ripmeester, J.A., Ratcliffe, C.I., Dutrizac, J.E., and Jambor, J.L., 1986. Hydronium ion in the alunite-jarosite group. Canadian Mineralogist, 24, 435-447.

Rye, R.O., 1993. The evolution of magmatic fluids in the epithermal environment: The stable-isotope perspective. Economic Geology, 88, 733-753.

Rye, R.O., and Alpers, C.N., 1997. The stable-isotope geochemistry of jarosite. USGS Open File Report 97-88., 28 p.

Rye, R.O., Bethke, P.M., and Wasserman, M.D., 1992. The stable-isotope geochemistry of acid sulfate alteration. Economic Geology, 87, 225-262.

Rye, R.O, and Stoffregen, R.E., 1995. Jarosite-water oxygen and hydrogen isotope fractionations: preliminary experimental data. Economic Geology, 90, 2336-2342.

Sandeman, H.A., Archibald, D.A.; Grant, J.W.; Villneuve, M.E. and Ford, F.D., 1999. Characterisation of the chemical composition and ^{40}Ar-^{39}Ar systematics of intralaboratory standard MAC-83 biotite. *In* Radiogenic Age and Isotopic Studies: Report 12; Geological Survey of Canada, Current Research 1999-F, 13-26.

Schwab, R.G., Herold, H, Gotz, C. and de Oliveira, N.P., 1990. Compounds of the crandallite type: Synthesis and properties of pure rare earth element phosphates. Neues Jahrbuch fuer Mineralogie, 6, 241-254.

Schoen, R., White, D.E., and Hemley, J.J., 1974. Argillization by descending acid at Steamboat Springs, Nevada. Clays and Clay Minerals, 22, 1-22.

Siddeley, G. and Areneda, R., 1985. Gold-silver occurences of the El Indio belt, Chile. Geology of the Andes and its relation to mineral and energy resources, symposium, Santiago, Chile, 18 p.

Sillitoe, R.H., 1993. Epithermal models: Genetic types, geometric controls, and shallow features. *In* Kirkham, R.V., Sinclair, W.D., Thorpe, R.I., and Duke, J.M., eds., Mineral Deposit Modelling. Geological Association of Canada, Special paper 40, 403-417.

Sillitoe, R.H., 1999. Styles of high sulfidation gold, silver and copper mineralization in the porphyry and epithermal environments. PacRim '99. Bali, Indonesia, 10-13 October, Proceedings, p. 29-44.

Sillitoe, R.H., McKee, E.H., and Vila T., 1991. Reconnaissance K-Ar geochronology of the Maricunga gold-silver belt, northern Chile. Economic Geology, 86, 1261-1270.

Simmons, S.F., and Brown, P.R.L., 1990. Mineralogic, alteration, and fluid inclusion studies of epithermal gold-bearing veins at the Mt. Muro prospect, central Kalimantan (Borneo), Indonesia: Geology, geochemistry, origin, and exploration. Journal of Geochemical Exploration, 35, 63-104.

Steiger, R. H. and Jäger, E., 1977. Subcommission on geochronology: convention on the use of decay constants in geo- and cosmochronology. Earth and Planetary Science Letters, 36, 359-362.

Stroffregen, R., 1987. Genesis of acid-sulfate alteration and Au-Cu-Ag mineralization at Summitville, Colorado. Economic Geology, 82, 1575-1591.

Stoffregen, R.E. and Alpers, C.N., 1987. Woodhouseite and svanbergite in hydrothermal ore deposits: Products of apatite destruction during advanced argillic alteration. Canadian Mineralogist, 25, 201-211.

Stoffregen, R.E. and Alpers, C.N., 1992. Observations on the unit-cell dimensions, H_2O contents, and δD values of natural and synthetic alunite. American Mineralogist, 77, 1092-1098.

Stoffregen, R.E., Alpers, C.N, and Jambor, J.L., 2000. Alunite-jarosite crystallography, thermodynamics, and geochronology. *In* Alpers, C.N., Jambor, J.L., and Nordstrom, D.K.,

eds., Sulfate Minerals; Crystallography, Geochemistry, and Environmental Significance. Reviews in Mineralogy and Geochemistry, vol. 40, 454-480.

Stoffregen, R.E., and Cygan, G., 1990. An experimental study of Na-K exchange between alunite and aqueous sulfate solutions. American Mineralogist. 75, 209-220.

Stoffregen, R.E., Rye, R.O., and Wasserman, M.D., 1994. Experimental studies of alunite: I. ^{18}O-^{16}O and D-H fractionation factors between alunite and water at 250-450°C. Geochimica et Cosmochimica Acta, 58, 903-916.

Terakado, Y., and Fujitani, T., 1998. Behavior of rare earth elements and other trace elements during interactions between acidic hydrothermal solutions and silicic volcanic rokcs, southwestern Japan. Geochimica et Cosmochimica Acta, 62, 1903-1917.

Thompson, A.J.B, 1992. Alunite compositions and textures: Relationships to precious metal mineralization. *In* New Developments in Lithogeochemistry, Mineral Deposit Research Unit Short Course #8, 20-21 February.

Thompson, A.J.B., Hauff, P.L., and Robitaille, A.J. 1999. Alteration mapping in exploration: Application of short-wave infrared (SWIR) spectroscopy. Society of Economic Geologists Newsletter, 39, , October 1999.

Vasconcelos, P.M., 1999. $^{40}Ar/^{39}Ar$ geochronology of supergene processes in ore deposits. *In* Lambert, D.D., Ruiz, J., eds., Application of radiogenic Isotopes to Ore Deposits Research and Exploration. Reviews in Economic Geology vol 12, 73-113.

Vasconcelos, P.M., Brimhall, G.H., Becker, T.M., and Renne, P.R., 1994. $^{40}Ar/^{39}Ar$ analysis of supergene jarosite and alunite: Implications to the paleoweathering history of the western USA and West Africa. Geochimica et Cosmochimica Acta, 58, 401-420.

Wasserman, M.D., Rye, R.O., Bethke, P.M., and Arribas, Jr., A., 1992. Methods for separation and total stable-isotope analysis of alunite. Open file report 92-9, US Department of the Interior, Geological Survey.

Wood, S.A., 1990. The aqueous geochemistry of the rare-earth elements and yttrium 1. Review of available low-temperature data for inorganic complexes and the inorganic REE speciation of natural waters. Chemical Geology, 82, 159-186.

Chapter 5

ALUNITE–NATROALUNITE STABILITY RELATIONS

INTRODUCTION

Acid-sulfate alteration is defined as the assemblage alunite, quartz ± clays (kaolinite, dickite, pyrophyllite) and pyrite (Hemley and Jones, 1964; Meyer and Hemley, 1967). Empirical evidence and thermodynamic models indicate that acid-sulfate alteration forms under conditions of low pH and highly oxidized fluid chemistry (Holland, 1965; Henley and McNabb, 1978; Stoffregen, 1987), but experimental data on the relation of alunite and alunite-group minerals to other alteration minerals is limited. The only data available on stability relations for minerals in the K_2O-Al_2O_3-SiO_2-H_2O-SO_3 system are provided by Hemley et al. (1969), who examined reactions between alunite, kaolinite/pyrophyllite, muscovite, and K-feldspar.

Likewise, little information is available regarding occurrences of natroalunite and the nature of the alunite-natroalunite solid-solution. The substitution of Na^+ for K^+ is the most common substitution in natural alunite (Stoffregen et al., 2000) and the temperature dependence of this reaction is of particular interest in mineral exploration. Recent studies (e.g., Aoki, 1991; Aoki et al., 1993; Thompson, 1992; Arribas et al., 1995) suggest that higher Na contents are characteristic of higher temperature environments of formation, and thus may indicate ore-proximal alteration zones. Alunite from lower temperature environments has been reported to have more K-rich compositions (e.g., Arribas et al., 1995; A.J.B. Thompson, unpub. data), although few studies suggest that a range of K- and Na-rich compositions can occur (e.g., Stoffregen and Alpers, 1992; Zotov, 1971; Reyes, 1990). Experimental data for the alunite-natroalunite solid-solution is only available from Stoffregen and Cygan (1990), who developed a mixing model for the alunite-natroalunite alkali exchange reaction at 250° to 450°C. Their data are consistent with observations that higher Na contents are favored at higher temperatures. However, many other factors are likely to affect K/Na substitution in naturally occurring alunite, including host-rock composition and nature of source fluids, the latter of which has not been addressed to date.

Based on the scarcity of information available regarding equilibrium relations of alunite, natroalunite, and associated alteration minerals, the goals of this chapter are:

1. To compare the stability relations of alunite and natroalunite with associated alteration minerals in the K_2O/Na_2O-Al_2O_3-SiO_2-SO_3-H_2O systems. This comparison also provides a means to evaluate the experimental results and thermodynamic calculations of Hemley et al. (1969) in light of more recent thermodynamic data.
2. To predict the effect of fluid composition, and K/Na fluid ratios in particular, on the composition of the alunite-natroalunite solid-solution.

The range of alunite-natroalunite solid-solution in the El Indio–Pascua Belt, and controls on Na substitution, are also discussed.

STABILITY RELATIONS IN THE K_2O/Na_2O-Al_2O_3-SiO_2-H_2O-SO_3 SYSTEM

The stability relations of alunite and associated alteration minerals (kaolinite, pyrophyllite, muscovite, and K-feldspar) were first examined experimentally by Hemley et al. (1969). These experiments were conducted only for the K_2O-Al_2O_3-SiO_2-H_2O-SO_3 system at 200°, 300 °, and 380 °C and 15,000 psi total pressure. Experimental results were expressed in terms of molar concentrations of H_2SO_4 and K_2SO_4 and were transformed into activity–activity plots on the basis of dissociation calculations (Hemley et al., 1969). Invariant points for the reactions were also evaluated independently of the experimental results using thermodynamic data for all phases. Thermodynamic properties (see Table 3 in Hemley et al., 1969) for most minerals were evaluated by Hemley et al. (1969) using high-temperature thermodynamic data from Robie and Waldbaum (1968) or by extrapolating low-temperature data according to the heat-capacity method of Criss and Cobble (1964). Standard free-energy data for alunite were calculated from the experiments of Shomate et al. (1946).

The calculated invariant points of Hemley et al. (1969) did not agree with their experimental results. However, more recent thermodynamic data are now available for several minerals in the K_2O-Al_2O_3-SiO_2-H_2O-SO_3 system (Helgeson et al., 1978). These data, and data for all Na-equivalent minerals, are used to construct updated activity–activity diagrams and to compare the equilibrium conditions of formation for alunite- and natroalunite-bearing acid-sulfate assemblages.

Methods and Results:

Balanced reactions among minerals in the K_2O-Al_2O_3-SiO_2-H_2O-SO_3 system (i.e. alunite, kaolinite, pyrophyllite, muscovite, and K-feldspar) are given in Appendix D. Equations involving natroalunite and all of the Na analogues of the K mineals were also determined (Appendix D). Standard molal Gibbs free energies for each reaction were calculated using SUPCRT92, a software package which permits the calculation of thermodynamic properties for minerals, gases, aqueous species, and reactions at specified P and T conditions (Johnson et al., 1992). The SUPCRT92 thermodynamic database was modified to include data for natroalunite from Stoffregen and Cygan (1990). All reactions were determined at 200°, 300 ° and 380 °C, and 1000 bars in the presence of quartz. These P–T conditions were chosen to allow comparison with the experiments of Hemley et al. (1969). Mineral stability fields at various P–T conditions were determined by plotting $\log(aX^+)^2(aSO_4)$ versus $\log(aH^+)^2(aSO_4)$, where X = either K or Na (Hemley et al., 1969; Stoffregen, 1987), and aSO_4 is the thermodynamic activity of SO_4 in fluid (and likewise for all other species).

Activity diagrams calculated for the system K_2O-Al_2O_3-SiO_2-H_2O-SO_3 are shown in Figure 5.1. These plots indicate that:

- Alunite is stable at increasingly higher pH values with increasing temperature, at fixed a_{SO4}.
- The activity of K^+ required at equilibrium among alunite, muscovite, and kaolinite decreases with increasing temperature (at fixed a_{SO4}).
- With increasing temperature, the stability field of muscovite shrinks relative to those of kaolinite and K-feldspar.
- Equilibrium relations are relatively insensitive to pressure (Fig. 5.2), within the range of epithermal conditions. Changes in pressure (at this scale) affect only the absolute position, but not the relations of the stability fields.

Activity diagrams calculated for the system Na_2O-Al_2O_3-SiO_2-H_2O-SO_3 are shown in Figure 5.3. These plots indicate that:

- The effects of temperature and pressure in the Na_2O and K_2O systems are similar. Natroalunite is also stable at increasingly higher pH values and lower Na activities with increasing temperature, at fixed a_{SO4}.

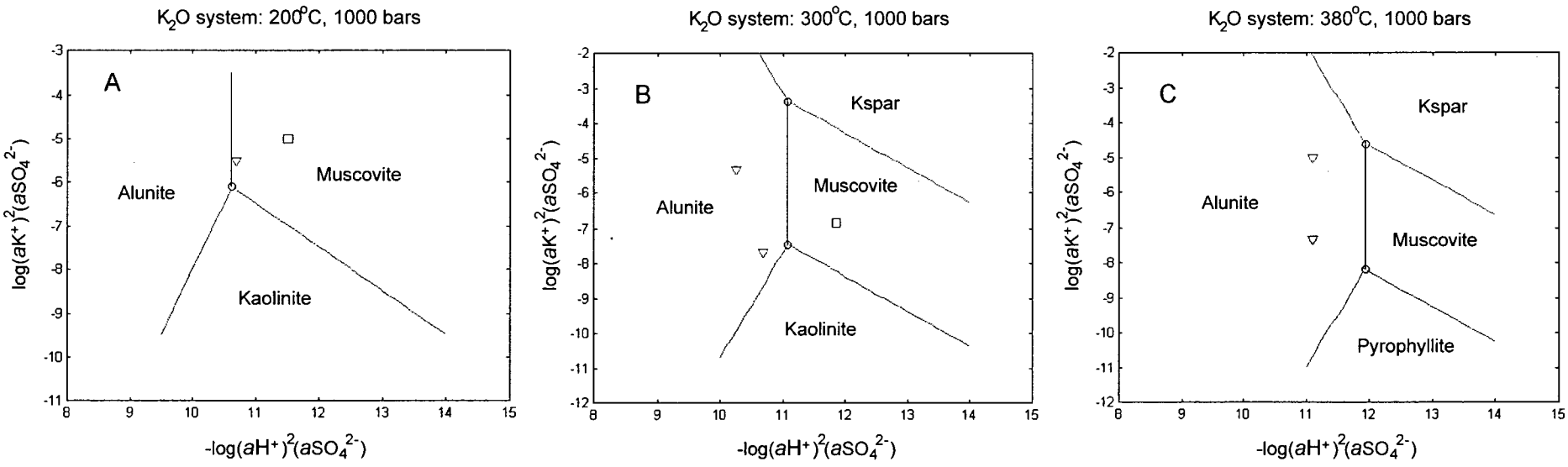

Figure 5.1. Calculated stability diagrams for the system K_2O-Al_2O_3-SiO_2-H_2O-SO_3 at (a) 200°, (b) 300° and (c) 380 °C, and 1000 bars. □ = thermodynamic triple point calculated by Hemley et al. (1969). Calculations above 300°C not possible because high temperature data for pyrophyllite was not available. ∇= equilibrium triple point based on dissociation constants from Hemley et al. (1969).

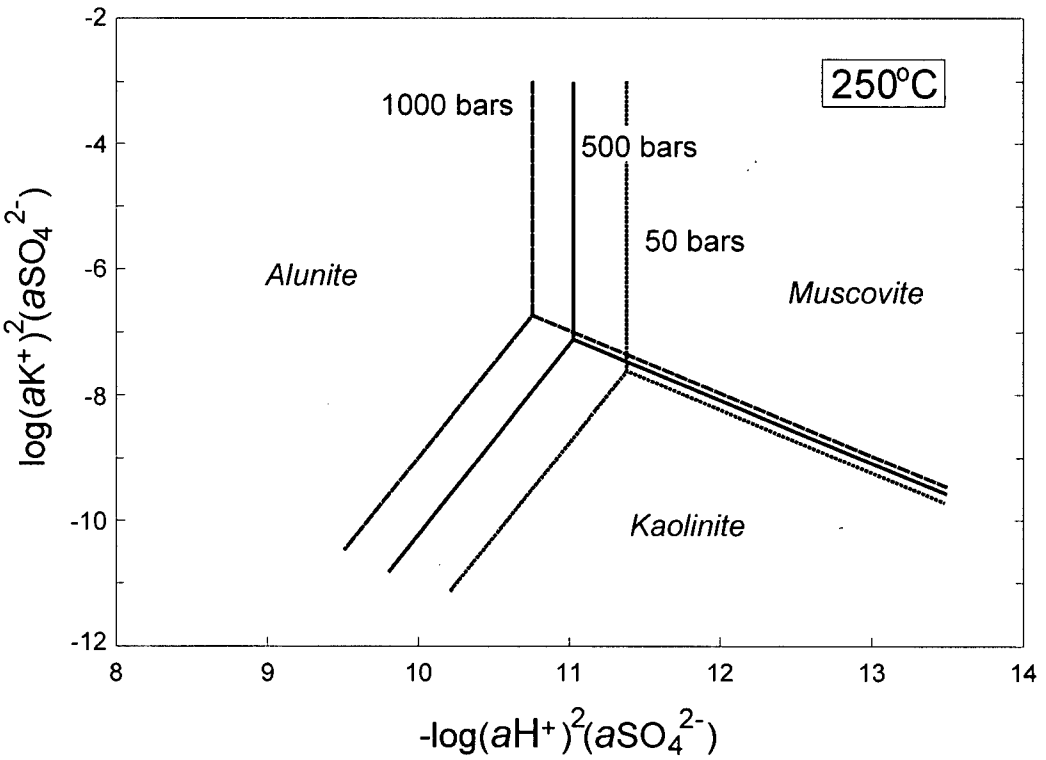

Figure 5.2. Effect of pressure on the stability of alunite relative to kaolinite and muscovite in the system K_2O-Al_2O_3-SiO_2-H_2O-SO_3..

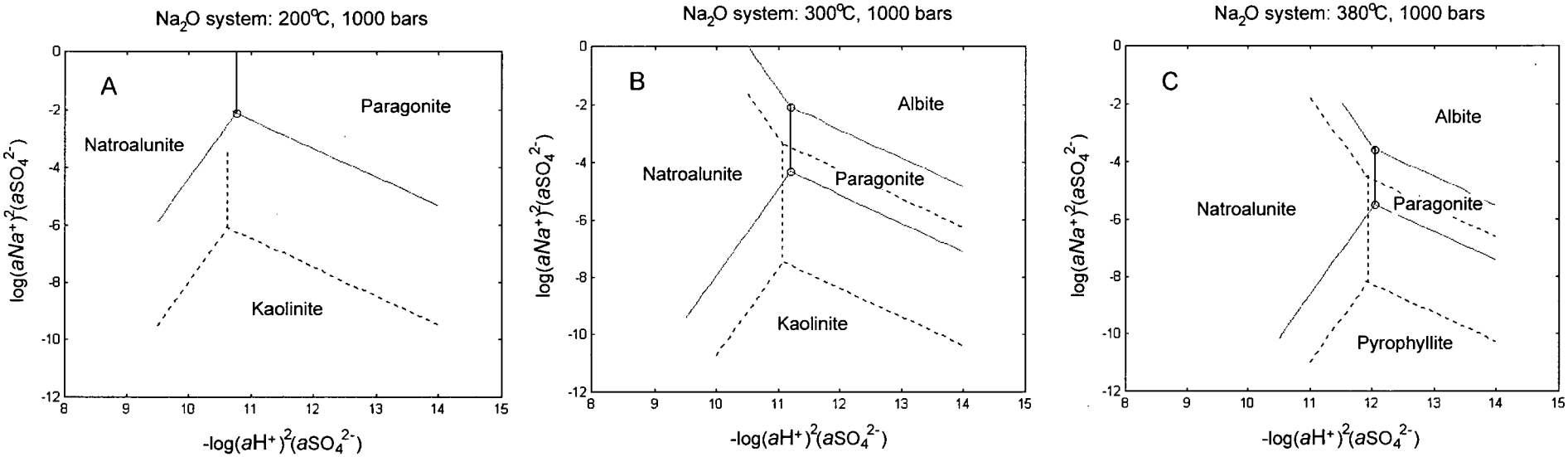

Figure 5.3. Calculated stability diagrams for the system Na_2O-Al_2O_3-SiO_2-H_2O-SO_3 at (a) 200°, (b) 300° and (c) 380 °C, and 1000 bars. Dashed lines represent equivalent boundaries in the K_2O system.

- Significantly higher aqueous Na^+ activity is required for equilibrium between natroalunite and kaolinite/pyrophyllite than for K^+ activity in the equivalent K_2O system (at fixed a_{SO4}). Slightly higher pH values are also required at equilibrium.

Paragonite is uncommon in natural systems and to our knowledge, has not been reported to occur in high sulfidation environments. A much more accurate representation of Na-bearing acid sulfate alteration is the assemblage natroalunite + kaolinite/pyrophyllite + muscovite/illite. We can approximate this assemblage in the K_2O-Al_2O_3-SiO_2-H_2O-SO_3 system by using the mixing model of Stoffregen and Cygan (1990) for the alunite-natroalunite solid-solution. The activity of various alunite compositions (ranging from $X_{Kaln,aln}$ = 0.2 to 1.0, where X is the mole fraction of alunite in alunite–natroalunite solid-solution: Appendix D) can be calculated to illustrate the effects of partial Na-substitution in alunite relative to other alteration phases (Fig. 5.4). As shown, increasing the Na content of alunite expands its stability field relative to kaolinite/pyrophyllite. Equilibrium among these minerals occurs at lower aqueous K^+ concentrations, as expected, and slightly higher pH values at all temperatures studied (assuming constant a_{SO4}) . The magnitude of this change is typically small (about 1 to 1.5 log units K_2SO_4) and appears to be greatest at intermediate temperatures (i.e., 350°C).

Interpretation of Results:

- In this study, the thermodynamic equilibria calculated on the basis of data in Helgeson et al. (1978) and Stoffregen and Cygan (1990) are much closer to the dissociation-constant triple points than the thermodynamic calculations of Hemley et al. (1969). Our calculations of the alunite-kaolinite-muscovite invariant point are within 0.5 log units of experimental H_2SO_4 and K_2SO_4 results at 200° and 300°C. The difference is slightly greater at 380°C (up to 1 log unit). Recent thermodynamic data cannot be compared directly to the experimental results of Hemley et al. (1969) without further determination of dissociation effects for K^+ and H^+ aqueous species.
- The pressure conditions (1000 bars) used in these activity models are higher than expected for alteration in most areas of the El Indio Belt, and for many high sulfidation systems in general. However, we have shown that phase relations are relatively insensitive to pressure, which is consistent with the experimental results of Hemley et al. (1969). General relations

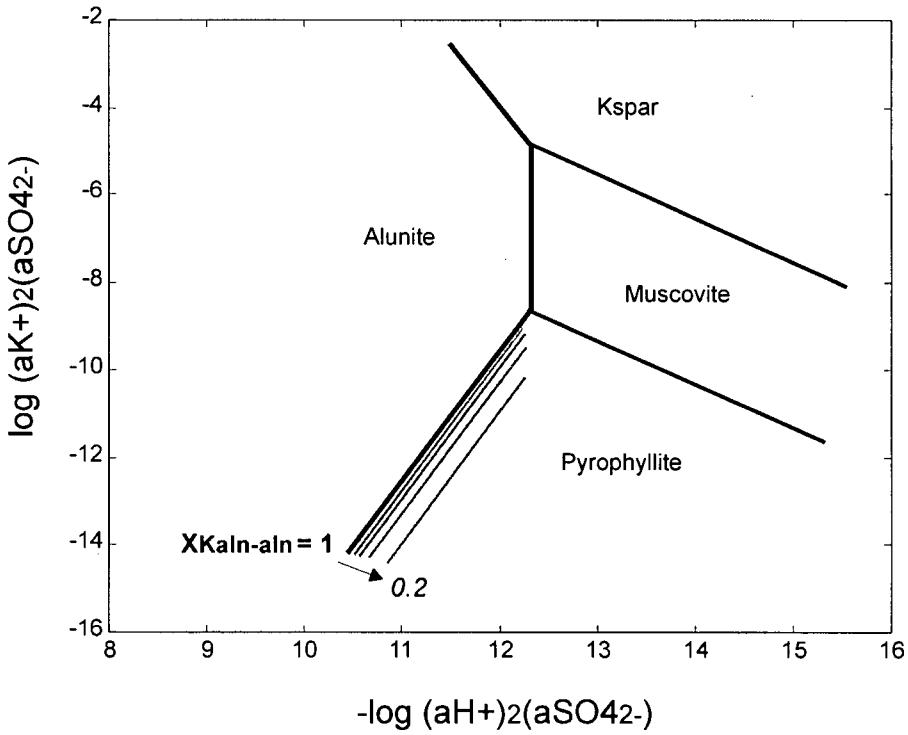

Figure 5.4. Effect of variable alunite Na substitution on the K_2O-AL_2O_3-SIO_2-H_2O-SO_3 system. Dashed lines represent $X_{Kaln\text{-}aln}$ = 1.0, 0.8, 0.6, 0.4, and 0.2.

illustrated here can therefore be applied to high sulfidation environments, regardless of P of formation.

- Activity–activity diagrams indicate that both end-member alunite and natroalunite (and various intermediate compositions) are stable relative to kaolinite/pyrophyllite and micas at temperatures typical of acid-sulfate alteration (about 200-350°C). At constant sulfate concentrations, the natroalunite-kaolinite (or pyrophyllite) assemblage is stable to higher pH values than potassium equivalents.
- The assemblages alunite/natroalunite + kaolinite (or pyrophyllite) and alunite/natroalunite + kaolinite + muscovite (or illite) are common in naturally occurring systems. Muscovite (or illite) are rarely observed in the El Indio Belt but are present elsewhere, particularly in the roots of some magmatic-hydrothermal systems (e.g., Hedenquist et al., 2000; Sillitoe, 1999). The shrinkage of the mica field at high temperatures (Figs 5.1 and 5.3) suggests that small changes in H^+ and a_{K+} would be sufficient to move from an assemblage containing pyrophyllite to one containing K-feldspar. This may explain why sericite is relatively rare in high sulfidation systems, and the El Indio Belt in particular. Detailed short-wave infrared (SWIR) analyses at Pascua, for example, have shown that advanced argillic and acid-sulfate assemblages can occur directly adjacent to relatively fresh, K-feldspar bearing granites, without an intermediate sericitic or illitic alteration zone.
- To our knowledge, an equilibrium assemblage of alunite + K-feldspar or alunite + K-feldspar + muscovite has not been reported in naturally occurring systems. This apparent absence suggests that the elevated K_2SO_4 concentrations required to stabilize such assemblages are rarely, if ever, obtained in nature (Hemley et al., 1969).
- The metastable formation of alunite must also be considered in natural systems. As noted by Hemley et al. (1969), the rate of crystallization of silicate minerals at low temperatures is much slower relative to sulfate minerals. It is therefore possible that alunite–natroalunite could form from the breakdown of feldspathic rocks under conditions that would otherwise produce K-mica or kaolinite, if equilibrium were established. Also, disequilibrium acid-sulfate assemblages in high sulfidation deposits are likely, due to the overprinting or telescoping of different alteration assemblages. In the El Indio Belt in particular, late-stage (lower temperature) alteration commonly overprints higher temperature assemblages. This overprint can lead to complex phase relations that do not represent equilibrium conditions.

EFFECTS OF FLUID COMPOSITION ON THE ALUNITE–NATROALUNITE SOLID-SOLUTION

Thermodynamic data for natroalunite (Table 5.1) were determined from the alkali-exchange experiments of Stoffregen and Cygan (1990), who examined the reaction:

$$KAl_3(SO_4)_2(OH)_6 + Na^+ = NaAl_3(SO_4)_2(OH)_6 + K^+ \qquad (5.1)$$

The distribution coefficient (K_d) for reaction (5.1) is defined as:

$$K_d = \left[\frac{X_{Na+}/X_{K+}}{m_{Na+}/m_{K+}} \right]$$

where X_{Na} indicates the mole fraction of Na in the solid, and m is the molality in aqueous solution. Experimentally determined values of $\ln K_d$ and X_{Na} were fit by Stoffregen and Cygan (1990) using a subregular Margules model, in order to describe the nonlinear variations in their data. Results from their study indicate that natroalunite is favoured at higher temperatures, because the equilibrium constant for reaction 5.1 decreases with decreasing temperature.

Table 5.1. Estimated thermodynamic properties of natroalunite at 25°C and 1 bar (Stoffregen and Cygan, 1990).

ΔG_f	-4622.40 ± 1.91 kJ·mol^{-1}
ΔH_f	-5131.97 kJ·mol^{-1}
S	321.08 J·K·mol^{-1}
V	141.15 cm^3·mol^{-1}
C_p (a)	641.5 J·K^{-1}·mol^{-1}
C_p (b)	-7.87×10^{-3} J·K^{-2}·mol^{-1}
C_p (c)	-234.12×10^5 J·K·mol^{-1}

The mixing model developed by Stoffregen and Cygan (1990) can also be used to examine the effect of fluid composition, particularly K/Na contents of a source fluid, on the composition of alunite-natroalunite solid-solution. Using reaction 5.1, the activity of both alunite and natroalunite can be modeled against variable fluid compositions assuming either:

(a) Ideal solid-solution - This is the simplest model and nearly fits data from Stoffregen and Alpers (1992) on unit-cell dimensions for samples on the alunite-natroalunite binary.

(b) Non-ideal solid-solution - This model is most consistent with the findings of Stoffregen and Cygan (1990).

Both models require calculating log K for reaction 5.1 knowing that:

$$K_{5.1} = \frac{[a_{\text{Naln, aln}}][a_{K+,fl}]}{[a_{\text{Kaln, aln}}][a_{Na+,fl}]}$$

Where $a_{\text{Naln,aln}}$ = activity of natroalunite in the solid phase,

$a_{\text{Kaln,aln}}$ = activity of alunite in the solid phase,

$a_{\text{K+ fl}}$ = activity of K^+ in the fluid phase,

$a_{\text{Na+ fl}}$ = activity of Na^+ in the fluid phase.

Re-arranging this expression gives:

$$K_{5.1} = \left[\frac{a_{Naln}}{a_{\text{Kaln}}}\right]_{\text{aln}}\left[\frac{a_{K+}}{a_{Na+}}\right]_{fl} \tag{5.3}$$

The value of K is fixed and calculable at various P and T conditions. All reactions in this study were calculated for 500 and 1000 bars pressure, and for temperatures ranging from 25° to 450°C, using SUPCRT92 (Johnson et al., 1992).

a) Ideal Solid-solution

In an ideal solution: $a_{\text{Kaln,aln}} = X_{\text{Kaln,aln}}$ and $a_{\text{Kaln,aln}} = 1 - a_{\text{Naln,aln}}$ (e.g., Nordstrom and Munoz, 1985). Rearranging equation 5.3 gives:

$$\left(\frac{a_{K+}}{a_{Na+}}\right)_{fl} = \frac{K_{5.1}}{a_{\text{Naln,aln}}} - K_{5.1} \tag{5.4}$$

Equation 5.4 can be determined over a range of $X_{\text{Kaln,aln}}$ = 0.1 to 0.9 and plotted against temperature (Fig. 5.5a). Pressure has a minimal effect on the behavior of the solid-solution, as illustrated in Figure 5.5b.

b) Non-ideal Solid-solution

The activity of a phase in asymmetric (sub-regular) binary solid-solutions can be calculated from measured Margules parameters (e.g., Anderson and Crerar, 1993):

$$RT \ln \gamma_1 = (2W_{G2} - W_{G1})X_2^{\,2} + 2(W_{G1} - W_{G2})X_2^{\,3} \tag{5.5}$$

and,

$$a_i^{P,T} = X_i^{P,T} * \gamma_i^{P,T} \tag{5.6}$$

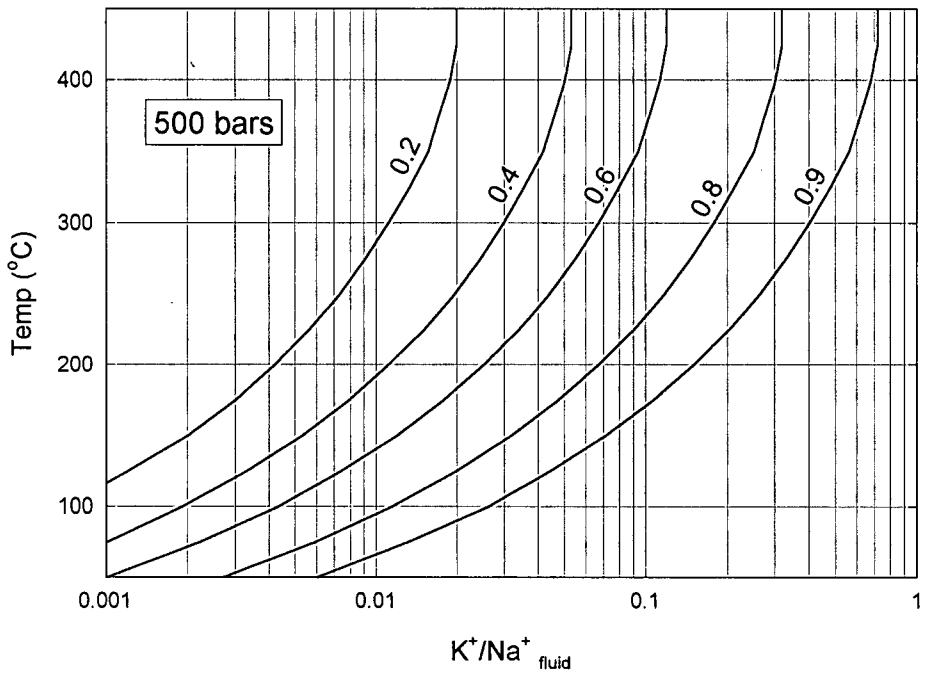

Figure 5.5a. Model fluid/composition curves for an ideal alunite-natroalunite solid solution at 500 bars pressure. Lines represent molar fraction of alunite (i.e., $X_{Kaln\text{-}aln}$).

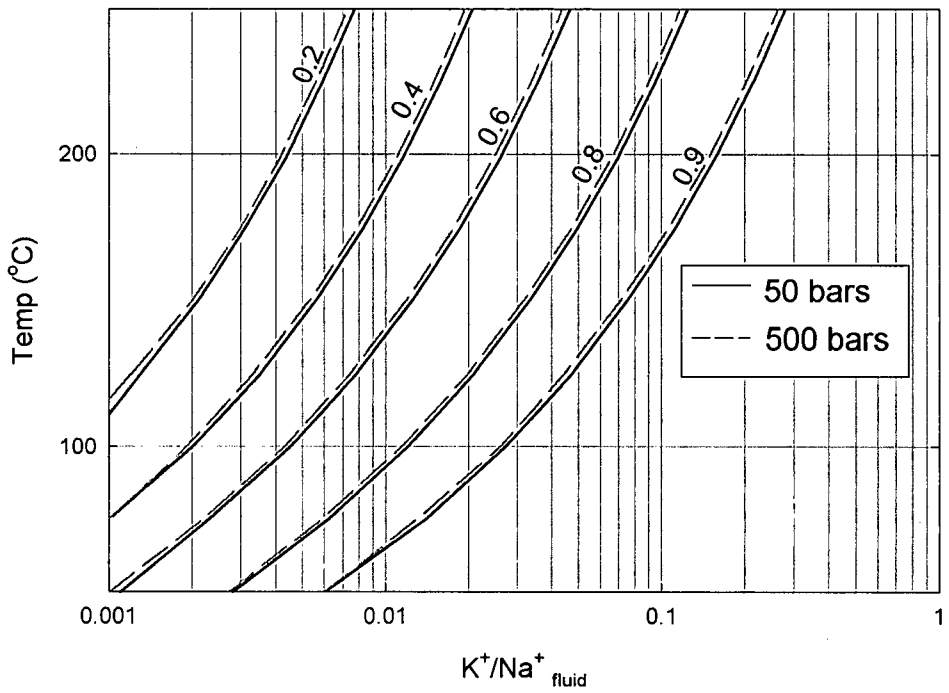

Figure 5.5b. Model fluid/composition curves for an ideal alunite-natroalunite solid solution at variable pressure. Lines represent molar fraction of alunite (i.e., $X_{Kaln\text{-}aln}$).

where W_G = Margules term for phases 1 or 2

γ_1 = activity coefficient for phase 1

For the purposes of this study, phases 1 and 2 are alunite and natroalunite, respectively.

Mixing parameters (W_G) were determined by Stoffregen and Cygan (1990) for alunite and natroalunite at 250°C, 500 bars; 350°C, 500 bars; and 450°C, 1000 bars (Table 5.2).

Table 5.2. Estimates of ln $K_{(5.1)}$ and Margules parameters for alunite-natroalunite mixing reaction from Stoffregen and Cygan (1990). 1σ error estimates given in parentheses.

	ln $K_{(5.1)}$	$W_{G,Na}$ ($J \cdot mol^{-1}$)	$W_{G,K}$ ($J \cdot mol^{-1}$)
450°C, 1000 bars	-0.99 (0.05)	1837 (427)	3159 (435)
350°C, 500 bars	-1.73 (0.26)	2867 (1050)	4785 (1229)
250°C, 500 bars	-2.56 (0.42)	4668 (2091)	6443 (4836)

Equations for the variation of $W_{G,Na}$ and $W_{G,K}$ with temperature (e.g., Essene, 1982) were generated based on a least-squares regression (Appendix D). Using these estimates for $W_{G,Na}$ and $W_{G,K}$ in equations 5.5 and 5.6, activity values for both alunite and natroalunite were calculated for a range of solid-solution compositions ($X_{Kaln,aln}$ = 0.1 to 0.9 at 500 and 1000 bars, and 100° to 450 °C : Appendix D).

Calculated activity values for alunite and natroalunite are input into equation 5.3, which can be re-arranged as:

$$\left(\frac{a_{K+}}{a_{Na+}}\right)_{fl} = K_{5.1}\left[\frac{a_{Kaln,aln}}{a_{Naln,aln}}\right] \qquad (5.7)$$

Plotting equation 5.7 at variable temperatures shows the combined effects of temperature and K^+/Na^+ fluid activity on the composition of alunite-natroalunite solid-solution (Fig. 5.6). These ionic species (K^+ and Na^+) will dominate at lower temperatures in the magmatic-hydrothermal environment (region I, Fig. 5.7), but complexes of Cl may be significant at higher temperatures (region III, Fig. 5.7). We can represent these higher temperature conditions using $KCl^o/NaCl^o$ species as follows:

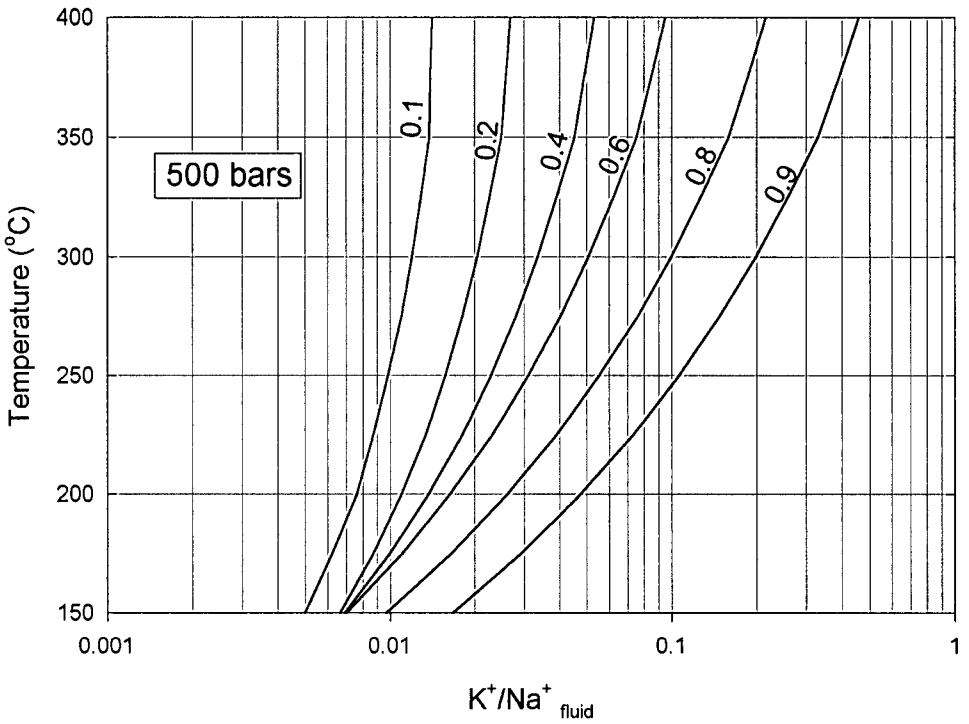

Figure 5.6. Effect of temperature and fluid K^+/Na^+ fluid composition on a non-ideal alunite-natroalunite solid solution, 500 bars. Lines represent molar fraction of alunite (i.e. $X_{Kaln,aln}$).

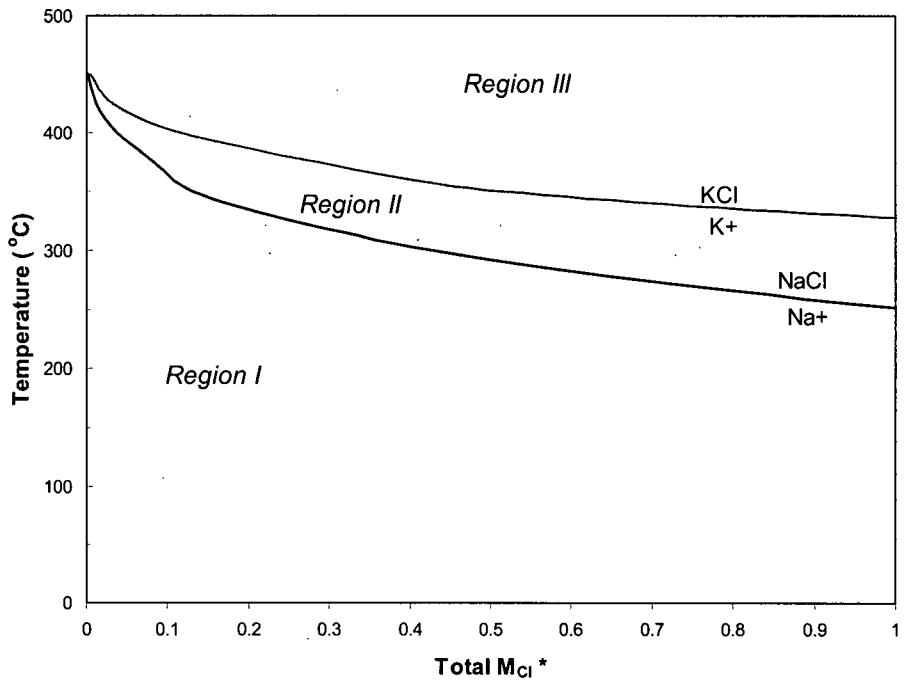

Figure 5.7. Dominance fields for K/Na species, based on equilibrium calculations (see Appendix D for details. Region I = K^+ and Na^+; Region II = K^+ and $NaCl^o$; Region III = KCl^o and $NaCl^o$.

$$K^+ + NaCl^o = Na^+ + KCl^o \qquad (5.8)$$

Knowing $\log K_{5.8} = \log\left(\frac{a_{Na+}}{a_{K+}}\right) + \log\left(\frac{a_{KCl}}{a_{NaCl}}\right)$

Re-arranging this equation gives:

$$\log\left(\frac{a_{KCl}}{a_{NaCl}}\right) = \log K_{5.8} - \log\left(\frac{a_{Na+}}{a_{K+}}\right) \qquad (5.9)$$

Log K for reaction 5.8 can be calculated at P,T using K^+/Na^+ activities calculated previously (reaction 5.7). Reaction 5.9 can be plotted in the same manner as the previous reactions (Fig. 5.8).

At intermediate temperatures (region II; Fig. 5.7), neither paired ionic species nor complexes of Cl are predominant. Instead, NaCl predominates over Na^+, but K^+ predominates over KCl. In this temperature range, therefore there is need to consider the reaction:

$$KAl_3(SO_4)_2(OH)_6\ K + NaCl = NaAl_3(SO_4)_2(OH)_6 + K^+ + Cl^- \qquad (5.10)$$

To plot this reaction, assumptions must be made concerning the activity of Cl^- in solution. However, under conditions typical of high sulfidation systems (i.e., total salinity less than about 0.5 M), this region is relatively small and will not be considered further.

Discussion:

- The calculations indicate that the alunite-natroalunite solid-solution is relatively insensitive to change in pressure. Varying the pressure from 500 to 1000 bars shifts equilibrium temperature determinations by less than ±10°C and fluid ratios by less than 0.1 log units K/Na, in both the ideal and non-ideal solid-solution models. These errors are likely smaller than the uncertainty in the thermodynamic calculations.
- The alunite-natroalunite solid-solution approaches calculated ideal behavior at high temperatures (e.g., above about 400°C). At low temperatures, large differences are observed between the ideal and non-ideal models (Figs 5.5 and 5.6). The latter consistently predicts higher Na contents in alunite formed at constant temperature and fluid K^+/Na^+ activities.

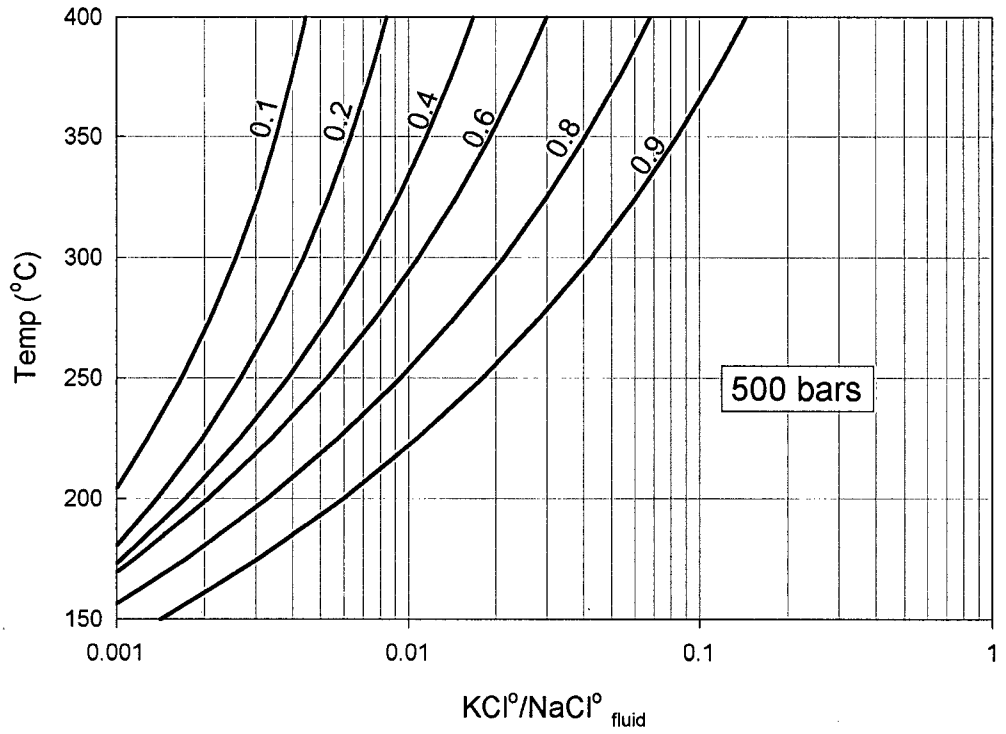

Figure 5.8. Effect of temperature and fluid KCl/NaCl fluid composition on a non-ideal alunite-natroalunite solid solution, 500 bars. Lines represent molar fraction of alunite (i.e. $X_{Kaln,aln}$).

- Overall, higher temperatures favor greater substitution of Na in alunite under both ideal and non-ideal conditions, at constant fluid K/Na ratios. This increase is consistent with the experimental results of Stoffregen and Cygan (1990) and is consistent with empirical observations of several magmatic-hydrothermal systems (e.g., Aoki, 1991; Thompson, 1992; Stoffregen et al., 2000 and references therein).

- At low to intermediate temperatures (i.e. 150-225°C), the non-ideal solid-solution model (Fig. 5.6) predicts that a large range of equilibrium alunite compositions ($X_{Kaln-aln}$ = about 0.2 to 0.6) can form from a very narrow range of fluid compositions. However, at higher temperatures, our model predicts that more than an order of magnitude change in K/Na fluid content is required to precipitate both alunite and natroalunite end-member compositions, at equilibrium. This suggests that small-scale zoning between end-member alunite-natroalunite compositions at high temperature is unlikely the result of changes in compositions of the bulk fluid (*see further discussion below*).

- The calculations indicate that low K/Na fluid ratios are required for significant Na-substitution in alunite at all temperatures (at equilibrium). For example, at temperatures typical of magmatic-hydrothermal alteration (e.g., 200-350°C), fluid K/Na activities <0.01 are required to form nearly pure natroalunite (Figs. 5.6 and 5.8). Geochemical data for K/Na in active volcanic systems (e.g., fumaroles, volcanic gas condensates) are scarce, but a few studies suggest that molar K/Na ratios range between 0.1 to 0.8 (Reed, 1997; Giggenbach, 1997; Symonds et al., 1990). This range is well within a field for nearly pure alunite, according to our models. These conditions are consistent with the formation of nearly pure magmatic steam alunite but magmatic-hydrothermal alunite typically show a much greater degree of compositional variability (this study; Rye, 1993; Stoffregen et al, 2000). This suggests that the chemistry of alteration minerals is affected by factors other than simply equilibrium temperature and fluid composition. This is not surprising, given the dynamic nature of the magmatic-hydrothermal environment and the complexity of magma-fluid-rock interactions.

CONTROLS ON ALUNITE-NATROALUNITE COMPOSITIONS IN THE EL INDIO-PASCUA BELT

The compositional variability of alunite and alunite-group minerals in the El Indio-Pascua Belt has been described in previous chapters. Alunite K/Na ratios are of interest in this region because of their potential use as an indicator for higher temperature (e.g., magmatic-hydrothermal) alteration that is directly associated with Au ± Cu, Ag mineralization at several deposits and prospects, including Pascua-Lama, Tambo, El Indio, and Del Carmen. The effects of depositional temperature on the composition of the alunite–natroalunite solid-solution in the El Indio-Pascua Belt are discussed below. The influence of fluid composition on alunite mineral chemistry is also addressed.

Depositional Temperature

Geochemical data for alunite-group minerals from this study indicate that higher depositional temperatures favor a greater range of Na-substitution. Electron microprobe (EPMA) data (Fig. 5.9) show that magmatic-hydrothermal alunite has a much larger range in Na substitution (Fig. 5.9), and nearly twice the average Na content (0.17 m.p.f.u.), than steam-heated (averaging 0.07 m.p.f.u. Na) or late-stage and supergene alteration (0.09 m.p.f.u. Na). Estimated temperatures of deposition for magmatic-hydrothermal alunite range from about 140° to 380°C, compared with lower-temperature steam-heated (*ca.* 90-180°C), and late stage alteration (*ca.* 60-150°C), on the basis of stable isotope, fluid inclusion, and paragenetic evidence (Chapters 2 and 3). Differences in K:Na contents are likely exaggerated by the larger data-set for higher temperature occurrences; quantitative data for low-temperature alunite are limited by the small grain size of most samples. However, these differences are statistically significant at a 95% confidence level, based on t-test results (Appendix A). EPMA data are also supplemented by qualitative SEM-EDS analyses of more than 125 polished thin sections and individual grain mounts that have shown similar trends.

Geochemical data provide further evidence for two stages of magmatic-hydrothermal alteration (AS I and AS II; details see Chapter 2) at the Pascua deposit. A correlation between alunite Na content and increasing depth (and by inference, temperature) is evident for AS II alteration (Fig. 5.10) that occurs in banded alunite-sulfide veins and in the matrix of mineralized breccias. An earlier stage of acid sulfate alteration minerals (AS I) occurs as aggregates and disseminations in wallrock over a large areal extent. The distribution of AS I alteration is irregular and strongly structurally controlled, and there is no consistent relation between alunite

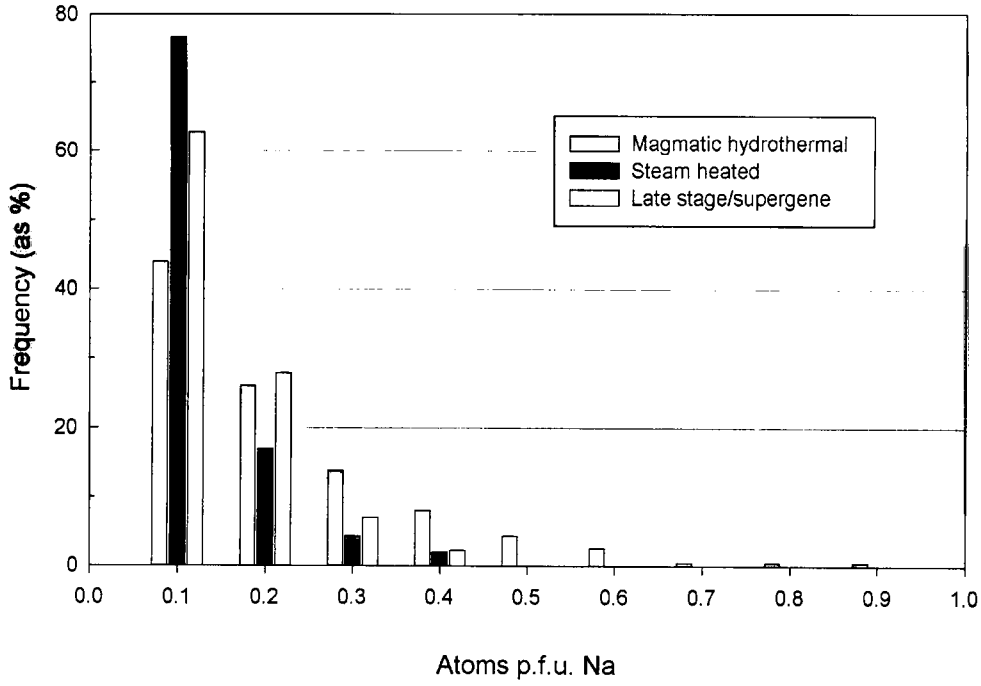

Figure 5.9. Histogram showing the range of Na substitution in alunite from 3 environments of acid sulfate alteration (Rye et al., 1992). Based on EPMA data from El Indio-Pascua Belt properties, including Pascua-Lama, El Indio, Tambo, Del Carmen, and Salitrales. Details of analytical procedures given in Appendix B. Total number analyses (*n*): magmatic-hydrothermal $n = 976$; steam heated $n = 47$; late stage and apparent supergene $n = 43$.

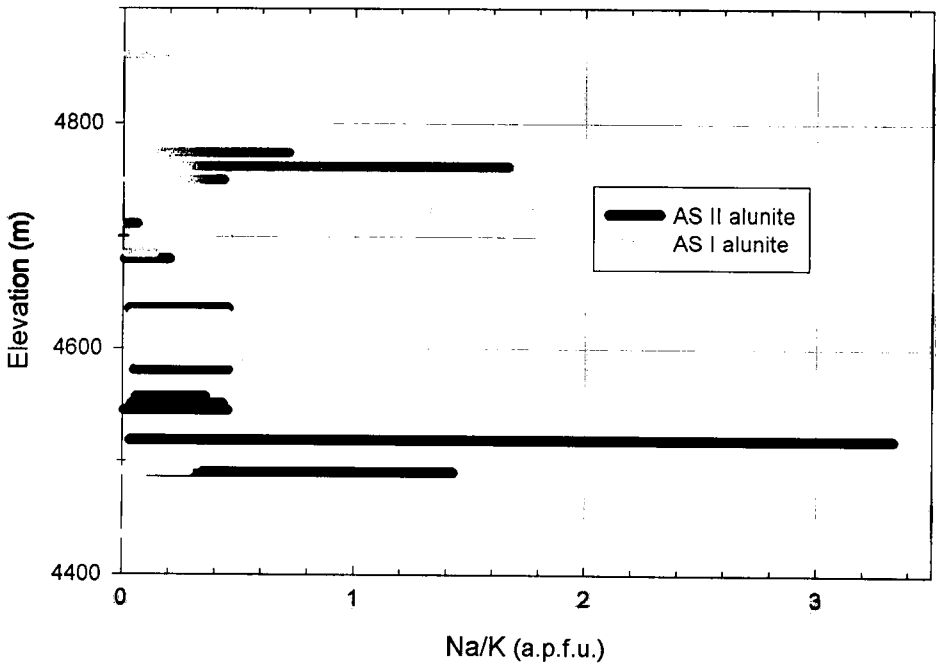

Figure 5.10. Range of K/Na ratios for Pascua AS I and AS II alunite with elevation. Based on EPMA results for a total of *n* data points (AS I $n = 335$; AS II $n = 331$).

Na content and depth. Instead, the influence of temperature on this earlier assemblage is evident from correlations between alunite geochemistry and the mineralogy of associated clays (Fig. 5.11). Alunite associated with pyrophyllite has lower average K contents than alunite associated with dickite (statistically significant at 95% confidence level, based on t-test results: Appendix A). In hydrothermal systems, pyrophyllite typically forms between *ca.* 200° to 350°C, whereas dickite forms at temperatures less than *ca.* 200° to 250°C (Hemley et al., 1980; Reyes, 1990).

Fluid Composition

The effects of source-fluid composition on alunite–natroalunite solid-solution are difficult to quantify, given the complexity of natural systems. Both local and distal scale fluid controls on alunite geochemistry can be inferred in the El Indio-Pascua Belt, however, given constraints from the solid-solution models presented above.

Local controls

Complex geochemical zoning and banded alunite-natroalunite crystals are common at several localities in the El Indio Belt (e.g., Del Carmen: Fig. 5.12). There is significant debate in the literature as to whether oscillatory zoning in hydrothermal minerals reflects local or large-scale variations in fluid composition (see discussions in Shore and Fowler, 1996, and Crowe et al., 2001). Our solid-solution models (Fig. 5.6 and 5.8) predict that more than an order of magnitude change in K/Na fluid content is required to precipitate both alunite and natroalunite end-members (at equilibrium). Such large shifts in bulk fluid composition are unlikely in the natural environment, particularly in the short time periods required to form zoned crystals. Zoning between end-member alunite and natroalunite is therefore unlikely the result of changes in bulk fluid compositions and may be attributed to more local effects such as supersaturation or crystallographic controls, analogous to the mechanisms inferred by Putnis et al. (1995) and Prieto et al. (1997) from their porous-media solid-solution experiments.

Distal controls

On a larger scale, extrinsic variations in fluid composition (e.g., due to lithological variations, fluid:rock interaction) can be shown to affect bulk alunite-natroalunite compositions. Data from the Del Carmen project in particular suggest that host-rock chemistry can affect the composition of alunite-natroalunite solid-solution. Magmatic-hydrothermal alunite in this area is less K-rich on average (Table 5.3) than that from the nearby El Indio-Tambo district (this study;

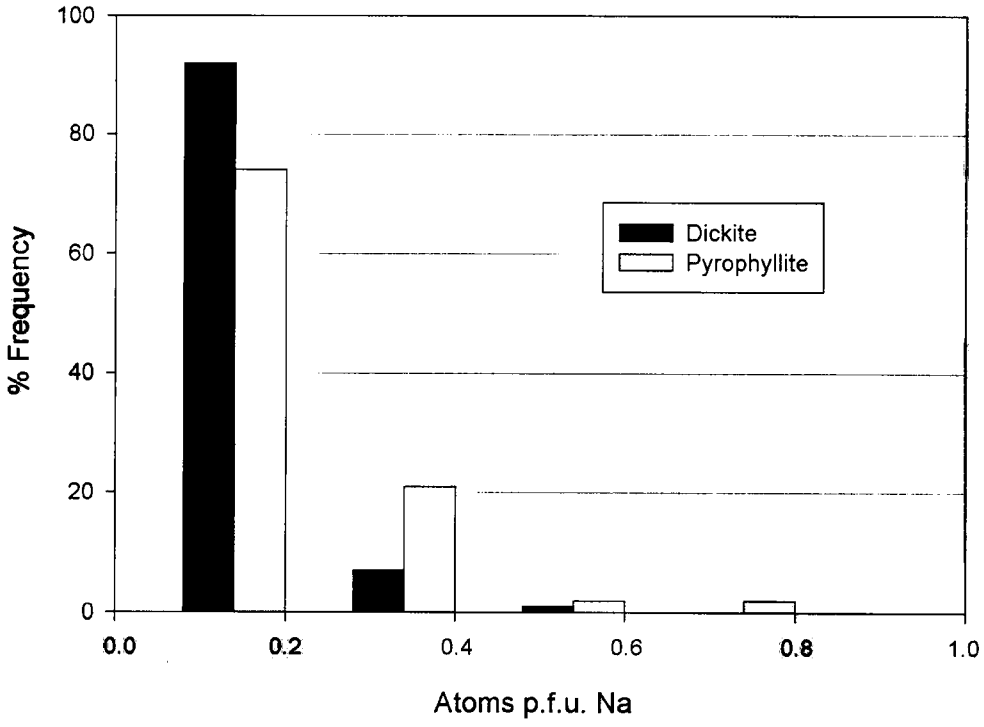

Figure 5.11. Histogram showing alunite Na contents for Pascua alteration (stage AS I) based on dominant clay mineralogy. Alunite data based on EPMA results for a total of *n* analyses (dickite series, $n = 99$; pyrophyllite series, $n = 137$). Clay identification by SWIR analysis (PIMA).

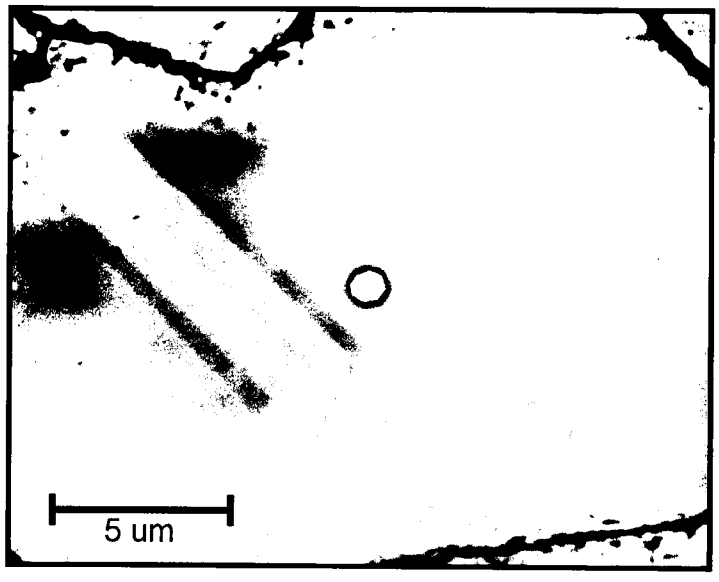

Figure 5.12. SEM backscatter image showing oscillatory zoning between Na-rich (dark) and K-rich (light) compositions in Del Carmen alunite. Bright circle in centre due to beam damage.

Bennet, 1995) and the Pascua-Lama area. K-depletion is attributed to increased Na substitution in Del Carmen alunite, based on EPMA (Fig. 5.13) and SWIR results. The style, timing, and characteristics of alteration are relatively consistent for all three regions (this study; Bissig, 2001), but their host lithologies differ. Alteration at Del Carmen is hosted primarily in the andesitic Cerro de las Tórtolas Formation and the contemporaneous Infiernillo Intrusive Unit (Noriega and Perez, 1997). This unit has higher average Na_2O/K_2O than either the Tilito Formation, which hosts the El Indio-Tambo deposits, or Pastos Blancos Group intrusions in the Pascua area (Table 5.4: Bissig, 2001). Intense, acid sulfate alteration of the andesitic host rock likely resulted in higher Na/K in the alteration fluids, which is reflected in the composition of the Del Carmen alunite. Variations in host-rock composition are most likely to influence alunite that forms directly from wallrock reaction with low fluid:rock ratios, rather than alunite deposited as open-space fill in veins and breccia matrices.

Table 5.3. Summary of EPMA Na data for magmatic-hydrothermal alunite from Del Carmen compared to the rest of the El Indio-Pascua Belt. Statistical analysis is based on recalculated atoms per formula unit Na for *n* analyses in each group. Standard deviation (σ), t-statistic, degrees of freedom (DF), and probability at 95% confidence level (p) are given: based on SYSTAT t-test (details Appendix A).

Group	*n*	Mean	σ	t value	DF	p
El Indio-Pascua Belt	909	0.158	0.134	-6.529	70.6	0.000
Del Carmen	66	0.301	0.175			

In contrast, the solid-solution models presented earlier also predict that very small changes in fluid composition could precipitate a range of alunite-natroalunite solid-solution at low temperatures. Fluid variation of this magnitude may be present in the near-surface environment because of variable mixing between magmatic fluids and meteoric waters and variable fluid:rock ratios. Significant variation in alunite composition has been recorded for other low-temperature (supergene or sedimentary) acid-sulfate environments (e.g., Stoffregen and Alpers, 1992; Hemley et al., 1969; Stoffregen et al., 2000). However, data from the El Indio-Pascua belt do not exhibit similar variation. Late-stage and supergene alunite from this study is K-dominant and rarely contains greater than 0.3 m.p.f.u. Na substitution (Fig. 5.9), even

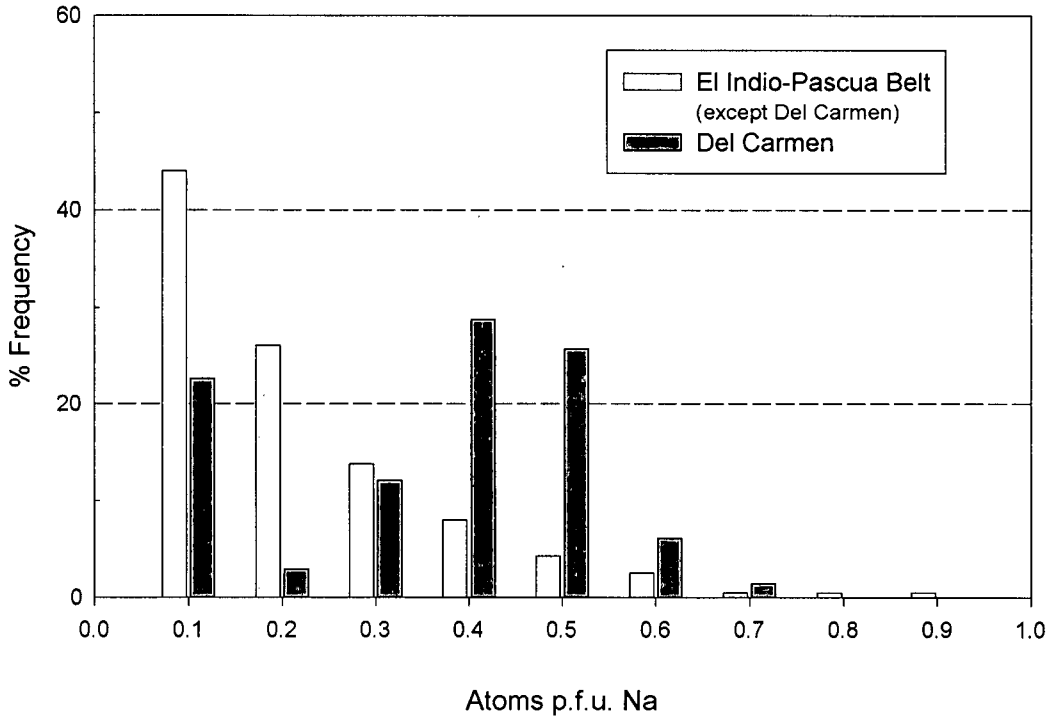

Figure 5.13. Histrogram showing alunite Na contents fro Del Carmen magmatic-hydrothermal alunite versus magmatic-hydrothermal alunite from all other El Indio-Pascua Belt properties. Alunite data based on EPMA results for a total of *n* analyses (Del Carmen series, *n* = 66; El Indio-Pascua Belt, *n* = 909).

Table 5.4. Average major element geochemistry for host lithologies from the Del Carmen (Infiernillo; n=5), Tambo (Tilito; n=3), and Pascua (Colorado Unit, n=1) areas. Data from Bissig (2001).

Unit	Cerro de las Tórtolas (Infiernillo)	Tilito	Pastos Blancos (Chollay)
Deposit	**Del Carmen**	**El Indio-Tambo**	**Pascua**
SiO_2	62.22	62.12	76.35
Al_2O_3	16.39	16.39	12.28
TiO_2	0.74	0.66	0.08
Fe_2O_3 (Fe total)	5.32	5.05	0.82
MnO	0.09	0.09	0.05
MgO	2.43	1.59	0.11
CaO	4.22	4.35	0.36
Na_2O	3.74	2.89	3.32
K_2O	2.57	4.24	4.39
P_2O_5	0.19	0.16	0.01
Total	98.00	97.63	97.79
Na_2O/K_2O	1.5	0.7	0.8

though significant mixing between meteoric and magmatic fluids is indicated by stable isotopic results (details see Chapters 2 and 3). These findings indicate that large-scale fluctuations in source-fluid composition did not result in variable alunite-natroalunite compositions in low-temperature assemblages. Data suggest that equilibrium conditions were rarely achieved in the near-surface environment, or that temperature exerted the greatest influence on the composition of alunite–natroalunite solid-solution.

Summary

- Geochemical results from the El Indio–Pascua Belt are consistent with our solid-solution model calculations, as well as with experimental (Stoffregen and Cygan, 1990) and empirical evidence (e.g., Stoffregen et al., 2000). Data suggest that higher temperatures of formation favor increased incorporation of solid-solution Na in alunite.
- In the magmatic-hydrothermal environment, both depositional temperature and large-scale fluid chemistry may affect average alunite–natroalunite compositions. Intracrystalline zonation or chemical banding between alunite and natroalunite compositions is likely due to local supersaturation effects or crystallographic controls.
- Large-scale fluid controls on alunite chemistry are not evident in low-temperature alteration. Alunite-natroalunite chemistry is most likely influenced by depositional temperatures or disequilibrium conditions.

REFERENCES

Andersen, G.M. and Crerar, D.A, 1993. Thermodynamics in Geochemistry; The Equilibrium Model. Oxford University Press, New York.

Aoki, M., 1991. Mineralogical features and genesis of alunite solid-solution in high temperature magmatic-hydrothermal systems. Journal of the Geological Survey of Japan, 277, 31-32.

Aoki, M., Comsti, E.C., Lazo, F.B., and Matsuhisa, Y., 1993. Advanced argillic alteration and geochemistry of alunite in an evolving hydrothermal system at Baguio, northern Luzon, Phillipines. Resource Geology, 43, 155-164.

Arribas, A., Jr., Cunningham, C.G., Rytuba, J.J., Rye, R.O., Kelly, W.C., McKee, E.H., Podwysocky, M.H., and Tosdal, R.M., 1995. Geology, geochronology, fluid inclusions, and stable isotope geochemistry of the Rodalquilar Au alunite deposit, Spain. Economic Geology, 90, 795-822.

Bennet, R.E., 1995. A combined hydrothermal alteration study and exploration target evaluation of the Tambo mining district, El Indio mineral belt, Region IV, Chile. Internal report for Companìa Minera San José Ltda.

Bissig, T., 2001. Metallogenesis of the Miocene El Indio-Pascua gold-silver-copper belt, Chile/Argentina: Geodynamic, geomorphological and petrochemical controls on epithermal mineralization. Unpublished Ph.D. thesis, Queen's University.

Crowe, D.E., Riciputi, L.R., Bezenek, S., Ignatiev, A., 2001. Oxygen isotope and trace element zoning in hydrothermal garnets: Windows into large-scale fluid-flow behavior. Geology, 29, 479-482.

Essene, E.J., 1982. Geologic thermometry and barometry. *In* Ferry, J.M., ed., Characterization of metamorphism through mineral equilibria. Reviews in Mineralogy, Vol. 10.

Giggenbach, W.F., 1997. The origin and evolution of fluids in magmatic-hydrothermal systems. *In* Barnes, H.L., ed., Geochemistry of Hydrothermal Ore Deposits, 3rd Ed. John Wiley and Sons, Inc., 737-796.

Helgeson, H.C., Delany, J.M, Nesbitt, H.W., and Bird, D.K., 1978. Summary and critique of the thermodynamic properties of rock-forming minerals. Amererican Journal of Science, 278A, 229 p.

Hemley, J.J., Hostetler, P.B., Gude, A.J., and Mountjoy, W.T., 1969. Some stability relations of alunite. Economic Geology, 64, 599-612.

Hemley, J.J., and Jones, W.R., 1964. Chemical aspects of hydrothermal alteration with emphasis of hydrogen metasomatism. Economic Geology, 59, 538-569.

Hemley, J.J., Montoy, J.W., Marinenko, J.W., and Luce, R.W., 1980. Equilibria in the system Al_2O_3-SiO_2-H_2O and some general implications for alteration/mineralization processes. Economic Geology, 75, 210-228.

Henley, R.W., and McNabb, 1978. Magmatic vapor plumes and ground-water interaction in porphyry copper emplacement. Economic Geology, 73, 1-20.

Holland, H.D., 1965. Some applications of thermodynamic data to problems of ore deposits, II. Mineral assemblages and the composition of ore-forming fluids. Economic Geology, 60, 1101-1166.

Johnson, J.W., Oelkers, E.H., and Helgeson, H.C., 1992. SUPCRT92: A software package for calculating the standard molal thermodynamic properties of minerals, gases, aqueous species, and reactions from 1 to 5000 bar and 0 to 1000°C. Computers and Geosciences, 18, 899-947.

Meyer, C.A. and Hemley, J.J., 1967. Wall rock alteration. *In* Barnes, H.L., ed., Geochemistry of Hydrothermal Ore Deposits, New York, Holt, Rinehart, and Winston, 166-235.

Nordstrom, D.K, and Munoz, J.L., 1985. Geochemical Thermodynamics. Benjamin/Cummings Publishing Co., Menlo Park, CA., 477 p.

Noriega, J. and Perez, L., 1997. Proyecto Del Carmen - Informe temporada 1997. Internal report. Barrick Gold Corporation.

Prieto, M., Feernandez-Gonzalez, A., Putnis, A., and Fernandez-Diaz, L., 1997. Nucleation, growth, and zoning phenomena in cystallizing $(Ba,Sr)CO_3$, $Ba(SO_4,CrO_4)$, $(Ba,Sr)SO_4$, and $(Cd,Ca)CO_3$ solid-solutions from aqueous solutions. Geochimica et Cosmochimica Acta, 61, 3383-3397.

Putnis, A., Prieto, M., and Fernandez-Diaz, L., 1995. Fluid supersaturation and crystallization in porous media. Geological Magazine, 132, 1-13.

Reed, M.H., 1997. Hydrothermal alteration and its relationship to ore fluid composition. *In* Barnes, H.L., ed., Geochemistry of Hydrothermal Ore Deposits, 3rd Ed. John Wiley and Sons, Inc., 303-366.

Reyes, A.G., 1990. Petrology of Philippine geothermal systems and the application of alteration mineralogy to their assessment. Journal of Volcanology and Geothermal Research, 43, 279-309.

Robie, R.A. and Waldbaum, D.R., 1968. Thermodynamic properties of minerals and related substances at 298.15 degrees K (25.0 degrees C) and one atmosphere (1.013 bars) pressure and at higher temperatures. U.S. Geological Survery Bulletin 1968.

Rye, R.O., 1993. The evolution of magmatic fluids in the epithermal environment: The stable isotope perspective. Economic Geology, 88, 733-753.

Rye, R.O, Bethke, P.M., and Wasserman, M.D., 1992. The stable isotope geochemistry of acid sulfate alteration. Economic Geology, 87, 225 - 262.

Shomate, C.H., 1946. Heat of formation of alunite. U.S. Bureau of Mines Technical Paper 688.

Shore, M., and Fowler, A.D., 1996. Oscillatory zoning in minerals: A common phenomenon. Canadian Mineralogist, 34, 1111-1126.

Stoffregen, R., 1987. Genesis of acid-sulfate alteration and Au-Cu-Ag mineralization at Summitville, Colorado. Economic Geology, 82, 1575-1591.

Stoffregen, R.E. and Alpers, C.N., 1992. Observations on the unit-cell dimensions, H_2O contents, and δD values of natural and synthetic alunite. American Mineralogist, 77, 1092-1098.

Stoffregen, R.E., Alpers, C.N., and Jambor, J.L., 2000. Alunite-jarosite crystallography, thermodynamics, and geochronology. Reviews in Mineralogy, 40, 453-479.

Stoffregen, R.E., and Cygan, G.L., 1990. An experimental study of Na-K exchange between alunite and aqueous sulphate solutions. American Mineralogist, 75, 209-220.

Symonds, R.B., Tose, W.I., Gerlach, T.N., Briggs, P.H., and Harmon, R.S., 1990. Evaluation of gases, condensates, and SO_2 emissions from Augustine volcano, Alaska: the degassing of a Cl-rich volcanic system. Bulletin of Volcanology, 52, 355-374.

Thompson, A.J.B, 1992. Alunite compositions and textures: Relationships to precious metal mineralization. *In* New Developments in Lithogeochemistry, Mineral Deposit Research Unit Short Course #8, 20-21 February.

Zotov, A.V., 1971. Dependence of the composition of alunite on the temperature of its formation. Geochemistry International, 71-75.

Chapter 6

FORMATION OF HIGH SULFIDATION PRECIOUS METAL DEPOSITS: NEW EVIDENCE FROM THE EL INDIO-PASCUA BELT, CHILE.

INTRODUCTION

High sulfidation deposits are a class of epithermal gold ± copper, silver deposit that are characterized by the presence of high-sulfidation state minerals (e.g., enargite and luzonite) and acid sulfate alteration assemblages (e.g., quartz, alunite, kaolinite, pyrophyllite: Hedenquist, 1987; Arribas, 1995). Deposits of this type were previously termed enargite-gold (Ashley, 1982), high sulfur (Bonham, 1984; 1986), quartz-alunite gold (Berger, 1986), acid-sulfate (Heald et al, 1987), and alunite-kaolinite (Hayba et al., 1985), in reference to the alteration mineralogy or conditions of formation.

Over the last ten years, a consensus has emerged on the origin of high sulfidation deposits and their environment of formation (e.g., White and Hedenquist, 1990; Sillitoe, 1993; Arribas, 1995; Hedenquist and Arribas, 1999; Cooke and Simmons, 2000). Most researchers, however, recognize unresolved questions in the genetic model for these deposits, particularly the precise controls on mineralizing processes.

The El Indio-Pascua Belt, spanning the Chile-Argentina border, is one of the world's largest concentrations of high sulfidation deposits and related regional alteration. The belt has been the subject of intensive exploration for approximately twenty years, resulting in the development of several mines (e.g., El Indio, Tambo), delineation of extensive resources (e.g., Pascua-Lama, Veladero), and discovery of numerous mineralized alteration zones. El Indio-Pascua Belt systems are typically well preserved, due to favorable tectonic and climatic conditions. The belt therefore provides an excellent site for evaluating models for high sulfidation deposits. Barrick Gold Corporation, the predominant land-holder and explorer in the region, has sponsored considerable research in the belt over the last five years. Results reported herein summarize the geological framework determined for high sulfidation systems at both a regional- and deposit- scale. In particular, we highlight research on the nature and

occurrence of alunite throughout the El Indio-Pascua Belt, and implications of this research for the characteristics of source fluids. These results provide important constraints on the genetic model for deposits specifically within this belt, and to high sulfidation environments in general.

THE HIGH SULFIDATION MODEL

Following the realization that high sulfidation precious metal systems constitute a distinct class of deposit, research has focused on the mineralizing environment and ore-forming processes at specific deposits (e.g., Stoffregen, 1987; Vennemann et al., 1993; Sillitoe and Lorsen, 1994; Arribas et al., 1995; Hedenquist et al., 1998; Jannas et al., 1999). Research on these deposits is hindered by the pervasive nature of alteration, the depth of oxidation, and the lack of good quality fluid inclusions. Regardless, the major elements of the genetic model are broadly accepted as follows:

- Deposits form in subduction-related arc settings during regional magmatism. Typically deposits occur in volcanic centers and mineralization is coeval with local volcanic rocks and related intrusions.
- Some deposits occur peripheral to and/or above porphyry and related mineral deposits of the same age.
- In many deposits, pervasive pre-ore, acid sulfate alteration is widespread. This alteration formed from acid fluids dominated by oxidized sulfur species (e.g. $SO_{2(g)}$, HSO_4^-, SO_4^{2-}). Acidity was generated by the condensation of magmatic vapors with disproportionation or dissociation of SO_2 and HCl, respectively.
- Mineralization postdates regional alteration and is focused in veins, breccia zones, and permeable or reactive lithologies. The composition of ore-fluids is poorly constrained. These fluids are typically inferred to be less acidic and less oxidized than the early alteration fluids, and possibly of mixed magmatic-meteoric origin. This two-stage model is invoked to explain localized mineralization and conversely, the lack of mineralization in many regional alteration zones (lithocaps). The timing and nature of these specific mineralizing events, the processes of metal transport and deposition, and the relation of mineralization to the paleosurface are poorly understood.

In this paper, we address several of these questions using data from the El Indio-Pascua Belt to provide new constraints. Unlike many high sulfidation deposits, alunite is temporally and genetically related to ore throughout the El Indio-Pascua Belt, and hence provides direct information on mineralizing processes. We focus on the textural, chemical, and isotopic characteristics of alunite to determine the nature of both alteration and ore-forming fluids, and the physio-chemical environment of mineral deposition. ^{40}Ar-^{39}Ar dating of alunite-group minerals (alunite and jarosite in particular) provides additional temporal constraints on processes in these systems.

THE EL INDIO-PASCUA BELT

A) Tectonic setting

The El Indio-Pascua Belt is situated in the Central Andean Cordillera Principal and straddles the Chile-Argentina border between Latitudes 29°20' and 30°30' S (Fig. 6.1). The belt is located in the middle of the "flat slab" segment of the Andes. The mineralized systems in this region formed in the late Miocene (6-9.5 Ma) after the initiation of slab flattening and crustal thickening (Kay et al, 1999; Bissig, 2001; Kay and Mpodozis, 2001).

The El Indio-Pascua Belt lies between two other well-known mineralized areas, the Maricunga porphyry Au and high sulfidation Au-Ag belt to the north (26-28° S), and the Los Pelambres–El Teniente porphyry Cu-Mo belt to the south (32-34° S). The Maricunga Belt occurs at the northern margin or transition zone of the "flat slab" region, but the mineralized systems in the belt formed before or during the very early stages of slab flattening, 24-20 and 14-13 Ma respectively (Vila and Sillitoe, 1991; Muntean and Einaudi, 2001). Both periods of mineralization in the Maricunga Belt host porphyry Au +/- Cu and high sulfidation epithermal Au-Ag deposits that are spatially associated with partially eroded andesitic to dacitic calc-alkaline volcanoes (Vila and Sillitoe, 1991). Widespread barren steam-heated alteration occurs in the Maricunga belt, interpreted to have formed above and extending laterally from porphyry centres (Vila and Sillitoe, 1991). At La Pepa, gold-enargite-barite mineralization and associated alunitic alteration are interpreted to have formed in the late-stages of a porphyry system from the escape of supercritical magmatic fluids that cooled and boiled upon ascent (Muntean and Einaudi, 2001).

In contrast to the early to middle Miocene mineralization in the Maricunga Belt, porphyry Cu-Mo deposits in the Los Pelambres–El Teniente district formed in the late Miocene,

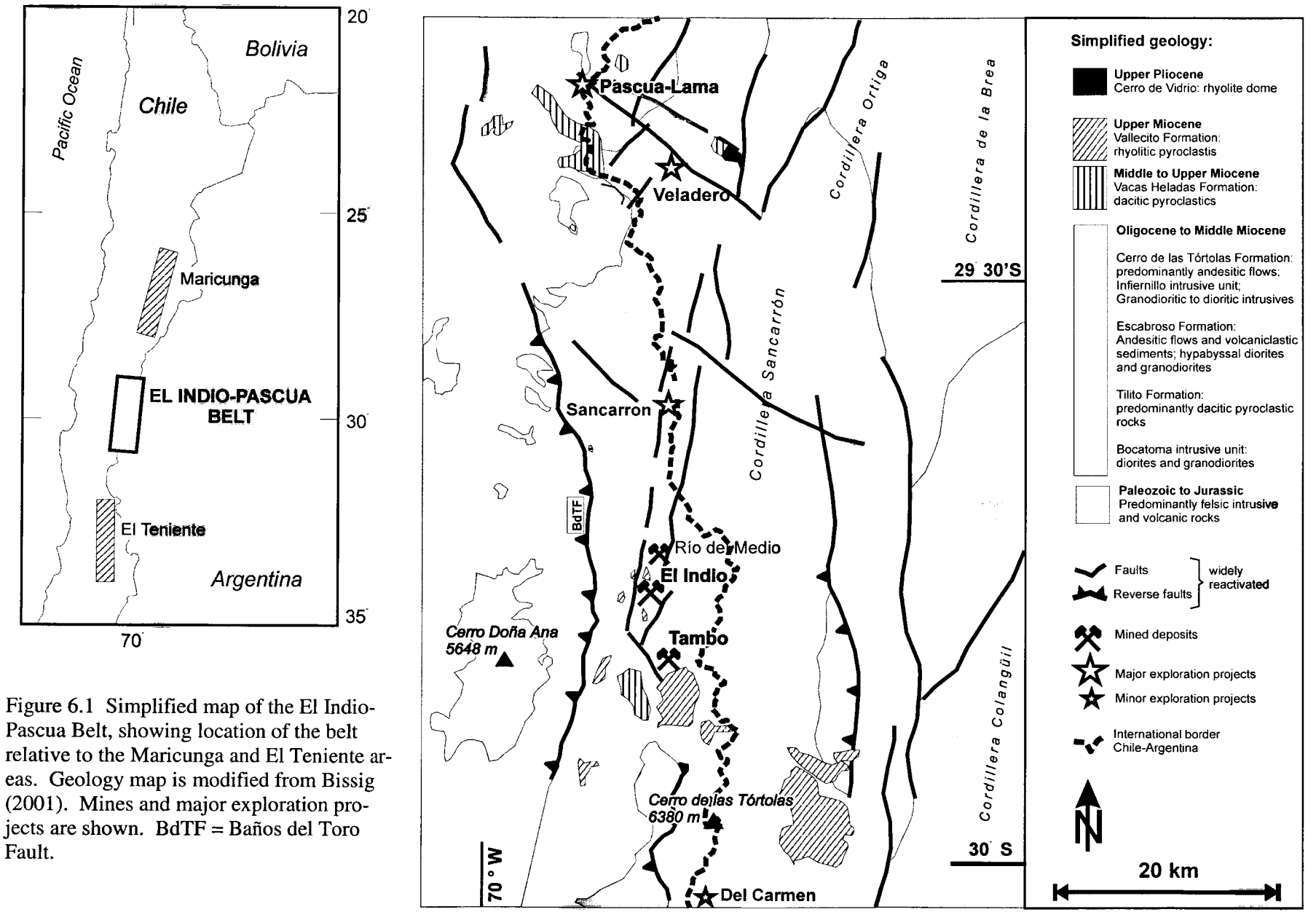

Figure 6.1 Simplified map of the El Indio-Pascua Belt, showing location of the belt relative to the Maricunga and El Teniente areas. Geology map is modified from Bissig (2001). Mines and major exploration projects are shown. BdTF = Baños del Toro Fault.

10-5 Ma (Skews and Stern, 1994; Kay et al, 1999), overlapping the timing of high sulfidation systems in the El Indio-Pascua Belt. The Los Pelambres–El Teniente deposits formed on the southern margin of the "flat slab" zone after crustal thickening. An increase in Sm/Yb ratios in volcanic and intrusive rocks temporally associated with the porphyry deposits is interpreted to reflect a change from amphibole to garnet stability during increasing dehydration of a lower crustal source region during crustal thickening (Kay et al., 1999; Kay and Mpodozis, 2001). A similar model is proposed for the adakitic suites of the same age in the El Indio-Pascua Belt (Kay and Mpodozis, 2001), although Bissig (2001) suggests an alternative model in which the distinctive Sm/Yb ratios and HREE signatures reflect hornblende and garnet stability related to increasing pressure and water fugacity in the source region. Regardless, there is evidence for involvement of the lower crust in the formation of magmas in both the El Indio-Pascua and Los Pelambres – El Teniente Belts. The similar timing and tectono-petrological setting suggests that mineralization in both belts could have formed from similar systems now preserved at different erosional levels. Support for this comes from the relatively high exhumation rates of 3 mm/year reported for the El Teniente region (Kurtz et al., 1997), contrasting with the relatively well preserved pediplain surfaces and shallow alteration zones in the El Indio-Pascua Belt. The metallogenic signature however, particularly the lack of gold and importance of tourmaline in the Los Pelambres – El Teniente Belt, differs between the two belts suggesting that probable differences exist between unexposed deep parts of the El Indio-Pascua Belt and the Cu-Mo porphyry deposits of Los Pelambres, Los Bronces and El Teniente.

B) Regional Geology

El Indio-Pascua Belt occurs within a NNE-SSW striking tectonic depression bound by the steeply dipping Baños del Toro fault to the west and opposing structures in the Valle del Cura region in the east. Within this block, an Upper Paleozoic to lower Jurassic basement, predominantly composed of calc-alkaline felsic intrusive suites and volcanic rocks (Martin et al., 1999), is overlain by up to 1500 m of Tertiary subaerial volcanic strata. The latter are extensively preserved in the southern part of the belt, where the Tambo and El Indio mines are located, but are less widespread in the northern extremity of the district near Pascua-Lama and Veladero (Martin et al., 1995; Maksaev et al., 1984). The Tertiary volcanic sequence (summarized after Bissig, 2001, and Martin et al., 1995) comprises predominantly volcanic and volcaniclastic rocks of the Tilito Formation (27 to 23 Ma), the Escabroso Group (21 to 17.5 Ma) and the Cerro de las Tortolas Formation (17 to 14 Ma). Magmatism decreased markedly

thereafter. Isolated tuffs of the Vacas Heladas Formation erupted between 12.7 and 11 Ma. A single 7.8 Ma dacite dike, the only igneous rock coeval with the mineralization in the district, is reported from Pascua (Bissig, 2001). The Vallecito Formation (6.2 to 5.5 Ma) is limited to the Valle de Cura region (Ramos et al., 1989) and local occurrences in the El Indio-Tambo area. Volcanism finally ceased in the Upper Pliocene after the eruption of the 2 Ma Cerro de Vidrio rhyolite dome in the northeast part of the belt (Bissig, 2001).

Decreasing magmatism after 14 Ma coincides with a change in the composition of the volcanic rocks from high K calc-alkaline suites, possibly derived from partial melting of upper mantle underplated basalts, to adakitic suites of lower or middle crustal origin (Bissig, 2001). An increase in the water fugacity in the lower crustal source region, postulated to explain the adakitic suites (Bissig, 2001), may reflect fluids derived from the flattening slab. These slab-derived fluids may also have increased the concentration of sulfur and chlorine in the source region, thus enhancing the potential for magmas that would generate metal-rich fluids upon crystallization (Bissig, 2001). Hence, a causative relation may exist between slab-flattening, crustal thickening, and the initiation of major mineralizing systems in the El Indio-Pascua Belt.

HIGH SULFIDATION SYSTEMS IN THE EL INDIO-PASCUA BELT

The largest high sulfidation systems in the El Indio-Pascua Belt include the world-class El Indio Mine (10 Moz gold produced), the giant Pascua-Lama (18.6 Moz Au, 630 Moz Ag) and Veladero (ca. 15.6 Moz Au, 230 Moz Ag) projects, and the Tambo deposit (0.8 Moz gold produced), which was recently closed. These systems have been at least partially described in previous publications (Table 6.1). Data for smaller occurrences such as Sancarron and Del Carmen are available only through internal reports to Barrick Gold Corporation. In the following section, we summarize the characteristics of each of these systems with particular reference to pre-mineral alteration, mineralization (Table 6.2), and late-stage and peripheral alteration events (Table 6.3).

Pre-Mineral Alteration

Barren hydrothermal activity of Oligocene to early-late Miocene age is recognized throughout the El Indio-Pascua Belt (Fig. 6.2). The oldest recorded alteration in the region comprises 36 Ma sericitic and potassic alteration of basement rocks in the Potrerillos prospect, about 7 km south of Pascua (Bissig, 2001). Larger alunite-bearing alteration zones are

Table 6.1. Geology and approximate size of selected high sulfidation deposits and prospects in the El Indio-Pascua Belt.

Deposit/ Prospect	Approx. areal extent of alt (km^2)	Host rock	Host rock composition	Age of host	Selected References[1]
Pascua-Lama	10	Pastos Blancos Group	Dacitic to granodioritic intrusions (and rare dacitic tuffs)	Upper Paleozoic to Lower Jurassic [2]	Chouinard and Williams-Jones (1999), Bissig (2001)
Veladero	10	-	Dacitic volcanic tuffs and volcanic breccias	-	Jones *et al.* (1999)
Tambo	7	Tilito Fm	Dacitic to rhyolitic volcanic tuffs	23-25 Ma [3]	Jannas (1995), Jannas *et al.* (1999)
El Indio	6	Tilito Fm	Dacitic to rhyolitic volcanic tuffs	23-25 Ma [3]	Jannas (1995), Jannas *et al.* (1999)
Del Carmen	4	Cerro de las Tortolas	Andesite to dacite flows and lesser volcanic tuffs	15-16 Ma [3]	Noriega and Perez (1997)
Sancarrón	4	Tilito Fm	Dacitic to rhyolitic lithic crystal tuffs	23-25 Ma [3]	Williams (1998)

[1] other than this study.
[2] Martin *et al.* (1999).
[3] data from Bissig (2001).

Table 6.2. Characteristics of ore and hypogene alteration assemblages for major deposits and exploration prospects.

Deposit/ Prospect	Au (10^3 kg)	Age of Mineralization (Ma)[2]	Styles of Mineralization	Ore-related Minerals	Age of Alteration (Ma)[2]	Hypogene Alteration
Pascua-Lama	>550	8.8 – 8.1	Breccias, veins, disseminations	En, py, qtz, alun, S, cal, bar, cv, gn, cpy, st, Fe-slf, jar, scrd	9.5 - 8.0	SL, AS, AG, PP (VQ)
Veladero	485	-	Breccias	Qtz, alun	11.0 - 8.0	SL, AS, AG, PP
Tambo	25	8.0 - 8.9	Breccias, veins	Bar, alun, qtz, tel, en, gn, wal, jar, scrd	7.3 - 11.0	AS, AG, PP (SL)
El Indio	>310	6.2 - 7.8	Veins	Qtz, mi, kao, py, en, tenn, slfsts, sph, gn, cal, alun[1]	6.2 - 9.4	SR, SL, AG
Del Carmen	-	-	Breccias, disseminations	Qtz, chalc, py, en, alun, mi, bis, Ag	-	SL, AS, AG, PP (VQ)
Sancarron	<5	7.7 - 7.9	Breccias, veins	Alun, jar, qtz, py, en	-	SL, AS, AG

Mineral abbreviations: Ag = native silver, bis = bismuthinite, alun = alunite, bar = barite, cal = calaverite, chalc = chalcedony, cpy = chalcopyrite, cv = covellite, en = enargite, Fe-slf = Fe-sulfates, gn = galena, jar = jarosite, kao = kaolinite, mi = Kmica (including sericite and illite), py = pyrite, qtz = quartz, S = native sulfur, scrd = scorodite, slfsts = sulfosalts, sph = sphalerite, st = stibnite, tel = tellurides, tenn = tennantite, wal = walthierite, op = opal. Alteration assemblages: vuggy quartz (VQ), silicic (SL), sericitic (SR), acid sulfate (AS) argillic (AG), propylitic (PP). Rare alteration types indicated by parentheses.

[1] alunite only associated with banded alunite-sulfide veins in Campana and Brechita-Huantina areas.
[2] data from this study and Bissig (2001).

Table 6.3. Characterisitics of late stage and near-surface processes.

Deposit/ Prospect	Magmatic steam occurences	Present-day thickness of SH zone (m)	SH mineralogy[1]	LS ± SP mineralogy
Pascua-Lama	Coarse-gr veins and breccia matrix	50 – 100	qtz -S (kao-alun-op)	Alun, jar, scrd, gyp, Fe-slf
Veladero	-	100	qtz-S (op)	Jar
Tambo	Banded veins, powdery cystalline masses, coarse-gr breccia matrix	40	qtz-S (kao-alun)	Alun, jar, scrd
Del Carmen	-	25	qtz-S	Gyp, jar
Sancarron	-	25	qtz-S (alun)	Jar, gyp, scrd, alun

Mineral and alteration abbreviations: see Table 2.
[1] Qtz may include cristobalite, trydimite, and residual silica.

recognized at Sanco (20 Ma) and Paso Deidad (17 Ma) in Chile, and Veladero Sur (15 Ma) and Lama Central (14 to 13 Ma) in Argentina. Alteration in these regions consists of either disseminated quartz-alunite (± topaz) assemblages or coarse-grained alunite veins and breccia matrix fill.

Barren alteration similar in age to the Vacas Heladas Formation (12.7 to 11 Ma) is typically found in the vicinity of major ore deposits. Pre-mineral acid sulfate alteration in both the El Indio-Tambo and Pascua-Lama districts is characterized by fine intergrowths of alunite-quartz ± clays that selectively replaced feldspar crystals and tuff fragments in the host rock. Alteration is widespread, and grades laterally to argillic and propylitic assemblages. Vuggy quartz is rare. Stable-isotope data for pre-mineral alunite in both districts indicate that alteration is of magmatic-hydrothermal origin (Fig. 6.3).

Slightly younger alteration is also recorded in the Tambo area. Coarse-grained magmatic-hydrothermal alunite sampled from the cement of a small, barren breccia (Brecha Sylvestre) has been dated at 10 Ma (Bissig, 2001). Porcellaneous vein alunite (10 Ma), interpreted to be of steam-heated origin (Bissig, 2001), is also widespread in the Fabiana region.

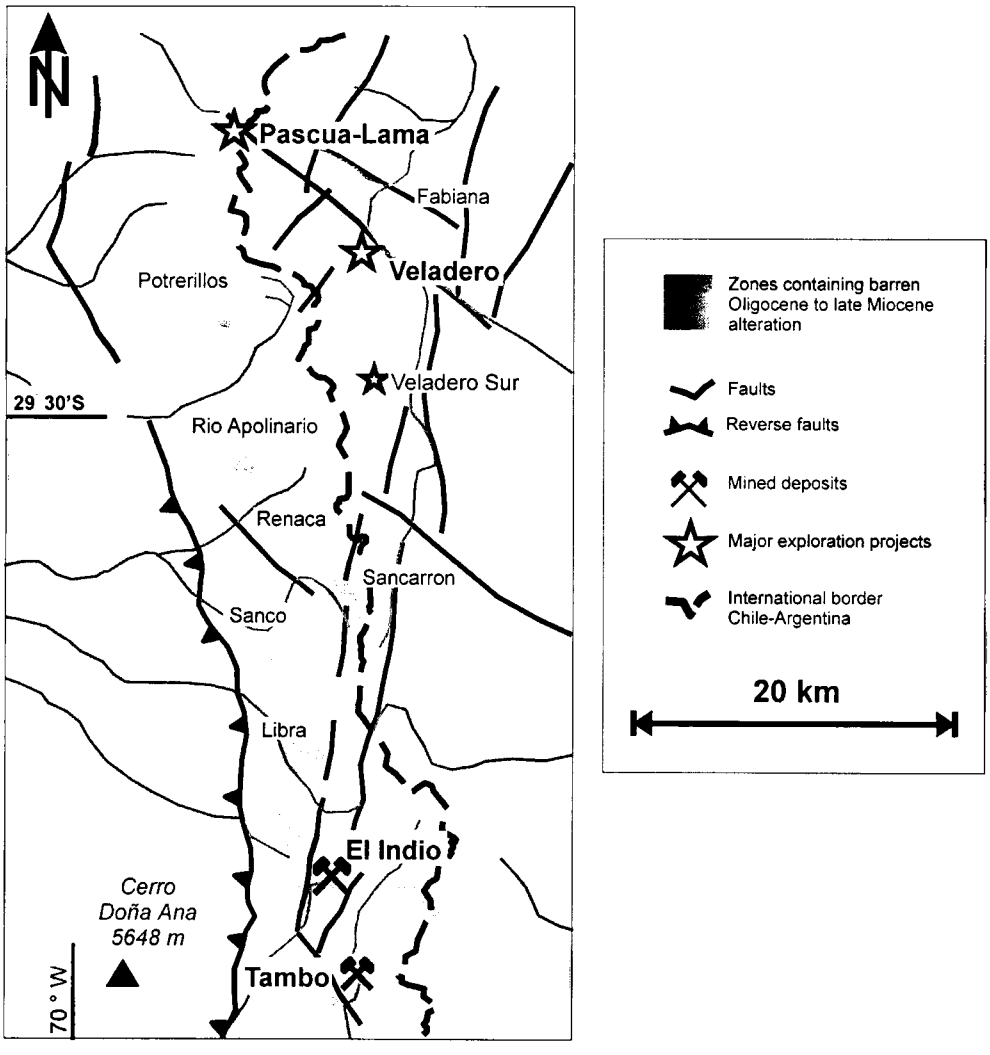

Figure 6.2. Map of the El Indio-Pascua Belt showing zones of Oligocene to Upper Miocene hydrothermal alteration that is not associated with known mineralization. Modified from Bissig (2001) based on ^{40}Ar-^{39}Ar age determinations of alteration minerals (alunite, sericite).

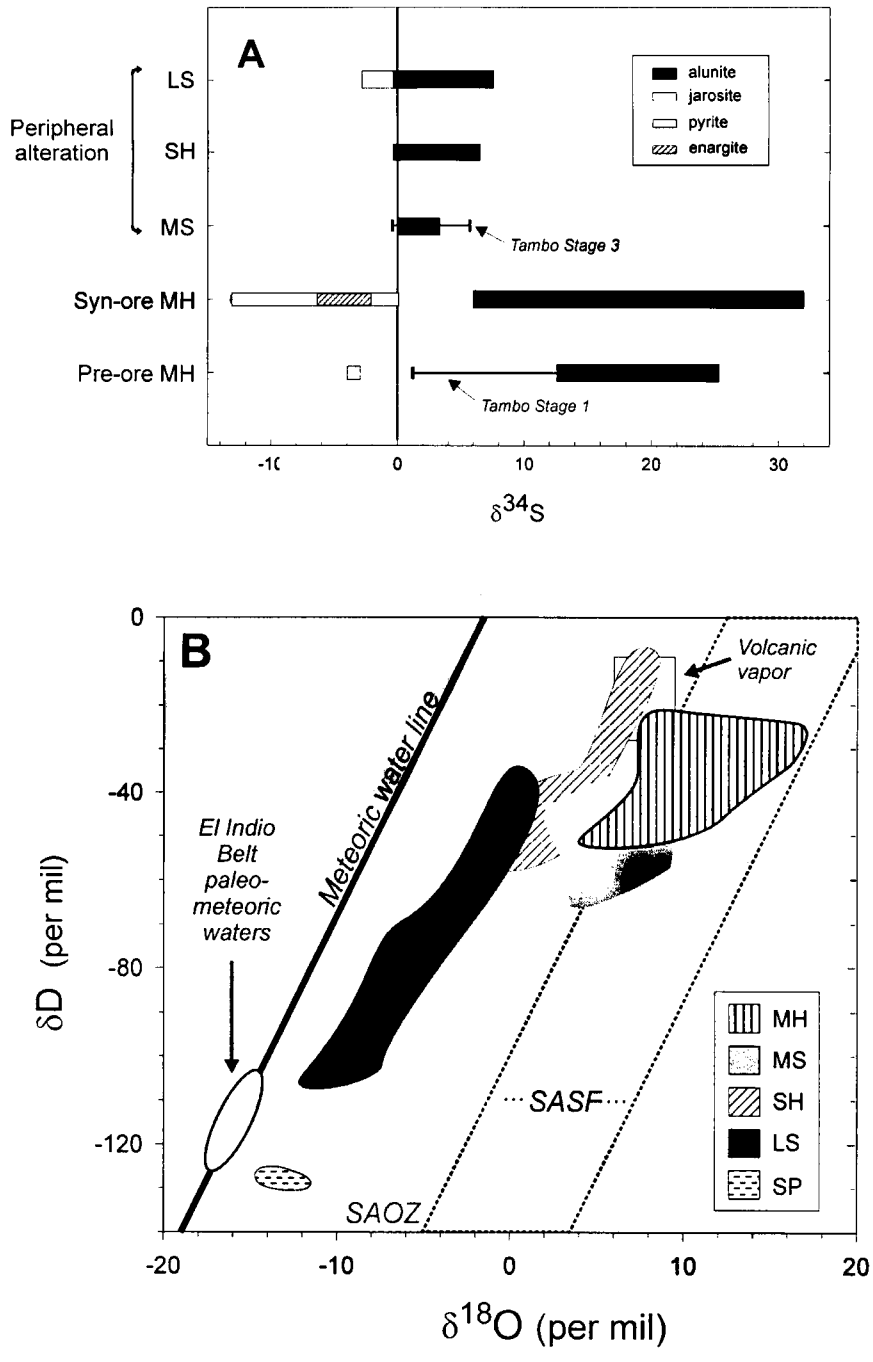

Figure 6.3. Summary of stable isotope data for alunite and associated minerals from the El Indio-Pascua Belt.

A) Sulfur isotope relations for alunite, jarosite, and associated sulfide for pre-ore, syn-ore, and peripheral stages of alteration.

B) Range of calculated deuterium and oxygen fluid compositions in equilibrium with alunite and jarosite samples. Fractionation factors taken from Stoffregen et al (1994) and Rye and Alpers (1997). Temperatures used for calculations are derived from textural, $\Delta^{34}S_{alun\text{-}py}$, and $\Delta^{18}O_{SO4\text{-}OH}$ isotope data. Lines and fields are MWL = meteoric water line of Craig (1961); Volcanic vapor = range of water compositions discharged from high temperature fumaroles (Giggenbach, 1992); SASF (light grey) = supergene alunite SO_4 field; and SAOZ = supergene alunite OH zone as described in Rye et al. (1992). Also shown (hatched circle) is the estimated composition of paleo-meteoric waters (B. Taylor, pers. comm.). Abbreviations used: MH = magmatic-hydrothermal, MS = magmatic steam, SH = steam-heated, LV = late vein, SP = supergene jarosite (Pascua).

Mineralization

Economic Au-Ag-Cu mineralization throughout the El Indio-Pascua Belt is confined to a narrow interval of about 9.5 to 6 Ma (Table 6.2: Bissig, 2001). There is no evidence for coeval volcanism, with the exception of one 7.8 Ma dike in the Pascua district (Bissig, 2001). High sulfidation systems are typically complex, and often several stages or styles of ore deposition are recognized. Copper mineralization is significant only at Pascua-Lama, El Indio, and Sancarron. All other systems are gold (± silver) dominant.

Alunite is common and is usually intimately intergrown with, or host to, either sulfide-rich (e.g., Pascua-Lama, Del Carmen) or sulfide-poor (e.g., Tambo, Veladero) ore (Fig. 6.4). Stable-isotope data for this alunite are consistent with a magmatic-hydrothermal origin, although a late-stage of gold deposition at Tambo is hosted in alunite with a magmatic steam signature (Chap. 3). Temperatures of ore deposition (based on fluid inclusion and $\Delta^{34}S_{alun\text{-}py}$ data) range between 180° to 320°C, and the available data indicate that mineralizing fluids were dilute with salinities less than about 4 wt% NaCl equivalent (this study; Beane et al, 1988; Jannas et al, 1999).

The El Indio deposit is distinctive from other systems in the region. Alunite is rare, only occurring in patchy kaolinite and sericite-bearing alteration assemblages in the proximity of the Campana, Viento, and Mula Muerta copper veins and as banded alunite-enargite-pyrite veins in the Campana and Brechita-Huantina areas (Jannas et al, 1999). The latter veins are typical of the high sulfidation systems in the region, but the majority of the El Indio veins have characteristics of low sulfidation systems (Jannas et al., 1999; Bissig, 2001) and will not be discussed further in this paper.

Post-mineralization and peripheral alteration

Detailed studies in the Pascua-Lama and El Indio-Tambo regions have identified several stages of alteration that post-date precious metal mineralization (Table 6.3). These include coarse-grained, banded alunite ± hematite magmatic steam veins in the Tambo deposit. Alunite of similar origin is recognized at Pascua at high elevations. Thin veinlets and disseminations of alunite ± jarosite are also common in both districts. These have the textural character of supergene veins found in many high sulfidation deposits but stable-isotope evidence indicates that alunite in these assemblages in the El Indio-Pascua Belt is not typical of a supergene origin (Fig. 6.3). Instead, the veins are interpreted to have occurred from the oxidation of sulfide

species in mixed magmatic-meteoric fluids at moderate temperatures (*ca.* 85° to 100°C; see Chapter 2 and 3). True supergene processes are recognized only at Pascua, where jarosite with a supergene isotope signature was dated at 7.98 ± 0.43 Ma (Chapter 2).

Steam-heated acid sulfate alteration is recognized throughout the El Indio-Pascua Belt. Alteration is characterized by surficial, blanket-type alteration zones with quartz ± kaolinite, native sulfur, and trace alunite. While the geometry and mineralogy of these zones is typical of steamed-heated alteration around many high and low sulfidation epithermal deposits, isotopic signatures of alunite in the El Indio-Pascua examples indicate a strong magmatic component to the source fluids, which is not typical of most steam-heated systems. Dating of alunite by ^{40}Ar-^{39}Ar methods demonstrates that alteration is contemporaneous with precious metal mineralization at both Tambo and Pascua. Slightly younger (7.7 ± 0.2 Ma: Bissig, 2001), widespread steam-heated alteration in the Azufreras area, about 3 km west of Tambo, is not associated with any known mineralization at depth.

No significant alteration younger than Vallecito age volcanism (5.5–6.2 Ma: Bissig, 2001) has been recognized in the El Indio-Pascua Belt, although on-going hydrothermal activity is evident from small geothermal hot springs in the El Indio and Veladero areas.

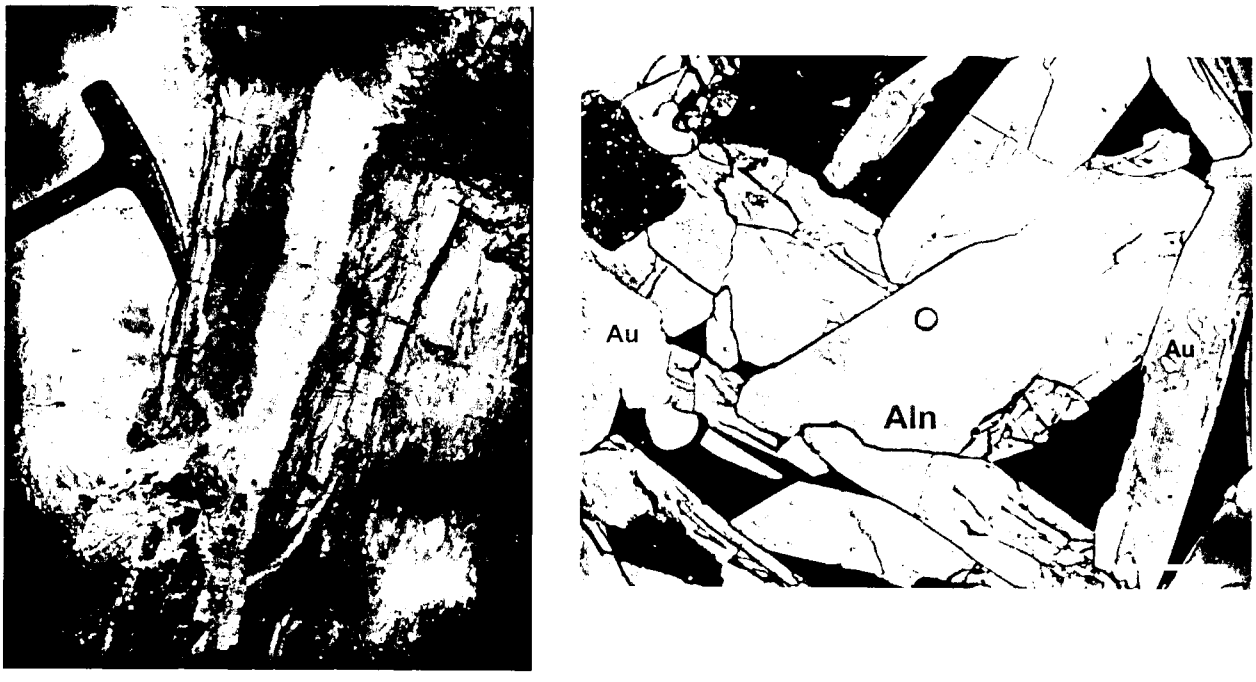

Figure 6.4. A) *on left.* Banded alunite-enargite-pyrite vein, Pascua deposit (Maria Tunnel, sample PS-17). B) *on right.* Native Au (white) associated with alunite (grey) from Tambo (Wendy deposit, DDH-92a , 206.7m; SEM backscatter image). Bright circle in centre of image due to electron beam damage. Scale bar = 25 μm.

DISCUSSION: COMPARISON TO OTHER HIGH SULFIDATION SYSTEMS

1. The origin and importance of early alteration

Economic mineralization in the El Indio-Pascua Belt was preceded by the development of numerous and widespread barren alteration zones (Bissig, 2001). Pre-mineral, barren alteration is typical of most high sulfidation systems and may be an important factor in the development of some economic deposits. In the ore environment, permeability generated by early stage leaching and residual silica may control fluid flow and subsequent metal deposition (e.g., Stoffregen, 1987; Sillitoe, 1993). At a larger scale, early magmatic activity related to pre-mineral alteration may also provide a source of metals that can be remobilized and incorporated in later ore-forming events.

Several reasons have been postulated for the lack of mineralization in early alteration. In the most popular model, it is suggested that early alteration formed from magmatic vapors which were not capable of transporting metals (Arribas, 1995; Cooke and Simmons, 2000). As discussed below, however, there is considerable evidence from El Indio-Pascua and other data for vapor transport of metals and hence an alternative model is needed to explain the lack of mineralization in early alteration.

Stable-isotope evidence indicates that magmatic fluids responsible for both alteration and mineralization in magmatic-hydrothermal systems are decoupled from their magma source (Rye, 1993). These fluids have equilibrated with lower temperature rocks before being released into the epithermal environment (Rye, 1993; Deen et al., 1994). Fluids and metals therefore may be stored in the region between the water-rich carapace of the magma and the brittle-ductile transition (Rye, 1993). Fluids exsolved from a crystallizing magma may be stored in this zone temporarily, only to be released by episodic rupture of the brittle-plastic transition (Fournier, 1999). Fournier (1999) argues that the accumulation of significant fluids will only occur after a considerable body of plastic rock has formed as a result of magmas encountering rocks that have been heated to successively higher temperatures by previous igneous activity. If correct, sufficient metal-rich fluids will not be present until late in the development of a magmatic-hydrothermal system, and conversely, early alteration will be derived from metal-poor fluids and hence will not be mineralized.

2. Mineralizing processes

While there is general consensus that source of fluids and metals in high sulfidation

deposits is magmatic (e.g. Hedenquist and Lowenstern, 1994; Arribas, 1995; Cooke and Simmons, 2000), there is still considerable uncertainty regarding the physical nature of the ore fluids. In particular, the relative contributions of vapor versus hypersaline liquid to the transport and deposition of gold, silver, and copper are the cause of much debate. In a recent summary, Cooke and Simmons (2000) outlined current models for high sulfidation mineralization, based on fluid inclusion and isotopic studies from several deposits. Three possible fluid types were discussed:

a) Low-salinity, acid waters with high concentrations of reduced sulfur and hydrosulfide-complexed metals. These fluids could either result from the mixing of magmatic volatiles with meteoric waters (Sillitoe, 1983; Arribas, 1995), particularly under high pressure conditions (Hedenquist, 1995), or from the base of a rising magmatic vapor plume (Rye, 1993).
b) Acidic brines derived from an exsolved magmatic fluid with chlorine-complexed metals.
c) Reduced magmatic vapors capable of transporting gold and copper in the vapor phase as volatile species.

A variation on (a) was recently proposed by Muntean and Einaudi (2001) for epithermal mineralization in the Maricunga Belt. They suggest that high sulfidation gold ore at La Pepa formed simultaneously with quartz-alunite alteration following the condensation of a moderately saline, supercritical fluid into shallow meteoric waters.

In the El Indio-Pascua Belt, stable-isotope data from ore-related alunite show no evidence for non-magmatic fluids (Fig. 6.3) and a fluid mixing model therefore appears unlikely. Ore-stage fluid inclusions are typically vapor-rich with salinities less than 4 wt% NaCl equivalent (this study; Beane et al, 1988; Jannas et al, 1999). Although slightly higher salinities are recorded locally (up to 10 wt% NaCl equiv.), there is no evidence for a significant hypersaline fluid component in any deposit. In several of the deposits in the El Indio-Pascua Belt, alunite is intergrown with, or host to, ore minerals and is therefore considered to be contemporaneous with gold (± copper) deposition (e.g., Fig. 6.4). This alunite has textural, geochemical, and stable-isotope characteristics consistent with condensation from a magmatic vapor plume (e.g., Rye et al, 1992; Rye, 1993), supporting a vapor transport–condensation model for El Indio-Pascua deposits.

Support for vapor transport comes from recent studies of metal fractionation between magmatic brines and high-temperature vapors in fluid and melt inclusions which have demonstrated the considerable capacity of magmatic vapors to transport metals such as copper

and gold (Lowenstern et al., 1991; Heinrich et al., 1992; Shinohara, 1994; Audétat et al., 1998; Heinrich et al., 1999; Ulrich et al., 1999). In some cases, gold, silver, and copper are shown to partition preferentially into a high-pressure vapor phase (Heinrich et al., 1999). These results are particularly significant to epithermal mineralization, given the much larger mobility and mass flux of a vapor phase relative to the brine.

The occurrence of significant alunite as gangue to gold (and copper) mineralization in the El Indio-Pascua Belt is unusual. Similar assemblages are reported only in la Mejicana deposit, Nevados del Famatina District, Argentina (Losada-Calderon and McPhail, 1996). The intimate association of sulfide and sulfates has implications for ore-fluid chemistry in each of these environments. In most high sulfidation systems, ore fluids are considered to be relatively reduced, with gold transported as either bisulfide- or chloride-complexed species (as summarized in Cooke and Simmons, 2000). Thermochemical models for the Pascua APE-stage ore (Fig. 6.5), however, indicate that acidic and relatively more oxidized fluid conditions are required to deposit the alunite-enargite-pyrite-S^{o} assemblage. Under these conditions, the bulk of Au transport may still be attributed to $Au(HS)^{o}$ complexes, in accordance with the experimental predictions of Benning and Seward (1995).

The chemistry of high sulfidation ore fluids will also affect the relation of copper and gold mineralization. In several systems, gold deposition is preceded by an earlier stage of copper mineralization (e.g., Hedenquist et al., 1998; Jannas et al., 1999). This phenomenon has been attributed to the progressive reduction, and possibly neutralization, of mineralizing fluids. This relation does not apply in the El Indio-Pascua Belt. New geological and geochronological data from El Indio indicate that the distinction determined by Jannas et al. (1999) between early copper-stage and late gold-stage ore is no longer applicable (Bissig, 2001). At Pascua, gold is coeval with copper deposition (Chouinard and Williams-Jones, 1999).

In the El Indio-Pascua belt, the most likely model for the formation of the major mineralizing systems involves:

- release of vapor from magma and the overlying carapace below the brittle-ductile transition;
- transport of metals in vapor with eventual condensation of the vapor into previously condensed magmatic fluids;
- deposition of metals by either oxidation or boiling of the condensed fluid.

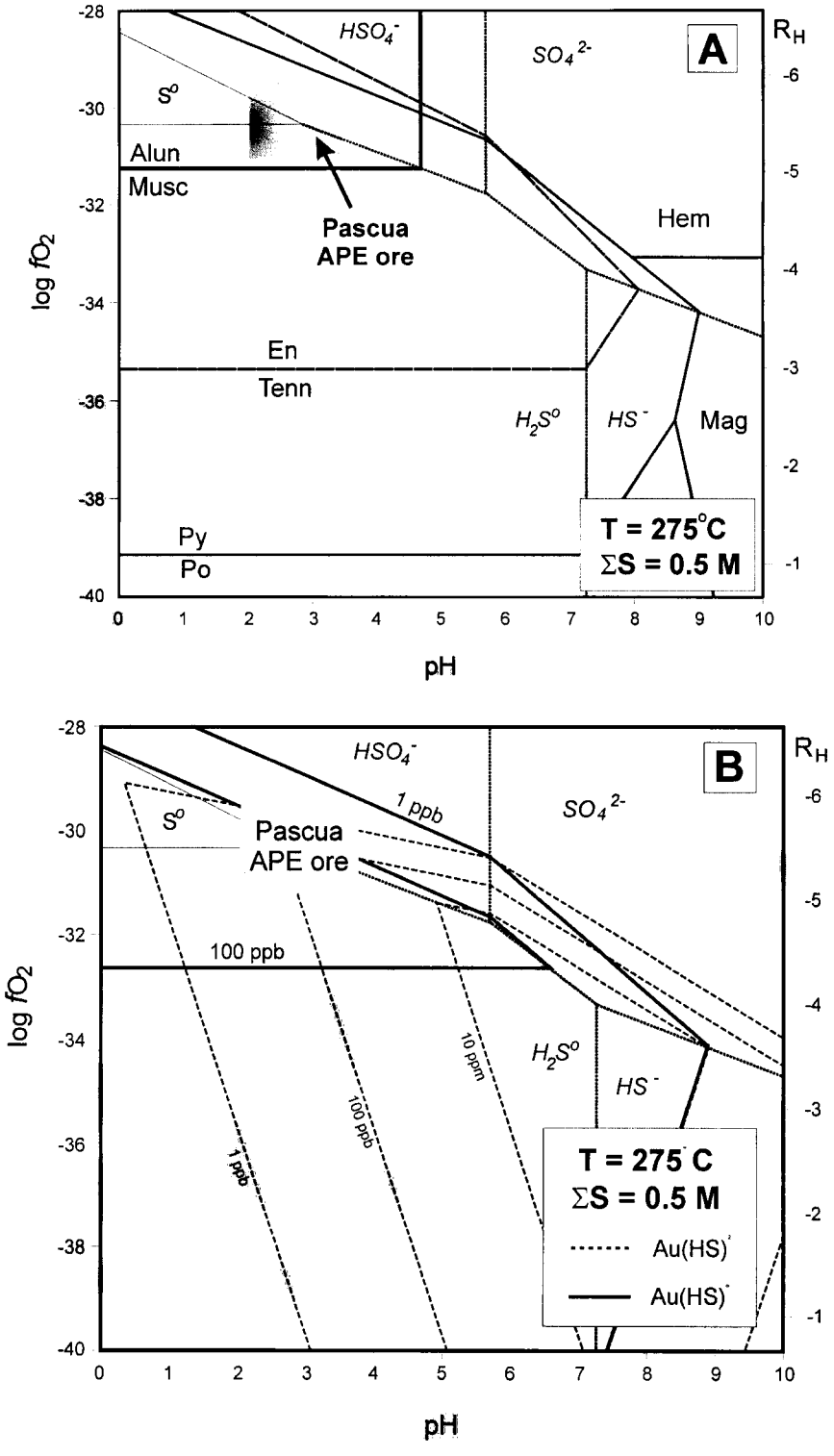

Figure 6.5. The Pascua alunite-pyrite-enargite (APE) mineralizing event in terms of pH and the fugacity of O_2 at 275°C and 0.5 molal total dissolved sulfur. A) Stability relations among minerals are calculated using reactions given in Appendix D. Pressure equals vapour saturation at temperature. The shaded grey area represents an estimate of APE ore fluids based on the stability fields of the mineral assemblage alunite, pyrite, enargite, and native sulfur. Mineral abbreviations: alunite (alun), enargite (en), hematite (hem), magnetite (mag), muscovite (musc), pyrrhotite (po), pyrite (py), native sulfur (S^o), tennantite (tenn). B) Calculated solubilities of gold hydrosulfide species based on data from Benning and Seward (1996). Details of calculations given in Appendix D.

3. Magmatic-hydrothermal to supergene transition

Late-stage processes in the El Indio-Pascua Belt include the deposition of magmatic steam alunite and late-stage acid sulfate alteration. The magmatic steam environment was originally defined by Rye et al. (1992) based on data for coarsely crystalline alunite veins from Marysvale, Utah (Cunningham et al., 1984). Documented occurrences of this type are rare however, and its origins are poorly understood. Alunite is thought to have crystallized directly from a magmatic vapor phase that ascended rapidly without loss of heat by conduction following the rapid decompression of the magma chamber (Rye, 1993; Fournier, 1999). Paragenetic relationships and ^{40}Ar-^{39}Ar results from Tambo indicate that magmatic steam alunite forms late in the development of the hydrothermal systems, following prolonged periods of magmatic-hydrothermal activity. A similar sequence of events is recorded at the Red Mountain deposit, Colorado (Bove et al., 1990; Rye et al., 1992). Alteration is typically unrelated to precious metal mineralization (Bove et al., 1990; Rye et al., 1992, Rye, 1993, this study), although a late-stage of gold deposition at Tambo (Stage 3) is hosted in alunite of magmatic steam origin. The presence of gold in this stage provides further support for vapor transport of metals, and furthermore suggests that gold may precipitate directly from vapor without prior condensation.

Late-stage alteration is responsible for significant oxidation and alunite ± jarosite deposition throughout the El Indio-Pascua Belt. In many deposits, this style of alteration is termed supergene and is related to weathering; however, much of this alteration in the El Indio-Pascua Belt is not strictly supergene in origin. Based on the stable isotopic composition of alunite, sulfate was derived either from the oxidation of precursor sulfides or aqueous sulfur species, and was incorporated into fluids of mixed magmatic-meteoric origin at moderate temperatures (*ca.* 85° to 100°C). Elevated trace metal contents in late-stage alunite suggest that these fluids were capable of either transporting or remobilizing metals from the primary hypogene ore assemblage. Similar processes are thought to be responsible for silver enrichment at high elevations in the Brecha Central area, Pascua (A. Chouinard, pers. comm.).

The timing and origin (hypogene versus supergene) of oxidation is the source of considerable debate in several high sulfidation deposits (e.g., Paradise Peak, Sillitoe and Lorson, 1994; Summitville, Stroffregen, 1987; Pierina, Noble et al. 1997; summarized in Sillitoe, 1999). Results from this study offer an alternative process intermediate to these two 'end-members'. A mixed magmatic-meteoric fluid composition, combined with moderate temperatures of deposition, rule out a true supergene – weathering origin for alunite.

Conversely, formation of this alunite in a shallow environment related to the probable paleosurface suggests similarities to steam-heated alunite and descending fluids rather than ascending hypogene processes. This type of alunite is therefore interpreted to be transitional among typical hypogene, steam-heated and supergene processes.

4. The near-surface environment

Extensive tabular zones of alteration are widespread at high elevations throughout the El Indio-Pascua Belt. These alteration zones have the characteristics of steam-heated alteration, however the stable-isotope evidence from alunite is not consistent with the expected meteoric fluid contribution for near-surface alteration. Instead, much of the water appears to be previously condensed magmatic vapors that either displaced or overwhelmed meteoric fluids in the host rock. We attribute these processes to the climatic and physiographic characteristics specific to the El Indio-Pascua Belt. In contrast to many high sulfidation deposits, mineralization in this belt was not associated with calderas or large volcanic edifices. Instead, the region was dominated by extensive sub-planar erosion surfaces that are now incised by Pliocene or younger fluvial and glacial processes (Bissig, 2001). Although the preservation of these surfaces and shallow level steam-heated alteration throughout the El Indio Belt implies limited erosion, pediment incision occurred in the Late Miocene and may have played a major role in controlling near-surface fluid dynamics (Bissig, 2001). Repeated incision depressed the water table and makes it unlikely that large lakes were present in this region of the Andes. This, combined with the onset of hyper-arid to arid conditions in northern Chile, would limit the availability of meteoric water in the upper part of the El Indio-Pascua high sulfidation systems. Prolonged magmatic-hydrothermal activity would therefore favor the accumulation of magmatic fluids within the hydrothermal system explaining the dominant magmatic isotopic signature in alunite that formed close to the paleosurface.

CONSTRAINTS ON THE HIGH SULFIDATION MODEL

The El Indio-Pascua Belt is one of the world's largest high sulfidation districts, comprising several mined deposits, extensive resources, and widespread alteration zones. Geological constraints provided by regional- (e.g., Martin et al., 1999; Kay et al., 1999; Bissig, 2001) and deposit-scale (e.g., Jannas et al., 1999; Chouinard and Williams-Jones, 1999; Jones et

al., 1999) studies have provided a detailed framework in which to examine shallow-level magmatic-hydrothermal processes. Several conclusions can be drawn from this study:

1. The largest deposits in the El Indio-Pascua Belt are characterized by multiple alteration and mineralizing events. Episodic magmatic-hydrothermal activity is typically recorded over several million years. Barren alteration events may be important for the development of subsequent economic mineralization – both as local permeability controls, and potentially as a source of metals that can be remobilized by later magmatic activity.
2. Alunite is coeval with gold (± copper) deposition. This alunite typically has characteristics consistent with a magmatic-hydrothermal origin. Syn-ore magmatic steam alunite is recognized only at the Tambo deposit.
3. The abundance of alunite associated with precious-metal mineralization requires relatively oxidizing and acidic fluids. These findings are not consistent with a near-neutral, reduced ore-fluid that is inferred for many high sulfidation deposits (e.g., Hedenquist et al., 1998).
4. Limited fluid inclusion data indicate the majority of the ore-fluids were vapor-rich. Based on the currently accepted model for the origin of magmatic steam alunite (see Chap. 3), the presence of mineralization in magmatic steam alunite at Tambo implies vapor transport of gold and deposition directly from vapor without prior condensation. This study is consistent with emerging evidence from other systems indicating the importance of vapor transport for metals in high sulfidation systems.
5. Alteration and mineralization were dominated by magmatic fluids, even in the near-surface environment. This is attributed to the displacement or dilution of meteoric fluids by condensed magmatic vapors due to prolonged magmatic activity, an arid climate, and depressed water tables resulting from repeated incision.

These characteristics provide important constraints to the high sulfidation genetic model in the El Indio-Pascua Belt. These characteristics reflect specific features of the belt including:

- multiple periods of magmatism prior to mineralization but limited evidence for magmatic activity similar in age to mineralization – no evidence for major volcanic edifices related to mineralizing centres;
- semi-arid climatic conditions - which, combined with landforms (Bissig, 2001), suggest limited availability of meteoric water;

- slab-flattening, crustal thickening and the generation of magmas from lower crustal source regions modified by slab-derived fluids (Bissig, 2001);
- uplift, incision but limited overall erosion – contrasting with the Los Pelambres – El Teniente Belt to the south;
- repeated magmatic-hydrothermal events resulting in widespread pre-mineral alteration, zones of mineralization focused in breccias and veins, and post-ore alteration all of which were dominated by magmatic fluids.

These features may be present in other areas but are clearly absent from the majority of high sulfidation deposits. Genetic models for these systems need to be re-evaluated in the light of this study with the recognition that a range of area-specific processes may operate successfully to form high sulfidation deposits. It is likely, however, that the particular characteristics of the El Indio - Pascua Belt relate to the formation and preservation of the prolific mineralizing systems in this region.

REFERENCES

Arribas, A., Jr., 1995. Characteristics of high sulfidation epithermal deposits, and their relation to magmatic fluids. *In* Thompson, J.F.H., ed., Magmas, Fluids and Ore Deposits. Mineralogical Association of Canada Short Course Notes, 23, 419-454.

Arribas, A., Jr., Cunningham, C.G., Rytuba, J.J., Rye, R.O., Kelly, W.C., McKee, E.H., Podwysocky, M.H., and Tosdal, R.M., 1995. Geology, geochronology, fluid inclusions, and stable-isotope geochemistry of the Rodalquilar Au alunite deposit, Spain. Economic Geology, 90, 795-822.

Ashley, R.P., 1982. Occurrence model for enargite-gold deposits. U.S. Geological Survey Open File Report 82-795, 144-147.

Audétat, A., Günther, D., and Heinrich, C.A., 1998. Formation of magmatic-hydrothermal ore deposit: Insights with LA-ICP-MS analysis of fluid inclusions. Science, 279, 2091-2094.

Beane, R.E., 1988. Hydrothermal alteration and mineralization at the Nevada prospect, Chile. Internal report for Barrick Gold.

Bennet, R.E., 1995. A combined hydrothermal alteration study and exploration target evaluation of the Tambo mining district, El Indio mineral belt, Region IV, Chile. Internal

report for Companìa Minera San José Ltda.

Benning, L.G., and Seward, T.M., 1996. Hydrosulfide complexing of Au(I) in hydrothermal solutions from 150-400°C and 500-1500 bar. Geochimica et Cosmochimica Acta, 60, 1849-1872.

Berger, B.R, 1986. Descriptive model of epithermal quartz-alunite Au. *In* Cox, D.P., and Singer, D.A., eds., Mineral Deposit Models. U.S. Geological Survey Bulletin 1693, p.158.

Bissig, T., 2001. Metallogenesis of the Miocene El Indio-Pascua gold-silver-copper belt, Chile/ Argentina: Geodynamic, geomorphological and petrochemical controls on epithermal mineralization. Unpublished Ph.D. thesis, Queen's University.

Bodnar, R.J., 1995. Fluid-inclusion evidence for a magmatic source of metals in porphyry copper deposits. Mineralogical Association of Canada Short Course Series, v. 23, 139-152.

Bonham, H.F., Jr, 1984. Three major types of epithermal precious metal deposits. Geological Society of America Abstracts with Program, 16, 449.

Bonham, H.F., Jr., 1986. Models for volcanic-hosted epithermal precious metal deposits: A review. *In* Proceedings of the International Volcanological Congress, Symposium 5, Hamilton, New Zealand 1986. Aukland, New Zealand, 13-17.

Bove, D.J., Rye, R.O., and Hon, K., 1990. Evolution of the Red Mountain alunite deposits, Lake City, Colorado. US Geological Survey Open File Report, 90-0235.

Chouinard, A. and Williams-Jones, A.E. 1999. Mineralogy and petrography of ore and alteration assemblages at the Pascua Au-Ag-Cu deposit, Chile. Internal for Barrick Gold and Barrick Chile Ltda.

Cooke, D.R. and Simmons, S.F., 2000. Characterisitcs and genesis of epithermal gold deposits. *In* Hagemann. S.G., and Brown, P.E., eds., Reviews in Economic Geology, v. 13, 221-244.

Craig, H., 1961. Isotopic variations in meteoric waters. Science, 133, 1702-1703.

Cunningham, C.G., Rye, R.O., Steven, T.A., and Mehnert, H.H., 1984. Origins and exploration signficance of replacement and vein-type alunite deposits in the Marysvale volcanic field, west central Utah. Economic Geology, 79, 50-71.

Deen, J.A., Rye, R.O., Munoz, J.L., and Drexler, J.W., 1994. The magmatic hydrothermal system at Julcani, Peru: Evidence from fluid inclusions and hydrogen and oxygen isotopes. Economic Geology, 89, 1924-1938.

Fournier, 1999. Hydrothermal processes related to movement of fluid from plastic into brittle rock in the magmatic-hydrothermal environment. Economic Geology, 94, 1193-1212.

Hayba, D.O., Bethke, P.M., Heald, P, and Foley, N.K., 1985. Geologic, mineralogic, and

geochemical characteristics of volcanic-hosted epithermal precious-metal deposits. Reviews in Economic Geology, 2, 129-167.

Heald, P., Foley, N.K., and Hayba, D.O., 1987. Comparative anatomy of volcanic-hosted epithermal deposits: acid-sulfate and adularia-sericite types. Economic Geology, 82, 1-26.

Hedenquist, J.W., 1995. The ascent of magmatic fluid: Discharge versus mineralization. *In* Thompson, J.F.H., ed., Magmas, Fluids, and Ore Deposits. Mineralogical Association of Canada Shortcourse Series, v. 23, 263-289.

Hedenquist, J.W., 1987. Mineralization asscoiated with volcanic-related hydrothermal systems in the Circum-Pacific basin. *In* Horn, M.K., ed., Transactions of the Fourth Circum-Pacific Energy and Mineral Resources Conference, August, 1986. Singapore, American Association of Petroleum Geologists, Tulsa, OK, 513-524.

Hedenquist, J.W. and Arribas, A., Jr., 1999. Epithermal gold deposits: I. Hydrothermal processes in intrusion-related systems, and II. Characteristics, examples, and origin of epithermal gold deposits. *In* F. Molnar, J. Lexa, and J.W. Hedenquist, eds., Epithermal Mineralization of the Western Carpathians. Society of Economic Geologists, Guidebook Series, 31, 13-63.

Hedenquist, J.W., Arribas, Jr., A., and Reynolds, T.J., 1998. Evolution of an intrusion-centered hydrothermal system: Far Southeast-Lepanto porphyry and epithermal Cu-Au deposits, Phillipines. Economic Geology, 93, 373-404.

Hedenquist, J.W. and Lowenstern, J.B., 1994. The role of magmas in the formation of hydrothermal ore deposits. Nature, 370, 519-527.

Heinrich, C.A., Gunther, D., Audetat, A., Ulrich, T., and Frischknecht, R., 1999. Metal fractionation between magmatic brine and vapor, determined by microanalysis of fluid inclusions. Geology, 27, 755-758.

Heinrich, C.A., Ryan, C.G., Mernagh, T.P., and Eadington, P.J., 1992. Segregation of ore metals between magmatic brine and vapor: A fluid inclusion study using PIXE micranalysis. Economic Geology, 87, 1566-1583.

Jannus, R.R., 1995. Reduced and oxidized high sulfidation deposits of the El Indio deposit, Chile. Unpublished Ph.D. thesis, Harvard University, USA, 421 p.

Jannas, R.R., Bowers, T.S., Petersen, U., Beane, R.E., 1999. High-sulfidation deposit types in the El Indio District, Chile. *In* B.J. Skinner, ed., Geology and ore deposits of the Central Andes. SEG Special Publication #7, 27-59.

Jones, P.J., Martinez, R.D., Vitaller, A.O., Chavez, I., Carrizo, M.M., La Motte, M.G., and

Riveros, S.E., 1999. El depósito epithermal aurífero Veladero, San Juan. *In* Zappettini, E. O., ed., Recursos Minerales de la República Argentina. Instituto de Geología y Recursos Minerales SEGEMAR, Anales 35, 1673-1648.

Kay, S.M., Mpodozis, C., and Coira, B., 1999. Neogene magmatism, tectonism, and mineral deposits of the Central Andes (22° to 33° S latitude). *In* Skinner, B.J., ed., Geology and Ore Deposits of the Central Andes, SEG Special Publication #7, 27-59.

Kay, S.M., and Mpdozis, C., 2001. Central Andean ore deposits linked to evolving shallow subduction systems and thickening crust. GSA Today, 11, 4-9.

Kurtz, A.C., Kay, S.M., Charrier, R., Farrar, E., 1997. Geochronology of Miocene plutons and exhumation history of the El Teniente region, central Chile (34-35 degrees S). Revista Geologica de Chile, 24, 75-90.

Losada-Calderon, A.J., and McPhail, D.C., 1996. Porphyry and high-sulfidation epithermal mineralization in the Nevados del Famatina Mining District, Argentina. *In* Camus, F., Sillitoe, R.H., and Petersen, R., eds., Andean copper deposits: New discoveries, mineralization, styles, and metallogeny. Society of Economic Geologists Special Publication No. 5, 91-118.

Lowenstern, J.B., Mahood, G.A., Rivers, M.L., and Sutton, S.R., 1991. Evidence for extreme partitioning of copper into a magmatic vapor phase. Science, 257, 1405-1409.

Maksaev, V., Moscoso, R., Mpodozis, C., and Nasi, C., 1984. Las unidades volcánicas y plutonicas del cenozoico superior en la Alta Cordillera del Norte Chico (29°-31°S): Geología, alteración hidrothermal y mineralisacion. Revista Geológica de Chile, 21, 11-51.

Martin, M, Clavero, J., and Mpodozis, C., 1995. Estudio geologico regional del Franja El Indio, Cordillera de Coquimbo. Servicio National de Geologia y Minera, Santiago, Chile. Registered report IR-95-06, 232p.

Martin, M.W., Clavero, J.R., Mpodozis, C., 1999. Late Paleozoic to Early Jurassic tectonic development of the high Andean Principal Cordillera, El Indio Region, Chile (29-30°S). Journal of South American Earth Sciences, 12, 33-49.

Muntean, J.L., and Einaudi, M.T., 2001. Porphyry-epithermal transition: Maricunga Belt, Northern Chile. Economic Geology, 96, 1445-1472.

Noble, D.C., Park-Li, B., Henderson, W.B., and Vital, C.E., 1997. Hypogene oxidation and late deposition of precious metals in the Pierina high-sulfidation deposit and other volcanic and sedimentary rock-hosted gold systems. *In* 9th Congreso Peruano de Geología, Resúmenes Extendidos. Sociedad Geológica del Perú, Publicación Especial 1, 121-127.

Noriega, J. and Perez, L., 1997. Proyecto Del Carmen - Informe temporada 1997. Internal report for Barrick Exploraciones, S.A.

Ramos, V. A., Mahlburg Kay, S, Page, R. N. and Munizaga, F., 1989. La ignimbrita Vacas Heladas y el cese del volcanismo en el Valle del Cura, Provincia de San Juan. Revista Asociación Geológica Argentina, 44, 336-352.

Rye, R.O., 1993. The evolution of magmatic fluids in the epithermal environment: The stable-isotope perspective. Economic Geology, 88, 733-753.

Rye, R.O., Bethke, P.M., and Wasserman, M.D., 1992. The stable-isotope geochemistry of acid sulfate alteration. Economic Geology, 87, 225-262.

Shinohara, H., 1994. Exsolution of immiscible apor and liquid phases from a crystallizing silicate melt: Implications for chlorine and metal transport. Geochimica et Cosmochimica Acta, 58, 5215-5221.

Sillitoe, R.H., 1983. Enargite-bearing massive sulfide deposits high in porphyry copper systems. Economic Geology, 78, 348-352.

Sillitoe, R.H., 1993. Epithermal models: Genetic types, geometric controls, and shallow features. *In* R.V. Kirkham, W.D. Sinclair, R.I. Thorpe and J.M. Duke, eds., Mineral Deposit Modelling. Geological Association of Canada Special Paper 40, 403-417.

Sillitoe, R.H., 1999. Styles of high sulfidation gold, silver and copper mineralization in the porphyry and epithermal environments. PacRim '99. Bali, Indonesia, 10-13 October, Proceedings, 29-44.

Sillitoe, R.H., and Lorson, R,C, 1994. Epithermal gold-silver-mercury deposits at Paradise Peak, Nevada: Ore controls, porphyry gold association, detachment faulting, and supergene oxidation. Economic Geology, 89, 1228-1248.

Skewes, M.A., and Stern, C.R., 1994. Tectonic trigger for the formation of late Miocene Cu-rich breccia pipes in the Andes of central Chile. Geology, 22, 551-554.

Stroffregen, R., 1987. Genesis of acid-sulfate alteration and Au-Cu-Ag mineralization at Summitville, Colorado. Economic Geology, 82, 1575-1591.

Ulrich, T., Gunther, D. and Heinrich, C.A., 1999. Gold concentrations of magmatic brines and the metal budget of porphyry copper deposits. Nature, 399, 676-679.

Venneman, T.W., Muntean, J.L., Kesler, S.E., O'Neil, J.R., Valley, J.W., and Russell, N., 1993. Stable-isotope evidence for magmatic fluids in the Pueblo Viejo epithermal acid sulfate Au-Ag deposit, Dominican Republic. Economic Geology, 88, 55-71.

Vila, T., and Sillitoe, R.H., 1991. Gold-rich porphyry systems in the Maricunga Belt, northern

Chile. Economic Geology, 86, 1238-1260.

White, N.C., and Hedenquist, J.W., 1990. Epithermal environments and styles of mineralization: variations and their causes, and guidelines for exploration. Journal of Geochemical Exploration, 36, 445-474.

APPENDIX A: GEOCHEMICAL ANALYSIS

A.1 Analytical techniques: Electron Microprobe

Electron probe microanalysis (EPMA) of alunite and alunite-group minerals is difficult. The thermal sensitivity of these minerals results in extreme volatilization of alkali elements and suitable analytical standards are generally unavailable (A.J.B. Thompson and E.U. Petersen, 1992). Optimum analytical conditions needed to be determined at the start of this study, as outlined below. The standard used in this study is a sample of Marysvale Christmas vein alunite supplied by Roger Stoffregen.

A) Analytical parameters

Of all the major elements in alunite-group minerals, Na and K are particularly sensitive to volatilization. This results in a relative increase in measured concentrations of Al and S. Visible beam damage is also common. As a result, standard EPMA operating conditions with long count times cannot be used. Conditions must be optimized to balance long count times (for better precision) while minimizing volatilization of the alkali elements. Published information on analytical parameters used for the analysis of alunite are scarce. Selected values are given in Table A1.

Table A1: Published EPMA analytical parameters for alunite–group minerals ("-" denotes data not provided).

Source	KeV	nA	Spot size (μm)	Time (s)	Comments
Thompson and Petersen (written, comm.)	10	20	20	<40	Time = total analysis time. Did not determine Fe
Stoffregen and Alpers (1987)	15	12-22	10-30	-	
Muntean *et al* (1990)	10	-	10-20	-	
Scott (1990)	20	10	20	5	No sample damage noted
Li *et al* (1992)	10-12	4-5	3-6	15/30	15 sec for K and Na; 30 sec for all other elements
Cho and Kim (1993)	15	5	5	-	

Optimum EPMA analytical conditions for this study were determined by a series of experiments to test the effect of changing accelerating potential, beam current, spot size, and total analysis time on alunite grains. Two alunite samples were used; the Marysvale alunite standard and Na-rich alunite from Del Carmen (determined from PIMA analysis). All data in this study were collected on a fully automated Cameca SX-50 microprobe with four wavelength dispersive spectrometers, a fully-integrated Kevex 8000 energy-dispersive system, and synthetic multi-layer diffracting crystals for the analysis of light elements.

Results from these experiments are summarized below. Variations in recorded counts are considered significant (at a 95% confidence level) when total counts per interval exceed the

initial response ± 2σ. Counts are defined as the number of Kα X-rays measured by each detector.

- The effects of volatilization are shown in Fig A1. Counts recorded for K are significantly reduced while those for S and Al increase over time.
- A minimum 15 KeV voltage is required for the determination of Fe. Our results indicate that the rate of K loss remains constant at increasing accelerating voltage (from 10 to 15 KeV; determined at constant beam size (both 20 μm and 15 μm) and 20 nA). However, overall count rates are approximately 4 times higher at 15 KeV (versus 10 KeV).
- Counting experiments with changing accelerating current were determined between 5 and 20 nA. Total response is greatest at highest current values, but sample damage is also more pronounced
- The effect of varying beam size was determined between 10 to 40 μm (Fig. A2a,b). At 15 KeV and 10 nA, beam sizes ≥ 20 μm show no significant decrease in K at count times up to 3 minutes. At 10 μm however, significant K loss occurs after about 55 seconds. At 15 μm, K counts are stable to at least 130 seconds.
  - Our results confirm that Na is more volatile than K. Significant loss in Na counts occurs after approximately 45 seconds at 10μm beam size. Increasing the spot size to 15 μm increases the stability of Na to at least 65 seconds; and to 150 seconds at 20μm. A similar trend occurs using 10 KeV and 20 nA, from 10 to 20 μm (Fig A2c).
- Total analysis time:
  - Under the conditions 15 KeV, 10 nA, and 20 μm, Na is stable for at least 130 seconds, and longer for K (Fig. A3).
  - At 15 μm, Na is stable for 94 seconds on average, and a minimum of 65 seconds. For K, counts are stable to an average of 130 seconds and a minimum of 85 seconds.

In general, results indicate that using a larger beam will increase the optimum analytical time, but also results in reduced resolution. This is particularly significant when analyzing small grains or finely zoned crystals. Using a beam sizes larger than 20 μm is impractical for the purposes of this thesis, due to the small grain size of several alunite samples and small-scale compositional zoning. Spot size less than 15 μm however do not allow for adequate analysis times.

Conclusions:

Optimum analytical conditions are determined to be 15 KeV, 10 nA,15 μm, with a total analysis time under 65 seconds. Elements are arranged on the 4 spectrometers as indicated in Table A2.

Table A2: Configuration of spectrometers (Spec) for alunite analyses.

	Count time (s)	*Background time (x2)*	*Spec. 1*	*Spec. 2*	*Spec. 3*	*Spec. 4*
Crystal:			**LIF**	**TAP**	**PET**	**PET**
Pass 1	12	6	Fe	Na	K	S
Pass 2	10	5		Al	P	Ca
Pass 3	10	5		Sr	Ba	

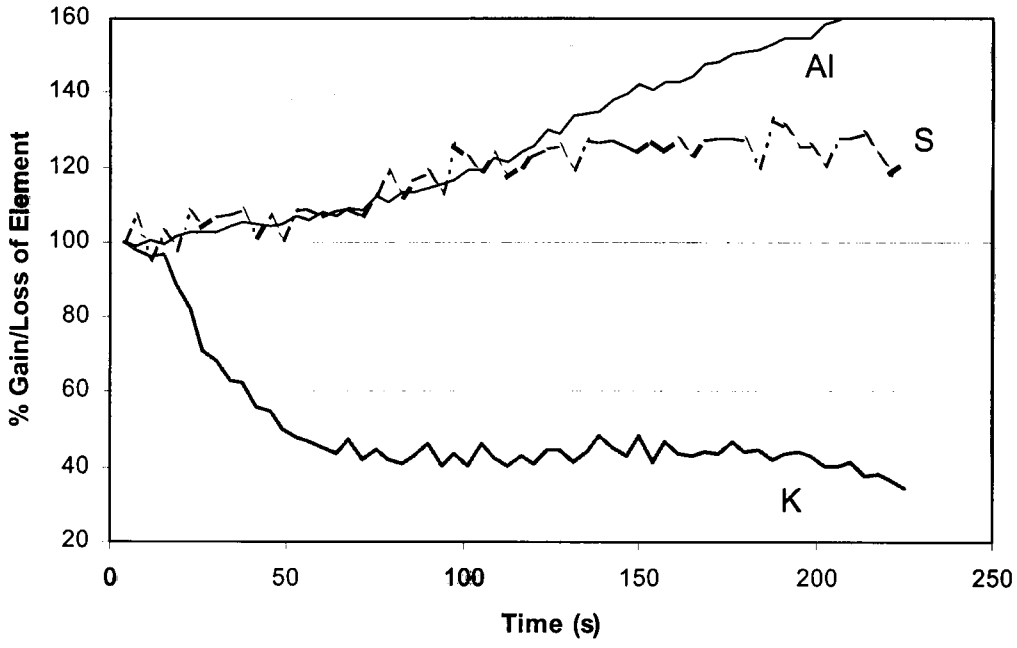

Figure A1. Effects of volatilization for K, S, and Al. Analytical conditions: 10 KeV, 20 nA, 10 um.

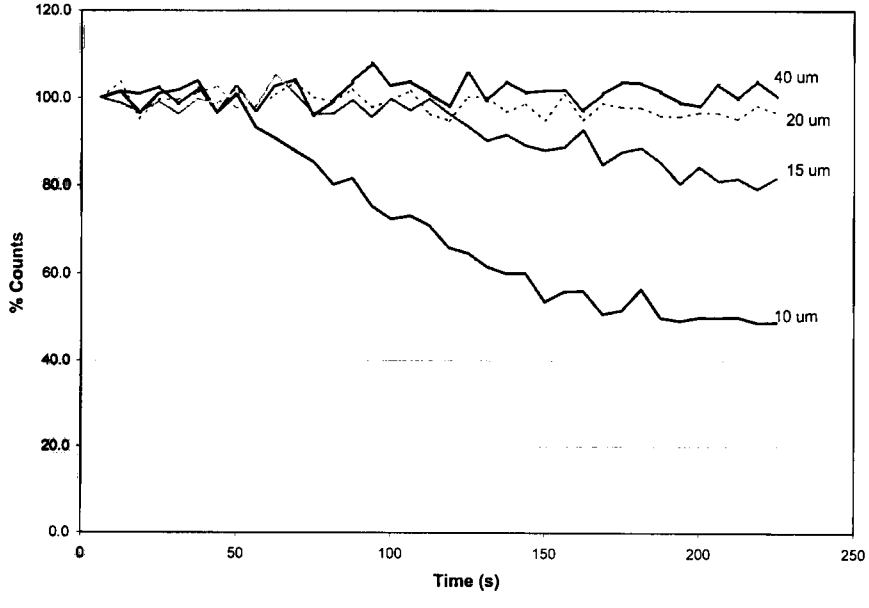

Figure A2a. Counting statistics (given as percentage of original number of counts) for K at 15 KeV, 10nA, and variable beam size.

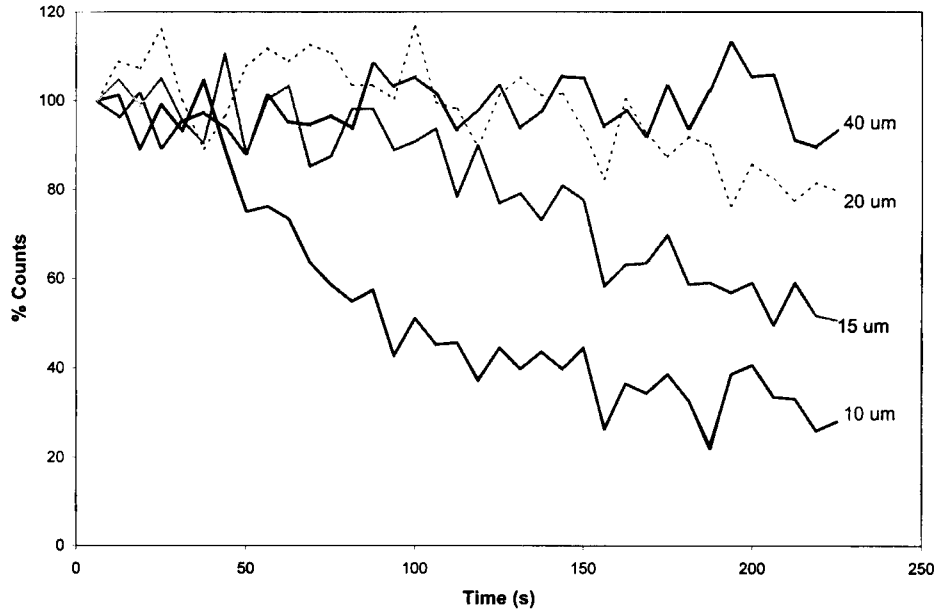

Figure A2b. Counting statistics (given as percentage of original number of counts) for Na at 15 KeV, 10nA, and variable beam size.

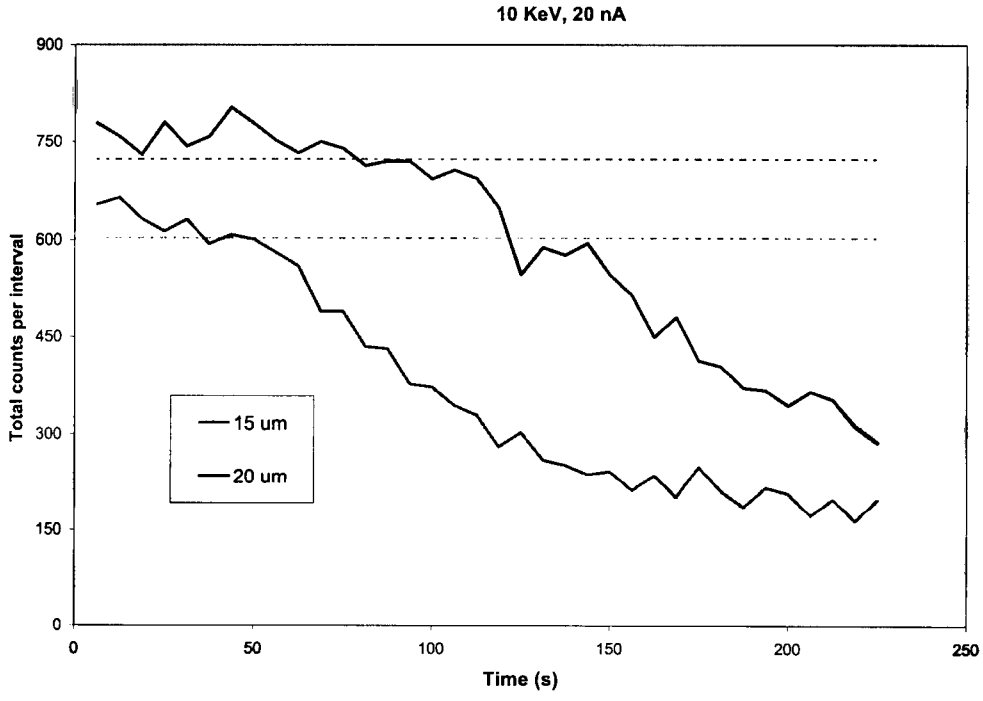

Figure A2c. Counting statistics (given as total counts per time interval) for Na at 10 KeV, 20nA, and variable beam size. Dashed lines represent 2σ limit on initial analysis for each beam size.

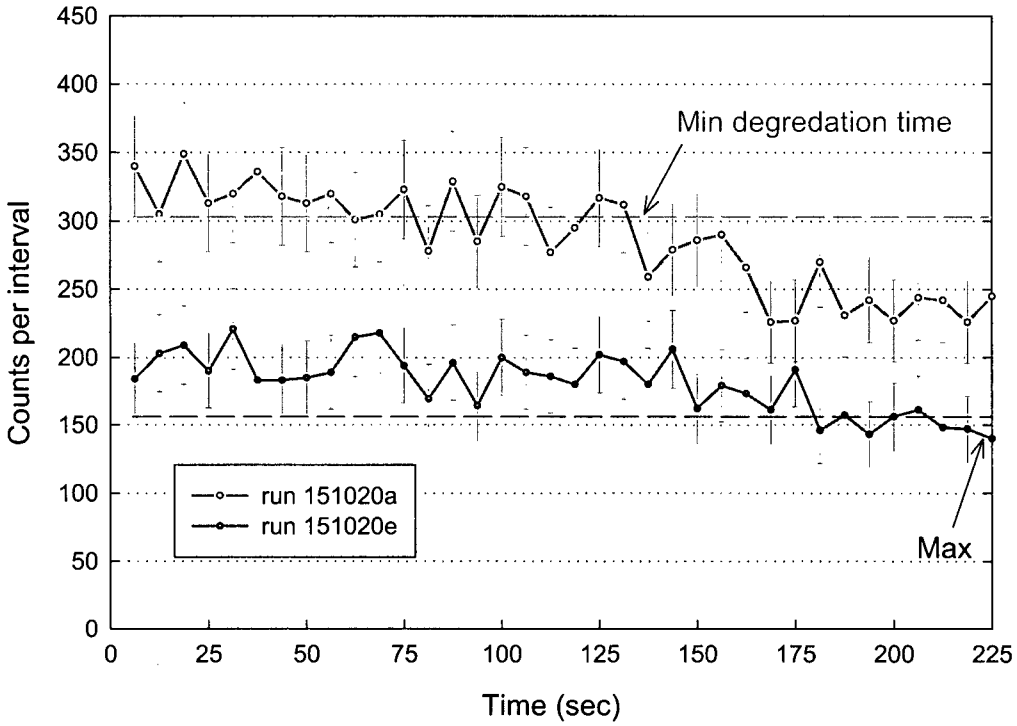

Fig. A3. Na counting statistics at 15 KeV, 10nA, and 20 um. Error bars represent ± 2σ limit on each analysis. Minimum degradation time given as time when total number of counts per interval is less than original count ± 2σ. Minimum and maximum values are taken from 6 replicate analyses at specified analytical conditions.

B) Analytical standard

A.J.B. Thompson and E.U. Petersen (written comm.) determined that higher quality EPMA data is generated using alunite as an analytical standard, rather than combining standards from other minerals. No alunite standard was available at UBC at the start of this project but a sample of Marysvale Christmas vein alunite was supplied by Roger Stoffregen (Table A3; from Stoffregen and Alpers, 1987). This material has been used in previous studies by Roger Stoffregen (Stoffregen and Alpers, 1987; Stoffregen and Alpers, 1992).

Table A3. Composition of Marysvale alunite from Stoffregen and Alpers (1987). n.d. = not detected. Methods of recalculation are not specified.

Oxide	Weight % Oxide
K_2O	10.84
Na_2O	0.19
CaO	n.d.
SrO	0.31
BaO	n.d.
Al_2O_3	36.92
SO_3	36.94
P_2O_5	0.86
H_2O	13.05[1]
Total	**99.11**

Element	Number of moles
K	0.952
Na	0.024
Ca	n.d.
Sr	0.12
Ba	n.d.
Al	2.998
S	1.91
P	0.049
OH	6.003

[1] Weight % H_2O calculated on basis of observed values of calcium, strontium, phosphorus, and sulfur.

The Marysvale material was sent to Erich Petersen for analysis using a synthetic alunite standard for independent verification of the chemical composition. Only the elements K, Na, Ca, S, P, Al and S were analyzed (Table A4). The presence of elements Fe, Pb, As, and Ba was checked by line scan (for a total of 16.7 minutes) – none were detected.

	Measured Wt % Element									Calculated Moles Per Formula Unit							
Analysis #	**K**	**Na**	**Ca**	**Al**	**P**	**S**	**H**	**O**	**Sum**	**K**	**Na**	**Ca**	**Al**	**P**	**S**	**H**	**O**
10	8.18	0.12	0.04	18.29	0.33	15.65	1.42	53.22	**97.25**	0.89	0.02	0.00	2.87	0.05	2.07	6.01	14.09
35	8.81	0.05	0.00	18.93	0.17	15.10	1.42	52.84	**97.31**	0.96	0.01	0.00	2.98	0.02	2.00	6.03	14.01
47	8.43	0.25	0.00	18.48	0.50	15.21	1.42	53.02	**97.31**	0.91	0.05	0.00	2.90	0.07	2.01	6.02	14.04
34	8.84	0.17	0.00	18.83	0.20	15.08	1.42	52.81	**97.34**	0.96	0.03	0.00	2.96	0.03	2.00	6.02	14.00
15	8.84	0.03	0.04	18.87	0.32	15.00	1.42	52.85	**97.37**	0.96	0.01	0.00	2.97	0.04	1.98	6.02	14.01
54	9.41	0.10	0.00	18.69	0.00	15.16	1.42	52.64	**97.42**	1.02	0.02	0.00	2.94	0.00	2.01	6.03	13.98
63	9.18	0.05	0.06	18.89	0.29	14.85	1.42	52.70	**97.45**	1.00	0.01	0.01	2.97	0.04	1.97	6.03	13.98
23	9.38	0.11	0.08	18.40	0.20	15.18	1.42	52.70	**97.46**	1.02	0.02	0.01	2.90	0.03	2.01	6.03	13.99
29	9.18	0.02	0.03	18.61	0.29	15.13	1.42	52.83	**97.49**	1.00	0.00	0.00	2.93	0.04	2.00	6.02	14.01
40	8.49	0.09	0.01	18.61	0.28	15.45	1.42	53.17	**97.52**	0.92	0.02	0.00	2.92	0.04	2.04	6.01	14.06
18	8.42	0.13	0.00	18.97	0.13	15.34	1.42	53.13	**97.53**	0.91	0.02	0.00	2.97	0.02	2.02	6.01	14.04
45	8.51	0.21	0.02	18.55	0.52	15.26	1.42	53.19	**97.68**	0.92	0.04	0.00	2.91	0.07	2.01	6.00	14.05
58	8.53	0.14	0.03	18.46	0.47	15.40	1.42	53.25	**97.70**	0.92	0.03	0.00	2.89	0.06	2.03	6.00	14.06
64	8.96	0.29	0.00	18.52	0.33	15.24	1.42	53.01	**97.77**	0.97	0.05	0.00	2.90	0.05	2.01	6.01	14.01
13	8.72	0.11	0.00	18.53	0.42	15.37	1.42	53.21	**97.78**	0.94	0.02	0.00	2.90	0.06	2.03	6.00	14.05
51	8.84	0.13	0.00	18.92	0.24	15.18	1.42	53.08	**97.81**	0.96	0.02	0.00	2.96	0.03	2.00	6.00	14.02
46	8.70	0.30	0.00	18.33	0.43	15.46	1.42	53.25	**97.89**	0.94	0.05	0.00	2.87	0.06	2.04	5.99	14.05
53	8.95	0.13	0.06	18.73	0.28	15.27	1.42	53.13	**97.96**	0.97	0.02	0.01	2.93	0.04	2.01	6.00	14.03
48	9.35	0.08	0.00	19.11	0.07	15.06	1.42	52.93	**98.01**	1.01	0.01	0.00	2.99	0.01	1.99	6.00	13.98
52	8.72	0.20	0.02	18.35	0.29	15.66	1.42	53.36	**98.02**	0.94	0.04	0.00	2.87	0.04	2.06	5.99	14.06
66	8.76	0.09	0.02	18.53	0.49	15.41	1.42	53.37	**98.09**	0.94	0.02	0.00	2.89	0.07	2.03	5.99	14.06
12	8.48	0.22	0.02	18.50	0.32	15.73	1.42	53.60	**98.28**	0.91	0.04	0.00	2.88	0.04	2.06	5.97	14.09
9	9.00	0.17	0.00	18.94	0.00	15.68	1.42	53.58	**98.78**	0.97	0.03	0.00	2.94	0.00	2.05	5.96	14.05
67	8.61	0.17	0.12	18.41	0.40	15.84	1.42	53.84	**98.81**	0.92	0.03	0.01	2.86	0.05	2.07	5.95	14.10
7	8.92	0.14	0.04	18.69	0.06	15.87	1.42	53.70	**98.84**	0.96	0.03	0.00	2.90	0.01	2.08	5.95	14.07
59	8.96	0.19	0.00	18.42	0.29	15.84	1.42	53.74	**98.85**	0.96	0.03	0.00	2.86	0.04	2.07	5.95	14.08
62	9.08	0.15	0.00	18.88	0.52	15.26	1.42	53.58	**98.88**	0.97	0.03	0.00	2.93	0.07	2.00	5.96	14.04
61	8.81	0.20	0.04	18.41	0.31	15.91	1.42	53.83	**98.92**	0.94	0.04	0.00	2.86	0.04	2.08	5.95	14.09
50	9.26	0.14	0.00	19.15	0.13	15.41	1.42	53.56	**99.06**	0.99	0.02	0.00	2.97	0.02	2.01	5.95	14.03
65	8.53	0.16	0.01	19.04	0.36	15.66	1.42	54.02	**99.20**	0.91	0.03	0.00	2.95	0.05	2.04	5.93	14.10
24	8.91	0.16	0.01	18.80	0.29	15.75	1.42	53.93	**99.28**	0.95	0.03	0.00	2.91	0.04	2.05	5.93	14.08
49	9.59	0.07	0.00	19.41	0.06	15.27	1.42	53.54	**99.35**	1.03	0.01	0.00	3.01	0.01	1.99	5.94	14.01
39	8.87	0.05	0.03	18.98	0.46	15.60	1.42	54.03	**99.44**	0.95	0.01	0.00	2.93	0.06	2.03	5.92	14.09
55	9.21	0.16	0.00	19.23	0.11	15.64	1.42	53.96	**99.73**	0.98	0.03	0.00	2.97	0.01	2.03	5.92	14.05
36	9.35	0.10	0.00	18.95	0.13	15.82	1.42	54.00	**99.76**	1.00	0.02	0.00	2.93	0.02	2.06	5.92	14.07
43	8.78	0.15	0.09	18.39	0.26	16.33	1.42	54.40	**99.82**	0.93	0.03	0.01	2.83	0.04	2.12	5.90	14.14
16	9.25	0.21	0.00	18.91	0.24	15.83	1.42	54.15	**100.01**	0.98	0.04	0.00	2.91	0.03	2.05	5.90	14.07
17	9.19	0.24	0.00	18.99	0.22	15.97	1.42	54.41	**100.43**	0.97	0.04	0.00	2.92	0.03	2.06	5.88	14.09
26	9.55	0.06	0.01	18.83	0.22	16.67	1.42	55.33	**102.09**	1.00	0.01	0.00	2.86	0.03	2.13	5.81	14.16

Table A4. EPMA data for Marysvale alunite using synthetic alunite standard. O determined by charge balance. Recalculation based on $TO_4 = 2$.

Table A5a. Average weight % oxide data for Marysvale standard, determined from EPMA data given in Table A4 (n=39: E. Petersen data).

	Weight % Oxide
K_2O	10.74
Na_2O	0.19
CaO	0.003
SrO	n.a.
BaO	n.a.
Al_2O_3	35.38
SO_3	38.71
P_2O_5	0.62
H_2O	13.05
Total	**98.71**

Table A5b. Error estimates for Marysvale alunite based on n = 39 analyses (E. Petersen data).

Element	2σ	% Precision*
K	0.68	7.7
Na	0.14	95.6
Ca	0.06	290.6
Al	0.56	3.0
S	0.75	4.9
P	0.29	105.7

** calculated at 95% confidence limit.*

As indicated in Table A5b, precision values for major elements are all better than 8%. Precision estimates for Na, Ca, and P are much larger, due to their low abundance (close to detection limit). Low precision values are also likely due to the extremely short count times per element. Overall, results from the Petersen and Stoffregen and Alpers (1987) data sets are comparable. With the exception of Al, all of Petersen's measured weight percent oxide data is the same as the published values, at the 95% confidence level. Published values for Al falls just slightly outside of the 2σ limit measured by Petersen. This variation may be attributed to the omission of Sr in the Petersen analyses.

C) Methods of Recalculation

Given the general formula for alunite-group minerals as: $DG_3(TO_4)_2$ $(OH,H_2O)_6$, recalculation of chemical formulas can be done on the basis of:

a) $G_3(TO_4)_2 = 5$; used by Thompson and Petersen (1995).
b) $TO_4 = 2$; recommended by Jambor (1999) since substitution in both D and G sites used in method (a) are common within the alunite-jarosite family.

Both methods were compared with data reported in Stoffregen and Alpers (1987) for the Marysvale alunite standard and both give molar concentrations comparable to the published data.

Based on the recommendation of Jambor (pers. comm.) all data in this study is recalculated using method (b), with charge balance to determine OH.

D) Detection Limits

EPMA detection limits for all elements are given in Table A6. Limits represent 3σ values (approximately; see SAMx, 1997) averaged for n = 150 analyses.

Table A6. EPMA detection limits.

Element	Detection Limit (weight %)
Na	0.09
Al	0.05
P	0.12
S	0.15
K	0.08
Ca	0.06
Fe	0.12
Sr	0.11
Ba	0.23

E) Error Estimation

Error estimates for major elements K, S, and Al were calculated from analyses of the Marysvale alunite standard (Table A7)- measured throughout this study. Table A7 also includes error estimates for minor and trace elements. As shown, precision values are significantly higher than for major elements, due to their low abundance in the Marysvale sample.

Table A7. Error and precision estimates for major elements K, S, Al. Also shown is data for minor elements (see discussion in text). Based on weight percent oxide results for Marysvale alunite standard, n=128. Precision determined at 95% confidence limit.

Element	2σ	% Precision
K	0.80	9.0
S	0.36	2.5
Al	0.46	2.4
Na	*0.09*	*68.7*
Ca	*0.01*	*>100*
Ba	*0.13*	*>100*
P	*0.19*	*65.3*
Sr	*0.16*	*80.9*

Estimation of error for Na (and other trace elements) is problematic, given their low abundance in the Marysvale standard. For Na, a better estimate can be taken from replicate analyses of more Na-rich alunite from Del Carmen (Table A8). Data were measured on a single alunite

grain *ca.* 1 cm in length. SEM-EDS analysis indicated that the grain is relatively homogeneous, but some Na- and K- compositional zoning was present nonetheless. Therefore, the 2σ value determined here (0.77) is a maximum error estimate, albeit more realistic than that estimated from the Marysvale sample.

Table A8. Estimation of Na analytical error, based on replicate analyses of Del Carmen alunite.

Sample #	Weight % Element
dc3a-2	2.32
dc3a-3	2.36
dc3a-4	1.80
dc3a-5	1.44
dc3a-7	1.74
dc3a-8	2.09
dc3a-9	2.24
dc3a-10	2.12
dc3a-11	1.90
dc3a-12	1.62
dc3a-13	1.45
dc3a-14	2.64
dc3a-15	1.74
dc3a-16	1.89
dc3a-18	1.31
dc3a-19	1.46
2σ	**0.77**
% Precision*	**40.90**

** at 95% confidence level.*

F) Statistical analysis

The significance of variations in EPMA data between different populations (Chap. 2 to 5) was determined using t-tests. Data were analyzed in SYSTAT at a 95% confidence level, using the separate variance method. Data below detection limits were not included in these calculations. Statistical parameters are listed in the following table.

	Group	*n*	Mean	σ	t value	DF	p
Pascua K content (a.p.f.u.)	AS I	351	0.887	0.137	2.215	617.7	0.027
	AS II	315	0.861	0.162			
	AS II	315	0.861	0.162	-8.445	166.6	0.000
	AS III	29	0.958	0.037			
	AS I and II	666	0.875	0.150	-9.207	80.0	0.000
	AS III	29	0.958	0.037			
	AS I and II	666	0.875	0.150	-3.859	38.4	0.000
	LV	32	0.945	0.097			
	AS II (no Lama)	274	0.886	0.144	-6.657	105.7	0.000
	Lama	78	0.737	0.183			
	AS I with dickite	100	0.953	0.097	5.018	234.6	0.000
	AS I with pyrophyllite	137	0.876	0.139			
Tambo K content (a.p.f.u.)	Stage 1	80	0.808	0.231	3.935	86.2	0.000
	Stage 2	59	0.579	0.400			
	Stage 2	59	0.579	0.400	-5.663	71.2	0.000
	Stage 3	76	0.890	0.153			
	Stage 2	59	0.579	0.400	-5.391	70.1	0.000
	Banded vein	33	0.875	0.100			
	Stage 2	59	0.579	0.400	-6.291	65.1	0.000
	LV	11	0.919	0.048			
All EI Indio-Pascua Belt Na content (a.p.f.u.)	MH (no DC)	909	0.158	0.134	-6.529	70.6	0.000
	DC	66	0.301	0.175			
	All MH	976	0.168	0.141	6.409	55.2	0.000
	All LV	43	0.087	0.078			

Abbreviations: σ = standard deviation, DF = degrees of freedom, p = probability, MH = magmatic-hydrothermal, DC = Del Carmen. Groups listed according to paragenetic stages defined in Chap. 2 and 3.

A2. ANALYTICAL METHODS: Geochemistry of Alunite Separates

A) Sample Preparation

Samples chosen for detailed geochemical analysis (Table A9) were selected based on their distribution, paragenetic relationships, and sample size. Approximately 1 gram samples were required and considerable effort was spent to obtain pure separates. Samples were initially crushed and physically separated, wherever possible. Samples were then treated using a 1:1 HF/H_2O solution following the method of Wasserman et al (1992) to remove silicates prior to analysis. The purity of separates was verified by X-ray diffraction (XRD) but trace amounts (ie. approximately < 10 volume %) of quartz, clays, or other impurities may be present. Note: sample selection was limited by the large sample size required for analyses (ie. minimum 1 gram for complete element suite).

B) Analysis

Samples were analysed by ALS Chemex (Table A10). For REE analysis, a prepared sample (0.200 gram) was added to lithium metaborate flux (0.90 gram), mixed well and fused in a furnace at 1050°C. The resulting melt was then cooled and dissolved in 100 ml of 4% nitric acid. This solution was analyzed by inductively coupled plasma - mass spectrometry. Detection limits given in Table A11a.

All other elements were analyzed using a prepared sample (0.500 gram) that was digested with perchloric, nitric and hydrofluoric acids to dryness. The residue was taken up in a volume of 25 ml of 10% hydrochloric acid and the resulting solution is analyzed by inductively coupled plasma-atomic emission spectrometry, to check base metal concentrations. Samples that met the criteria for analyses (ie., base metal concentrations are less than 1%, with the exception of Ag, and Bi, which have upper analytical limits of 100 and 1000 ppm, respectively) were then diluted and analysed by ICP-MS. Results are corrected for spectral inter-element interferences. Detection limits listed in Table A11b.

C) Error Estimates

A total of eleven samples (nine for REE) were analyzed in duplicate (Table A12). Error estimates were calculated according to Thompson and Howarth (1978), at 95% confidence limit, 90^{th} percentile. Errors for selected elements given in Table A13.

Overall, ICP-MS data for elements of interest (e.g. K, Al, Na, P, Sr, Ba, Ca, REE) are within acceptable error. Higher error estimates for trace elements are attributed to both analytical error and sample heterogeneities (e.g., presence of inclusions). Other elements are present in variable amounts, typically close to detection limits, and data is generally not reproducible.

Table A9. List of samples for ICP-MS analysis with short descriptions.

Deposit	Lab #	Sample #	Paragenetic stage	Description
Pascua	P09	DDH-137a, 23m	AS I	Qtz-alun alteration of granodiorite
	P11	DDH-195a, 242	AS I	Qtz-aln-py alteration
	P02	DDH-137a, 114m	AS II	Alun-en-py from Bx Central Sur
	P06	PS-18-16d	AS II	Alun-en with minor quartz from Maria Tunnel
	P05	PS-99-03	AS II	Alun associated with sulfide in matrix of Bx Central
	P17	DDH-154, 311m	LV	Thin, white fine-grained alun vein
	P15	LM-20, 160m	LV	Alun-jar from matrix of surficial bx
	P-SH	DDH-119, 34-47m	SH	Alun-sil and trace kao from surficial SH zone
	P32	PS-26c	AS III	Coarse-grained alun from surface of Bx Central
Tambo	T09	WND-92a, 190m	1	Qtz-alun alteration of tuff
	T10	WND-92a, 291m	1	Qtz-alun alteration; contains approx. 35 wt% alun
	T01	RA-01	2	Coarse alun-bar-walth from Reina vein
	T27	LN-09	2	Alun-bar in Kimberly Oueste bx
	T05*	WND-92a, 207m	2-3	Alun in matrix of Wendy bx; visible Au
	T28	WND-92a, 82.7	3	Alun in matrix of Wendy bx
	T04	WND-86, 155.0m	3	Alun in matrix of Wendy bx
	T03b	LN-24	3	Coarse qtz-alun bx in Kimberly Oueste
	T22	WND-92a, 37.5m	3	Alun in matrix of Kimberly bx
	T25*	CS-01b	3	Qtz-aln-bar bx in Canto Sur
	T03a*	LN-24	3?	Fx alun overgrowing bx in Kimberly Oueste
	T02A	CS-08	LV	Qtz-aln-bar bx from Canto Sur
	T11	KBD-85, 125.7m	LV	Thin alun-jar vein
	T17	KB-40	SH	Alun-qtz-kao from SH zone
	T32	WN-07	MS	Alun-hem vein
	T44	KB-float	MS	Banded alun ± hem vein
	T33	KB-01	MS	Banded alun ± hem vein
	T14	KB-09	Ca veins	Thin pink alun-huang vein
	B03	BxS-03	BxS	Alun in matrix of Bx Sylvestre
Del Carmen	D03	DC-03		Coarse, vug-filling alun
El Indio	BH1	BH-01A		Alun-sulfide; Brechita-Huantina vein
	CMP1	CMP-01		Alun with trace en; Campana vein

Mineral abbreviations: alunite (alun), quartz (qtz), walthierite (wal), jarosite (jar), enargite (en), huangite (huag).
* uncertain paragenesis.

Table A10. ICP-MS data for El Indio-Pascua Belt alunite. Blank = not analyzed. > = above max detection.

		Pascua								
Sample #		P09	P11	P02	P06	P05	P17	P15	P-SH	P32
Na	wt %	0.37	0.73		1.26	0.49	0.54	1.16	0.98	0.31
Mg		<0.01	<0.01		<0.01	<0.01	<0.01	<0.01	0.01	<0.01
Al		5.59	10.15		18.3	18.3	20.1	19.35	18.35	22.4
K		2.11	3.5		6.5	7.96	8.59	7.66	7.17	>10.00
Ca		0.03	0.01		0.03	<0.01	0.12	0.03	0.07	<0.01
Ti		0.01	0.09		<0.01	<0.01	<0.01	0.06	0.47	0.01
Fe		0.24	0.02		0.01	0.01	0.11	0.73	0.13	0.21
P	ppm	110	140		470	580	2260	790	740	840
Sr		n/a	185		878	137	2400	685	1095	615
Ba		220	250		6170	6120	2180	1240	1140	1720
Pb		340	562		696	2530	3170	128	688	1765
Mn		20	<5		<5	<5	<5	<5	5	<5
Ag		3.45	2.7		1.2	0.4	1.4	0.4	1	2.8
Cu		n/a	12		22	122	27	28	54	21
Bi		13.1	10.4		0.15	0.35	0.2	0.55	0.9	4.45
Zn		16	2		<2	18	48	<2	2	<2
Ni		4.2	3		3	14	4	4	10	3
Co		0.8	1.6		<1.0	<1.0	<1.0	1	<1.0	<1.0
Cr		311	7		36	25	15	5	40	61
Mo		0.8	0.2		<1.0	<1.0	<1.0	1	1	<1.0
Sb		12.2	23		1	5	1.5	2	4	31
Cs		0.1	0.15		<0.25	<0.25	0.5	<0.25	<0.25	<0.25
La		13	11		7	14	26	37	37	47
Ce		25.3	26		10.9	16.65	46.3	45.2	52.1	41.9
Li		0.6	1		1	2	1	1	2	<1.0
Rb		2.2	3.4		6	9	15	50	53	8
Y		0.5	0.9		0.5	0.5	2	2.5	2	0.5
Nb		2.2	13.2		<1.0	<1.0	<1.0	2	13	<1.0
Be		0.05	<0.05		<0.25	<0.25	0.5	<0.25	<0.25	<0.25
Cd		0.06	0.18		<0.10	<0.10	<0.10	<0.10	<0.10	0.1
Ga		15.5	38.9		30	127	60	33	76.5	238
Ta		0.35	1.1		<0.25	<0.25	<0.25	0.25	1	<0.25
Te		0.2	0.2		<0.25	0.25	0.25	1.25	1	0.25
Tl		0.02	0.02		<0.10	0.2	0.4	0.4	0.2	0.1
Th		5.8	2.6		3	8	13	5	11	9
W		1.5	3.7		5	14.5	65.5	1.5	2.5	19
V		7	18		40	71	64	55	198	95
La		15	14.8	39	17.5	20	32	39	37.5	39
Ce		29.5	26.8	48.5	19.5	20	65	51.5	54.5	33
Pr		3.2	2.7	3.7	1.5	1.7	8.7	4.5	5.5	1.4
Nd		8.5	5.8	9	3.5	4	37	14	16.5	2
Sm		1	0.4	1.5	0.3	0.4	11.3	2.3	2	0.1
Eu		0.1	<0.1	0.2	0.1	<1.0	2.8	0.4	0.4	<0.1
Gd		0.5	0.2	1	0.2	0.3	11.1	1.7	1.4	0.1
Tb		<0.1	<0.1	0.1	<0.1	<0.1	1.3	0.2	0.1	<0.1
Dy		0.3	0.4	0.1	<0.1	0.1	3.6	1	0.8	<0.1
Ho		<0.1	0.1	<0.1	<0.1	<0.1	0.3	0.2	0.1	<0.1
Er		0.1	0.7	<0.1	<0.1	<0.1	0.3	0.6	0.6	<0.1
Tm		<0.1	0.1	<0.1	<0.1	<0.1	<0.1	<0.1	0.1	<0.1
Yb		0.2	1.6	0.2	<0.1	<0.1	0.3	0.8	0.9	<0.1
Lu		<0.1	0.4	<0.1	<0.1	<0.1	<0.1	0.1	0.1	<0.1

Table A10. (Continued.)

		Tambo									
Sample #		T09	T10	T01	T27	T05	T28	T04	T03b	T22	T25
Na	wt %	0.51	0.52	0.43	0.75	0.62	1	0.37	0.4	0.47	0.34
Mg		0.01	0.01	<0.01	<0.01	<0.01	<0.01	<0.01	<0.01	<0.01	<0.01
Al		10.3	6.75	17.3	20.7	19.8	20.4	20.4	18.95	20.9	18.35
K		3.81	2.48	6.86	8.35	8.42	8.2	9.22	8.38	9.14	5.52
Ca		0.06	0.04	0.03	0.05	0.04	0.08	0.04	0.03	0.05	0.12
Ti		0.07	0.11	<0.01	<0.01	<0.01	0.13	<0.01	<0.01	<0.01	<0.01
Fe		2.43	0.26	0.5	0.04	0.05	0.27	0.12	0.15	0.1	0.13
P	ppm	300	380	1570	120	900	1270	1210	1180	1700	1000
Sr		652	208	511	461	483	1580	696	411	728	727
Ba		340	630	4080	3850	840	1470	600	3600	280	6410
Pb		112	856	1515	1745	2030	338	608	251	428	630
Mn		<5	15	<5	<5	<5	<5	80	<5	<5	<5
Ag		2.8	0.85	79.4	4	0.2	3	21.4	5.8	0.2	7.3
Cu		1215	10	32	20	16	69	53	17	18	2
Bi		22	1.54	6.54	0.8	0.6	32	102	13.4	2.25	3.81
Zn		2	2	<2	2	10	46	48	6	<2	<2
Ni		<1.0	4.2	12.4	2	2	346	4	2	3	0.2
Co		4	0.6	<0.2	<1.0	<1.0	1	<1.0	<1.0	<1.0	<0.2
Cr		4	279	23	9	15	148	29	15	12	31
Mo		1	1	0.2	<1.0	<1.0	15	11	<1.0	1	0.2
Sb		>	11.3	317	10	12.5	15	29.5	10	31	12
Cs		>	0.6	0.15	<0.25	<0.25	0.5	<0.25	<0.25	<0.25	0.05
La		>	23	7.5	6	27	30	81	62	112	37
Ce		86.5	40.3	7.26	6.7	44.8	62.1	104	122.5	221	82
Li		>	0.6	4.6	<1.0	3	2	1	<1.0	6	0.6
Rb		>	4.6	7	28	14	86	18	29	24	33.4
Y		>	2.1	0.3	<0.5	0.5	1.5	9.5	0.5	1.5	0.2
Nb		>	13.4	<0.2	<1.0	<1.0	8	22	<1.0	<1.0	1
Be		<0.50	0.3	<0.05	<0.25	0.25	1	1	<0.25	<0.25	<0.05
Cd		<0.50	<0.02	0.06	<0.10	<0.10	0.2	0.1	<0.10	<0.10	<0.02
Ga		>	9.8	185	91	105.5	44	73.5	27	13.5	26.6
Ta		>	1.2	<0.05	<0.25	<0.25	0.5	0.75	<0.25	<0.25	0.05
Te		>	0.1	38.2	1.25	0.25	4.5	1	0.5	<0.25	5.25
Tl		>	0.06	0.2	0.1	0.1	0.9	<0.10	0.1	0.2	0.16
Th		>	7.8	3.8	<1.0	6	8	9	11	18	1.2
W		<10.0	3.6	98	14.5	12	5	28	5	1.5	4.5
V		35	22	98	62	143	79	114	52	57	85
La		45.5	25.5	10.5				66.5			90.3
Ce		86.5	45	9.5				79.5			81.3
Pr		9.2	4.3	0.6				4.1			5.1
Nd		25	11.5	1.5				6			6.8
Sm		3.3	1.6	0.2				0.2			0.1
Eu		0.3	0.3	0.2				0.2			0.1
Gd		1.8	1.3	0.1				0.3			0.1
Tb		0.1	0.3	<0.1				<0.1			<0.1
Dy		1	1.1	<0.1				0.2			<0.1
Ho		0.2	0.3	<0.1				<0.1			<0.1
Er		0.9	1.1	<0.1				<0.1			<0.1
Tm		0.1	0.3	<0.1				<0.1			<0.1
Yb		1.4	1.6	<0.1				0.1			<0.1
Lu		0.1	0.3	<0.1				<0.1			<0.1

Table A10. (Continued.)

		Tambo								
Sample #		T03a	T02A	T11	T17	T32	T33	T34	T14	B03
Na	wt %	0.78	0.19	0.44	0.23	0.32	0.34	0.52	1.01	0.6
Mg		<0.01	<0.01	<0.01	<0.01	<0.01	<0.01	<0.01	<0.01	<0.01
Al		17.5	18	19.85	19.1	17.2	20.4	18.15	21.4	20.3
K		6.67	7.7	9.22	8.94	6.57	8.9	6.31	2.23	8.83
Ca		0.03	0.09	0.05	0.04	0.02	0.04	0.05	3.47	0.03
Ti		<0.01	<0.01	0.03	0.05	<0.01	<0.01	<0.01	<0.01	0.01
Fe		0.07	0.18	2.1	0.01	0.51	0.09	0.09	0.01	0.04
P	ppm	370	1580	1490	940	1020	2300	1510	630	680
Sr		329	677	2760	353	560	1535	832	246	511
Ba		2190	2430	2140	1030	410	1120	960	830	650
Pb		380	2240	486	916	600	580	530	59	1700
Mn		<5	<5	<5	<5	<5	5	5	<5	<5
Ag		7.4	7.9	3	1.4	<0.05	<0.20	1.35	<0.20	0.8
Cu		<1	1	44	44	<1	18	2	18	25
Bi		23.7	5.98	32.3	1	72.1	0.3	17.7	0.55	29.2
Zn		<2	<2	70	18	2	<2	2	8	2
Ni		1.8	10.4	2	6	0.2	3	0.6	4	27
Co		<0.2	<0.2	<1.0	<1.0	<0.2	<1.0	0.2	<1.0	<1.0
Cr		9	60	32	21	12	17	13	4	20
Mo		0.6	0.2	4	<1.0	4.4	<1.0	0.2	<1.0	3
Sb		48.4	14.3	14.5	10	25.2	28.5	93.3	0.5	78.5
Cs		0.15	0.05	0.75	<0.25	0.15	<0.25	0.05	0.25	<0.25
La		2.5	45.5	28	24	59.5	164	71	49	25
Ce		12	31.3	45.8	40.3	96.5	208	167.5	110	34
Li		0.6	2	1	<1.0	1	<1.0	6	6	1
Rb		30.2	38	22	67	17.2	15	15.4	66	10
Y		0.2	0.1	1.5	1.5	0.5	1	0.8	0.5	0.5
Nb		0.4	<0.2	<1.0	6	0.2	<1.0	<0.2	<1.0	<1.0
Be		<0.05	<0.05	0.25	<0.25	<0.05	<0.25	0.1	0.25	<0.25
Cd		<0.02	0.06	<0.10	<0.10	<0.02	<0.10	<0.02	0.1	<0.10
Ga		50	354	65.5	51.5	83.5	267	51.7	22	89.5
Ta		0.05	<0.05	<0.25	0.25	<0.05	<0.25	<0.05	<0.25	<0.25
Te		1.1	2.45	1.75	0.5	0.6	<0.25	3.1	<0.25	1.25
Tl		0.1	0.96	0.2	0.2	0.14	<0.10	0.06	0.6	0.2
Th		0.4	4	8	7	7.8	18	11.4	5	6
W		8.6	3	4	0.5	2.4	<0.5	5.2	<0.5	3
V		100	107	217	83	65	83	69	48	127
La		6.8	77	29	47.5	74	156	89	48	24.5
Ce		12.5	47	50	85	96.5	198	167.5	109.5	33
Pr		1.4	2.1	5.9	8.7	6.3	13.4	14.9	15.5	3
Nd		3.8	3	22	27.5	9	24	26.5	65.5	8
Sm		0.6	0.2	5	3.7	0.4	1.1	1.2	16.8	0.6
Eu		0.2	0.4	0.9	0.5	<0.1	0.3	0.1	2.5	0.1
Gd		0.4	0.1	3.2	2.3	0.4	1	0.7	9.3	0.5
Tb		<0.1	<0.1	0.4	0.2	<0.1	0.1	<0.1	0.6	<0.1
Dy		<0.1	<0.1	1.1	0.7	<0.1	0.3	0.1	0.7	0.1
Ho		<0.1	<0.1	0.1	0.1	<0.1	<0.1	<0.1	<0.1	<0.1
Er		<0.1	<0.1	0.3	0.5	<0.1	0.1	<0.1	<0.1	0.1
Tm		<0.1	<0.1	<0.1	<0.1	<0.1	<0.1	<0.1	<0.1	<0.1
Yb		<0.1	0.1	0.3	0.8	<0.1	0.1	<0.1	0.1	0.1
Lu		<0.1	<0.1	<0.1	0.1	<0.1	<0.1	<0.1	<0.1	<0.1

Table A10. (Continued.)

		Del Carmen	El Indio	
Sample #		D03	BH-01	CMP-01
Na	wt %	2.17	1.01	1.53
Mg		<0.01	<0.01	<0.01
Al		18.4	17.5	18.55
K		4.65	6.23	5.91
Ca		0.03	0.01	0.19
Ti		<0.01	<0.01	<0.01
Fe		0.06	0.03	0.05
P	ppm	470	1050	280
Sr		1185	239	341
Ba		1240	1300	630
Pb		83	3360	169
Mn		<5	5	<5
Ag		0.25	0.1	2
Cu		<1	76	58
Bi		0.79	1.28	19.9
Zn		<2	50	4
Ni		0.8	0.2	0.4
Co		<0.2	0.2	0.6
Cr		15	11	25
Mo		1	<0.2	0.2
Sb		3.3	14.7	14.7
Cs		0.05	0.1	0.1
La		4.5	15	3
Ce		5.5	50	9
Li		21.6	20.6	2
Rb		4.6	13.4	26
Y		0.3	1	0.1
Nb		<0.2	<0.2	<0.2
Be		<0.05	0.15	0.2
Cd		<0.02	0.02	0.08
Ga		2.2	18.9	21.6
Ta		<0.05	<0.05	<0.05
Te		0.3	0.95	0.9
Tl		0.08	0.16	0.36
Th		1	5.6	0.8
W		1	47.6	1.8
V		40	61	175
La		7.5	23	4.8
Ce		5.5	50	9
Pr		0.3	5.3	1
Nd		0.5	11	2.3
Sm		<0.1	0.8	0.1
Eu		<0.1	0.1	<0.1
Gd		<0.1	0.6	<0.1
Tb		<0.1	<0.1	<0.1
Dy		<0.1	0.2	<0.1
Ho		<0.1	<0.1	<0.1
Er		<0.1	<0.1	<0.1
Tm		<0.1	<0.1	<0.1
Yb		<0.1	<0.1	<0.1
Lu		<0.1	<0.1	<0.1

Table A11a. Limits of detection for REE analysis.

Element	Detection Limit	Upper Limit
Ce	0.5 ppm	1 %
Dy	0.1 ppm	0.1 %
Er	0.1 ppm	0.1 %
Eu	0.1 ppm	0.1 %
Gd	0.1 ppm	0.1 %
Ho	0.1 ppm	0.1 %
La	0.5 ppm	1 %
Lu	0.1 ppm	0.1 %
Nd	0.5 ppm	1.0 %
Pr	0.1 ppm	0.1 %
Sm	0.1 ppm	0.1 %
Tb	0.1 ppm	0.1 %
Tm	0.1 ppm	0.1 %
Yb	0.1 ppm	0.1 %

Table A11b. Limits of detection: trace element ICP-MS analysis.

Element	Detection Limit	Upper Limit
Al	0.01%	25 %
Ba	0.5 ppm	1 %
Be	0.05 ppm	1000 ppm
Bi	0.01 ppm	1 %
Cd	0.02 ppm	500 ppm
Ca	0.01%	25 %
Ce	0.01 ppm	500 ppm
Cs	0.05 ppm	500 ppm
Cr	1 ppm	1 %
Co	0.1 ppm	1 %
Cu	0.2 ppm	1 %
Ga	0.05 ppm	500 ppm
Ge	0.05 ppm	500 ppm
In	0.01 ppm	100 ppm
Fe	0.01%	25 %
Pb	0.5 ppm	1 %
Li	0.2 ppm	500 ppm
Mg	0.01%	15 %
Mn	5 ppm	1 %
Mo	0.05 ppm	1 %
Ni	0.2 ppm	1 %
Nb	0.1 ppm	500 ppm
P	10 ppm	1 %
K	0.01%	10 %
Rb	0.1 ppm	500 ppm
Ag	0.05 ppm	100 ppm
Na	0.01%	10 %
Sr	0.2 ppm	1 %
Ta	0.05 ppm	100 ppm
Te	0.05 ppm	500 ppm
Tl	0.02 ppm	500 ppm
Th	0.2 ppm	500 ppm
Ti	0.01%	10 %
W	0.1 ppm	1 %
U	0.1 ppm	500 ppm
V	1 ppm	1 %
Y	0.1 ppm	500 ppm
Zn	2 ppm	1 %

Table A12. Duplicate ICP-MS data for El Indio-Pascua Belt alunite.

		DUPLICATES											
Sample #		T04	Dup	T33	Dup	T14	Dup	T32	Dup	T34	Dup	P11	Dup
Na	wt %	0.37	0.32	0.34	0.3	1.01	0.96	0.33	0.32	0.52	0.5	0.73	0.71
Mg		<0.01	<0.01	<0.01	<0.01	<0.01	<0.01	<0.01	<0.01	<0.01	<0.01	<0.01	<0.01
Al		20.4	20.2	20.4	20.1	21.4	18.25	17.5	17.2	18.15	16.65	10.15	10.2
K		9.22	9.14	8.9	8.92	2.23	2.12	7.28	6.57	6.31	6.78	3.5	2.69
Ca		0.04	0.01	0.04	0.04	3.47	2.74	0.01	0.02	0.05	0.04	0.01	0.01
Ti		<0.01	<0.01	<0.01	<0.01	<0.01	<0.01	<0.01	<0.01	<0.01	<0.01	0.09	0.1
Fe		0.12	<0.01	0.09	0.1	0.01	0.01	0.53	0.51	0.09	0.05	0.02	0.01
P	ppm	1210	1210	2300	2320	630	530	1030	1020	1510	1320	140	130
Sr		696	698	1535	1495	246	206	573	560	832	769	185	189.5
Ba		600	600	1120	1100	830	800	440	410	960	830	250	210
Pb		608	612	580	578	59	59	620	600	530	478	562	546
Mn		80	<5	5	10	<5	<5	<5	<5	5	<5	<5	<5
Ag		21.4	15	<0.20	0.2	<0.20	<0.20	<0.05	<0.05	1.35	1.35	2.7	2.65
Cu		53	97	18	20	18	18	<1	<1	2	3	12	12
Bi		102	95.6	0.3	1.55	0.55	0.15	73	72.1	17.7	16.6	10.4	10.2
Zn		48	2	<2	<2	8	10	<2	2	2	2	2	2
Ni		4	4	3	3	4	3	<0.2	0.2	0.6	<0.2	3	2.8
Co		<1.0	<1.0	<1.0	<1.0	<1.0	<1.0	<0.2	<0.2	0.2	<0.2	1.6	1.6
Cr		29	18	17	47	4	3	12	12	13	11	7	6
Mo		11	10	<1.0	<1.0	<1.0	<1.0	4.8	4.4	0.2	0.2	0.2	0.2
Sb		29.5	28.5	28.5	28.5	0.5	0.5	24.8	25.2	93.3	99.6	23	22.3
Cs		<0.25	<0.25	<0.25	<0.25	0.25	0.25	0.15	0.15	0.05	0.05	0.15	0.15
La		81	58	164	174	49	43	63.5	59.5	71	90.5	11	13
Ce		104	67.8	208	217	110	97.1	95.5	96.5	167.5	167	26	27.5
Li		1	<1.0	<1.0	<1.0	6	5	0.8	1	6	4	1	0.8
Rb		18	15	15	19	66	63	18.8	17.2	15.4	15.4	3.4	2.8
Y		9.5	0.5	1	1	0.5	0.5	0.4	0.5	0.8	0.6	0.9	0.8
Nb		22	<1.0	<1.0	<1.0	<1.0	<1.0	<0.2	0.2	<0.2	<0.2	13.2	13
Be		1	<0.25	<0.25	<0.25	0.25	1	<0.05	<0.05	0.1	<0.05	<0.05	<0.05
Cd		0.1	<0.10	<0.10	<0.10	0.1	0.2	<0.02	<0.02	<0.02	<0.02	0.18	0.04
Ga		73.5	69	267	262	22	20	84.2	83.5	51.7	42.4	38.9	36.1
Ta		0.75	<0.25	<0.25	<0.25	<0.25	<0.25	<0.05	<0.05	<0.05	<0.05	1.1	1.1
Te		1	0.75	<0.25	0.25	<0.25	<0.25	0.65	0.6	3.1	2.5	0.2	0.25
Tl		<0.10	<0.10	<0.10	<0.10	0.6	0.5	0.12	0.14	0.06	0.06	0.02	<0.02
Th		9	6	18	15	5	3	8.4	7.8	11.4	10.4	2.6	3.8
W		28	26	<0.5	1	<0.5	7.5	2.3	2.4	5.2	4.2	3.7	3.9
V		114	117	83	83	48	42	66	65	69	60	18	16
La		66.5		156		48	48	73.5	74	89	89.5	14.8	15
Ce		79.5		198		109.5	109.5	95.5	96.5	167.5	167	26.8	27.5
Pr		4.1		13.4		15.5	15.4	6	6.3	14.9	15.1	2.7	2.7
Nd		6		24		65.5	64.5	8.5	9	26.5	26.5	5.8	6
Sm		0.2		1.1		16.8	16.5	0.4	0.4	1.2	1.4	0.4	0.4
Eu		0.2		0.3		2.5	2.4	<0.1	<0.1	0.1	0.1	<0.1	<0.1
Gd		0.3		1		9.3	9.3	0.3	0.4	0.7	1	0.2	0.2
Tb		<0.1		0.1		0.6	0.6	<0.1	<0.1	<0.1	<0.1	<0.1	<0.1
Dy		0.2		0.3		0.7	0.7	<0.1	<0.1	0.1	0.1	0.4	0.4
Ho		<0.1		<0.1		<0.1	<0.1	<0.1	<0.1	<0.1	<0.1	0.1	<0.1
Er		<0.1		0.1		<0.1	<0.1	<0.1	<0.1	<0.1	<0.1	0.7	0.6
Tm		<0.1		<0.1		<0.1	<0.1	<0.1	<0.1	<0.1	<0.1	0.1	0.1
Yb		0.1		0.1		0.1	0.1	<0.1	<0.1	<0.1	<0.1	1.6	1.5
Lu		<0.1		<0.1		<0.1	<0.1	<0.1	<0.1	<0.1	<0.1	0.4	0.3

Table A12. (Continued.)

		DUPLICATES									
Sample #		T09	Dup	T25	Dup	T03a	Dup	T27	Dup	CMP-01	Dup
Na	wt %	0.51	0.53	0.34	0.32	0.78	0.75	0.75	0.47	1.53	1.53
Mg		0.01	0.01	<0.01	<0.01	<0.01	0.03	<0.01	<0.01	<0.01	<0.01
Al		10.3	10.45	18.35	17.5	17.5	17.1	20.7	11.45	18.55	18.55
K		3.81	4.04	5.52	5.37	6.67	6.35	8.35	3.66	5.91	6.13
Ca		0.06	0.06	0.12	0.1	0.03	0.16	0.05	0.02	0.19	0.19
Ti		0.07	0.07	<0.01	<0.01	<0.01	<0.01	<0.01	<0.01	<0.01	<0.01
Fe		2.43	2.33	0.13	0.1	0.07	0.07	0.04	0.14	0.05	0.05
P	ppm	300	320	1000	940	370	390	120	70	280	300
Sr		652	683	727	534	329	346	461	216	341	330
Ba		340	340	6410	6510	2190	1970	3850	1550	630	640
Pb		112	120	630	420	380	468	1745	948	169	171
Mn		<5	<5	<5	<5	<5	<5	<5	<5	<5	<5
Ag		2.8	2.6	7.3	6.85	7.4	6.95	4	6.35	2	1.95
Cu		1215	1220	2	3	<1	<1	20	4	58	57
Bi		22	22	3.81	3.66	23.7	23.8	0.8	1.62	19.9	19.7
Zn		2	6	<2	<2	<2	<2	2	<2	4	4
Ni		<1.0	<1.0	0.2	<0.2	1.8	0.2	2	0.6	0.4	0.6
Co		4	4	<0.2	<0.2	<0.2	<0.2	<1.0	<0.2	0.6	0.6
Cr		4	3	31	29	9	9	9	6	25	24
Mo		1	1	0.2	0.2	0.6	0.4	<1.0	<0.2	0.2	0.2
Sb		>	>	12	11.2	48.4	45.4	10	16.9	14.7	14
Cs		>	>	0.05	0.05	0.15	0.35	<0.25	0.25	0.1	0.1
La		>	>	37	28.5	2.5	4.5	6	5	3	3
Ce		86.5	86.5	82	80.5	12	13	6.7	5.5	9	9
Li		>	>	0.6	0.6	0.6	0.8	<1.0	0.6	2	1.8
Rb		>	>	33.4	31.4	30.2	30.2	28	15.2	26	26.2
Y		>	>	0.2	0.2	0.2	0.9	<0.5	0.1	0.1	0.2
Nb		>	>	1	0.8	0.4	0.4	<1.0	0.2	<0.2	<0.2
Be		<0.50	<0.50	<0.05	<0.05	<0.05	0.05	<0.25	<0.05	0.2	0.15
Cd		<0.50	<0.50	<0.02	<0.02	<0.02	<0.02	<0.10	<0.02	0.08	0.08
Ga		>	>	26.6	25.3	50	45.7	91	59.3	21.6	20.6
Ta		>	>	0.05	0.05	0.05	<0.05	<0.25	<0.05	<0.05	<0.05
Te		>	>	5.25	5.7	1.1	1.15	1.25	3	0.9	0.7
Tl		>	>	0.16	0.12	0.1	0.1	0.1	0.08	0.36	0.36
Th		>	>	1.2	1	0.4	1.2	<1.0	0.2	0.8	0.8
W		<10.0	<10.0	4.5	4.1	8.6	8.1	14.5	8.4	1.8	1.9
V		35	33	85	79	100	98	62	29	175	180
La		45.5	45	90.3	89	6.8	7		8	4.8	5
Ce		86.5	86.5	81.3	80.5	12.5	13		5.5	9	9
Pr		9.2	9.2	5.1	5	1.4	1.5		0.3	1	1
Nd		25	24.5	6.8	6.5	3.8	4		0.5	2.3	2
Sm		3.3	3.2	0.1	0.1	0.6	0.6		<0.1	0.1	0.1
Eu		0.3	0.3	0.1	0.1	0.2	0.1		0.1	<0.1	<0.1
Gd		1.8	1.8	0.1	0.1	0.4	0.4		<0.1	<0.1	<0.1
Tb		0.1	0.2	<0.1	<0.1	<0.1	<0.1		<0.1	<0.1	<0.1
Dy		1	1	<0.1	<0.1	<0.1	<0.1		<0.1	<0.1	<0.1
Ho		0.2	0.2	<0.1	<0.1	<0.1	<0.1		<0.1	<0.1	<0.1
Er		0.9	1	<0.1	<0.1	<0.1	<0.1		<0.1	<0.1	<0.1
Tm		0.1	0.1	<0.1	<0.1	<0.1	<0.1		<0.1	<0.1	<0.1
Yb		1.4	1.4	<0.1	<0.1	<0.1	<0.1		<0.1	<0.1	<0.1
Lu		0.1	0.2	<0.1	<0.1	<0.1	<0.1		<0.1	<0.1	<0.1

Table A13. Thompson and Howarth (1978) error analysis for selected elements.

	Total Error (%)*
Major elements: K, Al	10
Minor (and trace) elements: Na, P, Sr, Sb, Bi	10
Trace elements: Ba, Ca	15
Trace elements: Ag, Cu	22
Trace elements: Fe, Zn	55
REE: La, Ce, Pr, Sm	5
REE: Nd, Eu	10

* error better than given value at 95% confidence limit, 90th percentile.

REFERENCES

Cho, H.G. and Kim, S.J., 1993. Oscillatory zoning in alunite from the Sungsan mine, Korea. N. Jb. Miner. Mh., 4, 185-192.

Jambor, J.L., 1999. Nomenclature of the alunite-jarosite family. Internal report for the CNNMN.

Li, G., Peacor, D.R., Essene, E.J., Brosnahan, D.R., and Beane, R.E., 1992. Walthierite and huangite; two new minerals of the alunite group from the Coquimbo region, Chile. American Mineralogist, 77, 1275-1284.

Muntean, J.L., Kesler, S.E., Russel, N., and Polcabci, J., 1990. Evolution of the Monte Negro acid-sulfate Au-Ag deposit, Peublo Viejo, Dominican Republic; Important factors in grade development. Economic Geology, 85, 1738-1758.

Petersen, E.U., and Thompson, A.J.B., 1992. Analysis of alunite and other thermally sensitive minerals. Microprobe Analyst (Internal report for the Dept. of Geology and Geophysics, University of Utah), April, 2-6.

SAMx, 1997. SAMx-XMAS Reference Manual – Version 5.0 Fourth Edition. Pp. 9-24,25.

Scott, K.M., 1987. Solid solution in, and classification of, gossan-derived members of the alunite-jarosite family, northwest Queensland, Australia. American Mineralogist, 72, 178-187.

Scott, K.M., 1990. Origin of alunite- and jarosite-group minerals in the Mt. Leyshon epithermal gold deposit, northeast Queensland, Australia. American Mineralogist, 75, 1176-1181.

Stoffregen, R.E. and Alpers, C.N., 1987. Woodhouseite and svanbergite in hydrothermal ore deposits: Products of apatite destruction during advanced argillic alteration. Canadian Mineralogist, 25, 201-211.

Stoffregen, R.E. and Alpers, C.N., 1992. Observations on the unit-cell dimensions, H2O contents, and δD values of natural and synthetic alunite. American Mineralogist, 77, 1092-1098.

Thompson, M., and Howarth, R.J., 1978. A new approach to the estimation of analytical precision. Journal of Geochemical Exploration, 9, 1, 23-30.

APPENDIX B: STABLE ISOTOPE ANALYSIS

Stable isotope analyses were carried out to constrain the origin of acid sulfate alteration at the Pascua, Tambo, El Indio, and Del Carmen properties. Samples were selected from drill core, underground workings, and various surface localities. All analyses were completed at the USGS lab facilities in Denver, Colorado in collaboration with R.O. Rye. Complete isotope systematics (δD, $\delta^{18}O_{SO4}$, $\delta^{18}O_{OH}$, and $\delta^{34}S$) were determined for over 60 alunite samples and 1 jarosite sample. $\delta^{34}S$ data for coexisting sulfides, jarosite, and barite were also obtained. Methods of mineral separation and analysis are based on the work of Wasserman et al. (1992) and are summarized below.

Sample Preparation

Most samples consist of fine-grained intergrowths of alunite ± quartz, clays (kaolinite, dickite, pyrophyllite, etc.), pyrite. The separation method of Wasserman et al.. (1992) involves physical separation by repeated suspension and elutriation, and chemical purification by controlled dissolution in HF (to remove silicates) and NaOH (to obtain pure kaolinite). The purity of each separate was checked optically and by X-ray diffraction analyses. In several instances, separations were not successful and the samples could not be used for further analysis. Specific considerations for each mineral group are outlined as follows:

Alunite (and barite): Coarse-grained alunite samples could usually be separated easily by hand-picking. For finer-grained samples, and those intermixed with silicates, treatment using a 1:1 HF/H_2O solution following the method of Wasserman et al. (1992) was required to remove impurities. Often multiple dissolutions were required to obtain a pure separate. This method was typically unsuccessful on samples containing pyrophyllite. Detailed sampling across growth zones in coarsely crystalline alunite veins was completed by micro-drilling (using a small hand-held drill with a diamond bit). Thick (approximately 2 cm) slabs of the vein material were used, and sampled at *ca.* 25 to 50 mm intervals.

Sulfides: The majority of sulfides (pyrite and enargite) were separated by careful hand-picking. In a few cases, heavy liquid separation using methylene iodide (MEI) was required in order to obtain a pure separate.

Clays: The separation of clay minerals proved to be very difficult and time consuming, since fine-grained quartz and/or alunite was commonly present. Approximately 50-100 g of material was crushed in a mortar and sieved to remove larger quartz grains and silicified clots (>425μm). Fine grained material was disagregated using an ultrasonic probe and separated by settling in a water column, followed by high speed centrifugation.

Analytical methods

Detailed analytical procedures for alunite, sulfide, and clay samples are outlined in Wasserman et al. (1992). Several methods have been updated since this initial study however, and are specified below. Duplicate analyses and standards were run routinely for all procedures. Standard errors are reported in the following discussions, based on Thompson and Howarth error

analysis (short method: Thompson and Howarth, 1978). All precision estimates are given as 95% confidence level at 90th percentile.

Sulfur: $\delta^{34}S$ analyses were determined by an on-line method using an elemental analyzer coupled to a Micromass Optima mass spectrometer following Giesemann et al. (1994). Analytical precision is better than 3% (n = 22).

Hydrogen: δD analyses of alunite, jarosite, and kaolinite were performed by a step heated technique modified from Godfrey (1962). Analytical error is better than 10% (n=10).

Oxygen: $\delta^{18}O$ data was collected for both sulfate and hydroxyl groups in alunite and jarosite. Two different analytical methods were used.

a) Samples were initially analyzed using the conventional BrF_5 method described in Wasserman et al. (1992). $\delta^{18}O_{SO4}$ analysis requires the dissolution of alunite in a hot NaOH solution and precipitation of sulfate as $BaSO_4$. The $BaSO_4$ precipitate is then analysed by fluorination with BrF_5 at 580°C following the standard analytical procedure of Clayton and Mayeda (1963), and as used by Pickthorn and O'Neil (1985). Analytical precision is estimated at ± 0.15‰ (Wasserman et al., 1992).

$\delta^{18}O_{OH}$ is determined by material balance using the total O isotopic composition of alunite and $\delta^{18}O_{SO4}$ results. The total isotopic composition is measured by fluorination with BrF_5 as described above. The fluorination of alunite produces 50±1% yield of O_2 from the SO_4 site and 100% from the OH site. The $\delta^{18}O_{OH}$ can be calculated using the mass balance equation:

$$\delta^{18}OBrF_5 \text{ alunite} = 0.40\ [\ \delta^{18}O_{SO4(GR\text{-}FI)} \text{ alunite}\ ] + 0.60\ \delta^{18}O_{OH}$$

$\delta^{18}O_{SO4\ (GR\text{-}FI)}$ alunite represents the experimentally determined fractionation for O (10.5 ‰ at the Denver facility) produced by fluorination of alunite. Analytical precision is about ± 0.3‰ (Wasserman et al., 1992).

b) A new method of sulfate oxygen analysis ('continuous flow method') was being developed by R.O. Rye and C. Kester at the USGS facility at the time of my study. This method eliminates the fluorination procedure and will significantly reduce the analytical time required for sulfate minerals. Analyses are done by pyrolysis with a Finnigan TC/EA coupled to a Finnigan Delta Plus XL mass spectrometer using continuous flow methods modified from Kornexl et al. (1999). Both total alunite oxygen and $\delta^{18}O_{SO4}$ analyses on $BaSO_4$ precipitates can be run. $\delta^{18}O_{OH}$ is then calculated using the mass balance equation for alunite:

$$\delta^{18}O_{OH} = \frac{\delta^{18}O_{total} - 0.60\left(\delta^{18}O_{SO4}\right)}{0.40}$$

Precision is estimated at better than 4% for $\delta^{18}O_{SO4}$ (n=14), and 3% for $\delta^{18}O_{total}$ (n=5).

Sample descriptions and analytical results

Brief descriptions for all samples included in this study are given in Tables B1. Isotope data is presented in Tables B2 to B4. All oxygen and hydrogen isotope values are given relative to Standard Mean Ocean Water. Sulfur isotope values are given in relation to troilite from the Canyon Diablo meteorite. In addition, $\delta^{34}S$ analyses were made on several large alunite crystals and banded alunite veins in order to determine the variability of $\delta^{34}S$ (Table B5).

Area	Sample	Lab #	Stage[1]	Elev. (m)	Description
PASCUA	**Alunite:**				
	DDH-137A, 23.1m	P09a	AS I	4665	Qtz-alun alteration of host rock
	DDH-184, 441.3m	P10a	AS I	4616	Qtz-alun alteration of host rock
	DDH-195A, 242.0m	P11a	AS I	4612	Qtz-alun alteration of host rock
	DDH-154, 185.9m	P12a	AS I	4570	Qtz-alun-dick alteration; Frontera
	LM-20, 94.8m	P13a	AS I	4990	Qtz-alun-py alteration of host rock
	DDH-116, 289.5m	P21a	AS I	4435	Qtz-alun alteration; Lama
	DDH-152, 107.0m	P22a	AS I	4630	Qtz-alun-dick alteration; Frontera
	PSD-98-108, 374m	P23a	AS I	4435	Qtz-alun-pyl-zuny alteration
	DDH-017, 122.5	P24a	AS I	4369	Qtz-alun-pyl alteration; near Esperanza
	DDH-017, 108.0m	P28a	AS I	4369	Qtz-alun-pyl alteration; near Esperanza
	DDH-168, 260m	P33a	AS I	4647	Qtz-alun-pyl alteration
	DDH-116, 157.0m	P01a	AS II	4551	Alun-py-enarg banded vein
	DDH-137A, 113.9m	P02a	AS II	4580	Brecha Central Sur matrix; alun-enarg-py
	DDH-137A, 152.1m	P03a	AS II	4544	Alun-py-enarg banded vein
	DDH-154, 224.3m	P04a	AS II	4545	Matrix alun-enarg-py; Frontera
	PS-99-03	P05a	AS II	4680	Brecha Central matrix; alun-enarg-py-S
	PS-98-16d	P06a	AS II	4674	Alun-enarg vein; Tunel Maria
	LM-03, 301.0m	P07a	AS II	4519	Alun-py-enarg vein; Lama
	DDH-172, 435.1m	P25a	AS II	4393	Alun vein overgrown by jar; Frontera
	Annick 440	P27a	AS II	4680	Brecha Central matrix; alun-enarg-py
	PS-26c	P32a	AS III	4995	Near-surface, coarse matrix alun
	DDH-129, 111.6m	P14a	LV	4582	Alun-jar vein
	LM-20, 160.1m	P15a	LV	4960	Alun-jar matrix; Lama
	DR-368NE, PM-33	P16a	LV	4680	Alun-jar +/- silica vein; Tunel Alex
	DDH-154, 310.5m	P17a	LV	4489	Alun +/- jar vein
	DDH-119, 47.7m	P18a	SH	4994	Alun-sil +/- kao, S; near surface
	DDH-122, 4.3m	P19a	SH	5089	Alun-sil +/- kao, S; near surface
	DDH-119. 34.0m	P20a	SH	5006	Alun-sil +/- kao, S; near surface
	DDH-057, 76.5m	P26a	Esp	4873	Alun in bx matrix; Esperanza
	Jarosite:				
	DDH-135, 162.7m	Pj30	SP	4528	Jar +/- alun vein cutting QA alteration
	DDH-198, 168m	Pj31	SP	4718	Matrix of opaline qtz bx
	Barite:				
	Annick 440	Pb29	AS II	4680	Barite breccia matrix in Dr-440-SE
	Pyrite:				
	DDH-137A, 113.9m	P02p	AS II	4580	Brecha Central Sur matrix; alun-enarg-py
	DDH-137A, 152.1m	P03p	AS II	4544	Alun-py-enarg banded vein
	LM-03, 301.0m	P07p	AS II	4519	Alun-py-enarg vein; Lama
	Enargite:				
	DDH-137A, 113.9m	P02e	AS II	4580	Brecha Central Sur matrix; alun-enarg-py
	DDH-154, 224.3m	P04e	AS II	4545	Matrix alun-enarg-py; Frontera
	PS-98-16d	P06e	AS II	4674	Alun-enarg vein; Tunel Maria
	LM-03a, 433m	P08e	AS II	4398	Massive vein enarg

Table B1. Stable isotope sample descriptions and sample numbers. Abbreviated mineral names; alunite (alun), quartz (qtz), kaolinite (kao), dickite (dick), pyrophyllite (pyl), walthierite (wal), jarosite (jar), enargite (enarg), pyrite (py), hematite (hem), zunyite (zuny), native sulfur (S). Other abbreviations: Wendy (WN), Kimberly (KB), Kimberly West (KBw), Reina (RN), Canto Sur (CS). [1] *See descriptions in Chap. 2 (Pascua) and Chap. 3 (Tambo).*

Area	Sample	Lab #	Stage[1]	Elev. (m)	Description
TAMBO	**Alunite:**				
	WND-92A, 190.0m	T09a	1	4113	WN; Qtz-alun alteration
	WND-92A, 290.8m	T10a	1	4135	WN; Qtz-alun alteration
	KBD-85, 16.0m	T16a	1	4113	KB; Qtz-alun-pyl alt
	KBD-85, 306.8m	T29a	1	3887	KB; Qtz-alun alteration
	KBD-85, 94.1m	T30a	1	4052	KB; Qtz-alun alteration
	WND-92a, 82.7m	T31a	1	4090	WN; Qtz-alun-dick alteration
	RA-01	T01a	2	4010	RN; Vein alun with bar, walth, Au
	RA-4, 41.6m	T24a	2	4025	RN; Coarse alun with walth
	CS-29	T26a	2	4522	CS; Fine-grained alun, bar with Au
	CS-01b	T27a	3	4474	CS; Alun with bar in breccia matrix
	CS-08	T02b	3	4474	CS; Matrix alun over barite
	LN-24	T03a	3?	4130	KBw; Matrix alun, overgrowing T03b
	LN-24	T03b	3	4130	KBw; Matrix alun, overgrowing qtz
	WND-86, 155.0m	T04a	3	4017	WN; Matrix alun, with scorodite
	WND-86, 237m	T06a	3	3960	WN; Matrix alun hosting enarg
	CS-04	T20a	3	4475	CS; Matrix alun
	WND-92a, 37.5m	T21a	3	4080	WN; Matrix alun hosting enarg
	WND-92a, 231.8m	T22a	3	4122	WN; Matrix alun
	KB-43	T23a	3	4075	KB; Matrix alun
	LN-09	T25a	2	4240	KBw; Matrix alun with bar, qtz
	WND-92a, 13.7m	T28a	3?	4075	WN; powdery, near-surface matrix alun
	KB-08	T36a	3	4050	KB; Matrix alun with scorodite
	KB-47	T07a	MS		KB; Mine sample
	KB-33B	T08a	MS	4100	KB; Coarse banded vein with hem
	WN-07	T32a	MS	4180	WN; Banded vein with hem
	KB-01	T33a	MS	4050	KB; Coarse banded vein
	KB-44	T34a	MS	4075	KB; Coarse banded vein with hem
	KB-37B	T13a	SH	4480	KB; Near-surface qtz-kao-alun-S alteration
	KB-40	T17a	SH	4460	KB; Near-surface qtz-kao-alun-S alteration
	WN-14	T18a	SH	4450	CE; Powdery qtz-alun veinlets, near-surface
	CS-08	T02a	LV	4474	CS; Fine-gr. alun-jar overgrowing Stage 3 alun
	KBD-85, 306.8m - V	T11a	LV	3887	KB; Alun-jar veinlet cross-cutting Stage 1 alteration
	KBD-85, 125.7m	T12a	LV	4027	KB; Alun-qtz (jar) veinlet cross-cutting wallrock
	WND-86, 226.5m	T15a	LV	3969	WN; Brown jar-alun vein
	KB-09	T14a	Ca	4060	KB; Thin, pink veinlet cross-cutting altered tuff
	LN-02	T35a	Ca	4260	KBw; Thin, pink veinlet cross-cutting altered tuff
	BxS-03	B03a	BxS	4400	Breccia Sylvestre; matrix only
	BxS-05	B05a	BxS	4400	Breccia Sylvestre; matrix only
	Barite:				
	RA-01	Tb01	2	4050	RN; Coarse vein fill, associated with T01a
	CS-08	Tb02	2	4474	CS; Coarse matrix crystals associated with alun
	CS-30	Tb03	2	4396	CS; Coarse matrix crystals, mineralized
BRECHITA-HUANTINA VEIN	BH-01	BH-01	alun	4185	Coarse alun adjacent BH-02
	BH-02	BH-02	alun	4185	Banded alun-py-enarg-qtz vein
		BH-02p	pyrite		
		BH-02e	enargite		
CAMPANA B VEIN	CMP-01	C-01	alun		Massive med-grained alun, trace en
DEL CARMEN	DC-03a	D-03	alun		Coarse-grained, vug-filling alun
	DC-98-27-06	D-06	alun		Med-grained alun associated with enarg

Table B1. *(Continued)*

Table B2. All stable isotope data for El Indio-Pascua Belt alunite. All data reported in per mil. Replicate analyses separate by "/".

					I	II		III		IV				III
Description					BrF_5					Continuous Flow				
Sample	Lab #	Stage	δD	$\delta^{34}S$	$\delta^{18}O_{total}$	$\delta^{18}O_{SO4}$	$\delta^{18}O_{OH}$	Δ SO4-OH	Temp (°C)	$\delta^{18}O_{total}$	$\delta^{18}O_{SO4}$	$\delta^{18}O_{OH}$	Δ SO4-OH	Temp (°C)
Pascua:														
DDH-137A, 23.1m	P09a	AS I	-37	24.7	9.6		9.2	10.7	10	13.0	19.9	2.7	17.3	-50
DDH-184, 441.3m	P10a	AS I	-52	22.0	9.1		12.4	1.4	1200	14.2	13.8	14.8	-1.0	n/a
DDH-195A, 242.0m	P11a	AS I	-34/-31	24.5	10.2		12.2	4.7	190	16.6	16.9	16.2	0.7	n/a
DDH-154, 185.9m	P12a	AS I	-52	15.7	8.3					12.6				
LM-20, 94.8m	P13a	AS I	-27/-31	21.0	13.1	20.4	14.7	5.7	140	18.1	20.7	14.2	6.5	110
DDH-116, 289.5m	P21a	AS I		15.4/15.2										
DDH-152, 107.0m	P22a	AS I		12.6										
PSD-98-108, 374m	P23a	AS I	-43	18.5/18.5	8.0	15.6	9.4	6.2	120					
DDH-017, 122.5	P24a	AS I		17.2/17.0										
DDH-017, 108.0m	P28a	AS I		16.7										
DDH-168, 260m	P33a	AS I	-27	20.4										
DDH-116, 157.0m	P01a	AS II	-46	17.6	9.0		10.9	4.9	180	13.1	15.8	9.1	6.8	100
DDH-137A, 113.9m	P02a	AS II	-34	19.8/19.7	10.5	16.5	13.0	3.5	290	14.5				
DDH-137A, 152.1m	P03a	AS II	-51	14.7	12.4	17.3	15.6	1.7	790	16.1	17.4	14.2	3.2	320
DDH-154, 224.3m	P04a	AS II	-45/-42	22.2	8.8	15.7	10.7	5.0	170	13.0	15.7	9.0	6.8	100
PS-99-03	P05a	AS II	-41	14.1	11.5		13.6	4.4	210	16.4	18	14.0	4.0	240
PS-98-16d	P06a	AS II	-40	24.7	10.2		10.4	9.2	40	12.6	19.6	2.1	17.5	#
DDH-172, 435.1m	P25a	AS II	-47	18.9/19.0/18.7						15.3/14.9	15.6	14.4	1.3	1520
LM-03, 301.0m	P07a	AS II		17.8/18.0	9.3									
Annick 440	P27a	AS II	-36	12.6						17.1	18.2	15.5	2.8	400
PS-26c	P32a	AS III	-41	2.8	12.2		13.5	6.5	110	16.5	20.3/20.5	10.7	9.7	30
DDH-129, 111.6m	P14a	LV	-40	7.0						17.9/17.7	20.7	13.5	7.3	80
DR-368NE, PM-33	P16a	LV	-72	4.3	5.4		9.0	0.7	n/a		9.7			
DDH-154, 310.5m	P17a	LV	-77/-80	6.2	4.4/4.7	12.9	5.5	7.4	80	10.0	12.7/12.6	6.0	6.8	100
LM-20, 160.1m	P15a	SH	-48	1.6	10.9	19.7	11.5	8.2	60	16.7	19.1	13.1	6.0	130
DDH-119, 47.7m	P18a	SH	-42	-0.1	10.7/10.9		13.2	3.7	270		16.9			
DDH-122, 4.3m	P19a	SH	-68	6.1										
DDH-119. 34.0m	P20a	SH	-58	2.4/2.3	11.6	18.7	13.3	5.4	150		18.8/19.2			
DDH-057, 76.5m	P26a	Esp	-35	18.3	10.5		12.4	5.0	170	14.1	17.4	9.2	8.3	60

Description						I	II		III		IV			III
					BrF5					Continuous Flow				
Sample	Lab #	Stage	δD	$\delta^{34}S$	$\delta^{18}O_{total}$	$\delta^{18}O_{SO4}$	$\delta^{18}O_{OH}$	Δ SO4-OH	Temp (°C)	$\delta^{18}O_{total}$	$\delta^{18}O_{SO4}$	$\delta^{18}O_{OH}$	Δ SO4-OH	Temp (°C)
Tambo:														
WND-92A, 190.0m	T09a	1	-98	6.2	2.1	9.4	3.7	5.7	140		8.4			
WND-92A, 290.8m	T10a	1	-53	22.1	8.5		10.1	5.7	140	13.5	15.8	10.1	5.8	140
KBD-85, 16.0m	T16a	1		7.2	11.3									
KBD-85, 306.8m	T29a	1	-32	23.1	11.6		14.3	2.9	380		17.2			
KBD-85, 94.1m	T30a	1	-30	1.1	12.8		14.3	6.0	130	16.8	20.3	11.6	8.8	50
WND-92a, 82.7m	T31a	1		12.4										
RA-01	T01a	2	-28	27.3/27.2	13.8		15.5	5.5	150	19.7/17.9	20.9/21.1	15.5	5.5	150
RA-4, 41.6m	T24a	2	-27	27.4	14.0		16.3	4.0	240	17.1	20.3	12.3	8.0	70
CS-29	T26a	2	-55	27.5/27.1	9.2		10.8	5.7	140	13.4	16.5	8.8	7.8	70
CS-01b	T27a	3	-42	25.7	13.2		15.3	4.5	200		19.7/19.9			
CS-08	T02b	3	-75/-81	1.8	2.5	10.5	3.6	6.9	100	7.7	10.1	4.1	6.0	130
LN-24	T03a	3?	-47	5.9/5.1	11.1		13.2	4.5	200	16.3	17.7	14.2	3.5	290
LN-24	T03b	3	-46	1.3	11.5		12.8	6.4	110	16.6	19.2	12.7	6.5	110
WND-86, 155.0m	T04a	3	-63	1.7	7.2	15.6	8.1	7.5	80	11.9	15	7.3	7.8	70
WND-86, 237m	T06a	3	-85	1.7	4.3		5.7	6.2	120	8.0	11.9	2.2	9.8	30
CS-04	T20a	3	-41	-0.2						20.0				
WND-92a, 37.5m	T21a	3	-80	1.7	5.4		4.9	11	10	9.9/9.0	15.9	-0.1	16.0	#
WND-92a, 231.8m	T22a	3	-54	2.8	12.8		14.7	5.0	170	15.8	19.9/19.5	10.0	9.7	30
KB-43	T23a	3	-79	0.7						15.4				
LN-09	T25a	2	-35/-41	2.1	13.8		16.4	3.2	330		19.6			
WND-92a, 13.7m	T28a	3?	-98	2.8	2.7		3.6	7.5	80		11.1			
KB-08	T36a	3	-51	3.5	10.5		12.0	6.0	130	14.2	18.3/17.6	8.5	9.5	30
KB-47	T07a	MS	-40	0.5/0.5	12.6	20.2	14.0	6.2	120	17.4	20.5	12.8	7.8	70
KB-33B	T08a	MS	-48	1.1	7.8	16.0	8.8	7.2	90	13.5	16.4	9.2	7.2	80
WN-07	T32a	MS	-68/-70	1.3/1.5	8.3		9.7	6.2	120	2.1/12.1/11.5	15.9	5.9	10.0	30
KB-01	T33a	MS	-60	0.4						17.5	18.8	15.6	3.3	320
KB-44	T34a	MS	-74	0.3							11.3			
KB-37B	T13a	SH	-53	5.9	11.0/7.2		12.3	6.5	110	12.9/12.7	18.8	3.8	15.0	#
KB-40	T17a	SH	-16/-8	4.9	16.7	23.2	18.8	4.4	210	22.7	23.1/23.7	21.5	2.0	620
WN-14	T18a	SH	-62	16.6						14.0	15.4	11.9	3.5	290

Table B2. (Continued)

							I	*II*		*III*				*IV*	*III*
Description					**BrF_5**						**Continuous Flow**				
Sample	**Lab #**	**Stage**	**δD**	**$\delta^{34}S$**	**$\delta^{18}O_{total}$**	**$\delta^{18}O_{SO4}$**	**$\delta^{18}O_{OH}$**	**Δ SO4-OH**	**Temp (°C)**	**$\delta^{18}O_{total}$**	**$\delta^{18}O_{SO4}$**	**$\delta^{18}O_{OH}$**	**Δ SO4-OH**	**Temp (°C)**
CS-08	T02a	LV	-110/-112	-0.2	1.6		2.5	7.5	80	6.2/5.0/4.9	10.2/9.8	0.5	9.5	30
KBD-85, 306.8m - V	T11a	LV	-110	5.4	-0.3		1.3	5.7	140		7.0			
KBD-85, 125.7m	T12a	LV	-57	2.1/1.9	8.3		9.8	5.9	130	14.5	15.7	12.7	3.0	360
WND-86, 226.5m	T15a	LV	-68	4.2/4.4	8.3	16.5	9.3	7.2	90	13.7	16.1	10.1	6.0	130
KB-09	T14a	Ca	-120/-115	1.8	2.7	11.7	3.2	8.5	50		10.3			
LN-02	T35a	Ca	-56	9.2	12.9		14.2	6.4	110	15.8	20.8/20.3	8.6	12.0	0
BxS-03	B03a	BxS	-44	15.3	7.9	15.2	9.5	5.7	140		13.8/14.1			
BxS-05	B05a	BxS	-45	14.9	9.6		10.0	8.7	50	13.1/12.2	18.7	3.7	15.0	#
Other El Indio-Pascua Belt:														
BH-01	BH-01		-50	6.2	10.0		12.2	4.2	230		16.1/16.6	12.2		
BH-02	BH-02		-49	7.2	8.9		12.4	1.0	4360		13.4	12.4		
CMP-01	C-01		-104	10.1	1.0	5.7	-1.5	7.2	90		4.9/5.3/5.2			
DC-03a	D-03		-52	31.5	10.0		12.5	3.4	310	13.1	16.0/15.7	8.9		
DC-98-27-06	D-06		-86	28.6/28.3	18.5		20.6	4.5	200	22.0/22.3	25.1	17.9		

Table B2. (Continued.)

I Data from barite precipitate.

II $\delta^{18}O_{OH} = \delta^{18}OBrF_5 - (B*(\delta^{18}OGR\text{-}D)\text{-}E)/C$

Where: A = SO_4 yield factor = 0.50
B = SO_4 molar ratio = 0.40
C = OH molar ratio = 0.60
D = sulfate factor GR-BRF5 = 8.4
E = cation depend. factor = -0.50

* $\delta^{18}O_{SO4\text{-}flow}$ data used to calculate $\delta^{18}O_{OH}$, for comparison, where $\delta^{18}O_{SO4\text{-}BrF5}$ unavailable.

III sulfate-hydroxil $^{18}O = ax + b$ where a = 0.80, b = 1.00 (R.O. Rye, unpub. data)

IV $\delta^{18}O_{OH} = (\delta^{18}O \text{ flow} - (0.6*\delta^{18}O_{SO4}))/0.4$

					I	II		III		IV				III
Description					BrF_5					Continuous Flow				
Sample	Lab #	Stage	δD	$\delta^{34}S$	$\delta^{18}O_{total}$	$\delta^{18}O_{SO4}$	$\delta^{18}O_{OH}$	Δ SO4-OH	Temp (°C)	$\delta^{18}O_{total}$	$\delta^{18}O_{SO4}$	$\delta^{18}O_{OH}$	Δ SO4-OH	Temp (°C)
Jarosite:														
DDH-135, 162.7m	Pj30	SP	-129	-2.5	0.0									
DDH-198, 168m	Pj31	SP	-178	3.3/3.3	-0.7						4.8/4.2	2.3		
Barite:														
Annick 440	Pb29	AS II		22.1							14.4			
RA-01	Tb01	2		26.8		13.8					13.5/14.1			
CS-08	Tb02	2		24.5		17.3					17.3			
CS-30	Tb03	2		23.8		17.1					17.1			

Table B3. Stable isotope data for El Indio-Pascua Belt jarosite and barite. All data given as per mil. Replicate analyses denoted by '/'.

Sample	Lab #	Stage	$\delta^{34}S$
Pyrite:			
DDH-137A, 113.9m	P02p	AS II	-3.8
DDH-137A, 152.1m	P03p	AS II	-5.3
LM-03, 301.0m	P07p	AS II	-3.4/-3.3
BH-02p			-12.9/-12.8
Enargite:			
DDH-137A, 113.9m	P02e	AS II	-6.0/-5.9
DDH-154, 224.3m	P04e	AS II	-3.6/-3.5
PS-98-16d	P06e	AS II	-4.5
LM-03a, 433m	P08e	AS II	-5.6/-5.5
BH-02e			-3.7

Table B4. Sulfur isotope data for El Indio-Pascua Belt sulfides. All data given as per mil. Replicate analyses denoted by '/'.

Source	Sample Type	Sample #	Area	Analysis #	$\delta^{34}S$ (per mil)
Tambo	Magmatic Steam Veins	KB-02a	Kimberly	1	-0.1
				2	0.8
				3	1.1
				4	1.6
				5	1.8
				6	1.0
				7	0.7
				8	0.6
				9	-1.1
				10	-0.2
				11	0.0
				12	-0.4
				13	-0.4
				14	-0.5
				15	-0.1
				16	0.8
				17	-0.8
				18	-0.2
				19	0.4
		KB-02b	Kimberly	1	0.4
				2	-0.2
				3	0.1
				4	-0.2
				5	0.0
				6	-0.7
				7	0.2
				8	0.1
				9	-0.7
				10	0.2
		WN-07	Wendy	1	1.4
				2	1.1
				3	1.4
				4	1.7
	Stage 3 alunite	CS-08	Canto Sur	1 (base)	2.0
				2 (mid)	2.0
				3 (top)	1.0
		WND-86, 155.0m	Wendy	coarse	1.3
				fine	1.5
		KB-34	Kimberly	coarse	1.3
				fine	0.9/1.2
Del Carmen	Coarse vug alunite	DC-03a		yellow	31.1
				pink	31.4
Brechita-Huantina	Banded vein alunite	BH-01		A	7
				B	1.6/0.3*
				C	8.9
				D	7.7
				E	6.2
		BH-02		A	7.2
				B	3.9/3.8
				C	7.8

Table B5. Additional $\delta^{34}S$ data for El Indio-Pascua Belt alunite representing multiple analyses from banded veins or individual crystals. * *sample contaminated by pyrite.*

References

Clayton, R.N. and Mayeda, T.K., 1963. The use of bromine pentafluoride in the extraction of oxygen from oxides and silicates for isotopic analysis; Geochim. et Cosmochim. Acta, v. 27, 43-52.

Gieseman, A., Jager, H.J., Norman, A.L., Krouse, H.R., and Brand, W.A., 1994. On-line sulfur-isotope determination using and elemental analyzer coupled to a mass spectrometer, Analytical Chemistry, 65, 18.

Godfrey, J.D., 1962. The deuterium content of natural waters and other substances, Geochim. et Cosmochim. Acta, 27, 43-52.

Kornexl, Barbara E., Matthias Gehre, Reiner Höfling, and Roland A. Werner, 1999. On-line d18O measurement of organic and inorganic substances. Rapid Communications in Mass Spectrometry 13, 1685-1693.

Pickthorn, W.J., and O'Neil, J.R., 1985. 18O relations in alunite mineral: potential single mineral thermometer (abst). Geol. Soc. of America Abstracts with Programs, v. 17 (7), 686.

Thompson, M., and Howarth, R.J., 1978. A new approach to the estimation of analytical precision. Journal of Geochemical Exploration, 9, 1, 23-30.

Wasserman, M.D., Rye, R.O., Bethke, P.M., and Arribas, Jr., A., 1992. Methods for separation and total stable isotope analysis of alunite. Open file report 92-9, US Department of the Interior, Geological Survey.

APPENDIX C: ^{40}AR-^{39}AR GEOCHRONOLOGY

Analytical Methods

All analyses were carried out at the Queen's University ^{40}Ar-^{39}Ar laboratory. For each sample *ca.* 10 mg material, was wrapped in Al-foil, and the resulting disks stacked vertically, together with further samples of similar age, into a 11.5 cm long and 2.0 cm diameter container. The container was then irradiated with fast neutrons for 7.5 hours at McMaster nuclear reactor in Hamilton, Canada. Standards (flux monitors) were located at ca. 0.5-1 cm intervals along the irradiation container and J-values for individual samples were determined by second-order polynomial interpolation. The J-values for the samples discussed in this study were *ca.* 2.4 x 10^{-3} and varied by less than 0.02 x 10^{-3}.

All samples, including the monitors, were placed in small pits (ca. ½-1 mm diameter) drilled in a Cu sample-holder that was placed beneath the sapphire view-port of a small, bakeable, stainless-steel chamber connected to an ultra-high vacuum purification system. Monitors were fused using LEXEL 3500 argon-ion laser-beam, for step-heating the alunites, the beam was defocused to cover the entire sample. Heating periods are *ca.* 3 minutes at increasing power settings (0.25 to 3.0 W). The evolved gas, after purification using a cold-trap with liquid N_2 and an SAES C50 getter (*ca.* 5 minutes), was admitted to an on-line, MAP 216 mass spectrometer, with a Bäur Signer source and an electron multiplier (set to a gain of 100 over the Faraday). Blanks, measured routinely, were subtracted from the subsequent sample gas-fractions. Measured argon-isotope peak heights were extrapolated to zero-time, normalized to the ^{40}Ar/^{36}Ar atmospheric ratio (295.5) using measured values of atmospheric argon, and corrected for neutron-induced ^{40}Ar from potassium, ^{39}Ar and ^{36}Ar from calcium (using production ratios of Onstott and Peacock, 1987), and ^{36}Ar from chlorine (Roddick, 1983).

Dates and errors (all given at 2σ) are calculated using formulae given by Dalrymple et al. (1981), and the constants recommended by Steiger and Jäger (1977). The inter-laboratory standard (flux-monitor) used is Mac-83 biotite (Sandeman et al., 1997) with the most recent published age of 24.36 ± 0.17 Ma (2σ; Sandeman et al. 1999).

Analytical Data

Details of ^{40}Ar-^{39}Ar data used to calculate reported ages for Pascua and Tambo alunite (Tables 2.5 and 3.4, respectively) are given (Table C1). Age spectrum plots for all samples are shown in Figure C.1.

Table C1. Detailed geochronologic data for Pascua and Tambo alunite.

Laser Power	^{40}Ar	^{39}Ar	^{38}Ar	^{37}Ar	^{36}Ar	Blank ^{40}Ar	Ca/K	% ^{40}Ar	% ^{39}Ar	$^{40}Ar/^{39}Ar_K$	Age +/- 2σ
TU-128: sample P05, mass 1.0mg, J value = 0.002389 +/- 0.000026											
0.75	0.043 (0.003)	0.010 (0.002)	0.003 (0.002)	0.003 (0.002)	0.003 (0.002)	0.046	0.000	0.03	-0.01	3.228 (435.046)	13.86 (1860.69)
1.50	125.652 (0.157)	0.549 (0.011)	0.107 (0.013)	0.005 (0.005)	0.434 (0.010)	0.054	0.043	98.32	4.97	3.922 (5.840)	16.83 (24.93)
2.25	49.506 (0.087)	5.458 (0.030)	0.187 (0.014)	0.003 (0.003)	0.137 (0.004)	0.077	0.000	77.44	50.32	2.034 (0.246)	8.75 (1.05)
3.00	26.303 (0.047)	4.898 (0.022)	0.151 (0.005)	0.003 (0.002)	0.060 (0.002)	0.050	0.000	61.98	44.72	2.050 (0.137)	8.81 (0.59)
TU-129: sample Pj31, mass 1.0mg, J value = 0.002391 +/- 0.000028											
0.5	273.177 (0.315)	1.562 (0.025)	0.245 (0.023)	0.011 (0.008)	0.934 (0.021)	0.049	0.048	97.54	2.63	4.339 (4.079)	18.62 (17.42)
1.0	182.182 (0.236)	24.571 (0.111)	0.441 (0.018)	0.007 (0.005)	0.475 (0.013)	0.051	0.002	74.20	41.68	1.898 (0.155)	8.17 (0.67)
1.5	144.326 (0.194)	18.312 (0.085)	0.354 (0.020)	0.005 (0.005)	0.387 (0.009)	0.052	0.001	76.27	31.05	1.855 (0.151)	7.99 (0.65)
1.75	87.993 (0.138)	10.778 (0.052)	0.212 (0.013)	0.005 (0.004)	0.243 (0.007)	0.060	0.001	78.13	18.27	1.770 (0.198)	7.62 (0.85)
2.0	43.322 (0.075)	2.602 (0.018)	0.083 (0.008)	0.004 (0.003)	0.138 (0.005)	0.082	0.000	89.38	4.39	1.760 (0.533)	7.58 (2.29)
2.5	31.732 (0.048)	0.479 (0.004)	0.046 (0.003)	0.003 (0.002)	0.112 (0.003)	0.051	0.011	98.28	0.79	1.145 (1.913)	4.93 (8.23)
3.5	18.479 (0.023)	0.026 (0.002)	0.026 (0.002)	0.002 (0.002)	0.064 (0.002)	0.065	0.000	96.74	0.82	1.229 (1.254)	5.29 (5.39)
4.5	25.111 (0.034)	0.232 (0.003)	0.035 (0.003)	0.002 (0.001)	0.090 (0.002)	0.066	0.000	100.10	0.38	-0.147 (2.915)	-0.64 (12.58)
sample P11, mass 1.0mg											
0.50	0.527(0.099)	0.473 (0.109)	0.221 (0.113)	0.142 (0.026)	0.146 (0.036)	0.401	1.498	8003.51	52.72	-87.740 (31.010)	-424.98 (169.37)
0.80	6.300 (0.021)	0.052 (0.003)	0.010 (0.002)	0.004 (0.002)	0.026 (0.002)	0.027	0.126	100.10	4.31	-0.190 (16.094)	-0.82 69.49
1.25	5.747 (0.016)	0.063 (0.003)	0.011 (0.003)	0.004 (0.002)	0.023 (0.002)	0.011	0.047	99.39	5.45	0.670 (13.153)	2.89 (56.67)
1.75	6.409 (0.020)	0.119 (0.003)	0.012 (0.002)	0.005 (0.002)	0.025 (0.002)	0.007	0.049	97.01	11.88	1.727 (5.300)	7.44 (22.78)
2.25	3.048 (0.025)	0.062 (0.004)	0.008 (0.003)	0.004 (0.002)	0.014 (0.002)	0.007	0.153	96.39	5.34	2.095 (12.628)	9.02 (54.22)
3.00	2.515 (0.012)	0.126 (0.003)	0.008 (0.002)	0.004 (0.002)	0.012 (0.002)	0.003	0.030	90.50	12.60	1.870 (6.039)	8.05 (25.94)
3.75	2.166 (0.012)	0.083 (0.004)	0.008 (0.002)	0.004 (0.002)	0.011 (0.002)	0.003	0.036	91.36	7.71	2.352 (9.094)	10.12 (39.02)
sample P17, mass 1.0mg											
0.25	30.545 (0.055)	0.030 (0.004)	0.027 (0.004)	0.005 (0.002)	0.113 (0.003)	0.758	0.523	101.44	0.06	-41.024 (83.941)	-185.84 (400.53)
0.50	76.182 (0.126)	0.042 (0.004)	0.061 (0.007)	0.006 (0.003)	0.276 (0.006)	0.787	0.322	102.01	0.12	-76.334 (92.694)	-362.72 (487.87)
1.00	230.053 (0.247)	0.127 (0.011)	0.172 (0.017)	0.011 (0.009)	0.805 (0.018)	0.611	0.309	99.59	0.62	8.815 (50.139)	37.55 (211.38)
1.50	340.313 (0.405)	1.015 (0.022)	0.283 (0.029)	0.021 (0.012)	1.171 (0.025)	0.042	0.082	98.10	5.76	6.519 (7.672)	27.84 (32.52)
2.00	214.056 (0.263)	5.081 (0.034)	0.308 (0.018)	0.018 (0.005)	0.712 (0.015)	0.010	0.013	94.49	29.29	2.316 (0.918)	9.94 (3.93)
2.75	196.569 (0.237)	11.105 (0.058)	0.435 (0.020)	0.031 (0.005)	0.619 (0.014)	0.012	0.012	89.43	64.15	1.855 (0.371)	7.97 (1.59)

Laser Power	^{40}Ar	^{39}Ar	^{38}Ar	^{37}Ar	^{36}Ar	Blank ^{40}Ar	Ca/K	% ^{40}Ar	% ^{39}Ar	$^{40}Ar/^{39}Ar_K$	Age +/- 2σ
TB-110: sample T01, mass 1.0mg, J value = 0.002400 +/- 0.000038											
1.00	45.421(0.105)	6.291 (0.032)	0.501 (0.013)	0.008 (0.002)	0.119 (0.003)	0.209	0.003	72.35	16.01	1.979 (0.157)	8.55 (0.67)
1.75	40.547 (0.057)	16.025 (0.065)	1.427 (0.025)	0.010 (0.002)	0.031 (0.002)	0.205	0.002	18.88	40.86	2.031 (0.045)	8.77 (0.19)
2.40	31.260 (0.084)	13.594 (0.059)	1.454 (0.025)	0.008 (0.002)	0.017 (0.002)	0.203	0.001	11.16	34.66	2.018 (0.046)	8.72 (0.20)
3.00	7.667 (0.035)	3.337 (0.017)	0.420 (0.011)	0.006 (0.002)	0.007 (0.002)	0.201	0.003	9.92	8.47	2.013 (0.170)	8.69 (0.73)
TB-104: sample T02a, mass 1.0mg, J value = 0.002399 +/- 0.000036											
0.25	1.685 (0.010)	0.231 (0.004)	0.013 (0.003)	0.005 (0.002)	0.010 (0.002)	0.192	0.019	101.90	0.32	-0.167 (2.486)	-0.72 (10.77)
0.75	12.027 (0.029)	6.417 (0.028)	0.091 (0.006)	0.011 (0.002)	0.010 (0.002)	0.196	0.005	13.47	9.69	1.583 (0.086)	6.84 (0.37)
1.25	78.215 (0.172)	45.459 (0.185)	0.579 (0.017)	0.053 (0.004)	0.009 (0.003)	0.349	0.005	1.09	68.83	1.679 (0.024)	7.25 (0.10)
1.75	22.513 (0.042)	12.945 (0.053)	0.170 (0.008)	0.019 (0.003)	0.006 (0.002)	0.201	0.005	2.03	19.58	1.675 (0.046)	7.23 (0.20)
2.50	2.198 (0.013)	1.064 (0.007)	0.020 (0.003)	0.006 (0.002)	0.006 (0.002)	0.193	0.008	15.09	1.58	1.617 (0.573)	6.98 (2.47)
TB-106: sample T10a, mass 1.0mg, J value = 0.002388 +/- 0.000026											
0.30	7.590 (0.025)	0.030 (0.003)	0.013 (0.003)	0.005 (0.002)	0.031 (0.002)	0.295	0.292	102.50	0.05	-14.588 (56.327)	-63.97 (251.42)
1.02	12.385 (0.033)	0.124 (0.004)	0.021 (0.004)	0.007 (0.002)	0.048 (0.003)	0.300	0.133	100.53	0.41	-0.641 (7.632)	-2.76 (32.93)
1.50	10.747 (0.034)	1.356 (0.008)	0.036 (0.003)	0.009 (0.002)	0.031 (0.002)	0.296	0.019	69.43	5.12	2.379 (0.493)	10.22 (2.11)
2.00	26.698 (0.057)	6.574 (0.030)	0.102 (0.005)	0.015 (0.002)	0.039 (0.003)	0.302	0.008	36.23	25.12	2.558 (0.118)	10.99 (0.51)
2.50	43.118 (0.079)	9.433 (0.039)	0.146 (0.008)	0.018 (0.002)	0.071 (0.003)	0.305	0.007	43.65	36.07	2.553 (0.090)	10.97 (0.38)
3.00	40.421 (0.065)	8.689 (0.036)	0.138 (0.005)	0.015 (0.002)	0.068 (0.003)	0.305	0.006	44.22	33.23	2.571 (0.095)	11.04 (0.41)
TB-101: sample T17, mass 1.0mg, J value = 0.002396 +/- 0.000032											
0.25	42.654 (0.074)	0.039 (0.004)	0.041 (0.004)	0.006 (0.002)	0.155 (0.004)	0.244	0.326	100.62	0.05	-25.199 (108.552)	-112.35 (499.38)
0.50	47.627 (0.072)	0.093 (0.004)	0.043 (0.005)	0.006 (0.002)	0.172 (0.004)	0.245	0.080	100.52	0.33	-3.895 (18.094)	-16.91 (78.95)
0.80	52.666 (0.087)	1.562 (0.009)	0.082 (0.004)	0.007 (0.002)	0.178 (0.004)	0.247	0.006	94.26	7.95	1.949 (0.773)	8.41 (3.32)
1.25	47.648 (0.074)	7.637 (0.032)	0.215 (0.009)	0.011 (0.002)	0.116 (0.003)	0.248	0.004	66.69	39.47	2.061 (0.126)	8.89 (0.54)
1.75	32.199 (0.057)	5.247 (0.024)	0.162 (0.007)	0.009 (0.002)	0.079 (0.003)	0.244	0.004	66.14	27.07	2.060 (0.151)	8.88 (0.65)
2.50	31.137 (0.053)	4.870 (0.022)	0.138 (0.006)	0.008 (0.002)	0.079 (0.003)	0.242	0.003	67.81	25.12	2.041 (0.167)	8.80 (0.72)

Table C.1. *Continued.*

Table C.1. *Continued.*

Laser Power	^{40}Ar	^{39}Ar	^{38}Ar	^{37}Ar	^{36}Ar	Blank ^{40}Ar	Ca/K	% ^{40}Ar	% ^{39}Ar	$^{40}Ar/^{39}Ar_K$	Age +/- 2σ
TB-111: sample T33, mass 1.0mg, J value = 0.002402 +/- 0.000040											
0.50	48.027 (0.106)	0.389 (0.005)	0.052 (0.005)	0.006 (0.002)	0.171 (0.004)	0.222	0.005	99.19	9.67	1.026 (3.136)	4.44 (13.56)
1.00	89.334 (0.149)	2.117 (0.017)	0.097 (0.008)	0.008 (0.004)	0.304 (0.007)	0.341	0.006	95.88	54.98	1.737 (1.009)	7.51 (4.36)
2.75	11.646 (0.028)	1.365 (0.009)	0.031 (0.004)	0.007 (0.002)	0.036 (0.002)	0.216	0.009	78.12	35.35	1.846 (0.520)	7.98 (2.24)
TB-103: sample T35, mass 1.0mg, J value = 0.002397 +/- 0.000034											
0.75	5.992 (0.020)	1.472 (0.008)	0.029 (0.003)	0.045 (0.002)	0.015 (0.002)	0.142	0.139	51.69	8.90	1.923 (0.449)	8.30 (1.93)
1.25	17.827 (0.043)	7.041 (0.031)	0.108 (0.005)	0.206 (0.004)	0.017 (0.002)	0.146	0.141	19.48	42.89	2.012 (0.088)	8.68 (0.38)
1.75	11.710 (0.029)	4.751 (0.021)	0.071 (0.004)	0.157 (0.004)	0.012 (0.002)	0.146	0.159	18.68	28.91	1.971 (0.141)	8.50 (0.61)
2.50	6.952 (0.035)	2.553 (0.018)	0.042 (0.007)	0.116 (0.005)	0.010 (0.003)	0.330	0.215	22.22	15.45	2.021 (0.361)	8.72 (1.55)
3.00	2.023 (0.010)	0.653 (0.005)	0.016 (0.003)	0.038 (0.002)	0.006 (0.002)	0.193	0.259	28.03	3.85	2.073 (0.786)	8.94 (3.38)

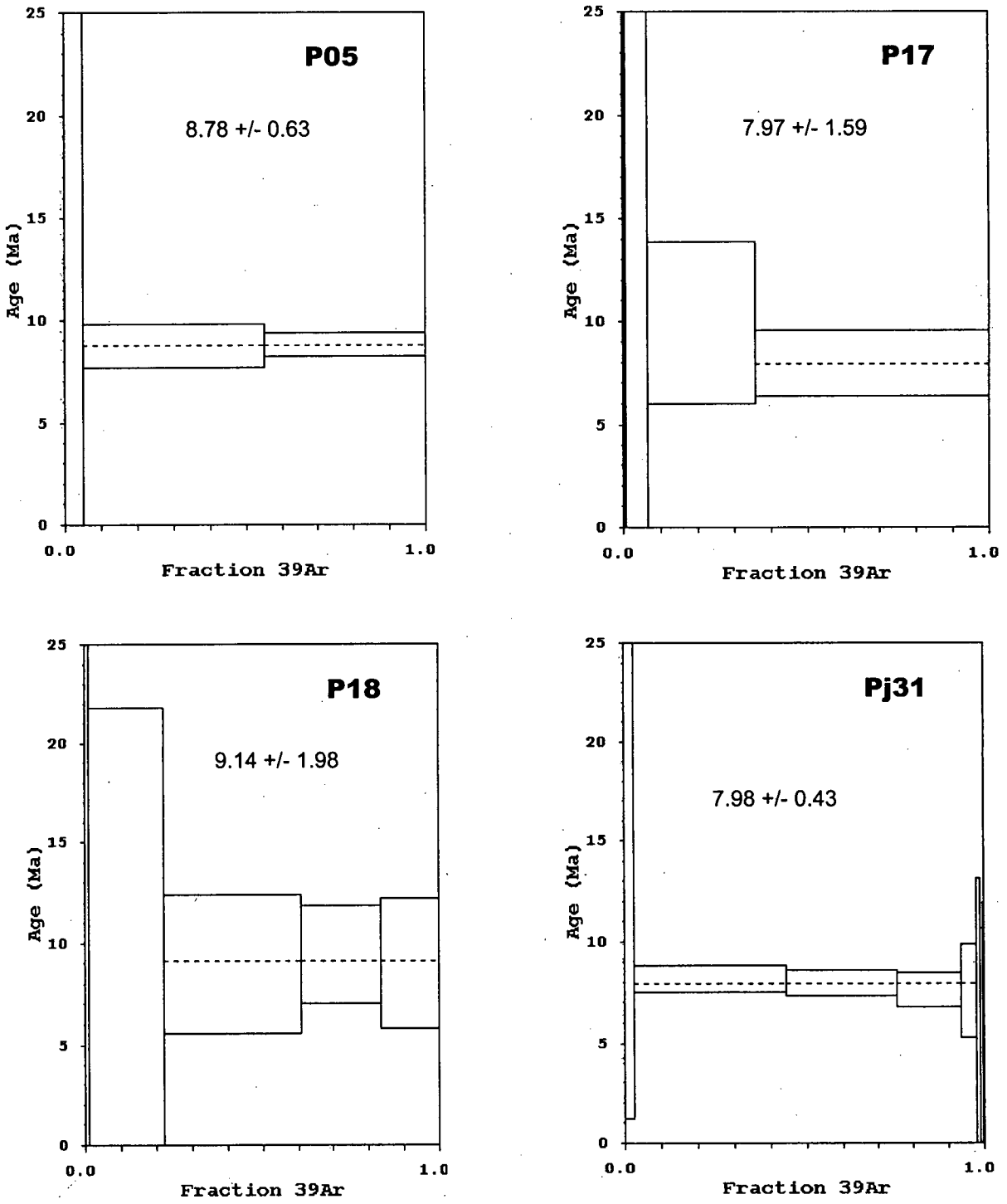

Figure C.1. Age spectra for El Indio-Pascua Belt alunite. Sample number as shown. Dashed line represents step included in plateau age.

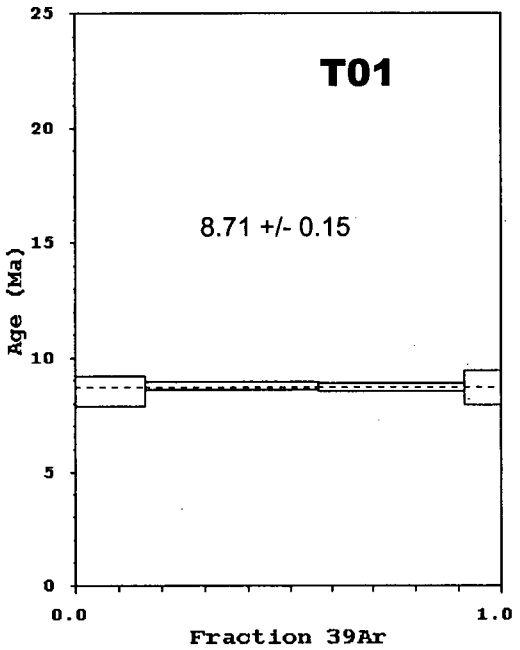

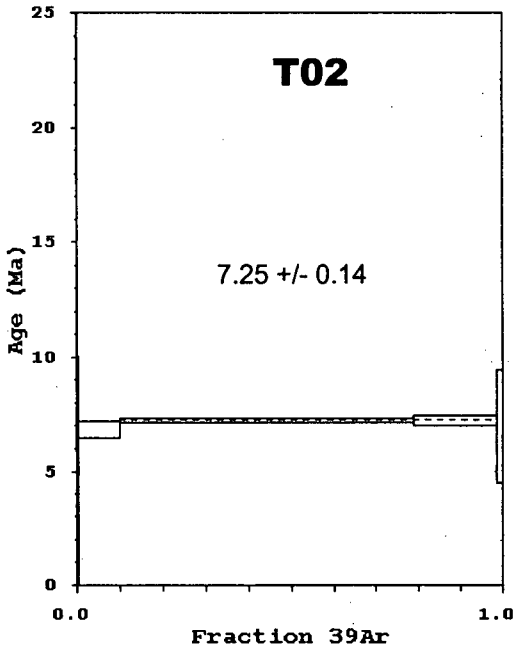

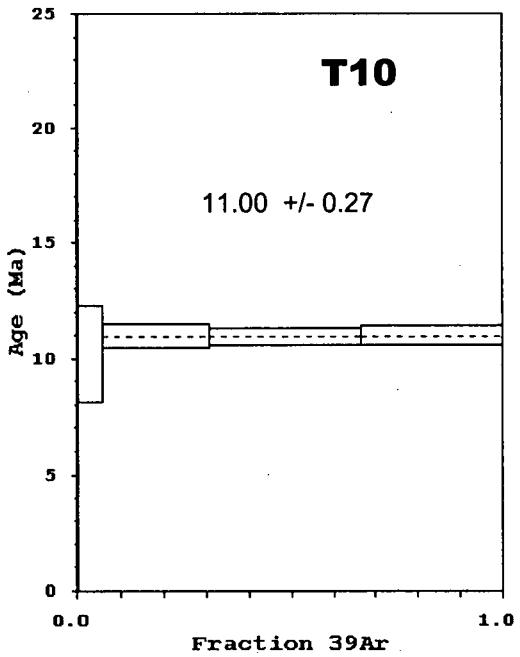

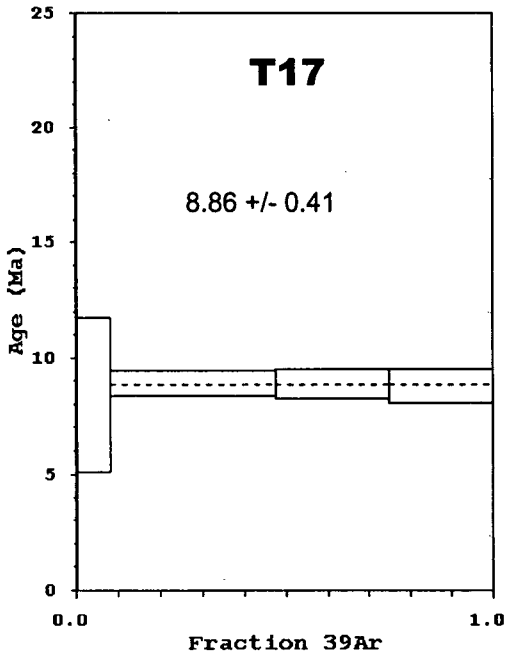

Figure C.1. Continued...

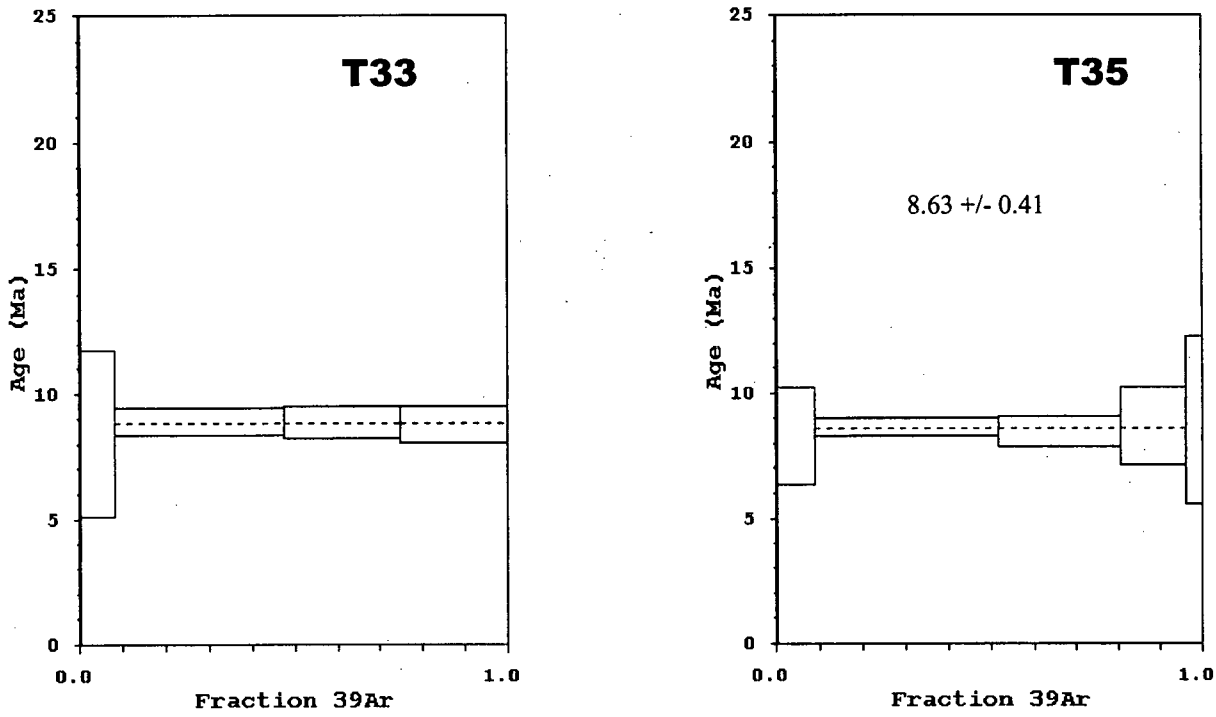

Figure C.1. Continued....

REFERENCES

Dalrymple, G. B., Alexander, Jr., E.C., Lanphere, M. A., and Kraker, G. P., 1981: Irradiation of samples for $^{40}Ar/^{39}Ar$ dating using the Geological Survey TRIGA reactor. US Geological Survey Professional Paper 1176, 55 p.

Onstott, T. C. and Peakock, M. W., 1987: Argon retentivity of hornblendes; a field experiment in a slowly cooled metamorphic terrane, Geochimica et Cosmochimica Acta, 51 (11), p. 2891-2903.

Roddick, J. C., 1983: High-precision intercalibration of 40Ar-39Ar standards. Geochimica et Cosmochimica Acta, 47, 887-898.

Sandeman, H.A., Clark, A.H., Farrar E. and Arroyo, G., 1997: Lithostratigraphy, petrology and ^{40}Ar-^{39}Ar geochronology of the Crucero Supergroup, Puno Department, SE Peru; Journal of South American Earth Sciences, v. 10, p. 223-245.

Sandeman, H.A., Archibald, D.A.; Grant, J.W.; Villneuve, M.E. and Ford, F.D. 1999: Characterisation of the chemical composition and ^{40}Ar-^{39}Ar systematics of intralaboratory standard MAC-83 biotite; in Radiogenic Age and Isotopic Studies: Report 12; Geological Survey of Canada, Current Research 1999-F, p.13-26.

Steiger, R. H. and Jäger, E., 1977: Subcommission on geochronology: convention on the use of decay constants in geo- and cosmochronology. Earth Planet. Sci. Letters, 36, 359-362.

APPENDIX D: THERMODYNAMIC DATA AND CALCULATIONS

This appendix includes thermodynamic data and details of calculations used in:
1) Chapter 2: pH-fO2 diagram for Pascua APE event (Fig. 2-15).
2) Chapter 5: activity diagrams and alunite-natroalunite solid solution models.

A) pH-LOG fO_2 DIAGRAM

Balanced reactions for all mineral and S-species reactions are given in Table D1. Log K values for all reactions were generated in SUPCRT92 (Johnson et al., 1992), with the exception of enargite-tennantite reactions. These are based on thermochemical approximations from Craig and Barton (1973). ΔG for the sulfidation reaction (Craig and Barton, 1973):

$$2/3 \text{ tenn} + S_2 = 8/3 \text{ enarg}$$

is calculated at 275°C and combined with reactions D15 through D19.

Caution must be taken when combining thermodynamic databases, but this method is justified since:

- Standard state properties of S_2 are equivalent in the Craig and Barton (1973) and SUPCRT92 database - which is based on Helgeson data (e.g. Helgeson et al., 1978).
- Only balanced reactions are used for the purposes of this diagram. Thermodynamic properties for individual elements are not calculated and therefore there is no concern regarding the compatibility of ΔG_f in the two databases.

Au solubility as $Au(HS)_2^-$

Reliable thermodynamic data for the $Au(HS)_2^-$ complex does not exist in the SUPCRT92 (and updates) database (Wood, 1998; Wood and Samson, 1998). The most reliable thermodyamic data for this species comes from the experimental data for reaction D22 from Benning and Seward (1996).

$$Au(s) + 2\ H_2S^o + HS^- = Au(HS)_2^- + \tfrac{1}{2}\ H_2\ (g) \qquad (D22)$$

Log K for reaction D22 is given at SWVP and temperatures (at 50°C intervals) between 150° and 350°C. Data is compatible with the SUPCRT database. For this study, log K at 275 °C is taken as –0.995; determined by the midpoint between 250° and 300 °C.

Balanced reactions are given in Table D2. Table D3 gives equations based on variable Au concentrations.

Table D1. Reactions and equations for boundaries on log fO_2-pH diagram at 275°C (Fig. 2-15).

Rxn #		Balanced Reaction	Log K	Equation (ΣS=0.05 M)
D1	Py-mag (HS^- field)	$FeS_2 + 6H_2O = Fe_3O_4 + 6HS^- + 6H^+ + O_2$	-95.992	$fO_2 = 6pH - 88.186$
D2	Py-mag (SO_4^{2-} field)	$3FeS_2 + 6H_2O + 11O_2 = Fe_3O_4 + 6SO_4^{2-} + 12H^+$	260.167	$fO_2 = -^{12}/_{11}\,pH - 22.942$
D3	Hem-mag	$1/3Fe_3O_4 + 1/12O_2 = ½\ Fe_2O_3$	33.060	$fO_2 = -33.060$
D4	Hem-py (SO_4^{2-} field)	$2FeS_2 + 4H_2O + 15/2O_2 = Fe_2O_3 + 4SO_4^{2-} + 8\ H^+$	178.955	$fO_2 = -^{8}/_{7.5}\,pH - 24.555$
D5	Hem-py (HSO_4^- field)	$2FeS_2 + 4H_2O + 15/2O_2 = Fe_2O_3 + 4HSO_4^- + 4H^+$	201.756	$fO_2 = -^{4}/_{7.5}\,pH - 27.595$
D6	Aln-musc (H_2S field)	$KAl_3(SO_4)_2(OH)_6 + 3SiO_2 = KAl_2(AlSi_3)O_{10}(OH)_2 + 2H_2S + 4O_2$	-127.585	$fO_2 = -31.246$
D7	Aln-musc (HSO_4^- field)	$KAl_3(SO_4)_2(OH)_6 + 3SiO_2 = KAl_2(AlSi_3)O_{10}(OH)_2 + 2HSO_4^- + 2H^+$	-11.982	$pH = 4.690$
D8	Po-mag	$3FeS + 3H_2O + ½\ O_2 = Fe_3O_4 + 3HS^- + 3H^+$	-11.627	$fO_2 = -6pH + 15.448$
D9	Po-py (H_2S field)	$FeS + ½\ O_2 + H_2S = FeS_2 + H_2O$	20.863	$fO_2 = -39.124$
D10	Po-py (HS^- field)	$FeS + ½\ O_2 + HS^- + H^+ = FeS_2 + H_2O$	28.122	$fO_2 = 2pH - 53.642$
D11	En-tn (H_2S field)*	$8Cu_3AsS_4 + 6H_2O = 2Cu_{12}As_4S_{13} + 6H_2S + 3O_2$		
D12	En-tn (HS^- field)*	$8Cu_3AsS_4 + 6H_2O = 2Cu_{12}As_4S_{13} + 6HS^- + 6H+\ 3O_2$		
D13	En-tn (SO_4^{2-} field)*	$8Cu_3AsS_4 + 6H_2O + 9O_2 = 2Cu_{12}As_4S_{13} + 6SO_4^{2-} + 12H^+$		
D14	En-tn (HSO_4^- field)*	$8Cu_3AsS_4 + 6H_2O + 9O_2 = 2Cu_{12}As_4S_{13} + 6HSO_4^- + 6H^+$		
D15	H_2S - HS^-	$H_2S = HS^- + H^+$	-7.258	$pH = 7.258$
D16	HSO_4^- - SO_4^{2-}	$HSO_4^- = SO_4^{2-} + H^+$	-5.700	$pH = 5.700$
D17	H_2S - HSO_4^-	$H_2S + 2O_2 = HSO_4^- + H^+$	57.802	$fO_2 = -½\ pH - 28.901$
D18	H_2S - SO_4^{2-}	$H_2S + 2O_2 = SO_4^{2-} + 2H^+$	52.101	$fO_2 = -pH - 26.051$
D19	HS^- - SO_4^{2-}	$HS^- + 2O_2 = SO_4^{2-} + H^+$	59.360	$fO_2 = -½\ pH - 29.68$
D20	S^o - HSO_4^-	$2S^o + 2H_2O + 3O_2 = 2HSO_4^- + 2\ H^+$	82.675	$fO_2 = -^{2}/_{3}\,pH - 28.425$
D21	S^o - H_2S	$2S^o + 2H_2O = 2H_2S + O_2$	-32.928	$fO_2 = -30.326$

Mineral abbreviations: pyrite (py); magnetite (mag); hematite (hem), alunite (aln), musc (musc), pyrrhotite (po), enargtite (en), tennantite (tn).
* See discussion in text regarding calculations of enargite-tennantite reactions.

Table D2. Balanced reactions and calculated log K values for Au as $Au(HS)_2^-$.

Rxn #	S-species field	Balanced Reaction	Log K (SWVP, 275°C)
D23	H_2S	$Au(s) + 2\ H_2S^o + ¼\ O_2\ (g) = Au(HS)_2^- + ½\ H_2O + H^+$	1.227
D24	SO_4^{2-}	$Au(s) + 2\ SO_4^{2-} + 3\ H^+ = Au(HS)_2^- + ½\ H_2O + 15/4\ O_2\ (g)$	-102.976
D25	HS-	$Au(s) + 2\ HS^- + H^+ + ¼\ O_2\ (g) = Au(HS)_2^- + ½\ H_2O$	15.743
D26	HSO_4^-	$Au(s) + 2\ HSO_4^- + H^+ = Au(HS)_2^- + ½\ H_2O + 15/4\ O_2\ (g)$	-114.376

Table D3. Equations for Au as $Au(HS)_2^-$ calculated at 275°C and variable Au concentrations.

Rxn #	Au concentration	Equation (S=0.05 M)
D23	1 ppb	$fO_2 = -4\ pH - 27.674$
	100 pbb	$fO_2 = -4\ pH - 19.674$
	10 ppm	$fO_2 = -4\ pH - 11.674$
D24	1 ppb	$fO_2 = -{}^4/_5\ pH - 25.942$
	100 pbb	$fO_2 = -{}^4/_5\ pH - 26.476$
	10 ppm	$fO_2 = -{}^4/_5\ pH - 27.009$
D25	1 ppb	$fO_2 = 4\ pH - 85.740$
	100 pbb	$fO_2 = 4\ pH - 77.740$
	10 ppm	$fO_2 = 4\ pH - 69.740$
D26	1 ppb	$fO_2 = -{}^4/_{15}\ pH - 28.982$
	100 pbb	$fO_2 = -{}^4/_{15}\ pH - 29.516$
	10 ppm	$fO_2 = -{}^4/_{15}\ pH - 30.049$

Au solubility as $Au(HS)^o$

Again, the best estimate of Au solubility as $Au(HS)^o$ is taken from Benning and Seward (1996):

$$Au(s) + 2\ H_2S^o = Au(HS)^o + ½\ H_2\ (g) \qquad (D27)$$

Log K of reaction at D27 at SWVP and 275°C = -6.320 (Benning and Seward, 1996) - determined by mid-point between 250° and 300°C. Balanced reactions given in Table D4. Table D5 gives equations based on variable Au concentrations.

Table D4. Balanced reactions and calculated log K values for Au as $Au(HS)^o$.

Rxn #	S-species field	Balanced Reaction	Log K (SWVP, 275°C)
D28	H_2S	$Au(s) + 2\ H_2S^o + ¼\ O_2\ (g) = Au(HS)^o + ½\ H_2O$	3.160
D29	SO_4^{2-}	$2Au(s) + 2\ SO_4^{2-} + 4\ H^+ = 2Au(HS)^o + H_2O + 7/2\ O_2\ (g)$	-97.883
D30	HS-	$Au(s) + HS^- + H^+ + ¼\ O_2\ (g) = Au(HS)^o + ½\ H_2O$	10.418
D31	HSO_4^-	$2Au(s) + 2\ HSO_4^- + 2\ H^+ = 2Au(HS)^o + H_2O + 7/2\ O_2\ (g)$	-109.285

Table D5. Equations for Au as $Au(HS)^{\circ}$ calculated at 275°C and variable Au concentrations.

Reaction #	Au concentration	Equation (S=0.05 M)
D28	1 ppb	$fO_2 = -40.612$
	100 pbb	$fO_2 = -32.612$
	10 ppm	$fO_2 = -24.612$
D29	1 ppb	$fO_2 = 4\ pH - 69.644$
	100 pbb	$fO_2 = 4\ pH - 61.644$
	10 ppm	$fO_2 = 4\ pH - 53.644$
D30	1 ppb	$fO_2 = -^{8}/_{7}\ pH - 23.971$
	100 pbb	$fO_2 = -^{8}/_{7}\ pH - 25.113$
	10 ppm	$fO_2 = -^{8}/_{7}\ pH - 26.256$
D31	1 ppb	$fO_2 = -^{4}/_{7}\ pH - 27.228$
	100 pbb	$fO_2 = -^{4}/_{7}\ pH - 28.371$
	10 ppm	$fO_2 = -^{4}/_{7}\ pH - 29.140$

Solubility of Au as $AuCl_2^-$

The best estimate for Au solubility as $AuCl_2^-$ is taken from Svjenski et al. (1997), as recommended by Wood and Samson (1998):

$$Au + 2Cl^- + H^+ = AuCl_2^- + \tfrac{1}{2} H_2(g) \qquad (D32)$$

Balanced reactions given in Table D6.

Table D6. Equations for Au as $AuCl_2^-$ (Svjenski et al., 1997) at 275°C and variable total Cl contents.

Cl total (M)	Au concentration	Equation (S=0.05 M)
1	1 ppb	$fO_2 = 4\ pH - 47.736$
	100 pbb	$fO_2 = 4\ pH - 39.736$
	10 ppm	$fO_2 = 4pH - 31.736$
0.5	1 ppb	$fO_2 = 4\ pH - 45.330$
	100 pbb	$fO_2 = 4\ pH - 37.330$
	10 ppm	$fO_2 = 4\ pH - 29.330$

B) ALUNITE-NATROALUNITE STABILITY RELATIONSHIPS

Activity diagrams

All thermodynamic data used in this study is taken from an updated SUPCRT92 database called 'slop98' (available on the GeoPigs website) which was modified to:

a) include thermodynamic data for natroalunite from Stoffregen and Cygan (1990)
b) correct the alunite unit cell volume from a double to single unit cell. This mistake was noticed by Li et al. (1995).

Balanced reactions and calculated log K values used in K_2O/Na_2O-Al_2O_3-SiO_2-SO_3-H_2O systems are given in Table D7. In all reactions, quartz is used instead of aqueous silica (as in Hemley et al., 1969). Log K values are all generated in SUPCRT92 at specified P and T intervals.

Table D7. Balanced reactions and calculated log K values in K_2O/Na_2O-Al_2O_3-SiO_2-SO_3-H_2O systems.

Rxn #	PHASES	Balanced Reaction	Log K 200°C, 1000 bars	Log K 300°C, 1000 bars	Log K 380°C, 1000 bars
D33	Musc to alun	$KAl_2(AlSi_3)O_{10}(OH)_2 + 4H^+ + 2SO_4^{2-} = KAl_3(SO_4)_2(OH)_6 + 3SiO_2$	21.251	22.153	23.855
D34	Kao to alun	$3Al_2Si_2O_5(OH)_4 + 6H^+ + 2K^+ + 4SO_4^{2-} = 2KAl_3(SO_4)_2(OH)_6 + 6SiO_2 + 3H_2O$	37.984	40.688	44.666
D35	Pyl to alun	$3Al_2Si_4O_{10}(OH)_2 + 6H^+ + 2K^+ + 4SO_4^{2-} = 2KAl_3(SO_4)_2(OH)_6 + 12SiO_2$	39.253	40.735	43.971
D36	Musc to kao	$2KAl_2(AlSi_3)O_{10}(OH)_2 + 2H^+ + 3H_2O = 3Al_2Si_2O_5(OH)_4 + 2K^+$	4.518	3.618	3.043
D37	Musc to pyl	$2KAl_2(AlSi_3)O_{10}(OH)_2 + 2H^+ + 6SiO_2 = 3Al_2Si_4O_{10}(OH)_2 + 2K^+$	3.248	3.572	3.738
D38	Kspar to alun	$3K(AlSi_3)O_8 + 6H^+ + 2SO_4^{2-} = KAl_3(SO_4)_2(OH)_6 + 2K^+ + 9SiO_2$	29.540	29.877	31.213
D39	Kspar to musc	$3K(AlSi_3)O_8 + 2H^+ = KAl_2(AlSi_3)O_{10}(OH)_2 + 2K^+ + 6SiO_2$	8.289	7.724	7.358
D40	Par to nalun	$NaAl_2(AlSi_3)O_{10}(OH)_2 + 4H^+ 2SO_4^{2-} = NaAl_3(SO_4)_2(OH)_6 + 3SiO_2$	21.515	22.395	24.082
D41	Kao to nalun	$3Al_2Si_2O_5(OH)_4 + 6H^+ + 2Na^+ + 4SO_4^{2-} = 2NaAl_3(SO_4)_2(OH)_6 + 6SiO_2 + 3H_2O$	34.383	37.931	42.313
D42	Pyl to nalun	$3Al_2Si_4O_{10}(OH)_2 + 6H^+ + 2Na^+ + 4SO_4^{2-} = 2NaAl_3(SO_4)_2(OH)_6 + 12SiO_2$	35.652	37.978	41.619
D43	Alb to nalun	$3Na(AlSi_3)O_8 + 6H^+ + 2SO_4^{2-} = NaAl_3(SO_4)_2(OH)_6 + 2Na^+ + 9SiO_2$	31.879	31.525	32.545
D44	Alb to par	$3Na(AlSi_3)O_8 + 2H^+ = NaAl_2(AlSi_3)O_{10}(OH)_2 + 2Na^+ + 6SiO_2$	10.364	9.130	8.462
D45	Par to kao	$2NaAl_2(AlSi_3)O_{10}(OH)_2 + 2H^+ + 3H_2O = 3Al_2Si_2O_5(OH)_4 + 2Na^+$	8.647	6.858	5.852
D46	Par to pyl	$2NaAl_2(AlSi_3)O_{10}(OH)_2 + 2H^+ + 6SiO_2 = 3Al_2Si_4O_{10}(OH)_2 + 2Na^+$	7.378	6.812	6.546

Table D8. Calculated log K for reaction 5.1 at selected P and T conditions.

Pressure (bars)	Temp (°C)	Log K
500	50	-3.178
	150	-2.102
	250	-1.536
	350	-1.205
	450	-1.100
1000	50	-3.209
	150	-2.126
	250	-1.560
	350	-1.242
	450	-1.064

Solid solution models

a) Modelling of the ideal solid solution requires log K values for reaction 5.1:

$$KAl_3(SO_4)_2(OH)_6 + Na^+ = NaAl_3(SO_4)_2(OH)_6 + K^+ \qquad (5.1)$$

Calculated log K values are given in Table D8.

b) Equations for $W_{G,Na}$ and $W_{G,K}$ are generated based on the equation:

$$W_G = W_H + PW_V - TW_S \quad \text{(e.g. Essene, 1982)} \qquad (D47)$$

Assuming the effect of P is negligible, then equation D47 becomes:

$$W_G = W_H - TW_S$$

These parameters were determined by least-squares regression of the parameters given in Stoffregen and Cygan (1990; see Table 5.2).

For alunite: $W_H = 1.5028$, $W_S = -1.6420$

For natroalunite: $W_H = 1.1945$, $W_S = -1.4155$

c) Activty coefficients of alunite and natroalunite (Table D9) were calculated according to the expression (Anderson and Crerar, 1993):

$$RT \ln \gamma_1 = (2W_{G2} - W_{G1})X_2^{\ 2} + 2(W_{G1} - W_{G2})X_2^{\ 3} \qquad (5.5)$$

d) Figures 5.6 and 5.8 were determined by calculating the dominant K and Na species in the temperature and pressure range of interest (e.g. 500 bars, 150-450°C; Fig. 5.7). The species considered were K^+, KCl^o, and KOH^o - and Na equivalents.

The dominant species were determined at pH = 3 and total fluid chlorinity of about 5 to 10 weight % equivalent NaCl. These conditions were chosen to approximate the enviroment of alteration (± ore deposition) in high sulfidation environments. All thermodynamic data and equations were generated in SUPCRT92, using the modified slop98 database.

The concentration of OH- species was neglible at all temperatures and salinities of interest.

The predominance fields of KCl^o versus K^+ species (and Na equivalents) can be approximated by the equation:

$$K^+ + Cl^- = KCl^o \qquad (D48)$$

And knowing that:

$$K_{D48} = \frac{KCl_{aq}}{[K^+][Cl^-]}$$

Log K of reaction D48 is given in Table D10 (and Na-equivalents in Table D11). This reaction can be plotted for KCl = K^+ at any given concentration of Cl^-. The activity coefficient for Cl^- is estimated according to the Brønsted-Guggenheim equation (Nordstrom and Munoz, 1985) over the temperature and salinity range of interest. Calculations indicate that γCl^- ranges from about 0.45 to 0.6, and averages about 0.5. This average value is used to plot the curves in Fig. 5.7.

Table D9. Calculated activity coefficients (Y) for alunite and natroalunite at selected temperature intervals.

Temp (°C)	$X_{Kaln\text{-}aln}$	$Y_{Kaln\text{-}aln}$	$X_{Naln\text{-}aln}$	$Y_{Naln\text{-}aln}$	Temp (°C)	$X_{Kaln\text{-}aln}$	$Y_{Kaln\text{-}aln}$	$X_{Naln\text{-}aln}$	$Y_{Naln\text{-}aln}$
	1.0	1.0000	0.0	0.0000		1.0	1.0000	0.0	0.0000
	0.9	0.9110	0.1	0.4344		0.9	0.9063	0.1	0.2500
	0.8	0.8437	0.2	0.6897		0.8	0.8254	0.2	0.4362
	0.7	0.7977	0.3	0.8212		0.7	0.7570	0.3	0.5688
150	0.6	0.7716	0.4	0.8755	250	0.6	0.6992	0.4	0.6604
	0.5	0.7634	0.5	0.8878		0.5	0.6491	0.5	0.7239
	0.4	0.7684	0.6	0.8833		0.4	0.6010	0.6	0.7710
	0.3	0.7740	0.7	0.8796		0.3	0.5450	0.7	0.8124
	0.2	0.7451	0.8	0.8898		0.2	0.4612	0.8	0.8577
	0.1	0.5826	0.9	0.9254		0.1	0.3090	0.9	0.9166
	0.0	0.0000	1.0	1.0000		0.0	0.0000	1.0	1.0000
	1.0	1.0000	0.0	0.0000		1.0	1.0000	0.0	0.0000
	0.9	0.9031	0.1	0.1717		0.9	0.9008	0.1	0.1309
	0.8	0.8132	0.2	0.3195		0.8	0.8045	0.2	0.2551
	0.7	0.7305	0.3	0.4432		0.7	0.7120	0.3	0.3701
350	0.6	0.6540	0.4	0.5454	450	0.6	0.6231	0.4	0.4749
	0.5	0.5813	0.5	0.6302		0.5	0.5368	0.5	0.5701
	0.4	0.5087	0.6	0.7030		0.4	0.4508	0.6	0.6576
	0.3	0.4294	0.7	0.7697		0.3	0.3615	0.7	0.7402
	0.2	0.3330	0.8	0.8366		0.2	0.2631	0.8	0.8217
	0.1	0.2009	0.9	0.9107		0.1	0.1471	0.9	0.9065
	0.0	0.0000	1.0	1.0000		0.0	0.0000	1.0	1.0000

Table D10. log K for reaction $K^+ + Cl^- = KCl^o$ (calculated using SUPCRT92).

Pressure	Temp(°C)	log K
500 bars	50	-2.339
	100	-1.825
	150	-1.364
	200	-0.926
	250	-0.482
	300	-0.001
	350	0.590
	400	1.236
	450	2.666

Table D11. log K for reaction $Na^+ + Cl^- = NaCl^o$ (calculated using SUPCRT92).

Pressure	Temp(°C)	log K
500 bars	50	-0.745
	100	-0.533
	150	-0.294
	200	-0.024
	250	0.288
	300	0.668
	350	1.184
	400	1.737
	450	3.054

REFERENCES

Andersen, G.M. and Crerar, D.A., 1993. Thermodynamics in Geochemistry; The equilibrium model. Oxford University Press, New York.

Benning, L.G., and Seward, T.M., 1996. Hydrosulfide complexing of Au(I) in hydrothermal solutions from 150-400oC and 500-1500 bar. Geochimica et Cosmochimica Acta, 60, 1849-1872.

Craig, J.R., and Barton, P.B.Jr., 1973. Thermochemical approximations for sulfosalts. Economic Geology, 68, 493-506.

Essene, E.J., 1982. Geologic thermometry and barometry. In Characterization of metamorphism through mineral equilibria. Ferry, J.M., ed. Reviews in Mineralogy, Vol. 10.

Helgeson, H.C., Delany, J.M., Nesbitt, H.W., and Bird, D.K., 1978. Summary and critique of the thermodynamic properties of rock-formning minerals. American Journal of Science, v. 278-A, 229p.

Hemley, J.J., Hostetler, P.B., Gude, A.J., and Mountjoy, W.T., 1969. Some stability relations of alunite. Economic Geology, 64, 6, 599-612.

Johnson, J.W, Oelkers, E.H.,a nd Helgeson, H.C., 1992. SUPCRT92: A software package for calculating the standard molal thermodynamic properties of minerals, gases, aqueous species and reactions from 1 to 5000 bar and 0 to 1000°C. Computers and Geosciences, 18, 7, 899-947.

Li, G., Peacor, D.R., Essene, E.J., Brosnahan, D.R., and Beane, R.E., 1992, Walthierite and huangite; two new minerals of the alunite group from the Coquimbo region, Chile. American Mineralogist, 77, 1275-1284.

Nordstrom, D.K., and Munoz, J.L., 1994. Geochemical Thermodynamics. Boston: Blackwell Scientific Publications, 2nd Ed., 493 p.

Wood, S.A., 1998. Calculation of Activity-Activity and log fO2-pH diagrams. In: Techniques in hydrothermal ore deposits geology. Eds. Richards, J.P., and Larson, P.B. Reviews in Economic Geology v. 10, 81-96.

Wood, S.A., and Samson, I, M., 1998. Solubility of ore minerals and complexation of ore metals in hydrothermal solutions. In: Techniques in hydrothermal ore deposits geology. Eds. Richards, J.P., and Larson, P.B. Reviews in Economic Geology.10, 33-80.

Stoffregen, R.E., and Cygan, G.L., 1990. An experimental study of Na-K exchange between alunite and aqueous sulphate solutions. American Mineralogist, 75, 209-220.

Sverjensky, D.A., Shock, E.L., and Helgeson, H.C., 1997. Prediction of the thermodynamic properties of aqueous metal complexes to 1000°C and 5kb. Geochimica et Cosmochimica Acta, 61, 7, 1359-1412.

APPENDIX E: PIMA ANALYSIS AND INTERPRETATION

Short-wave infrared (SWIR) analyses were used throughout this study to identify minerals present within hydrothermal alteration assemblages. A PIMA (portable infrared mineral analyzer) instrument was used in all cases. These spectrometers detect the energy generated by vibrations within molecular bonds, in the 1300 to 2500 nm region of the electromagnetic spectrum (Thompson *et al.*, 1999). SWIR is particularly sensitive to certain molecules and radicals, including OH, H_2O, NH_4, CO_3, and cation-OH bonds such as Al-OH, Mg-OH, and Fe-OH. Minerals are distinguished on the basis of distinctive features and wavelength positions, and by the character of the SWIR profile. SWIR spectroscopy is suitable for many alteration minerals such as phylosilicates, clays, carbonates, and selected sulfates – including alunite (Thompson *et al.*, 1999).

A total of over 5000 PIMA spectra were collected from the El Indio-Pascua Belt. This includes samples analyzed in the field (during 1998 and 1999 field seasons), and additional samples from the Pascua district that were run in Vancouver as part of a larger alteration mapping project for the Tunnel Alex area.

Methods of Analysis

Samples were selected from drill core, RDH chips, surface outcrops, and underground exposures. Considerable care was taken to select representative samples, while avoiding abundant sulfide or surficial sulfates that can obscure the resulting spectra. Each sample was analyzed twice, whenever possible. Specific features (e.g., cross-cutting veins, breccia fragments, etc.) were analysed separately.

Data were processed using PIMAView 3.0 software and the SPECMIN database (Hauff, 1993). Additional reference spectra were provided by A.J.B. Thompson.

Mineral identification is reported on a scale of 1 to 4, based on confidence in the spectral interpretation (4 = strong signature, no doubt in the interpretation; 1 = tentative identification, suggestion of the mineral presence).

Pascua-Lama Alteration Study

The majority of samples analysed in this study were from the Pascua-Lama district. Samples were taken every 10-20 metres from the Alex Tunnel and selected drill core along cross-sections CA-EW, and CA-00 (Chap. 2). Several drill holes located roughly within the 4680 level were also sampled to supplement the Alex Tunnel data.

An example of PIMA data interpretation for all DDH samples are summarized in the accompanying tables. The 'Feature' column refers to the position of ca. 1480 alunite feature (in nm). Mineral abbreviations used: alunite (alun), kaolinite (kao), dickite (dick), pyrophyllite (pyl), illite (ill), jarosite (jar), silica (sil), gypsum (gyp), smectite (smect), alunogen (alung), diaspore (dsp).

DDH #	PIMA sample #	Depth (m)	Elevation (m.a.s.l.)	UTM coordinates		Mineral Identification								Comments
				Easting	Northing	alun	*feature*	kao	dick	pyl	ill	jar	other	
17	pd01701	59.1	4369.0	400246.9	6325.3	4	1481.5							
	pd01702	73.3	4369.0	400257.0	6315.3	4	1481.9							
	pd01703	108.0	4369.0	400281.7	6291.0	4	1481.9			3				
	pd01704	122.5	4369.0	400292.1	6280.8	4	1481.5			3				
	pd01705	127.2	4369.0	400295.4	6277.5	3	1481.1			2				
	pd01706	144.0	4369.0	400307.4	6265.8	4	1481.7					tr		
	pd01707	150.0	4369.0	400311.7	6261.6	3	1482.0							
	pd01708	159.0	4369.0	400318.1	6255.3	2	1481.1	?		1				
37	pd03701	0.5	4762.6	400059.2	6356.2								sil	
	pd03702	14.0	4752.3	400059.2	6356.2								sil	
	pd03703	40.0	4732.4	400059.2	6356.2			?				?	sil	
	pd03704	50.0	4724.7	400059.2	6356.2			tr				?	sil, tr gyp	
	pd03705	68.0	4710.9	400059.2	6356.2								qtz-sil	
	pd03706	83.0	4699.4	400059.2	6356.2								sil	
	pd03707	100.0	4686.4	400059.2	6356.2	4	1480.9							
	pd03708	108.5	4679.9	400059.2	6356.2	3	1481.5			3				
	pd03709a	124.0	4668.0	400059.2	6356.2	4	1482.6							breccia fragment only
	pd03709b	124.0	4668.0	400059.2	6356.2	3	1479.5					2		matrix with small fragments
	pd03709c	124.0	4668.0	400059.2	6356.2	2	1482.0							darker grey matrix
	pd03710	126.5	4666.1	400059.2	6356.2	4	1481.1							
	pd03711	138.0	4657.3	400059.2	6356.2	4	1482.0							dike
	pd03712	167.0	4635.1	400059.2	6356.2	4	1482.2		3					
41	pd04101	2.0	4764.9	399820.9	6301.8	tr		4						
	pd04102	4.0	4764.8	399820.9	6301.8	2	1480.1	4						
	pd04103	12.5	4764.3	399820.9	6301.8			?			4		smect?	
	pd04104	21.0	4763.9	399820.9	6301.8						?			
	pd04105	38.6	4763.0	399820.9	6301.8			2			2		gyp	
	pd04106	41.7	4762.8	399820.9	6301.8	1	1481.2							
	pd04107	53.0	4762.2	399820.9	6301.8								sil	
	pd04108	59.0	4761.9	399820.9	6301.8								sil	
	pd04109	80.1	4760.8	399820.9	6301.8								sil	
70	pd07001	3.0	4914.2	399796.6	6301.3							?	sil	
	pd07002	13.0	4904.8	399796.6	6301.3								sil	
	pd07003	25.0	4893.5	399796.6	6301.3								sil	
	pd07004	33.4	4885.6	399796.6	6301.3								sil	
	pd07005	41.3	4878.2	399796.6	6301.3							?	sil	

DDH #	PIMA sample #	Depth (m)	Elevation (m.a.s.l.)	UTM coordinates		Mineral Identification								Comments
				Easting	Northing	alun	*feature*	kao	dick	pyl	ill	jar	other	
	pd07007	66.0	4855.0	399796.6	6301.3								sil	
	pd07008	80.0	4841.8	399796.6	6301.3						4		gyp	
	pd07009	95.2	4827.5	399796.6	6301.3						2		sil or smect	
	pd07010	117.4	4806.7	399796.6	6301.3			?			2		smect	
	pd07011	125.0	4799.5	399796.6	6301.3			3						
	pd07012	133.0	4792.0	399796.6	6301.3			4			?		sil	
	pd07013	146.3	4779.5	399796.6	6301.3	3					?	1	sil	
	pd07014	154.2	4772.1	399796.6	6301.3	2							alunog?	
	pd07015	163.6	4763.3	399796.6	6301.3	4						2		
	pd07016	173.7	4753.8	399796.6	6301.3	2		3						
	pd07017	184.5	4743.6	399796.6	6301.3						3		sil?	
	pd07018	192.5	4736.1	399796.6	6301.3			4						
	pd07019	206.7	4722.8	399796.6	6301.3			4						
103	644301	4.0	400416.8	6756485.0	4685.3	4	1478.0					1		
	644302	24.0	400398.8	6756492.2	4689.9	4	1479.1							
104A	644303	4.0	400429.8	6756479.4	4683.8	1						2	dsp	
	644304	24.0	400446.7	6756468.8	4685.1	4	1477.2					2		
	644305	41.0	400461.1	6756459.9	4686.3	1						4		
	644306	67.0	400483.2	6756446.2	4688.0	4	1477.5					1		
	644307	88.0	400501.0	6756435.1	4689.4	3	1479.0			2				
	644308	110.0	400519.6	6756423.6	4690.9	4	1478.8							
	644309	130.0	400536.6	6756413.0	4692.2	4	1478.4					2		
116	pd11601	64.2	4630.4	400766.0	6209.2	3	1479.9	3						
	pd11602	67.5	4627.5	400766.6	6207.7	2	1480.5	1						
	pd11603	72.8	4623.0	400767.5	6205.2	4	1481.1							
	pd11604	79.2	4617.4	400768.7	6202.2	3	1481.5		2					
	pd11605	83.0	4614.1	400769.4	6200.5	1	1481.4		4					
	pd11606	87.0	4610.7	400770.1	6198.6	4	1481.3							
	pd11607	91.7	4606.6	400770.9	6196.4	4	1481.3							
	pd11608	99.2	4600.1	400772.3	6192.9	4	1481.2							
	pd11609a	103.0	4596.8	400773.0	6191.1	4	1480.5							yellow breccia matrix
	pd11609b	103.0	4596.8	400773.0	6191.1	4	1481.4							breccia fragment only
	pd11610	107.0	4593.3	400773.7	6189.3	3	1480.3							
	pd11611a	114.0	4587.3	400774.9	6186.0	2	1482.0							wallrock adjacent to vein
	pd11611b	114.0	4587.3	400774.9	6186.0	4	1481.2							vein only

DDH #	PIMA sample #	Depth (m)	Elevation (m.a.s.l.)	UTM coordinates		Mineral Identification								Comments
				Easting	Northing	alun	*feature*	kao	dick	pyl	ill	jar	other	
	pd11612a	117.6	4584.2	400775.6	6184.3	4	1481.3							breccia matrix
	pd11612b	117.6	4584.2	400775.6	6184.3	4	1482.2							fragments only
	pd11613	122.0	4580.3	400776.4	6182.3	1	1483.2		4					
	pd11614	127.0	4576.0	400777.3	6179.9	4	1482.9					?		
	pd11615	132.0	4571.7	400778.2	6177.6	4	1482.3			tr				
	pd11616	136.1	4568.1	400778.9	6175.7	2	1482.1		4					
	pd11617	142.3	4562.8	400780.0	6172.8	4	1482.5							
	pd11618	148.8	4557.1	400781.2	6169.7	4	1481.9			2				
	pd11619	153.0	4553.5	400781.9	6167.8	3	1481.8							
	pd11620	156.0	4550.9	400782.5	6166.4	3	1482.0		3					
	pd11621	163.8	4544.1	400783.9	6162.7	4	1482.2			tr				
	pd11622	168.0	4540.5	400784.6	6160.8	4	1482.1		3					
	pd11623	173.0	4536.2	400785.5	6158.4	2	1481.5			3				
	pd11624	178.4	4531.5	400786.5	6155.9	4	1481.2			1		3		
	pd11625	183.5	4527.1	400787.4	6153.5	4	1481.6							
	pd11626	188.4	4522.8	400788.3	6151.3	3	1481.6		2	3				
	pd11627	191.8	4519.9	400788.9	6149.7	4	1481.3			2				
	pd11628	196.0	4516.3	400789.6	6147.7	3	1481.6			1		1		
	pd11629	203.0	4510.2	400790.9	6144.4	4	1481.9			3			dsp?	
	pd11630	207.8	4506.0	400791.7	6142.2	4	1482.4					1		
	pd11631	211.9	4502.5	400792.5	6140.3	1		1			?		smect?	
	pd11632	217.0	4498.1	400793.4	6137.9	4	1480.5			3				
	pd11633	223.4	4492.5	400794.5	6134.9	3	1480.2			4		1	dsp?	
	pd11634	229.0	4487.7	400795.5	6132.3	4	1481.0			tr		1		
	pd11635	233.0	4484.2	400796.2	6130.4	3	1480.7		2			1		
	pd11636	237.9	4480.0	400797.1	6128.2	2	1482.1		3					
	pd11637	242.0	4476.4	400797.9	6126.2	4	1482.2			3			tr dsp?	
	pd11638	246.5	4472.5	400798.7	6124.1	4	1482.1			4				
	pd11639	253.0	4466.9	400799.8	6121.1	4	1482.4			4				
	pd11640	257.5	4463.0	400800.6	6119.0	2	1480.1			4		2		
	pd11641	263.4	4457.9	400801.7	6116.2	4	1482.3			2		tr	tr dsp?	
	pd11642	267.2	4454.6	400802.4	6114.5	4	1481.8							
	pd11643	272.8	4449.7	400803.4	6111.9	4	1482.0			1			tr dsp?	
	pd11644	278.7	4444.6	400804.4	6109.1	3	1482.0			4			tr dsp?	
	pd11645	283.2	4440.7	400805.2	6107.0	3	1481.7			3		1		

DDH #	PIMA sample #	Depth (m)	Elevation (m.a.s.l.)	UTM coordinates		Mineral Identification								Comments
				Easting	Northing	alun	*feature*	kao	dick	pyl	ill	jar	other	
	pd11646	289.5	4435.3	400806.4	6104.1	4	1482.7			2				
	pd11647	292.5	4432.7	400806.9	6102.7	3	1483.3			4				
	pd11648	298.5	4427.5	400808.0	6099.9	3	1483.9	1						
	pd11649	303.1	4423.5	400808.8	6097.7	4	1483.9			1				
	pd11650	307.5	4419.7	400809.6	6095.7	3	1481.7			?		2	tr dsp?	
	pd11651	314.5	4413.6	400810.9	6092.4	4	1482.5							
	pd11652	318.6	4410.1	400811.6	6090.5	4	1484.3		3					
	pd11653	323.9	4405.5	400812.5	6088.0	2	1483.5		tr					
	pd11654	327.9	4402.0	400813.3	6086.1	2	1484.4		3					
119	pd11901	2.0	5033.4	400874.0	6380.8								sil	
	pd11902	7.5	5029.1	400875.5	6382.9								sil	
	pd11903	14.0	5024.0	400877.3	6385.4								sil	
	pd11904	18.1	5020.7	400878.4	6387.0								sil	
	pd11905	22.2	5017.5	400879.5	6388.5								sil	
	pd11906	29.0	5012.1	400881.3	6391.2	3	1482.4						tr sil	
	pd11907	34.0	5008.2	400882.7	6393.1	4	1482.0							
	pd11908	37.8	5005.2	400883.7	6394.5	4	1483.3							
	pd11909	43.3	5000.9	400885.2	6396.7	4	1483.4							
	pd11910	47.7	4997.4	400886.3	6398.3	2	1483.3						tr sil	
	pd11911	52.1	4993.9	400887.5	6400.0	2	1483.0						sil	
	pd11912	57.6	4989.6	400889.0	6402.2	3	1482.8						sil	
	pd11913	63.0	4985.4	400890.5	6404.2	2	1483.1					tr	tr sil	
	pd11914	68.2	4981.3	400891.9	6406.2	2	1483.4							
	pd11915	72.0	4978.3	400892.9	6407.7	2	1479.4					3	tr sil	
	pd11916a	77.0	4974.3	400894.2	6409.6			4				2	sil	wallrock
	pd11916b	77.0	4974.3	400894.2	6409.6	4	1482.2							vein only
	pd11917	83.2	4969.4	400895.9	6412.0			4						
	pd11918	87.6	4966.0	400897.1	6413.7			3						
	pd11920	97.4	4958.2	400899.7	6417.5			3						
	pd11921	102.3	4954.4	400901.0	6419.3			4						
	pd11922a	109.0	4949.1	400902.9	6421.9	3	1482.1							mostly breccia matrix
	pd11922b	109.0	4949.1	400902.9	6421.9	tr								mostly breccia fragments
	pd11923	112.8	4946.1	400903.9	6423.4	4	1481.0							
	pd11924	117.2	4942.6	400905.1	6425.1	3	1480.6							
	pd11925	123.0	4938.1	400906.6	6427.3	2	1481.1	3						

DDH #	PIMA sample #	Depth (m)	Elevation (m.a.s.l.)	UTM coordinates		Mineral Identification								Comments
				Easting	Northing	alun	*feature*	kao	dick	pyl	ill	jar	other	
	pd11926	127.1	4934.8	400907.7	6428.9	tr		4						
	pd11927	134.0	4929.4	400909.6	6431.5	3	1481.9	3						
	pd11928	137.2	4926.9	400910.4	6432.8	tr		4						
	pd11929	142.7	4922.6	400911.9	6434.9	1	1479.3	4						
	pd11930	148.7	4917.8	400913.5	6437.2	?		3				1		
	pd11931	153.0	4914.4	400914.7	6438.8	1	1480.1	3						
	pd11932	157.5	4910.9	400915.9	6440.6	4	1481.1	1						
	pd11933	163.5	4906.2	400917.5	6442.9	1	1481.1	1					sil?	
	pd11934	167.3	4903.2	400918.6	6444.3	1	1482.3		3					
	pd11935	172.5	4899.1	400920.0	6446.3	tr							qtz?	
	pd11936	177.4	4895.2	400921.3	6448.2	4	1480.4							
	pd11937	182.2	4891.4	400922.6	6450.1	4	1480.3							
	pd11938	187.0	4887.6	400923.9	6451.9	3	1479.9						sil	
	pd11939	192.3	4883.5	400925.3	6454.0			4						
	pd11940	198.0	4879.0	400926.8	6456.1						4			
	pd11941	202.2	4875.7	400927.9	6457.8	1	1480.5	4						
	pd11942	206.8	4872.0	400929.2	6459.5			3			tr			
	pd11943	213.0	4867.2	400930.9	6461.9						1		sil	
	pd11944	219.2	4862.3	400932.5	6464.3						1		sil	
	pd11945	222.5	4859.7	400933.4	6465.6			4			1		sil?	
	pd11946	227.1	4856.0	400934.7	6467.3						4	tr		
	pd11947	233.5	4851.0	400936.4	6469.8	1	1478.8	3			?			
	pd11948	237.2	4848.1	400937.4	6471.2	1	1479.6	1			2		tr sil	
	pd11949	243.4	4843.2	400939.0	6473.6	tr		2			2			
	pd11950	248.2	4839.4	400940.3	6475.4						1		sil	
	pd11951	254.0	4834.8	400941.9	6477.7	1	1481.9	tr	4					
	pd11952	257.7	4831.9	400942.9	6479.1	1	1479.8						sil?	
	pd11953	261.3	4829.1	400943.9	6480.5	3	1479.9	4						
	pd11954	267.0	4824.6	400945.4	6482.7	2	1480.6	3			1			
	pd11955	271.0	4821.4	400946.5	6484.2			4						
	pd11956	276.4	4817.2	400947.9	6486.3	2	1476.0	4			?	tr		
	pd11957	284.5	4810.8	400950.1	6489.4	1	1480.5	?			1		sil	
	pd11958	288.2	4807.9	400951.1	6490.8	?		1			1		gyp	
	pd11959	293.6	4803.6	400952.6	6492.9						4		smect?	
	pd11960	296.5	4801.4	400953.3	6494.0	?		4			?	?	sil?	

DDH #	PIMA sample #	Depth (m)	Elevation (m.a.s.l.)	UTM coordinates		Mineral Identification								Comments
				Easting	Northing	alun	*feature*	kao	dick	pyl	ill	jar	other	
	pd11961	303.2	4796.1	400955.1	6496.6			4				tr	?	
	pd11962	307.3	4792.8	400956.2	6498.2			3				tr	?	
	pd11963	313.6	4787.9	400957.9	6500.6			2			3		smect?	
	pd11964	316.7	4785.4	400958.8	6501.8	1	1479.2	4						
	pd11965	323.8	4779.8	400960.7	6504.5	3	1480.4		4					
	pd11966	327.6	4776.8	400961.7	6506.0	1	1481.3	3						
	pd11967	334.1	4771.7	400963.5	6508.5	2	1481.3		3					
	pd11968	336.8	4769.6	400964.2	6509.5	4	1481.1		4					
	pd11969	343.3	4764.5	400965.9	6512.0						4		smect?	
	pd11970	348.2	4760.6	400967.3	6513.9			?			4		gyp	
	pd11971	353.9	4756.1	400968.8	6516.1	1	1481.7	2	2					
	pd11972	358.5	4752.5	400970.0	6517.9	tr			4					
	pd11973	361.0	4750.5	400970.7	6518.8	tr		4						
	pd11974	367.8	4745.2	400972.5	6521.4						4		smect?	
	pd11975	371.8	4742.0	400973.6	6523.0	2	1481.3	3						
	pd11976	379.0	4736.3	400975.6	6525.8	tr		4				tr		
	pd11977	383.8	4732.6	400976.8	6527.6	3	1481.8	4	?					
	pd11978	388.0	4729.3	400978.0	6529.2						1	2	sil	
	pd11979	392.3	4725.9	400979.1	6530.9	2	1481.3	4						
	pd11978	398.5	4721.0	400980.8	6533.3	3	1481.5		3					
126	pd12601	3.2	4682.9	400832.3	6398.6	4								
	pd12602	14.7	4671.8	400829.6	6397.3	2			3					
	pd12603	26.2	4660.7	400827.0	6395.9	?								too much sulfide, noisy pattern
	pd12604	36.2	4651.0	400824.7	6394.7	1				3			alunog	
	pd12605	47.1	4640.5	400822.1	6393.5	3								
	pd12606	55.1	4632.8	400820.3	6392.5								alunog	
	pd12607	67.6	4620.7	400817.4	6391.1								alunog	
	pd12608	74.5	4614.0	400815.8	6390.2	3				4			dsp	
	pd12609	86.4	4602.5	400813.1	6388.8	2							dsp?	
	pd12610	95.8	4593.5	400810.9	6387.7									noisy pattern
	pd12611	103.9	4585.6	400809.0	6386.8	3				3				
	pd12612	117.0	4573.0	400806.0	6385.3	3				2			dsp?	
	pd12613	123.0	4567.2	400804.6	6384.5	tr							alunog	banded vein only
	pd12614	134.0	4556.6	400802.1	6383.3								alunog	noisy pattern
	pd12615	143.6	4547.3	400799.9	6382.1	4								

DDH #	PIMA sample #	Depth (m)	Elevation (m.a.s.l.)	UTM coordinates		Mineral Identification								Comments
				Easting	Northing	alun	*feature*	kao	dick	pyl	ill	jar	other	
127	pd12701	46.2	4639.9	400625.5	6386.1	4						tr		
	pd12702	55.3	4631.4	400624.0	6383.2	4								
	pd12703	67.2	4620.3	400622.0	6379.4	4							alunog?	
	pd12704a	76.0	4612.0	400620.5	6376.7	4								breccia matrix
	pd12704b	76.0	4612.0	400620.5	6376.7	3							sil	mostly breccia fragments
	pd12705	83.9	4604.7	400619.2	6374.2	4								
	pd12706	94.1	4595.2	400617.5	6370.9	4								
	pd12707a	105.8	4584.2	400615.5	6367.2	4								only breccia fragment
	pd12707b	105.8	4584.2	400615.5	6367.2	4						tr		only breccia matrix
	pd12708	114.9	4575.7	400614.0	6364.3	4								
	pd12709	123.9	4567.3	400612.5	6361.5	4								
	pd12710	135.8	4556.2	400610.5	6357.7	4				4				
	pd12711	147.6	4545.2	400608.5	6354.0	4						2		
	pd12712	154.5	4538.8	400607.3	6351.8	3				2			alunog?	or dsp?
	pd12713	164.3	4529.6	400605.7	6348.7	4								
	pd12714	178.0	4516.8	400603.4	6344.4	4				?				
	pd12715	184.9	4510.4	400602.2	6342.2	4				3		2		
	pd12716	194.7	4501.2	400600.5	6339.1	4						1		
	pd12717	205.3	4491.3	400598.8	6335.7	3				4				
	pd12718	216.1	4481.3	400596.9	6332.3	4				4				
	pd12719	225.0	4472.9	400595.4	6329.5	4				4		1		
	pd12720	232.5	4465.9	400594.2	6327.1	4				4		1		
	pd12721	243.0	4456.1	400592.4	6323.8	4						3		
132	pd13201a	89.0	4599.1	400791.9	6272.9	4	1480.7							banded aln-sulfide vein only
	pd13201b	89.0	4599.1	400791.9	6272.9	1	1482.6						sil	wallrock
	pd13202	91.9	4596.2	400792.3	6272.7	4	1481.7						sil?	
	pd13203	98.5	4589.7	400793.1	6272.0	4	1481.6							
	pd13204	102.0	4586.3	400793.5	6271.7	3	1481.9							
	pd13205	108.0	4580.3	400794.2	6271.1	4	1482.1					tr		
	pd13206a	114.2	4574.2	400795.0	6270.5	4	1481.9							mostly breccia matrix
	pd13206b	114.2	4574.2	400795.0	6270.5	4	1481.7							only pink breccia fragment
	pd13207	117.5	4570.9	400795.4	6270.1	4	1483.0							
	pd13208a	121.0	4567.5	400795.8	6269.8	3	1483.0							mostly breccia matrix
	pd13208b	121.0	4567.5	400795.8	6269.8	4	1482.7							only breccia clasts
	pd13209a	127.3	4561.3	400796.6	6269.2	tr							dsp?	mostly breccia matrix

DDH #	PIMA sample #	Depth (m)	Elevation (m.a.s.l.)	UTM coordinates		Mineral Identification								Comments
				Easting	Northing	alun	*feature*	kao	dick	pyl	ill	jar	other	
	pd13209b	127.3	4561.3	400796.6	6269.2								sil + dsp?	only breccia clasts
	pd13210	132.8	4555.8	400797.2	6268.6	4	1482.9							
	pd13211a	138.4	4550.3	400797.9	6268.1	1	1482.2						sil?	wallrock adj to vein
	pd13211b	138.4	4550.3	400797.9	6268.1	3	1480.5							vein only
	pd13212a	142.7	4546.1	400798.4	6267.7	3	1482.8							wallrock adj to vein
	pd13212b	142.7	4546.1	400798.4	6267.7	4	1482.7							vein only
	pd13214	152.2	4536.7	400799.6	6266.7	3	1480.5					3		
	pd13215	157.0	4531.9	400800.2	6266.2	4	1484.6							
	pd13216	164.3	4524.7	400801.1	6265.5	4	1485.9							
	pd13217	167.5	4521.6	400801.5	6265.2	3	1484.2					tr		
	pd13218	171.5	4517.6	400801.9	6264.8	3	1482.9			4				
	pd13219	177.6	4511.6	400802.7	6264.2	4	1483.9			1				
	pd13220	181.0	4508.2	400803.1	6263.9	4	1484.4			1				
	pd13221	187.0	4502.3	400803.8	6263.3	4	1484.3			3				
	pd13222	192.5	4496.9	400804.5	6262.7	4	1483.7			1				
	pd13223	197.0	4492.4	400805.0	6262.3	1	1481.2					2		
	pd13224	203.1	4486.4	400805.8	6261.7	4	1483.8							
	pd13225	207.0	4482.5	400806.3	6261.3	2	1481.4			4		2		
	pd13226	211.7	4477.9	400806.8	6260.9	4	1482.0			1		4		
	pd13227	217.4	4472.3	400807.5	6260.3	4	1482.7	?						
	pd13228	224.0	4465.8	400808.3	6259.6	3	1483.5					2		
	pd13229	227.0	4462.8	400808.7	6259.4	3	1483.1			1		tr	sil?	
	pd13230	231.5	4458.4	400809.2	6258.9	2	1482.7	?	2			2		
135	pd13502	11.0	4674.0	400715.4	6365.4								sil+alunog?	
	pd13503	20.0	4665.1	400715.8	6366.1	3							alunog?	
	pd13504	37.7	4647.4	400716.5	6367.4	2							alunog?	
	pd13505	47.0	4638.2	400716.9	6368.1								sil	
	pd13506	56.3	4628.9	400717.2	6368.9								sil	
	pd13507	68.0	4617.3	400717.7	6369.8	4							alunog?	
	pd13509	84.4	4600.9	400718.3	6371.1	4								
	pd13510a	117.7	4567.7	400719.7	6373.6	4						2		
	pd13510b	117.7	4567.7	400719.7	6373.6	4						1		
	pd13513	157.4	4528.2	400721.2	6376.7	4				1		2		
	pd13515	174.5	4511.2	400721.9	6378.1	4						3		
	pd13516	184.0	4501.7	400722.3	6378.8	4						3		

DDH #	PIMA sample #	Depth (m)	Elevation (m.a.s.l.)	UTM coordinates		Mineral Identification								Comments
				Easting	Northing	alun	*feature*	kao	dick	pyl	ill	jar	other	
	pd13517a	192.0	4493.7	400722.6	6379.4	4				?				
	pd13517b	192.0	4493.7	400722.6	6379.4	4						tr		
	pd13518	204.6	4481.2	400723.1	6380.4	1						3	sil?	
	pd13519a	210.8	4475.0	400723.3	6380.9	4						2		
	pd13519b	210.8	4475.0	400723.3	6380.9	4						4		
	pd13520	222.8	4463.0	400723.8	6381.8	4						tr		
	pd13521	229.0	4456.9	400724.1	6382.3	4				3				
	pd13522	236.2	4449.7	400724.3	6382.8	3				4				
137	pd13701	2.9	4685.3	400780.1	6052.3	3	1482			2				
	pd13702	7.6	4680.9	400778.5	6052.8	4	1482.3					1		
	pd13203	14.1	4674.8	400776.4	6053.6	4	1483.7							
	pd13704	17.9	4671.2	400775.2	6054.0	4	1482.9							
	pd13705	23.1	4666.3	400773.5	6054.6	4	1483.7							
	pd13706a	27.2	4662.4	400772.2	6055.0	4	1482.6							
	pd13706b	32.9	4657.1	400770.4	6055.7								sil	only breccia matrix
	pd13706c	32.9	4657.1	400770.4	6055.7								sil	breccia clast only
	pd13707a	38	4652.3	400768.7	6056.2								sil, qtz	only breccia matrix
	pd13707b	38	4652.3	400768.7	6056.2	tr							sil	breccia clast only
	pd13708a	41.3	4649.2	400767.6	6056.6	4	1483.7							only breccia matrix
	pd13708b	41.3	4649.2	400767.6	6056.6	4	1483.9							breccia clast only
	pd13709a	45.7	4645.1	400766.2	6057.1	4	1484							mostly breccia matrix (yellow)
	pd13709b	45.7	4645.1	400766.2	6057.1	4	1483.8							mostly pink breccia matrix
	pd13709c	45.7	4645.1	400766.2	6057.1	4	1484							breccia clast only
	pd13710a	51.7	4639.4	400764.3	6057.8	4	1483.7							breccia clast only
	pd13710b	51.7	4639.4	400764.3	6057.8	4	1483.4							only breccia matrix
	pd13711a	56.1	4635.3	400762.9	6058.2	4	1481.8							only breccia matrix
	pd13711b	56.1	4635.3	400762.9	6058.2	4	1483.7							breccia clast only
	pd13712	64.2	4627.7	400760.2	6059.1	4	1481.8							
	pd13713a	68	4624.1	400759.0	6059.6	4	1481.1							breccia clast only
	pd13713b	68	4624.1	400759.0	6059.6	4	1481.5							only breccia matrix
	pd13714a	72.3	4620.1	400757.6	6060.1	4	1481.7							breccia clast only
	pd13714b	72.3	4620.1	400757.6	6060.1	4	1481.3							only breccia matrix
	pd13715	79	4613.8	400755.5	6060.8	2	1480.8							
	pd13716	84.6	4608.5	400753.6	6061.4	4	1481.6							
	pd13717	87.1	4606.2	400752.8	6061.7	4	1481.4							

DDH #	PIMA sample #	Depth (m)	Elevation (m.a.s.l.)	UTM coordinates		Mineral Identification								Comments
				Easting	Northing	alun	*feature*	kao	dick	pyl	ill	jar	other	
	pd13718a	93.8	4599.9	400750.7	6062.4	4	1481.4		4					breccia clast
	pd13718b	93.8	4599.9	400750.7	6062.4	4	1483.1							only breccia matrix
	pd13719	97.7	4596.2	400749.4	6062.9	3	1482.2		4					
	pd13720	103	4591.2	400747.7	6063.5	2	1481.8	2	3					
	pd13721a	106.5	4587.9	400746.6	6063.9	3	1481.5		2					breccia clast
	pd13721b	106.5	4587.9	400746.6	6063.9	4	1482.7	?	1					breccia matrix
	pd13722a	113.9	4581.0	400744.2	6064.7	3	1483		2					breccia clast
	pd13722b	113.9	4581.0	400744.2	6064.7	4	1483.6							breccia matrix
	pd13723	117.2	4577.9	400743.1	6065.1	3	1482.3		?					
	pd13724	122.6	4572.8	400741.4	6065.7	1	1481.5		3		?			
	pd13725	127.3	4568.4	400739.8	6066.2	4	1482.1							
	pd13726a	133.6	4562.5	400737.8	6066.9	4	1483.1							
	pd13726b	133.6	4562.5	400737.8	6066.9	4	1482.7							
	pd13727a	138.8	4557.6	400736.1	6067.5	4	1481.7					2		
	pd13727b	138.8	4557.6	400736.1	6067.5	4	1481.9					2		
	pd13728	143.8	4552.9	400734.5	6068.0	4	1482							
	pd13729	147	4549.9	400733.5	6068.4	4	1481.5					1		
	pd13730	151.8	4545.4	400731.9	6068.9	4	1483			3				
	pd13731	158.3	4539.2	400729.8	6069.6	4	1483.8							
	pd13732	162.5	4535.3	400728.4	6070.1	4	1482.6			3				
	pd13733	168.2	4529.9	400726.6	6070.7	4	1482.1			4				
	pd13734	173.6	4524.9	400724.9	6071.3	4	1482.5							
	pd13735	176.5	4522.1	400723.9	6071.7	4	1480.5		2		1	1		
	pd13736	183.9	4515.2	400721.5	6072.5	4	1481.6							
	pd13737	186.5	4512.7	400720.7	6072.8	4	1480.3							
	pd13738	192.5	4507.1	400718.7	6073.4	3	1480.8	?		2		2		
	pd13739	197	4502.9	400717.3	6073.9	4	1482.3			1				
	pd13740	204	4496.3	400715.0	6074.7	3	1480.9			1		2		
	pd13741	209.1	4491.5	400713.4	6075.3	3	1481.5			4		1		
154	pd15401	1.2	4689.2	401136.1	6375.9			4						
	pd15402	2.2	4688.6	401136.9	6376.0			4						
	pd15403	13	4681.6	401145.0	6377.4						1		sil, smect	
	pd15404	16	4679.7	401147.3	6377.8			4						
	pd15405	22.8	4675.3	401152.4	6378.7			2			1			
	pd15406	27.2	4672.5	401155.7	6379.3			2			?		sil	

DDH #	PIMA sample #	Depth (m)	Elevation (m.a.s.l.)	UTM coordinates		Mineral Identification								Comments
				Easting	Northing	alun	*feature*	kao	dick	pyl	ill	jar	other	
	pd15407	31.4	4669.8	401158.9	6379.9			3						
	pd15408	36	4666.9	401162.4	6380.5						3		smect?	
	pd15409	41.5	4663.3	401166.5	6381.2			?			2		sil	
	pd15410	45.1	4661.0	401169.2	6381.7	2		4						
	pd15411	52	4656.6	401174.4	6382.6			3						
	pd15412	56	4654.0	401177.4	6383.1	4								
	pd15413	62	4650.1	401182.0	6383.9	3								
	pd15414	64.3	4648.7	401183.7	6384.3								smect	
	pd15415	71	4644.4	401188.8	6385.1	4								
	pd15416	79	4639.2	401194.8	6386.2	4			2					
	pd15417	83.8	4636.1	401198.4	6386.8	2							sil or smect?	
	pd15418	88.3	4633.2	401201.8	6387.4	3							alunog?	
	pd15419	92.8	4630.3	401205.2	6388.0								sil	
	pd15420	97.3	4627.5	401208.6	6388.6	3			3					
	pd15421	102	4624.4	401212.1	6389.3	?							sil	
	pd15422	107.3	4621.0	401216.1	6390.0	1							sil	
	pd15423a	112.5	4617.7	401220.1	6390.7	4								breccia clast
	pd15423b	112.5	4617.7	401220.1	6390.7	4								breccia matrix
	pd15425a	121.3	4612.0	401226.7	6391.8	1								breccia clast
	pd15425b	121.3	4612.0	401226.7	6391.8	4								breccia matrix
	pd15426a	125.5	4609.3	401229.9	6392.4	4								breccia clast
	pd15426b	125.5	4609.3	401229.9	6392.4	2								mostly matrix
	pd15427	130.4	4606.2	401233.6	6393.0	4								both matrix and clasts
	pd15428a	135.1	4603.2	401237.1	6393.7	2								breccia clast
	pd15428b	135.1	4603.2	401237.1	6393.7	2							dsp?	mostly matrix
	pd15429a	141	4599.4	401241.6	6394.5	2								breccia clast
	pd15429b	141	4599.4	401241.6	6394.5	3								both matrix and clasts
	pd15430	146.5	4595.8	401245.7	6395.2	4								
	pd15431	151.3	4592.7	401249.3	6395.8	4								
	pd15432	156.6	4589.3	401253.3	6396.5	2								
	pd15433a	160.9	4586.6	401256.6	6397.1	?							sil + aluno	mostly breccia clasts
	pd15433b	160.9	4586.6	401256.6	6397.1	4								mostly matrix
	pd15434a	167.8	4582.1	401261.8	6398.0	3								breccia clast
	pd15434b	167.8	4582.1	401261.8	6398.0	4							alunog	breccia matrix
	pd15435	172	4579.4	401265.0	6398.6	4								

DDH #	PIMA sample #	Depth (m)	Elevation (m.a.s.l.)	UTM coordinates		Mineral Identification								Comments
				Easting	Northing	alun	*feature*	kao	dick	pyl	ill	jar	other	
	pd15436	178	4575.6	401269.5	6399.4	4				1				
	pd15437	181.9	4573.1	401272.4	6399.9	4								
	pd15438	185.9	4570.5	401275.4	6400.4	4			3					
	pd15439	191.5	4566.9	401279.7	6401.2	4						tr		
	pd15440	197.6	4563.0	401284.3	6402.0	4				tr				
	pd15441	203.2	4559.4	401288.5	6402.7	4				2				
	pd15442	207.5	4556.6	401291.7	6403.3	3			2	3				
	pd15443	214	4552.4	401296.6	6404.2	4				4				
	pd15444	219	4549.2	401300.4	6404.8	4				3				
	pd15446	229	4542.8	401308.0	6406.2	4				3				
	pd15447	233	4540.2	401311.0	6406.7	4				4				
	pd15448	235.8	4538.4	401313.1	6407.1	4				4				
	pd15449	241.8	4534.6	401317.6	6407.9	4				4				
	pd15450	247.7	4530.8	401322.1	6408.6	4				?				
	pd15451	253	4527.4	401326.1	6409.4	4				5				
	pd15452	258	4524.2	401329.8	6410.0	4								
	pd15453	263.3	4520.8	401333.8	6410.7	4				?				
	pd15454	268.8	4517.2	401338.0	6411.5	4				4				
	pd15455	270.5	4516.1	401339.3	6411.7	4				3				
	pd15456	279.7	4510.2	401346.2	6412.9	4				?				
	pd15457	282	4508.7	401347.9	6413.2	3				4				
	pd15458	289.6	4503.8	401353.7	6414.2	4				4				
	pd15460	299.3	4497.6	401361.0	6415.5	4								
	pd15461	300.5	4496.8	401361.9	6415.7	4				3				
	pd15462	306	4493.3	401366.0	6416.4	4				2				
	pd15463a	310.5	4490.4	401369.4	6417.0	4								wallrock
	pd15463b	310.5	4490.4	401369.4	6417.0	4						?		thin yellow vein
	pd15463c	310.5	4490.4	401369.4	6417.0	4								thicker crystalline vein
	pd15464	310.7	4490.3	401369.6	6417.0	4								
	pd15465	316.6	4486.5	401374.0	6417.8			4						
161	pd16101	1	4692.5	401134.2	6376.0	1		2?						
	pd16102	11.3	4697.8	401126.5	6380.4			3					sil	
	pd16103	23.8	4704.3	401117.2	6385.8			?			2			
	pd16104	32.5	4708.7	401110.8	6389.5						4			
	pd16105	41.3	4713.3	401104.2	6393.3						2		tr gyp	

DDH #	PIMA sample #	Depth (m)	Elevation (m.a.s.l.)	UTM coordinates		Mineral Identification								Comments
				Easting	Northing	alun	*feature*	kao	dick	pyl	ill	jar	other	
	pd16107	61.5	4723.7	401089.2	6402.0						1		sil	
	pd16108	71.6	4728.9	401081.7	6406.3			?			2		sil	
	pd16109	84.9	4735.7	401071.9	6412.0			2?						noisy pattern
	pd16110a	90	4738.4	401068.1	6414.2						4	1		wallrock
	pd16110b	90	4738.4	401068.1	6414.2						?	tr	gyp	white vein
	pd16111	101.6	4744.3	401059.5	6419.1	tr		2						
	pd16112	112.9	4750.1	401051.1	6424.0								sil	
	pd16113	123	4755.3	401043.6	6428.3								sil	
	pd16114	132.6	4760.3	401036.5	6432.4			?					sil	
	pd16115	142.2	4765.2	401029.3	6436.5								sil	
	pd16116	152.3	4770.4	401021.8	6440.9			1					sil	
	pd16117	162.9	4775.9	401014.0	6445.4								sil	
	pd16118	174.8	4782.0	401005.1	6450.5			tr					sil	
	pd16119	182.4	4785.9	400999.5	6453.8								sil	
	pd16120	194.5	4792.2	400990.5	6459.0			?					sil	
	pd16121	202.6	4796.3	400984.5	6462.4			1					sil + alunog	
	pd16122	214.3	4802.4	400975.8	6467.4								sil + ?	
	pd16123	221	4805.8	400970.8	6470.3			3					sil	
	pd16124	244.8	4818.1	400953.2	6480.5								sil?	too noisy
	pd16125	251.6	4821.6	400948.1	6483.4									too noisy
	pd16127	276.5	4834.4	400929.6	6494.1			2					sil	
	pd16128	283	4837.8	400924.8	6496.9			1					sil?	
	pd16129	296.8	4844.9	400914.6	6502.8			?			?		sil	
168	644310	5	400705.8	6756359.3	4686.3								sil	
	644311	25	400688.7	6756349.4	4683.6	4	1480.2							
	644312	50	400667.4	6756336.7	4680.2								sil	
	644313	70	400650.4	6756326.4	4677.5	2	1479.9							noisy spectrum
	644314	89	400634.1	6756317.0	4674.9	3	1479.5		4					
	644315	101	400623.8	6756311.1	4673.3	2	1478.7		2				dsp	
	644316	122	400605.8	6756300.7	4670.4	4	1479.4							
	644317	142	400588.7	6756290.8	4667.7	3	1479.8		4					
	644318	164	400569.6	6756280.2	4664.7	3	1479.4							
	644319	186	400550.3	6756270.2	4661.5	4	1479.1							
	644320	200	400538.1	6756263.6	4659.5	2	1479.8		4				tr dsp	
	644321	220	400520.6	6756254.3	4656.6	3	1480.5		1				dsp?	

DDH #	PIMA sample #	Depth (m)	Elevation (m.a.s.l.)	UTM coordinates		Mineral Identification								Comments
				Easting	Northing	alun	*feature*	kao	dick	pyl	ill	jar	other	
	644322	240	400502.8	6756245.6	4653.8	4	1479.6							
	644323	260	400484.8	6756237.5	4651.0	4	1480.1							
	644324	283	400463.8	6756228.6	4647.8	3	1480.8		2					minor noise
	644325	302	400446.0	6756222.5	4645.0	4	1481.2							
	644326	320	400429.2	6756216.7	4642.5	4	1480.1							
172	pd17201	252	4523.0	401427.3	6476.8	4				3				
	pd17202	260.5	4517.6	401433.8	6477.4	4								
	pd17203	271.2	4510.7	401442.0	6478.1	4								
	pd17204	279	4505.7	401447.9	6478.6	4				4				
	pd17205	290.2	4498.5	401456.5	6479.4	4				3				
	pd17206a	302.5	4490.6	401465.8	6480.2	3						1		breccia clast
	pd17206b	302.5	4490.6	401465.8	6480.2	?		?					sil	mostly breccia matrix
	pd17207a	304.2	4489.5	401467.1	6480.3			3					sil	breccia clast
	pd17207b	304.2	4489.5	401467.1	6480.3	?		2?	?				sil	mostly breccia matrix
	pd17208	312.7	4484.0	401473.6	6480.9	4				4				
	pd17209	321	4478.7	401480.0	6481.4	4				3				
	pd17210	329.7	4473.1	401486.6	6482.0	4			1	4				
	pd17211	342	4465.2	401496.0	6482.8	4								
	pd17212	351.5	4459.1	401503.2	6483.5	4				4				
	pd17213	364.5	4450.7	401513.2	6484.3	4								
	pd17214	372.2	4445.8	401519.0	6484.8	4				4				
	pd17215	387	4436.2	401530.3	6485.8	4				4				
	pd17216	395	4431.1	401536.4	6486.4	3				4				
	pd17217	402.9	4426.0	401542.5	6486.9	4								
	pd17218	414.1	4418.8	401551.0	6487.6	4				3				
	pd17219	422.5	4413.4	401557.4	6488.2	4				4				
	pd17220a	435.1	4405.3	401567.0	6489.0	2				4				wallrock
	pd17220b	435.1	4405.3	401567.0	6489.0	4						1		vein only
	pd1721a	436	4404.7	401567.7	6489.1	4				4				wallrock
	pd17221a	436	4404.7	401567.7	6489.1	4						3		vein only
	pd17222	449	4396.4	401577.6	6490.0	4								
174	644327	8	400954.3	6756223.4	4691.2	1			1					noisy spectrum
	644328	28	400973.3	6756218.1	4694.6	2	1478.1							
	644329	48	400992.2	6756212.5	4697.7	3	1477.9	2						
	644330	68	401011.0	6756206.5	4700.7	2	1478.2							noisy patterns

DDH #	PIMA sample #	Depth (m)	Elevation (m.a.s.l.)	UTM coordinates		Mineral Identification								Comments
				Easting	Northing	alun	*feature*	kao	dick	pyl	ill	jar	other	
	644331	88	401029.7	6756200.2	4703.9	1								noisy spectrum
	644332	108	401048.3	6756193.5	4706.9	3	1479.5		1					minor noise
	644333	130	401068.8	6756186.1	4710.4			tr					sil	
	644334	150	401087.1	6756178.8	4713.6								sil	
	644335	170	401105.4	6756171.3	4716.7								sil	noisy spectrum
	644336	190	401123.5	6756163.5	4719.8								sil	feature at 2100 nm
	644337	210	401141.4	6756155.1	4723.0								sil	+/- argillics, feature at 2100 nm
	644338	230	401159.1	6756146.4	4726.2								sil	+/- argillics
	644339	250	401176.5	6756137.1	4729.8								sil	minor noise
	644340	270	401193.6	6756127.4	4733.4			2					tr gyp	
	644341	290	401210.6	6756117.4	4736.8			3						
	644342	308	401225.8	6756108.2	4739.9	?							sil	
	644343	330	401244.1	6756096.6	4743.3			2						
	644344	350	401260.5	6756085.6	4746.5					?			sil	
	644345	370	401276.6	6756074.1	4749.6								sil	+/- argillics
	644346	390	401292.6	6756062.5	4752.7									noisy spectrum
184	pd18401	301.9	4740.2	401029.8	6699.4			?			2		sil	
	pd18402	307.8	4741.2	401026.1	6703.9						2		sil	
	pd18403	311.5	4741.7	401023.7	6706.7						1		sil	
	pd18404	317.1	4742.6	401020.2	6710.9						1		sil	
	pd18405	323.5	4743.6	401016.1	6715.8						?		chl	
	pd18406	327	4744.2	401013.9	6718.4						2			
	pd18407	332.8	4745.1	401010.2	6722.8						4	tr		
	pd18408	337.5	4745.8	401007.2	6726.4						3	?		
	pd18409	344	4746.8	401003.1	6731.3						1		qtz	
	pd18410	349	4747.6	400999.9	6735.1						2		smect	
	pd18411	352.3	4748.1	400997.8	6737.6			2			2		smect?	
	pd18412	358	4749.0	400994.2	6741.9	tr	1481.8		4					
	pd18413	363	4749.8	400991.0	6745.7	?		?			3		smect?	
	pd18414	367	4750.4	400988.5	6748.7	?					3		smect	
	pd18415	371.5	4751.1	400985.6	6752.1	tr	1481.1		4					
	pd18416	377.3	4752.0	400982.0	6756.5			3			?			
	pd18417	383.7	4753.0	400977.9	6761.3			?	2		2			
	pd18418	388.8	4753.8	400974.7	6765.2						4		smect? chl?	
	pd18419	394	4754.6	400971.4	6769.1			2			2		smect?	

DDH #	PIMA sample #	Depth (m)	Elevation (m.a.s.l.)	UTM coordinates		Mineral Identification								Comments
				Easting	Northing	alun	*feature*	kao	dick	pyl	ill	jar	other	
	pd18420	396.8	4755.1	400969.6	6771.2			?			?		smect	
	pd18421	403	4756.0	400965.6	6775.9								chl	
	pd18422	407	4756.7	400963.1	6778.9			?			2		smect	
	pd18423	412.8	4757.6	400959.4	6783.3								chl	
	pd18424	418.2	4758.4	400956.0	6787.4						4			
	pd18425a	422.5	4759.1	400953.3	6790.7			?			2	?	smect	
	pd18425b	422.5	4759.1	400953.3	6790.7						1		sil	
	pd18426	427.8	4759.9	400949.9	6794.7						1	tr	sil, smect?	
	pd18427	433.2	4760.8	400946.5	6798.8			?			4			
	pd18428	436.6	4761.3	400944.3	6801.3			tr			1		sil	
	pd18429	441.3	4762.0	400941.3	6804.9	4	1484.4							
	pd18430	447	4762.9	400937.7	6809.2	2	1482.2		4				dsp?	
192	pd19201	142.1	4748.3	400844.7	6133.5	4	1480.9		4					
	pd19202	146.4	4750.0	400841.8	6130.8			?					sil	
	pd19203	153.3	4752.9	400837.2	6126.5	2	1481.4		4					
	pd19204	157	4754.4	400834.7	6124.2	2	1481							
	pd19205	164.5	4757.4	400829.7	6119.5	3	1480.9		4					
	pd19206	166.9	4758.4	400828.1	6118.0	4	1480.5		4					
	pd19208	178.5	4763.1	400820.3	6110.8	2	1480.6						qtz	
	pd19209	185.6	4766.0	400815.6	6106.4	3	1480.9		2					
	pd19210	191	4768.2	400812.0	6103.0	4	1481.4		4					
	pd19211	197.7	4770.9	400807.5	6098.8	2	1481.8		4					
	pd19501	2.5	4692.4	400776.0	6039.7	4	1481.7							
	pd19502	7.5	4694.1	400773.4	6035.8	3	1481.7		4					
	pd19503	14.3	4696.4	400769.8	6030.5	3	1481.5							
	pd19504	17	4697.3	400768.4	6028.4	4	1481.7							
	pd19505	22	4699.0	400765.7	6024.5	4	1482.7							
	pd19506	27.6	4700.9	400762.8	6020.1	2	1482.7		4					
	pd19507	32	4702.4	400760.5	6016.7	3	1480.9							
	pd19508	37.9	4704.5	400757.4	6012.1	4	1482.2		2					
	pd19509	42.1	4705.9	400755.2	6008.8	4	1481.2	1	4					
	pd19510	47.5	4707.7	400752.3	6004.6	4	1482.3	1	3					
	pd19511	53	4709.6	400749.5	6000.3	4	1481.3	?			2			
	pd19512	57.1	4711.0	400747.3	5997.1	3	1482.5		2					
	pd19513	62.5	4712.9	400744.5	5992.9	4	1481.1		2			tr		

DDH #	PIMA sample #	Depth (m)	Elevation (m.a.s.l.)	UTM coordinates		Mineral Identification								Comments
				Easting	Northing	alun	*feature*	kao	dick	pyl	ill	jar	other	
	pd19514	66.9	4714.4	400742.1	5989.5	4	1481.2		3					
	pd19515	73	4716.5	400738.9	5984.7	4	1479.9							
	pd11616	77.4	4718.0	400736.6	5981.3	3	1480.4	4						
	pd19517	83.1	4719.9	400733.6	5976.9	4	1481.3							
	pd19518	88	4721.6	400731.1	5973.0	4	1480.2							
	pd19519a	91.7	4722.9	400729.1	5970.2	tr		3			?			
	pd19519b	91.7	4722.9	400729.1	5970.2	4	1479.8						smect	
	pd19520	98.6	4725.2	400725.5	5964.8	4	1481.2						ill-smect?	
	pd19521	104	4727.1	400722.7	5960.6	2	1481	4						
	pd18522	108	4728.4	400720.5	5957.5	2	1481.7						tr dsp?	
	pd19523	111.7	4729.7	400718.6	5954.6	3	1480.9					2	sil?	
	pd19524	118.7	4732.1	400714.9	5949.1	tr							sil	
	pd19525	122.9	4733.5	400712.7	5945.9	4	1481.7					3		
	pd19526	127.5	4735.1	400710.3	5942.3	3	1482.8	?	3					
	pd19527	133.1	4737.0	400707.4	5937.9	4	1482.5					tr		
	pd19528	137.1	4738.4	400705.3	5934.8	4	1483.1		1					
	pd19529	142.6	4740.3	400702.4	5930.5	2	1483		2					
	pd19530	148.5	4742.3	400699.3	5925.9	4	1481.1							
	pd19531	153.8	4744.1	400696.5	5921.8	2	1481					1	dsp?	
	pd19532	158.5	4745.7	400694.0	5918.1	2	1479.5						sil?	
	pd19533	162.8	4747.2	400691.8	5914.8	2	1479.6	4						
	pd19534	166	4748.3	400690.1	5912.3	?		1			2	1		
	pd19535	172.8	4750.6	400686.5	5907.0	1	1480.3		3					
	pd19536	176.5	4751.9	400684.6	5904.1	3	1480.8							
	pd19537	184.1	4754.5	400680.6	5898.2			1			1	1	sil	
	pd19538	188.4	4755.9	400678.3	5894.8	3	1481.1	1						
	pd19539	191.7	4757.1	400676.6	5892.3	4	1480.8							
	pd19540	196	4758.5	400674.3	5888.9	4	1480.3					1		
	pd19541	202	4760.6	400671.2	5884.2	3	1480.3						sil	
	pd19542	209	4763.0	400667.5	5878.8	3	1481.2	?			?	tr		
	pd19543a	213.7	4764.6	400665.0	5875.1	2	1481.3	1						unoxidized wallrock
	pd19543b	213.7	4764.6	400665.0	5875.1	1	1476.7	2				4		with significant disseminated jarosi
	pd19544	218	4766.1	400662.7	5871.8	4	1482.2							
	pd19545	232	4770.8	400655.4	5860.9	4	1482.2	tr						
	pd19546	236.3	4772.3	400653.1	5857.5	4	1481.4							

DDH #	PIMA sample #	Depth (m)	Elevation (m.a.s.l.)	UTM coordinates		Mineral Identification								Comments
				Easting	Northing	alun	*feature*	kao	dick	pyl	ill	jar	other	
	pd19547	242	4774.3	400650.1	5853.1	4	1484.4							
	pd19548	249	4776.7	400646.5	5847.6	4	1482.6							
	pd19549	252	4777.7	400644.9	5845.3	3	1483.9						sil or dsp?	
	pd19550	258	4779.7	400641.7	5840.6	4	1482.6							
	pd19551	263	4781.5	400639.1	5836.7	3	1482.2	1						
	pd19552	266	4782.5	400637.5	5834.4	3	1481.7	2						
	pd19553	272	4784.5	400634.4	5829.7	4	1484.1							
	pd19554	278	4786.6	400631.2	5825.0	4	1483.3							
	pd19555	284.5	4788.8	400627.8	5820.0	4	1482.4							
203	pd20301	2.5	4696.8	401262.0	6385.4								sil + arg?	
	pd20302a	17.5	4705.4	401249.7	6386.7	1								wallrock
	pd20302b	17.5	4705.4	401249.7	6386.7	4							alunog?	vein only
	pd20303	30.5	4712.9	401239.2	6387.8	2							sil	
	pd20304	41	4718.9	401230.6	6388.7	2			4				alunog?	
	pd20305	53	4725.8	401220.8	6389.7	2			2					
	pd20306	64.5	4732.4	401211.5	6390.7	tr		2			2?			
	pd20307a	74.8	4738.3	401203.1	6391.6			4						wallrock
	pd20307b	74.8	4738.3	401203.1	6391.6	4		?			4?			vein only
	pd20308	83.5	4743.3	401196.0	6392.3						3		sil	
	pd20309	93	4748.7	401188.2	6393.2						1		sil	
	pd20310	107.9	4757.3	401176.1	6394.4			tr			1		sil	
	pd20311	116.1	4762.0	401169.4	6395.1			3			?		sil?	
	pd20312	126	4767.7	401161.4	6396.0						?		sil	
	pd20313	134	4772.3	401154.8	6396.7			4						
	pd20314	145.4	4778.8	401145.5	6397.6			2			?		sil	
	pd20315	156.4	4785.1	401136.6	6398.6	?		3			2			
	pd20316a	163.5	4789.2	401130.8	6399.2	3								wallrock
	pd20316b	163.5	4789.2	401130.8	6399.2	4								vein only
	pd20317a	167.4	4791.4	401127.6	6399.5								alunog	wallrock
	pd20317b	167.4	4791.4	401127.6	6399.5	4								vein only
	pd20318	173.2	4794.7	401122.9	6400.0	4								